2001: a symplectic odyssey

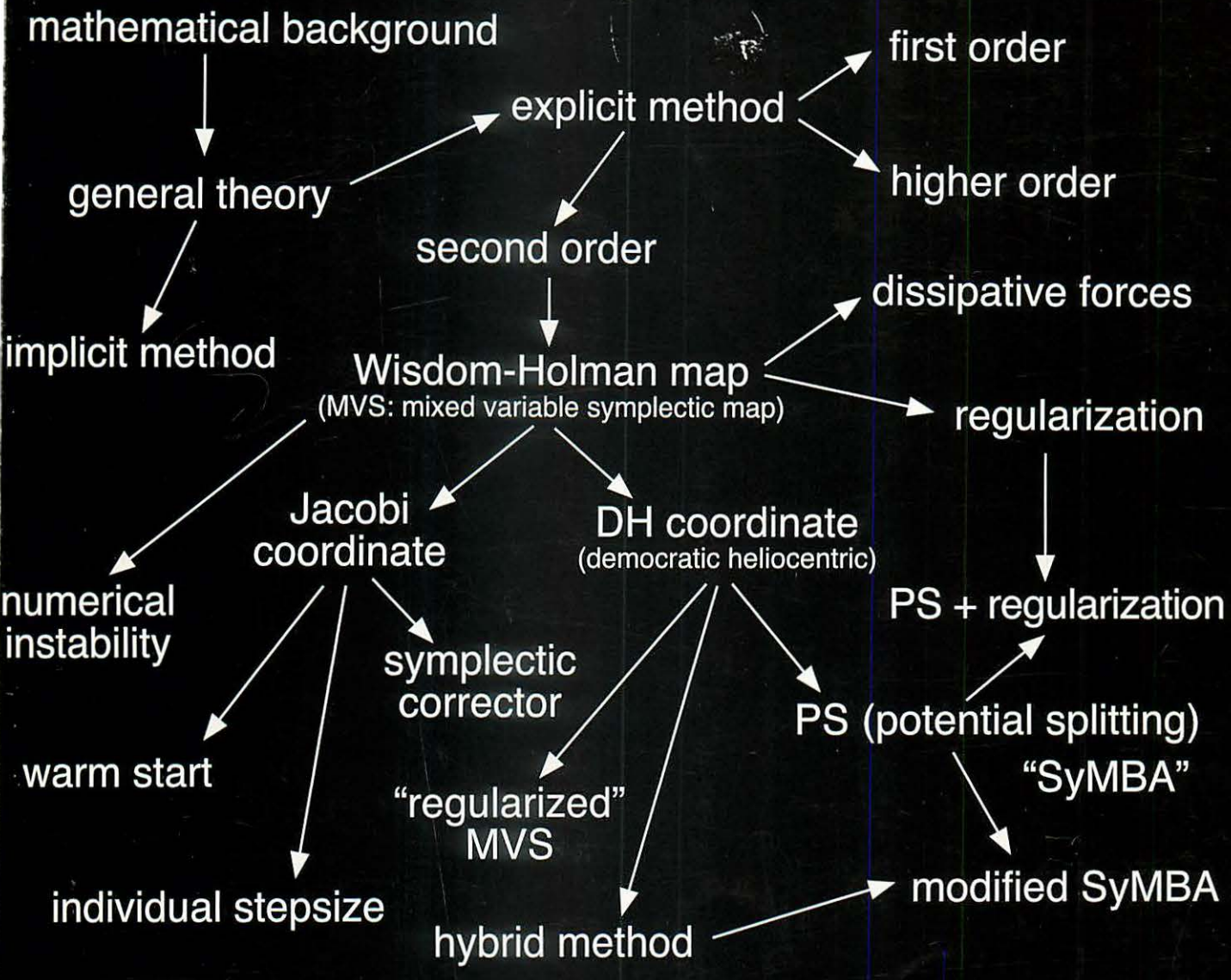

Proceedings of the 33rd Symposium on Celestial Mechanics

March 16-18, 2001 at Kusatsu-Onsen, Gumma, Japan

Eiichiro Kokubo, Takashi Ito & Hideyoshi Arakida (eds.)

天体力学N体力学研究会　(2001年3月16日 - 3月18日　国立大学共同利用施設 草津セミナーハウスにて)

草津天体力学N体力学研究会集録

平成13年3月16日–18日

群馬県草津温泉草津セミナーハウス

2001: a symplectic odyssey
シンプレクティック積分法の輝き

Proceedings of the 33rd Symposium on Celestial Mechanics

March 16–18, 2001 at Kusatsu-Onsen, Gunma, Japan

Editors: E. Kokubo, T. Ito, and H. Arakida

Preface/序文

2000年度の天体力学N体力学研究会(通称草津N体)は、2001年3月16日から18日にかけてまだ雪の残る群馬県草津温泉の草津セミナーハウスにて滞在型研究会の形で開催されました。口頭発表が16件、ポスター発表が18件あり、参加者は大学院生からシニア研究者までの42名を数えました。

草津N体のメインテーマは、2001: a symplectic odyssey –シンプレクティック積分法の輝き–ということで、常微分方程式の数値解法の1つであるシンプレクティック積分法でした。シンプレクティック積分法には、ハミルトン系に適用した場合、エネルギーなどに永年誤差が現れない、という良い性質があります。そして様々な天体力学的応用が提案されています。今回はシンプレクティック積分法に関して、2つの招待講演を企画しました。まずシンプレクティック積分法の基礎的な理論について国立天文台の吉田春夫氏にレビューしていただきました。そしてシンプレクティック積分法の天体力学的応用について国立天文台の伊藤孝士氏にレビューをしてもらいました。興味深くわかりやすいレビューをしていただいた両氏にはこの場を借りて感謝したいと思います。シンプレクティック積分法の輝きを感じてもらえましたでしょうか。もしそうなら世話人としてうれいし限りです。

研究会運営にあたっては草津セミナーハウスのスタッフの方々に大変お世話になりました。「天文の先生はワインがお好きなんですね」と温かく見守っていただきました。厚くお礼申し上げます。

平成13年初秋 世話人代表 小久保英一郎

Editors/世話人

小久保英一郎 (Kokubo, Eiichiro) 国立天文台理論天文学研究系
kokubo@th.nao.ac.jp

伊藤孝士 (Ito, Takashi) 国立天文台天文学データ解析計算センター
tito@cc.nao.ac.jp

荒木田英禎 (Arakida, Hideyoshi) 総合研究大学院大学
h.arakida@nao.ac.jp

Cover/表紙

Road map of symplectic integrators (Ito p.19)
シンプレクティック積分法のロードマップ (伊藤 p.19)

Table of Contents/目次

"2001: a symplectic odyssey" Feature Articles

Formation of Planetary Systems

Extrasolar Planetary Systems

Solar System Dynamics

Dynamics of Artificial Satellites

Theory of Dynamical Systems

Others

ELSEVIER

23 April 2001

Physics Letters A 282 (2001) 276–283

PHYSICS LETTERS A

www.elsevier.nl/locate/pla

Non-existence of the modified first integral by symplectic integration methods

Haruo Yoshida

National Astronomical Observatory of Japan, Mitaka, Tokyo 181-8588, Japan

Received 2 February 2001; accepted 9 March 2001
Communicated by A.P. Fordy

Abstract

It is known that the symplectic mapping obtained as a symplectic integration method is formally an exact time evolution of the modified Hamiltonian which is close to the original Hamiltonian. In the case when the original Hamiltonian has an additional first integral, it is shown that the modified first integral, which is defined to be an integral for the modified Hamiltonian, does not necessarily exist in general. This non-existence of the modified first integral is demonstrated by an example of the 2D harmonic oscillator with an integer frequency ratio. © 2001 Elsevier Science B.V. All rights reserved.

1. Introduction

Symplectic integration method (symplectic integrator) is a numerical integration method for Hamiltonian systems which is designed to conserve the property that the method (mapping)

$$\big(q(t), p(t)\big) \to \big(q(t+\tau), p(t+\tau)\big) \tag{1}$$

for one step, $\tau = \Delta t$, is exactly symplectic as the original Hamiltonian flow. It is known that for general Hamiltonian systems, implicit symplectic methods such as implicit Runge–Kutta methods always exist. On the other hand, for a Hamiltonian of the form $H = T(p) + V(q)$, explicit methods are easily constructed [6,10]. For a review, see [4,8,11].

When a symplectic method is applied to a concrete example, it is observed that although the value of Hamiltonian is not conserved at each step, the error does not grow monotonically and remains in some finite width. This phenomena can be explained naively by the fact that any symplectic method is a rigorous time-τ evolution of the *modified Hamiltonian*, which is close to the original Hamiltonian [2,11].

For an nth-order symplectic method, this modified Hamiltonian takes the form

$$\tilde{H} = H + \tau^n H_n + \cdots \tag{2}$$

with H_n a differential polynomial of H. As a consequence, the error of Hamiltonian remains as the order of $o(\tau^n)$ forever, if the series converges and if the round-off error is neglected. However, since this series diverges in general, any rigorous statement can be claimed only after a truncation of the series at some finite order. As a result of the truncation, it turns out that the error of Hamiltonian remains as the order of $o(\tau^n)$ for an exponentially long time interval [1,3].

Suppose now that the given Hamiltonian system is integrable and that there exists a first integral (integral of motion, conserved quantity) besides the Hamiltonian. Then there is no guarantee that this first integral is also well conserved by the symplectic

E-mail address: h.yoshida@nao.ac.jp (H. Yoshida).

0375-9601/01/$ – see front matter
PII: S0375-9601(01)00186-4

method as in the case of Hamiltonian. Good numerical methods, such as symplectic methods, are expected to respect the integrability of the original system. Indeed, one can observe that the additional integrals are also well conserved in many examples. However, this is not always the case.

In this Letter it is shown that there are some first integrals which are not well conserved by symplectic methods and that for these first integrals, the modified first integral which may guarantee the near-conservation of the first integral, does not exist. This unfortunate fact can be demonstrated in the 2D harmonic oscillator with an integer frequency ratio.

Section 2 gives a minimum knowledge on explicit symplectic methods with the form of the modified Hamiltonian and introduces the modified first integral. In some special case the modified first integral seems to exist formally. Section 3 reviews the 2D harmonic oscillator. It is noted that if the frequency ratio is an integer, a special first integral exists which makes the system super-integrable. In Section 4, it is shown that the modified first integral does not exist for this first integral of the 2D harmonic oscillator, except for the isotropic case. The non-existence of the modified first integral is explained by the violation of the super-integrability of the modified Hamiltonian. Finally, Section 5 is devoted to concluding remarks.

2. Modified Hamiltonian and modified first integral

For a Hamiltonian system of the form

$$H = T(p) + V(q), \tag{3}$$

the first-order, explicit Euler method gives the mapping $(q, p) \to (q', p')$ with

$$q' = q + \tau\left(\frac{\partial T}{\partial p}\right)_{p=p},$$
$$p' = p - \tau\left(\frac{\partial V}{\partial q}\right)_{q=q}. \tag{4}$$

On the other hand, the symplectic Euler method which is again a first-order explicit method gives the mapping

$$q' = q + \tau\left(\frac{\partial T}{\partial p}\right)_{p=p},$$
$$p' = p - \tau\left(\frac{\partial V}{\partial q}\right)_{q=q'}. \tag{5}$$

Mapping (5) is known to be an exact time-τ evolution of the *modified Hamiltonian* given by

$$\tilde{H} = H_0 + \tau H_1 + \tau^2 H_2 + \cdots, \tag{6}$$

where $H_0 = H$ and

$$H_1 = \frac{1}{2} H_p H_q,$$
$$H_2 = \frac{1}{12}(H_{qq'} H_p H_{p'} + H_{pp'} H_q H_{q'}),$$
$$H_3 = \frac{1}{12} H_{pp'} H_{qq''} H_{p''} H_{q'}, \quad \ldots, \tag{7}$$

with the notations

$$H_p H_q := \sum_i H_{p_i} H_{q_i} := \sum_i \frac{\partial H}{\partial p_i}\frac{\partial H}{\partial q_i},$$
$$H_{qq'} H_p H_{p'} := \sum_{i,j} H_{q_i q_j} H_{p_i} H_{p_j}, \quad \ldots, \tag{8}$$

and, consequently, $\tilde{H}$ is conserved by mapping (5) in a quite formal sense. For the derivation of series (6), see [11]. This series, which comes from the Baker–Campbell–Hausdorff (BCH) formula [9], diverges in general. It should be noted that for a non-symplectic integration method such as the explicit Euler method (4), this kind of series does not exist with differential polynomials of Hamiltonian as its coefficients.

Suppose now that there exists an additional first integral $\Phi = \text{const}$ for a given Hamiltonian of the form (3), i.e., there exists a function $\Phi(q, p)$ such that the Poisson bracket of Φ and H vanishes,

$$\{\Phi, H\} := \Phi_q H_p - \Phi_p H_q = 0. \tag{9}$$

For this first integral, let us try to construct a series for the *modified first integral* of the form

$$\tilde{\Phi} = \Phi_0 + \tau\Phi_1 + \tau^2\Phi_2 + \cdots. \tag{10}$$

This modified first integral, which is defined to be a first integral of the modified Hamiltonian (6), and consequently which is conserved by the symplectic Euler method (4) formally, must satisfy the condition

$$\{\tilde{\Phi}, \tilde{H}\} = 0. \tag{11}$$

Once such a series is obtained, it would be possible to repeat the same game for the modified Hamiltonian,

that is, to truncate the series at a finite order to conclude the near-conservation of the first integral Φ for an exponentially long time interval.

Substituting series (6) and (10) into condition (11), and equating the coefficient of each power of τ equal to zero, we have a sequence of conditions

$$\{\Phi_0, H_0\} = 0, \tag{12}$$

$$\{\Phi_1, H_0\} + \{\Phi_0, H_1\} = 0, \tag{13}$$

$$\{\Phi_2, H_0\} + \{\Phi_1, H_1\} + \{\Phi_0, H_2\} = 0, \tag{14}$$

$$\{\Phi_3, H_0\} + \{\Phi_2, H_1\} + \{\Phi_1, H_2\} + \{\Phi_0, H_3\} = 0, \tag{15}$$

which successively determine $\Phi_0, \Phi_1, \Phi_2, \ldots$. Obviously one can take $\Phi_0 = \Phi$. For a Hamiltonian of the form (3), it is found that Φ_1 which satisfies (13) is given by

$$\Phi_1 = \frac{1}{2}\Phi_q H_p = \frac{1}{2}\Phi_p H_q. \tag{16}$$

These two expressions for Φ_1 are identical since $\Phi_q H_p - \Phi_p H_q = \{\Phi, H\} = 0$. An example of this Φ_1 already appeared in [5] for an integrable Hénon–Heiles Hamiltonian. Proof of (16) is a straightforward computation. Indeed, from (7) and (16), one computes

$$\begin{aligned} &2\big(\{\Phi_1, H_0\} + \{\Phi_0, H_1\}\big) \\ &\quad = (\Phi_q H_p)_{q'} H_{p'} - (\Phi_q H_p)_{p'} H_{q'} + \Phi_{q'}(H_p H_q)_{p'} \\ &\qquad - \Phi_{p'}(H_p H_q)_{q'} \\ &\quad = (\Phi_{qq'} H_{p'} - \Phi_{p'} H_{qq'} - \Phi_{qp'} H_{q'}) H_p \\ &\quad = (\Phi_{q'} H_{p'} - \Phi_{p'} H_{q'})_q H_p \\ &\quad = \{\Phi, H\}_q H_p \\ &\quad = 0. \end{aligned} \tag{17}$$

Although there is a difficulty if we try to find out Φ_2 in general cases, there is a particular case where Φ_2 and Φ_3 are found rather easily. This is the case when the first integral Φ has the form

$$\Phi = F(p) + G(q). \tag{18}$$

For a first integral of this form, it can be shown that

$$\Phi_2 = \frac{1}{12}(\Phi_{qq'} H_p H_{p'} + \Phi_{pp'} H_q H_{q'}) \tag{19}$$

and

$$\Phi_3 = \frac{1}{12}\Phi_{pp'} H_{qq''} H_{p''} H_{q'} \tag{20}$$

satisfy conditions (14) and (15), respectively. Proof of expressions (19) and (20) is again a straightforward computation. Note that Φ_1, Φ_2, Φ_3 of (16), (19), and (20) reduce to H_1, H_2, H_3 of (7) by the mechanical substitution $\Phi \to H$, which is a natural consequence since the Hamiltonian H is a first integral of the form (18). It is strongly conjectured that Φ_n $(n \geqslant 4)$ in general are also given as differential polynomials of H and Φ.

A second-order symplectic method (leap-frog or Verlet method) for a Hamiltonian of the form (3) is given by the mapping $(q, p) \to (q', p')$ with

$$\begin{aligned} q^* &= q + \frac{\tau}{2}\left(\frac{\partial T}{\partial p}\right)_{p=p}, \\ p' &= p - \tau\left(\frac{\partial V}{\partial q}\right)_{q=q^*}, \\ q' &= q^* + \frac{\tau}{2}\left(\frac{\partial T}{\partial p}\right)_{p=p'}. \end{aligned} \tag{21}$$

For this mapping, the modified Hamiltonian is given by

$$\tilde{H} = H_0 + \tau^2 H_2 + \tau^4 H_4 + \cdots \tag{22}$$

with $H_0 = H$ and [11]

$$H_2 = \frac{1}{12}H_{pp'} H_q H_{q'} - \frac{1}{24}H_{qq'} H_p H_{p'}. \tag{23}$$

The corresponding modified first integral takes the form

$$\tilde{\Phi} = \Phi_0 + \tau^2 \Phi_2 + \tau^4 \Phi_4 + \cdots \tag{24}$$

with $\Phi_0 = \Phi$. For a general first integral, it is difficult to find Φ_2 which must satisfy

$$\{\Phi_2, H_0\} + \{\Phi_0, H_2\} = 0. \tag{25}$$

However, again for a first integral of the form (18), it is found that

$$\Phi_2 = \frac{1}{12}\Phi_{pp'} H_q H_{q'} - \frac{1}{24}\Phi_{qq'} H_p H_{p'} \tag{26}$$

satisfies condition (25). For this second-order symplectic method, it is also conjectured that the modified first integral (24) exists with differential polynomial of H and Φ as its coefficients Φ_i. Although there is a case where the modified first integral seems to exists, there is another case where such an object does not exist, as will be seen in the following sections. This implies that the modified first integral does not exist in general.

3. 2D harmonic oscillator with an integer frequency ratio

The two-dimensional (2D) harmonic oscillator is described by the Hamiltonian

$$H=\frac{1}{2}\left(p_1^2+p_2^2\right)+\frac{1}{2}\left(\omega_1^2q_1^2+\omega_2^2q_2^2\right) \tag{27}$$

with two constant frequencies ω_1 and ω_2. From the equations of motion

$$\ddot{q}_1+\omega_1^2q_1=0, \qquad \ddot{q}_2+\omega_2^2q_2=0, \tag{28}$$

one can immediately obtain the general solution

$$q_1=c_1\sin(\omega_1t+\delta_1), \qquad q_2=c_2\sin(\omega_2t+\delta_2),$$
$$p_1=\dot{q}_1, \qquad p_2=\dot{q}_2, \tag{29}$$

where $c_1, c_2, \delta_1, \delta_2$ are arbitrary integration constants. This system is always integrable with the second integral of motion, say,

$$\Phi=\frac{1}{2}\left(p_1^2-p_2^2\right)+\frac{1}{2}\left(\omega_1^2q_1^2-\omega_2^2q_2^2\right). \tag{30}$$

When the frequency ratio is an integer, or more generally a rational number, there exists an additional polynomial first integral. Let us assume that $\omega_1=1/m$, $\omega_2=1/n$ with integers m, n and put

$$\theta_1=\frac{1}{m}t+\delta_1, \qquad \theta_2=\frac{1}{n}t+\delta_2. \tag{31}$$

Then the expressions

$$\Phi'=c_1^mc_2^n\cos(m\delta_1-n\delta_2),$$
$$\Phi''=c_1^mc_2^n\sin(m\delta_1-n\delta_2), \tag{32}$$

both of which are obviously first integrals of the original system (27), can be written as homogeneous polynomials of q and p. In fact, since $m\theta_1-n\theta_2=m\delta_1-n\delta_2$,

$$\begin{aligned}\Phi'&=c_1^mc_2^n\cos(m\theta_1-n\theta_2)\\&=c_1^m\cos(m\theta_1)c_2^n\cos(n\theta_2)\\&\quad+c_1^m\sin(m\theta_1)c_2^n\sin(n\theta_2)\end{aligned} \tag{33}$$

and

$$\begin{aligned}\Phi''&=c_1^mc_2^n\sin(m\theta_1-n\theta_2)\\&=c_1^m\sin(m\theta_1)c_2^n\cos(n\theta_2)\\&\quad-c_1^m\cos(m\theta_1)c_2^n\sin(n\theta_2),\end{aligned} \tag{34}$$

and these quantities can be represented as homogeneous polynomials of

$$q_1=c_1\sin\theta_1, \qquad q_2=c_2\sin\theta_2,$$
$$p_1=\frac{c_1}{m}\cos\theta_1, \qquad p_2=\frac{c_2}{n}\cos\theta_2. \tag{35}$$

For example, when $m=n=1$,

$$\Phi'=p_1p_2+q_1q_2, \qquad \Phi''=q_1p_2-p_1q_2, \tag{36}$$

and when $m=1, n=2$,

$$\Phi'=p_1\left(4p_2^2-q_2^2\right)+4q_1p_2q_2,$$
$$\Phi''=q_1\left(4p_2^2-q_2^2\right)-4p_1p_2q_2, \tag{37}$$

and so on. Note that among four first integrals H, Φ, Φ' and Φ'', there exists one algebraic relation

$$(\Phi')^2+(\Phi'')^2=m^{2m}n^{2n}(H+\Phi)^m(H-\Phi)^n, \tag{38}$$

so that there are only three functionally independent first integrals for Hamiltonian system (27). The existence of this additional integral Φ' makes the system *super-integrable*, that is, any bounded orbit is a periodic orbit. For super-integrable systems, see, for example, [7] and references therein.

Fig. 1 shows the orbit of 2D harmonic oscillator in (q_1, q_2) plane for (a) $(m,n)=(1,1)$, (b) $(m,n)=(1,2)$, (c) $(m,n)=(1,3)$, and (d) $(m,n)=(1,4)$ with a common initial condition, $(q_1, q_2, p_1, p_2)=(0.0, 1.0, 1.0, 0.0)$ at $t=0$. It is easily observed that while q_2 oscillates once, q_1 oscillates n times. It should be noted that if the frequency ratio is an irrational number, then a single orbit will fill the whole box area $-1\leqslant q_1\leqslant 1$, $-1\leqslant q_2\leqslant 1$ completely as $t\to\pm\infty$, which is a generic situation for ordinary integrable systems.

4. Non-existence of the modified first integral

In this section we show that Φ_2 does not exist as a differential polynomial of H and Φ for general pair of a Hamiltonian and a first integral. This assumption on Φ_2 is not artificial, since if Φ_2 exists, Φ_2 must reduce to H_2 of (7) by the mechanical substitution $H\to\Phi$, and H_2 is a differential polynomial of H. For this purpose it suffices to show the non-existence of Φ_2 in an example of the 2D harmonic oscillator (27) with

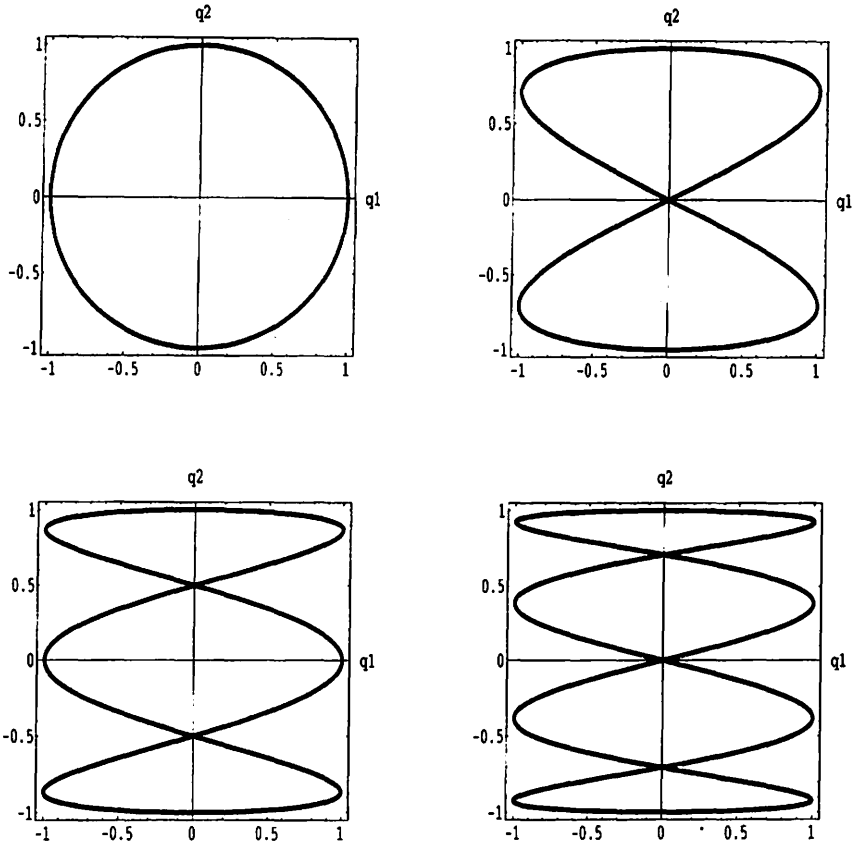

Fig. 1. Orbits of harmonic oscillator with frequency ratio 1 : 1, 1 : 2, 1 : 3, and 1 : 4.

$m = 1$ and $n = 2$, that is, the pair of

$$H = H_0 = \frac{1}{2}(p_1^2 + p_2^2) + \frac{1}{2}\left(q_1^2 + \frac{1}{4}q_2^2\right) \tag{39}$$

and

$$\Phi = \Phi_0 = p_1(4p_2^2 - q_2^2) + 4q_1p_2q_2. \tag{40}$$

Direct computation of (7) and (16) yields

$$H_1 = \frac{1}{2}p_1q_1 + \frac{1}{8}p_2q_2,$$
$$\Phi_1 = p_1p_2q_2 + 2p_2^2q_1, \tag{41}$$

and

$$H_2 = \frac{1}{12}(p_1^2 + q_1^2) + \frac{1}{48}\left(p_2^2 + \frac{1}{4}q_2^2\right). \tag{42}$$

If these expressions are substituted into $\{\Phi_0, H_2\}$ and $\{\Phi_1, H_1\}$, Eq. (14) reduces to

$$\{\Phi_2, H_0\} = -\frac{1}{8}q_1q_2^2. \tag{43}$$

On the other hand, if the general solution of the original H_0 system

$$q_1 = c_1\sin(t + \delta_1), \qquad p_1 = c_1\cos(t + \delta_1),$$
$$q_2 = c_2\sin\left(\frac{t}{2} + \delta_2\right),$$
$$p_2 = \frac{c_2}{2}\cos\left(\frac{t}{2} + \delta_2\right) \tag{44}$$

is substituted into the right-hand side of (43), and if we remark that $\{\Phi_2, H_0\}$ is equal to the time derivative of Φ_2 along this solution, Eq. (43) further reduces to

$$\frac{d\Phi_2}{dt} = -\frac{1}{8}c_1c_2^2\sin(t + \delta_1)\sin^2\left(\frac{t}{2} + \delta_2\right)$$
$$= \frac{1}{32}c_1c_2^2[\sin(\delta_1 - 2\delta_2) - 2\sin(t + \delta_1) + \sin(2t + \delta_1 + 2\delta_2)]. \tag{45}$$

Suppose now that Φ_2 is given as a differential polynomial of H and Φ, and consequently, a polynomial of q and p. Then Φ_2 expressed by the general solution (44) becomes a trigonometric polynomial of t. Thus $d\Phi_2/dt$ is a trigonometric polynomial of t without constant terms. On the other hand, the right-hand side of (45) contains a constant term $1/32c_1c_2^2\sin(\delta_1-2\delta_2)$ for generic values of δ_1 and δ_2, which is a obvious contradiction. Thus Φ_2 as a polynomial of q and p cannot exist. This proves that Φ_2 does not exist as a differential polynomial of H and Φ.

This logic of non-existence proof *beautifully fails* if we try to find out Φ_1 from (13) in the same way. First, after computation of $\{\Phi_0, H_1\}$, Eq. (13) reduces to

$$\{\Phi_1, H_0\} = 3p_1p_2^2 - 2p_2q_1q_2 - \frac{1}{4}p_1q_2^2. \tag{46}$$

Then, by substitution (44), it further reduces to

$$\frac{d\Phi_1}{dt} = \frac{1}{4}c_1c_2^2\left[\cos(t+\delta_1) + 2\cos(2t+\delta_1+2\delta_2)\right]. \tag{47}$$

Note that the right-hand side of this equation is a trigonometric polynomial without a constant term. Integration once yields

$$\Phi_1 = \frac{1}{4}c_1c_2^2\left[\sin(t+\delta_1) + \sin(2t+\delta_1+2\delta_2)\right] \tag{48}$$

which can be rewritten as

$$\Phi_1 = p_1p_2q_2 + 2p_2^2q_1 \tag{49}$$

by the inverse substitution of (44). Thus the known expression of Φ_1 is recovered.

This proof of non-existence of Φ_2 works similarly for the sequence $m=1$, $n=2,3,4,\ldots$ of the 2D harmonic oscillator with the first integral (32). It also works for the second-order symplectic method (21). The isotropic case ($m=n=1$) is an exception, and indeed Φ_2 does exist. In this case, starting with

$$H = H_0 = \frac{1}{2}(p_1^2+p_2^2) + \frac{1}{2}(q_1^2+q_2^2) \tag{50}$$

and

$$\Phi = \Phi_0 = p_1p_2 + q_1q_2, \tag{51}$$

one finds

$$H_1 = \frac{1}{2}(p_1q_1 + p_2q_2),$$
$$\Phi_1 = \frac{1}{2}(p_2q_1 + p_1q_2), \tag{52}$$

and

$$H_2 = \frac{1}{12}(p_1^2+q_1^2+p_2^2+q_2^2). \tag{53}$$

Then, since $\{\Phi_0, H_2\} = \{\Phi_1, H_1\} = 0$, condition (14) reduces to

$$\{\Phi_2, H_0\} = 0, \tag{54}$$

and there is no constant term in the right-hand side. Since Φ is of the form (18), we know already that Φ_2 is given by (19) which yields

$$\Phi_2 = \frac{1}{6}(p_1p_2 + q_1q_2), \tag{55}$$

and this Φ_2 certainly satisfies condition (54). Furthermore it can be checked that

$$\tilde{\Phi} = p_1p_2 + q_1q_2 + \frac{\tau}{2}(p_2q_1 + p_1q_2) \tag{56}$$

is an exact integral for the symplectic mapping obtained as the symplectic Euler method.

The speciality of the isotropic case ($n=1$) can be explained by the expression of the modified Hamiltonian (6). For the original Hamiltonian

$$H = \frac{1}{2}(p_1^2+q_1^2) + \frac{1}{2}\left(p_2^2 + \frac{1}{n^2}q_2^2\right) \tag{57}$$

with an integer n, the modified Hamiltonian (6) takes the form

$$\begin{aligned}\tilde{H} = {} & \frac{1}{2}(p_1^2+q_1^2) + \frac{\tau}{2}p_1q_1 + \frac{\tau^2}{12}(p_1^2+q_1^2) + \cdots \\ & + \frac{1}{2}\left(p_2^2 + \frac{1}{n^2}q_2^2\right) + \frac{\tau}{2n^2}p_2q_2 \\ & + \frac{\tau^2}{12n^2}\left(p_2^2 + \frac{1}{n^2}q_2^2\right) + \cdots\end{aligned} \tag{58}$$

and reduces to

$$\begin{aligned}\tilde{H} = {} & \left[1 + \frac{\tau^2}{6} + \cdots\right]\left[\frac{1}{2}(p_1^2+q_1^2) + \frac{\tau}{2}p_1q_1\right] \\ & + \left[1 + \frac{\tau^2}{6n^2} + \cdots\right] \\ & \times \left[\frac{1}{2}\left(p_2^2 + \frac{1}{n^2}q_2^2\right) + \frac{\tau}{2n^2}p_2q_2\right]\end{aligned} \tag{59}$$

which again represents a 2D harmonic oscillator with new frequencies Ω_1 and Ω_2. Although the case when $n=1$ is again a super-integrable isotropic system, the new frequency ratio is no more integer for general

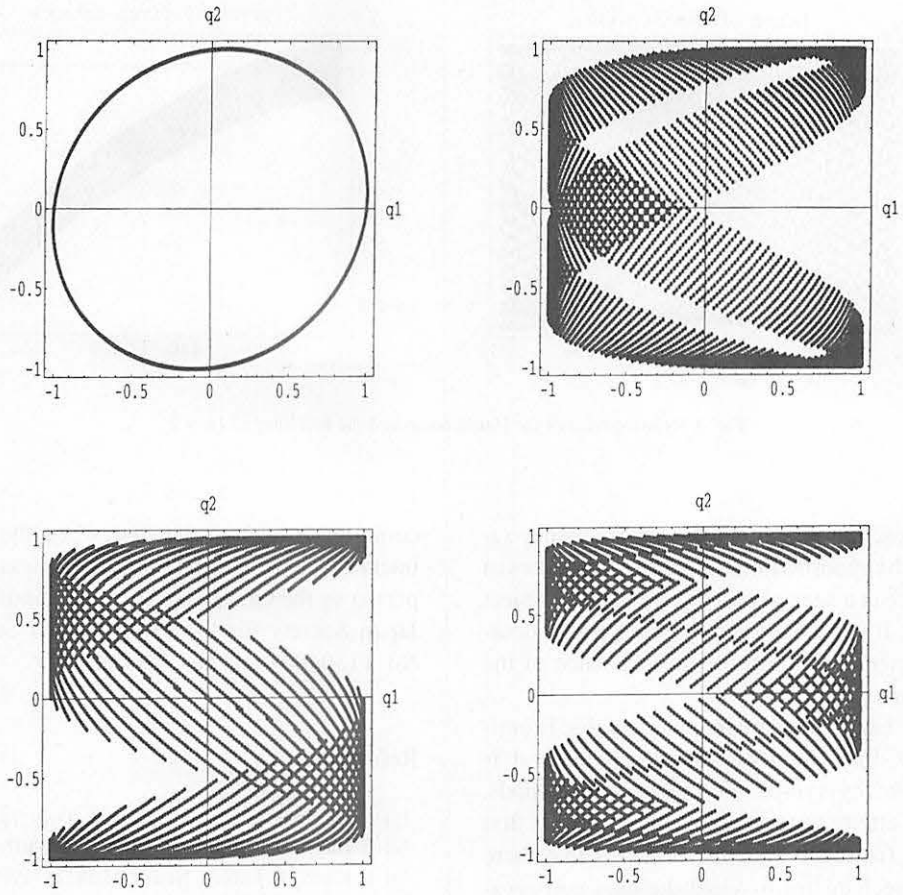

Fig. 2. Orbits of Fig. 1 obtained by the symplectic Euler method ($\tau = 0.2$).

cases, $n = 2, 3, 4, \ldots$ when $\tau > 0$. Up to the second order of τ, this new frequency ratio is given by

$$\frac{\Omega_1}{\Omega_2} = \frac{(1+\tau^2/6+\cdots)\sqrt{1-\tau^2/4}}{(1+\tau^2/6n^2+\cdots)(1/n)\sqrt{1-\tau^2/4n^2}} = n\left(1+\frac{n^2-1}{24n^2}\tau^2+\cdots\right) \tag{60}$$

which is equal to n only when $n = 1$. This violation of super-integrability is the reason of the non-existence of the modified first integral, and in particular, Φ_2.

Fig. 2 shows the same set of orbits as in Fig. 1 obtained numerically by the symplectic Euler method (5) for 5000 steps with the time step $\tau = 0.2$. Except the case $n = 1$, large deviation from the original periodic orbit is observed because of the violation of super-integrability and/or non-existence of the modified first integral. Fig. 3 shows the relative error of (a) Hamiltonian (39) and (b) the first integral (40) in the case of $n = 2$ for the orbit shown in Fig. 2. Similar couple of figures are obtained for other $n = 3, 4, \ldots$ cases, but not for the isotropic ($n = 1$) case. Non-existence of the modified first integral is related with such a large variation of the error.

5. Concluding remarks

In this Letter it is shown that the modified first integral, which is defined to be an integral of the modified Hamiltonian, does not necessarily exist in general. The non-existence proof is given easily in the case of

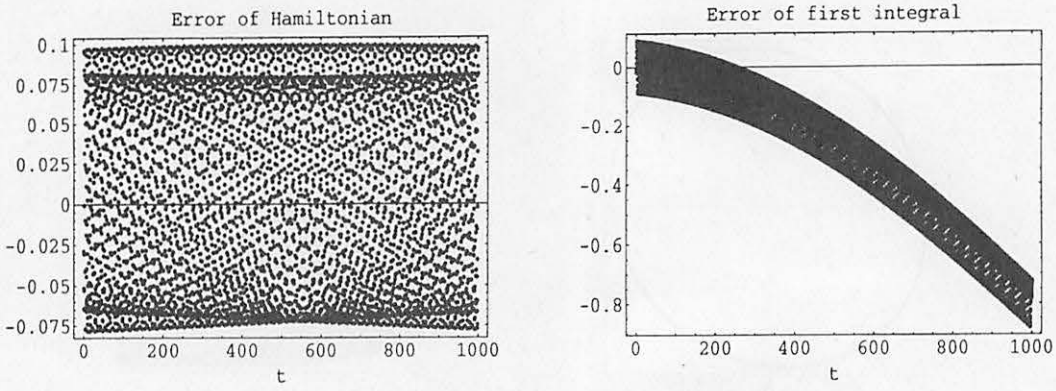

Fig. 3. Relative error of the Hamiltonian and the first integral ($n = 2$).

2D harmonic oscillator with an integer frequency ratio. Although the modified first integral does not exist in general, there is a special case where such an object seems to exist. It is an open problem to give a necessary and sufficient condition for the existence of the modified first integral.

On the other hand, there are many integrable Hamiltonian systems for which the additional integral is nearly conserved by symplectic integration methods, although easy attempts to find out the modified first integral failed for these systems. It seems that there are different mechanisms to yield the near conservation of the first integral, and one of them is certainly the existence of the modified first integral.

Acknowledgements

The author thanks K. Nakagawa for calling attention to the 2D harmonic oscillator with an integer frequency ratio. He is also indebted to A. Murua for communications on the case when the modified first integral seems to exist. This work was partially supported by the Grants-in-Aid for Scientific Research of Japan Society for the Promotion of Science (JSPS), No. 11304004 and No. 12640227.

References

[1] G. Benettin, A. Giorgilli, J. Statist. Phys. 74 (1994) 1117.
[2] E. Hairer, Ann. Numer. Math. 1 (1994) 107.
[3] E. Hairer, C. Lubich, Numer. Math. 76 (1997) 441.
[4] E. Hairer, S.P. Nørsett, G. Wanner, Solving Ordinary Differential Equations 1, 2nd rev. ed., Springer, 1993.
[5] X.H. Liao, L. Liu, Celest. Mech. Dyn. Astron. 63 (1995) 113.
[6] R.I. McLachlan, SIAM J. Sci. Comput. 16 (1995) 151.
[7] M.F. Ranada, J. Math. Phys. 38 (1997) 4165.
[8] J.M. Sanz-Serna, M.P. Calvo, Numerical Hamiltonian Problems, Chapman and Hall, 1994.
[9] V.S. Varadarajan, Lie Groups, Lie Algebras and Their Representations, Prentice-Hall, 1974.
[10] H. Yoshida, Phys. Lett. A 150 (1990) 262.
[11] H. Yoshida, Celest. Mech. Dyn. Astron. 56 (1993) 27.

NON-EXISTENCE OF THE MODIFIED FIRST INTEGRAL BY SYMPLECTIC INTEGRATION METHODS II: KEPLER PROBLEM

HARUO YOSHIDA
National Astronomical Observatory of Japan, Mitaka, Tokyo 181-8588, Japan
e-mail : h.yoshida@nao.ac.jp

Received: .....; Accepted: .....

Abstract. Symplectic integration methods conserve the Hamiltonian quite well because of the existence of the modified Hamiltonian as a formal conserved quantity. For a first integral of a given Hamiltonian system, the modified first integral is defined to be a formal first integral for the modified Hamiltonian. It is shown that the Runge-Lenz vector of the Kepler problem is not well conserved by symplectic methods, and that the corresponding modified first integral does not exist. This conclusion is given for an one-parameter family of symplectic methods including the symplectic Euler method and the Störmer/Verlet method.

Keywords: Symplectic integration method, modified Hamiltonian, modified first integral, Kepler problem, Runge-Lenz vector

1. Introduction

The symplectic integration method (symplectic integrator), which is already a must for a long time integration of the solar system motion, conserves the energy of the system (Hamiltonian) quite well. In fact an n-th order symplectic method keeps the error of the Hamiltonian of the order of $O(\tau^n)$ for an exponentially long time, where $\tau = \Delta t$ is the constant step size of integration (Benettin and Giorgilli, 1994; Hairer and Lubich, 1997; Reich, 1999). This favorite behavior is guaranteed by the existence of the *modified Hamiltonian*,

$$H = H_0 + \tau^n H_n + \cdots \tag{1}$$

which is defined to be a formal integral of motion for the symplectic method considered. For example, for a Hamiltonian of the form

$$H = T(p) + V(q), \tag{2}$$

the symplectic Euler method, which is a first order explicit symplectic method, gives the mapping $(q,p) \to (q',p')$ with

$$q' = q + \tau \left(\frac{\partial T}{\partial p}\right)_{p=p}, \quad p' = p - \tau \left(\frac{\partial V}{\partial q}\right)_{q=q'}. \tag{3}$$

Celestial Mechanics and Dynamical Astronomy **00:** 1–10, 2001.

This mapping (3) is known to be an exact time-τ evolution of the modified Hamiltonian given by

$$\tilde{H} = H_0 + \tau H_1 + \tau^2 H_2 + \cdots \tag{4}$$

where $H_0 = H$ and

$$H_1 = \frac{1}{2} H_p H_q, \quad H_2 = \frac{1}{12}(H_{qq} H_p^2 + H_{pp} H_q^2), \quad \cdots \tag{5}$$

with the notations,

$$H_p H_q := \sum_i H_{p_i} H_{q_i}, \quad H_{qq} H_p^2 := \sum_{i,j} H_{q_i q_j} H_{p_i} H_{p_j}, \quad \cdots \tag{6}$$

and consequently, $\tilde{H}$ is conserved by the mapping (3) formally (Yoshida, 1993; Hairer et al., 1993; Sanz-Serna and Calvo, 1994). This series is just a re-interpretation of the Baker-Campbell-Hausdorff (BCH) formula (Varadarajan, 1974), and diverges in general. Since the modified Hamiltonian, which is a quantity close to the original Hamiltonian, is conserved, the error of the Hamiltonian cannot grow so easily and the favorite property of the symplectic method follows. It should be mentioned that the existence of the modified Hamiltonian is guaranteed for more general Hamiltonians and for more general symplectic methods (Hairer, 1994).

Suppose now that a given Hamiltonian system has an additional first integral. Then it is often observed that this first integral is also conserved quite well by symplectic methods. However, this is not always the case. For example, the Runge-Lenz vector, which is a first integral of the Kepler problem and which makes the Kepler problem super-integrable, is not well conserved by symplectic methods. As a consequence of this fact, the pericenter of the elliptic orbit moves secularly.

In a recent publication (Yoshida, 2001) it was shown that the modified first integral, which is defied to be a first integral for the modified Hamiltonian, does not exist in general. The proof was given by an example of 2D harmonic oscillator with an integer frequency ratio. In this paper it is shown that the proof similarly works for the Kepler problem and that the modified first integral for the Runge-Lenz vector does not exist.

Section 2 gives a short review of the Kepler problem to introduce the set of first integrals and its general solution in a form of Fourier expansion. Conservation of these first integrals by the symplectic Euler method is tested in Section 3. Section 4 starts with the precise definition of the modified first integral, and gives the proof of the non-existence of it for the Runge-Lenz vector. The proof of non-existence is extended to an one-parameter family of symplectic methods in Section 5.

2. 2D Kepler problem: First integrals and its general solution

The 2D (2-dimensional) Kepler problem is defined by the Hamiltonian

$$H = \frac{1}{2}(p_1^2 + p_2^2) - \frac{1}{r} \tag{7}$$

with $r = \sqrt{q_1^2 + q_2^2}$. First integrals of this system are the Hamiltonian (7), the angular momentum

$$h = q_1 p_2 - q_2 p_1, \tag{8}$$

and the *Runge-Lenz vector*, $\boldsymbol{e} = (e_1, e_2)$, defined by

$$e_1 = +p_2(q_1 p_2 - q_2 p_1) - \frac{q_1}{r}, \quad e_2 = -p_1(q_1 p_2 - q_2 p_1) - \frac{q_2}{r}. \tag{9}$$

For the derivation of the Runge-Lenz vector as a first integral, see for example Pollard (1966). Among these four first integrals of the Kepler problem, (H, h, e_1, e_2), there exists one algebraic relation

$$2Hh^2 + 1 = e_1^2 + e_2^2, \tag{10}$$

so that only three integrals are functionally independent. With these three first integrals, the 2D Kepler problem (7) is called *super-integrable*, and consequently all bounded orbits are periodic. Indeed, when the value of Hamiltonian (7) is negative, the orbit is an ellipse with its focus at the origin. Then the Runge-Lenz vector ($\boldsymbol{e}$) is a constant vector which has a length equal to the eccentricity e and points to the pericenter of the orbit.

The elliptic orbit is expressed in polar coordinates (r, f) as

$$r = \frac{h^2}{1 + e\cos f}, \tag{11}$$

where

$$h^2 = a(1 - e^2), \quad a = -1/(2H), \tag{12}$$

and

$$e_1 = e\cos\varpi, \quad e_2 = e\sin\varpi. \tag{13}$$

Here a is called the *semi-major axis* and angles f and ϖ are called the *true anomaly* and the *longitude of pericenter*, respectively.

The position (q_1^*, q_2^*) and velocity (p_1^*, p_2^*) are expressed, in Cartesian coordinates in which the direction of the pericenter equals to q_1^*-axis, by

$$q_1^* = r\cos f, \quad q_2^* = r\sin f, \quad p_1^* = -\frac{\sin f}{h}, \quad p_2^* = \frac{e + \cos f}{h}. \tag{14}$$

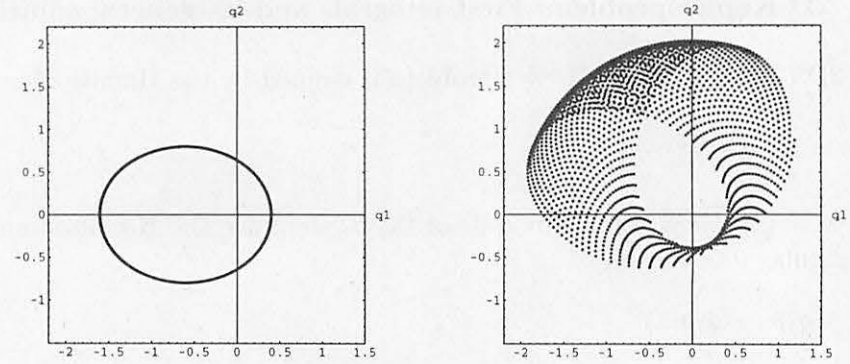

Figure 1. An elliptic orbit and an orbit obtained by the symplectic Euler method

Finally the position (q_1, q_2) and velocity (p_1, p_2) in the inertial frame are given by the rotation of the angle ϖ, i.e.,

$$\begin{pmatrix} q_1 \\ q_2 \end{pmatrix} = M \begin{pmatrix} q_1^* \\ q_2^* \end{pmatrix}, \quad \begin{pmatrix} p_1 \\ p_2 \end{pmatrix} = M \begin{pmatrix} p_1^* \\ p_2^* \end{pmatrix}, \quad M = \begin{pmatrix} \cos\varpi & -\sin\varpi \\ \sin\varpi & \cos\varpi \end{pmatrix}. \tag{15}$$

Fourier expansions of several quantities for the elliptic motion are known as follows (Brouwer and Clemence, 1961);

$$\frac{r}{a} = 1 + \frac{e^2}{2} - 2e \sum_{m=1}^{\infty} \frac{1}{m} J'_m(me) \cos ml, \tag{16}$$

$$\frac{a}{r} = 1 + 2 \sum_{m=1}^{\infty} J_m(me) \cos ml, \tag{17}$$

$$\cos f = -e + \frac{2(1-e^2)}{e} \sum_{m=1}^{\infty} J_m(me) \cos ml, \tag{18}$$

$$\sin f = 2\sqrt{1-e^2} \sum_{m=1}^{\infty} J'_m(me) \sin ml, \tag{19}$$

where

$$l = n(t - t_0), \quad n = a^{-3/2}, \tag{20}$$

called the *mean anomaly* (l) and the *mean motion* (n), and $J_m(x)$ denotes the Bessel function. Therefore the position (q_1, q_2) and velocity (p_1, p_2), all of which are periodic functions of t, are expressed in the form of Fourier series of time t. These expressions constitute the general solution of the 2D Kepler problem (7), with 4 integration constants, a, e, ϖ and t_0.

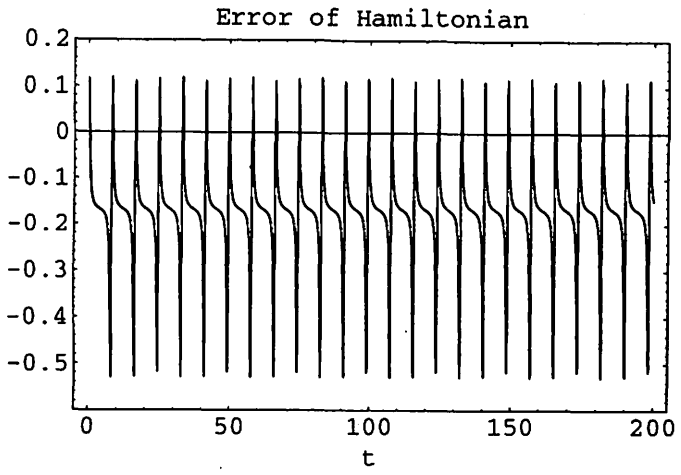

Figure 2. Relative error of Hamiltonian H by the symplectic Euler method

3. Conservation of first integrals by the symplectic Euler method

Fig. 1 shows an elliptic orbit and an orbit obtained by the symplectic Euler method (3) with the initial condition, $(q_1, q_2, p_1, p_2) = (0.4, 0.0, 0.0, 2.0)$, for 2000 steps with the step size $\tau = 0.1$. With this initial condition, the semi-major axis, the eccentricity, and the orbital period are $a = 1$, $e = 0.6$, and $T = 2\pi$, respectively. Fig.2, Fig.3, and Fig.4 show the relative error of the Hamiltonian H, of the angular momentum h, and of the Runge-Lenz integral e_1 along this orbit. In general, the relative error $\Delta\Phi$ of a first integral $\Phi(q,p)$ is computed by

$$\Delta\Phi = \frac{\Phi(q(t),p(t)) - \Phi(q(0),p(0))}{\Phi(q(0),p(0))}. \tag{21}$$

Although the error of Hamiltonian oscillate with a large amplitude, it does not start to grow secularly which is consistent with the general theory. As for the angular momentum integral (8), the microscopic error was caused only by rounding-off errors, since (8) is conserved exactly by the symplectic Euler method (3). This fact is seen since (8) is an integral not only for the total Hamiltonian (7), but also for the kinetic energy part $H = T(p)$ and the potential energy part $H = V(q)$ separately, and the symplectic Euler method (3) is just a composition of flows generated by $H = T(p)$ and $H = V(q)$. On the other hand the Runge-Lenz integral e_1 is not kept well conserved, which is responsible for the secular move of the pericenter of the elliptic orbit observed in Fig.1.

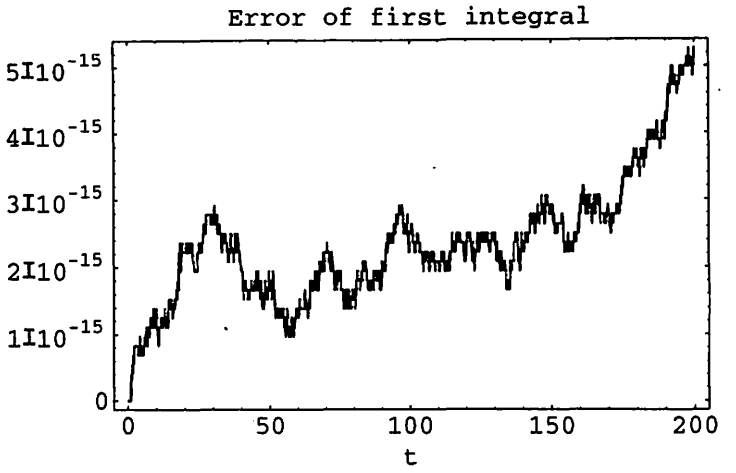

Figure 3. Relative error of the angular momentum h by the symplectic Euler method

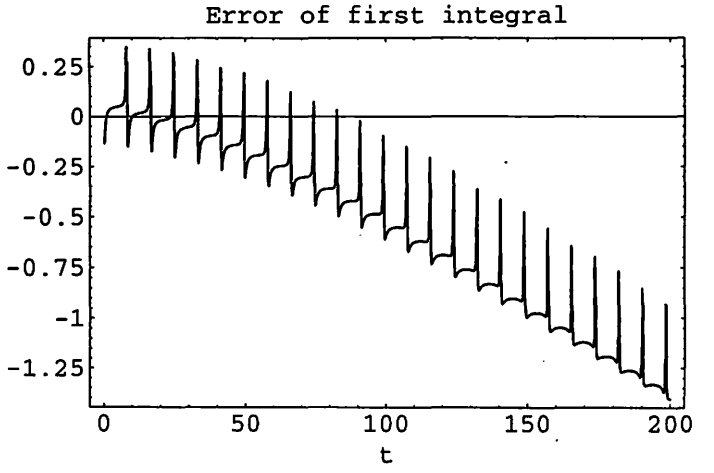

Figure 4. Relative error of the Runge-Lenz integral e_1 by the symplectic Euler method

4. Non-existence of the modified first integral

For the Hamiltonian of the 2D Kepler problem (7), the first two terms of the modified Hamiltonian (5) are computed to be

$$H_1 = \frac{q_1 p_1 + q_2 p_2}{2r^3}, \tag{22}$$

and

$$H_2 = \frac{p_1^2(-2q_1^2 + q_2^2) + p_2^2(q_1^2 - 2q_2^2) - 6p_1 p_2 q_1 q_2 + r}{12r^5}. \tag{23}$$

For a first integral Φ of the original Hamiltonian system (2), the modified first integral $\tilde{\Phi}$ is defined to be a first integral of the modified Hamiltonian $\tilde{H}$, i.e.,

$$\tilde{\Phi} = \Phi_0 + \tau\Phi_1 + \tau^2\Phi_2 + \cdots, \tag{24}$$

such that

$$\{\tilde{\Phi}, \tilde{H}\} = 0. \tag{25}$$

Substituting (4) and (24) into (25), and expanding (25) in powers of τ, we obtain a sequence of conditions

$$\{\Phi_0, H_0\} = 0, \tag{26}$$

$$\{\Phi_1, H_0\} + \{\Phi_0, H_1\} = 0, \tag{27}$$

$$\{\Phi_2, H_0\} + \{\Phi_1, H_1\} + \{\Phi_0, H_2\} = 0, \tag{28}$$

which successively determine $\Phi_0, \Phi_1, \Phi_2, \ldots$. Obviously one can take $\Phi_0 = \Phi$, and it is known (Yoshida, 2001) that

$$\Phi_1 = \frac{1}{2}\Phi_q H_p = \frac{1}{2}\Phi_p H_q. \tag{29}$$

The modified first integral for the angular momentum integral $\Phi = h$ can be taken equal to the original Φ, i.e.,

$$\tilde{\Phi} = \Phi, \tag{30}$$

and consequently, the angular momentum integral is exactly conserved by the symplectic Euler method as seen before. As for the modified first integral for the first component of the Runge-Lenz vector, $\Phi \doteq e_1$, expression (29) gives

$$\Phi_1 = \frac{q_2(q_1p_2 - q_2p_1)}{2r^3}. \tag{31}$$

However, the next term Φ_2 is shown not to exist.

Suppose that Φ_2 is a differential polynomial of H and Φ, which is a natural postulate for Φ_2. This is because Φ_2 must reduce to H_2 of (5) when $\Phi = H$ and H_2 is a differential polynomial of H. Then Φ_2 becomes a polynomial of q, p and $1/r$. Now we shall show that Φ_2 cannot be a polynomial of q, p and $1/r$. The condition (28) which determines Φ_2 reads

$$\{\Phi_2, H_0\} = F(q,p) := -\{\Phi_1, H_1\} - \{\Phi_0, H_2\}. \tag{32}$$

Along the solution of the Kepler problem, the left hand side of (32) equals to $d\Phi_2/dt$. Thus $d\Phi_2/dt = F(q,p)$. On the other hand, a straightforward computation shows that the right hand side of (32) reduces to

$$F(q,p) = -\frac{h}{4r^7}\left[p_1^2q_2(-4q_1^2 + q_2^2) + p_2^2q_2(3q_1^2 - 2q_2^2) + 2p_1p_2q_1(q_1^2 - 4q_2^2)\right], \tag{33}$$

where h is the angular momentum integral (8). Suppose now that Φ_2 is a polynomial of q, p and $1/r$. Then by the substitution of the general solution of the elliptic motion, Φ_2 becomes a Fourier series of t, and consequently $d\Phi_2/dt$ must become a Fourier series of t without constant terms. However, the computation below shows that there exists a constant term in $F(q,p)$ which is given by

$$\langle F(q,p)\rangle_t = -\frac{ne(4+e^2)}{16h^6}\sin\varpi. \tag{34}$$

This implies that Φ_2 cannot be a polynomial of q, p and $1/r$, and consequently, cannot be a differential polynomial of H and Φ.

The constant term of $F(q,p)$, which is expressed by a Fourier series of time t, is obtained by the average of t over the period $T = 2\pi/n$, i.e.,

$$\langle F(q,p)\rangle_t = \frac{1}{T}\int_0^T F(q(t),p(t))dt. \tag{35}$$

By the change of integration variable,

$$dt = \frac{r^2}{h}df, \tag{36}$$

which comes from the Kepler's third law, $r^2df/dt = q_1p_2 - q_2p_1 = h$, integral (35) changes to

$$\langle F(q,p)\rangle_t = \frac{n}{2\pi h}\int_0^{2\pi} r^2F(q,p)df. \tag{37}$$

Substitution of the expressions (14) and (15) into (33), and the final substitution (11) yields

$$\begin{aligned}\frac{n}{2\pi h}r^2F(q,p) = \frac{n}{32\pi h^6}(1+e\cos f)^2\left[e^2\sin(f-\varpi)\right.\\ \left.+2(-2+e^2)\sin(f+\varpi) - 8e\sin(2f+\varpi) - 5e^2\sin(3f+\varpi)\right],\end{aligned} \tag{38}$$

for which, integration by f over the period 2π gives the final expression (34).

It should be mentioned here that if we take $\Phi = e_2$, the second component of the Runge-Lenz vector, the quantity which corresponds to (34) becomes

$$\langle F(q,p)\rangle_t = +\frac{ne(4+e^2)}{16h^6}\cos\varpi, \tag{39}$$

and the same conclusion follows for $\Phi = e_2$ as for the non-existence of the modified first integral.

5. Extension to an one-parameter family of symplectic methods

So far the symplectic method used in this paper is the first order, symplectic Euler method (3), which comes from the approximation

$$\exp[\tau(A+B)] = \exp(\tau A)\exp(\tau B) + O(\tau^2) \tag{40}$$

for non-commuting operators A and B (Yoshida, 1993). One can slightly generalizes the symplectic Euler method, by introducing a parameter x, to

$$\exp[\tau(A+B)] = \exp[x\tau A]\exp[\tau B]\exp[(1-x)\tau A] + O(\tau^2) \tag{41}$$

which gives the mapping $(q,p) \to (q',p')$ with

$$\begin{aligned} q^* &= q + x\tau \left(\frac{\partial T}{\partial p}\right)_{p=p}, \quad p' = p - \tau \left(\frac{\partial V}{\partial q}\right)_{q=q^*}, \\ q' &= q^* + (1-x)\tau \left(\frac{\partial T}{\partial p}\right)_{p=p'}. \end{aligned} \tag{42}$$

This method (42) reduces to the symplectic Euler method (3) when $x = 1$, and to its dual one when $x = 0$. When $x = 1/2$, this mapping gives a second order method, known as the Störmer/Verlet method.

In what follows it is shown that the same conclusion is given about the non-existence of the modified first integral also by this extension. For the method (42), the modified Hamiltonian is computed to be

$$H_1 = (x-1/2)H_pH_q, \quad H_2 = \frac{1}{12}\left[(1-6x(1-x))H_{qq}H_p^2 + H_{pp}H_q^2\right], \tag{43}$$

which, of course, reduces to expression (5) when $x = 1$. Starting with these expressions one can repeat the same game as before. The first order term of the modified first integral (29) is generalized to

$$\Phi_1 = (x-1/2)\Phi_q H_p = (x-1/2)\Phi_p H_q. \tag{44}$$

For the 2D Kepler Hamiltonian (7) and the Runge-Lenz integral $\Phi = e_1$, expressions (43) and (44) give

$$H_1 = (x-1/2)\frac{q_1p_1 + q_2p_2}{r^3}, \quad \Phi_1 = (x-1/2)\frac{q_2(q_1p_2 - q_2p_1)}{r^3}, \tag{45}$$

and

$$H_2 = \frac{X[p_1^2(-2q_1^2+q_2^2) + p_2^2(q_1^2-2q_2^2) - 6p_1p_2q_1q_2] + r}{12r^5}, \tag{46}$$

with $X = 1 - 6x(1-x)$. Now the expression (33) for $F(q,p)$ in the case of $x = 1$ is generalized to

$$\begin{aligned} F(q,p) = &-\frac{x(1-x)hq_2}{r^6} \\ &-X\frac{h}{4r^7}\left[p_1^2q_2(-4q_1^2+q_2^2) + p_2^2q_2(3q_1^2-2q_2^2) + 2p_1p_2q_1(q_1^2-4q_2^2)\right]. \end{aligned} \tag{47}$$

However, a straightforward computation shows that the final expression for the time average $\langle F(q,p)\rangle_t$ is exactly the same as before and equals to (34), which is independent of the value of parameter x. The deep reason of this unexpected phenomena is not well understood at this moment.

Anyway the computation above shows that the non-existence of the modified first integral for the Runge-Lenz vector of the Kepler problem is established not only for the symplectic Euler method (3) but also for the one-parameter family of symplectic methods (42). It is an open question whether there exists a symplectic integration method which conserves the Runge-Lenz vector well and the corresponding modified first integral exists.

6. Acknowledgements

The author would like to thank G. Contopoulos and A. Giorgilli for useful discussions. This work was partially supported by the Grants-in-Aid for Scientific Research of Japan Society for the Promotion of Science (JSPS), No.11304004 and No.12640227.

References

Benettin, G. and Giorgilli, A.: 1994, 'On the Hamiltonian interpolation of near-to-the-identity symplectic mappings with application to symplectic integration algorithms', *J. Statist. Phys.* **74**, 1117–1143.

Brouwer, D. and Clemence, G.: 1961, *Methods of Celestial Mechanics*, Academic Press.

Hairer, E.: 1994, 'Backward analysis of numerical integration and symplectic methods', *Ann. Numer. Math.* **1**, 107–132.

Hairer, E. and Lubich, C.: 1997, 'The lifespan of backward error analysis for numerical integrators', *Numer. Math.* **76**, 441–462.

Hairer, E., Nørsett, S.P., and Wanner, G.: 1993, *Solving Ordinary Differential Equations I* (2nd revised edition), Springer-Verlag.

Pollard, H.: 1966, *Mathematical Introduction to Celestial Mechanics*, Prentice-Hall.

Reich, S.: 1999, 'Backward error analysis for numerical integrators', *SIAM J. Numer. Anal.* **36**, 1549–1570.

Sanz-Serna, J.M. and Calvo, M.P.: 1994, *Numerical Hamiltonian Problems*, Chapman and Hall.

Varadarajan, V.S.: 1974, *Lie groups, Lie algebras and their representations*, Prentice-Hall.

Yoshida, H.: 1993, 'Recent progress in the theory and application of symplectic integrators', *Celest. Mech. Dyn. Astron.* **56**, 27–43.

Yoshida, H.: 2001, 'Non-existence of the modified first integral by symplectic integration methods', *Phys. Lett. A* **282**, 276–283.

Application of Symplectic Integrators in Dynamical Astronomy
シンプレクティク数値積分法の天体力学的応用

Takashi Ito (tito@cc.nao.ac.jp)
伊藤孝士 (国立天文台天文学データ解析計算センター)
National Astronomical Observatory, Mitaka, Tokyo 181-8588, Japan

Various enhancement of symplectic integrators are reviewed from the viewpoint of dynamical astronomy, especially in our solar system dynamics: mixed variable method (Wisdom-Holman map), warm start, individual stepsize method, several techniques handling close encounters (democratic heliocentric coordinate (DH), symplectic massive body algorithm (SyMBA), hybrid method, modified SyMBA), and a regularization method by Mikkola.

0. はじめに

シンプレクティク数値積分法の基礎と背景、その良い性質については本巻の吉田春夫氏の記事に詳しく記されている通りである。本稿では吉田記事の内容を踏まえ、実際の天体の運動、とりわけ太陽重力場が支配的な太陽系内の天体の運動に対してシンプレクティク数値積分法を応用する際の手法の幾つかを概観する。まずシンプレクティク数値積分法の復習を行い、Wisdom-Holman map と呼ばれる混合変数型の方法を説明する。Wisdom-Holman map はシンプレクティク数値積分法の今日の発展の礎となった記念碑的な手法であり、なおかつ現在でも大いに現役として活躍する手法である。然る後に warm start と呼ばれる特殊な出発方法を説明し、固定刻み幅 WH map の応用例のひとつとして独立刻み幅を実装する方法について触れる。後半は天体同士の近接遭遇を扱う方法についての解説である。シンプレクティク数値積分法は本然的に可変刻み幅と馴染まず、それ故に天体同士の近接遭遇を苦手にしていたが、近年になってポテンシャルの分割・Democratic Heliocentric method (DH)・Symplectic Massive Body Algorithm (SyMBA)・ハイブリッド法・修正 SyMBA など、近接遭遇に対応できる各種の方法が工夫されて来た。これらの方法の概念を解説し、応用の可能性について触れる。最後は S. Mikkola によって開拓された来たシンプレクティク数値積分法と正則化の融合領域について簡単に述べる。なお、図表は筆者がオリジナルに作製したものだけを掲載し、参考文献からの直接の引用は避けた。参考文献の図で重要なものについては図の番号のみを記しているし、末尾に添付した PowerPoint のスライドには当該図の主要なものを掲載してある。

参考までに、図 1 にはシンプレクティク数値積分法の基本から天体力学的応用までの発展を概観した系統樹を示す。ここに示された枝はシンプレクティク数値積分法研究のごく一部であり、現時点で筆者が認識している部分に過ぎないことに留意する必要がある。シンプレクティク数値積分法に関してはその基礎および応用に関して膨大な数の新しい論文が次々と発表され続けており、その進歩が已む気配は全く無い。

1. シンプレクティク数値積分法の基礎

本節は吉田春夫氏の記事の復習に該当する。より詳細については吉田記事、また Yoshida (1990b, 1992, 1993), 吉田 (1995, 1997), Gladman et al. (1991), Sanz-Serna & Calvo (1994) などの文献を参照していただきたい。

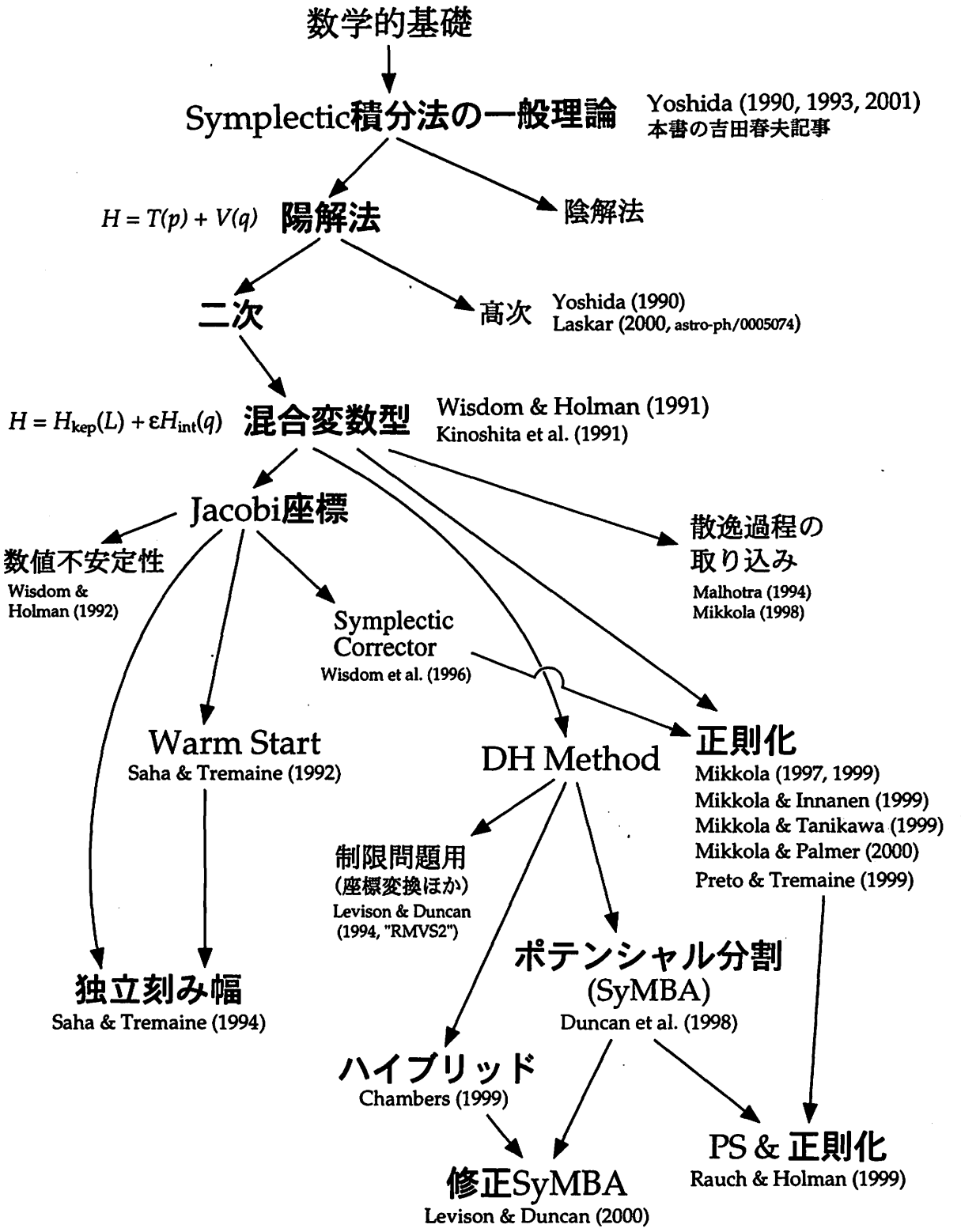

図 1. [A part of the development tree of symplectic integrators] シンプレクティク数値積分法の発展系統樹の一部。矢印の流れはほぼ歴史的な時間の経過にも合致している。本稿で解説するのは主として図中のゴシックあるいは Palatino フォントで記された項目である。

ハミルトニアンを H, 一般化座標を q, 共役な運動量を p, 時刻を t と書くと、ハミルトンの正準運動方程式は以下のように書ける。

$$\frac{dq}{dt} = \frac{\partial H}{\partial p}, \quad \frac{dp}{dt} = -\frac{\partial H}{\partial q}. \tag{1}$$

上記二本の式をまとめると以下のようになる。

$$\frac{dz}{dt} = \{z, H(z)\}, \tag{2}$$

但し z は q または p, 括弧 $\{,\}$ はいわゆる Poisson 括弧である。ここで微分演算子$\{\ ,G\}$を以下のように導入する。

$$\{\ ,G\}\,F \equiv \{F,G\}. \tag{3}$$

すると、ハミルトンの運動方程式 (2) は以下のように書ける。

$$\frac{dz}{dt} = \{\ ,H\}\,z. \tag{4}$$

この方程式 (4) について、時刻 $t=0$ から $t=\tau$ までの $z(t)$ の時間発展を表現する形式的な解は以下のように書ける。但し以下は飽くまで形式的な解であることに留意する必要がある。私達が必要な形に「解けた」わけではない。

$$z(\tau) = \left[e^{\tau\{\ ,H\}}\right] z(0). \tag{5}$$

ここで、以下のように分割可能なハミルトニアンを考える。例えば$T(p)$ は運動エネルギー, $V(q)$ はポテンシャルエネルギーである。このようにハミルトニアンが分割可能であることは、シンプレクティク数値積分法のもっとも基礎的な前提のひとつである。

$$H = T(p) + V(q). \tag{6}$$

すると形式的な解 (5) は

$$z(\tau) = \left[e^{\tau(A+B)}\right] z(0), \tag{7}$$

となる。但し

$$A \equiv \{\ ,T\}, \quad B \equiv \{\ ,V\}, \tag{8}$$

である。ここで、$T(p)$, $V(q)$ はそれぞれ独立には積分可能であるとする。即ち

$$z_A(\tau) = \left[e^{\tau A}\right] z_A(0), \quad z_B(\tau) = \left[e^{\tau B}\right] z_B(0), \tag{9}$$

の両方が個別には求積可能であることを意味する。ここで登場するのが吉田記事にも出て来た BCH (Baker–Campbell–Hausdorff) 公式である。BCH 公式を適用した一次のシンプレクティク数値積分法の公式は以下のようになる。

$$e^{\tau\{\ ,T\}} e^{\tau\{\ ,V\}} = e^{\tau\{\ ,\tilde{H}_{1st}\}}, \tag{10}$$

但し

$$\tilde{H}_{1st} = T + V + \frac{\tau}{2}\{T,V\} + \frac{\tau^2}{12}(\{\{T,V\},V\} + \{\{V,T\},T\}) + \frac{\tau^3}{24}\{\{\{T,V\},V\},T\} + \cdots, \tag{11}$$

である。二次の公式も同様にして

$$e^{\frac{\tau}{2}\{\ ,T\}}e^{\tau\{\ ,V\}}e^{\frac{\tau}{2}\{\ ,T\}} = e^{\tau\{\ ,\tilde{H}_{2nd}\}}, \tag{12}$$

但し

$$\tilde{H}_{2nd} = T + V + \tau^2\left(\frac{1}{12}\{\{T,V\},V\} - \frac{1}{24}\{\{V,T\},T\}\right) + O(\tau^4), \tag{13}$$

となる。同様にして n 次の公式と代理ハミルトニアン (surrogate Hamiltonian) $\tilde{H}_n$ は以下のようになる。H_{err} は誤差ハミルトニアン (error Hamiltonian) と呼ばれている。

$$\tilde{H}_n = H + H_{err} + O(\tau^{n+1}), \tag{14}$$

2. 混合変数型の方法

シンプレクティク数値積分法の一次の公式 (10) や二次の公式 (12) は汎用の方法であったが、太陽系天体の場合には太陽の重力が支配的であるという特徴がある。この特徴を考慮し、シンプレクティク数値積分の実行効率を大いに高めることができる。この方法は Wisdom & Holman (1991, 1992) および Kinoshita et al. (1991) に於いて発案され、その後の応用的シンプレクティク数値積分法の発展に極めて大きな貢献を果たした。本稿ではこの方法を Wisdom-Holman map あるいは WH map と呼ぶことにする。

2.1 Wisdom-Holman map

太陽系のように中心星の重力が支配的な系では、ハミルトニアンの分割を以下のようにすることが出来る。

$$H = H_{kep} + \epsilon H_{int}. \tag{15}$$

H_{kep} は中心星周りのケプラー運動を表すハミルトニアン、ϵH_{int} は惑星同士の相互作用を表すハミルトニアンである。式 (15) 右辺第二項の係数 ϵ は、ケプラー運動ハミルトニアンが相互作用ハミルトニアンに比べて非常に大きいということを形式的に表すために付加したものである。

ハミルトニアンを (15) のように分割した場合、二次の公式を用いて書き下した誤差ハミルトニアンは以下のようになる。

$$\begin{aligned} H_{err} &= \frac{\tau^2}{12}\left\{\left\{H_{kep},\epsilon H_{int}\right\},\epsilon H_{int}\right\} - \frac{\tau^2}{24}\left\{\left\{\epsilon H_{int},H_{kep}\right\},H_{kep}\right\} + O(\tau^4) \\ &= \frac{\epsilon\tau^2}{24}\left\{\left\{H_{kep},H_{int}\right\},H_{kep}\right\} + O(\epsilon^2\tau^2) + O(\tau^4). \end{aligned} \tag{16}$$

式 (16) が意味するところは即ち、シンプレクティク数値積分法による誤差が τ^2 から $\epsilon\tau^2$ に低減されているということである。惑星運動の場合、摂動の大きさ ϵ は摂動関数の大きさのオーダー、つまり惑星質量と太陽質量の比に相当する。太陽系であれば、木星質量が太陽質量の 1/1000 であることを考えると大雑把に言って

$$\epsilon H_{int} \sim 10^{-3} H_{kep}, \tag{17}$$

となる。ハミルトニアンの分割 (15) を用いた新しいシンプレクティク数値積分法で使われる時間ステップを τ_{new} とし、従来の方法と誤差の程度を等しくする、すなわち H_{err} の主要項を同じ大きさに保とうとすると、二次の方法ならば

$$\epsilon\tau_{new}^2 \sim \tau^2, \tag{18}$$

となるので、結局

$$\therefore \tau_{new} \sim \epsilon^{-\frac{1}{2}}\tau \sim 32\tau, \tag{19}$$

となる。即ち、ハミルトニアンの分割として (15) で表される方法を採用すると、従来の方法 (6) に比べて一桁以上の高速化が実現されることになる。もちろん刻み幅を不変に保てばこの新しい方法は従来の方法に比べて誤差ハミルトニアンの大きさがϵ倍に小さく、高い精度を実現できる。

ちなみに n 次の公式を考えると、刻み幅は

$$\tau_{new} \sim \epsilon^{-\frac{1}{n}}\tau \tag{20}$$

となる。新しい刻み幅が$\epsilon^{-\frac{1}{n}}$に比例することから、(15) の分割方法は次数が低いほど高速化の効率が高いことがわかる。WH map としては専ら二次の方法が用いられている所以である。

前述した微分演算子を用いて新しい公式による時間発展を記述すると、一ステップ (時間τ) 分は以下のようになる。

$$e^{\frac{\tau}{2}\{\ ,H_{kep}\}}e^{\tau\{\ ,\epsilon H_{int}\}}e^{\frac{\tau}{2}\{\ ,H_{kep}\}}. \tag{21}$$

式 (21) を複数個連ねた実際のスキームは以下のようになる。

$$e^{\frac{\tau}{2}\{\ ,H_{kep}\}}e^{\tau\{\ ,\epsilon H_{int}\}}e^{\tau\{\ ,H_{kep}\}}e^{\tau\{\ ,\epsilon H_{int}\}}\cdots e^{\tau\{\ ,\epsilon H_{int}\}}e^{\frac{\tau}{2}\{\ ,H_{kep}\}}. \tag{22}$$

ここで $H_{kep}(L)$ は軌道要素 (Delauney 変数) で積分可能, $H_{int}(q)$ は直交座標で積分可能である。もう少し具体的に書けば以下のようになる。

$$\begin{aligned} H &= H_{kep} + \epsilon H_{int} \\ &= H_{kep}(L) + \epsilon H_{int}(L, G, H, l, g, h) \\ &= H_{kep}(\boldsymbol{q}, \boldsymbol{p}) + \epsilon H_{int}(\boldsymbol{q}), \end{aligned} \tag{23}$$

式 (23) のように二種類の変数が混在することから、この新しいシンプレクティク数値積分法は混合変数型の方法とも呼ばれる。式 (23) を見てわかるように、この新しいハミルトニアンの分割方法は H_{kep}とϵH_{int}の評価 (これらのハミルトニアンに支配された系の時間進化。ハミルトニアンの偏微分の計算と言っても良い) の度に変数変換が必要であり、従来の方法に比べるとその分でやや計算の効率が落ちる。但しこの変数変換は Gauss の fg 法など (Danby, 1992) を用いて比較的高速な実装を実現することが可能である。

参考までに Gauss の fg 法の概要を述べておく。$\boldsymbol{r}_0 = \boldsymbol{r}(t_0)$ と $\boldsymbol{v}_0 = \boldsymbol{v}(t_0)$ をそれぞれ時刻 t_0に於ける天体のケプラー軌道上の位置ベクトルと速度ベクトルとする。この二種のベクトルは平行ではないと仮定する。つまり、軌道の角運動量は 0 ではないとする。軌道運動は平面内に限る。$\boldsymbol{r}(t)$ を時刻 t に於けるケプラー軌道上の位置ベクトル、$\boldsymbol{v}(t)$ を時刻 t に於ける速度ベクトルとすると、初期の位置ベクトル$\boldsymbol{r}_0$と速度ベクトル$\boldsymbol{v}_0$は定ベクトルであるから、一意に確定するスカラ関数 f と gを用いてこの$\boldsymbol{r}(t)$ と$\boldsymbol{v}(t)$ を以下のように記述することができる。

$$\boldsymbol{r}(t) = f(t, t_0)\boldsymbol{r}_0 + g(t, t_0)\boldsymbol{v}_0, \tag{24}$$

$$\boldsymbol{v}(t) = \dot{f}(t, t_0)\boldsymbol{r}_0 + \dot{g}(t, t_0)\boldsymbol{v}_0, \tag{25}$$

但し

$$\dot{f} = \frac{df}{dt}, \quad \dot{g} = \frac{dg}{dt}, \tag{26}$$

である。$f, g, \dot{f}, \dot{g}$の具体的な関数形と値に関する詳細は Danby (1992) や Battin (1987) に記されている。

参考までに、WH map を用いて太陽系全9惑星の軌道運動を±40億年以上数値積分した例 (Ito and Tanikawa, 2001a) に於ける全エネルギーと全角運動量の保存状況を図2に示す。この数値積分では10^{12}個近い時間ステップ数が踏まれているが、全エネルギー (図2下) に永年誤差は見られず、相対誤差10^{-9}以内程度で良好に保存している。一方、全角運動量 (図2上) は全般的には相対誤差10^{-11}で保存している。陽解法のシンプレクティク数値積分に於いては角運動量に相当する量が厳密に保存されるため (Yoshida, 1990a)、数値的な誤差は打ち切り誤差 (truncation error) ではなく丸め誤差 (round-off error) に支配されるためである。なお、角運動量の相対誤差には何らかの永年的な変化が発現しているように見えるが、これは数値積分を実行した各種計算機の OS や数学関数の実装方法に於ける丸め誤差処理方法の違いに起因するものであることが確認されている (Ito, 2000)。実際のところ、丸め誤差の見地から見て許容範囲内の WH map 実行環境を提供する計算機はさほど多くはない。PC 上の FreeBSD や Linux はおおむね合格である。HP-UX, ひと昔前の Solaris (2.5.1 まで) や IRIX (6.2 まで) も何とか許容範囲にある。けれども alpha 系の OSF/1 や Tru64 UNIX, および Solaris や IRIX の新しい版の数学関数は丸め誤差の処理に殆ど気を使っておらず、精度の高いシンプレクティク数値積分法の実行にはまったく不向きでることが判明している。

2.2 Jacobi 座標

その定式化の過程を見れば明らかなように、混合変数型のシンプレクティク数値積分法で用いられるハミルトニアンには以下のような形式が要請される。

1. ケプラー項部分が二体問題を表すハミルトニアン $H_{kep} = \frac{p^2}{2m} - \frac{\mu}{r}$ と同等、あるいはこの和の形に書ける。

2. 相互作用項が$\epsilon H_{int} = V(\boldsymbol{r})$ という相互距離のみの関数である。

けれども太陽中心座標 (heliocentric) や重心中心座標 (barycentric) は上記の要請を満たすことができない。例えば重心中心の座標でハミルトニアンを書き下してみると

$$\begin{aligned} H &= \sum_{i=0}^{N} \frac{\boldsymbol{p}_i^2}{2m_i} + \left(-\sum_{i=1}^{N} \frac{Gm_0m_i}{|\boldsymbol{r}_i - \boldsymbol{r}_0|} + \sum_{i=1}^{N} \frac{Gm_0m_i}{|\boldsymbol{r}_i - \boldsymbol{r}_0|} \right) - \sum_{i=0}^{N} \sum_{j=i+1}^{N} \frac{Gm_im_j}{|\boldsymbol{r}_i - \boldsymbol{r}_j|} \\ &= \frac{\boldsymbol{p}_0^2}{2m_0} + \sum_{i=1}^{N} \left(\frac{\boldsymbol{p}_i^2}{2m_i} - \frac{Gm_0m_i}{|\boldsymbol{r}_i - \boldsymbol{r}_0|} \right) + \sum_{i=1}^{N} \frac{Gm_0m_i}{|\boldsymbol{r}_i - \boldsymbol{r}_0|} - \left(\sum_{j=1}^{N} \frac{Gm_0m_j}{|\boldsymbol{r}_0 - \boldsymbol{r}_j|} + \sum_{i=1}^{N} \sum_{j=i+1}^{N} \frac{Gm_im_j}{|\boldsymbol{r}_i - \boldsymbol{r}_j|} \right) \\ &= \frac{\boldsymbol{p}_0^2}{2m_0} + \sum_{i=1}^{N} \left(\frac{\boldsymbol{p}_i^2}{2m_i} - \frac{Gm_0m_i}{|\boldsymbol{r}_i - \boldsymbol{r}_0|} \right) - \sum_{i=1}^{N} \sum_{j=i+1}^{N} \frac{Gm_im_j}{|\boldsymbol{r}_i - \boldsymbol{r}_j|}, \end{aligned} \tag{27}$$

のようになり、太陽の運動エネルギー$\boldsymbol{p}_0^2/2m_0$がH_{kep}にもϵH_{int}にも分類不能になってしまう。混合変数型の WH map を実装するためには、ハミルトニアンを私達が望む形に分割できるための正準変数の組が必要なのである。幸いなことに、私達の要請を満たす正準変数の組は存在する。いわゆる Jacobi 座標と呼ばれるものがそれであり、以下の$\tilde{\boldsymbol{r}}_i$のように定義される (Plummer, 1960)。

$$\tilde{\boldsymbol{r}}_i = \boldsymbol{r}_i - \frac{1}{\sigma_{i-1}} \sum_{j=1}^{i-1} m_j \boldsymbol{r}_j, \tag{28}$$

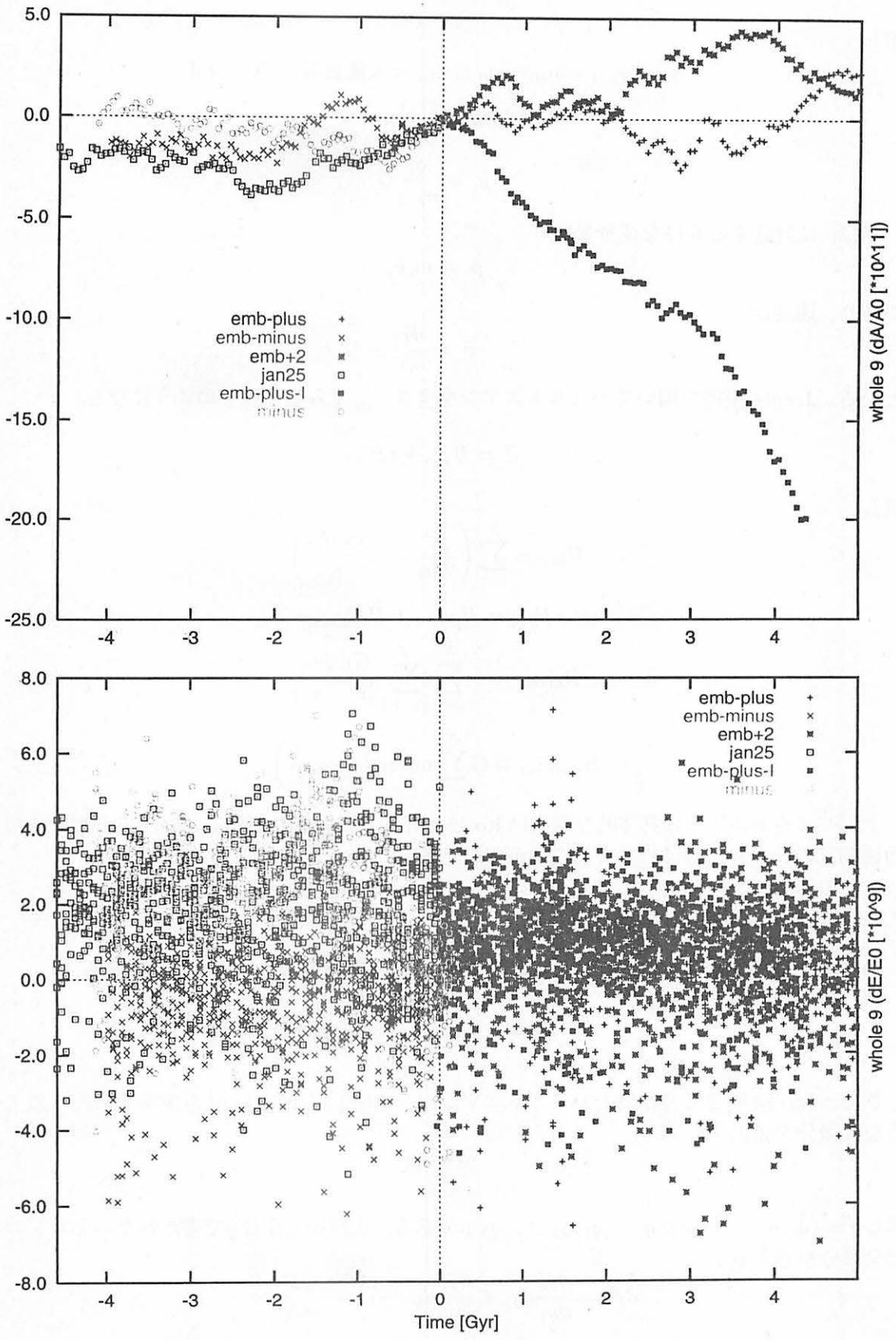

図 2. [An example of relative errors in orbital energy and angular momentum of planetary motions] WH map による数値積分での全エネルギーと全角運動量の相対的な保存の例。複数の異なる初期値から出発した数値積分の結果を重ねてプロットしている。

但し

$$\sigma_i = \sigma_{i-1} + m_i, \quad \sigma_0 = m_0 = \text{太陽質量}, \quad \sigma_{-1} \equiv 0, \tag{29}$$

$$\tilde{m}_i = \frac{\sigma_{i-1}}{\sigma_i} m_i, \tag{30}$$

$$\tilde{\mu}_i = \frac{\sigma_i}{\sigma_{i-1}} G, \tag{31}$$

座標$\tilde{\boldsymbol{r}}_i$に対応する共役な運動量は

$$\tilde{\boldsymbol{p}}_i = \tilde{m}_i \tilde{\boldsymbol{v}}_i, \tag{32}$$

であり、速度は

$$\tilde{\boldsymbol{v}}_i = \frac{d\tilde{\boldsymbol{r}}_i}{dt}. \tag{33}$$

となる。Jacobi 座標を用いてハミルトニアンを書き下してみると以下のようになる。

$$H = H_{kep} + \epsilon H_{int}, \tag{34}$$

但し

$$H_{kep} = \sum_{i=1}^{N} \left(\frac{\tilde{\boldsymbol{p}}_i^2}{2\tilde{m}_i} - \tilde{\mu}_i \frac{\tilde{m}_i m_0}{\tilde{r}_i} \right), \tag{35}$$

$$\epsilon H_{int} = H_{direct} + H_{indirect}, \tag{36}$$

$$H_{direct} = -\sum_{i=1}^{N} \sum_{j=i+1}^{N} \frac{G m_i m_j}{|\boldsymbol{r}_i - \boldsymbol{r}_j|}, \tag{37}$$

$$H_{indirect} = G \sum_{i=1}^{N} m_i m_0 \left(\frac{1}{\tilde{r}_i} - \frac{1}{r_i} \right). \tag{38}$$

上記ハミルトニアンの具体的な導出は Ito (2000) などに記されている。Jacobi 座標で表現する角運動量の表式も同様にして得ることが可能である。

2.2.1 Jacobi 座標による偏微分

Jacobi 座標の定義式は (28) だが、これを成分表記で以下のように書くことにする。

$$\tilde{q}_i = q_i - \frac{1}{\sigma_{i-1}} \sum_{j<i} m_j q_j. \tag{39}$$

さて、Jacobi 座標で書かれたハミルトニアンから出発して WH map を実装する際、以下のような偏微分が頻出する。

$$\frac{\partial H(\boldsymbol{q})}{\partial \tilde{q}_i}, \tag{40}$$

但し$\tilde{\boldsymbol{q}} = (\tilde{q}_1, \tilde{q}_2, \ldots, \tilde{q}_N)$, $\boldsymbol{q} = (q_1, q_2, \ldots, q_N)$ である。太陽中心座標$\boldsymbol{q}$で書かれたハミルトニアンの全微分を考えると

$$dH = \frac{\partial H}{\partial q_1} dq_1 + \frac{\partial H}{\partial q_2} dq_2 + \ldots + \frac{\partial H}{\partial q_N} dq_N, \tag{41}$$

なので、結局 (40) は

$$\frac{\partial H(\boldsymbol{q})}{\partial \tilde{q}_i} = \frac{\partial H}{\partial q_1}\frac{\partial q_1}{\partial \tilde{q}_i} + \frac{\partial H}{\partial q_2}\frac{\partial q_2}{\partial \tilde{q}_i} + \ldots + \frac{\partial H}{\partial q_N}\frac{\partial q_N}{\partial \tilde{q}_i} \tag{42}$$

$$= \sum_{j=1}^{N} \frac{\partial H}{\partial q_j}\frac{\partial q_j}{\partial \tilde{q}_i}, \tag{43}$$

となる。この偏微分$\partial q_j/\partial \tilde{q}_i$を計算する作業は、(39) の逆変換が

$$q_i = \tilde{q}_i + \sum_{j<i} \frac{m_j \tilde{q}_j}{\sigma_j}, \tag{44}$$

であることを確認する作業と聯関している。以下ではこのことを確認してみる。

まず式 (39) を行列形式で書くと

$$\begin{pmatrix} \tilde{q}_1 \\ \tilde{q}_2 \\ \tilde{q}_3 \\ \vdots \\ \tilde{q}_N \end{pmatrix} = \begin{pmatrix} q_1 \\ -\frac{m_1}{\sigma_1}q_1 + q_2 \\ -\frac{m_1}{\sigma_2}q_1 - \frac{m_2}{\sigma_2}q_2 + q_3 \\ \vdots \\ -\frac{m_1}{\sigma_{N-1}}q_1 - \frac{m_2}{\sigma_{N-1}}q_2 - \cdots - \frac{m_{N-1}}{\sigma_{N-1}}q_{N-1} + q_N \end{pmatrix}$$

$$= \begin{pmatrix} 1 & & & & 0 \\ -\frac{m_1}{\sigma_1} & 1 & & & \\ -\frac{m_1}{\sigma_2} & -\frac{m_2}{\sigma_2} & 1 & & \\ \vdots & \vdots & \vdots & \ddots & \\ -\frac{m_1}{\sigma_{N-1}} & -\frac{m_2}{\sigma_{N-1}} & \cdots & -\frac{m_{N-1}}{\sigma_{N-1}} & 1 \end{pmatrix} \begin{pmatrix} q_1 \\ q_2 \\ q_3 \\ \vdots \\ q_N \end{pmatrix}, \tag{45}$$

となる。これを

$$\tilde{\boldsymbol{q}} = A\boldsymbol{q}, \tag{46}$$

と書くことにする。同様に (44) も

$$\begin{pmatrix} q_1 \\ q_2 \\ q_3 \\ \vdots \\ q_N \end{pmatrix} = \begin{pmatrix} \tilde{q}_1 \\ \frac{m_1}{\sigma_1}\tilde{q}_1 + \tilde{q}_2 \\ \frac{m_1}{\sigma_1}\tilde{q}_1 + \frac{m_2}{\sigma_2}\tilde{q}_2 + \tilde{q}_3 \\ \vdots \\ \frac{m_1}{\sigma_1}\tilde{q}_1 + \frac{m_2}{\sigma_2}\tilde{q}_2 + \frac{m_3}{\sigma_3}\tilde{q}_3 + \cdots + \frac{m_{N-1}}{\sigma_{N-1}}\tilde{q}_{N-1} + \tilde{q}_N \end{pmatrix}$$

$$= \begin{pmatrix} 1 & & & & 0 \\ \frac{m_1}{\sigma_1} & 1 & & & \\ \frac{m_1}{\sigma_1} & \frac{m_2}{\sigma_2} & 1 & & \\ \vdots & \vdots & \vdots & \ddots & \\ \frac{m_1}{\sigma_1} & \frac{m_2}{\sigma_2} & \cdots & \frac{m_{N-1}}{\sigma_{N-1}} & 1 \end{pmatrix} \begin{pmatrix} \tilde{q}_1 \\ \tilde{q}_2 \\ \tilde{q}_3 \\ \vdots \\ \tilde{q}_N \end{pmatrix}, \tag{47}$$

となるので、これを

$$\boldsymbol{q} = B\tilde{\boldsymbol{q}}, \tag{48}$$

と書く。行列 A の i 行目は

$$\underset{(i-1\text{列})}{-\frac{m_1}{\sigma_{i-1}}} \quad \underset{}{-\frac{m_2}{\sigma_{i-1}}} \quad \cdots \quad \underset{(i\text{列})}{-\frac{m_{i-1}}{\sigma_{i-1}}} \quad \underset{(i+1\text{列})}{1} \quad 0 \quad \cdots \quad 0 \tag{49}$$

であり、行列 B の j 列目は

$$\begin{matrix} 0 & \\ \vdots & \\ 0 & (j-1\text{行}) \\ 1 & (j\text{行}) \\ \frac{m_j}{\sigma_j} & (j+1\text{行}) \\ \vdots & \\ \frac{m_j}{\sigma_j} & \end{matrix} \tag{50}$$

となっている。

(i) $i=j$ の場合　明らかに

$$(AB)_{ij} = (AB)_{ii} = 1 \times 1 = 1, \tag{51}$$

である。従って積行列 AB の対角成分は 1 になる。

(ii) $i<j$ の場合　(49) より、A の i 行目の第 $i+1$ 成分以降は 0 となる。(50) より、B の j 列目の第 $j-1$ 成分以前は 0 となる。従って

$$(AB)_{ij} = \sum_{k=1}^{N} A_{ik}B_{kj} = 0, \tag{52}$$

となる。

(iii) $i>j$ の場合　(49)(50) より、$(AB)_{ij}$ のうち 0 でない積を産み出すのは、A の i 行目および B の j 列目の第 j 成分から第 i 成分までのみである。従って

$$\begin{aligned}
(AB)_{ij} &= \sum_{k=1}^{N} A_{ik}B_{kj} = \sum_{k=j}^{i} A_{ik}B_{kj} \\
&= \underbrace{-\frac{m_j}{\sigma_{i-1}} \times 1}_{k=j} + \underbrace{\left(-\frac{m_{j+1}}{\sigma_{i-1}} - \cdots - \frac{m_{i-1}}{\sigma_{i-1}}\right) \times \frac{m_j}{\sigma_j}}_{k=j+1,\ldots,i-1} + \underbrace{1 \times \frac{m_j}{\sigma_j}}_{k=i} \\
&= -\frac{m_j}{\sigma_{i-1}} - \frac{m_j}{\sigma_j\sigma_{i-1}} \underbrace{\sum_{k=j+1}^{i-1} m_k}_{=\sigma_{i-1}-\sigma_j} + \frac{m_j}{\sigma_j} \\
&= \frac{1}{\sigma_{i-1}}\left[-m_j - \frac{m_j}{\sigma_j}(\sigma_{i-1}-\sigma_j)\right] + \frac{m_j}{\sigma_j} \\
&= \frac{m_j}{\sigma_{i-1}}\left(-1 - \frac{\sigma_{i-1}}{\sigma_j} + 1\right) + \frac{m_j}{\sigma_j}
\end{aligned}$$

$$= -\frac{m_j}{\sigma_j} + \frac{m_j}{\sigma_j}$$
$$= 0. \tag{53}$$

(51)(52)(53) より、積行列 ABは単位行列であることが示された。これにより、(39) と (44) は互いに逆変換になっていることがわかる。それに加え、式 (47) の一行目を見るまでもなく、懸案の偏微分係数の値はここまでの過程で

$$\frac{\partial q_j}{\partial \tilde{q}_i} = B_{ij} = \begin{cases} \frac{m_i}{\sigma_i}, & (i < j) \\ 1, & (i = j) \\ 0, & (i > j) \end{cases} \tag{54}$$

であることが明らかに判明した。

3. Warm Start

シンプレクティク数値積分法が包含する誤差、特に平均近点離角などの角変数の誤差は、軌道半長径などの作用変数の平均的誤差に由来している。ここでは作用変数を一般に Jと書くことにすると、その平均的誤差とは以下のようなものである。

$$\left\langle \tilde{J} - J \right\rangle, \tag{55}$$

但し$\tilde{J}$は代理系 (surrogate system) の作用変数であり、$\langle\rangle$は時間平均を表すものとする。例えば、軌道半長径 a の時間平均誤差Δa に由来する平均近点離角 lの誤差Δlは、二体問題の諸公式からすぐに以下のように見積もられる。n は平均運動を表す。

$$\Delta l \propto \int \frac{\Delta a}{a} n dt, \tag{56}$$

このような角変数の永年誤差はシンプレクティク数値積分法では時間の一次に比例するに留まるとは言え、長い積分期間の間には重大な大きさに成り得る。これをなるべく小さくするための工夫が warm start と呼ばれる特殊な数値積分の開始方法である (Saha and Tremaine, 1992)。

Warm start の原理は非常に簡単である。まず、刻み幅$\tau \to 0$ の極限では代理系のハミルトニアン$\tilde{H}$は真の系のハミルトニアン Hに等しく、従って作用変数$\tilde{J}$も Jに一致する。この状況から出発し、刻み幅τを徐々に大きくして行くと、最終的には代理系ハミルトニアン$\tilde{H}$は真の系のハミルトニアンから誤差分だけずれる。

$$\tilde{H}(\sim H) \to H + H_{err}. \tag{57}$$

この時のポイントは「徐々に」という点である。ハミルトン力学系のいわゆる断熱定理により、系を記述する或る種のパラメータ (この場合には刻み幅τ) が非常にゆっくりと変化した場合にエネルギーは一般に変化するが、作用変数は変化しない (戸田, 1994)。即ち作用変数は断熱不変量 (adiabatic invariants) であり、

$$\tilde{J} \sim J, \tag{58}$$

となるのである。

3.1 Warm Start のもう少し詳しい説明

Warm start によってシンプレクティク数値積分法の角変数の誤差が低減できることの本質的な理由は、前述の断熱定理の適用で尽きている。が、ここではもう少し定量的な解説を試みてみる。以下の説明は基本的に Saha & Tremaine (1992) に沿ってはいるが、当該論文の記載はかなり直感的かつ抽象的であり、あまつさえ一部は不正確である。本稿ではその辺りを記載を修正しながら話を進める。が、完全に厳密な論理展開にはなっていないかもしれない部分があることをあらかじめお断りしておく。

WH map に於ける代理系のハミルトニアン$\tilde{H}$と真の系のハミルトニアン Hの関係が以下であることは何度も述べた通りである。

$$\tilde{H} = H + H_{err}, \tag{59}$$

$$H = H_{kep} + \epsilon H_{int}, \tag{60}$$

$$H_{err} = \frac{\epsilon\tau^2}{24}\{\{H_{kep}, H_{int}\}, H_{kep}\} + O(\epsilon^2\tau^2). \tag{61}$$

以下の議論では、誤差ハミルトニアン H_{err}を真の系のハミルトニアン $H = H_{kep} + \epsilon H_{int}$に対する摂動と看做し、摂動論を適用して解を求めるという方針を採用する。

代理系および真の系に於ける作用変数と角変数を具体的に以下のように記す。

$$\begin{cases} \text{代理系の作用変数} & \tilde{\boldsymbol{J}} = (\tilde{J}_1, \tilde{J}_2, \tilde{J}_3) \\ \text{代理系の角変数} & \tilde{\boldsymbol{\theta}} = (\tilde{\theta}_1, \tilde{\theta}_2, \tilde{\theta}_3) \end{cases}$$

$$\begin{cases} \text{真の系の作用変数} & \boldsymbol{J} = (J_1, J_2, J_3) \\ \text{真の系の角変数} & \boldsymbol{\theta} = (\theta_1, \theta_2, \theta_3) \end{cases}$$

ケプラー運動を表すハミルニトアン H_{kep}に関しては、作用変数と角変数は以下のような Delauney 変数で記述することにする。実際には H_{kep}は L のみの関数である。

$$\begin{cases} H_{kep}\text{の作用変数} & \boldsymbol{L} = (L, G, H) \\ H_{kep}\text{の角変数} & \boldsymbol{l} = (l, g, h) \end{cases}$$

WH map で扱うような問題では Hと H_{kep}の差がせいぜい $O(\epsilon)$ であることを私達は知っている。従って、それぞれの作用変数および角変数に関する差異も以下のようになる[1]。

$$\begin{aligned} J_1 &= L + O(\epsilon), \quad \theta_1 = l + O(\epsilon), \\ J_2 &= G + O(\epsilon), \quad \theta_2 = g + O(\epsilon), \\ J_3 &= H + O(\epsilon), \quad \theta_3 = h + O(\epsilon). \end{aligned} \tag{63}$$

[1]ここの言い回しは極めて直感的だが、以下のように考えると理解できた気になるかもしれない。後述する正準変換摂動論を適用すると、例えば真の系に於ける作用変数 J_1は一次の近似の範囲内で

$$J_1 = \overline{J_1} - \epsilon\frac{\partial}{\partial\theta_1}\int \left(H_{int} - \overline{H_{int}}\right) dt, \tag{62}$$

と表すことができる。ここで$\overline{J_1}$は積分可能な時間平均ハミルトニアン$\left\langle H_{kep}(\overline{J_1})\right\rangle$の作用変数、つまり L に相当するものである。$H = H_{kep} + \epsilon H_{int}$の場合を考えれば一目瞭然だが、$\epsilon \to 0$ なら $H \to H_{kep}$で且つ $J_1 \to \overline{J_1}$となるのだから、$\overline{J_1}$は L と同等である。従って J_1と L_1は $O(\epsilon)$ の違いしか無い。他の変数に関しても同様である。

ここで H_{kep} は L のみの関数 ($H_{kep} = -\sum_i \frac{\mu_i^2}{2L_i^2}$) なので、$J_2$, J_3, θ_1, θ_2, θ_3 に対する H_{kep} の依存性はすべて $O(\epsilon)$ の大きさに限られる。より具体的に書けば以下のようになる。式 (63) より $J_1 = L + O(\epsilon)$ なので、これを

$$L = J_1 + \epsilon, \tag{64}$$

と書くことにすると、

$$\begin{aligned} H_{kep} &= H_{kep}(L) \\ &= H_{kep}(J_1 + \epsilon) \\ &= H_{kep}(J_1) + \frac{\partial H_{kep}(J_1)}{\partial J_1}\epsilon + \frac{1}{2}\frac{\partial^2 H_{kep}(J_1)}{\partial {J_1}^2}\epsilon^2 + \cdots, \end{aligned} \tag{65}$$

となる。従って、式 (65) を偏微分すると $\frac{\partial H_{kep}}{\partial J_1}$ については $O(1)$ の量が残るが、それ以外は

$$\frac{\partial H_{kep}}{\partial J_2} = O(\epsilon), \quad \frac{\partial H_{kep}}{\partial J_3} = O(\epsilon), \tag{66}$$

$$\frac{\partial H_{kep}}{\partial \theta_1} = O(\epsilon), \quad \frac{\partial H_{kep}}{\partial \theta_2} = O(\epsilon), \quad \frac{\partial H_{kep}}{\partial \theta_3} = O(\epsilon), \tag{67}$$

となる。これが上述した「J_2, J_3, θ_1, θ_2, θ_3 に対する H_{kep} の依存性はすべて $O(\epsilon)$ の大きさに限られる」の意味である。

式 (67) を式 (61) に代入し、Poisson 括弧 $\{,\}$ を真の系の正準変数 $(\boldsymbol{J}, \boldsymbol{\theta})$ で評価し、誤差ハミルトニアン H_{err} を書き直してみる。すると、$O(\epsilon)$ までの近似では誤差ハミルトニアンには $\frac{\partial H_{kep}}{\partial J_1}$ を含む項しか残らないことがすぐにわかる。式 (61) を見ればわかるように、誤差ハミルトニアン H_{err} には元々 ϵ のファクターが掛かっているからである。

$$H_{err} = -\frac{\epsilon\tau^2}{24}\left(\frac{\partial H_{kep}}{\partial J_1}\right)^2\left(\frac{\partial^2 H_{int}}{\partial {\theta_1}^2}\right) + O(\epsilon^2\tau^2). \tag{68}$$

ここで、私達は太陽系の惑星運動のように有界な運動のみを念頭に置いていることを思い出そう。すると、式 (68) の $\frac{\partial^2 H_{int}}{\partial {\theta_1}^2}$ は周期項のみで構成されていなければならないことがわかる。仮に $\frac{\partial^2 H_{int}}{\partial {\theta_1}^2}$ 内に定数項が含まれており、例えば

$$\frac{\partial^2 H_{int}}{\partial {\theta_1}^2} = C_1, \tag{69}$$

のような状況だとすれば、これを θ_1 で積分することで

$$\frac{\partial H_{int}}{\partial \theta_1} = C_1\theta_1 + C_2, \tag{70}$$

となる。C_2 は別種の積分定数である。H_{int} に関する作用変数のひとつ $J_{1,H_{int}}$ を

$$\frac{dJ_{1,H_{int}}}{dt} = \frac{\partial H_{int}}{\partial \theta_1} = C_1\theta_1 + C_2, \tag{71}$$

と置くことで定めると、(71) を時間で積分することで

$$J_{1,H_{int}} = C_2 t + f(\theta_1; t), \tag{72}$$

を得る。ここで $f(\theta_1;t)$ はθ_1と t の関数である。式(72)の意味するところは、もし式(68)の$\frac{\partial^2 H_{int}}{\partial \theta_1^2}$に定数項が含まれているなら、作用変数 $J_{1,H_{int}}$には時刻に比例する永年項が現れるということである。少なくとも私達は有界な運動を扱っているのだから、時刻に比例する作用変数の永年変化とは縁が無いはずである。従って式(68)の$\frac{\partial^2 H_{int}}{\partial \theta_1^2}$には定数項は無く、周期項のみを含むということになる。$\frac{\partial^2 H_{int}}{\partial \theta_1^2}$が周期項だけで表されるという事実は、惑星間摂動を表す摂動関数の中に "生の" 角変数$\boldsymbol{\theta}$が現れては来ないということをも意味する。摂動関数内の角変数は、すべて $\sin\boldsymbol{\theta}$や $\cos\boldsymbol{\theta}$と言った周期関数の形で現れる。

以上より、$O(\epsilon)$ までの近似範囲内では誤差ハミルトニアン H_{err}は周期項のみを含み、永年項を含まないことがわかる。従って H_{err}の時間平均値は以下のようになる。

$$\langle H_{err}\rangle = O(\epsilon^2\tau^2). \tag{73}$$

式(73)が表す事実は後に、warm start の誤差低減原理に於いて本質的な役割を果たす。

本節では以降、WH map を一種の摂動問題として扱う。即ち、積分可能なハミルトニアン Hに対して摂動 H_{err}が加わった$\tilde{H} = H + H_{err}$ という系を解く問題として WH map を扱うのである。以下の議論では H_{kep}, ϵH_{int}, H_{err}をそれぞれ

$$H_{kep} \to H_0, \quad \epsilon H_{int} \to H_1, \quad H_{err} \to H_2, \tag{74}$$

と置き換えて話を進める。下添字 0, 1, 2 は各項に関する摂動のオーダーと捉えても悪くはない。

3.1.1 真の系

真の系を支配するハミルトニアンは以下である。

$$H(\boldsymbol{J},\boldsymbol{\theta}) = H_0(\boldsymbol{J}) + H_1(\boldsymbol{J},\boldsymbol{\theta}). \tag{75}$$

$H_0(\boldsymbol{J})$ は $H_{kep}(\boldsymbol{L})$ に$\boldsymbol{L} = \boldsymbol{J}$を代入したものである (実際には H_{kep}が L のみの関数であることは既述なので、厳密な書き方とは言えない)。Hori (1966, 1967) や Deprit (1969) の摂動論を用いると、或る母関数を用いて Hを角変数$\boldsymbol{\theta}$を含まない以下のような形に正準変換することができる。

$$H^*(\boldsymbol{J}^*) = H_0^*(\boldsymbol{J}^*) + H_1^*(\boldsymbol{J}^*). \tag{76}$$

式(76)での上添字 *は当該変数が正準変換されたものであることを示す。以下の議論でも同様である。Hori (1966, 1967) らの理論に従うと、$O(\epsilon)$ までの近似で

$$H_0^*(\boldsymbol{J}^*) = H_0(\boldsymbol{J}^*), \tag{77}$$

$$H_1^*(\boldsymbol{J}^*) = \langle H_1(\boldsymbol{J}^*,\boldsymbol{\theta}^*)\rangle_{\theta^*}, \tag{78}$$

$$W_{real} = \int (H_1 - H_1^*)dt^*, \tag{79}$$

となる。但しW_{real}は正準変換の母関数であり、下添字$\langle\rangle_{\theta^*}$は角変数$\boldsymbol{\theta}^*$に関する平均化を表す。この正準変換により元々の $H(\boldsymbol{J},\boldsymbol{\theta})$ が積分可能な形 $H^*(\boldsymbol{J}^*)$ に変換されるので、新しい作用変数$\boldsymbol{J}^*$の解を得ることができる。となれば、$O(\epsilon)$ までの近似での最終的な解は$\boldsymbol{J}$は以下のようになる。

$$\begin{aligned} \boldsymbol{J} &= \boldsymbol{J}^* + \{\boldsymbol{J}^*, W_{real}\} \\ &= \boldsymbol{J}^* - \frac{\partial W_{real}}{\partial \boldsymbol{\theta}^*}. \end{aligned} \tag{80}$$

3.1.2 代理系

代理系のハミルトニアンは以下のように表すことができる。

$$\begin{aligned}\tilde{H}(\tilde{\boldsymbol{J}},\tilde{\boldsymbol{\theta}}) &= H(\tilde{\boldsymbol{J}},\tilde{\boldsymbol{\theta}}) + H_{err}(\tilde{\boldsymbol{J}},\tilde{\boldsymbol{\theta}}) \\ &= H_0(\tilde{\boldsymbol{J}}) + H_1(\tilde{\boldsymbol{J}},\tilde{\boldsymbol{\theta}}) + H_2(\tilde{\boldsymbol{J}},\tilde{\boldsymbol{\theta}}).\end{aligned} \tag{81}$$

$H_0(\tilde{\boldsymbol{J}})$ は例によって $H_{kep}(\boldsymbol{L})$ に $\boldsymbol{L}=\tilde{\boldsymbol{J}}$ を代入したようなものである。

ここでは、$H_1+H_2=\epsilon H_{int}+H_{err}$ をひとまとめにして摂動を受けたハミルトン系と捉えることにする。母関数 W_{surr} を用いた正準変換を行って角変数 $\tilde{\boldsymbol{\theta}}$ を除去すると、真の系の場合と同様に以下のような結果を得る。

$$\tilde{H}^*(\tilde{\boldsymbol{J}}^*) = H_0^*(\tilde{\boldsymbol{J}}^*) + H_1^*(\tilde{\boldsymbol{J}}^*) + H_2^*(\tilde{\boldsymbol{J}}^*), \tag{82}$$

但し

$$H_0^*(\tilde{\boldsymbol{J}}^*) = H_0(\tilde{\boldsymbol{J}}^*), \tag{83}$$

$$H_1^*(\tilde{\boldsymbol{J}}^*) = \left\langle H_1(\tilde{\boldsymbol{J}}^*,\tilde{\boldsymbol{\theta}}^*)\right\rangle_{\tilde{\theta}^*}, \tag{84}$$

$$H_2^*(\tilde{\boldsymbol{J}}^*) = \left\langle H_2(\tilde{\boldsymbol{J}}^*,\tilde{\boldsymbol{\theta}}^*)\right\rangle_{\tilde{\theta}^*}, \tag{85}$$

$$W_{surr} = \int \left[(H_1+H_2)-(H_1^*+H_2^*)\right] dt^*. \tag{86}$$

この正準変換によって元々の $\tilde{H}(\tilde{\boldsymbol{J}},\tilde{\boldsymbol{\theta}})$ が積分可能な形 $\tilde{H}^*(\tilde{\boldsymbol{J}}^*)$ に変換されるので、解 $\tilde{\boldsymbol{J}}^*$ を得ることができる。最終的な $\tilde{\boldsymbol{J}}$ の形は以下のようになる。

$$\begin{aligned}\tilde{\boldsymbol{J}} &= \tilde{\boldsymbol{J}}^* + \{\tilde{\boldsymbol{J}}^*, W_{surr}\} \\ &= \tilde{\boldsymbol{J}}^* - \frac{\partial W_{surr}}{\partial \tilde{\boldsymbol{\theta}}^*}.\end{aligned} \tag{87}$$

3.1.3 真の系と代理系の差異

以上のようにして得られた真の系と代理系の解を比較するために、式 (87) から式 (80) を差し引いてみる。

$$\begin{aligned}\tilde{\boldsymbol{J}}-\boldsymbol{J} &= \left(\tilde{\boldsymbol{J}}^* - \frac{\partial W_{surr}}{\partial \tilde{\boldsymbol{\theta}}^*}\right) - \left(\boldsymbol{J}^* - \frac{\partial W_{real}}{\partial \boldsymbol{\theta}^*}\right) \\ &= \tilde{\boldsymbol{J}}^* - \boldsymbol{J}^* - \left(\frac{\partial W_{surr}}{\partial \tilde{\boldsymbol{\theta}}^*} - \frac{\partial W_{real}}{\partial \boldsymbol{\theta}^*}\right) \\ &= \tilde{\boldsymbol{J}}^* - \boldsymbol{J}^* - \frac{\partial}{\partial \boldsymbol{\theta}^*}\int \left[(H_1+H_2-H_1^*-H_2^*)-(H_1-H_1^*)\right] dt^* \\ &= \tilde{\boldsymbol{J}}^* - \boldsymbol{J}^* - \frac{\partial}{\partial \boldsymbol{\theta}^*}\int (H_2-H_2^*)\, dt^*.\end{aligned} \tag{88}$$

なお式 (88) の二行目から三行目に掛けては、右辺の第三項と第四項が ϵ の大きさであることを考慮して $\partial/\partial\tilde{\boldsymbol{\theta}}^*$ と $\partial/\partial\boldsymbol{\theta}^*$ を同一視したことに留意すること。

式 (88) の第三項は周期項のみで構成されているので、時間平均した値 (永年値) は 0 になる。従って、代理系と真の系の作用変数の差の時間平均値は以下のようになる。

$$\left\langle \tilde{\boldsymbol{J}}-\boldsymbol{J}\right\rangle = \langle\tilde{\boldsymbol{J}}\rangle - \langle\boldsymbol{J}\rangle = \tilde{\boldsymbol{J}}^* - \boldsymbol{J}^*. \tag{89}$$

この結果 (89) は重要な示唆を持っている。私達が知りたいのは作用変数$\tilde{J}$またはJの永年誤差による角変数の数値誤差、すなわちシンプレクティク数値積分法での代理系と真の系に於ける角変数の差異である。けれども式 (89) が示す$\langle\tilde{J}\rangle - \langle J\rangle = \tilde{J}^{\star} - J^{\star}$ という事実は、作用変数$\tilde{J}$またはJの永年部分に関する議論を、これらの作用変数を正準変換して周期項を消去したもの ($\tilde{J}^{\star}$や$J^{\star}$) に関する議論に持ち込むことができることを意味している[2]。

この結果に留意し、正準変換された代理系ハミルトニアン (82) に話を戻そう。式 (73) で表現された注目すべき事実、つまり$O(\epsilon)$までの近似では$\langle H_{\epsilon rr}\rangle = \langle H_2\rangle = 0$ であることより、

$$H_2^{\star}(J^{\star}) = 0, \tag{90}$$

が$O(\epsilon)$までの近似で成立する。従って結局

$$\begin{aligned} \tilde{H}^{\star}(\tilde{J}^{\star}) &= H_0^{\star}(\tilde{J}^{\star}) + H_1^{\star}(\tilde{J}^{\star}), \\ &= H(\tilde{J}^{\star}), \end{aligned} \tag{91}$$

であることがわかる。これ故、正準変換された代理系に於ける正準周波数すなち$\tilde{\omega}^{\star}(\tilde{J}^{\star})$は、$O(\epsilon)$までの近似で以下のようになる。

$$\begin{aligned} \tilde{\omega}^{\star}(\tilde{J}^{\star}) \equiv \frac{\partial \tilde{H}^{\star}(\tilde{J}^{\star})}{\partial \tilde{J}^{\star}} &= \frac{\partial H^{\star}(\tilde{J}^{\star})}{\partial \tilde{J}^{\star}} \\ &= \omega^{\star}(\tilde{J}^{\star}). \end{aligned} \tag{92}$$

これは結局、$\tilde{\omega}^{\star}(\tilde{J}^{\star})$が (正準変換された) 代理系の作用変数を代入した (正準変換された) 真の系$H^{\star}$のハミルトニアンに於ける正準周波数$\omega^{\star}(\tilde{J}^{\star})$に等しいことを意味している。

話が長くなったが、ここで私達の本来の動機に戻ろう。私達が本当に知りたかったのは、真の系H (あるいはそれが正準変換された$H^{\star}$) における正準周波数であると言うことができる。それは式 (92) に於ける$\tilde{\omega}^{\star}(\tilde{J}^{\star})$ではなく、$\omega^{\star}(\tilde{J}^{\star})$でもなく、以下である。

$$\omega^{\star}(J^{\star}) \equiv \frac{\partial H^{\star}(J^{\star})}{\partial J^{\star}}. \tag{93}$$

けれども式 (92) から、もし

$$\tilde{J}^{\star} = J^{\star}, \tag{94}$$

が何らかの条件で満たされるのであれば、

$$\omega^{\star}(J^{\star}) = \omega^{\star}(\tilde{J}^{\star}) = \tilde{\omega}^{\star}(\tilde{J}^{\star}), \tag{95}$$

という関係が成立することがわかる。式 (95) が成立すれば、代理系$\tilde{\omega}^{\star}(\tilde{J}^{\star})$の正準周波数は$O(\epsilon)$までの近似で真の系の正準周波数$\omega^{\star}(J^{\star})$と等しくなる。このことは角変数$\boldsymbol{\theta}$の数値誤差の大きな低減に直結する。シンプレクティク数値積分法に於ける角変数の数値誤差は時刻に比例して増えて行くからである。

以上のような原理を背景とし、シンプレクティク数値積分の開始時のみならず積分の最中にも式 (94) が成立するための工夫が、断熱定理を基礎とした warm start である。

[2]これに関して、Saha & Tremaine (1992) の p. 1636 にある記載は妙である。同ページ左段、(19a)(19b) の次の段落には以下のような記載がある。"Since $\tilde{J}$ is fixed in the surrogate system ($\tilde{H}$), and J is fixed in the real system (H). ..." ここで "fixed" が『不動の/一定した』を意味すると思うと、正準変換を行う以前の変数である$\tilde{J}$やJは周期項を含んでいるのだから、明らかに "fixed" ではない。従って Saha & Tremaine (1992) の上記記載で用いられている$\tilde{J}, J$は、本来は短周期成分に関して平均化された変数$\tilde{J}^{*}, J^{*}$を意味しているべきものである。

3.2 Warm Start の実装

Warm start の実装は困難なものではなく、以下のような手法を用いて容易に実装が可能である。

1. 数値積分の初期刻み幅τを非常に小さく取る。

2. 刻み幅τを徐々に大きくする。

3. 刻み幅τが望むべき値にまで大きくなったら固定し、本番の数値積分を開始する。

上記の 1. と 2. に於いては代理系ハミルトニアン$\hat{H}$は一定ではないので、厳密な意味ではこれはシンプレクティク数値積分ではない。Warm start が「特殊な始動方法」("special start-up procedure") と呼ばれる所以である。

ところで、実際の数値積分に於いては以下のような手続きがより適していることが Saha and Tremaine (1992) らに記載されている。

0. Warm Start で用いるステップ数を確定する。ここではSステップとする。

1. 本積分の刻み幅をτとするが、時刻$t=0$から刻み幅$\tau_0=\frac{\tau}{4S}$でシンプレクティク数値積分法を稼働させ、Sステップ進行する。一ステップごとに刻み幅をτ_0ずつ増す。すなわち刻み幅は$\tau_0,\ 2\tau_0,\ 3\tau_0,\ \ldots,\ S\tau_0$となる。

2. Sステップ進行したら、積分方向を反転させて$2S$ステップ進む。ここでも一ステップごとに刻み幅をτ_0ずつ増す。すなわち刻み幅は$(S+1)\tau_0,\ (S+2)\tau_0,\ \ldots,\ 3S\tau_0$となる。

3. $S+2S=3S$ステップ進行したら、再び積分方向を反転させてSステップ進む。ここでも一ステップごとに刻み幅をτ_0ずつ増す。すなわち刻み幅は$(3S+1)\tau_0,\ (3S+2)\tau_0,\ \ldots,\ 4S\tau_0$となる。

4. これにて刻み幅は$4S\tau_0=\tau$となるので、この値に固定し、本積分を開始する。

上記の手続きで注目すべきことは、3. が終了する時刻、すなわち本積分を開始すべき時点の時刻がちょうど$t=0$になっていることである。つまり、前進する区間 1. と区間 3. の長さの合計が後退する区間 2. に等しくなっているのである (図 3)。このことは以下のように示される。

$$\begin{aligned} T_1(=\text{手続き 1. を行う期間}) &= \tau_0+2\tau_0+3\tau_0+\ldots+S\tau_0 \\ &= \frac{S(S+1)}{2}\tau_0, \end{aligned} \tag{96}$$

$$\begin{aligned} T_2(=\text{手続き 2. を行う期間}) &= (S+1)\tau_0+(S+2)\tau_0+(S+3)\tau_0+\ldots+3S\tau_0 \\ &= \left(\frac{3S(3S+1)}{2}-\frac{S(S+1)}{2}\right)\tau_0 \\ &= \left(4S^2+S\right)\tau_0, \end{aligned} \tag{97}$$

$$\begin{aligned} T_3(=\text{手続き 3. を行う期間}) &= (3S+1)\tau_0+(3S+2)\tau_0+(3S+3)\tau_0+\ldots+4S\tau_0 \\ &= \left(\frac{4S(4S+1)}{2}-\frac{3S(3S+1)}{2}\right)\tau_0, \end{aligned} \tag{98}$$

従って

$$\begin{aligned} T_1 + T_3 &= \left(\frac{S(S+1)}{2} + \frac{4S(4S+1)}{2} - \frac{3S(3S+1)}{2} \right) \cdot \tau_0 \\ &= \left(4S^2 + S \right) \tau_0 \\ &= T_2, \end{aligned} \tag{99}$$

となるのである。なお太陽系の力学に関する諸問題では $S \sim 5000$ とすれば十分に warm start が効力を発揮し、誤差が軽減されることが経験的にわかっている。

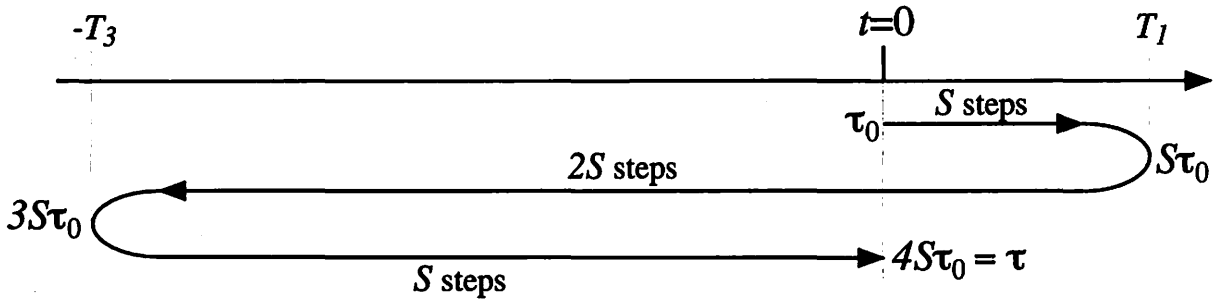

図 3. [A schematic illustration of the warm start] Warm start の模式図。初期刻み幅τ_0で出発して Sステップ進み、$2S$ステップ戻り、再び Sステップ進むと丁度出発点 $t = 0$ に戻って来る ($|T_1| + |T_3| = |T_2|$)。

3.3 Warm start の数値例

太陽–小惑星–木星の三体系を例に取り、warm start の効果を確認するための数値積分を行った。小惑星としてはいわゆる四大小惑星 (Ceres, Pallas, Juno, Vesta) を対象とし、すべての天体の軌道要素と質量は現在の値を用いた。具体的には、5×10^4年間の数値積分を warm start を使った場合と使わなかった場合 (cold start を呼ぶ) で出発し、平均近点離角 lの計算誤差を計測した。誤差計測の基準としては非常に小さな刻み幅 ($\tau = 0.125$ 日) を用いた試験的数値積分を行い、その解を真の解と仮定した。誤差の評価は、この擬似的な真の解と本積分 ($\tau = 40$ 日) の解との差を計測することで行った。例えば図 4は Ceres についての数値結果であるが、warm start を使った本積分での平均近点離角の誤差は、cold start による本積分での平均近点離角の誤差と比べて圧倒的に小さくなっていることがわかる。他の小惑星についても同様である (図 5, 図 6, 図 7)。かくして warm start は、その実装が極めて簡単であるにも関わらず効果的に誤差を減らし得る有益な方法であることが判明した。

4. 独立刻み幅 (individual stepsize method)

太陽系の惑星運動を考えてみると、最内惑星の水星の公転周期は 90 日未満であるのに対して最外惑星の冥王星は 250 年近い公転周期を持つ。通常は最内惑星の公転周期が刻み幅決定の目安になるが、水星の公転周期を基準にして冥王星の軌道進化を数値積分するのは明らかに無駄が多いように思える。ここでは、こうした背景から産まれた独立刻み幅の方法 (individual stepsize method)

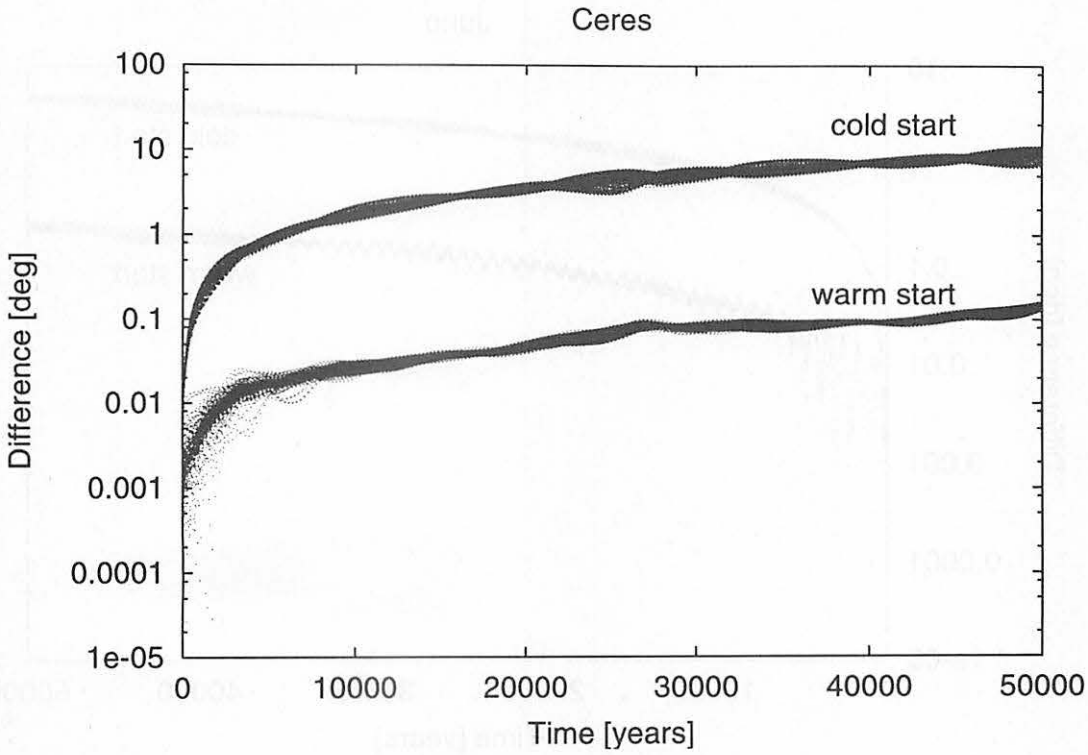

図 4. An example of warm start (errors in mean anomaly): (1) Ceres.

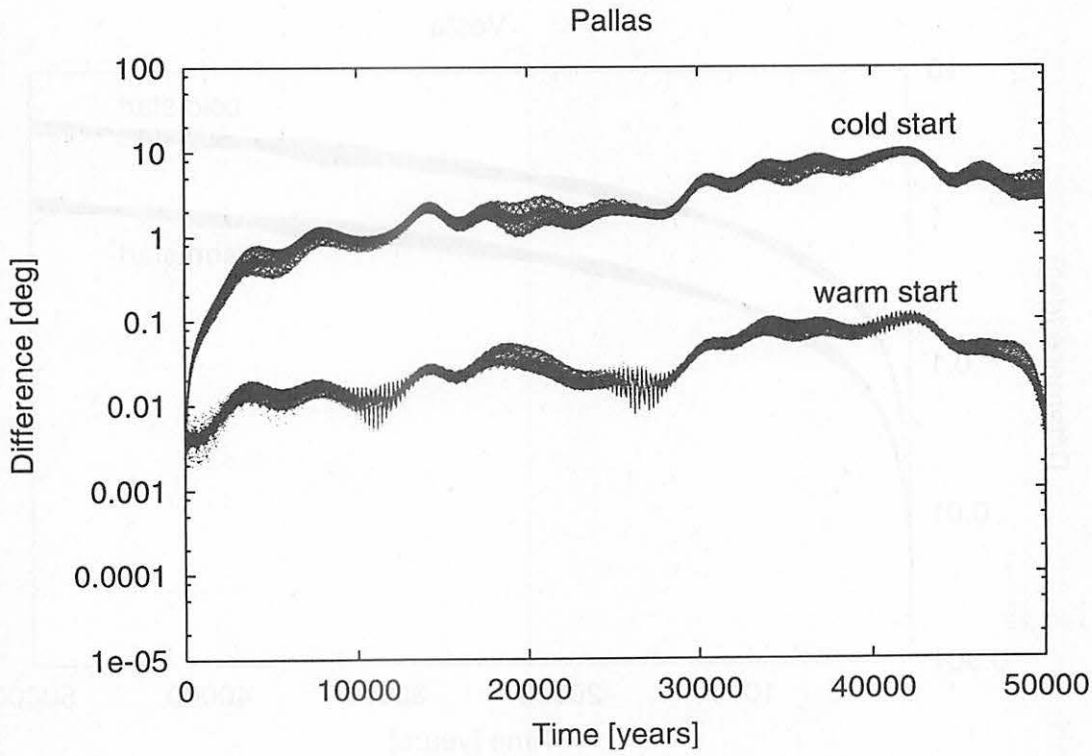

図 5. An example of warm start (errors in mean anomaly): (2) Pallas.

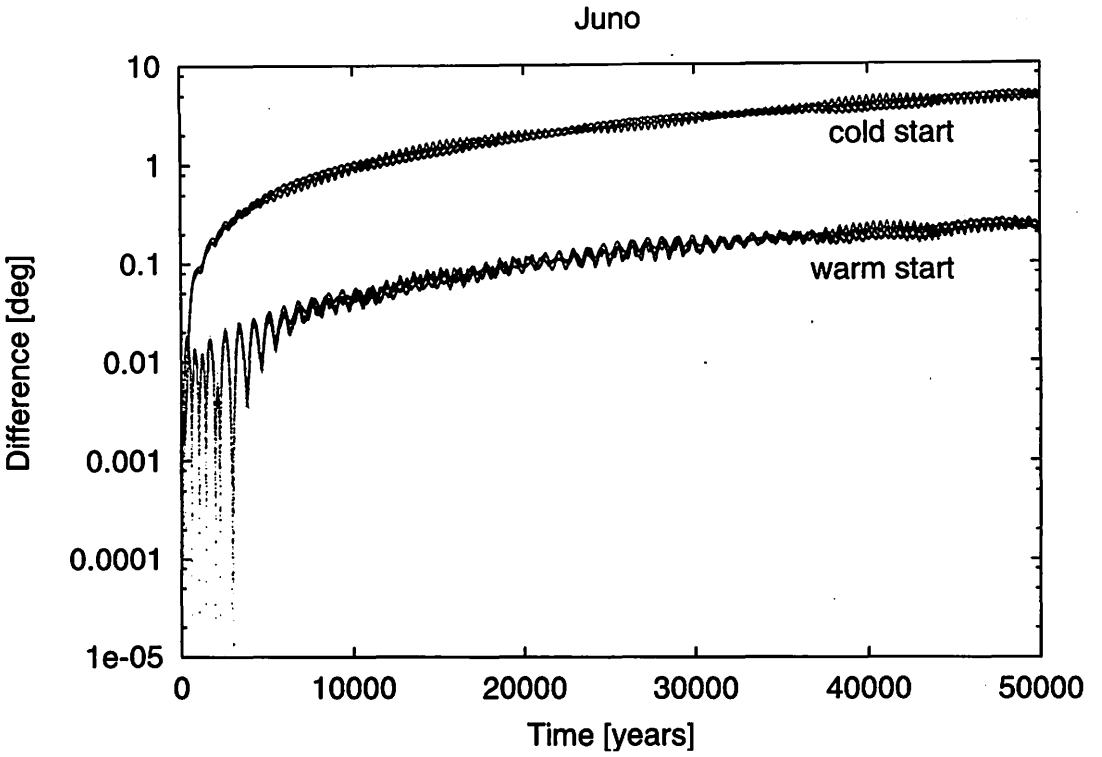

図 6. An example of warm start (errors in mean anomaly): (3) Juno.

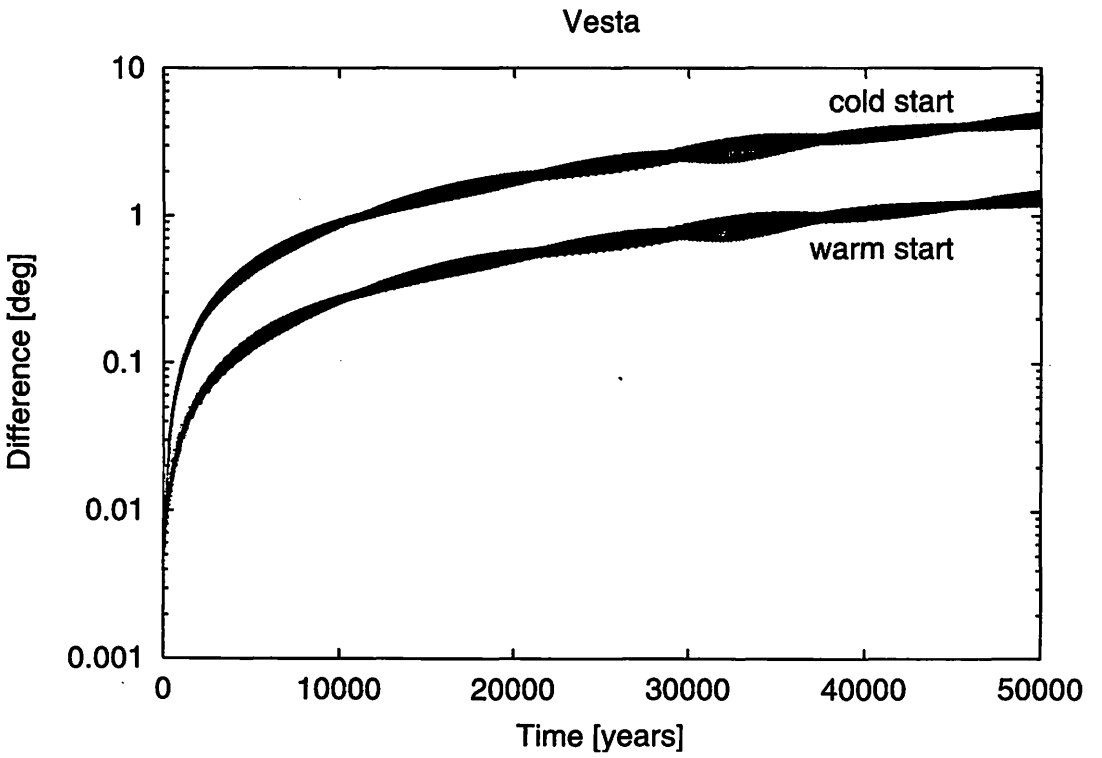

図 7. An example of warm start (errors in mean anomaly): (4) Vesta.

について概観する (Saha and Tremaine, 1994)。なおここで言う独立刻み幅とは、各天体ごとに独立 (individual) ではあるが数値積分全般を通して固定された (fixed) ものであり、いわゆる可変 (variable) 刻み幅ではない。シンプレクティク数値積分法が可変刻み幅の方法に馴染まないことについては Gladman et al. (1991) や Yoshida (1993) らに記されている通りである。

4.1 ケプラー運動時計と相互作用時計

前述したように、中心星の重力が支配的な系でのハミルトニアン分割は以下のようになる。

$$H = H_{kep} + \epsilon H_{int}. \tag{100}$$

ここで、H_{kep}とϵH_{int}はそれぞれ時計 Kと Iに対応すると考える。

- K ··· 各天体は各自の接触軌道上をケプラー運動する。天体間の相互作用は働かない。
- I ··· 各天体の位置は不動。天体間で運動量の交換が行われる。

通常の WH map を例に取って Kと Iの時間発展を書き下すと以下のようになる。

$$\begin{aligned}
&\left\langle K\text{を}\tfrac{1}{2}\tau\text{進める}\right\rangle \\
&\left\langle I\text{を}\tau\text{進める}\right\rangle \\
&\left\langle K\text{を}\tfrac{1}{2}\tau\text{進める}\right\rangle
\end{aligned}$$

上記は一ステップ (刻み幅τ分) のみの話であり、数値積分全体では以下のようになる。

$$\begin{aligned}
&\left\langle K\text{を}\tfrac{1}{2}\tau\text{進める}\right\rangle \\
&\textbf{loop} \\
&\quad \left\langle I\text{を}\tau\text{進める}\right\rangle \\
&\quad \left\langle \text{出力が必要なら } \textbf{loop} \text{ を抜ける}\right\rangle \\
&\quad \left\langle K\text{を}\tau\text{進める}\right\rangle \\
&\textbf{end loop} \\
&\left\langle K\text{を}\tfrac{1}{2}\tau\text{進める}\right\rangle
\end{aligned}$$

更に話を進め、惑星が N個ある場合を考える。この時は、ハミルトニアン H_{kep}とϵH_{int}を以下のように分割する。

$$H_{kep} = \sum_{i=1}^{N} H_{kep,i}, \quad \epsilon H_{int} = \sum_{i=1}^{N} H_{int,i}, \tag{101}$$

但し $H_{kep,i}$と $H_{int,i}$はそれぞれ以下のような意味を持つ。

- $H_{kep,i}$ ··· 天体 i のケプラー運動を表すハミルトニアン
- $H_{int,i}$ ··· 天体 i に対する天体 $i+1, \cdots, N$の相互作用を表すハミルトニアン

具体例として $N = 2$ の場合の二ステップ (2τ) 分を書き下してみる。$H_{int,2} = 0$ であることに注意すると以下のようになる。

$$\left\langle K_1\text{を}\tfrac{1}{2}\tau, K_2\text{を}\tfrac{1}{2}\tau\text{進める}\right\rangle$$
$$\quad\left\langle I_1\text{を}\tau\text{進める}\right\rangle$$
$$\quad\left\langle K_1\text{を}\tau, K_2\text{を}\tau\text{進める}\right\rangle$$
$$\quad\left\langle I_1\text{を}\tau\text{進める}\right\rangle$$
$$\left\langle K_1\text{を}\tfrac{1}{2}\tau, K_2\text{を}\tfrac{1}{2}\tau\text{進める}\right\rangle$$

同様にして $N = 3$ の場合の三ステップ (3τ) 分は以下のようになる。この場合には $H_{int,3} = 0$ である。

$$\left\langle K_1\text{を}\tfrac{1}{2}\tau, K_2\text{を}\tfrac{1}{2}\tau, K_3\text{を}\tfrac{1}{2}\tau\text{進める}\right\rangle$$
$$\quad\left\langle I_1\text{を}\tau, I_2\text{を}\tau\text{進める}\right\rangle$$
$$\quad\left\langle K_1\text{を}\tau, K_2\text{を}\tau, K_3\text{を}\tau\text{進める}\right\rangle$$
$$\quad\left\langle I_1\text{を}\tau, I_2\text{を}\tau\text{進める}\right\rangle$$
$$\quad\left\langle K_1\text{を}\tau, K_2\text{を}\tau\text{進める}\right\rangle$$
$$\quad\left\langle I_1\text{を}\tau, I_2\text{を}\tau\text{進める}\right\rangle$$
$$\left\langle K_1\text{を}\tfrac{1}{2}\tau, K_2\text{を}\tfrac{1}{2}\tau, K_3\text{を}\tfrac{1}{2}\tau\text{進める}\right\rangle$$

4.2 再帰呼び出しを使う方法

以上の背景を頭に入れれば、独立刻み幅スキームの構築方針が自ずから以下のように定められる。以下の要件を満たすようにスキームを作れば良い。

1. 各ステップ中に出て来る同一の K_i, I_i はなるべくまとめる。
2. 各ステップの終わりにはどの時計 K_i, I_i も同じだけ進んでいる。
3. 各ステップの途中でも各時計間の同期がなるべく保たれる。

上記項目を満たす独立刻み幅スキーム構築のために利用できる Poisson 括弧の性質としては以下が挙げられる。いずれも $H_{kep,i}$ や $H_{int,i}$ の定義から容易に導出が可能なものばかりなので、興味を持った読者は自分で試してみると良い。

$$\left\{H_{kep,i}, H_{kep,j}\right\} = 0, \quad \left\{H_{int,i}, H_{int,j}\right\} = 0, \tag{102}$$

$$\left\{H_{kep,i}, H_{int,j}\right\} = 0. \quad (j > i) \tag{103}$$

独立刻み幅を実装するスキームは一意ではない。ここでは Saha & Tremaine (1994) に例示された再帰型のスキームに従って解説を行う。再帰呼び出しを用いるスキームでは、天体 i に刻み幅 τ_i を割り当て、以下のようなソースコードイメージによって独立刻み幅スキームを実装する。

procedure TICK(i)
$$\quad\left\langle K_i\text{を}\tfrac{1}{2}\tau_i\text{進める}\right\rangle$$
$$\quad\left\langle I_i\text{を}\tau_i\text{進める}\right\rangle$$
$$\quad\textbf{if } i > 1$$

```
        loop τ_i/τ_{i-1} 回
          call TICK(i − 1)
        end loop
      end if
      ⟨K_i を (1/2)τ_i 進める⟩
end TICK
```

上記のスキームで N 体系の時間進化を時間 τ_N だけ追うには、単に

```
call TICK(N)
```

とすれば良い。具体的に $N = 2$ の場合 (call TICK(2)) を書き下すと、$\tau_2 = 2\tau_1$ であるから以下のようになる。ここで I_2 は実際には何もしないので、無視して良いことに留意する。

```
⟨K_2 を (1/2)τ_2 進める⟩
⟨I_2 を τ_2 進める⟩
    ⟨K_1 を (1/2)τ_1 進める⟩
    ⟨I_1 を τ_1 進める⟩
    ⟨K_1 を (1/2)τ_1 進める⟩
    ⟨K_1 を (1/2)τ_1 進める⟩
    ⟨I_1 を τ_1 進める⟩
    ⟨K_1 を (1/2)τ_1 進める⟩
⟨K_2 を (1/2)τ_2 進める⟩
```

4.3 再帰呼び出しを使わない方法

上述した再帰呼び出し型のスキームの例をよく見ると、ケプラー運動時計 K_1 の進行が $\tau_1/2+\tau_1/2$ に分割されていることがわかる。これは即ちケプラー方程式の求解を二度繰り返す必要があることを意味しており、計算効率悪化の原因となる。この欠点を改善するために、非再帰型のスキームが考案されている。非再帰型のスキームも勿論一意ではないが、例えば以下のようになる。

```
⟨すべての i について K_i を (1/2)τ_i 進める⟩
loop
    ⟨K_i が I_i よりも後になって変更されたすべての i に関して, I_i を τ_i 進める⟩
    ⟨すべての I_i が等しく, 出力が要求される場合には exit loop⟩
    loop for i = 1, ··· , N
        ⟨i = 1 または K_i + (1/2)τ_i ≤ K_{i-1} ならば, K_i を τ_i 進める⟩
    end loop
end loop
⟨すべての i について K_i を (1/2)τ_i 進める⟩
```

例として $N = 2$ の場合を書き下すと、$\tau_2 = 2\tau_1$ であるから

$\langle K_1$を$\frac{1}{2}\tau_1, K_2$を$\frac{1}{2}\tau_2$進める$\rangle$
$\langle I_1$をτ_1進める$\rangle$
$\langle K_1$をτ_1進める$\rangle$
$\langle I_1$をτ_1進める$\rangle$
$\langle K_1$を$\frac{1}{2}\tau_1, K_2$を$\frac{1}{2}\tau_2$進める$\rangle$

となる。一見してわかるように、スキームの中盤に於いてK_1が一気にτ_1進められる分だけ、非再帰型の方法が再帰型の方法に比べて計算量が少なくて済む。このことは$N = 3$ (call TICK(3))の場合を考えるとより明白である。$N = 3$の場合には$\tau_3 = 2\tau_2 = 4\tau_1$であることに注意し、再帰型スキームと非再帰型スキームの実際を書き下すと以下のようになる。非再帰型スキームは再帰型スキームよりも四段階も少ない手間で一ステップ分の数値積分を終えることができる。この差異はNが大きくなるとますます拡大し、非再帰型のスキームが有利になって行く。

再帰型

$\langle K_3$を$\frac{1}{2}\tau_3$進める$\rangle$
$\langle I_3$をτ_3進める$\rangle$
  $\langle K_2$を$\frac{1}{2}\tau_2$進める$\rangle$
  $\langle I_2$をτ_2進める$\rangle$
    $\langle K_1$を$\frac{1}{2}\tau_1$進める$\rangle$
    $\langle I_1$をτ_1進める$\rangle$
    $\langle K_1$を$\frac{1}{2}\tau_1$進める$\rangle$
    $\langle K_1$を$\frac{1}{2}\tau_1$進める$\rangle$
    $\langle I_1$をτ_1進める$\rangle$
    $\langle K_1$を$\frac{1}{2}\tau_1$進める$\rangle$
  $\langle K_2$を$\frac{1}{2}\tau_2$進める$\rangle$
  $\langle K_2$を$\frac{1}{2}\tau_2$進める$\rangle$
  $\langle I_2$をτ_2進める$\rangle$
    $\langle K_1$を$\frac{1}{2}\tau_1$進める$\rangle$
    $\langle I_1$をτ_1進める$\rangle$
    $\langle K_1$を$\frac{1}{2}\tau_1$進める$\rangle$
    $\langle K_1$を$\frac{1}{2}\tau_1$進める$\rangle$
    $\langle I_1$をτ_1進める$\rangle$
    $\langle K_1$を$\frac{1}{2}\tau_1$進める$\rangle$
  $\langle K_2$を$\frac{1}{2}\tau_2$進める$\rangle$
$\langle K_3$を$\frac{1}{2}\tau_3$進める$\rangle$

非再帰型

$\langle K_3$を$\frac{1}{2}\tau_3$進める$\rangle$
$\langle K_2$を$\frac{1}{2}\tau_2$進める$\rangle$
$\langle K_1$を$\frac{1}{2}\tau_1$進める$\rangle$
  $\langle I_3$をτ_3進める$\rangle$
  $\langle I_2$をτ_2進める$\rangle$
  $\langle I_1$をτ_2進める$\rangle$
    $\langle K_1$をτ_1進める$\rangle$
  $\langle I_1$をτ_2進める$\rangle$
    $\langle K_1$をτ_1進める$\rangle$
  $\langle I_1$をτ_2進める$\rangle$
    $\langle K_1$をτ_1進める$\rangle$
    $\langle K_2$をτ_2進める$\rangle$
  $\langle I_1$をτ_1進める$\rangle$
  $\langle I_2$をτ_2進める$\rangle$
$\langle K_3$を$\frac{1}{2}\tau_3$進める$\rangle$
$\langle K_2$を$\frac{1}{2}\tau_2$進める$\rangle$
$\langle K_1$を$\frac{1}{2}\tau_1$進める$\rangle$

こうした独立刻み幅のスキームを用いても、誤差ハミルトニアンの大きさがτ^2より大きくなることはない。$N = 2$の場合の非再帰型スキームに於ける誤差ハミルトニアンの例を以下に示す。以下の形は上の非再帰型スキームにBCH公式を繰り返し適用することで得られたものである。

$$
\begin{aligned}
H_{err} &= \frac{\tau^2}{12}\Big(\Big\{\Big\{H_{kep,1}, H_{int,1}\Big\}, H_{int,1}\Big\} + \frac{1}{2}\Big\{\Big\{H_{kep,1}, H_{int,1}\Big\}, H_{kep,1}\Big\} \\
&+ 4\Big\{\Big\{H_{kep,2}, H_{int,1}\Big\}, H_{int,1}\Big\} + 2\Big\{\Big\{H_{kep,2}, H_{int,1}\Big\}, H_{kep,2}\Big\} \\
&+ 4\Big\{\Big\{H_{kep,2}, H_{int,1}\Big\}, H_{kep,1}\Big\}\Big) + O(\tau^4). \qquad (104)
\end{aligned}
$$

独立刻み幅スキームを用いることによる肝心の計算効率の向上だが、まずは

- $\Delta t_{K,i} \equiv$ 時計 K_i を一ステップ進めるのに必要な時間
- $\Delta t_{I,i} \equiv$ 時計 I_i を一ステップ進めるのに必要な時間

と定義する。すると、独立刻み幅スキームと共通刻み幅スキームとの実計算時間の比は以下のようになる。

$$
\frac{\text{独立刻み幅}}{\text{共通刻み幅}} = \frac{\displaystyle\sum_{i=1}^{N}\left[\frac{\Delta t_{K,i}}{\tau_i} + (N-i)\frac{\Delta t_{I,i}}{\tau_i}\right]}{\dfrac{N\Delta t_K}{\tau} + \dfrac{N(N-1)\Delta t_I}{2\tau}} = \begin{cases} 0.28 & (\text{if } \Delta t_K \gg \Delta t_I) \\ 0.46 & (\text{if } \Delta t_K \ll \Delta t_I) \end{cases} . \qquad (105)
$$

Saha & Tremaine (1994) の Fig. 1 と Fig. 2 では太陽系 9 惑星の軌道進化の数値積分を独立刻み幅と共通刻み幅のスキームで実行し、誤差を比較している。この時には式 (105) の比の値は 0.43 になっており、独立刻み幅を用いることによって 2 倍以上の高速化が実現されていることがわかる。

独立刻み幅のスキームは、太陽系惑星ように (1) 円軌道に近くて (2) 階層的で (3) 安定な軌道を周回する天体の数値積分には適していると言える。この三条件がすべて揃っていない天体の軌道に向いている方法ではない。

5. 近接遭遇への対応

天体同志の近接遭遇 (close encounter) が発生する場合、天体の運動はケプラー運動から大きく外れる。従ってこの場合には generic な WH map をそのまま適用することは出来ない。Generic WH map は天体の運行がケプラー運動に近いということを大前提に置いているからである。一般に close encounter を正確に計算し切ることは如何なる数値積分法にとっても難関と言えるが、ここ数年の間にシンプレクティク性を損わずに近接遭遇を乗り切る計算方法が提案され始めた。本節ではそうした方法の幾つかを紹介する。

5.1 ポテンシャル分割の概念

近接遭遇に対応できるシンプレクティク数値積分法の代表的な例は、Skeel & Biesiadecki (1994) らのアイディアを元にした Lee et al. (1997) および Duncan et al. (1998) によって提案されている。この方法は、近接遭遇する天体が作るポテンシャルを幾つものポテンシャルの和に再帰的に分割するというアイディアを基本として構成されている。直感的なイメージは以下のようになる。

1. 或る天体の周囲に同心球状の薄い殻を何枚も置く。外側の大きな球殻には大きな刻み幅を対応させ、内側の小さな球殻には小さな刻み幅を対応させる。

2. もう一方の天体が接近すると、相手の天体の球殻を通過して行く。

3. 天体が球殻を通過してもうひとつの天体に近付く度に、刻み幅を小さくする。天体が遠ざかって球殻を抜けて行く場合には、刻み幅を大きくする。

ここでは、前述した相互作用ハミルトニアンϵH_{int}に相当するポテンシャルエネルギーを

$$H_V = -\frac{Gm_0m_1}{r}, \tag{106}$$

と書くことにする。ポテンシャルH_Vを分割するとは、即ちH_Vを

$$H_V = \sum_{k=0}^{\infty} V_k, \tag{107}$$

というV_kの和に分けて考えることを意味している。H_Tを運動エネルギーとしてハミルトニアン全体を書くと

$$H = H_T + \sum_{k=0}^{\infty} V_k, \tag{108}$$

となる。なお、ここでの実装としてはポテンシャルH_Vを分割してV_kの和にするのではなく、ポテンシャルを偏微分して得られる力$\boldsymbol{F}$を分割して$\boldsymbol{F}_k$の和の形にする。その方がシンプレクティク数値積分法の実装上の手間が少ないからである。上述した「球殻通過」のイメージは、或るカットオフ半径R_kを定義し、以下を満たすように力F_kを分割することで具現化される。

1. すべてのrに関して$\boldsymbol{F}(r) = \sum_{k=0}^{\infty} \boldsymbol{F}_k(r)$,

2. $r > R_k$ $(k \geq 1)$ ならば $\boldsymbol{F}_k = 0$,

また、力$\boldsymbol{F}_k$と刻み幅τ_kとの関係は以下のようにする。

- 力$\boldsymbol{F}_k$が関与する場合の刻み幅はτ_k
- τ_k/τ_{k+1}は固定された整数 (ここではM)

この辺の話はやや面倒であるが、Duncan et al. (1998) の Fig. 1 などを参照にすると理解しやすい。例として、一回分割 (半径R_1を超えた接近遭遇) に於ける二次のスキームを書き下す。この時は$\tau_0 = M\tau_1$である。

$$\begin{aligned} e^{\tau_0\{\,,H\}} &= e^{\tau_0\left\{\,,H_T+V_0+\sum_{k=1}^{\infty}V_k\right\}} \\ &\approx e^{\frac{\tau_0}{2}\{\,,V_0\}}e^{\tau_0\left\{\,,H_T+\sum_{k=1}^{\infty}V_k\right\}}e^{\frac{\tau_0}{2}\{\,,V_0\}} \\ &\approx e^{\frac{\tau_0}{2}\{\,,V_0\}}\left[e^{\frac{\tau_1}{2}\{\,,V_1\}}e^{\tau_1\left\{\,,H_T+\sum_{k=2}^{\infty}V_k\right\}}e^{\frac{\tau_1}{2}\{\,,V_1\}}\right]^M e^{\frac{\tau_0}{2}\{\,,V_0\}}. \end{aligned} \tag{109}$$

上記のスキームに BCH 公式を適用すると、第k階層の再帰分割スキームから出て来る誤差ハミルトニアンが以下のようになることを簡単に示すことができる。

$$H_{err,k} = \frac{\tau_k^2}{12}\left\{\{V_k, H_T\}, H_T + \frac{1}{2}V_k + \sum_{l=k+1}^{\infty} V_l\right\} + O(\tau_k^4). \tag{110}$$

同様にして、再帰分割を無限回繰り返した後の誤差ハミルトニアンは以下のようになる。

$$H_{err} = \sum_{k=0}^{\infty} \left[\frac{\tau_k^2}{12} \left\{ \{V_k, H_T\}, H_T + \frac{1}{2} V_k + \sum_{l=k+1}^{\infty} V_l \right\} + O(\tau_k^4) \right]. \tag{111}$$

無限回の再帰分割を繰り返せば式 (111) の右辺は無限級数になるが、実際には天体の最接近距離のところで再帰分割が行われなくなるので、級数も有限で打ち切られる。

なお、ここで述べた刻み幅縮小の方法は飽くまで固定 (fixed) した刻み幅を再帰的に分割するに過ぎず、可変 (variable) 刻み幅ではない。その意味で Duncan et al. (1998) で述べられた方法は、当該論文のタイトルにあるように "multiple stepsize" method と呼ぶべきものである。

5.2 ポテンシャル分割の実装

ポテンシャル分割方法の具体例を示す前に、ポテンシャルを以下のように書き直しておく。

$$H_V = \sum_{k=0}^{\infty} V_k = \tilde{V}_0 + (\tilde{V}_1 - \tilde{V}_0) + (\tilde{V}_2 - \tilde{V}_1) + \cdots, \tag{112}$$

但し

$$\tilde{V}_0 = V_0, \quad V_k = \tilde{V}_k - \tilde{V}_{k-1} \quad (k \geq 1), \quad \tilde{V}_k = \sum_{l=0}^{k} V_l. \tag{113}$$

繰り返しになるが、実際にはポテンシャル V ではなく力 $\boldsymbol{F}$ を分割する。即ち、以降は

$$\tilde{\boldsymbol{F}}_k = -\frac{\partial \tilde{V}_k}{\partial \boldsymbol{q}}, \tag{114}$$

を満たす $\tilde{\boldsymbol{F}}_k$ を考慮の対象とする。力の分割は、$\left|\tilde{\boldsymbol{F}}_{k-1}\right|$ が

1. $R_k < r$ では r^{-2} に比例し、
2. $R_{k+1} \leq r \leq R_k$ でスムーズに減少し、
3. $r < R_{k+1}$ では 0,

という要請を満たすように実装する。例えば以下のようになる。

$$\tilde{\boldsymbol{F}}_{k-1} = \begin{cases} -\dfrac{\boldsymbol{q}}{r^3}, & (R_k \leq r) \\ -f_l\left(\dfrac{R_k - r}{R_k - R_{k+1}}\right) \dfrac{\boldsymbol{q}}{r^3}, & (R_{k+1} \leq r < R_k) \\ 0. & (r < R_{k+1}) \end{cases} \tag{115}$$

ここで関数 $f_l(x)$ は x に関する $2l+1$ 次の多項式であり、

$$f_l(0) = 1, \quad f_l(1) = 0, \tag{116}$$

である必要がある。V_k の二階微分までを滑らかにする ($l = 1$) 例は

$$f_l(x) = 2x^3 - 3x^2 + 1, \tag{117}$$

などがあり、V_k の四階微分までを滑らかにする ($l = 3$) 例は

$$f_l(x) = 20x^7 - 70x^6 + 84x^5 - 35x^4 + 4, \tag{118}$$

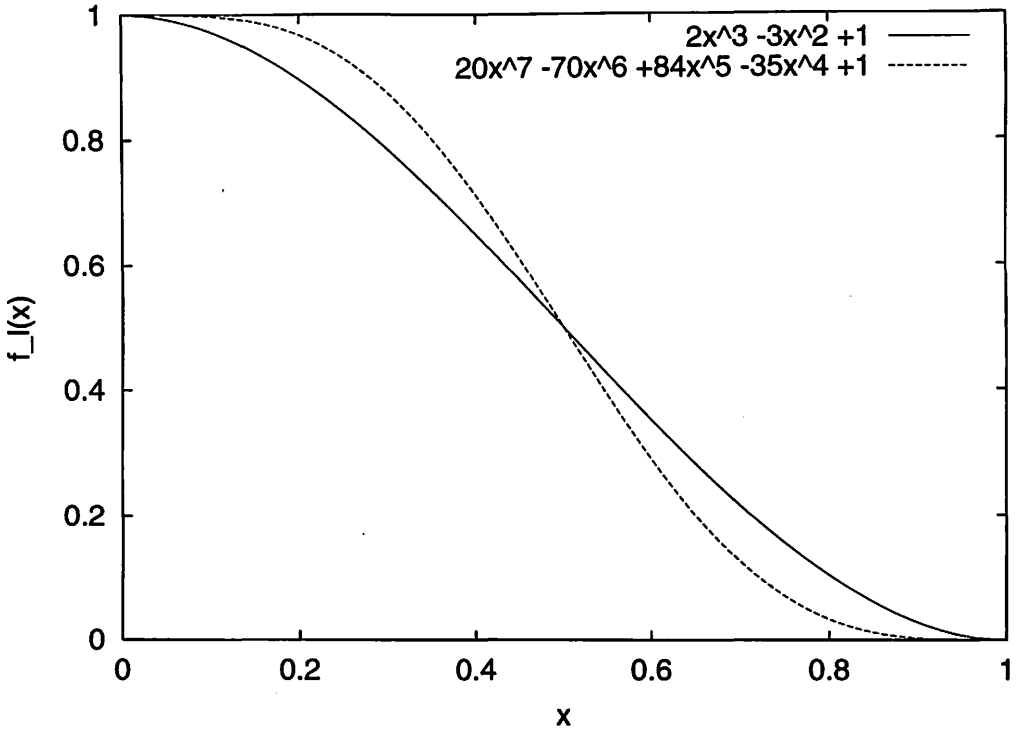

図 8. [An example of $f_l(x)$] $f_l(x) = 2x^3 - 3x^2 + 1$ と $f_l(x) = 20x^7 - 70x^6 + 84x^5 - 35x^4 + 4$.

などがある。これら f_l の具体例は図 8 に示されている。

上述したポテンシャル分割のスキームは、原理的にはそのまま惑星同志の近接遭遇に応用が可能である。けれども現実には generic WH map への適用は簡単とは言えない。この理由をひとことで説明することは難しいが、以下のような状況を考えれば良い。Generic WH map のハミルトニアンは Jacobi 座標を用いて書かれており、ケプラー項 H_{kep} (35), 相互作用直接項 H_{dir} (37), 相互作用間接項 H_{ind} (38) に分割されている。このうち直接項 H_{dir} はすぐに分割可能な形をしているが、間接項 H_{ind} は Jacobi 座標と太陽中心 (heliocentric) 座標が混じっており、容易にポテンシャル分割のスキームに乗らないからである。このことを別の言い方で言うと以下のようになる。相互作用の直接項 H_{dir} を分割して作る二次のスキームとして以下のようなものがすぐに思い付く。

$$
\begin{aligned}
& e^{\tau_0\{\,,H_{kep}+\epsilon H_{int}\}} \\
& \quad \approx e^{\frac{\tau_0}{2}\{\,,\epsilon H_{int}\}} e^{\tau_0\{\,,H_{kep}\}} e^{\frac{\tau_0}{2}\{\,,\epsilon H_{int}\}} \\
& \quad = e^{\frac{\tau_0}{2}\{\,,H_{ind}\}} e^{\frac{\tau_0}{2}\{\,,H_{dir}\}} e^{\tau_0\{\,,H_{kep}\}} e^{\frac{\tau_0}{2}\{\,,H_{dir}\}} e^{\frac{\tau_0}{2}\{\,,H_{ind}\}} \\
& \quad \approx e^{\frac{\tau_0}{2}\{\,,H_{ind}\}} \left[e^{\frac{\tau_1}{2}\{\,,H_{dir,1}\}} e^{\tau_1\{\,,H_{kep}+\sum_{i=2}^{\infty} H_{dir,i}\}} e^{\frac{\tau_1}{2}\{\,,H_{dir,1}\}} \right]^M e^{\frac{\tau_0}{2}\{\,,H_{dir}\}} \\
& \quad \approx \cdots .
\end{aligned}
\tag{119}
$$

ここで考えてみると、相互作用ハミルトニアンの間接項 H_{ind} は各天体がそれぞれ異なる中心を回っている (これは Jacobi 座標の定義のようなもの) ことに対する或る種の補正であると捉えることができる。この補正は各天体の接触軌道上での位置の変化、即ち H_{kep} による時間発展と同様の刻み幅で計算される必要がある。然るに、式 (119) のスキームでは H_{ind} が大外ループに置かれたままであり、H_{kep} と同じ刻み幅では評価されない。このことは計算誤差の蓄積を招く。上述し

たポテンシャル分割スキームを generic な WH map にそのまま適用できないのは、以上のような理由に拠っている。

5.3 Democratic Heliocentric Method

ポテンシャル分割スキームと generic WH map の相性が良くはなく、その理由が Jacobi 座標を用いたことにあることは前節で述べた。では、Jacobi 座標以外に WH map 的な混合変数型のシンプレクティク数値積分法を実現する正準変数の組はあるのだろうか？この問いに対する回答を与えるのが民主的太陽中心座標 (Democratic Heliocentric coordinate (あるいは method), 以下では DH と略記) であり、以下のように表現される。

$$\boldsymbol{Q}_i = \begin{cases} \boldsymbol{q}_i - \boldsymbol{q}_0, & (i = 1, \cdots, N) \\ \dfrac{1}{m_{tot}} \displaystyle\sum_{j=0}^{N} m_j \boldsymbol{q}_j, & (i = 0) \end{cases} \tag{120}$$

$$\boldsymbol{P}_i = \begin{cases} \boldsymbol{p}_i - \dfrac{m_i}{m_{tot}} \displaystyle\sum_{j=0}^{N} \boldsymbol{p}_j, & (i = 1, \cdots, N) \\ \displaystyle\sum_{j=0}^{N} \boldsymbol{p}_j, & (i = 0) \end{cases} \tag{121}$$

但し $m_{tot} = \sum_{j=0}^{N} m_j$ は系の全質量である。$\boldsymbol{Q}_i$ と $\boldsymbol{P}_i$ は互いに正準共役である。

DH 座標の物理的意義は単純で、位置座標の原点を中心天体 (heliocentric) に取り、運動量の原点を重心 (barycentric) に取った座標系である。このように座標と運動量についての二種類の原点が存在することから、DH 座標は混合中心座標 (mixed-centre coordinate) とも呼ばれている。

DH 座標で表わしたハミルトニアンは以下のようになる。ここで重要なことは、ハミルトニアンが generic WH map の場合の二分割とは異なり、以下のように三分割されることである[3]。

$$H = H_{Kep} + H_{Sun} + H_{int}, \tag{122}$$

$$H_{Kep} = \sum_{i=1}^{N} \left(\frac{|\boldsymbol{P}_i|^2}{2m_i} - \frac{G m_i m_0}{|\boldsymbol{Q}_i|} \right), \tag{123}$$

$$H_{Sun} = \frac{1}{2m_0} \left| \sum_{i=1}^{N} \boldsymbol{P}_i \right|^2, \tag{124}$$

$$H_{int} = -\sum_{i=1}^{N-1} \sum_{j=i+1}^{N} \frac{G m_i m_j}{\left| \boldsymbol{Q}_i - \boldsymbol{Q}_j \right|}. \tag{125}$$

新しいハミルトニアン H_{Kep}, H_{Sun}, H_{int} を用いた二次のシンプレクティク数値積分スキームは以下のように書くことができる。式 (126) では、$\{H_{Sun}, H_{int}\} = 0$ という事実を用いて $e^{\frac{\tau}{2}\{\cdot, H_{int}\}}$ と $e^{\frac{\tau}{2}\{\cdot, H_{Sun}\}}$ の順番を入れ替えていることに留意せよ。

$$e^{\frac{\tau}{2}\{\cdot, H_{Sun}\}} e^{\frac{\tau}{2}\{\cdot, H_{int}\}} e^{\tau\{\cdot, H_{Kep}\}} e^{\frac{\tau}{2}\{\cdot, H_{int}\}} e^{\frac{\tau}{2}\{\cdot, H_{Sun}\}}. \tag{126}$$

式 (126) で表されるスキームの意味するところは以下である。

[3] この辺から ϵH_{int} を単に H_{int}, H_{kep} を H_{Kep}, H_{sun} を H_{Sun} などと表記する場合が増えて来るが、気にしない。

1. H_{Sun}由来の位置座標の変化 (linear drift)。具体的には $\frac{\tau}{2}\frac{\partial H_{Sun}}{\partial \boldsymbol{P}_i} = \frac{\tau}{2m_0}\sum \boldsymbol{P}_i$.

2. H_{int}由来の運動量変化 (kick)。$\tau/2$ 分。

3. 瞬時のケプラー軌道に沿った位置の変化 drift, τ分。

4. 再び kick, $\tau/2$ 分。

5. 再び linear drift, $\tau/2$ 分。

DH 座標を使ったシンプレクティク数値積分法の長所と短所は以下のように纏められる。

- 全惑星が共通中心を周回するので、前述した multiple stepsize method によく馴染む。
- 天体の順序が入れ変わっても数値計算の誤差が増大しない。Jacobi 座標を用いた generic WH map の場合には、天体の順序が入れ替わると計算誤差が増大するという報告がある (Chambers and Wetherill, 1998)。DH を使えばそのような心配はない。
- 惑星の近点が小さくなる場合 (長楕円軌道) には計算誤差が増大する。但しこれは generic WH map に於いても同様である。

最初の長所は次節以降で述べる SyMBA スキームの構築に直結するものである。最後の短所の改善については後の節で述べられる。

5.4 Symplectic Massive Body Algorithm — SyMBA

ここまで来れば、ポテンシャル分割スキームと DH method を組み合わせ、近接遭遇にも対応できる multiple stepsize のシンプレクティク数値積分法を構築することができる。

$$
\begin{aligned}
& e^{\tau_0\{\ ,H_{Sun}+H_{int}+H_{Kep}\}} \\
& \quad \approx e^{\frac{\tau_0}{2}\{\ ,H_{Sun}\}} e^{\frac{\tau_0}{2}\{\ ,H_{int}\}} e^{\tau_0\{\ ,H_{Kep}\}} e^{\frac{\tau_0}{2}\{\ ,H_{int}\}} e^{\frac{\tau_0}{2}\{\ ,H_{Sun}\}} \\
& \quad \approx e^{\frac{\tau_0}{2}\{\ ,H_{Sun}\}} \left[e^{\frac{\tau_1}{2}\{\ ,H_{int,1}\}} e^{\tau_1\{\ ,H_{Kep}+\sum_{i=2}^{\infty} H_{int,i}\}} e^{\frac{\tau_1}{2}\{\ ,H_{int,1}\}} \right]^M e^{\frac{\tau_0}{2}\{\ ,H_{Sun}\}} \\
& \quad \cdots .
\end{aligned}
\tag{127}
$$

式 (127) のスキームを用いた場合の誤差ハミルトニアンが以下のようになることもすぐにわかる。

$$
\begin{aligned}
H_{err} = & \frac{\tau_0^2}{12}\left\{\{H_{Sun},H_{Kep}\}\ ,H_{Kep}+\frac{1}{2}H_{Sun}\right\} \\
& +\sum_{k=0}^{\infty}\left[\frac{\tau_k^2}{12}\left\{\{H_{int,k},H_{Kep}\}\ ,H_{Kep}+\frac{1}{2}H_{int,k}+\sum_{l=k+1}^{\infty}H_{int,l}\right\}+O(\tau_k^4)\right].
\end{aligned}
\tag{128}
$$

Duncan et al. (1998) によって考案された上記のスキームは SyMBA (Symplectic Massive Body Algorithm) と呼ばれる。その出自から明らかなように、SyMBA は近接遭遇が無い状況では generic WH map と同様に高速な数値積分を実現し、近接遭遇が発生する場合には再帰的なポテンシャル分割を実行することによって高い精度を保つ。但し前述したように近点距離が近くなるような

軌道、即ち離心率が大きな天体の軌道を上手く扱うことはできない。近点距離が小さな軌道があると H_{Sun} が非常に大きくなり得、混合変数型シンプレクティク数値積分法の基本的前提である $H_{Kep} \gg H_{Sun}$ という条件が満たされなくなる可能性があるからである。また、上記の数式群を見てわかるようにSyMBAの実装には非常に面倒臭いコーディング作業が伴う。これは開発者のひとりであるHal Levison自身も認めるところであり、一般ユーザのためにSWIFTというプログラムパッケージが公開されている(後述)。

Duncan et al. (1998)の論文内では、SyMBAの性能を検証する例として連惑星系、質量を増した木星型惑星系、円制限三体問題、微惑星の重力フォーカシング効果、月の集積過程、らの数値実験について従来の方法との比較結果が示されている。その結果は当該論文中の図に示されているが、いずれの場合にもSyMBAは優秀なパフォーマンスを示し、(コードさえ完成していれば)実用に供し得るスキームであることが示されている。

5.5 A hybrid symplectic integrator

近接遭遇を扱うシンプレクティク数値積分法として、SyMBAとは独立に開発された方法が存在する(Chambers, 1999)。本節ではそれについて紹介する。

そもそもの問題は、天体同士が近接遭遇すると相互作用ハミルトニアン H_{int} が大きくなって H_{Kep} と同程度の大きさになり、generic WH mapでは誤差が増大してしまうという点にあった。本節で紹介する方法の要点は、H_{Kep} が解析的に解けないものになってしまっても良いので、H_{Kep} と H_{int} の大きさの比を $H_{Kep} \gg H_{int}$ に保ちたいという点にある。ここですぐに考え付く方法は、H_{int} のうち近接遭遇に関係する項を強制的に H_{Kep} に繰り込んでしまうことである。例えば以下のような方法が考えられる。

$$H_{Kep} = \sum_{i=1}^{N} \left(\frac{p_i^2}{2m_i} - \frac{Gm_0 m_i}{r_{i0}} \right) - \frac{Gm_\alpha m_\beta}{r_{\alpha\beta}}, \tag{129}$$

$$H_{int} = -G \sum_{i \neq \alpha} \sum_{j>i} \frac{m_i m_j}{r_{ij}} - \sum_{j>\alpha}^{j \neq \beta} \frac{m_\alpha m_j}{r_{\alpha j}}. \tag{130}$$

式(129)と式(130)はα番目とβ番目の天体が近接遭遇するケースを考えた H_{Kep} と H_{int} である。天体αと天体βが近接遭遇すれば距離 $r_{\alpha\beta}$ が小さくなり、項$-\frac{Gm_\alpha m_\beta}{r_{\alpha\beta}}$の絶対値が非常に大きくなり得る。この項を H_{int} から H_{Kep} へと強制的に移動することにより、$H_{Kep} \gg H_{int}$ の比に保つことができる。但しこの場合、H_{Kep} はケプラー運動以外の項を含むのでgeneric WH mapのように解析的に解くことは出来なくなる。しかしこのことはそれほど問題にはならない。H_{Kep} が解析的に解けなければ、補外法など従来型の数値積分法を用いて H_{Kep} の時間進化を機械ϵまでの精度で数値的に解いてやれば、結果的には解析的に解を求めることとの差異は無くなるからである。WH map的なシンプレクティク数値積分法を基本としながらも近接遭遇時には従来型の数値積分法を併用するこの方法はChambers (1999)よって提唱され、hybrid symplectic integratorあるいはhybrid methodと呼ばれている。

式(129)と式(130)は、近接遭遇時にハミルトニアン間で突如として項を移動することを意味している。けれどもこれでは代理系のハミルトニアンが或る時点に於いて唐突に不連続変化し、ハミルトニアンの偏微分(Poisson括弧)を組み合わせて作られる誤差ハミルトニアンが定義できなくなってしまう。これは明らかに好ましくない。近接遭遇に関係する項の移動を滑らかに行い、ハミルトニアンの偏微分がきちんと定義できるような方法を考えることが必要である。このために、SyMBAでも用いたような滑らかな関数 $K(r)$ を導入する。

$$H_{Kep} = \sum_{i=1}^{N} \left(\frac{p_i^2}{2m_i} - \frac{Gm_0 m_i}{r_{i0}} \right) - G \sum_{i=1}^{N} \sum_{j=i+1}^{N} \frac{m_i m_j}{r_{ij}} \left[1 - K(r_{ij}) \right], \tag{131}$$

$$H_{int} = -G \sum_{i=1}^{N} \sum_{j=i+1}^{N} \frac{m_i m_j}{r_{ij}} K(r_{ij}). \tag{132}$$

切り換え関数 Kの例としては以下のようなものがある (図9参照)。

$$K = \begin{cases} 0, & (y < 0) \\ \dfrac{y^2}{2y^2 - 2y + 1}, & (0 < y < 1) \\ 1, & (y > 1) \end{cases} \tag{133}$$

$$y = \frac{r_{ij} - 0.1 r_{crit}}{0.9 r_{crit}}, \tag{134}$$

但し r_{crit}は近接遭遇を定義するためのパラメータであり、具体的な値は扱う問題に依存する。Chambers (1999) の Figure 9 も参照せよ。なお hybrid integrator も DH 座標を用いて構築されるので、以下のハミルトニアン H_{Sun}も考慮に入れる必要がある。

$$H_{Sun} = \frac{1}{2m_0} \left(\sum_{i=1}^{N} \boldsymbol{p}_i \right)^2. \tag{135}$$

この hybrid integrator を用いた二次の積分スキームは SyMBA と全く同じである。

$$e^{\frac{\tau}{2}\{\ ,H_{Sun}\}} e^{\frac{\tau}{2}\{\ ,H_{int}\}} e^{\tau\{\ ,H_{Kep}\}} e^{\frac{\tau}{2}\{\ ,H_{int}\}} e^{\frac{\tau}{2}\{\ ,H_{Sun}\}}. \tag{136}$$

1. 各天体の位置は不変。各天体は、時間$\tau/2$ にわたり太陽を除く他の天体からの重力による加速度を受ける (H_{int}由来)。この加速度には $K(r_{ij})$ の重みが掛かっている。
2. 各天体の運動量は不変。各天体の位置はそれぞれ$\tau \sum_i \boldsymbol{p}_i / 2m_\odot$だけ変化する ($H_{Sun}$に由来する操作)。
3. 近接遭遇していない天体は太陽の周りのケプラー軌道上を時間τ分だけ進む。近接遭遇している天体に関しては、ケプラー項および $1 - K(r_{ij})$ の重みが掛かった近接相互作用項を時刻τ分だけ数値的に求め、時間進化の操作を行う。
4. ステップ 2. と同様。
5. ステップ 1. と同様。

Chambers (1999) の論文内では、この hybrid integrator の性能を検証する例として質量を増した外惑星系、制限三体問題、惑星胚 (原始惑星) の運動、周期彗星 Oterma の木星との近接遭遇、らの数値実験について従来の方法との比較結果が示されている。その結果は当該論文中の図に示されているが、いずれの場合にもこの hybrid integrator は優秀なパフォーマンスを示し、(コードさえ完成していれば) 実用に供し得るスキームであることが示されている。ちなみにこの方法は SyMBA に比べてコーディング作業の面倒もかなり軽減されていると思われる。

蓋しこの hybrid integrator も、近点距離が非常に小さくなる場合、つまり長楕円軌道天体の運動を精密に追い掛けることは難しい。その理由は SyMBA の場合と全く同様であり、近点距離の小さな軌道では H_{Sun}が非常に大きくなり得、混合変数型シンプレクティク数値積分法の基本的前提である $H_{Kep} \gg H_{Sun}$という条件が満たされなくなる可能性があるからである。

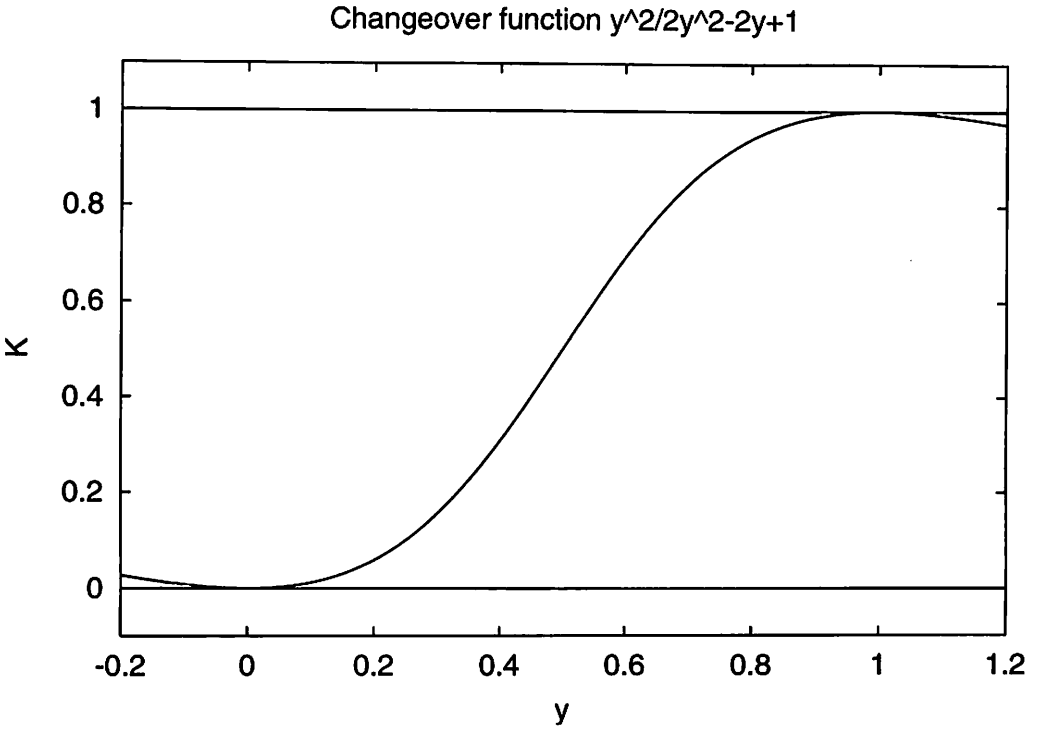

図 9. [An example of $K(r)$] 式 (133) で表現されるものをプロットした。

5.6 Modified SyMBA

前述したように、SyMBA や hybrid integrator の最大の欠点は長楕円軌道の天体を扱い難いことであった。けれども、この二つの方法の長所をうまく組み合わせることにより、この欠点を克服する方法を開発することができる (Levison and Duncan, 2000)。ここでの要点は、離心率が大きい軌道上で天体の近点距離が小さくなる事象を中心星との近接遭遇だと看做すことにある。具体的には、hybrid integrator の切り換え関数的考え方を SyMBA に移植し、天体の近点距離が小さくなった場合には該当する項を H_{Sun} から H_{Kep} に移動する。具体的なハミルトニアンは以下のようになる。

$$H = H'_{Kep} + H'_{Sun} + H_{int}, \tag{137}$$

$$H'_{Kep} = \sum_{i=1}^{N} \left(\frac{|\boldsymbol{P}_i|^2}{2m_i} - \frac{Gm_i m_0}{|\boldsymbol{Q}_i|} \right) + \frac{1}{2m_0} \left| \sum_{i=1}^{N} \boldsymbol{p}_i \right|^2 F(r_1, \cdots, r_n), \tag{138}$$

$$H'_{Sun} = \frac{1}{2m_0} \left| \sum_{i=1}^{N} \boldsymbol{P}_i \right|^2 \left[1 - F(r_1, \cdots, r_n) \right], \tag{139}$$

$$H_{int} = - \sum_{i=1}^{N-1} \sum_{j=i+1}^{N} \frac{Gm_i m_j}{\left| \boldsymbol{Q}_i - \boldsymbol{Q}_j \right|}. \tag{140}$$

上記のハミルトニアンを用いて修正された SyMBA は文字通り修正 SyMBA (modified SyMBA) と呼ばれている。H'_{Kep} 中の項 $\frac{1}{2m_0} \left| \sum_{i=1}^{N} \boldsymbol{p}_i \right|^2 F(r_1, \cdots, r_n)$ は任意の天体が主星に接近遭遇した場

合に H'_{Sun} から持ち込まれる項であり、切り替え関数 F によって滑らかにされている。F は

$$F(r_1,\cdots,r_N)=1-\prod_{i=1}^{N}[1-f(r_i)], \tag{141}$$

のような形をしており、$f(r_i)$ の例としては以下のようなものがある。R_1, R_2 は主星との近接遭遇を判定するための定数であり、具体的な値は問題に依存する。Levison & Duncan (2000) の Fig .2 も参照せよ。

$$f(r_i)=\begin{cases} 1, & (r_i<R_1) \\ 10\left(\dfrac{R_2-r_i}{R_2-R_1}\right)^6-15\left(\dfrac{R_2-r_i}{R_2-R_1}\right)^8+6\left(\dfrac{R_2-r_i}{R_2-R_1}\right)^{10}, & (R_1\le r_i\le R_2) \\ 0. & (r_i>R_2) \end{cases} \tag{142}$$

修正 SyMBA を用いた二次の積分スキームはオリジナルの SyMBA と全く同じである。

$$e^{\frac{\tau}{2}\{\ ,H'_{Sun}\}}e^{\frac{\tau}{2}\{\ ,H_{int}\}}e^{\tau\{\ ,H'_{Kep}\}}e^{\frac{\tau}{2}\{\ ,H_{int}\}}e^{\frac{\tau}{2}\{\ ,H'_{Sun}\}}. \tag{143}$$

Levison & Duncan (2000) の論文内では、この修正 SyMBA の性能を検証する例として木星と土星的な惑星の運動、連惑星系、円制限三体問題、らの数値実験について従来の方法との比較結果が示されている。その結果は当該論文中の図に示されているが、いずれの場合にもこの修正 SyMBA は優秀なパフォーマンスを示し、(コードさえ完成していれば) 実用に供し得るスキームであることが示されている。但し、修正 SyMBA のコーディング作業がオリジナル SyMBA の場合よりも更に面倒になっていることは明白である。

6. 正則化

ここで話の方向を少し変えてみる。Levi-Civita, Kustaanheimo-Stiefel に代表される正則化の方法は、シンプレクティク数値積分法が普及する以前から恒星系力学などの分野で日常的に用いられて来た (Stiefel and Scheifele, 1971)。代表的な KS (Kustaanheimo-Stiefel) 変換を例に取って説明すると以下のようになる。通常の位置ベクトル

$$\boldsymbol{r}=(x,y,z), \tag{144}$$

は、KS 変換による正則化によって四次元ベクトル

$$\boldsymbol{u}=(u_1,u_2,u_3,u_4), \tag{145}$$

に変換される。$\boldsymbol{r}$ と $\boldsymbol{u}$ の関係は

$$\boldsymbol{r}=(x,y,z,0)=L\boldsymbol{u}, \tag{146}$$

であり、変換行列 L は以下のようになる。

$$L=\begin{pmatrix} u_1 & -u_2 & -u_3 & u_4 \\ u_2 & u_1 & -u_4 & -u_3 \\ u_3 & u_4 & u_1 & u_2 \\ u_4 & -u_3 & u_2 & -u_1 \end{pmatrix}. \tag{147}$$

時刻を表す変数 t も同時に正則化される。

$$\frac{dt}{ds} = g(r). \tag{148}$$

但し $g(r)$ は時刻 t を正則化するための kernel function とも呼ばれる関数であり、

$$g(r) = r, \tag{149}$$

や

$$g(r) = r^{\frac{3}{2}}, \tag{150}$$

などの形が用いられる場合が多い (cf. Arakida & Fukushima 2000, 2001)。

正則化の手法は、シンプレクティク数値積分法が扱うハミルトン力学系に対しても素直に拡張することができる (Brumberg, 1995)。Mikkola (1997) は WH map の枠組に KS 変換を持ち込み、WH map の特徴を保ちながら正則化の最大の特徴である近接遭遇の対処を巧みに実装した。正則化の操作を行うことで、ハミルトニアン H は以下のような Γ に変換される。

$$\Gamma = g(r)\left[H(\boldsymbol{q}, \boldsymbol{p}, q_0) + p_0\right]. \tag{151}$$

ハミルトニアン Γ は時刻を陽に含むので次元が増える。古い時刻変数 t は一般化座標のひとつに、古いハミルトニアンの値は運動量のひとつになる。

$$p_0 = -H(0), \quad q_0 = t. \tag{152}$$

このような方法で実装された正則化 WH map の数値例が Mikkola (1997) の Figure 2 や Figure 3 に示されている。Mikkola (1997) での例は離心率の大きな階層的連星系であるが、Generic WH map では近接遭遇の度にエネルギーの保存状態が大きく変化するのに対し、正則化された WH map ではそのような誤差の増大が発現しないことが明らかである。計算時間の増大も無い。

シンプレクティク数値積分法を正則化するメリットは、単に近接遭遇を正確に扱えることのみではない。近接遭遇が無い系でも、正則化することによって generic WH map に比べて高速な計算が可能になる。このことは、generic WH map が接触軌道上の天体位置の変化 (いわゆる kick) を追うためにケプラー方程式の求解を必要とすることに原因がある。通常の直交座標を用いてケプラー問題を表す方程式を書き下すと、お馴染みの

$$\frac{d^2\boldsymbol{r}}{dt^2} + \mu\frac{\boldsymbol{r}}{r^3} = 0, \tag{153}$$

になる。だが、正則化すなわち $\boldsymbol{r}$ から $\boldsymbol{u}$ への変換を行うと、方程式 (153) は以下のようになる。h_k は天体の軌道エネルギーに相当する量であり、無摂動のケプラー運動では定数となる。

$$\frac{d^2\boldsymbol{u}}{ds^2} + \frac{h_k}{2}\boldsymbol{u} = 0. \tag{154}$$

方程式 (154) は $\boldsymbol{u}$ について明らかに線形であり、解 $\boldsymbol{u}$ は調和振動子の重ね合わせとして表現できる。出来る。即ち、kick の際にケプラー方程式を解くことを行わずとも済むようになるのである。このことが正則化された WH map の高い計算効率の要因となっている。

正則化の一般的な短所として、正則化する天体の組をあらかじめ特定する必要のあることが挙げられる。予想外の天体ペアが近接遭遇するような場合、正則化は有効に機能しない。しかし、例えば離心率の大きな太陽系外惑星の安定性を検証するような場合には、正則化されたシンプレクティク数値積分法は極めて高精度かつ効率的な計算方法として使用できる。WH map の各種の拡張の中でも、正則化は今後の発展がもっとも強く期待される領域である。詳細は Seppo Mikkola の一連の論文に記載されている (Mikkola and Innanen, 1999; Mikkola, 1999; Mikkola and Tanikawa, 1999; Mikkola and Palmer, 2000)。

7. その他

最後にシンプレクティク数値積分法の応用に際しての補足的情報、特にケプラー方程式の高速解法とシンプレクティク数値積分法のプログラムパッケージについて触れる。

7.1 ケプラー方程式の高速解法

WH map に於ける接触軌道上での天体の位置変化 (kick) に際してケプラー方程式を解く必要があることは繰り返して述べた。正則化しない WH map に於いて、$e^{\{\cdot,H_{kep}\}}$ の drift 部分の殆どの計算はケプラー方程式の求解に費やされると言っても良い。太陽系の惑星運動を WH map で数値積分した場合、$e^{\{\cdot,H_{kep}\}}$ と $e^{\{\cdot,H_{int}\}}$ との計算時間比は 3:7 程度であるから、ケプラー方程式の求解を効率化して kick の計算を高速化することには大きな意義がある。

u を離心近点離角とした場合のケプラー方程式

$$u - e\sin u = l, \tag{155}$$

の効率的な求解は前世紀以前から研究されて来た古典中の古典と言える課題であるが、数値計算全盛の現代を迎えてその解法は一変しつつある。離心率 e が小さな場合には、ケプラー方程式 (155) を解く場合にさほどの気を使う必要はない。Newton 法 (二次収束) や Halley 法 (三次収束) でも十分な精度と効率を得られる。けれども離心率 e が大きな場合には、従来の方法には大いに問題がある。収束が遅いというのはまだましな方で、酷い場合には逐次近似がまったく収束しない事態すら発生し得る。

その中で国立天文台の福島登志夫氏による一連の研究は画期的であり、精度と効率を高い水準で両立させた極めてユニークな解法に関する論文群が多く出版されている (Fukushima 1996, 1997a, 1997b, 1997c, 1998)。福島氏の一連の研究で提唱されている方法の特徴は、ケプラー方程式を求解する際に sin や cos といった超越関数を使わないという点にある。超越関数の値を計算する組込数学関数の呼び出しは一般に数値計算のボトルネックになり易く、これを回避することによる計算効率の向上は大きい。例えば Fukushima (1996) では、まず挟み撃ち法でケプラー方程式の近似解を得、次に三角関数を使わずにテイラー展開を用いたニュートン法を駆使して精密かつ高速に求解するという方法を採用する。この方法は従来の方法に比べて二倍以上は高速で、且つ離心率 e の全領域に於いて安定であるという良好な試験結果が得られている。福島登志夫氏の一連の仕事は楕円軌道の場合のみならず、双曲線軌道の場合やケプラー方程式がガウス型をしている場合など、多岐なる領域の問題に対応できるものである。また邦文の福島 (1982) はケプラー方程式を高速に解くための巧みな初期値の選び方に関する研究であり、その実装も極めて簡単である。

7.2 プログラムパッケージ

シンプレクティク数値積分法の実装 (ソースコードの作製作業) は極めて困難と言うほどではないが、非常に簡単というものでもない。特に本稿で述べたように WH map の拡張を行って行くとソースコードは次第に複雑になり、研究過程に於けるプログラミング作業の占める割合がどんどん増えて行く。そのような過程を嫌う一般ユーザに利用してもらうため、シンプレクティク数値積分法のプログラムパッケージが存在している。特に、前述した各種の応用的シンプレクティク数値積分法の考案者自身が開発しているプログラムパッケージは信用が置けるし、他のユーザによる使用事例も多くあるので、初心者が取り付くには悪くないと思える。

- SWIFT ··· Hal Levison, M.J. Duncan らのグループが開発。RMVS から SyMBA までのプログラム群を包含している。詳しくは Duncan et al. (1998) に記載されている。

- MERCURY ··· J.E. Chambers が開発。Hybrid integrator に必要なプログラム群が包括されている。詳しくは Chambers (1999) に記載されている。

けれども、シンプレクティク数値積分法の算法を十分に理解して天体力学的な応用的研究を進めようという人には、上記のようなプログラムパッケージの使用はお薦めできない。他人が書いたソースコードを完全に理解することは極めて困難であるし、勉強だと思っても効率が悪い。シンプレクティク数値積分法は天文学に於けるひとつの道具であるから、道具の動作原理を完全に理解しなければ先に進めないという原理主義者達は、何としてもソースコードを自前で開発して計算を行うべきであろう。

8. まとめ

本稿ではシンプレクティク数値積分法の天体力学的応用に関して長々と述べて来た。シンプレクティク数値積分法の改良に関する論文は現在でも毎月のように発表され続けており (cf. Breiter 1999; Chambers 2000; Laskar & Robutel 2000)、将来への歩みの速度は全く緩むことがないように思える。では結局どれがお薦めなのか？という問いに対しては、常套句のようであるが「万能な方法は無い」という回答しかあり得ない。どの方法もそれぞれ長所と短所を持っており、解くべき問題の性質や必要とされる精度によって選択肢の自由度は無数にある。強いて言えば、至るところで近接遭遇が頻繁に発生するような状況ではなく、大局的に見て摂動二体系に近いような状況に適用する場合には、正則化された WH map を使うべきであろう。正則化された WH map は離心率がどんなに大きくなっても精度を落とすことがないし、ケプラー方程式を解く手間が省けるので高速である。実際のところ、現在の太陽系や太陽系外の惑星運動は殆どの場合に「至るところで近接遭遇が頻繁に発生するような状況ではなく、大局的に見て摂動二体系に近いような状況」であり、まずは正則化された WH map の使用が基本ということが言えるであろう。一方で、惑星集積過程のように近接遭遇が頻繁に発生する系に於いては、任意の天体の組の近接遭遇に対応し、なおかつ離心率が大きな軌道も精度良く扱うことができる修正 SyMBA が有効な手法として活用できると思われる。修正 SyMBA について言えば、Levison らが示したオリジナルの方法に対して、近接遭遇する天体に座標中心を移動する force-center switching および Mikkola 的な正則化の手法を組み込むことにより、更に高い精度と効率を得られる可能性があるという報告がなされている (Rauch and Holman, 1999)。

ところで、近接遭遇が頻発する系にシンプレクティク数値積分法を適用する場合の心構えをひとつ述べておこう。太陽系天体の運動に於いて近接遭遇が重要になる局面と言えば、何と言っても惑星や衛星の集積過程が代表的である (Levison *et al.*, 1998; Chambers and Wetherill, 1998; Agnor *et al.*, 1999; Kominami and Ida, 2001)。そうした惑星集積の力学過程、特に N が小さな原始惑星系などの軌道進化をシンプレクティク数値積分法で計算するなら、SyMBA 的な方法が有効であることはすぐに想像が付く。しかしここで留意すべき点がある。有限サイズの天体の近接遭遇は遅かれ早かれ衝突合体あるいは衝突破壊に至る可能性が高いということである。天体が衝突合体を行えば必然的に系のハミルトニアンは全く別物になり、シンプレクティク数値積分法はそこで境界条件の初期化の如き作業を余儀なくされる。この問題はもちろん衝突頻度に依存するが、少なくとも衝突合体の回数だけのハミルトニアンの初期化が必要であり、その前後ではシン

プレクティク性の保存など彼岸の話となる。こうした状況に於いて、シンプレクティク数値積分法を使い続けることが本当に望ましい姿なのかどうかは甚だ疑わしい。こうした領域では Hermite scheme (Makino and Aarseth, 1992; Kokubo *et al.*, 1998) に代表されるような簡明かつ柔軟な数値解法が既に確立されており、敢えてシンプレクティク数値解法を持ち込む積極的理由はさほど強くはなかろう。シンプレクティク数値積分法は確かにハミルトン力学系では極めて強力かつ有効な手法ではあるが、それは飽くまで使用者が周囲の状況を完全に把握しているという前提に立った話であり、使い方を誤れば良い道具もその能力を発揮できないことは火を見るより明らかである。その意味で、シンプレクティク数値積分法は他一般の数値積分法と比べて使用者の見識が大いに問われる手法と言えるかもしれない。

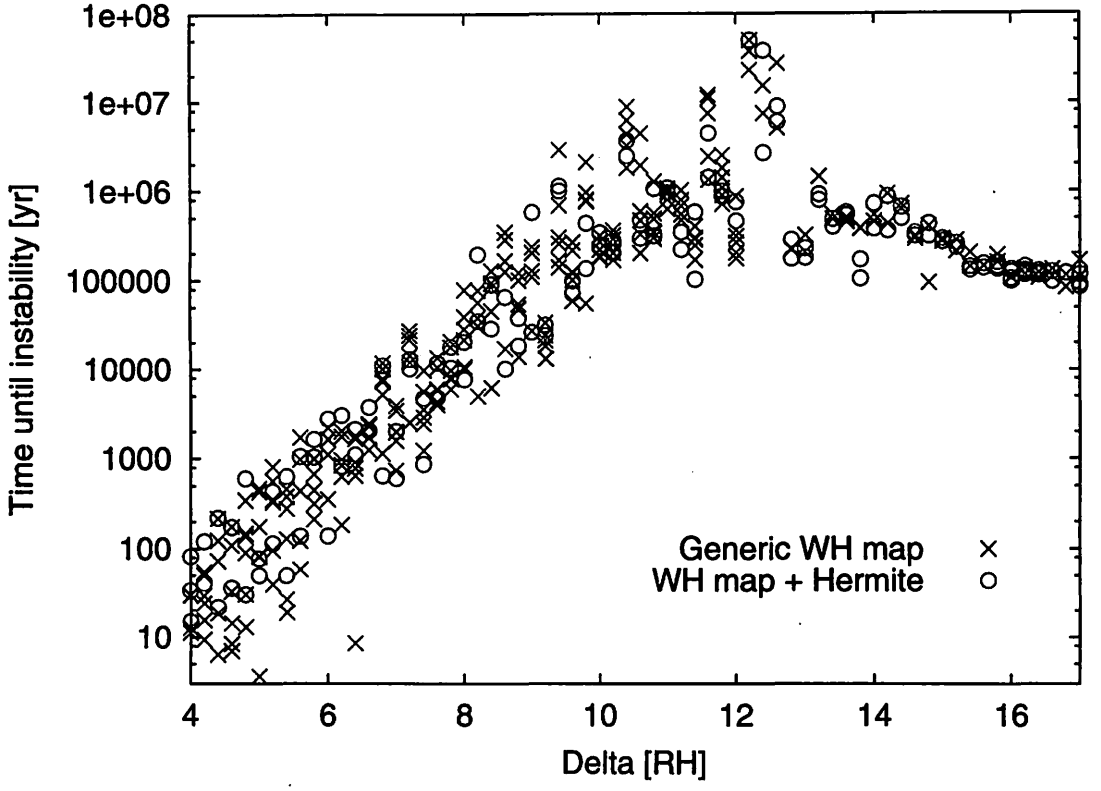

図 10. [A CWB diagram of terrestrial protoplanet systems (Ito & Tanikawa 1999)] 原始惑星系の CWB diagram の一例。横軸は相互 Hill 半径で規格化した原始惑星間の平均的間隔、縦軸は $1R_H$ 以内の近接遭遇が発生するまでの時間 (年)。×が generic な WH map での計算結果、○が generic な WH map と四次の Hermite scheme の混淆法での計算結果である。原始惑星の個数は 14, 最内天体の軌道半長径は 0.5AU, ランダム速度の初期値は $\langle e^2\rangle^{\frac{1}{2}} = 2\langle I^2\rangle^{\frac{1}{2}} = 0.005$ の Rayleigh 分布、原始惑星質量のばらつきは 10%, 間隔のばらつきは 0。パラメータの詳細については Ito & Tanikawa (1999) を参照のこと。

蛇足になるが、generic WH map が近接遭遇をどの程度まで扱えるのかを知る手掛りになる一例を示しておこう。SyMBA を提唱する Duncan et al. (1998) や Levison & Duncan (2000) によれば、二天体の相互 Hill 半径[4]の三倍以内程度 ($3R_H$) の近接遭遇が発生したら何らかの処置 (SyMBA 的な刻み幅の再帰分割やハミルトニアンの近接遭遇項の移動、あるいは force-center switching な

[4]二天体の質量を m_i, m_j, 主星 (質量 M) からの距離を r_i, r_j とすると、相互 Hill 半径 $R_H^{i,j}$ は以下のように定義さ

ど) を行うべきであるという記載がある。そのような忠告を無視し、Ito & Tanikawa (1999, 2001) では相互 Hill 半径の一倍 ($1R_H$) までの接近遭遇を刻み幅固定の WH map (warm start 付き) で計算した。対象となる系は地球型惑星領域の原始惑星系であり、木星と土星の摂動を考慮している。この時はまた、generic WH map で $1R_H$ までの近接遭遇を扱うことの妥当性を検証するために、二天体が $5R_H$ 以内に接近したら数値積分方法を WH map から四次の Hermite scheme へ変えた計算も行った。この場合にはシンプレクティク性の保存を犠牲にしていることになるが、近接遭遇の最中だけを取り出してみれば高い精度での計算が行われていると考えられる。ここでの generic WH map で用いた刻み幅は最内天体の公転周期の 1/20 程度であり、WH map を用いた標準的な数値積分にしばしば使われる値をそのまま採用した。近接遭遇を予期して予め刻み幅を小さくするような細工はしていない。この二通りの方法で数値積分を行い、初回の近接遭遇までに掛かった時間を (相互 Hill 半径で規格化した) 原始惑星の平均的間隔の関数として表示したのが図 10である[5]。縦軸の不安定時間が対数で描かれていることも理由のひとつだが、二者の計算方法で行った結果に定性的な違いはまったく無い。即ち $1R_H$ 程度までの近接遭遇であれば、generic WH map を用いても計算誤差についてそれほど神経質になることはないという結果が得られた。もちろんこれは、図 10のように多数の計算結果を並べて統計的な目で眺めたからこそ言える話である。個々の数値積分に関しては、generic WH map のみを用いた場合と Hermite scheme を併用した場合とで結果が大きく異なる場合があることもまた言を待たない。シンプレクティク数値積分法に限らず、どんなに高精度な数値積分法を用いたとしてもこの状況は同じである。

謝辞

今回の草津 N体研究会への参加にあたり、以下の方々には大変お世話になった。小久保英一郎さん (国立天文台理論天文学研究系) には講演を薦めていただき、荒木田英禎さん (総合研究大学院大学数物科学研究科天文科学専攻博士課程) には正則化の基本を教授をしていただき、谷川清隆さん (国立天文台理論天文学研究系) には講演の予行演習にて幾つかの重要な助言をいただき、吉田二美さん (神戸大学大学院自然科学研究科構造科学専攻博士課程) には MS PowerPoint の詳細な使用法を指導していただいた。この場を借りて深く御礼を申し上げる。

れる。

$$R_H^{i,j} = \left(\frac{m_i + m_j}{3M}\right)^{\frac{1}{3}} \left(\frac{r_i + r_j}{2}\right),$$

相互 Hill 半径は制限三体問題に於けるいわゆる Hill 近似から出て来る距離 (Nakazawa *et al.*, 1989a; Nakazawa *et al.*, 1989b; Gladman, 1993) であり、回転座標系上での天体の重力圏の大きさを表すものと思えば良い。

[5]図 10のようなダイアグラムは Chambers, Wetherill and Boss (1996) に於いて初めて示されたので、CWB diagram とも呼ばれる。Yoshinaga et al. (1999), Iwasaki et al. (2001) らも参照のこと。

参考文献

Agnor, C.B., Canup, R.M., and Levison, H.F. (1999) N-body simulations of late stage planetary formation with a simple fragmentation model, *Icarus*, **142**, 219–237.

Arakida, H. and Fukushima, T. (2000) Long-term integration error of Kustaanheimo-Stiefel regularized orbital motion, *Astron. J.*, **120**, 3333–3339.

Arakida, H. and Fukushima, T. (2001) Long-term integration error of Kustaanheimo-Stiefel regularized orbital motion. II. Method of variation of parameters, *Astron. J.*, **121**, 1764–1767.

Battin, R.H. (1987) *An Introduction to The Mathematics and Methods of ASTRODYNAMICS*, American Institute of Aeronautics and Astronautics, Inc., New York.

Breiter, S. (1999) Explicit symplectic integrator for highly eccentric orbits, *Celes. Mech. Dyn. Astron.*, **71**, 229–241.

Brumberg, V.A. (1995) *Analytical Techniques of Celestial Mechanics*, Springer-Verlag, New York.

Chambers, J.E. (1999) A hybrid symplectic integrator that permits close encounters between massive bodies, *Mon. Not. R. Astron. Soc.*, **304**, 793–799.

Chambers, J.E. and Murison, M.A. (2000) Pseudo-high-order symplectic integrators, *Astron. J.*, **119**, 425–433.

Chambers, J.E. and Wetherill, G.W. (1998) Making the terrestrial planets: N-body integrations of planetary embryos in three dimensions, *Icarus*, **136**, 304–327.

Danby, J.M.A. (1992) *Fundamentals of Celestial Mechanics (second edition, third printing)*, Willmann-Bell Inc., Richmond, Virginia.

Deprit, A. (1969) Canonical transformations depending on a small parameter, *Celes. Mech.*, **1**, 12–30.

Duncan, M.J., Levison, H.F., and Lee, M.H. (1998) A multiple time step symplectic algorithm for integrating close encounters, *Astron. J.*, **116**, 2067–2077.

Fukushima, T. (1996) A fast procedure solving Kepler's equation for elliptic case, *Astron. J.*, **112**, 2858–2861.

Fukushima, T. (1997a) A method solving Kepler's equation for hyperbolic case, *Celes. Mech. Dyn. Astron.*, **68**, 121–137.

Fukushima, T. (1997b) A method solving Kepler's equation without transcendental function evaluations, *Celes. Mech. Dyn. Astron.*, **66**, 309–319.

Fukushima, T. (1997c) A procedure solving the extended Kepler's equation for the hyperbolic case, *Astron. J.*, **113**, 1920–1924.

Fukushima, T. (1998) A fast procedure solving Gauss' form of Kepler's equation, *Celes. Mech. Dyn. Astron.*, **70**, 115–130.

Gladman, B. (1993) Dynamics of systems of two close planets, *Icarus*, **106**, 247–263.

Gladman, B., Duncan, M., and Candy, J. (1991) Symplectic integrators for long-term integrations in celestial mechanics, *Celes. Mech. Dyn. Astron.*, **52**, 221–240.

Hori, G. (1966) Theory of general perturbations with unspecified canonical variables, *Publ. Astron. Soc. Japan*, **18**, 287–296.

Hori, G. (1967) Non-linear coupling of two harmonic oscillations, *Publ. Astron. Soc. Japan*, **19**, 229–241.

Ito, T. (2000) *Stability and instability of planetary and protoplanetary systems*, PhD thesis, University of Tokyo, Tokyo.

Ito, T. and Tanikawa, K. (1999) Stability and instability of the terrestrial protoplanet system and their possible roles in the final stage of planet formation, *Icarus*, **139**, 336–349.

Ito, T. and Tanikawa, K. (2001a) Long-term integrations and stability of planetary orbits in our solar system, *Mon. Not. R. Astron. Soc.*, submitted.

Ito, T. and Tanikawa, K. (2001b) Stability of terrestrial protoplanet systems and alignment of orbital elements, *Publ. Astron. Soc. Japan*, **53**, 143–151.

Iwasaki, K., Tanaka, H., Nakazawa, K., and Emori, H. (2001) The gas-drag effect on the orbital instability of a protoplanet-system, *Publ. Astron. Soc. Japan*, **53**, 321–329.

Kinoshita, H., Yoshida, H., and Nakai, H. (1991) Symplectic integrators and their application to dynamical astronomy, *Celes. Mech. Dyn. Astron.*, **50**, 59–71.

Kokubo, E., Yoshinaga, K., and Makino, J. (1998) On a time-symmetric Hermite integrator for planetary N-body simulation, *Mon. Not. R. Astron. Soc.*, **297**, 1067–1072.

Kominami, J. and Ida, S. (2001) The effect of dynamical friction on formation of terrestrial planet, in *Proc. 33th Symp. Celes. Mech.*, National Astronomical Observatory, in press.

Laskar, J. and Robutel, P. (2000) High order symplectic integrators for perturbed Hamiltonian systems, preprint (astro-ph/0005074).

Lee, M.H., Duncan, M.J., and Levison, H.F. (1997) Variable time step integrators for long-term orbital integrations, *Astron. Soc. Pac. Conf. Ser.*, **123**, 32–37.

Levison, H.F. and Duncan, M.J. (1994) The long-term dynamical behavior of short-period comets, *Icarus*, **108**, 18–36.

Levison, H.F. and Duncan, M.J. (2000) Symplectically integrating close encounters with the Sun, *Astron. J.*, **120**, 2117–2123.

Levison, H.F., Lissauer, J.J., and Duncan, M.J. (1998) Modeling the diversity of outer planetary systems, *Astron. J.*, **116**, 1998–2014.

Makino, J. and Aarseth, S.J. (1992) On a Hermite integrator with Ahmad-Cohen scheme for gravitational many-body problems, *Publ. Astron. Soc. Japan*, **44**, 141–151.

Malhotra, R. (1994) A mapping method for the gravitational few-body problem with dissipation, *Celes. Mech. Dyn. Astron.*, **60**, 373–385.

Mikkola, S. (1997) Practical symplectic methods with time transformation for the few-body problem, *Celes. Mech. Dyn. Astron.*, **67**, 145–165.

Mikkola, S. (1998) Non-canonical perturbations in symplectic integration, *Celes. Mech. Dyn. Astron.*, **68**, 249–255.

Mikkola, S. (1999) Efficient symplectic integration of satellite orbits, *Celes. Mech. Dyn. Astron.*, **74**, 275–285.

Mikkola, S. and Innanen, K. (1999) Symplectic tangent map for planetary motions, *Celes. Mech. Dyn. Astron.*, **74**, 59–67.

Mikkola, S. and Palmer, P. (2000) Simple derivation of symplectic integrators with first order correctors, *Celes. Mech. Dyn. Astron.*, **77**, 305–317.

Mikkola, S. and Tanikawa, K. (1999) Explicit symplectic algorithms for time-transformed Hamiltonians, *Celes. Mech. Dyn. Astron.*, **74**, 287–295.

Nakazawa, K., Ida, S., and Nakagawa, Y. (1989a) Collisional probability of planetesimals revolving in the solar gravitational field I. Basic formulation, *Astron. Astrophys.*, **220**, 293–300.

Nakazawa, K., Ida, S., and Nakagawa, Y. (1989b) Collisional probability of planetesimals revolving in the solar gravitational field II. The validity of the two-body approximation, *Astron. Astrophys.*, **221**, 342–347.

Plummer, H.C. (1960) *An Introductory Treatise on Dynamical Astronomy*, Dover, New York.

Preto, M. and Tremaine, S. (1999) A class of symplectic integrators with adaptive time step for separable hamiltonian systems, *Astron. J.*, **118**, 2532–2541.

Rauch, K.P. and Holman, M. (1999) Dynamical chaos in the Wisdom-Holman integrator: origins and solutions, *Astron. J.*, **117**, 1087–1102.

Saha, P. and Tremaine, S. (1992) Symplectic integrators for solar system dynamics, *Astron. J.*, **104**, 1633–1640.

Saha, P. and Tremaine, S. (1994) Long-term planetary integrations with individual time steps, *Astron. J.*, **108**, 1962–1969.

Sanz-Serna, J.M. and Calvo, M.P. (1994) *Numerical Hamiltonian Problems*, Chapman & Hall, London.

Skeel, R.D. and Biesiadecki, J.J. (1994) Symplectic integration with variable stepsize, *Ann. Numer. Math.*, **1**, 191–198.

Stiefel, E.L. and Scheifele, G. (1971) *Linear and Regular Celestial Mechanics*, Springer-Verlag, New York.

Wisdom, J. and Holman, M. (1991) Symplectic maps for the N-body problem, *Astron. J.*, **102**, 1528–1538.

Wisdom, J. and Holman, M. (1992) Symplectic maps for the n-body problem: stability analysis, *Astron. J.*, **104**, 2022–2029.

Wisdom, J., Holman, M., and Touma, J. (1996) Symplectic correctors, in Marsden, J.E., Patrick, G.W., and Shadwick, W.F. eds., *Integration Algorithms and Classical Mechanics*, Vol. 10 of Fields Institute Communications, American Mathematical Society, Providence, Rhode Island, 217–244.

Yoshida, H. (1990a) Conserved quantities of symplectic integrators for Hamiltonian systems, preprint.

Yoshida, H. (1990b) Construction of higher order symplectic integrators, *Phys. Lett. A*, **150**, 262–268.

Yoshida, H. (1992) Symplectic integration for Hamiltonian systems: basic theory, in *Chaos, resonance and collective dynamical phenomena in the solar system*, Kluwer Academic publishers, Dordrecht, 407–412.

Yoshida, H. (1993) Recent progress in the theory and application of symplectic integrators, *Celes. Mech. Dyn. Astron.*, **56**, 27–43.

Yoshida, H. (2001) Non-existence of the modified first integral by symplectic integration method, *Phys. Lett. A*, **282**, 276–283.

Yoshinaga, K., Kokubo, E., and Makino, J. (1999) The stability of protoplanet systems, *Icarus*, **139**, 328–335.

戸田盛和 (1994) 一般力学 30 講, 物理学 30 講シリーズ, No. 1, 朝倉書店.

福島登志夫 (1982) Newton 反復に対する安定な出発値とその Kepler 方程式への応用, 第 15 回天体力学研究会集録, 国立天文台, 33–36.

吉田春夫 (1995) シンプレクティク数値解法, 数理科学, **384**, 37–46.

吉田春夫 (1997) ハミルトン力学系のためのシンプレクティク数値積分法, 共同研究「非線型現象の数理科学」・湘南レクチャー「非線型現象の数理」 論文集, 総合研究大学院大学, 68–83.

Symplectic数値解法の天体力学的応用
《ーユーザから見たレビューー》

伊藤孝士（国立天文台 データ解析センター）

$$H = H_A + H_B$$
$$H_A >> H_B$$

実際的、非網羅的、現象論的、羅列的、不誠実（?）

話の内容

- Symplectic積分法の復習
- 混合変数型 (WH map)
- warm start
- 近接遭遇への対処
  (DH, SyMBA, Hybrid, 修正SyMBA)
- 正則化 (KS変換)
- 補足・まとめ

目的(対象)別 Symplectic積分法の例

- 規則的(準周期的)で安定な軌道
  → Generic WH map — Wisdom & Holman (1991)
- 階層的で規則的な軌道 — 例. 太陽系の惑星運動
  → 独立刻み幅 — Saha & Tremaine (1992, 1994)
- 近接遭遇が頻発する系 — 例. 惑星集積過程 Duncan et al. (1998), Chambers (1999), Levison & Duncan (2000)
  → ポテンシャル分割, Hybrid
- 長楕円軌道、近接遭遇少 — 例. 彗星、人工衛星 Mikkola (1997, 1999), Mikkola & Tanikawa (1999)
  → 正則化

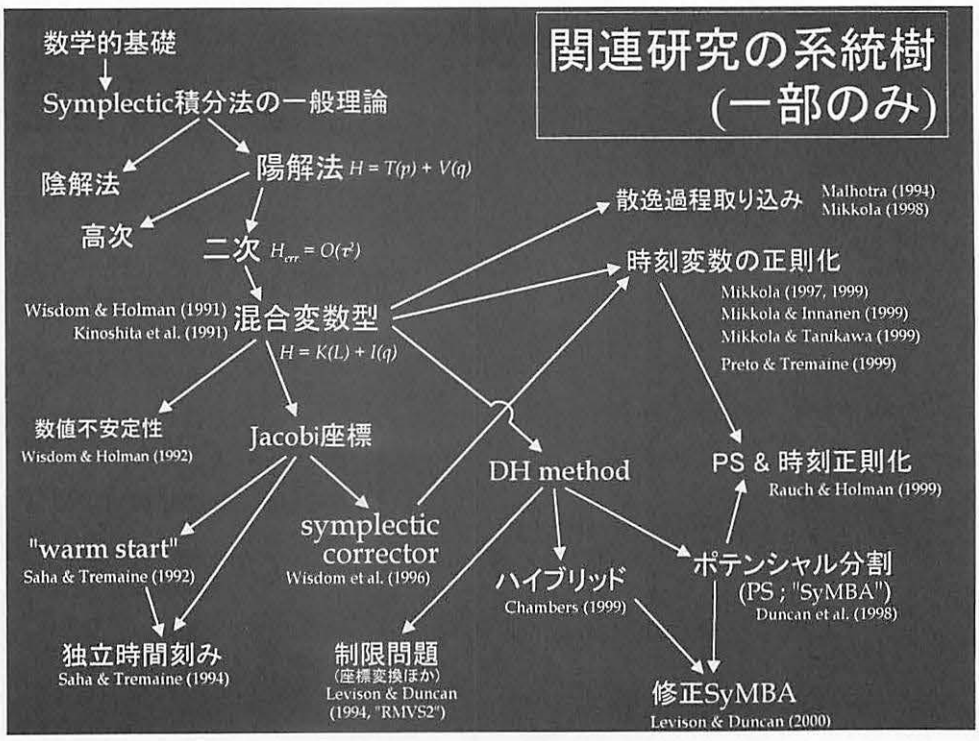

Symplectic積分法の復習

Yoshida (1993)ら

ハミルトンの運動方程式

$$\frac{dq}{dt} = \frac{\partial H}{\partial p}, \quad \frac{dp}{dt} = -\frac{\partial H}{\partial q}$$

Poisson括弧 $\{\ ,\ \}$ を使う $\quad \dfrac{dz}{dt} = \{z, H(z)\}$

微分演算子 $\{\ ,G\}$ を導入

$$\{\ , G\}\, F \equiv \{F, G\}$$

運動方程式は $\quad \dfrac{dz}{dt} = \{\ , H\}\, z$

$t=0$ から $t=\tau$ の形式解 $\quad z(\tau) = \left[e^{\tau\{\ , H\}}\right] z(0)$

分割可能なハミルトニアン $H = T(p) + V(q)$

T(p), V(q) それぞれは単独で積分可能

$$z_A(\tau) = \left[e^{\tau A}\right] z_A(0), \quad z_B(\tau) = \left[e^{\tau B}\right] z_B(0)$$

$$A \equiv \{\ , T\}, B \equiv \{\ , V\}$$

BCH公式を駆使した一次のsymplectic積分公式

$$e^{\tau\{\ ,T\}} e^{\tau\{\ ,V\}} = e^{\tau\left\{\ ,\tilde{H}_{1st}\right\}}$$

Surrogate Hamiltonian (代理ハミルトニアン)

$$\tilde{H}_{1st} = T + V + \frac{\tau}{2}\{T,V\} + \frac{\tau^2}{12}(\{\{T,V\},V\} + \{\{V,T\},T\}) + \frac{\tau^3}{24}\{\{\{T,V\},V\},T\} + \cdots$$

BCH公式を駆使した二次のsymplectic積分公式

$$e^{\frac{\tau}{2}\{\,,T\}}e^{\tau\{\,,V\}}e^{\frac{\tau}{2}\{\,,T\}} = e^{\tau\left\{\,,\tilde{H}_{2nd}\right\}}$$

Surrogate Hamiltonian

$$\tilde{H}_{2nd} = T + V + \tau^2\left(\frac{1}{12}\{\{T,V\},V\} - \frac{1}{24}\{\{V,T\},T\}\right) + O(\tau^4)$$

n 次公式の Surrogate Hamiltonian

$$\tilde{H}_n = H + H_{err} + O(\tau^{n+1})$$

Hamiltonianの分割は $H=T(p)+V(q)$ ばかりではない

. 分割可能かつ単独で積分可能ならば何でもOK

混合変数型の方法 (WH map)

中心天体の重力場が支配的な場合　Wisdom & Holman (1991)
Kinoshita et al. (1991)

$$H = H_{kep} + \epsilon H_{int}$$

$$H_{kep} = \sum_{i=1}^{N}\frac{\boldsymbol{p}_i^2}{2m_i}, \quad \epsilon H_{int} = -\sum_{i=1}^{N}\sum_{j=i+1}^{N}\frac{Gm_im_j}{|\boldsymbol{r}_i - \boldsymbol{r}_j|}$$

H_{kep}はDelauney変数で, εH_{int}は直交座標で積分可能

$$\begin{aligned} H &= H_{kep} + \epsilon H_{int} \\ &= \boxed{H_{kep}(L)} + \epsilon H_{int}(L,G,H,l,g,h) \\ &= H_{kep}(\boldsymbol{q},\boldsymbol{p}) + \boxed{\epsilon H_{int}(\boldsymbol{q})} \end{aligned}$$

二次のsymplectic積分公式

$$e^{\frac{\tau}{2}\left\{\,,H_{kep}\right\}}e^{\tau\{\,,H_{int}\}}e^{\frac{\tau}{2}\left\{\,,H_{kep}\right\}}$$

. 2種類の変数が混在 (要 座標変換)

誤差ハミルトニアン

$$H_{err} = \frac{\tau^2}{12}\{\{H_{kep}, \epsilon H_{int}\}, \epsilon H_{int}\} - \frac{\tau^2}{24}\{\{\epsilon H_{int}, H_{kep}\}, H_{kep}\} + O(\tau^4)$$

$$= \frac{\epsilon\tau^2}{24}\{\{H_{kep}, H_{int}\}, H_{kep}\} + O(\epsilon^2\tau^2) + O(\tau^4)$$

.同じ刻み幅で誤差が ε 倍に減少

新しい方法での刻み幅＝τ_{new}
従来の方法での刻み幅＝τ

H_{err}の主要項が同じ大きさと仮定→ $\epsilon\tau_{new}^2 \sim \tau^2$

例.太陽系の惑星運動 $\varepsilon \sim 10^{-3}$

$$\tau_{new} \sim \epsilon^{-\frac{1}{2}}\tau \sim 32\tau$$

cf. n 次の場合 $\tau_{new} \sim \epsilon^{-\frac{1}{n}}\tau$

低次の方法ほど高速化率が高い

混合変数型に分離したハミルトニアン

(1)ケプラー項部分 . $p^2/2m$ - μ/r の形, またはその和

(2)相互作用項部分 .相互距離のみの関数 $V(q)$

太陽中心または重心中心の座標系
→(1) を満たさない

例. 重心中心座標で書いたハミルトニアン

$$H = \sum_{i=0}^{N}\frac{\boldsymbol{p}_i^2}{2m_i} + \left(-\sum_{i=1}^{N}\frac{Gm_0m_i}{|\boldsymbol{r}_i-\boldsymbol{r}_0|} + \sum_{i=1}^{N}\frac{Gm_0m_i}{|\boldsymbol{r}_i-\boldsymbol{r}_0|}\right) - \sum_{i=0}^{N}\sum_{j=i+1}^{N}\frac{Gm_im_j}{|\boldsymbol{r}_i-\boldsymbol{r}_j|}$$

$$= \frac{\boldsymbol{p}_0^2}{2m_0} + \sum_{i=1}^{N}\left(\frac{\boldsymbol{p}_i^2}{2m_i} - \frac{Gm_0m_i}{|\boldsymbol{r}_i-\boldsymbol{r}_0|}\right) + \sum_{i=1}^{N}\frac{Gm_0m_i}{|\boldsymbol{r}_i-\boldsymbol{r}_0|} - \left(\sum_{j=1}^{N}\frac{Gm_0m_j}{|\boldsymbol{r}_0-\boldsymbol{r}_j|} + \sum_{i=1}^{N}\sum_{j=i+1}^{N}\frac{Gm_im_j}{|\boldsymbol{r}_i-\boldsymbol{r}_j|}\right)$$

$$= \boxed{\frac{\boldsymbol{p}_0^2}{2m_0}} + \sum_{i=1}^{N}\left(\frac{\boldsymbol{p}_i^2}{2m_i} - \frac{Gm_0m_i}{|\boldsymbol{r}_i-\boldsymbol{r}_0|}\right) - \sum_{i=1}^{N}\sum_{j=i+1}^{N}\frac{Gm_im_j}{|\boldsymbol{r}_i-\boldsymbol{r}_j|}$$

↳ H_{kep}, H_{int}のいずれにも分類不能

Jacobi座標

然るべき形にハミルトニアンを書き下す正準変数

$$\tilde{\boldsymbol{r}}_i = \boldsymbol{r}_i - \frac{1}{\sigma_{i-1}} \sum_{j=1}^{i-1} m_j \boldsymbol{r}_j \qquad \tilde{\boldsymbol{p}}_i = \tilde{m}_i \tilde{\boldsymbol{v}}_i$$

(i 番目天体の座標中心＝ i-1 番目天体までの重心)

$$\left[\begin{array}{c} \sigma_i = \sigma_{i-1} + m_i, \quad \sigma_0 = m_0 = M_\odot = 1, \quad \sigma_{-1} \equiv 0 \\ \tilde{m}_i = \frac{\sigma_{i-1}}{\sigma_i} m_i \qquad \tilde{\mu}_i = \frac{\sigma_i}{\sigma_{i-1}} G \qquad \tilde{\boldsymbol{v}}_i = \frac{d\tilde{\boldsymbol{r}}_i}{dt} \end{array} \right]$$

Jacobi座標で書いたハミルトニアン

$$H = H_{kep} + \epsilon H_{int}$$

$$\boxed{H_{kep} = \sum_{i=1}^{N} \left(\frac{\tilde{\boldsymbol{p}}_i^2}{2\tilde{m}_i} - \tilde{\mu}_i \frac{\tilde{m}_i m_0}{\tilde{r}_i} \right)}$$ ケプラー項

$$\epsilon H_{int} = H_{direct} + H_{indirect}$$ 相互作用

$$\boxed{H_{direct} = -\sum_{i=1}^{N} \sum_{j=i+1}^{N} \frac{G m_i m_j}{|\boldsymbol{r}_i - \boldsymbol{r}_j|}}$$ 直接項

$$\boxed{H_{indirect} = G \sum_{i=1}^{N} m_i m_0 \left(\frac{1}{\tilde{r}_i} - \frac{1}{r_i} \right)}$$ 間接項

Symplectic長期積分の例 Ito & Tanikawa (2001)

・太陽系の惑星運動（９惑星）
・約50億年×６種類

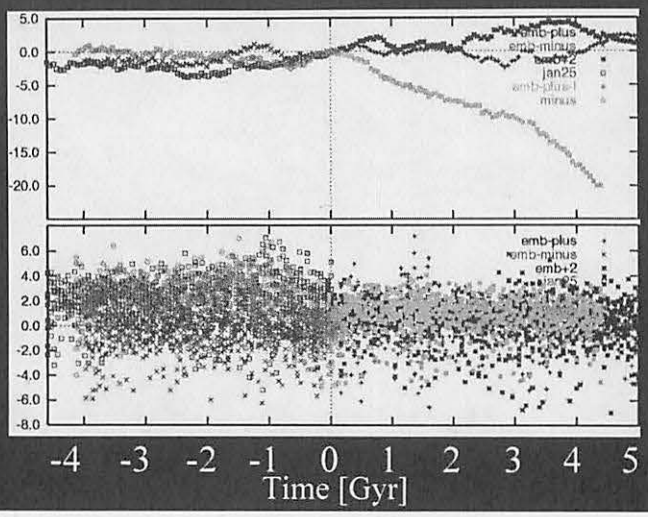

全角運動量
$\Delta L/L_0$
(10^{-11})

全エネルギー
$\Delta E/E_0$
(10^{-9})

角変数（惑星の経度など）の誤差要因

作用変数の“オフセット”

$$\left\langle \tilde{J} - J \right\rangle$$

例. $\Delta l \propto \int \frac{\Delta a}{a} n dt$

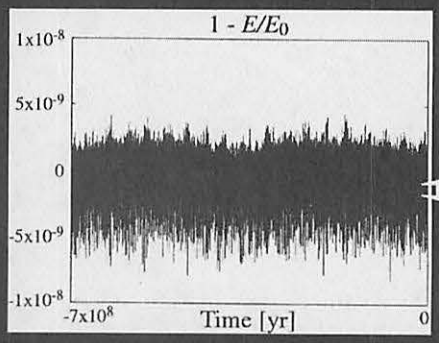

	Hamiltonian	作用変数
真の系	H	J
代理系	$\tilde{H}$	$\tilde{J}$

Warm Start の原理

刻み幅 $\tau \to 0$ の極限で

$$\tilde{H} \to H, \quad \tilde{J} \to J$$

徐々に刻み幅を増やす

$$\tilde{H}(\sim H) \to H + H_{err}$$

このとき作用変数の値は不変

$$\tilde{J} \sim J$$ （断熱不変量）

.角変数の永年誤差が減少する

Warm Start の実装

1. 非常に小さな刻み幅(τ_0)で計算を開始

$$\tilde{H} \to H, \quad \tilde{J} \to J$$

2. 徐々に(断熱的に)刻み幅を増やす

$$\tilde{H}(\sim H) \to H + H_{err}$$

3. 刻み幅が或る値(τ)になったら本積分を開始

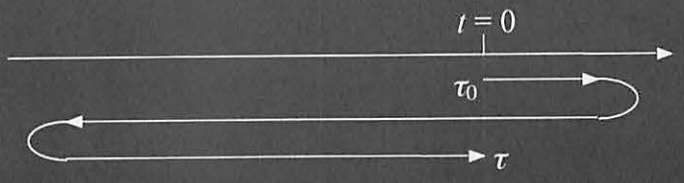

Saha & Tremaine (1992)

小惑星での例 Ito (2000)

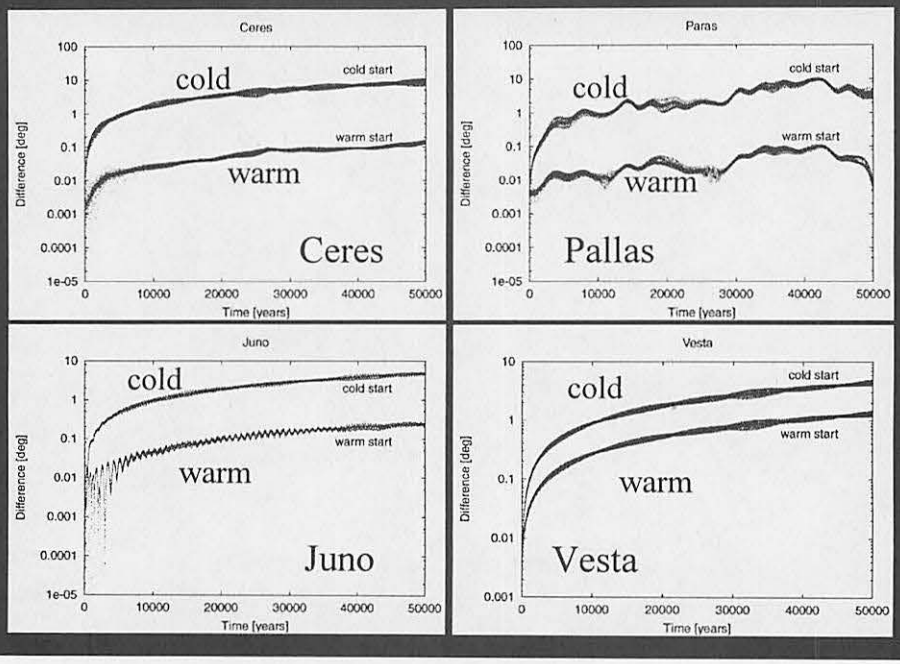

天体同志の近接遭遇がある場合

$$H_{direct} = -\sum_{i=1}^{N}\sum_{j=i+1}^{N}\frac{Gm_i m_j}{|\boldsymbol{r}_i - \boldsymbol{r}_j|}$$

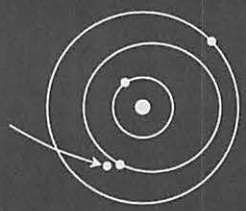

$H_{kep} >> H_{int}$ の仮定がもはや成り立たない

Generic WH map は使えない

---

(1) 刻み幅を細かくして凌ぐ

(2) 何とかして $H_{kep} >> H_{int}$ を維持する

(3) Symplectic以外の方法を考える

刻み幅を小さくして凌ぐ方法 (ポテンシャル分割)

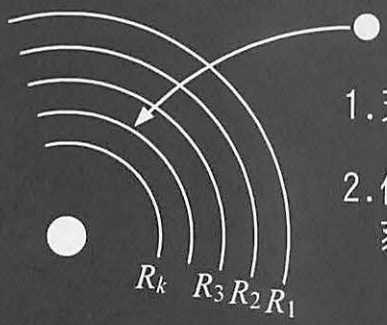

1. 天体の周囲に薄い殻を置く
2. 他の天体は殻を通過する毎に刻み幅を再帰的に減らす

ポテンシャル分割の概念 ($H = H_T + H_V$)

$$H_V = \sum_{k=0}^{\infty} V_k \quad (= -Gm_i m_j / r_{ij})$$

(実際にはポテンシャルではなく力を分割)

カットオフ半径R_kと力F_kの分割

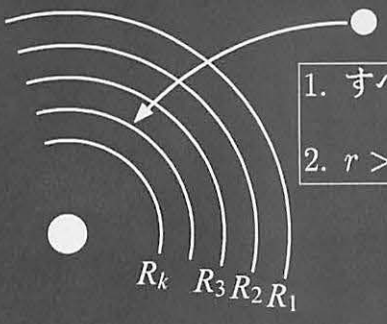

1. すべてのrに関して $\boldsymbol{F}(r) = \sum_{k=0}^{\infty} \boldsymbol{F}_k(r)$
2. $r > R_k$ $(k \geq 1)$ ならば $\boldsymbol{F}_k = 0$

(F_0を除く)

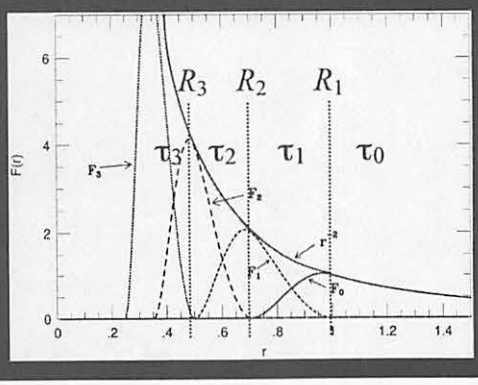

- F_kが関与するようになったら刻み幅を τ_k に変更
- τ_k / τ_{k+1} は固定された整数 (M)

Duncan et al. (1998)

例. 一回だけ再帰分割 ⇔ R_1以内の接近遭遇 ⇔V_1 (F_1)が関与

二次のスキームの例

$$e^{\tau_0\{\,,H\}} = \boxed{e^{\tau_0\left\{\,,H_T+V_0+\sum_{k=1}^{\infty}V_k\right\}}} \rightarrow \text{形式解} \qquad \text{Generic WH}$$

$$\approx \boxed{e^{\frac{\tau_0}{2}\{\,,V_0\}}e^{\tau_0\left\{\,,H_T+\sum_{k=1}^{\infty}V_k\right\}}e^{\frac{\tau_0}{2}\{\,,V_0\}}} \rightarrow \text{再帰的}M\text{分割}$$

$$\approx e^{\frac{\tau_0}{2}\{\,,V_0\}}\boxed{\left[e^{\frac{\tau_1}{2}\{\,,V_1\}}e^{\tau_1\left\{\,,H_T+\sum_{k=2}^{\infty}V_k\right\}}e^{\frac{\tau_1}{2}\{\,,V_1\}}\right]^M}e^{\frac{\tau_0}{2}\{\,,V_0\}}$$

第k階層の再帰分割による誤差ハミルトニアン

$$H_{err,k} = \frac{\tau_k^2}{12}\left\{\{V_k,H_T\},H_T+\frac{1}{2}V_k+\sum_{l=k+1}^{\infty}V_k\right\}+O(\tau_k^4)$$

再帰分割を繰り返した後の誤差ハミルトニアン

$$H_{err} = \sum_{k=0}^{\infty}\left[\frac{\tau_k^2}{12}\left\{\{V_k,H_T\},H_T+\frac{1}{2}V_k+\sum_{l=k+1}^{\infty}V_k\right\}+O(\tau_k^4)\right]$$

力$\boldsymbol{F}$の分割の具体例

便宜的なポテンシャルの書き直し

$$H_V = \sum_{k=0}^{\infty}V_k = \tilde{V}_0+(\tilde{V}_1-\tilde{V}_0)+(\tilde{V}_2-\tilde{V}_1)+\cdots$$

$$\tilde{V}_0 = V_0, \quad V_k = \tilde{V}_k-\tilde{V}_{k-1} \quad (k\geq 1), \quad \tilde{V}_k = \sum_{l=0}^{k}V_l$$

$\tilde{\boldsymbol{F}}_k = -\dfrac{\partial \tilde{V}_k}{\partial \boldsymbol{q}}$ が

1. $R_k < r$ では r^{-2}
2. $R_{k+1} \leq r \leq R_k$ でスムーズに減少
3. $r < R_{k+1}$ では0

を満たすように分割

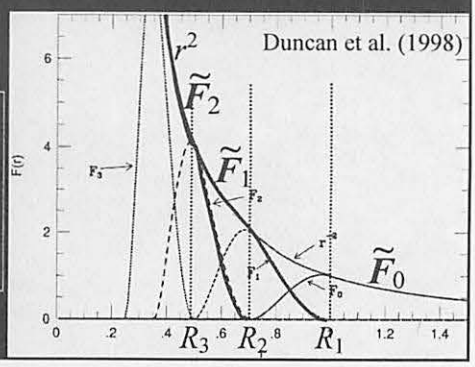

$\widetilde{F}_{k-1}$を好適に分割する関数の一例

$$\tilde{\boldsymbol{F}}_{k-1} = \begin{cases} -\dfrac{\boldsymbol{q}}{r^3} & (R_k \le r) \\ -f_l\left(\dfrac{R_k - r}{R_k - R_{k+1}}\right)\dfrac{\boldsymbol{q}}{r^3} & (R_{k+1} \le r < R_k) \\ 0 & (r < R_{k+1}) \end{cases}$$

$f_l(x)$ は x の $2l+1$ 次多項式

$f_l(0) = 1, \quad f_l(1) = 0$

$l = 1$: V_kの二階微分まで滑らか

$f_l(x) = 2x^3 - 3x^2 + 1$

$l = 3$: V_kの四階微分まで滑らか

$f_l(x) = 20x^7 - 70x^6 + 84x^5 - 35x^4 + 4$

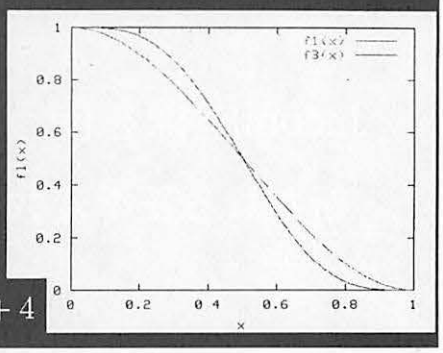

Generic WH mapへの応用

. 原理的には可能、しかし簡単ではない

Generic WH map の相互作用直接項 H_{dir}

$$H_{direct} = -\sum_{i=1}^{N}\sum_{j=i+1}^{N}\frac{Gm_im_j}{|\boldsymbol{r}_i - \boldsymbol{r}_j|}$$

→容易に分割可能な形

H_{dir} を分割して作る二次の再帰スキーム

$$e^{\tau_0\{\,,H_{kep}+H_{int}\}}$$

$$\approx e^{\frac{\tau_0}{2}\{\,,H_{int}\}}e^{\tau_0\{\,,H_{kep}\}}e^{\frac{\tau_0}{2}\{\,,H_{int}\}}$$

$$= e^{\frac{\tau_0}{2}\{\,,H_{ind}\}}e^{\frac{\tau_0}{2}\{\,,H_{dir}\}}e^{\tau_0\{\,,H_{kep}\}}e^{\frac{\tau_0}{2}\{\,,H_{dir}\}}e^{\frac{\tau_0}{2}\{\,,H_{ind}\}}$$

$$\approx e^{\frac{\tau_0}{2}\{\,,H_{ind}\}}\left[e^{\frac{\tau_1}{2}\{\,,H_{dir,1}\}}e^{\tau_1\{\,,H_{kep}+\sum_{i=2}^{\infty}H_{dir,i}\}}e^{\frac{\tau_1}{2}\{\,,H_{dir,1}\}}\right]^M e^{\frac{\tau_0}{2}\{\,,H_{dir}\}}$$

$$\approx \cdots$$

…うまく行かない

H_{indirect}も同時に再帰分割する必要あり

$$H_{indirect} = G\sum_{i=1}^{N} m_i m_0 \left(\frac{1}{\tilde{r}_i} - \frac{1}{r_i}\right)$$

Jacobi座標と太陽中心座標が混じっており、面倒

Jacobi座標を使うから物事がややこしい

新たなる正準変数の組を見い出す必要あり

PS法実装のためのJacobi座標以外の変数

・位置座標は太陽中心 (heliocentric)

・運動量は重心中心 (barycentric)

$$\boldsymbol{Q}_i = \begin{cases} \boldsymbol{q}_i - \boldsymbol{q}_0 & (i = 1, \cdots, n) \\ \dfrac{1}{m_{tot}} \displaystyle\sum_{j=0}^{n} m_j \boldsymbol{q}_j & (i = 0) \end{cases}$$

$$\boldsymbol{P}_i = \begin{cases} \boldsymbol{p}_i - \dfrac{m_i}{m_{tot}} \displaystyle\sum_{j=0}^{n} \boldsymbol{p}_j & (i = 1, \cdots, n) \\ \displaystyle\sum_{j=0}^{n} \boldsymbol{p}_j & (i = 0) \end{cases}$$

Democratic Heliocentric Method (DH)

(Mixed-centre coodinate)

DH座標で記述したハミルトニアン

$$H = H_{Kep} + H_{Sun} + H_{int}$$

$$H_{Kep} = \sum_{i=1}^{n} \left(\frac{|\boldsymbol{P}_i|^2}{2m_i} - \frac{Gm_i m_0}{|\boldsymbol{Q}_i|} \right)$$ ケプラー

$$H_{Sun} = \frac{1}{2m_0} \left| \sum_{i=1}^{n} \boldsymbol{P}_i \right|^2$$ 太陽の運動

$$H_{int} = -\sum_{i=1}^{n-1} \sum_{j=i+1}^{n} \frac{Gm_i m_j}{|\boldsymbol{Q}_i - \boldsymbol{Q}_j|}$$ 相互作用

DHを用いた二次のスキーム

$$e^{\frac{\tau}{2}\{\,,H_{Sun}\}} e^{\frac{\tau}{2}\{\,,H_{int}\}} e^{\tau\{\,,H_{Kep}\}} e^{\frac{\tau}{2}\{\,,H_{int}\}} e^{\frac{\tau}{2}\{\,,H_{Sun}\}}$$

1. H_{sun}由来の位置座標の変化, τ/2分 (linear drift)
2. H_{int}由来の運動量変化 (kick), τ/2分
3. H_{kep}配下の接触軌道上の運動 (drift), τ分
4. 再び kick, τ/2分
5. 再び linear drift, τ/2分

$$\frac{\tau}{2}\frac{\partial H_{Sun}}{\partial \boldsymbol{P}_i} = \frac{\tau}{2m_0}\sum \boldsymbol{P}_i$$

↑ 平行移動

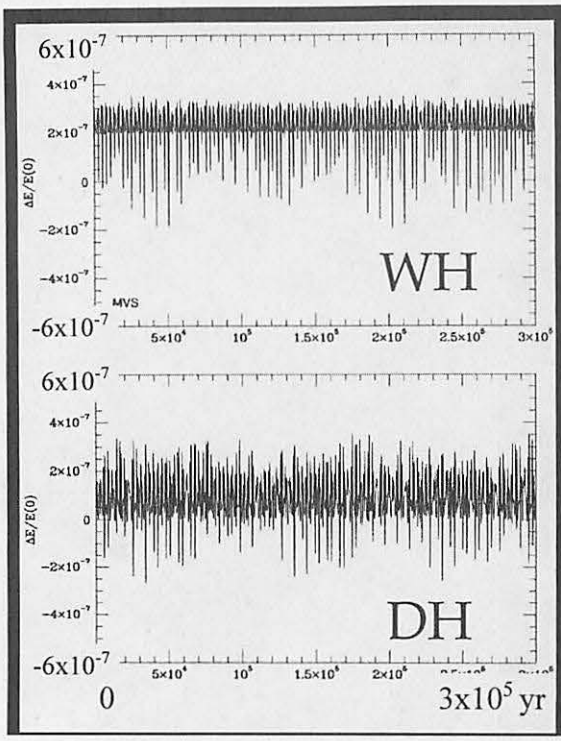

DHとWHの比較

$\Delta E/E_0$

木星型惑星４個

$\tau = 0.4$ yr

計算時間はほぼ同じ

Duncan et al. (1998)

Democratic Heliocentric
+
Potential Splitting

再帰型の二次スキーム

$$e_0^{\tau}\{\ ,\ H_{Sun}+H_{int}+H_{Kep}\}$$

→ 刻み幅τ_0の二次スキーム

$$\approx \boxed{e^{\frac{\tau_0}{2}\{\ ,H_{Sun}\}}e^{\frac{\tau_0}{2}\{\ ,H_{int}\}}e^{\tau_0\{\ ,H_{Kep}\}}e^{\frac{\tau_0}{2}\{\ ,H_{int}\}}e^{\frac{\tau_0}{2}\{\ ,H_{Sun}\}}}$$

$$\approx e^{\frac{\tau_0}{2}\{\ ,H_{Sun}\}}\left[e^{\frac{\tau_1}{2}\{\ ,H_{int,1}\}}e^{\tau_1\{\ ,H_{Kep}+\sum_{i=2}^{\infty}H_{int,i}\}}e^{\frac{\tau_1}{2}\{\ ,H_{int,1}\}}\right]^M e^{\frac{\tau_0}{2}\{\ ,H_{Sun}\}}$$

$\cdots$

→ 刻み幅を$\tau_1=\tau_0/M$に分割

Symplectic Massive Body Algorythm (SyMBA)

Duncan et al. (1998)

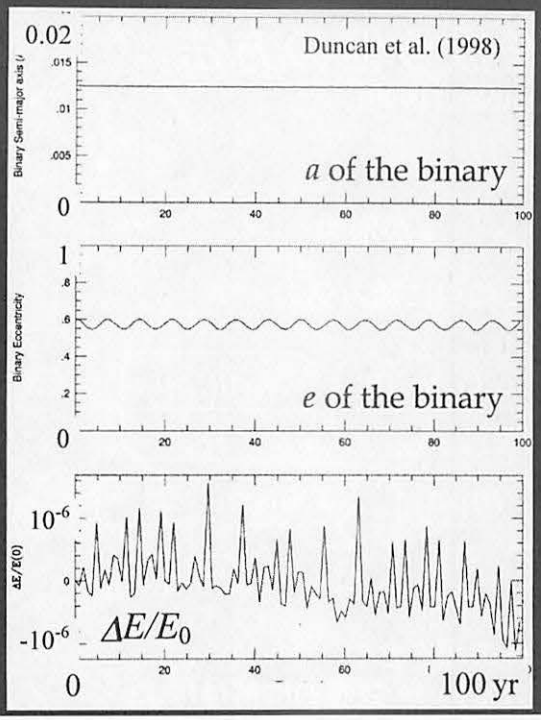

SyMBAの計算例 (連惑星)

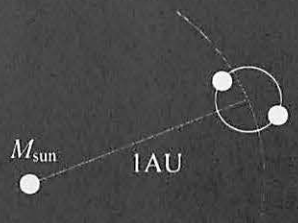

連惑星質量 $10^{-3}M_{\rm sun}\times 2$

連惑星 e_0= 0.6

連惑星 a_0= 0.0125AU

τ_0= 0.01 yr

再帰分割階層k = 4 - 6

誤差ハミルトニアン

$$H_{err}=\frac{\tau_0^2}{12}\left\{\{H_{Sun},H_{Kep}\},H_{Kep}+\frac{1}{2}H_{Sun}\right\}$$
$$+\sum_{k=0}^{\infty}\left[\frac{\tau_k^2}{12}\left\{\{V_k,H_{Kep}\},H_{Kep}+\frac{1}{2}V_k+\sum_{l=k+1}^{\infty}V_k\right\}+O(\tau_k^4)\right]$$

SyMBAの長所

・近接遭遇発生時には小さな刻み幅で計算
・それ以外では generic WH map と同程度の速度

SyMBAの短所

・大離心率の軌道を扱うのが苦手 ($H_{\rm Kep}\sim H_{\rm Sun}$)
・プログラムを書くのが大変

近接遭遇を扱う他の方法

Chambers (1999)

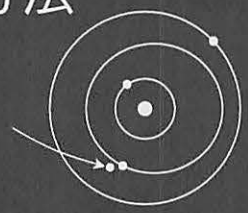

近接遭遇時 … $H_{\rm kep} \sim H_{\rm int}$

惑星α, βが接近 → $-Gm_\alpha m_\beta / r_{\alpha\beta}$ が増大

→ $-Gm_\alpha m_\beta / r_{\alpha\beta}$ を $H_{\rm kep}$に強引に組み込む

$$H_{Kep} = \sum_{i=1}^{N} \left(\frac{p_i^2}{2m_i} - \frac{Gm_\odot m_i}{r_{i\odot}} \right) - \frac{Gm_\alpha m_\beta}{r_{\alpha\beta}}$$

$$H_{int} = -G \sum_{i \neq \alpha} \sum_{j>i} \frac{m_i m_j}{r_{ij}} - \sum_{j>\alpha}^{j \neq \beta} \frac{m_\alpha m_j}{r_{\alpha j}}$$

$H_{\rm kep}$ はケプラー運動以外の項を含む
→ もはや解析的に解けない → 数値的に解けばよい

$H_{\rm kep}$と$H_{\rm int}$の間で滑らかに項を移動

$$H_{Kep} = \sum_{i=1}^{N} \left(\frac{p_i^2}{2m_i} - \frac{Gm_\odot m_i}{r_{i\odot}} \right) - G \sum_{i=1}^{N} \sum_{j=i+1}^{N} \frac{m_i m_j}{r_{ij}} [1 - K(r_{ij})]$$

$$H_{int} = -G \sum_{i=1}^{N} \sum_{j=i+1}^{N} \frac{m_i m_j}{r_{ij}} K(r_{ij})$$

(DHを使うため) $H_{Sun} = \frac{1}{2M_\odot} \left(\sum_{i=1}^{N} \boldsymbol{p}_i \right)^2$

切り替え関数 $K(r_{\rm ij})$：天体 i, j の近接遭遇に対応

$K(r_{ij})$ の一例

$$K = \begin{cases} 0 & (y < 0) \\ \dfrac{y^2}{2y^2 - 2y + 1} & (0 < y < 1) \\ 1 & (y > 1) \end{cases}$$

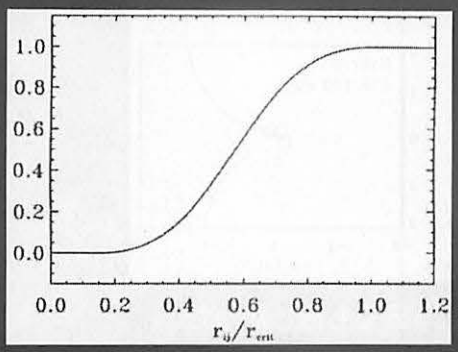

$$y = \frac{r_{ij} - 0.1 r_{crit}}{0.9 r_{crit}}$$

(r_{crit}はパラメータ)

Chambers (1999)

具体的なスキーム

$$e^{\frac{\tau}{2}\{\,,H_{Sun}\}} e^{\frac{\tau}{2}\{\,,H_{int}\}} e^{\tau\{\,,H_{Kep}\}} e^{\frac{\tau}{2}\{\,,H_{int}\}} e^{\frac{\tau}{2}\{\,,H_{Sun}\}}$$

1. H_{Sun} 由来の linear drift ($\tau/2$ 分)
2. $K(r_{ij})$ の重みが付いた H_{int} 由来の kick ($\tau/2$ 分)
3. [近接遭遇していない天体] $\tau/2$ 分の drift
   [近接遭遇している天体] 1-Kの重みを考慮した $\tau/2$ 分の drift を数値的に求める
4. 重み付き kick 再び ($\tau/2$ 分)
5. Linear drift 再び ($\tau/2$ 分)

解析的な方法と同様の精度が必要 → 機械εまでの補外法など

注・離心率が大きな軌道はやはり扱い難い

Hybrid methodの応用例

周期彗星 Oterma の木星接近

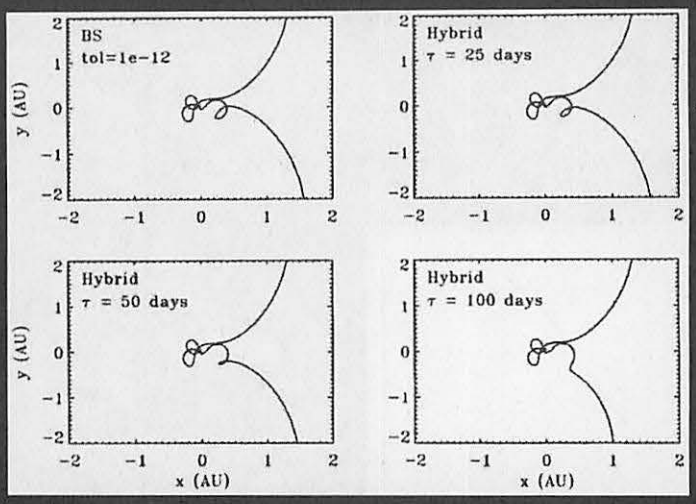

"BS"=補外法

$r_{crit} = 3r_{H,Jup}$

Chambers (1999)

「従来の WH map では τ=20日でも苦しかった。
Hybrid法を使えば τ=100日でも計算できる。」

SyMBA
Hybrid
} 近点距離が小さな軌道は苦手
(長い楕円軌道)

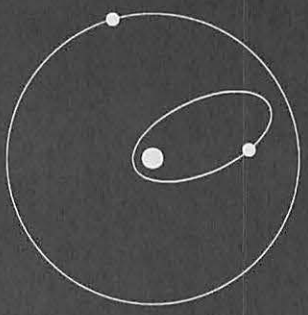

小さな近点距離
⇔中心星との近接遭遇

$$H = H_{kep} + H_{sun} + H_{int}$$

惑星同志の近接遭遇で↗
(PSで解決可能)

中心星との近接遭遇で↗
(Hybrid法の切り替え関数を持ち込む)

惑星の近点距離が小さくなったらH_{sun}の一部をH_{kep}に移動

修正SyMBA (SyMBA + Hybrid)

Levison & Duncan (2000)

$$H = H'_{Kep} + H'_{Sun} + H_{int}$$

$$H'_{Kep} = \sum_{i=1}^{n} \left(\frac{|\boldsymbol{P}_i|^2}{2m_i} - \frac{Gm_i m_0}{|\boldsymbol{Q}_i|} \right) + \frac{1}{2M_\odot} \left| \sum_{i=1}^{n} \boldsymbol{p}_i \right|^2 F(r_1, \cdots, r_n)$$

$$H'_{Sun} = \frac{1}{2m_0} \left| \sum_{i=1}^{n} \boldsymbol{P}_i \right|^2 [1 - F(r_1, \cdots, r_n)]$$

$$H_{int} = -\sum_{i=1}^{n-1} \sum_{j=i+1}^{n} \frac{Gm_i m_j}{|\boldsymbol{Q}_i - \boldsymbol{Q}_j|}$$

$F(r_1,...,r_n)$: Hybridの切り替え関数Kの拡張

$F(r_1,...,r_n)$ の一例

$$F(r_1, \cdots, r_n) = 1 - \prod_{i=1}^{n} [1 - f(r_i)]$$

$$f(r_i) = \begin{cases} 1 & (r_i < R_1) \\ 10\left(\frac{R_2 - r_i}{R_2 - R_1}\right)^6 - 15\left(\frac{R_2 - r_i}{R_2 - R_1}\right)^8 + 6\left(\frac{R_2 - r_i}{R_2 - R_1}\right)^{10} & (R_1 < r_i < R_2) \\ 0 & (r_i > R_2) \end{cases}$$

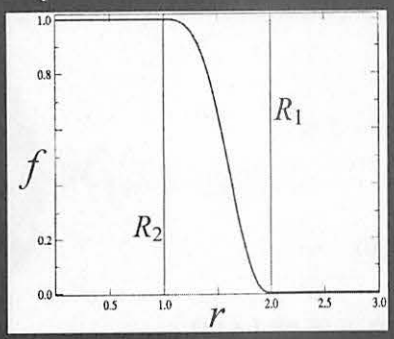

R_1, R_2 はパラメータ
(解くべき問題に依存)

滑らかであればあるほど
良い (導関数も)

Levison & Duncan (2000)

修正SyMBAでの計算例 (1)

・太陽＋木星＋土星

・土星の近点距離(⇔離心率)を変えて3000年計算

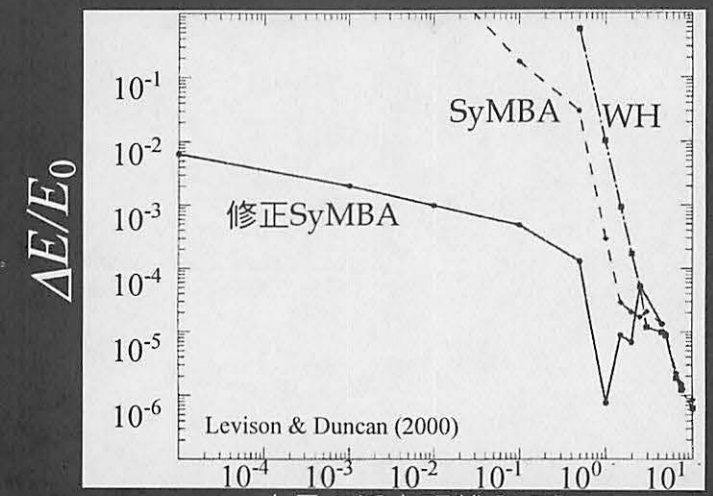

修正SyMBAでの計算例 (2)

・円制限三体問題 (太陽＋木星＋試験天体900個)

・10^4年間の計算でのJacobi定数Cの相対誤差

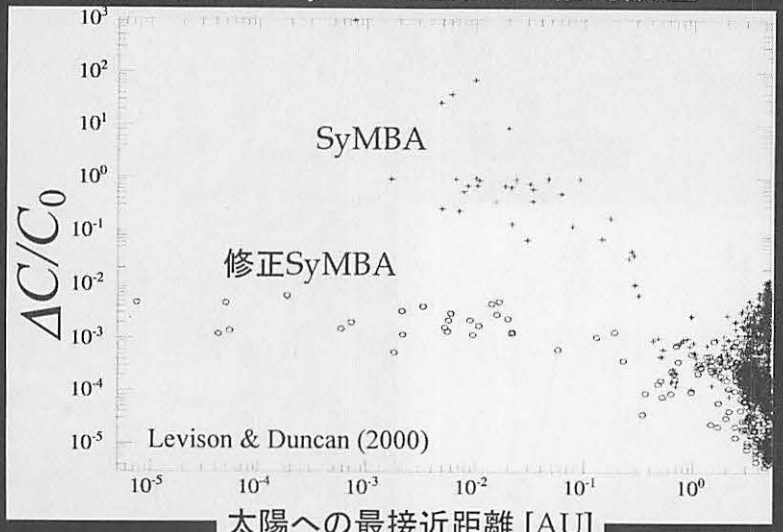

正則化しよう

WH map で長楕円軌道が扱い難い理由

時刻変数 t ∞ 平均近点離角 l

$l(t)$で均等分割 ⇔ 近点付近の解像度が悪い

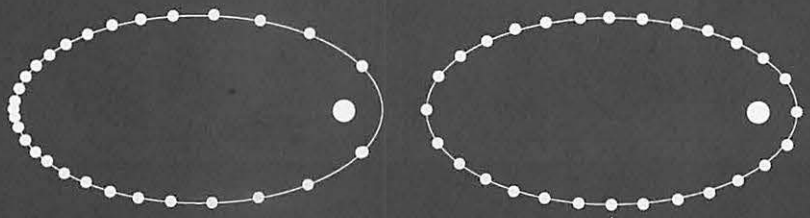

時刻変数を正則化して
近点付近の解像度を上げる

$$dt = g(r)ds$$

KS変換

時刻相当変数
∝ 離心近点離角(u)

時刻変数 $\dfrac{dt}{ds} = g(r)$ $\boxed{g(r) = r}$

座標

$$\boldsymbol{r} = (x, y, z) \longrightarrow \boldsymbol{u} = (u_1, u_2, u_3, u_4)$$

変換行列

$$\boldsymbol{r} = (x, y, z, 0) = L\boldsymbol{u} \qquad L = \begin{pmatrix} u_1 & -u_2 & -u_3 & u_4 \\ u_2 & u_1 & -u_4 & -u_3 \\ u_3 & u_4 & u_1 & u_2 \\ u_4 & -u_3 & u_2 & -u_1 \end{pmatrix}$$

ハミルトニアン

$$\Gamma = g(r)\left[H(\boldsymbol{q}, \boldsymbol{p}, q_0) + p_0\right]$$

$$p_0 = -H(0), \quad q_0 = t$$

正則化したWH mapでの計算例

階層的三体問題　Mikkola (1997)

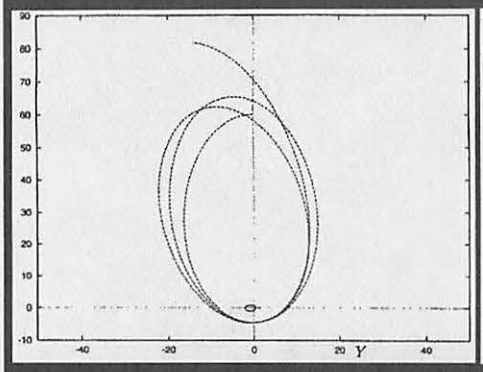

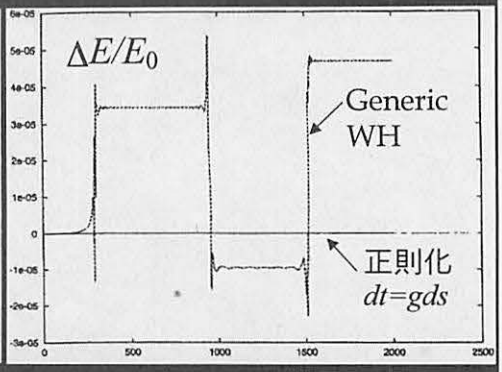

m_1=1, m_2=2, m_3=0.9

a_1=1.2, e_1=0.67

a_2=32, e_2=0.86

m_3の周期

注・この場合には
$g^{-1}=1/r_1 + 15/r_2$

正則化WH mapのもうひとつの長所

摂動二体問題的な系の場合には
Generic WH mapより速い

二体問題(ケプラー運動)を表す方程式

$$\frac{d^2\boldsymbol{r}}{dt^2} + \frac{\mu \boldsymbol{r}}{r^3} = 0$$

$$\frac{d^2\boldsymbol{u}}{ds^2} + \frac{h_k}{2}\boldsymbol{u} = 0$$

ケプラー運動から調和振動子へ

ケプラー方程式を解かなくても良い → 高速化

以下は補足事項など

補足1.

Generic WH map の drift ($H_{\rm kep}$)

→ほとんどがケプラー方程式の求解

$$\Delta l = \Delta u - e\cos u_0 \sin\Delta u + e\sin u_0 \left(1-\cos\Delta u\right)$$

例. 太陽系の惑星運動での計算量の比

drift ($H_{\rm kep}$) / kick ($H_{\rm int}$) ~ 3/7

- 離心率が小さい場合 . Newton法(二次収束), Halley法(三次収束)でも悪くはないが
- 離心率が大きい場合 . 従来の方法には問題が多い(収束が遅い、発散する、等)

福島登志夫氏による一連の仕事

- 福島(1980)．最適な初期値の選び方
- Fukushima (1996d, 1997a, 1997d, 1997g, 1998b)
  挟み撃ち法で近似解 → 三角関数を使わずに
  Newton法を適用して高速求解

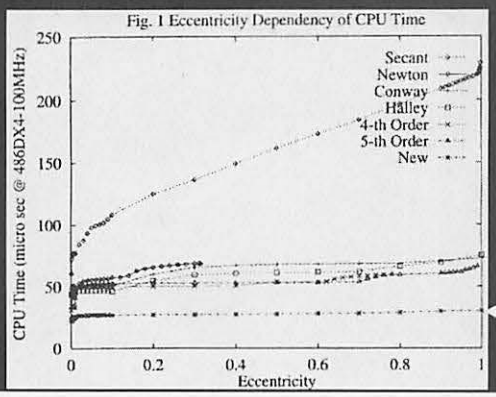

全離心率領域で
少なくとも二倍は
高速、かつ安定

← 福島方法 (1997d)

補足2. 独立刻み幅スキーム(概念のみ)

例. 太陽系の惑星運動

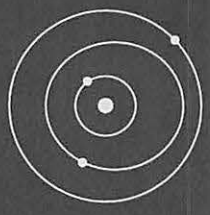

- 円軌道に近い
- 軌道交差・近接遭遇なし
- 階層構造に近い

全天体を同じ刻み幅で積分するのは勿体ない
→ 各天体に独立な刻み幅を割り振れないか？

$H = H_{kep} + H_{int}$

- H_{int} → 時計 I : 天体位置は不変。天体間で運動量を交換
- H_{kep} → 時計 K : 各天体が各自の接触軌道上をケプラー運動

惑星がN個ある場合 -- H_{kep}とH_{int}を分割

$$H_{kep} = \sum_{i=1}^{N} H_{kep,i}, \quad H_{int} = \sum_{i=1}^{N} H_{int,i}$$

$H_{kep,\,i}$: 天体 i のケプラー運動

$H_{int,\,i}$: 天体 i に対する天体 i+1, ..., N の相互作用

Generic WH map (N=2)

$\left\langle K_1\text{を}\frac{1}{2}\tau, K_2\text{を}\frac{1}{2}\tau\text{進める}\right\rangle$

$\quad\left\langle I_1\text{を}\tau\text{進める}\right\rangle$

$\quad\left\langle K_1\text{を}\tau, K_2\text{を}\tau\text{進める}\right\rangle$

$\quad\left\langle I_1\text{を}\tau\text{進める}\right\rangle$

$\left\langle K_1\text{を}\frac{1}{2}\tau, K_2\text{を}\frac{1}{2}\tau\text{進める}\right\rangle$

再帰呼び出しで独立刻みを実現

Saha & Tremaine (1992)

- 天体 i は刻み幅 τ_i
- τ_i/τ_{i-1} は整数

N体系の時間発展(τ_N間)

Call TICK(N)

procedure TICK(i)

$\quad\left\langle K_i\text{を}\frac{1}{2}\tau_i\text{進める}\right\rangle$

$\quad\left\langle I_i\text{を}\tau_i\text{進める}\right\rangle$

$\quad$**if** $i > 1$

$\quad\quad$**loop** τ_i/τ_{i-1} 回

$\quad\quad\quad$**call** TICK($i-1$)

$\quad\quad$**end loop**

$\quad$**end if**

$\quad\left\langle K_i\text{を}\frac{1}{2}\tau_i\text{進める}\right\rangle$

end TICK

$N=2$での例

独立刻み	共通刻み
Call TICK(2) : $\tau_2/2 = \tau_1 = \tau$	$\tau_2 = \tau_1 = \tau$
$\langle K_1$を$\frac{1}{2}\tau_1, K_2$を$\frac{\tau_2}{2}$進める$\rangle$	$\langle K_1$を$\frac{1}{2}\tau, K_2$を$\frac{1}{2}\tau$進める$\rangle$
$\langle I_1$をτ_1進める$\rangle$	$\langle I_1$をτ進める$\rangle$
$\langle K_1$をτ_1進める$\rangle$	$\langle K_1$をτ, K_2をτ進める$\rangle$
$\langle I_1$をτ_1進める$\rangle$	$\langle I_1$をτ進める$\rangle$
$\langle K_1$を$\frac{1}{2}\tau_1, K_2$を$\frac{\tau_2}{2}$進める$\rangle$	$\langle K_1$を$\frac{1}{2}\tau, K_2$を$\frac{1}{2}\tau$進める$\rangle$
K_1 : 3回	K_1 : 3回
K_2 : 2回	K_2 : 3回
I_1 : 2回	I_1 : 2回

どれくらい速くなるか

$\Delta t_{K,i}$　時計K_iを 1 step 進めるのに必要な計算時間

$\Delta t_{I,i}$　時計I_iを 1 step 進めるのに必要な計算時間

共通刻み幅スキームとの計算時間の比

$$\frac{\sum_{i=1}^{N}\left[\frac{\Delta t_{K,i}}{\tau_i}+(N-i)\frac{\Delta t_{I,i}}{\tau_i}\right]}{\frac{N\Delta t_K}{\tau}+\frac{N(N-1)\Delta t_I}{2\tau}}=\begin{cases}0.28 & (\text{if } \Delta t_K \gg \Delta t_I)\\ 0.46 & (\text{if } \Delta t_K \ll \Delta t_I)\end{cases}$$

準周期的・低離心率・階層的構造の系では使えるか

(まとめに代えて)

で結局、どれが良いのか？

万能な方法はない

- あちこちで近接遭遇がなく摂動二体系に近い場合　→正則化すべし
- 至る所で頻繁な近接遭遇が発生する系
  - 現在のところは修正SyMBAか？
    - + Force-Center Switching
    - + 正則化
    - によって高精度化が実現される可能性あり

(Rauch & Holman 1999)

とは言え

近接遭遇が頻繁に生じれば....

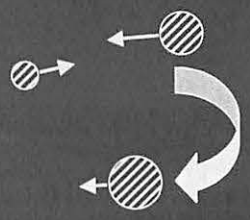

→早晩の衝突合体は必至

→Symplecticityなど彼岸の話

→Hermite scheme等の方が研究の turn-around time は短いことだろう

見識を持ってSymplectic積分法を使おう

補足3. プログラムパッケージ

SWIFT (SyMBAら)
H. Levison, M.J. Duncan らのグループが開発

MERCURY (Hybrid, 補外法ら)
J.E. Chambers らのグループが開発

本格的に使う人には、勧めません

算法を理解して自分で書きましょう

Special thanks to




E. Kokubo
K. Tanikawa
H. Arakida
F. Yoshida

THE DYNAMICS OF CIRCUMBINARY DISK WITH HIGH ECCENTRICITY BINARY

YUSUKE IMAEDA
Division of Theoretical Astrophysics
National Astronomical Observatory, Japan
Mitaka, Tokyo, 181-8588, Japan
imaeda@th.nao.ac.jp

AND

SHU-ICHIRO INUTSUKA
Department of Physics, Kyoto University
Kitashirakawa, Sakyo-ku, Kyoto, 606-8502, Japan
inutsuka@tap.scphys.kyoto-u.ac.jp

ABSTRACT

We investigate the tidal interaction between the circumbinary disk and the binary system with high eccentricity. Our investigation is focused on the final phase of the binary formation, when the gap between the binary star and the inner edge of the circumbinary disk is so large that the mass accretion from the circumbinary disk to the binary star is effectively terminated. From the numerical calculation with our modified SPH method specifically designed for modeling the shear flows, we have found that the $m = 1$ density enhancement is generated in the circumbinary disk if the eccentricity is sufficiently high. The density peak is always located at nearly 270° from the apastron of the secondary star. A simple analytical consideration shows that this standing structure is generated by the static component ($l = 0$ mode) of the $m = 1$ harmonic potential of the binary system. The interaction with ($m = 1, l = 0$) harmonic potential may play an important role in further mass accretion from the disk to the binary, since it enhances the eccentricity of the gas motion in the disk and provides a chance for more effective tidal interactions.

Subject headings: binary: formation, hydrodynamics, method: numerical

1. INTRODUCTION

Most of the stars in the Galaxy are the members of binary system or multiple system (Mathieu 1994). Its frequency may reach 80% in some estimation. Therefore, the investigation of the binary formation is as important as the single star formation to understand the star formation theory. It is worth noting that most of the binary have significantly large eccentricity. To study the effect of the high eccentricity is also important in the context of the comparison with the observation.

The effect of the binary on the gaseous disk has been investigated both analytically and numerically. We can find many analytical works about the interaction of the binary and the gaseous disk (Goldreich & Tremaine 1978a,b, 1979, 1980, 1981, 1982), but its application is limited to $e \sim 0$ since the treatment is linear. It is necessary to perform the non-linear calculation to investigate the high eccentricity binary. Artymowicz & Lubow (1994) has investigated the disk truncation process of the protoplanetary disk. They have used the standard SPH method as a numerical method and have found that the protoplanetary disk is truncated by the tidal effect and the circumbinary disk is formed. They have found that the truncation radius becomes $r_{\rm tr} \sim 3a$, where a is the semimajor axis of the binary. However, they did not argue the disk structure itself and concentrated on the truncation of the disk and the mass accretion flow from the disk to the binary (Artymowicz & Lubow 1996).

In this work, we investigate the later phase in the binary formation process. We calculate the disk dynamics after the disk is truncated tidally. This is the stage that the binary stars have been sufficiently evolved, already, and the mass accretion from the disk to the binary has been effectively terminated. We focus on the disk structure and investigate what structure is formed in the circumbinary disk due to the high eccentricity. We show the numerical method and results in §2. Analytic consideration about the numerical results are shown in the §3 and §4 is the summary.

2. EVOLUTION OF CIRCUMBINARY DISK WITH HIGHLY ECCENTRIC BINARY

We investigate the effect of the binary with high eccentricity on the circumbinary disk. When the binary has large eccentricity, the analytical treatment becomes quite difficult. Its application is limited only in the case of small eccentricity ($e \sim 0$). Therefore, we approach this process numerically.

2.1. *Numerical Method*

Artymowicz & Lubow (1994, 1996) investigated the evolution of the circumbinary disk with high eccentricity binary. They adopted standard SPH as the calculation method, which is widely used in the astrophysical hydrodynamics calculation. However, as we have pointed out in Imaeda & Inutsuka (2001a), the standard SPH method is quite inaccurate to study the long-term evolution of shear flows. It cannot follow the accurate density evolution. The error becomes as large as the initial density itself within the dynamical time scale. Thus, we use our newly im-

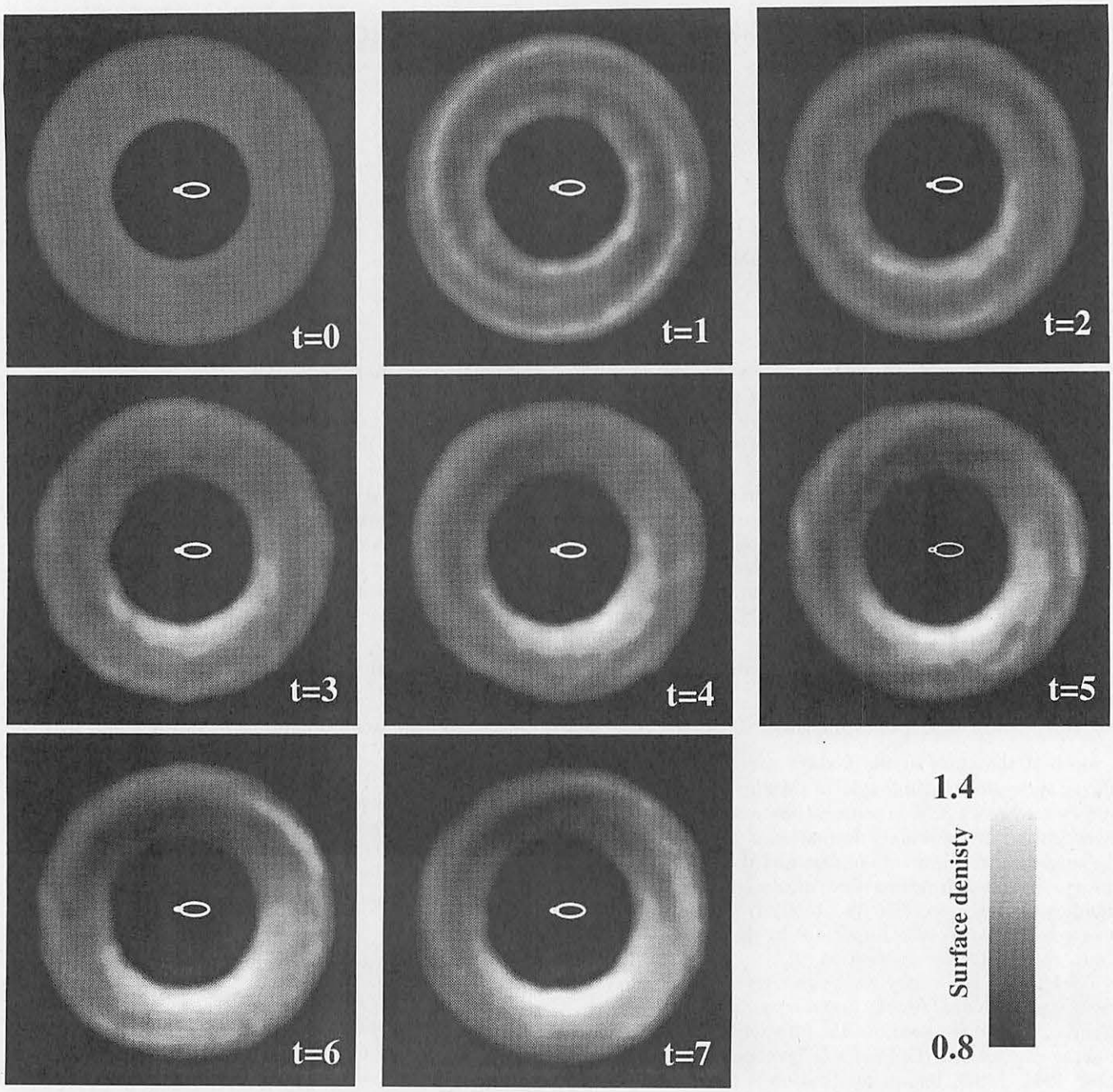

FIG. 1.— The evolution of the surface density of the circumbinary disk with high eccentricity binary. This is the extreme case of $e = 0.9$. We use the modified SPH for shear flows as the calculation scheme. The mass ratio of the binary is 4 : 1 and the semimajor axis of the binary is 0.173. The inner boundary is located at $r = 0.6$, while the outer boundary is located at $r = 1.4$. This means that we choose the truncation radius as $r_{\rm tr} \sim 3a$. We adopt free boundary condition. Typical gas temperature is $c_{s0} = 0.05$, which is normalized by the typical Kepler velocity, and two-dimensional approximation is adopted. Time is measured at the middle of the circumbinary disk, r=1. The white circles represent the orbit of the binary. The results are shown in the inertial frame. As the time proceeds, $m = 1$ standing wave emerges on the circumbinary disk, whose peak is roughly located at $\theta = 270°$ from the secondary apastron.

proved SPH method, which is suitable for the shear calculation. Our improvement reduces the density error to the acceptable level, which is due to assuring of local mass conservation property in the scheme. The precise procedure of the improved SPH calculation is elaborated in Imaeda & Inutsuka (2001a).

2.2. *Initial Conditions*

We calculate the gravitational interaction between the circumbinary disk and the eccentric binary. We start our calculation when the protoplanetary disk is truncated by the binary and the circumbinary disk is formed. The initial conditions of the calculation are the followings:

The semimajor axis of the binary is $a = 0.173$ for all the case. The mean motion of the binary is given by

$$\Omega_B = \sqrt{\frac{GM}{a^3}}, \tag{1}$$

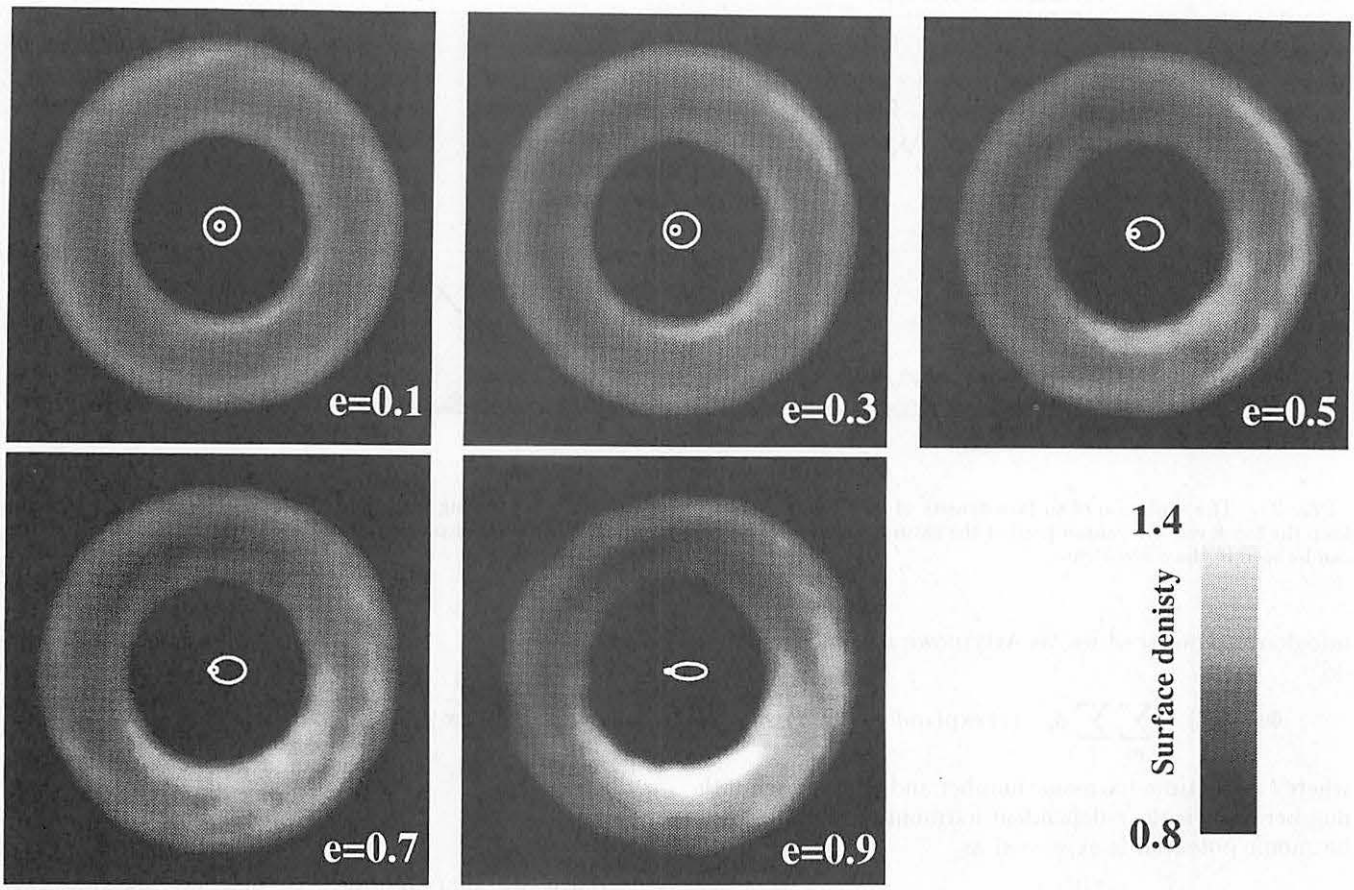

FIG. 2.— Surface density after seven rotational period of the circumbinary disk. Time is measured at the middle of the annulus ring. The eccentricity of the binary orbit ranges from 0.1 to 0.9. We observe the results in the inertial frame where the disk and the binary rotate in counter clockwise direction. The white circles represent the binary orbits. The mass ratio is 4 : 1. We can clearly see the $m = 1$ density structure in the high eccentricity case. The density peak emerges at $\sim 270°$ from the secondary apastron. This density structure does not rotate when we observe in the inertial frame.

where M is the total mass of the binary. Therefore, time periodicity of each simulation is identical. The mass ratio of the binary is 4 : 1 and the eccentricity is varied from $e = 0.1$ to $e = 0.9$. As a circumbinary disk, we consider the constant density disk, where we choose this constant value unity. At the inner and the outer boundaries, the density distribution has sharp edges, so that the disk model is an annulus ring. The inner boundary is located at $r = 0.6$, while the outer boundary is located at $r = 1.4$. This means that we choose the truncation radius as $r_{\rm tr} \sim 3a$. We adopt free boundary condition. Time is measured at the middle of the annulus ring, $r = 1$. Typical gas temperature is $c_{s0} = 0.05$, which is normalized by the typical Kepler velocity. Since the temperature of the disk is sufficiently low, we adopt two-dimensional calculation. We also neglect the self-gravity of the circumbinary disk since we are considering the latest phase of the binary evolution and expect that the disk is less massive than the total mass of the binary. Since the inner boundary of the circumbinary disk is distant from the binary orbit, gas accretion from the circumbinary disk to the binary is negligible. Starting from these initial conditions, we calculate the time evolution of the circumbinary disk. We observe the results in the *inertial frame* in which the disk and the binary rotate in *counter clockwise* direction.

2.3. *Numerical Results*

Figure 1 shows the surface density evolution of $e = 0.9$ case. We observe the results in the inertial frame. We can clearly see the $m = 1$ density structure in the circumbinary disk and this density structure does not rotate as the time proceeds. It appears as a standing wave and the density peak is roughly located at $\sim 270°$ from the secondary apastron. Figure 2 shows the surface density distribution after 7 rotational period for each eccentricity model. The amplitude of the $m = 1$ density mode is large when the eccentricity is large. We show the amplitude evolution of each mode in Figure 3. While the $m = 1$ mode is evolving, the amplitude of the other modes keep the low level. We cannot predict the saturation level of the $m = 1$ surface density in our present results, but the tendency of saturation can be seen in the $e = 0.7$ case.

3. ANALYTIC CONSIDERATION

To understand why the $m = 1$ mode emerges, we consider the results analytically.

3.1. *Decomposition of Gravitational Potential of Binary*

The binary motion is periodic about the θ-direction and the t-direction. We can decompose the external potential

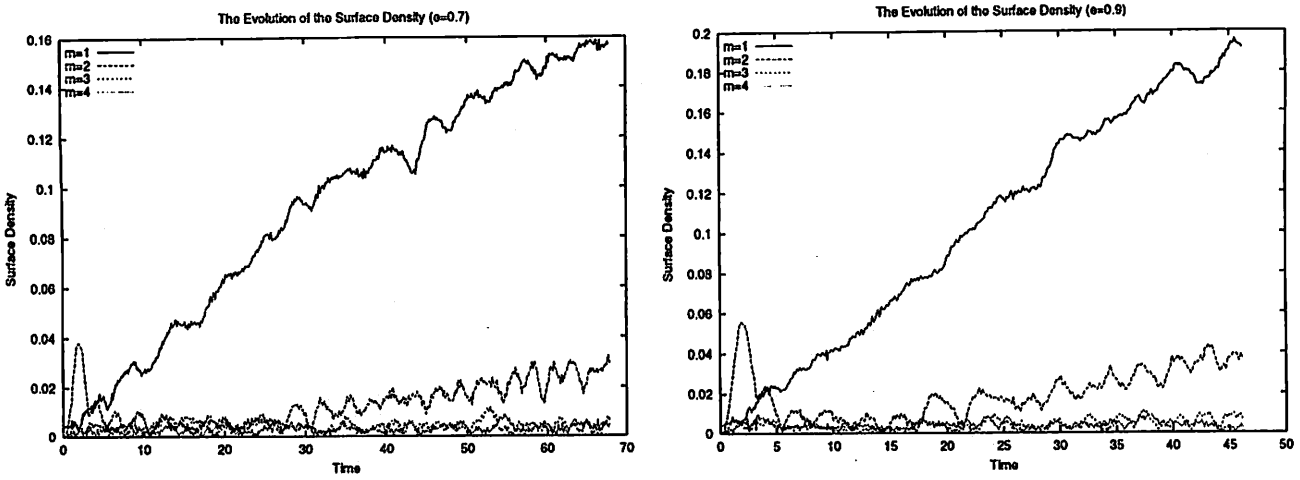

FIG. 3.— The evolution of surface density of each mode. While the $m = 1$ mode is evolving with time, the amplitude of the other modes keep the low level. We cannot predict the saturation level of the $m = 1$ surface density in our present results, but the tendency of saturation can be seen in the $e = 0.7$ case.

into double Fourier series, as Artymowicz & Lubow (1994) do,

$$\Phi(r,\theta,t) = \sum_m \sum_l \phi_{m,l}(r) \exp(im\theta - il\Omega_B t), \quad (2)$$

where l is the time-harmonic number and m is the azimuth number. $\phi_{m,l}$ is the r-dependent harmonic potential. Each harmonic potential is expressed as

$$\phi_{m,l}(r) = \frac{\Omega_B}{4\pi^2} \int_0^{2\pi/\Omega_B} dt \times \int_0^{2\pi} d\theta\ \Phi(r,\theta,t)\ \exp(-im\theta + il\Omega_B t), \quad (3)$$

and each (m,l) harmonic potential has the pattern speed of

$$\Omega_{m,l} = \frac{l}{m}\Omega_B. \quad (4)$$

Since the total potential is given by the sum of each gravitational source as

$$\Phi(r,\theta,t) = \sum_j -\frac{GM_j}{|r - r_j|} = -\frac{GM}{r} \sum_j \frac{q_j}{\sqrt{1 + \beta_j^2(t) - 2\beta_j(t)\cos(\theta - \theta_j(t))}}, \quad (5)$$

where

$$\beta_j(t) = \frac{r_j(t)}{r}. \quad (6)$$

we can write the (m,l) harmonic potential as

$$\phi_{m,l}(r) = -\frac{GM}{r} \sum_j q_j \times \frac{\Omega_B}{2\pi} \int_0^{2\pi/\Omega_B} F_{j;m}(t) \exp\left(-im\theta_j(t) + il\Omega_B t\right) dt, \quad (7)$$

where

$$F_{j;m}(t) = \frac{1}{2\pi} \int_0^{2\pi} \frac{\exp(-im\theta')}{\sqrt{1 + \beta_j(t)^2 - 2\beta_j(t)\cos\theta'}} d\theta'. \quad (8)$$

In equation (8), θ' is the angle from the j-th gravity source,

$$\theta' = \theta - \theta_j. \quad (9)$$

When the binary motion is circular, the equation (8) returns the constant value, since the distance from the mass center becomes constant. The exponent of equation (7) becomes

$$-im\theta_j(t) + il\Omega_B t = -i(m - l)\Omega_B t - im\theta_j(0). \quad (10)$$

Therefore, only the $m = l$ harmonic potentials have non-zero values, and f the other harmonic potentials vanish.

However, the situation is changed for the eccentric binary. In addition to $m = l$ harmonics, $l = m \pm 1$, $l = m \pm 2$, $l = m \pm 3$, $\cdots$ harmonic potentials have non-zero values and every harmonic potential contributes the angular momentum transport. The effect of $m \neq l$ potentials is essentially important in the case of eccentric binary.

3.2. *Corotation Resonance and Lindblad Resonance*

The binary and the disk interact each other through the location of resonance. The energy and the angular momentum are transferred through this interaction. There are two types of resonance. One is *corotation resonance* and the other is *Lindblad resonance.*

The corotation resonance occurs at the location where the pattern speed of the harmonic potential coincides with the rotational velocity of the fluid element,

$$\Omega(r) = \Omega_{m,l} = \frac{l}{m}\Omega_B, \quad (11)$$

where $\Omega_{m,l}$ is the pattern speed of (m,l) harmonic potential. When we view the (m,l) harmonic potential from the rotational frame with the angular velocity of $\Omega(r_{CR})$, it seems to be a static potential. Thus, the fluid elements

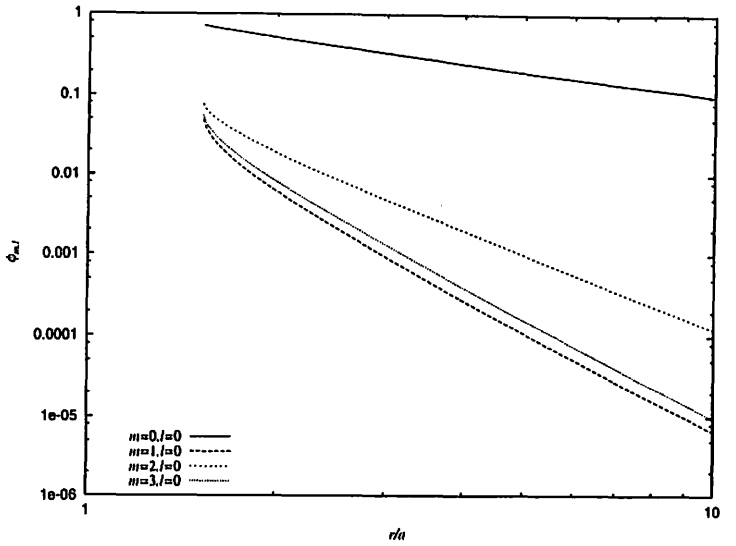

FIG. 4.— The amplitude of $(m,0)$ harmonic potentials. This is the case of $a = 0.173$, $e = 0.9$ and $M_1 : M_2 = 4 : 1$. The inner edge of the circumbinary disk model is roughly located at $r/a \sim 3$. Only $l = 0$ modes are presented. The $m = 0, l = 0$ mode scales as r^{-1}, the $m = 1, l = 0$ mode scales as r^{-4}, and the others scale as r^{-m-1}. The $m = 1, l = 0$ mode does not have the largest amplitude.

feel the one-way force. Thus, the energy and the angular momentum are strongly transferred.

The Lindblad resonance occurs at the location where the pattern speed coincides with its epicyclic (natural) frequency,

$$m(\Omega - \Omega_{m,l}) = \pm\kappa, \tag{12}$$

where κ is the epicyclic frequency. The fluid elements are exposed to the periodically varying external force, and its periodicity coincides with the natural frequency of the oscillation of the fluid element. Therefore, energy and momentum are strongly transferred.

Since the circumbinary disk is cool, we can neglect the pressure force in the 0-th order of argument. The motion of the disk is roughly approximated as Keplerian disk,

$$\kappa \simeq \Omega. \tag{13}$$

Using this approximation, the angular velocity at corotation resonance is expressed as

$$\Omega(r_{\rm CR}) = \frac{l}{m}\Omega_{\rm B}, \tag{14}$$

and the angular velocity at Lindblad resonance is

$$\Omega(r_{\rm LR}) = \frac{l}{m \pm 1}\Omega_{\rm B}. \tag{15}$$

Rewriting these relations in terms of the radial distance from the center of mass, the locations of the resonance in the Keplerian disk are expressed as follows:

$$r_{\rm CR} = \left(\frac{m}{l}\right)^{\frac{2}{3}} a, \tag{16}$$

$$r_{\rm LR} = \left(\frac{m \mp 1}{l}\right)^{\frac{2}{3}} a. \tag{17}$$

The case of the upper sign in the equation (17) is called the inner Lindblad resonance (ILR), while the lower is called the outer Lindblad resonance (OLR). We note that when we fix the number of m, relevantly outermost resonance corresponds to $l = 1$ mode. The location of resonance of larger l has smaller radius than the $(m, 1)$ resonance. If the location of resonance exists in the circumbinary disk, density waves are excited in the circumbinary disk and the corresponded structure, such as density structure, is formed.

3.3. *The Location of $m = 1$ Resonance*

We found that $m = 1$ mode is excited in the circumbinary disk with high eccentricity binary. As described in §3.2, the farthest resonance from the central star occurs at $l = 1$ resonance for each m. Among the resonance with the same m, OLR is the farthest, because we are considering a monotonically decreasing angular velocity distribution such as Keplerian disk. Thus, the furthest resonance for $m = 1$ is located at

$$r_{\rm OLR}(1,1) = 2^{\frac{2}{3}} a \approx 1.6a. \tag{18}$$

In our simulation, we set $a = 0.173$, and the furthest $m = 1$ resonance, OLR, is located about $r = 0.28$. On the other hand, the inner radius of the circumbinary disk is $r = 0.6$. Thus, there is no $m = 1$ resonance in our circumbinary disk model. The $m = 1$ wave cannot be excited in the circumbinary disk by the resonance. We can consider the resonance for $m \gg 1$ modes in the circumbinary disk, but it cannot explain $m = 1$ density structure.

Thus, we should consider another mode that was neglected previously. This is $m = 1$ and $l = 0$ ILR mode. In most cases, $l = 0$ mode is located at infinity, which is obvious from the equations (16) and (17). Thus, the $l = 0$ mode is always neglected in many previous astrophysical applications. However, we should pay an attention for $(m = 1, l = 0)$ ILR mode before discarding all of the $m = 1$ mode. In the equation (17), while the denominator vanishes, the numerator also vanishes for the

$(m = 1, l = 0)$ ILR mode. There is a possibility that the ILR radius becomes finite. Moreover, the $m = 1$ density structures seems to be stationary with time. The $l = 0$ mode corresponds to such a stationary mode.

From equation (15), the ILR is located where the condition,

$$m\Omega(r) - l\Omega_B = \kappa, \tag{19}$$

is satisfied. For $(m = 1, l = 0)$ mode, this condition becomes

$$\Omega(r) = \kappa. \tag{20}$$

This condition is exactly satisfied in Keplerian disk. The $(m = 1, l = 0)$ ILR is located everywhere in space, which means it is not localized. If the disk has non-zero temperature, this condition is not satisfied exactly, but the deviation from the Keplerian disk is not so large and it affects the disk structure strongly. We note here that the $(m = 1, l = 0)$ ILR has no significance in the case of the circular binary: As described in the previous subsection, the amplitude of the external force vanishes for all the $m \neq l$ mode, in the case of the circular binary. The $(m = 1, l = 0)$ ILR mode is important only in the case of eccentric binary.

3.4. *The Motion of a Test Particle in the $m = 1$ Perturbed Potential*

We perform simple test calculations to account for this $m = 1$ density structure seen in the Figure 2. The gravitational potential is decomposed into the (m, l) harmonic potentials. We calculate the orbit of a test particle under each component of the harmonic potential and investigate how it affects the test particle motion. Figure 4 shows the amplitudes of the harmonic potential of $l = 0$ case. The $m = 1$ harmonic potential scales as

$$\phi_{1,l} \propto r^{-4}, \tag{21}$$

where $r \gg 1$, and the other harmonic potentials scale as

$$\phi_{m,l} \propto r^{-m-1}. \tag{22}$$

The $m = 1$ harmonic potentials do not have the dependence of r^{-2}, but of r^{-4}, since we choose the origin of coordinate at the mass center of the binary.

We adopt the following power law potential as a model of (m, l) harmonic potentials:

$$\Phi_{0,0} = -\frac{GM}{r}, \tag{23}$$

$$\Phi_{1,0} = \epsilon_{1,0}\frac{GM}{r_0}\left(\frac{r}{r_0}\right)^{-4}\cos\theta, \tag{24}$$

$$\Phi_{2,0} = \epsilon_{2,0}\frac{GM}{r_0}\left(\frac{r}{r_0}\right)^{-3}\cos 2\theta, \tag{25}$$

$$\Phi_{3,0} = \epsilon_{3,0}\frac{GM}{r_0}\left(\frac{r}{r_0}\right)^{-4}\cos 3\theta, \tag{26}$$

where $\epsilon_{m,l}$ are the amplitudes of each harmonic potential. We considered the binary model of $a = 0.173$, $e = 0.9$, and $M_1 : M_2 = 4 : 1$ case, and determined the amplitude of each harmonic potential numerically. Figure 5 shows the evolution of orbital elements in each harmonic potential and in the combination of these potentials. The direction of $\theta = 0°$ is the direction of the secondary apastron and the rotational direction is counterclockwise. The initial condition of the test particle is circular when the perturbing potential is absent. We plot the value of $e\cos\varpi$ and $e\sin\varpi$, where e and ϖ are the eccentricity and the azimuth of periastron of the test particle, respectively. Though $m = 1, l = 0$ potential does not have the largest amplitude among many harmonic potentials, it greatly influences the test particle eccentricity. It is a natural consequence that only $m = 1, l = 0$ mode satisfies the condition of resonance. The periastron of the test particle is roughly aligned with the direction of $\theta = 90°$ from the secondary apastron, and the eccentricity grows with time.

Figure 6 shows the orbit of the test particle in the x-y plain under the model potential of $\Phi = \Phi_{0,0} + \Phi_{1,0}$. Owing to the small perturbation potential of $m = 1, l = 0$, the periastron and the apastron of the test particle orbit move toward $\theta = 270°$.

The eccentricity enhancement due to coupling with $m = 1$ mode is explained as follows: The evolution of angular momentum 0f each mode is written as

$$\frac{dL_{m,0}}{dt} = -\frac{\partial\Phi_{m,0}}{\partial\theta} = m\epsilon_{m,0}\frac{GM}{r_0}\left(\frac{r}{r_0}\right)^{-n}\sin m\theta. \tag{27}$$

We integrate the change of angular momentum over some elliptic orbit that has the form of

$$r = \frac{a(1-e^2)}{1 + e\cos(\theta - \theta_0)} \tag{28}$$

where a is the semimajor axis, e is the eccentricity, and θ_0 is the direction of periastron of the test particle, respectively. The change of angular momentum after one orbital period is expressed as

$$\Delta L_{m,0} = -m\epsilon_{m,0}\frac{GM}{r_0}\int_0^{2\pi/\Omega}\left(\frac{r}{r_0}\right)^{-n}\sin m\theta dt = m\epsilon_{m,0}\frac{GM}{r_0}\left(\frac{a}{r_0}\right)^{-n}\left(1-e^2\right)^{-n+\frac{3}{2}}\frac{1}{\Omega} \times \int_0^{2\pi}[1 + (n-2)e\cos(\theta - \theta_0)]\sin m\theta d\theta, \tag{29}$$

where we make the assumption of $e \ll 1$. Only $m = \pm 1$ mode can contribute to the angular momentum evolution. The mean evolution of the eccentricity is related with the change of angular momentum as

$$\frac{\Delta e}{\Delta t} = -\frac{1}{e}\sqrt{\frac{1-e^2}{GMa}}\frac{\Delta L}{\Delta t} \tag{30}$$

$$= -2\Omega\left(\frac{a}{r_0}\right)^{-3}\epsilon_{1,0}\sin\theta_0, \tag{31}$$

where $\Delta L = \Delta L_{1,0} + \Delta L_{-1,0}$, $m = 1$, $n = 4$, and we neglect the second order of e. Since $\theta = 0$ is the direction of apastron of the secondary, $\epsilon_{m,0}$ is negative. Thus, when $0° < \theta_0 < 180°$, the eccentricity grows, while $-180° < \theta_0 < 0°$, the eccentricity damps. The speed of eccentricity evolution is constant in the case of small e.

The above argument is for the case of the test particle, but the global feature is the same in the fluid dynamics. The fluid elements pass the binary with close orbit near the $\theta = 90°$ direction. On the other hand, the fluid elements pass the binary with distant orbit near the $\theta = 270°$ direction. Since

$$\dot{e} \propto a^{-\frac{9}{2}}, \tag{32}$$

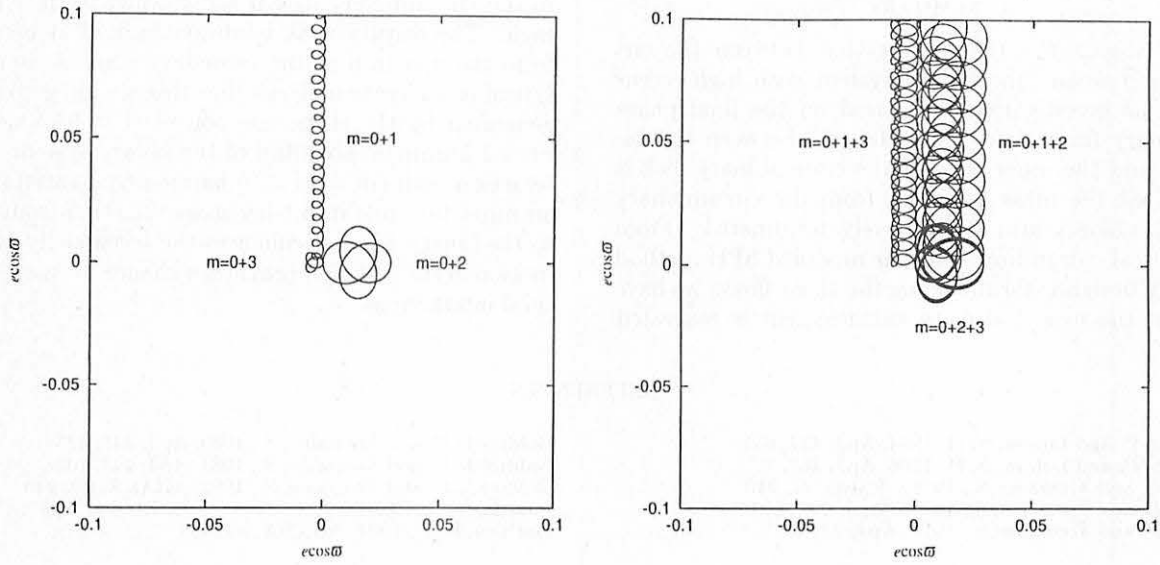

FIG. 5.— The evolution of eccentricity and the azimuth of periastron of the test particle. We plot the value of $e\cos\varpi$ and $e\sin\varpi$ on the x-y plane, where e and ϖ are the eccentricity and the azimuth of periastron, respectively. The left figure shows the orbital evolution of the test particle when $(m,0)$ harmonic potential exists as the small perturbation. We consider the unperturbed state of $(m=0, l=0)$, and $(m=1, l=0)$,$(m=2, l=0)$, and $(m=3, l=0)$ harmonic potential as perturbations, which are denoted as $m=0+1$, $m=0+2$, and $m=0+3$, respectively in the figure. The right figure also shows the orbital evolution of the test particle but two components of the harmonic potentials are included as the perturbation. The eccentricity of the test particle grows with time, when the $m=1, l=0$ harmonic potential exists. The periastron is aligned with the direction of $\theta = 90°$ from the perturbing potential peak.

the eccentricity of the inner part of the disk grows more rapidly. The density is reduced in the $\theta = 90°$ direction owing to gas expansion, while the density is enhanced in the $\theta = 270°$ direction owing to gas compression. Moreover, since the orbit of the fluid elements becomes eccentric, the stayover time at the apastron becomes longer, which makes the density at the apastron high. This is also contributes to the formation of $m = 1$ density structure with $\theta = 270°$ peak. Here, we mention about the circulation of the orbit of the fluid element. When the test particle moves freely under the potential of the binary, the direction of the periastron gradually rotates around the mass center. However, it seems that this circulation is not seen for the fluid calculation. It is understood that while the test particle moves freely, the fluid element continuously interact around the vicinity fluid by pressure or viscosity. The inner fluid element and the outer fluid element are coupled and the circulation motion would be suppressed. Thus, the interaction with $(m = 1, l = 0)$ harmonic potential may play an important role in further mass accretion from the disk to the binary, since it enhances the eccentricity of the gas motion in the disk and provides a chance for more effective tidal interactions.

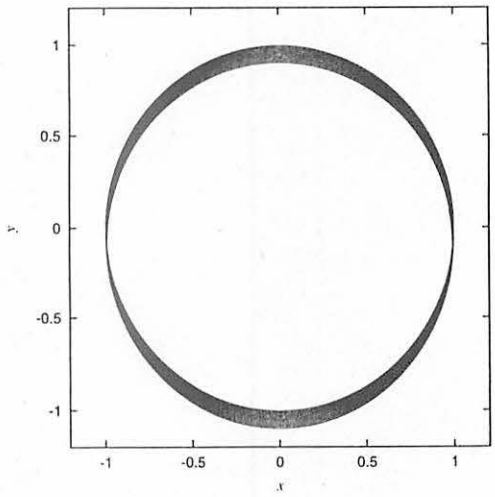

FIG. 6.— The orbit of the test particle under the model potential of $\Phi = \Phi_{0,0} + \Phi_{1,0}$. Owing to the small perturbation potential of $m=1, l=0$, the periastron and the apastron of the test particle orbit begins to move toward $\theta = 270°$.

4. SUMMARY

We investigate the tidal interaction between the circumbinary disk and the binary system with high eccentricity. Our investigation is focused on the final phase of the binary formation, when the gap between the binary star and the inner edge of the circumbinary disk is so large that the mass accretion from the circumbinary disk to the binary star is effectively terminated. From the numerical calculation with our modified SPH method specifically designed for modeling the shear flows, we have found that the $m = 1$ density enhancement is generated in the circumbinary disk if the eccentricity is sufficiently high. The density peak is always located at nearly 270° from the apastron of the secondary star. A simple analytical consideration shows that this standing structure is generated by the static component ($l = 0$ mode) of the $m = 1$ harmonic potential of the binary system. The interaction with ($m = 1, l = 0$) harmonic potential may play an important role in further mass accretion from the disk to the binary, since it enhances the eccentricity of the gas motion in the disk and provides a chance for more effective tidal interactions.

REFERENCES

Artymowicz, P. and Lubow, S. H. 1994, ApJ, 421, 651
Artymowicz, P. and Lubow, S. H. 1996, ApJ, 467, 77
Goldreich, P. and Tremaine, S., 1978a, Icarus, 34, 240
Goldreich, P. and Tremaine, S., 1978b, ApJ, 222, 850
Goldreich, P. and Tremaine, S., 1979, ApJ, 233, 857
Goldreich, P. and Tremaine, S., 1980, ApJ, 241, 425
Goldreich, P. and Tremaine, S., 1981, ApJ, 243, 1062
Goldreich, P. and Tremaine, S., 1982, ARA&A, 20, 249
Imaeda, Y. and Inutsuka, S. 2001a, submitted to ApJ
Mathieu, R. D. 1994, ARA&A, 32, 465

The Effect of Dynamical Friction on Formation of Terresrial Planet

Junko Kominami
E-mail: kominami@geo.titech.ac.jp
and
Shigeru Ida

Departmemt of Earth and Planetary Sciences,
Tokyo Institute of Technology,
Ookayama, Meguro-ku, Tokyo,152-8551, Japan

May,2001

Abstract

We performed the N-body simulation on proto planetary disk, including the effect of dynamical friction from the planetesimals and the disk gas. Mars-sized protoplanets are formed by accretion of planetesimals. The protoplanets are said to coagulate to form planets. The N-body simulation shows that the final eccentricity of the planets are around 0.1, which is about 10 times higher than that of the Earth and Venus(Chambers & Wetherill 1998). The high eccentricity is due to the instability of the orbits during the accretion of the protoplanets. Meanwhile, in order to make the protplanets to collide, the elevation of the eccentricity is essential.

We included gravitational interaction with the disk as dynamical friction and carried out the N-body simulation. The planets' final mass, spacial distribution, and eccentricity depend upon the strength of the dynamical friction. If the disk gas is partly depleted(0.1 - 1 % of minimum mass disk model), the protoplanets can grow to the size of about the Earth and Venus, and the eccentricity of such survived planets can be diminished within the nebular lifetime. Furthermore, since the gravitational drag is more effective on the larger mass, it is possible to explain why the eccentricity of smaller terrestrial planets; Mars and Mercury has relatively high eccentricity.

1 Introduction

Planets accrete form planetesimals. Runaway growth of the planetesimals results in rapid formation of protoplanets (Greenberg et al. 1978, Wetheril & Stewart 1989, Spaute et al. 1991,

Barge & Pellat 1991, Kokubo & Ida 1996, Inaba et al. 2001). Small number of planetesimals runs away, while most planetesimals remain small. Oligarchic growth follows the runaway growth, resulting in the similar-sized protoplanets with several Hill radius separation. The orbits of the protoplanets are almost circular and coplanar (Kokubo & Ida 1995, 1998, 2000, Weidenschilling et al. 1997).

Kokubo & Ida (1998, 2000) showed that about twenty Mars-sized protoplanets are finally formed as a result of the oligarchic growth, in the case of the minimum mass disk model (Weidenschilling 1977, Hayashi 1981). Mutual gravity among the protoplanets (Chambers et al. 1996, Yoshinaga et al. 1999, Iwasaki et al. 2001) and the seculer resonance from the giant planets (Ito & Tanikawa 1999, Nagasawa et al. 2000) may pump up eccentricity of the protoplanets. Then, orbital crossing begins and the accretion of the protoplanets starts.

Chambers & Wetherill (1998) and Agnor et al. (1999) calculated accretion of the protoplanets during the orbital crossing by N-body simulation, starting from initial conditions consistent with the oligarchic growth. In many cases, some of the resulting planets are as massive as Earth or Venus. However the eccentricity of the planets are rather high (~ 0.1). It is about 10 times the eccentricity of the Earth or Venus. This high eccentricity is the remnant of the orbital crossing of the protoplanets.

To make a planetary system that has planets with orbits and masses similar to those of the present terrestrial planets, the high eccentricity of the large planets has to be diminished. In order to diminish the eccentricity, some kind of drag force is needed. As will be discussed in section 2, the damping due to tidal interaction with a protoplanetary gas disk (Ward 1993,1989, Artymowicz 1993), which we will refer to as 'gravitational gas drag', is a good candidate; hydrodynamic gas drag and dynamical friction from the leftover planetesimals are too weak to diminish the eccentricity of the large planets in the final stage.

However, including such drag force might prevent orbital crossing of the protoplanets in the first place (Iwasaki et al. 2001) or lead to isolation between the protoplanets before sufficient coagulation to form Earth-sized planets.

Is there drag force that is weak enough not to prevent the growth of the planets to the Earth's size, but strong enough to damp the eccentricity of the Earth-sized planets before removal of the protoplanetary disk? The calculations we have carried out show that such strength of the drag is possible to exist as the gravitational gas drag due to a mostly depleted disk.

In this paper, we carried out N-body simulation to show if it is possible to make planets that are about the size of the Earth, and has nearly circuler orbit by including the gravitational drag force due to a mostly depleted disk. The drag force is expained in the next section. In section 3, the calculation method is explained. We show the result in section 4, and some discussions are made to present a possible consistent scenario to make terrestrial planets in section 5.

2 Garvitational Gas Drag

2.1 Effective Drag Force

There are possibly several types of drag force for the protoplanets that can be thought of.

One of such force is dynamical friction from the leftover planetesimals (e.g., Stewart & Wetherill 1988, Ida & Makino 1992). However, the result from the N-body calculation done by Kokubo & Ida (1998, 2000) shows that most planetesimals accretes to form protoplanets in the final stage of oligarchic growth; the total mass of the leftover planetesimals would not be

enough for effective dynamical friction. Therefore, dynamical friction from the planetesimals is not considered here.

Other forces are hydrodynamical gas drag (e.g., Adachi et al. 1976) and gravitational gas drag (Ward 1989, 1993, Artymowicz 1993). Comparison of the damping timescale of two forces shows that the hydrodynamical gas drag can be neglected in this case. Damping timescale of hydrodynamical gas drag is written as

$$\tau_{\rm hydro} \simeq \frac{M_{\rm p} v_{\rm rel}}{\pi r_{\rm p}^2 \rho_{\rm gas} v_{\rm rel}^2} \simeq 1.9 \times 10^7 e^{-1} \left(\frac{M_{\rm p}}{M_\oplus}\right)^{1/3} \times \left(\frac{\rho_{\rm gas}}{2 \times 10^{-9} {\rm gcm}^{-3}}\right)^{-1} \left(\frac{r}{1{\rm AU}}\right)^{1/2} {\rm years}, \quad (2.1)$$

where $v_{\rm rel}$ is relative velocity between a body and disk gas, which is $\sim e v_{\rm kep}$ ($v_{\rm kep}$: Keplerian velocity), M_p is the mass of the protoplanet, $r_{\rm p}$ is the radius of the protoplanet, and $\rho_{\rm gas}$ is the gas density (e.g., Adachi et al. 1976, Tanaka & Ida 1999). Supposing the minimum mass disk model ($\Sigma_{\rm gas}^{\rm min}$), this equation can be written as

$$\tau_{\rm hydro} \simeq 1.0 \times 10^6 \left(\frac{e}{0.01}\right)^{-1} \left(\frac{M}{M_\oplus}\right)^{1/3} \left(\frac{\Sigma}{\Sigma_{\rm gas}^{\rm min}}\right)^{-1} \left(\frac{r}{1{\rm AU}}\right)^{13/4} {\rm years}. \quad (2.2)$$

Since $\tau_{\rm hydro} \propto M^{1/3}$, hydrodynamical gas drag is more effective for a smaller body. On the other hand, gravitational gas drag is more effective for a larger body. Damping timescale of gravitational gas drag is written as

$$\tau_{\rm grav} \simeq \left(\frac{M_\odot}{M}\right) \left(\frac{M_\odot}{\Sigma_{\rm gas} r^2}\right) \left(\frac{c_{\rm s}}{v_{\rm kep}}\right)^4 \Omega_{\rm kep}^{-1}, \quad (2.3)$$

where $c_{\rm s}$ is sound velocity of the disk gas and $\Omega_{\rm kep}$ is Keplerian frequency (Ward 1989, 1993, Artymowitz 1993). Supposing the minimum mass disk model, this equation is written as

$$\tau_{\rm grav} \simeq 0.5 \times 10^3 \left(\frac{M}{M_\oplus}\right)^{-1} \left(\frac{r}{1{\rm AU}}\right)^2 \left(\frac{\Sigma}{\Sigma_{\rm gas}^{\rm min}}\right)^{-1} {\rm years}. \quad (2.4)$$

The ratio of the two timescales would be

$$\frac{\tau_{\rm hydro}}{\tau_{\rm grav}} \sim 2000 \left(\frac{e}{0.01}\right)^{-1} \left(\frac{M}{M_\oplus}\right)^{4/3} \left(\frac{r}{1{\rm AU}}\right)^{5/4}. \quad (2.5)$$

When the mass is less than $\sim 10^{25}$ g, the hydrodynamical gas drag is more effective than the gravitational gas drag. If it is larger than $\sim 10^{25}$ g, the gravitational gas drag is more effective (Ward 1993, Tanaka & Ida 1999).

So far, N-body simulation including the gravitational gas drag has not been done. N-body simulation of final accretion stage (e.g., Chambers & Wetherill 1998, Agnor et al. 1999) neglected the gravitational gas drag, maybe because they assume that gas disk is significantly depleted before completion of terrestrial planet formation. However, as shown in Eq.(2.4), the gravitational gas drag from significantly depleted gas disk is still important.

Note that the effect of dynamical friction is formally incorporated into the gravitational gas drag, because the dependence on planetary mass is the same. Actually, the damping time scale derived from Chadrasekhar's dynamical friction formula (Eq.(A4))is reduced to $\tau_{\rm grav}$ given by Eq.(2.3) by replacing velocity dispersion and surface density of the leftover planetesimals with sound velocity and surface density of gas disk, as shown in Appendix.

2.2 Drag Formula

We include the effects of the gravitational gas drag in N-body simulation by directly adding drag force ($\boldsymbol{f}_{\rm GD}$) to equations of motion as

$$\boldsymbol{f}_{\rm GD} = -\frac{\boldsymbol{v} - \boldsymbol{v}_{\rm gas}}{\tau_{\rm grav}}, \tag{2.6}$$

where $\boldsymbol{v}$ and $\boldsymbol{v}_{\rm gas}$ are the velocity of a protoplanet and of the gas velocity. We here assume the gas motion is non-inclined circular Keplerian motion. Equation (2.6) corresponds to Chadrasekhar's dynamical friction formula (Eq.(A1)) with the above mentioned replacement (see Appendix), which may support the inclusion of the gravitational gas drag as Eq. (2.6).

$\tau_{\rm grav}$ is written as

$$\tau_{\rm grav} = \tau_{\rm damp} \left(\frac{M}{M_\oplus}\right)^{-1} \left(\frac{r}{1{\rm AU}}\right)^2, \tag{2.7}$$

where $\tau_{\rm damp}$ is the damping timescale for a body with $M = M_\oplus$ at 1AU. We use $\tau_{\rm damp}$ as a parameter. With Eq. (2.4),

$$\tau_{\rm damp} = 500 \left(\frac{\Sigma_{\rm gas}}{\Sigma_{\rm gas}^{\rm min}}\right)^{-1} \ {\rm years}, \tag{2.8}$$

where $\Sigma_{\rm gas}^{\rm min}$ is gas surface density in the minimum mass model. As disk gas is depleted, $\tau_{\rm damp}$ increases.

3 Calculation Method

3.1 Initial Condition

We used the result of Kokubo & Ida (1998, 2000) to set up initial conditions. Fifteen protoplanets are placed with radial separation of 6-10 Hill radius, where Hill radius $r_{\rm H}$ is defined by

$$r_{\rm H} = \left(\frac{M}{3M_\odot}\right)^{1/3} r, \tag{3.1}$$

and random angular distribution. Each protoplanet has the mass of 0.2 times the mass of the Earth. Although the result of Kokubo & Ida (2000) shows that the mass distribution of the protoplanets made through the oligarchic growth has radial dependence, in order to simplify the problem, we set all protoplanets with equal mass. Calculation starts from the point when the orbital crossing occurs. The result of Kokubo & Ida (2000) shows that the eccentricity of the protoplanets are about $10^{-3} - 10^{-2}$, which means that the protoplanets have almost circular orbits. However, the protoplanets will eventually start orbital crossing on a timescale ($\tau_{\rm cross}$) depending on their orbital separation, mass (Chambers et al. 1996), initial eccentricity (Yoshinaga et al. 1999), and how much gas there is around the protoplanets (Iwasaki et al. 2001). The state we are investigating is after the onset of orbital crossing. It is rational to start the calculation with high eccentricity ($\gtrsim 10^{-2}$), supposing the state where orbital crossing is ready to start or has already been started. Iwasaki et al. (2001) shows that the eccentricity of the protoplanets secularly increases and orbital crossing starts if the damping timescale ($\tau_{\rm hydro}$

or $\tau_{\rm grav}$) is longer than $0.1\tau_{\rm cross}$ in the gas-free case (otherwise, orbital crossing is inhibited by the drag). In this case, the crossing time $\tau_{\rm cross}$ is the same as that in the gas-free case.

As to clarify the effect of the gas drag, the amount of the gas in the disk is constant during one run (section 4), The range of the constant damping timescale, $\tau_{\rm damp}$, is from 10^5 years to 10^8 year. For comparison, we also carried out runs with $\tau_{\rm damp} = 10^{15}$ years, which means the case with little gas. Each calculation has time span of 10^7 years because disk gas would not exist on a timescale much lomger than 10^7 years.

3.2 Orbital Integration

We integrate orbits with 4th order Hermite scheme (Makino & Aarseth 1992). The equation of motion of particle i is

$$\frac{{\rm d}\boldsymbol{v}_i}{{\rm d}t} = -\frac{GM_\odot}{|\boldsymbol{r}_i|^3}\boldsymbol{r}_i - \Sigma_{j\neq i}\frac{GM_j}{|\boldsymbol{r}_j-\boldsymbol{r}_i|^3}(\boldsymbol{r}_j-\boldsymbol{r}_i) - \frac{\boldsymbol{v}_i-\boldsymbol{v}_{\rm gas}}{\tau_{\rm grav}}. \tag{3.2}$$

The first term is the gravity from the sun. The second term is the mutual gravity between the protoplanets. And the last term is the gravitational drag from the disk gas. We include the dependence of the drag force on the mass and the location of the planet as Eq.(2.7).

When the protoplanets collide, perfect accretion is assumed.

The radius of the protoplanet is determined by the mass and the density as below.

$$r_{\rm p} = \left(\frac{3}{4\pi}\frac{M}{\rho_{\rm p}}\right)^{1/3}. \tag{3.3}$$

The density of the planets $\rho_{\rm p}$ is set to be 3 g/cm^3, which is a typical solid density of the terrestrial planets in our solar system.

4 Result

4.1 Numerical Results

We present the orbital evolution with $\tau_{\rm damp} = 10^{15}, 10^5, 10^7$ years in Figures 1a, 1b, and 1c, respectively. In all cases, initial orbital conditions are the same. Initially, orbital separation is $6r_{\rm H}$, $e =\sim 0.01$, and $i =\sim 0.01$. Solid lines represent the semimajor axis a. The dotted lines represent the pericenter and apocenter; the amplitude of the pericenter and apocenter is $2ea$, which is proportional to the eccentricity. The thickness of the solid line represents the mass of the planet.

Figure 1a shows the case with almost no gas ($\tau_{\rm damp} = 10^{15}$ years). Orbital crossing has not been finished even after 10^7 years. Totally, 8 coagulation events occurred before 10^7 years and some planets have grown to the size of the Earth or Venus.

Figure 2a shows the mass, eccentricity, and semimajor axis of surviving planets at 10^7 years. The largest planet at $a = 0.65$AU and the second largest at $a = 1.1$AU have the mass of $1.2M_\oplus$ and $0.8M_\oplus$. Although planets as massive as the Earth or Venus are made, the eccentricity is too large($e \simeq 0.05$) compared to that of the present Earth ($e \simeq 0.017$) or Venus ($e \simeq 0.0068$).

The high eccentricity is the remnant of eccentricity pumped up during orbital crossing ($e \sim 0.1$) by close encounters between the protoplanets. Collisional damping is not enough to

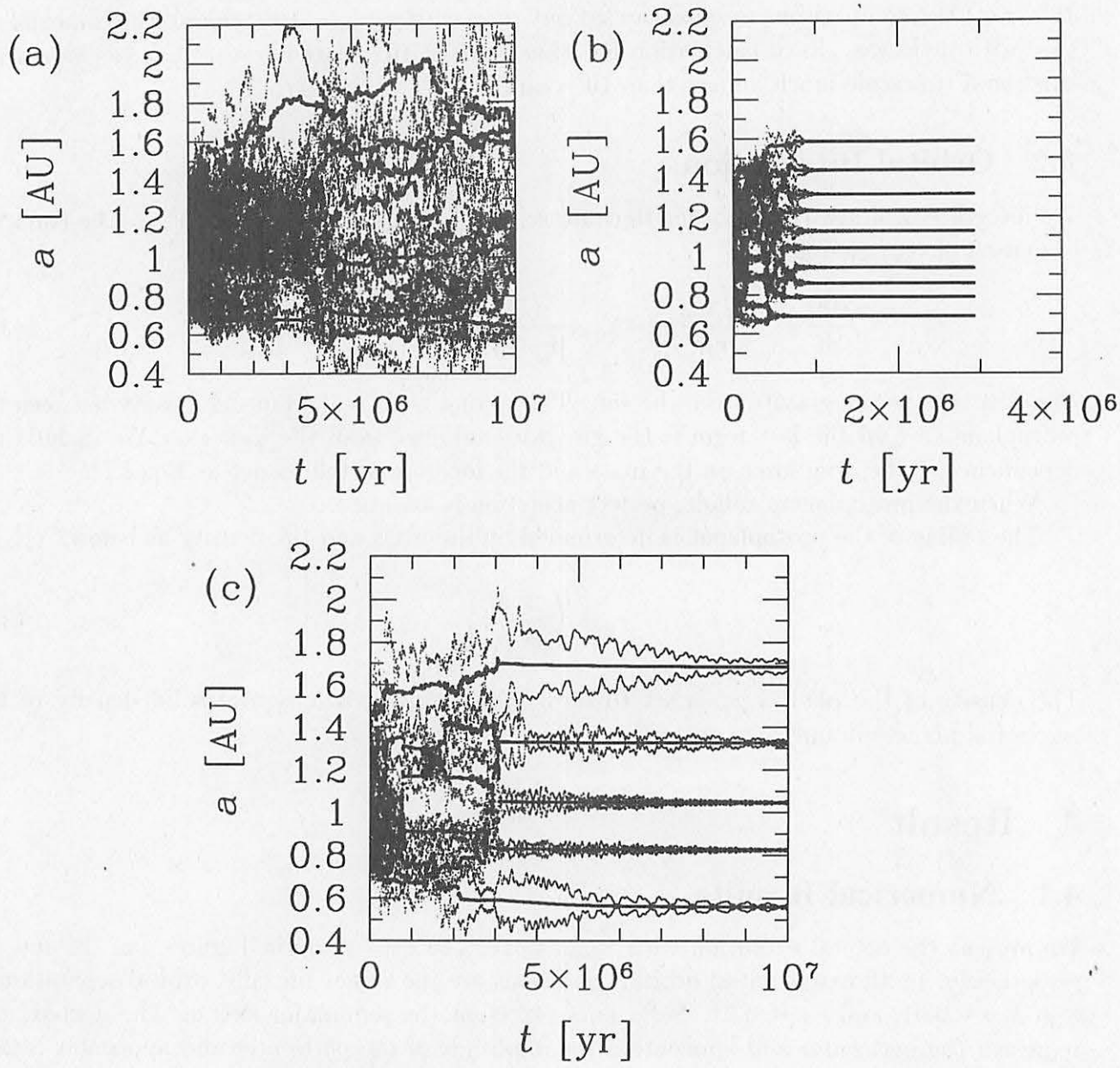

Figure 1: The figure shows the orbital evolution of the protoplanets. The x and y axis indicates the semimajor axis and time respectively. Dotted lines are the apocenters and pericenters. The solid lines are the semimajor axis of the accreting protoplanets. In (a), $\tau_{\rm damp} = 10^5$ years, which is equivalent to $\sim \Sigma_{\rm gas}^{\rm min}$ of gas. In (b), $\tau_{\rm damp} = 10^{15}$ years, which means the gas is mostly depleted. In (c), $\tau_{\rm damp} = 10^7$ years, which correspond to $\sim 10^{-3}\Sigma_{\rm gas}^{\rm min}$ of gas.

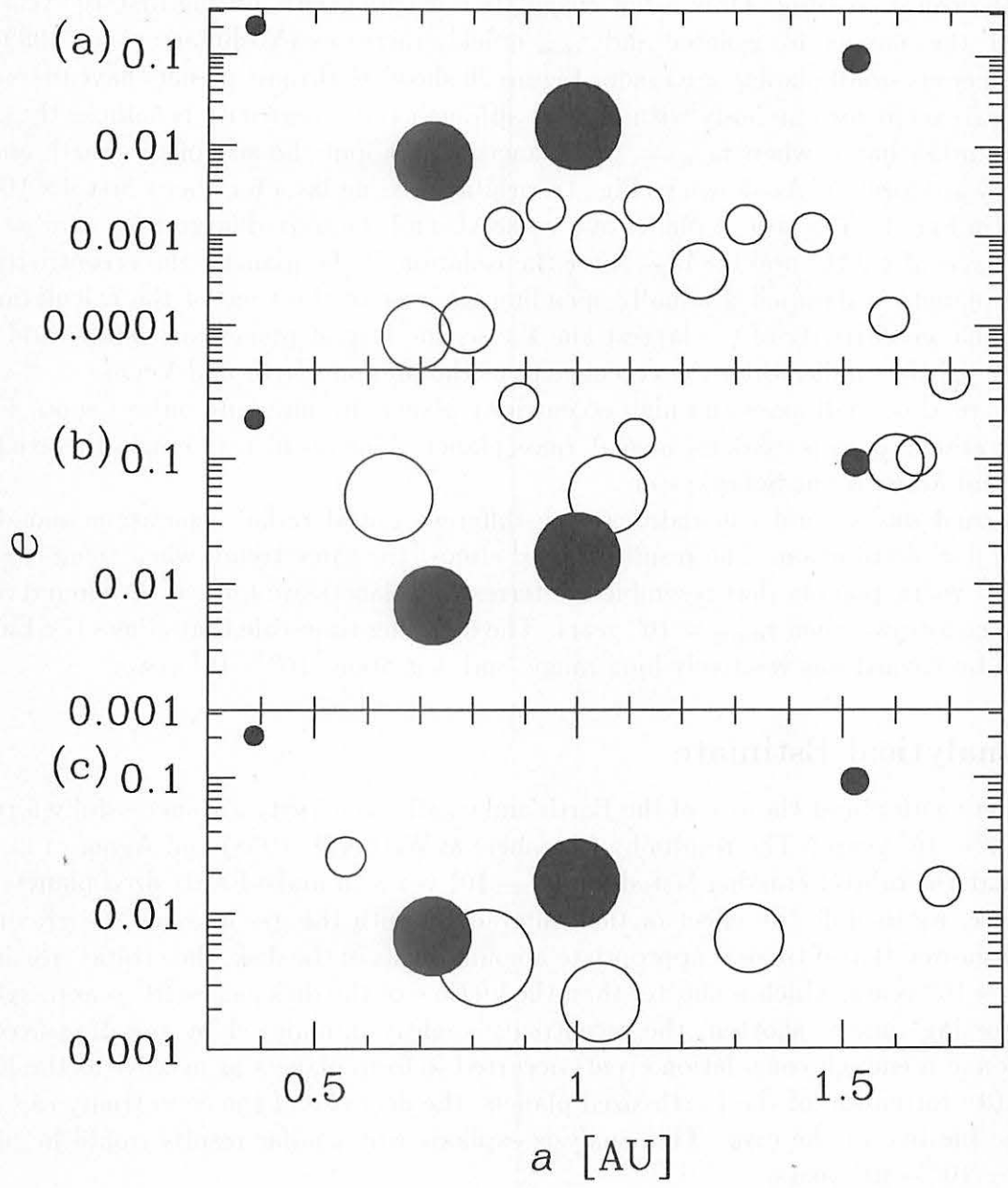

Figure 2: This figure shows the final mass and eccentricity of the planets after 10^7 years. The x and y axis are the semimajor axis and the eccentricity respectively. The area of the circles is proportional to the mass of the planets. White circles are the result of our calculations, and the black ones are terresrial planets in our Solar System. (a) is the result of the calculation of $\tau_{\rm damp} = 10^5$ years, (b) is $\tau_{\rm damp} = 10^{15}$ years and (c) is $\tau_{\rm damp} = 10^7$ years.

diminish e to ~ 0.01. This result is comparable to the results of Chmabers & Wetherill (1998) and Agnor et al. (1999).

Figure 1b shows the result with relatively strong drag ($\tau_{\rm damp} = 10^5$ years). In this case, the gravitational gas drag damps the eccentricity before the protoplanets can grow by colliding during the orbital crossing. Only a few coagulation events occurs during first 10^6 years. As e is damped, the planets are isolated and $\tau_{\rm cross}$ quickly increases (Yoshinaga et al. 1999). As a result, numerous small planets are made. Figure 2b shows that most planets have mass smaller than $0.4M_\oplus$ except for one body with $0.6M_\oplus$, although the eccentricity is sufficiently small.

On the other hand, when $\tau_{\rm damp} = 10^7$, planets with about the size of the Earth and small eccentricity are formed. As shown in Fig. 1c, orbital crossing lasts for about first 3×10^6 years. As shown in Fig. 1c, the largest planet at $a = 0.8$AU and the second largest one at $a = 1.05$AU have the mass of $1.2M_\oplus$ and $0.8M_\oplus$. After the isolation of the planets, the eccentricity of the surviving planets is damped gradually spending the rest of the time of the calculation (Fig. 1c). The final eccentricity of the largest and the second largest planets are 0.0047 and 0.0022, which are slightly smaller than the eccentricity of the present Earth and Venus.

There are also small mass and high eccentricity planets in inner and outer region (Fig. 2c). The gravitational drag is weak for a small mass planet. This result may eplain the existence of Mercury and Mars in our Solar system.

We carried out several calculations with different initial radial separation and different initial angular distribution. The results showed almost the same trend; when there is gas with $\tau_{\rm damp} = 10^7$ years, planets that resemble the terrestrial planets are formed. We found out that they are also formed when $\tau_{\rm damp} = 10^6$ years. The damping timescale that allows the Earth-like planets to be formed has relatively long range, and it is about $10^6 - 10^7$ years.

4.2 Analytical Estimate

Why planets with about the size of the Earth and small eccentricity are successfully formed for $\tau_{\rm damp} = 10^6 - 10^7$ years? The results by Chambers & Wetherill (1998) and Agnor et al. (1999) showed that the orbital crossing lasted for $10^7 - 10^8$ years to make Earth-sized planets.

However, we include the effect of tidal interaction with the gas disk, as the gravitational drag, and showed that if there is appropriate amount of gas in the disk, the orbital crossing time would be $\sim 10^6$ years, which is shorter than the lifetime of the disk gas($\sim 10^7$ years). Although orbital crossing time is shorten, the eccentricity slightly diminished by the drag accerelates coagulation and enough coagulation events occurred to form planets as massive as the Earth or Venus. After formation of the Earth-sized planets, the decrease of the eccentricity can happen within the lifetime of the disk. This analysis explains why similar results would be obtained for $\tau_{\rm damp} = 10^6 - 10^7$ years.

5 Conclusion and Discussion

We have investigated final accretion stage of terrestrial planet formation(giant impacts among the protoplanets), through N-body simulation, including the eccentricity damping caused by tidal interaction with remnant gas disk ('gravitational gas drag').

N-body simulations by Chambers & Wetherill (1998) and Agnor et al. (1999) showed that the giant impacts result in planets of about the size of the Earth, while the eccentricities of the planets tend to be significantly higher (~ 0.1) than the those of Earth and Venus (~ 0.01).

Collisional damping is not strong enough. In order to diminish the eccentricity, some kind of drag force should be incorporated. The inclusion of such strong drag force may prevent the orbital crossing of the protoplanets in the first place, not allowing the planets to grow sufficiently. However, we showed that the inclusion of the gravitational gas drag can successfully reproduce Earth-sized planets with eccentricities ~ 0.01.

In most runs, we start from 15 protoplanets with equal mass ($0.2M_\oplus$) and several Hill radius orbital separation and integrate the orbits for 10^7 years. The gravitational gas drag force is directly included in the equation of motion for orbital intergartion of the protoplanets, as Eq.(3.2). The amount of gas, which corresponds to $\tau_{\rm damp}$ (Eq.(2.8)), is fixed thoughout the calculation to see the effect of the presence of the gravitational gas drag. The parameter $\tau_{\rm damp}$ represents the eccentricity damping timescale for an Earth-sized planet at 1AU. The drag force depends on the mass of a protoplanet (M) and heliocentric distance (r) as $\propto M^{-1}r^2$ as Eq.(2.7).

When $\tau_{\rm damp} \lesssim 10^5$ years, since the drag force is too strong, it damps the eccentricity so quickly that the orbital crossing time does not last long enough to allow the planets to grow to the size of the Earth. When $\tau_{\rm damp} \gtrsim 10^8$ years, orbital crossing lasts throughout the calculation time and Earth-sized planets can be formed. However, the gas drag is too weak to diminish the eccentricity of the planets. The eccentricity is as large as ~ 0.1.

When $\tau_{\rm damp} = 10^6 - 10^7$ years, the orbital crossing stage lasts for $\sim 10^6$ years. Since the moderate damping of the eccentricity accelerates accretion of the protoplanets, some planets grow to the size of the Earth even during relatively short orbital crossing period. Their eccentricities are damped for the rest of the calculation time, resulting in the value of about 0.01. Usually, the large planets form at around 1AU. Also some small planets ($\sim 0.4M_\oplus$) that have relatively high eccentricity are formed at inner and outer part of the calculation area, which reflect the mass dependence of the drag force. These planets are analogous to Mars and Mercury in our Solar System. Therefore, if partly depleted gas exists in the disk when the orbital crossing begins, a planetary system similar to terrestrial planets can be formed.

Appendix

Dynamical Friction Timescale

Consider a planet with mass M and velocity $\boldsymbol{v}$ gravitationally interacting with a swarm of planetesimals with spatial density ρ, velocity dispersion $v_{\rm dis}$, and bulk velocity $\boldsymbol{v}_{\rm bulk}(v_{\rm bulk} \ll v_{\rm dis})$ If $v \ll v_{\rm dis}$, the Chandrasekhar dynamical friction formula for the drag force that is exerted on the planet is written as (e.g., Chandrasekhar 1943, Binney & Tremaine 1987)

$$\frac{d\boldsymbol{v}}{dt} \simeq -\frac{8}{3}\left(\frac{\pi}{2}\right)\ln\Lambda G^2\rho M\frac{\boldsymbol{v}-\boldsymbol{v}_{\rm bulk}}{{v_{\rm dis}}^3}, \tag{5.1}$$

where $\ln\Lambda$ expresses the effect of distant perturbations. For the system of a planet and planetesimals, $\ln\Lambda$ can be approximated to

$$\ln\Lambda \sim 3-5 \tag{5.2}$$

(Stewart & Ida 2000).

Since $\rho \sim \Sigma_{\rm solid}/(2v\Omega)(\Sigma_{\rm solid}$: the surface density of the planetesimals) and $G = v_{\rm kep}^2 r/M_\odot$, Eq.(5.1) reads as

$$\frac{d\boldsymbol{v}}{dt} = -\frac{\boldsymbol{v}-\boldsymbol{v}_{\rm bulk}}{\tau_{\rm DF}}, \tag{5.3}$$

where the damping timescale($\tau_{\rm DF}$) of the dynamical friction is

$$\tau_{\rm DF} = \frac{3}{2\pi\ln\Lambda}\left(\frac{M_\odot}{M}\right)\left(\frac{M_\odot}{\Sigma_{\rm solid}r^2}\right)\left(\frac{v_{\rm dis}}{v_{\rm kep}}\right)^4\Omega_{\rm kep}^{-1}. \tag{5.4}$$

Note that Eq.(5.4) is reduced to Eq.(2.3) except for a numerical factor by relacing $v_{\rm dis}$ and $\Sigma_{\rm solid}$ with $c_{\rm s}$ and $\Sigma_{\rm gas}$.

References

[1] Adachi, I.,C. Hayashi, and K. Nakazawa 1976. The gas drag effect on the elliptical motion of a solid body in the primordial solar nebula. *Prog. Theor. Phys.*,**56**,1756-1771.

[2] Agnor, C. B., R. M. Canup, and H. F. Levison 1999. On the character and consequences of large impacts in the late stage of terrestrial planet formation. *Icarus*,**142**,219-237.

[3] Artymowicz, P. 1993. Disk-satellite interacton via density wave and the eccentricity evolution of bodies embedded in disks. *Astron. J.*,**419**,166-180.

[4] Barge, P., and R. Pellat 1991. Mass spectrum and velocity dispersion during planetesimal accumullation. I. Accretion. *Icarus*,**93**,270-287.

[5] Chambers, J. E., G. W. Wetherill, and A. P. Boss 1996 The stability of multi-planet systems. *Icarus*,**119**,261-268.

[6] Chambers, J. E., and G. W. Wetherill 1998. Making the terrestrial planets: N-body integrations of planetary enbryos in three dimensions. *Icarus*,**136**,304-327.

[7] Greenberg, R., J. Wacker, W. K. Hartmann, and C. R. Chapman 1978. Planetesimals to planets: Numerical simulations and collisional evolution. *Icarus*,**35**,1-26.

[8] Hayashi, C. 1981. Structure of the solar nebula, growth and decay of magnetic fields and effects of magnetic and turbulent viscosities on the nebula. *Prog. Theor. Phys. Suppl.*,**70**,35-53.

[9] Inaba, S., H. Tanaka, K. Nakazawa, G. W. Wetherill, and E. Kokubo 2001. High-accuracy statistical simulation of planetary accretion: II. Comparison with N-body simulation. *Icarus*,**149**,235-250.

[10] Ito, T., and K. Tanikawa 1999. Stability and instability of the terrestrial protoplanet system and their possible roles in the final stage of planet formation. *Icarus*,**139**,336-349.

[11] Iwasaki, K., H. Tanaka, K. Nakazawa, and H. Emori 2001. The gas drag effect on the orbital instability of a protoplanet system. *Astron. Soc.*,**53**,321-329.

[12] Kokubo, E., and S. Ida 1995. Orbital evolution of protoplanets embedded in a swarm of planetesimals. *Icarus*,**114**,247-257.

[13] Kokubo, E., and S. Ida 1996. On runaway growth of planetesimals. *Icarus*,**123**,180-191.

[14] Kokubo, E., S. Ida 1998. Oligarchic growth of protoplanets. *Icarus*,**131**,171-178.

[15] Kokubo, E., and S. Ida 2000. Formation of protoplanets from planetesimals in the solar nebula. *Icarus*,**143**,15-27.

[16] Makino, J., and S. J. Aarseth 1992. On a hermite integrator with Ahmad-Cohen scheme for gravitational many-body problems. *Publ. Astron. Soc. Tpn.*,**44**,141-151.

[17] Nagasawa, M., H. Tanaka, and S. Ida 2000. Orbital evolution of asteroids during depletion of solar nebula. *Astron. J.*,**119**,1480-1497.

[18] Spaute, D., S. Weideschilling, D. R. Davis, and F. Marzari 1991. Accretional evolution of a planetesimal swarm: I. A new simulation. *Icarus*,**92**,147-164.

[19] Stewart, G. R., and G. W. Wetherill 1988. Evolution of planetesimal velocities. *Icarus*,**74**,542-553.

[20] Tanaka, H., and S. Ida 1999. Growth of migrating protoplanet. *Icarus*,**139**,350-366.

[21] Ward, W. R. 1989. On the rapid formation of giant planet cores. *Astrophys.J.Lett*,**345**,L99-L102.

[22] Ward, W. R. 1993. Density Wave In The Solar Nebula: Planetesimal Velocities. *ICARUS*,**106**,274-287.

[23] Weidenschilling, S. J. 1977b. The distribution of mass in the planetary system and solar nebula. *Astrophys. Space Sci.*,**51**,153-158.

[24] Weidenschilling, S. J.,D. Spaute, D. R. Davis, F. Marzari, and K. Ohtsuki 1997. Accretional evolution of a planetesimal swarm. 2. The terrestrial zone *Icarus*,**128**,429-455.

[25] Wetherill, G. W. and S. R. Stewart 1989. Accumulation of a swarm of small planetesimals. *Icarus*,**77**,330-357.

[26] Yoshinaga, K., E. Kokubo, and J. Makino 1999. The stability of protoplanet systems. *Icarus*,**139**,328-335.

Scattering of Cometary Planetesimals by Extrasolar Giant Planets and Metallicity of Their Host Stars

Shigeru Ida[1,2], Junko Kominami[1], and D.N.C. Lin[2]
(1) Tokyo Institute of Technology, (2) UCO/Lick Observatory

Abstract. We investigate shielding effect in extrasolar planetary systems and discuss its relation with the metallicity of the host stars. A giant planet can eject cometary objects, planetesimals that are scattered into inner region by outer giant planets, and can protect inner habitable planets against the impacts of the cometary objects. We integrate orbits of test particles thrown into the inner part of a planetary system, under the gravity of a host star and a giant planet. We calculate the probability of ejection of the test particles by perturbations of the giant planet as a function of its mass and semimajor axis. We find that a short-period planet cannot inhibit impacts onto the host star but a planet with large semimajor axis and/or large mass eject planetesimals to prevent contamination of metal to the host star. Our result may be consistent with observation of metallicity of the stars harboring extrasolar planets. Since the shielding effect does not only inhibit impacts onto the host star but also prevent inner habitable planets (if they exist) from being impacted by cometary planetesimals, habitability may be regulated by a giant planet(s).

1. Introduction

The stars known to harbor short-period extrasolar planets with period $P <$ 20 days tend to have larger metallicity [Fe/H] than the average population I stars in the solar neighborhood (Gonzalez 1997, 1998, 1999, 2000). The metallicity [Fe/H] is defined by

$$[\mathrm{Fe/H}] = \log_{10}\left[\frac{(\mathrm{Fe/H})_{\mathrm{star}}}{(\mathrm{Fe/H})_{\odot}}\right] \ \mathrm{dex}. \qquad (1)$$

Several of these stars are the most metal-rich stars ([Fe/H] $\sim$ 0.5 dex) so far known (Castro et al. 1997, Gonzalez 1999). The detection probability of the short-period planets is as high as 10% among metal-rich stars with [Fe/H] $>$ 0.20 dex in the solar neighborhood, while it is only $\sim$ 1% among non-biased sample of dwarf stars (Laughlin 2001).

Laughlin (2001) also showed that metallicity increases with stellar mass among the stars harboring short-period planets, and suggested that

this trend can be explained by accretion of rocky material with $\sim 30 M_\oplus$ onto the host stars during main-sequence phase. Convective zone mass of the Sun is only $0.02 M_\odot$ (Sackmann et al. 1993) and accreted rocky material may be mixed only in the convective zone. Accretion of rocky material with $\sim 30 M_\oplus$ onto a star with $1 M_\odot$ raises the metallicity of its convective zone by as large as 0.08 dex. Since the convective zone mass decreases with stellar mass (Forestini 1994), this effect is more important for a more massive star. Note that a pre-main sequence star is wholly convective and the convective region rapidly shrinks on a timescale $\sim 10^7$ years (Forestini 1994). [Fe/H] cannot be affected by the accretion of solid material during the pre-main sequence stage. Thus, Laughlin (2001) concluded that the observed trend of the increase in metallicity with stellar mass among the stars harboring short-period planets can be explained by accretion of rocky material after the host star proceeds to main sequence stage, when a planetary system has been mostly formed.

Murray et al. (1998) and Quillen & Holman (2000) showed through orbital calculation that mean-motion resonances of a giant planet can pump up eccentricities of planetesimals high enough to impact the host star. Quillen & Holman (2000) suggested that these impacts may enrich the metallicity of the host star, because such clearing of planetesimals occurs on a long timescale after formation of the giant planets and significant amount of rocky material may accrete after the host star's convective zone shrinks. Israelian et al. (2001) suggests that ^{6}Li abundance of HD82943 that harbors giant planets is explained by recent accretion of rocky material with $\sim 30 M_\oplus$.

On the other hand, Wetherill (1994) proposed "shielding effect" by Jupiter. The author showed that Jupiter's gravity ejects planetesimals that are scattered into inner region of the Solar system by outer giant planets (cometary objects) and protects terrestrial planets against the impacts of the cometary objects. If there is no Jupiter, lots of cometary objects impact the Earth and the Earth may be no longer habitable. To have H_2O ocean, a rocky planet must have nearly circular orbit with moderate semimajor axis. In addition to the orbital habitability, the habitability by the shielding effect may also be needed for actual habitability; habitability may be regulated by a giant planet(s).

Since the shielding effect does not only inhibit impacts onto inner habitable planets but also those onto the host star, the metallicity of a host star may indicate the habitability due to the shielding effect of terrestrial planets, if they exist, in a planetary system around the host star.

We investigate the shielding effect in extrasolar planetary systems and discuss its relation with the metallicity of the host stars. Carrying out Monte Carlo simulation, we will show that short-period planets cannot inhibit impacts onto the host stars but planets with large semimajor axis and/or large mass eject planetesimals to prevent contamination of metal to the host stars. We also transform the [Fe/H] data for the stars harboring

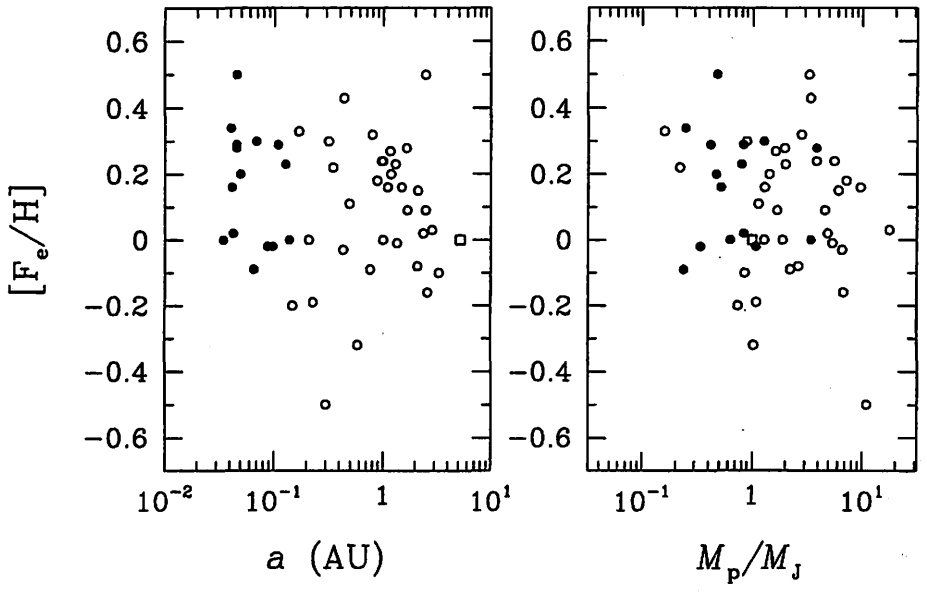

Figure 1. Metallicity, [Fe/H], of the stars known to harbor extrasolar planets, as a function of planetary semimajor axis $a_{\rm p}$ and that of the planetary mass $M_{\rm p}$. $M_{\rm J}$ is Jupiter's mass ($M_{\rm J} = 0.001 M_{\odot}$). For multiple planet systems, the largest planet is plotted. Filled circles and open circles represent planets with period $P < 20$ days and $P > 20$ days, respectively. Squares mean data of Jupiter and the Sun.

extrasolar planets to total amount of metal ($M_{\rm Fe}$) in the convective zone and find the trend that $M_{\rm Fe}$ is smaller for stars harboring more massive and larger semimajor axis planets, which would support the idea of "shielding effect".

2. Metal in Convective Zone

Figure 1 shows [Fe/H] of the stars known to harbor extrasolar planets, as a function of planetary semimajor axis $a_{\rm p}$ and that of the planetary mass $M_{\rm p}$. For multiple planet systems, the largest planet is plotted. Filled circles and open circles represent planets with period $P < 20$ days and $P > 20$ days, respectively. We used data at web sites "The Search for Extrasolar Planets" (http://exoplanets.org/) and "The Geneva Extrasolar Planet Search Programmes" (http://obswww.unige.ch/~udry/planet/planet.html). Jupiter in our Solar system is also shown with open squares.

The stars, in particular those harboring short-period planets, tend to be metal-rich, as already pointed out. However, we do not see any

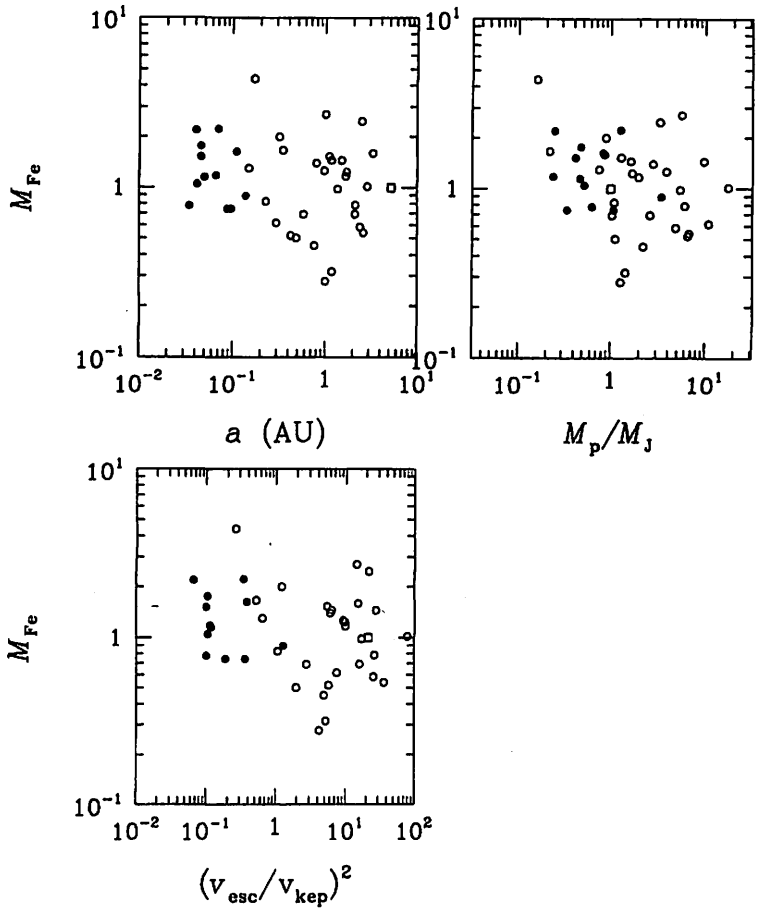

Figure 2. Total Fe mass in convective zone, $M_{\rm Fe}$, transformed by the data of Fig.1. The systems with $M_c < 0.5M_\oplus$ and $M_c > 1.2M_\oplus$ are excluded. A planet with too high eccentricity ($e > 0.09$) is also excluded. The plotted $M_{\rm Fe}$ is normalized by that of the Sun. Symbols are the same as those in Fig.1. $v_{\rm esc}$ is surface escape velocity of the planet and $v_{\rm kep}$ is Kepler velocity at a_p.

clear dependence on a_p or M_p. Since the convective zone mass sensitively depends on stellar mass, [Fe/H] is not a good physical quantity to measure the effect of accretion of solid material onto a host star. We estimate M_{Fe}, which is total Fe mass in convective zone, assuming that Fe is uniformly mixed in the convective zone with the observed value of [Fe/H]. Although the estimation of stellar mass, and hence that of the mass of convective zone, would include large uncertainty, M_{Fe} may be a better quantity than [Fe/H] for examining the shielding effect. Figure 2 shows M_{Fe} normalized by that of the Sun as a function of a_p, M_p, and $(v_{esc}/v_{kep})^2$, where v_{esc} is surface escape velocity of the planet and v_{kep} is Kepler velocity at a_p. $(v_{esc}/v_{kep})^2$ is a function of a_p and M_p. As discussed below, M_{Fe} may depend on a_p and M_p through $(v_{esc}/v_{kep})^2$. In Fig.2, the systems with $M_c < 0.5M_\oplus$ and $M_c > 1.2M_\oplus$ are excluded, because convective zone is too large in the former and too thin in the latter for the assumption that accreted solid material is uniformly mixed in the convective zone. A planet with too high eccentricity ($e > 0.9$) is also excluded. Compared with Figure 1, Figure 2 shows clearer dependence. M_{Fe} is smaller for larger a_p, M_p, or $(v_{esc}/v_{kep})^2$. As we will show below, a planet has stronger shielding effect if it has larger a_p, M_p, and/or $(v_{esc}/v_{kep})^2$. Hence, Figure 2 may reflect the shielding effect.

3. Model of Simulation

To investigate the shielding effect in extrasolar planetary systems, we carried out Monte Carlo simulation. We consider the system composed of a host star with mass M_c and a giant planet (mass M_p and physical radius r_p) orbiting the host star on a circular orbit. Test particles on a highly eccentric orbit is thrown into the system. The test particles correspond to planetesimals scattered by an outer giant planet(s). We integrate the particle orbit until the distance from the host star becomes larger than the initial value. If orbital eccentricity is pumped up to be larger than unity by the gravitational perturbations of the planet, or the particle collides with the host star or the planet, the integration is also stopped. Integrating many orbits with different phase angles and periastron distance for a fixed apastron distances p, we calculate the probability of ejection.

We here set $M_c = 1M_\odot$, but the ejection probability would be independent of M_c, if we express the probability as a function of $(v_{esc}/v_{kep})^2$, as explained below. We show the results with $p = 5$AU, but the ejection probability would also be almost independent of p.

We calculated the cases with $M_p = 1, 3, 10, 30M_J$, where M_J is Jupiter mass ($M_J = 0.001M_\odot$), and $a_p = 0.03, 0.1, 0.3, 1, 3$AU. For orbits of planetesimals, we examined the cases with $q = 0.1, 0.2, ...1.5a_p$. For each M_p, a_p, and q, 10^3-10^5 orbits with different initial longitudes of periastron are calculated so that statistical fluctuation in the probability is small enough. Semimajor axis a and orbital eccentricity e of the planetesimals are given

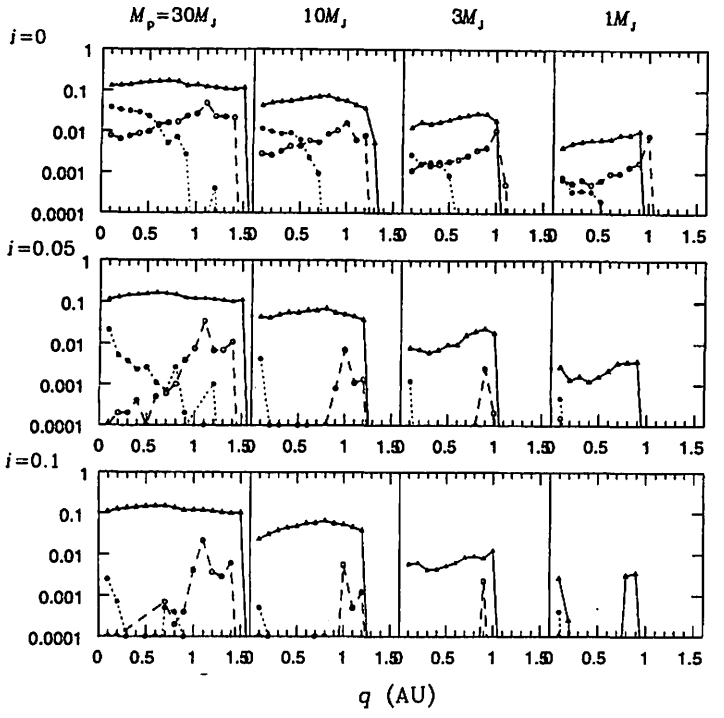

Figure 3. The ejection probability is shown with filled triangles as a function of planetary mass M_p, and periastron distance q and inclination i of planetesimal orbits. The semimajor axis of the planet a_p is 1AU. The collision probability with the host star (filled circles) and that with the planet (open circles) are also calculated, assuming that internal density of the planet is ~ 1 gcm^{-3} and physical radius of the host star is 0.01AU.

by $a = (p + q)/2$ and $e = 1 - q/a$. As explained below, in most cases we assume that the orbits of the planet and the planetesimals are coplanar.

4. Result

In Figure 3, the ejection probability is shown with filled triangles, as a function of M_p, q, and i for $a_p = 1$AU, where i is orbital inclination of the planetesimals. We also show the collision probability with the host star (filled circles) and that with the planet (open circles) assuming that internal density of the planet is ~ 1 gcm^{-3} and physical radius of the host star is 0.01AU.

We find that the ejection probability is hardly dependent on i as long as $i < 0.1$ radian, while the collision probabilities are dependent on i. Since we are concerned with the ejection probability, we hereafter focus on two-dimensional calculations ($i = 0$). The ejection probability is also almost

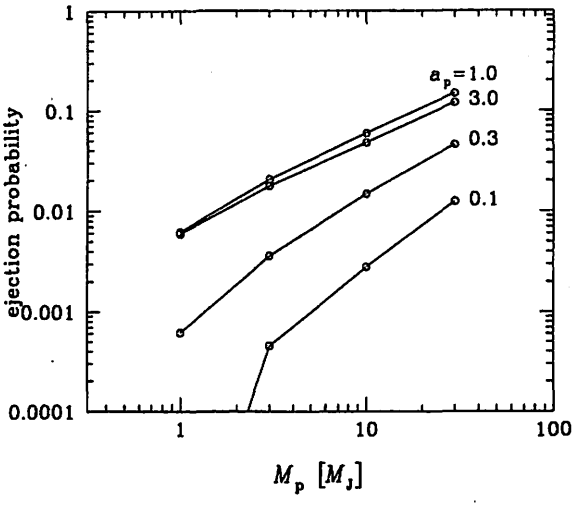

Figure 4. The average probability as a function of M_p and a_p. For $a_p = 0.03$AU, any ejection event is found.

independent of q as long as the orbits cross ($q < a_p$). Hence, we average the ejection probability over q for $q < a_p$.

The average probability is shown in Figure 4 as a function of M_p and a_p. In the calculations, $i = 0$ is adopted. The ejection probability strongly depends on M_p and a_p. It is smaller for smaller M_p and/or smaller a_p. For $a_p = 0.03$AU, we do not find any ejection event, because the planet is located so deeply in the potential of the host star that perturbation by $M_p \leq 30M_J$ cannot eject planetesimals. A short-period extrasolar planet cannot inhibit accretion of planetesimals at all, while a giant planet with larger a_p can inhibit impacts of planetesimals onto the host star as well as those onto habitable planets, if they exist. This trend would be consistent with the observed results in Figure 2.

The results with $a_p = 0.1$-1AU are well scaled by $(v_{esc}/v_{kep})^2$, where

$$\left(\frac{v_{esc}}{v_{kep}}\right)^2 \propto M_p^{2/3} a. \tag{2}$$

(The results with $a_p = 3$AU show different a-dependence, because p is close to a_p and scattering pattern may be different from the other cases.) This may be because v_{esc}^2 and v_{kep}^2 express available energy perturbation by the planet and the depth of gravitational potential of the host star. If v_{esc}^2/v_{kep}^2 is large, the planetesimals tend to be ejected by the planet. Thus, $(v_{esc}/v_{kep})^2$ would well indicate the ejection probability, but we need more quantitative analysis. Since $(v_{esc}/v_{kep})^2$ includes dependence on M_c [$(v_{esc}/v_{kep})^2 \propto M_c^{-1}$), we may also be able to apply the result to the cases with M_c other than $1M_\odot$. Note that M_c does not have a large variation

among the stars known to have extrasolar planets, dependence of the ejection probability on M_c would be small.

5. Discussion

Through the Monte Carlo simulation, we showed that that short-period planets cannot inhibit impacts of cometary planetesimals onto the host star, but planets with large semimajor axis and/or large mass effectively eject planetesimals. The transformed data of the observation of metallicity of the stars harboring extrasolar planets may support the model of the "shielding effect". The shielding effect does not only inhibit impacts onto the host star but also prevent inner habitable planet (if they exist) from being impacted by cometary planetesimals. Habitability may be regulated by a giant planet(s).

To discuss the shielding effect in more detail, in addition to the calculations with other p or M_c, we need similar calculations with a giant planet on an eccentric orbit, because most extrasolar planets so far discovered have eccentric orbits if they are not short-period planets. In this case, we also need to study orbital stability of inner habitable planets, since forced eccentricity due to the giant planet may easily destabilize the orbits of the inner habitable planets.

References

Castro, S., Rich, R. M., Grenon, M., Barbuy, B., & McCarthy, J. K. 1997, AJ, 114, 376

Forestini, M. 1994, A&A, 297, 183

Israelian, G., N. C. Santos, M. Mayor & R. Rebolo, 2001, Nature, 411, 6834

Laughlin. G. 2001, ApJ, 545, 1064

Gonzalez, G. 1997, MNRAS, 285, 403; 1998, A&A, 334, 221; 1999, MNRAS, 308, 447; 2000, ASP Conf. Ser., Disks, Planetesimals, and Planets, ed. F. Garzon, C. Eiroo, D. de Winter & T. J. Mahoney (San Francisco: ASP).

Murray, N., Hansen, B., Holman, M., & Tremaine, S. 1998 Science, 279, 69

Quillen, A. C., & Holman, M. 2000, AJ, 119, 397

Sackmann, I.-J., Boothroyd, A. I., & Kraemer, K. E. 1993, ApJ, 418, 457

Wetherill, G. 1994, Astrophys. Space Sci., 212, 23

The Effect of Dynamical Friction on the Orbital Instability of a Protoplanet System

K. IWASAKI, H. EMORI, AND K. NAKAZAWA

Department of Earth and Planetary Sciences, Faculty of Science
Tokyo Institute of Technology, Meguro-ku, Tokyo 152-8551, Japan

Abstract

We investigated the effect of the gravitational interaction (i.e., dynamical friction) with the nebular gas or planetesimal disk on the orbital instability of a protoplanet system. We considered an ideal protoplanet system, in which five protoplanets with the same mass of $1 \times 10^{-7}\,M_\odot$ are distributed with an equal separation distance, $\Delta\tilde{a}_0$, and their initial orbits are circular and coplanar. We pursued numerically the orbits of the five protoplanets suffering from the drag force which is proportional to the random velocity (i.e., the gravitational interaction with the gas or planetesimal disk). From our results, we found that the instability time, $T_{\rm inst}^{\rm df}$, becomes large drastically compared with the instability time under the drag-free condition, $T_{\rm inst}$, when $\Delta\tilde{a}_0$ excesses a certain critical separation distance, $(\Delta\tilde{a}_0)_{\rm crit}$. Furthermore, we obtained the empirical relation between $(\Delta\tilde{a}_0)_{\rm crit}$ and the surface mass density of the gas or planetesimal disk. Applying this relation to the minimum mass solar nebula, $(\Delta\tilde{a}_0)_{\rm crit}$ becomes about 6.1. Thus, for the occurence of an orbital instabilty in a realistic protoplanet system ($\Delta\tilde{a}_0 \simeq 10$), we must reduce the surface mass density of the nebular gas to about one-thousand times as large as that in the minimum mass nebula model.

1 Introduction

According to the standard scenario of the planetary formation, at the final stage of the planetary accretion, several tens of massive protoplanets, whose masses are of the order of the Martian mass, are formed through successive accretions of planetesimals in the present terrestrial planet region (Wetherill and Stewart 1989, Kokubo and Ida 1998, 2000). After the formation of the protoplanets, the orbital eccentricities increase in a stochastic manner owing to the mutual gravitational scattering and, after a while, there happens to occur the orbital crossing between protoplanets to become capable of colliding with each other. Through such collisions between protoplanets, they continue to grow increasing their mutual separation distance (owing to the decrease of the number of protoplanets). As a result, the present terrestrial planets are formed with the large orbital separations.

The orbital evolution of a multi-protoplanet system was investigated by Chambers et al.(1996) for the first time. They studied numerically the orbital behavior of the multi-protoplanet system composed of 3 to 20 protoplanets with equal mass ($1 \times 10^{-7} M_\odot$, $M_\odot$ being the solar mass), assuming that the protoplanets have initially the null orbital eccentricities and inclinations and are placed from 1AU with the same orbital separation distance, $\Delta\tilde{a}_0$. Note that the separation distance is scaled by the Hill radius, $r_{\rm H}$, which is defined by

$$r_{\rm H} = \frac{a_{10} + a_{20}}{2}\, h_{\rm PP}\,, \qquad (1)$$

where a_{10} and a_{20} are the initial semimajor axes of the two adjacent protoplanets. Furthermore, $h_{\rm PP}$ is the reduced Hill radius given by

$$h_{\rm PP} = \left[\frac{2M_{\rm P}}{3M_\odot}\right]^{\frac{1}{3}}\,, \qquad (2)$$

where $M_{\rm P}$ is the mass of the protoplanets. Through the long-term orbital calculations, they found that the orbital instability time, $T_{\rm inst}$, within which any two of the protoplanets come close within one Hill radius for the first time is expressed empirically as a function of $\Delta\tilde{a}_0$:

$$\log_{10} T_{\rm inst} = b\Delta\tilde{a}_0 + c\,, \qquad (3)$$

where b and c are numerical constants. The values of b and c are found to be

$$b = 0.765 \pm 0.030 \ \text{ and } \ c = -0.030 \pm 0.192 \qquad (4)$$

when the number of protoplanets, N, is five. These values are almost constant for $N \geq 5$.

However, it should be noted that the protoplanet system set up by Chambers et al. (1996) is highly idealized. Yoshinaga et al. (1999) focused on the system of protoplanets with finite random velocities (i.e., eccentricities and inclinations) and found that in such a protoplanet system the orbital instability time is shorten by several orders of magnitude. We must also question the assumption adopted in Chambers et al. that protoplanets orbit in a "vacuum space". Rather, it is natural to think that orbits of the protoplanets are influenced, not only by the mutual gravitational interaction, but also by the hydrodynamic gas drag due to the nebular gas and/or dynamical friction (i.e, gravitational interaction) originated by a swarm of planetesimals.

Iwasaki et al. (2001) studied a long-term orbital evolution of protoplanets suffering the gas-drag force by calculating orbits numerically. They considered an ideal

protoplanet system as those set up in Chambers et al. as well as the solar nebular gas rotating with a Keplerian circular velocity. Through a number of orbital calculations, they discovered that, under the gas-drag effect, the orbital instability time becomes enlarged in magnitude compared with that for the gas-free case (equation (3)), and that, the orbital instability does not occur substantially, when the initial orbital separation, $\Delta\tilde{a}_0$, is larger than the critical separation distance, $(\Delta\tilde{a}_0)_{\rm crit}$.

Furthermore, they found that the critical separation distance, $(\Delta\tilde{a}_0)_{\rm crit}$, can be written empirically as a function of the nebular gas density, ρ, and, obtained $(\Delta\tilde{a}_0)_{\rm crit} \simeq 10$ for the minimum mass nebula model ($\rho \simeq 1.0 \times 10^{-9}$ g cm^{-3} at 1AU given by Hayashi (1981)). On the basis of their results, they concluded that there occurs the orbital instability (followed by a collision) in the realistic protoplanet system with a typical orbital separation of about 5–10 in units of the Hill radius (Kokubo and Ida 1998, 2000), even if the protoplanets move round in the solar nebula.

It should be noted that the eccentricities of protoplanets are also depressed by the dynamical friction due to a swarm of planetesimals (i.e., the gravitational interaction with the planetesimal disk). Furthermore, in the final stage of the planetary accretion, the tidal interaction with the nebular gas (i.e., the gravitational interaction with the nebular gas disk) becomes important as the damping effect of the eccentricities (Ward 1988, Artymowicz 1993). Unfortunately, the results obtained by Iwasaki et al. (2001), mentioned above, cannot be applied for such cases. It is because that the dynamical friction and tidal interaction becomes intense in proportion to the random velocity of a protoplanet (Ida 1990, Artymowicz 1993), whereas the gas drag force is proportional to the square of the random velocity.

Therefore, in the present paper, we concentrate ourselves on studying the orbital instability of the protoplanet system under the action of the dynamical friction by a swarm of planetesimals and the tidal interaction with the nebular gas disk, both of which are proportional to the random velocity of a protoplanet.

2 Method of Orbital Calculations

2.1 Basic Equations

We calculate numerically the orbits of n protoplanets (in our present case, $n = 5$) revolving around the sun, including both of the mutual gravity and the drag force which is proportional to the random velocity of a protoplanet. The drag force acting on the i-th protoplanet, F_i is given by

$$F_i = \frac{1}{\tau_{\rm D}}\, u_i \,, \tag{5}$$

where u_i denotes the relative velocity vector of the i-th protoplanet from the Keplerian circular velocity, $v_{\rm K}$ (i.e., the random velocity of the protoplanet):

$$u_i = \dot{x}_i - v_{\rm K} \,. \tag{6}$$

In equation (5), $\tau_{\rm D}$ is the characteristic time constant. Adachi et al. (1976) investigated the effect of the drag force obeying equation (5) (i.e., the Stokes law in fluid dynamics) on the motion of a planetesimal orbiting around the sun. Through the orbital average of the motion of a planetesimal, they obtained the analytical formula of time variation of the orbital eccentricity, e, i.e.,

$$\frac{1}{e}\frac{de}{dt} = -\frac{1}{\tau_{\rm D}} \,. \tag{7}$$

In short, $\tau_{\rm D}$ represents the characteristic damping time of the eccentricity.

We can write down explicitly the expression of $\tau_{\rm D}$ depending on the kind of the drag force. Through a lot of orbital calculations, Ida (1990)obtained the damping rate of the eccentricity of a planetesimal due to the dynamical friction of a swarm of planetesimals. By applying his results to a protoplanet embedded in a swarm of planetesimals based on the minimum mass nebula model (Hayashi 1981), $\tau_{\rm D}$ is written as (Ida 1990)

$$\tau_{\rm D} = 3.9\times10^2 \left(\frac{v_m}{3\,h_{\rm P}\,v_{\rm K}}\right)^4 \left(\frac{M_{\rm P}}{1\times10^{-7}M_\odot}\right)^{\frac{1}{3}} \times \left(\frac{a}{1\,{\rm AU}}\right)^{-\frac{1}{2}} \left(\frac{\sigma_{\rm d}}{7.1\,{\rm g\,cm^{-2}}}\right)^{-1} T_{\rm K} \,, \tag{8}$$

where $\sigma_{\rm d}$ is the surface mass density of planetesimals at 1AU and $T_{\rm K}$ is the Keplerian period. In the above equation, $h_{\rm P}$ denotes the reduced Hill radius between the protoplanet and a planetesimal with the mass of m ($m \ll M_{\rm P}$) and is defined by

$$h_{\rm P} = \left(\frac{M_{\rm P}+m}{3M_\odot}\right)^{\frac{1}{3}} \simeq \left(\frac{M_{\rm P}}{3M_\odot}\right)^{\frac{1}{3}} . \tag{9}$$

Note that we assume the surface mass density, σ, varies with the distance from the sun, a, as $a^{-3/2}$ according to Hayashi (1981). It should be also noted that the above equation is valid only when the random velocity of a planetesimal, v_m, satisfies the following relation:

$$v_m = ({e_m}^2 + {i_m}^2)^{\frac{1}{2}}\, v_{\rm K} \;\geq 3 h_{\rm P} v_{\rm K} \,, \tag{10}$$

where e_m and i_m are the means of the eccentricity and inclination of planetesimals, respectively. The above assumption is always satisfied in our present case, since planetesimals have large random velocities because of the gravitational scatterings with massive protoplanets (Ida and Makino 1993).

Ward (1988) and Artymowicz (1993) calculated the tidal torque via density waves on the body embedded in a gaseous disk without a gap and estimated the damping rate of the eccentricity of the body. According to their results, for a protoplanet with small eccentricities ($ev_{\rm K} \ll c_{\rm s}$ where $c_{\rm s}$ is the sound velocity) embedded in the gas nebula, $\tau_{\rm D}$ is expressed by (Artymowicz 1993)

$$\tau_{\rm D} = 8.3\times10^9 \left(\frac{c_{\rm s}}{v_{\rm K}}\right)^4 \left(\frac{M_{\rm P}}{1\times10^{-7}M_\odot}\right)^{-1} \times \left(\frac{a}{1\,{\rm AU}}\right)^{-\frac{1}{2}} \left(\frac{\sigma_{\rm g}}{1.7\times10^3\,{\rm g\,cm^{-2}}}\right)^{-1} T_{\rm K} \,, \tag{11}$$

where σ_g denotes the surface density of the nebular gas at 1AU (we assume again that $\sigma \propto a^{-3/2}$).

2.2 Initial Condition

In order to see the orbital evolution of protoplanets under the influence of the drag force obeying equation (5), we calcutated numerically the orbits of the five protoplanets, including the drag force. We consider five protoplanets with the same mass of $1 \times 10^{-7}\, M_\odot$, which is about one-third of Martian mass, and their initial configuration in orbits is set up by the same way as those in Chambers et al. (1996) and Iwasaki et al. (2001), that is,

(a) The semimajor axis of the innermost protoplanet, a_1, is 1 AU,

(b) The five protoplanets are placed with an equal orbital separation, $\Delta\tilde{a}_0$,

(c) The orbital eccentricities and inclinations of five protoplanets are equally set to be zero,

and

(d) The azimuthal angles of positions of five protoplanets are selected randomly, but satisfying that the difference between the position angles of any two adjacent protoplanets is more than 20 degree.

As for the characteristic time constant, τ_D, we consider the following four cases:

$$\tau_D = 1.0\times10^3,\ 3.0\times10^3,\ 9.0\times10^3,\ \text{and}\ 2.7\times10^4\, T_K\ . \tag{12}$$

For each value of τ_D, we pursued orbits numerically changing the separation distance, $\Delta\tilde{a}_0$, from 3.6 to 6.6 with a step of 0.2:

$$\Delta\tilde{a}_0 = 3.6,\ 3.8,\ 4.0,\ \cdots,\ 6.4,\ \text{and}\ 6.6\ . \tag{13}$$

For an arbitrary set of τ_D and $\Delta\tilde{a}_0$, we make orbital simulations for ten cases with different phases in position angles according to assumption (d).

We integrate numerically the orbits of protoplanets by the use of a 4th-order $P(EC)^n$ Hermite scheme (Makino and Aarseth 1992, Kokubo et al. 1998, Kokubo and Makino 1998), which is quite the same as used in Iwasaki et al. (2001).

3 Results

Through a number of orbital calculations, we find the orbital instability time, $T_{\rm inst}^{\rm df}$, under the drag force obeying equation (5). Here, we adopt the same criterion for the occurrence of an orbital instability as those in Chambers et al. (1996) and Iwasaki et al. (2001), that is, a first approach of two protoplanets within one Hill radius. In order to save computational time, we stop our orbital calculations when the evolutionary time, t, exceeds the cut-off time, $T_{\rm stop}$, which is given by

$$T_{\rm stop} = 200 \times T_{\rm inst}\ . \tag{14}$$

In the above equation, $T_{\rm inst}$ denotes the instability time for the cases without the drag force, which is found empirically by Iwasaki et al. (2001) and is given by

$$\log_{10} T_{\rm inst} = 0.78\Delta\tilde{a}_0 - 0.15\ . \tag{15}$$

3.1 Instability Time

In figure 1, we plot the orbital instability time of the protoplanet system, $T_{\rm inst}^{\rm df}$, against the initial separation distance, $\Delta\tilde{a}_0$, for the case of $\tau_D = 9.0\times10^3\, T_K$. In this figure, the results for ten cases with different initial phases are plotted for each $\Delta\tilde{a}_0$. We can easily see that a protoplanet system becomes strongly stabilized owing to the drag force when $\Delta\tilde{a}_0$ excesses a certain critical value. In order to see the stability of a system in a quantitative manner, we divide an abscissa of figure 1 into three zones according to orbital behaviors of the ten cases with the same $\Delta\tilde{a}_0$, i.e., the "unstable" zone, the "transition" zone, and the "stable" zone by the same way as those in Iwasaki et al. (2001). In the unstable zone ($\Delta\tilde{a}_0 < 5.4$), all ten cases with the same $\Delta\tilde{a}_0$ experience the orbital instabilities within the time nearly equal to $T_{\rm inst}$. On the contrary, in the stable zone ($\Delta\tilde{a}_0 \geq 5.8$), all cases reach the cut-off time of orbital calculations, $T_{\rm stop}$, without the occurrence of the orbital instability. The above two zones are separated by the transition zone ($5.4 \leq \Delta\tilde{a}_0 < 5.8$), in which an orbital instability occurs in some cases whereas there occur no instabilities in the other cases.

The two vertical dotted lines in figure 1 denote the positions of the boundaries of the transition zone, that is, $(\Delta\tilde{a}_0)_1$ (the left dotted line) and $(\Delta\tilde{a}_0)_2$ (the right dotted line). The values of $(\Delta\tilde{a}_0)_1$ and $(\Delta\tilde{a}_0)_2$ for each τ_D are shown in Table 1. Here, we should note that, for any τ_D, the widths of the transition zone are small ($= 0.4$) compared with those of the unstable zone and the stable zone. In short, the system becomes drastically stabilized when $\Delta\tilde{a}_0$ excesses a narrow threshold which corresponds to the transition zone. Furthermore, we can readily see that the position of the transition zone is shifted toward a direction of large $\Delta\tilde{a}_0$ (in other words, the unstable zone spreads out) as τ_D increases (i.e., the intensity of the drag force decreases). This result means that the system becomes more unstable as the drag force weakens because of the decrease of the damping efficiency of eccentricities (see equation (7)).

Table 1: Boundaries of the transition zone, $(\Delta\tilde{a}_0)_1$ and $(\Delta\tilde{a}_0)_2$.

$\tau_D/\ 10^3\, T_k$	1.0	3.0	9.0	27
$(\Delta\tilde{a}_0)_1$	4.6	5.0	5.4	6.2
$(\Delta\tilde{a}_0)_2$	5.0	5.4	5.8	6.6

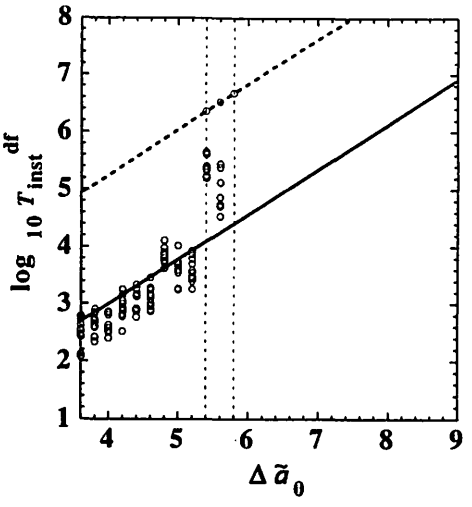

Figure 1: Instability time for the cases where the protoplanets suffer from the drag force obeying equation (5), ($T_{\rm inst}^{\rm df}$), as a function of $\Delta\tilde{a}_0$. This panel corresponds to the case of $\tau_{\rm D} = 9.0 \times 10^3\, T_{\rm K}$. The solid line presents $T_{\rm inst}$, given by equation (15), and the upper dotted line shows the cut-off time of calculations, $T_{\rm stop}(= 200 \times T_{\rm inst})$. Two vertical dotted lines denote the boundaries of the transition zone.

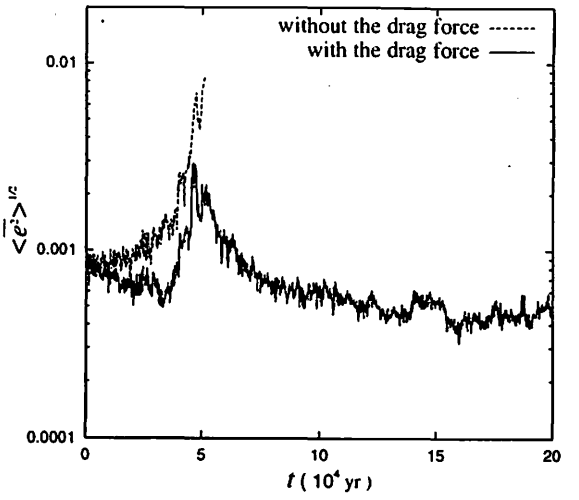

Figure 2: Time evolution of the root mean square of eccentricities of the five protoplanets for the case of ($\tau_{\rm D}$, $\Delta\tilde{a}_0$) = ($9.0 \times 10^3\, T_{\rm K}$, 5.6) (which is in the transition zone). The case without the drag force ($\Delta\tilde{a}_0 = 5.6$) are also shown. The onset of an orbital instability (i.e., an orbital crossing) is suppressed for the case with the drag force at $t \simeq 5 \times 10^4$ yr.

3.2 Comparison with the Case under the Gas-Drag Effect

As shown in the previous subsection, a protoplanet system whose separation distances are larger than a certain critical value, $(\Delta\tilde{a}_0)_1$, is strongly stabilized by the drag force obeying equation (5). In figure 2, we show the typical example of a system which is stabilized owing to the drag force. Figure 2 shows the time variation of the root mean square of eccentricities of the five protoplanets under the drag force, together with those for the drag-free case. At $t \simeq 5 \times 10^4$year, we observe a rapid increase and a following decrease in eccentricities of protoplanets for the case under the drag force, whereas the orbital crossing occurs for the case without the drag force at the almost same time. This event indicates that the occurrence of an orbital instability is prevented through the damping of eccentricities by the drag force as seen also in the cases under the gas-drag force (such an event is called a "falsely unstable event" in Iwasaki et al. (2001)).

Furthermore, such a rapid energy dissipation (i.e., a rapid decrease in eccentricities) leads to also a rapid orbital repulsion of protoplanets as a "falsely unstable event" in Iwasaki et al. does. The orbital repulsions play also an important role in stabilizing a system even under the drag force obeying equation (5) by the same way as those in Iwasaki et al. First, the expansion of the separation distances of protoplanets caused by an orbital repulsion stabilizes a system through the reduction in the strength of the mutual gravity between the protoplanets. Furthermore, the frequency of the onset of the orbital repulsions (which occurs many times in a same system) decreases as the separation distances, $\Delta\tilde{a}$, increases, since the time interval of such events is nearly equal to the instability time under the drag-free condition, $T_{\rm inst}$ when $\Delta\tilde{a}_0$ equals $\Delta\tilde{a}$ (see equation (3)). Consequently, a system is gradually stabilized through a number of the orbital repulsions.

Although the qualitative properties of the stabilizing mechanism are common in the drag force obeying equation (5) and the gas-drag force (i.e., the drag force which is proportional to the square of the random velocity), the degree of the stabilization under the above two kinds of drag forces are rather different. Figure 3 shows the evolutionary behaviors in the root mean square of the eccentricities of the five protoplanets for both of the case with the drag force obeying equation (5) and the case with the gas-drag force, where the characteristic damping time of eccentricities, $T_{\rm damp}$, which controls the intensities of the drag force, for both cases are equally set to be $1.7 \times 10^3\, T_{\rm K}$. Note that the damping time, $T_{\rm damp}$, during which the eccentricity decreases by a factor of $1/e$ owing to the gas-drag force, is inverse proportional to the eccentricity itself (Adachi et al. 1976), whereas the damping time due to the drag force obeying equation (5) (i.e., $\tau_{\rm D}$) does not depend on the eccentricity (see equation (7)). Here, for the eccentricity on which the damping time due to the gas-drag force depends, we substitute an eccentricity at the moment of the onset of an orbital crossing, $e_{\rm cross}$, i.e.,

$$e_{\rm cross} = \frac{1}{2}\, \Delta\tilde{a}_0\, h_{\rm PP}\ . \tag{16}$$

In both cases, first, the rapid increase in the eccentricities occurs at $t \simeq 5 \times 10^4$ yr and, right after the events, the eccentricities are damped owing to the drag forces, leaving the peaks of the eccentricities behind. In

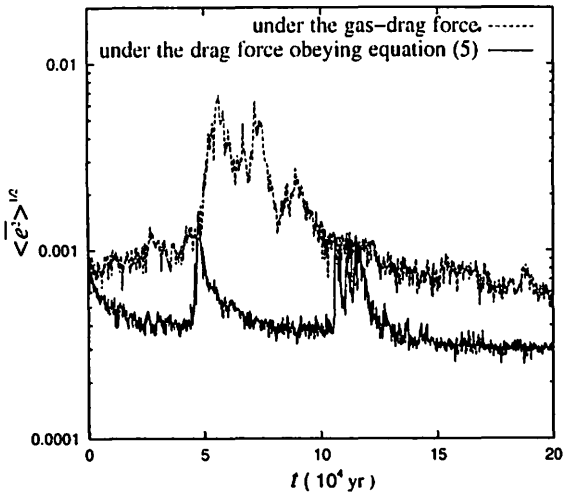

Figure 3: Time evolution of the root mean square of the eccentricities for both of the case with the drag force obeying equation (5) (solid line) and the case with the gas-drag force (dotted line). The characteristic damping time of the eccentricity, $T_{\rm damp}$, and $\Delta\tilde{a}_0$ for both cases are equally set to be $1.7 \times 10^3\, T_{\rm K}$ and 5.6, respectively. Sharp peaks of the eccentricities are seen in both cases at $t \simeq 5 \times 10^4$ yr.

spite of the sameness of $T_{\rm damp}$, the height of the peak under the drag force obeying equation (5) is considerably small compared with that under the gas-drag force. This is probably due to the difference in the e-dependence of the damping rate (which is proportional to an inverse of the damping time, $T_{\rm damp}$). For the cases with the gas-drag force, whose damping rate of the eccentricity is proportional to e, the damping effect becomes effective only at the late (high eccentricity) stage in the evolution of a system. On the other hand, for the cases with the drag force obeying equation (5) whose damping rate is independent of e, the damping effect works constantly. As a result, a system under the drag force obeying equation (5) is more strongly stabilized than a system under the gas-drag force and displays a low-peak behavior of eccentricities.

3.3 Critical Separation Distance

In subsection 3.1., we find that a protoplanet system suffering from the drag force obeying equation (5) experiences no orbital instabilities because of the strong stabilization due to the drag force, when $\Delta\tilde{a}_0$ is larger than a certain threshold (i.e., the transition zone). Furthermore, we see also that the position of the transition zone in the range of $\Delta\tilde{a}_0$ varies depending on $\tau_{\rm D}$ $(= T_{\rm damp})$, which controls the intensity of the drag force. In order to see the behavior of the transition zone against $T_{\rm damp}$ in detail, we introduce a critical separation distance, $(\Delta\tilde{a}_0)_{\rm crit}$, which represents a central value of the transition zone, i.e.,

$$(\Delta\tilde{a}_0)_{\rm crit} = \frac{(\Delta\tilde{a}_0)_1 + (\Delta\tilde{a}_0)_2}{2}\,, \qquad (17)$$

which is quite the same definition as that in Iwasaki et al. (2001). In figure 4, we plot $(\Delta\tilde{a}_0)_{\rm crit}$ as a function of the characteristic damping time of the eccentricity, $T_{\rm damp}$, for both of the case with the drag force obeying equation (5) (this study) and the case with the gas-drag force (Iwasaki et al. (2001)). In both cases, we can easily see that $(\Delta\tilde{a}_0)_{\rm crit}$ increases with a almost same inclination in proportion to a logarithm of $T_{\rm damp}$, although the heights of $(\Delta\tilde{a}_0)_{\rm crit}$ under the above two kinds of drag forces are different.

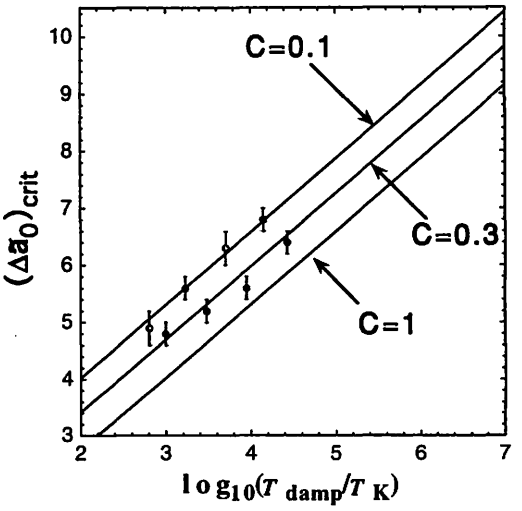

Figure 4: Critical separation distances, $(\Delta\tilde{a}_0)_{\rm crit}$, evaluated by our numerical calculations for both of the case under the drag force obeying equation (5) (filled circles) and the case under the gas-drag force (open circles) are plotted against $T_{\rm damp}$. Vertical error bars denote the widths of the transition zone $((\Delta\tilde{a}_0)_1 < \Delta\tilde{a}_0 < (\Delta\tilde{a}_0)_2)$. The critical values, which are evaluated by relation (19) are also shown for $C = 1$, $C = 0.3$, and $C = 0.1$, respectively.

The relation between $(\Delta\tilde{a}_0)_{\rm crit}$ and $T_{\rm damp}$ is also estimated on the basis of the following conjecture. As shown in subsection 3.1., a system with a small $\Delta\tilde{a}_0$ $(\Delta\tilde{a}_0 < (\Delta\tilde{a}_0)_{\rm crit})$ experiences an orbital instability, since the stirring time of the eccentricity due to the mutual gravity between the protoplanets is smaller than the damping time of the eccentricity due to the drag force, $T_{\rm damp}$. On the contrary, a system with a large $\Delta\tilde{a}_0$ $((\Delta\tilde{a}_0)_{\rm crit} < \Delta\tilde{a}_0)$ is stabilized owing to the drag force, since $T_{\rm damp}$ is smaller than the stirring time due to the mutual gravity. As a consequence, in the intermediate zone of $\Delta\tilde{a}_0$ $(\Delta\tilde{a}_0 \simeq (\Delta\tilde{a}_0)_{\rm crit})$, the stirring time of the eccentricity due to the mutual gravity must equilibrate with $T_{\rm damp}$. Here, the stirring time of the eccentricity due to the mutual gravity is supposed to be proportional to the orbital instability time under the drag-free condition, $T_{\rm inst}$. Therefore, when $\Delta\tilde{a}_0 = (\Delta\tilde{a}_0)_{\rm crit}$, we expect that the relation

$$T_{\rm damp} = C\, T_{\rm inst} \qquad (18)$$

is realized, where C is a numerical constant. Substituting equation (15) for $T_{\rm inst}$, we obtain the relation between $(\Delta\tilde{a}_0)_{\rm crit}$ and $T_{\rm damp}$, i.e.,

$$(\Delta\tilde{a}_0)_{\rm crit} = 1.28 \log_{10}[T_{\rm damp}/(C\, T_{\rm K})] + 0.19\,. \qquad (19)$$

In figure 4, the above estimated relation is also shown for $C = 1$, 0.3, and 0.1, respectively. First, we notice that the relation (19) for $C = 1$ does not fit the critical separation distances, $(\Delta\tilde{a}_0)_{\rm crit}$, which are found by our numerical calculations. This is reflected by the fact that, in an actual evolution of a system, the eccentricities of the protoplanets increase not uniformly but abruptly in the last limited period of the orbital instability time, $T_{\rm inst}$. Thus, in relation (18), we should balance only a small proportion of $T_{\rm inst}$ with $T_{\rm damp}$, in other words, set the value of C to be smaller than 1.

Second, we find that $(\Delta\tilde{a}_0)_{\rm crit}$ under the drag force obeying equation (5) follows the relation (19) for $C = 0.3$, although, as already shown in Iwasaki et al., the relation for $C = 0.1$ reproduces well the trend of $(\Delta\tilde{a}_0)_{\rm crit}$ under the gas-drag force. This is probably because, as pointed out in subsection 3.2., the damping effect of the eccentricities due to the drag force obeying equation (5) is constantly effective from the earlier stage in the evolution of a system, although the damping effect due to the gas-drag force becomes effective only in the later stage. Therefore, for the cases with the drag force obeying equation (5), $T_{\rm damp}$ in relation (18) must be balanced with a larger proportion of $T_{\rm inst}$ (i.e., $T_{\rm inst}$ with a larger value of C) compared with that for the cases with the gas-drag force. Consequently, $(\Delta\tilde{a}_0)_{\rm crit}$ under the drag force obeying equation (18) becomes small (i.e., the unstable zone is narrow) in comparison with that under the gas-drag force.

4 Summary and Conclusion

In the present study, we investigated the effect of the drag force which is proportional to the random velocity of a protoplanet on the orbital instability of a protoplanet system. For such purpose, we calculated numerically the orbits of protoplanets including both of the mutual gravity between protoplanets and the drag force. Our obtained results are summarized as follows.

(1) Under the drag force which is proportional to the random velocity of a protoplanet, the occurrence of an orbital instability of a protoplanet system is prevented more or less through damping of the eccentricities of the protoplanets.

(2) The effect of the drag force becomes remarkable, when the initial separation distance, $\Delta\tilde{a}_0$, excesses the critical separation distance, $(\Delta\tilde{a}_0)_{\rm crit}$, and, as a result, the orbital instability time under the drag force, $T^{\rm df}_{\rm inst}$ becomes more than 200 times as large as the orbital instability time under the drag-free condition, $T_{\rm inst}$. In short, a protoplanet system experiences no orbital instabilities substantially under such conditions.

(3) The value of $(\Delta\tilde{a}_0)_{\rm crit}$ depends on the characteristic damping time of the eccentricity due to the drag force, $\tau_{\rm D}$, and is estimated by the following relation, i.e.,

$$(\Delta\tilde{a}_0)_{\rm crit} = 1.3\log_{10}(\tau_{\rm D}/T_{\rm K}) + 0.86\,. \qquad (20)$$

Here, it should be noted that the above results are limited to the case with an ideal protoplanet system (in which the masses and radial spacings of protoplanets are equal, the initial orbital eccentricities and inclinations are zero, and the number of protoplanets, N, equals 5). According to Chambers et al. (1996), even in a system with dispersions of masses and spacings of protoplanets, the orbital instability time under the gas-free condition changes hardly from $T_{\rm inst}$ in equation (15). They also investigated the effect of the number of protoplanets and confirmed that for $N \geq 5$, the orbital instability time is almost constant independently of N. Furthermore, as pointed out in Iwasaki et al. (2001), the orbital repulsions will work as a stabilizing mechanism safely for larger N, since the typical length of a expansion in the separation distance caused by an orbital repulsion ($\leq 0.2\,r_{\rm H}$) is smaller than the width of the transition zone ($= 0.4\,r_{\rm H}$) even under the drag force obeying equation (5) (for details see Iwasaki et al. (2001)). As for initial eccentricities and inclinations of protoplanets, we need to perform additional simulations for a protoplanet system with initially finite eccentricities ($\geq 2\,h_{\rm PP}$) and inclinations ($\geq h_{\rm PP}$), since, in such a system, the orbital instability time is short by several orders of magnitude compared with that in an ideal system (Yoshinaga et al. 1999).

By evaluating the value of $\tau_{\rm D}$, we estimate the typical value of $(\Delta\tilde{a}_0)_{\rm crit}$ in an actual protoplanet system. First, we consider the effect of the dynamical friction due to a swarm of planetesimals. In order to determine the value of $\tau_{\rm D}$, we must know the mean of the eccentricities of planetesimals, $e_{\rm m}$. Ida and Makino (1993) showed that, in the presence of massive protoplanets, the eccentricities of planetesimals are determined by the balance between the stirring effect of the eccentricity due to the gravitational scattering with the protoplanets and the damping effect due to the gas-drag force by the solar nebular gas, i.e.,

$$e_{\rm m} = 7\left(\frac{m}{10^{23}{\rm g}}\right)^{\frac{1}{18}}\left(\frac{a}{1{\rm AU}}\right)^{\frac{27}{4}}\left(\frac{\rho_{\rm g}}{1\times10^{-9}{\rm g\,cm^{-3}}}\right)^{-\frac{1}{6}} h_{\rm P} \qquad (21)$$

where $\rho_{\rm g}$ is the density of the gas nebula at 1AU. Here, note that $e_{\rm m}$ depends on the gas density, $\rho_{\rm g}$, and, thus, the value of $\tau_{\rm D}$ varies according to the gas density, $\rho_{\rm g}$, even when the surface density of a swarm of planetesimals is fixed. Substituting $e_{\rm m}$ and $i_{\rm m}$ ($= 1/2\,e_{\rm m}$) for equation (8), we obtain from equations (8) and (20)

$$(\Delta\tilde{a}_0)_{\rm crit} = 7.5\,, \qquad (22)$$

where the gas density, $\rho_{\rm g}$, is set to be that in the minimum mass nebula model ($= 1\times10^{-9}{\rm g\,cm^{-3}}$) (Hayashi 1981). In the above, the surface mass density of planetesimals is supposed to be half as much as that in the minimum mass nebula model (we assume that a half of the solid mass is accreted on the protoplanets). Second, the effect of the tidal torque due to the density wave excited in the nebular gas disk is considered. On the basis of the gas nebula in the minimum gas nebula model where $c_{\rm s} \simeq 1.0\times10^{5}{\rm cm\,s^{-1}}$ at 1AU (Hayashi 1981), $(\Delta\tilde{a}_0)_{\rm crit}$

is evaluated from equations (11) and (20), i.e.,

$$(\Delta\tilde{a}_0)_{\rm crit} = 6.1\ , \qquad (23)$$

where, in equation (11), we substitute $3.0 \times 10^6 {\rm cm\ s^{-1}}$, which is the Keplerian circular velocity at 1AU, for $v_{\rm K}$.

According to Kokubo and Ida (1998) and (2000), the typical separation distance, $\Delta\tilde{a}_0$, between the protoplanets, which are formed through the accretion of planetesimals, is about 10 or less. Thus, for an actual protoplanet system to experience an orbital instability certainly, the critical separation distance, $(\Delta\tilde{a}_0)_{\rm crit}$ must be more than 10. However, as shown in the present study, taking into account the effect of the gravitational interaction (i.e., the dynamical friction and tidal interaction) with the gas and/or planetesimal disk, $(\Delta\tilde{a}_0)_{\rm crit}$ becomes 6.1, which is too small for the occurence of an orbital instability of a protoplanet system with a typical orbital separation.

Extrapolating the relation (20) with a larger value of $T_{\rm damp}$ than that in our parametric range, we understand that $(\Delta\tilde{a}_0)_{\rm crit}$ becomes as large as about 10 for both of the effect of the dynamical friction with a swarm of planetesimals (equation (8)) and the effect of the tidal interaction with the gas nebula (equation (11)), when the (surface) mass density of the gas nebula decreases to about one-thousand times as large as that in the minimum mass solar nebula model (the surface mass density of planetesimals does not need to be reduced). However, as mentioned above, these results are applicable only to a protoplanet system with initially small eccentricities and inclinations. Thus, for a system with large random velocities on initial configuration, maybe the orbital instability occurs, even when the surface mass density of the nebular gas is larger than the above value.

Chambers and Wetherill (1998) tried to reproduce the formation process of the terrestrial planets from the protoplanets by the long-term N-body calculations, including the perturbations by the Jupiter and Saturn, but no surroundings like the nebular gas or planetesimals. Their results showed that the planets formed in their simulations have commonly large eccentricities about 10 times as large as those of the present terrestrial planets. This implies that after the formation of the terrestrial planets, the nebular gas and/or planetesimals still remain around planets and decrease the eccentricities of the planets to those on the present level through the hydrodynamic gas drag by the nebular gas and/or gravitational interaction with the gas or planetesimal disk. On the other hand, if the drag force acting on the protoplanets is too intense, the onset of the orbital instability of a protoplanet system will be prevented and, as a result, the growth of protoplanets due to their mutual collisions will not start.

As a result of the present work, we find that a realistic protoplanet system experiences an orbital instability and is followed by the collisional evolution, when the surface mass density of the gas nebula decreases to about one-thousand times as large as that in the minimum mass solar nebula model. Furthermore, if such a gas nebula exists around the planets after the formation of the terrestrial planets, the eccentricity of a terrestrial type planet with the Earth mass can be reduced owing to the tidal interaction with the gas nebula within about 1×10^6 year, which is sufficiently small compared with the life time of the solar nebula ($\simeq 1 \times 10^7$ year). Thus, our result seems to support the scenario of the terrestrial planet formation mentioned above. However, from our simulation, we cannot elucidate whether or not the terrestrial planets will be actually formed through succesive collisions and accretions, suffering from the drag force due to the solar nebula. We hope that another simulations, which include both of the collisions end accretions between protoplanets and the effect of the drag force will be performed.

ACKNOWLEDGMENTS

The authors express their sincere gratitude to H.Tanaka and S. Ida for continuous encouragement and valuable advice. Numerical computaion was helped by SX-5/16 at the Computer Center of Tokyo Institute of Technology.

References

Adachi, I., Hayashi, C., & Nakazawa, K. 1976, Prog. Theor. Phys. 56, 1756

Artymowicz, P. 1993, ApJ 419, 166

Chambers, J. E., & Wetherill, G. W. 1998, Icarus 136, 304

Chambers, J. E., Wetherill, G. W., & Boss, A. P. 1996, Icarus 119, 261

Hayashi, C. 1981, Prog. Theor. Phys. Suppl. 70, 163

Ida, S. 1990, Icarus, 88, 129

Ida, S., & Makino, J. 1993, Icarus 106, 210

Ito, T., & Tanikawa, K. 1999, Icarus 139, 336

Ito, T., & Tanikawa, K. 2001, PASJ 53, 143

Iwasaki, K., Tanaka, H., Nakazawa, K, & Emori, H. 2001, PASJ 53, 321

Kokubo, E., & Ida, S. 1998, Icarus 131, 171

Kokubo, E., & Ida, S. 2000, Icarus 114, 247

Kokubo, E., & Makino, J. 1998, in Proceedings of the 30th symposium on celestical mechanics, ed T. Fukushima, T. Ito, T. Fuse, H. Umehara, p248

Kokubo, E., Yoshinaga, K., & Makino, J. 1998, MNRAS 297, 1067

Makino, J., & Aarseth, S. J. 1992, PASJ 44, 141

Ward, W. R. 1988, Icarus 73, 330

Wetherill, G. W., & Stewart, G. R. 1989, Icarus 77, 330

Yoshinaga, K., Kokubo, E., & Makino, J. 1999, Icarus 139, 328

The Effects of a Stellar Encounter on a Planetesimal Disk

Hiroshi Kobayashi and Shigeru Ida

Department of Earth and Planetary Sciences, Faculty of Science,
Tokyo Institute of Technology
2-12-1 Ookayama, Meguro, Tokyo 152-8551, Japan
Phone: +81-3-5734-2243
Fax : +81-3-5734-3538
E-mail: hkobayas@geo.titech.ac.jp,

Abstract

We investigate the effects of a passing stellar encounter on a planetesimal disk through analytical calculations as well as numerical simulations. We derive analytical formulae for orbital eccentricity (e) and inclination (i) of planetesimals pumped up by perturbations of a passing single star. Using the formulae, we derive the boundary radius ($a_{\rm planet}$) outside which planet formation is inhibited by the pumped-up e and i. We model a protoplanetary system as a disk of massless particles circularly orbiting a host star. The massless particles represent planetesimals. A single star as massive as the host star encounters the protoplanetary system. Numerical orbital simulations show that e and i are pumped strongly and have steep radial gradients in the outer region at $a \gtrsim 0.25D$ where D is pericenter distance of the encounter. In the in inner region, e and i are not change well and have power-law dependence on (a/D) as $e \propto (a/D)^{5/2}$ and $i \propto (a/D)^{3/2}$, independent of the encounter parameters. Since planet accretion is inhibited by e as small as 0.01, which is in the inner region, we focus on the weakly perturbed inner region to derive analytical formulae of the pumped-up e and i. We analytically reproduce the power-law dependence and explicitly give numerical factors of the power-law dependence as functions of encounter parameters. Using the formulae, we derive the boundary radius ($a_{\rm planet}$) of planet forming region as a function of dynamical parameters of a stellar cluster, assuming the protoplanetary system belongs to the stellar cluster. Since the radial gradient of e is so steep that the boundary is sharply determined. Planetesimal orbits are significantly modified beyond the boundary, while they are almost intact inside the boundary. We find $a_{\rm planet} \sim$ 40-60AU in the case of $D \sim$ 150-200AU. $D \sim$ 200AU may be likely to occur in a relatively dense cluster. We point out that the size of planetary systems ($a_{\rm planet}$) may be necessarily restricted to that comparable to the size of planet region ($\sim$ 30-40AU) of our Solar system. Similar sizes of inner hole radius of observed extrasolar dust-disks might be regulated by $a_{\rm planet}$, although we need to take into account migration processes of dust materials.

1 Introduction

In general, stars are born as members of an open cluster. Stellar clusters would evaporate on timescales more than 10^8 years (Kroupa 1995;1998). This evaporation would be caused by gravitational interactions between stars, so that many stars experience gravitational perturbations of the other stars during the evaporation. More than half of T Tauri stars have protoplanetary disks (e.g., Beckwith & Sargent 1996), which would eventually form planetary systems on timescales $10^6 - 10^9$ years (e.g., Safronov 1969, Wetherill 1980, Hayashi et al. 1986). Planetary systems would be affected by stellar encounters more or less during their formation stage.

In the standard model (e.g., Safronov 1969; Wetherill 1980; Hayashi et al. 1986), terrestrial planets and cores of jovian planets accrete from planetesimals that are formed in a protoplanetary disk. The accretion of jovian planet cores is followed by gas accretion onto the core when the core acquires critical mass $\sim 5 - 15 M_\oplus$ (e.g., Mizuno 1980; Bodenheimer & Pollack 1986; Ikoma *et al.* 2000).

The passing stellar encounters would pump up orbital eccentricity e and inclination i of planetesimals. The velocity dispersion between planetesimals is given by $\sim \sqrt{e^2 + i^2} v_{\rm kep}$, where i is given in unit of radian and $v_{\rm kep}$ is Keplerian velocity (e.g., Safronov 1969; Lissauer & Stewart 1993; Ohtsuki *et al.* 1993). If the velocity dispersion exceeds their surface escape velocity of the planetesimals, a collision between planetesimals results in disruption rather than accretion (e.g., Safronov 1969; Greenberg *et al.* 1978; Ohtsuki 1993). Then, planetesimal accretion would be forestalled. As shown in Eq. (30) in section 5, if pumped-up e and i are larger than 0.01, the velocity dispersion exceeds the surface escape velocity of planetesimals in the early stage. Therefore, only small orbital modifications ($e, i \gtrsim 0.01$) can give significant influence on planet formation.

As we will show in sections 3 and 4, the radial gradient of e and i is rather steep; e and i are highly pumped up in the outer planetesimal disk, while the inner disk is almost intact. The steep gradient leads

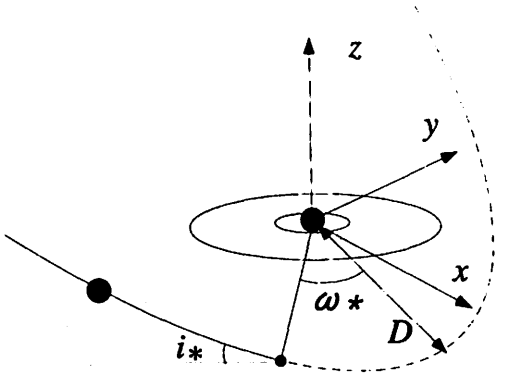

Figure 1: Encounter configuration in the frame centered at the primary star with mass M_1. The orbit of the passing star with mass M_2 is characterized by pericenter distance D, eccentricity e_*, inclination i_* and argument of perihelion ω_*. If length and mass are scaled by D and M_1, the encounter parameter are M_* ($= M_2/M_1$), e_*, i_* and ω_*.

to a sharp boundary of the disk that divides the strongly perturbed region where planet formation is inhibited and the intact region where planet formation keeps going. The boundary radius determines radial size of the region of a planetary system where planetary-sized bodies exist. Most planetesimals in the outermost region are ejected (and some of them are captured by the passing star), which would truncate the region of the planetary system where solid materials exist. Here we are concerned with the former size.

In the present paper, we derive analytical formulae of pumped-up e and i and discuss the effects on planetary formation. In section 2, we explain calculation models. In section 3, we show results of numerical simulations. The analytical formulae are derived in section 4. The e and i pumped up by stellar perturbations in the weakly perturbed inner regime are explicitly given as functions of heliocentric radius and parameters of stellar encounters. Using the analytical formulae, in section 5, we discuss the size of planet forming region as a function of parameters of stellar clusters. We will show the radius of planet forming region is likely to be 40-60AU, in the case of a dense cluster, which may be consistent with the Solar system.

2 Calculation Model and Basic Equations

We model a planetesimal disk as non-self-gravitating, collisionless particles that initially have coplanar circular orbits around a primary (host) star, because two-body relaxation time and mean collision time of planetesimals are much longer than encounter timescale that a passing star stay near a primary star. The particulate disk encounters a hypothetical passing star. The equation of motion of a planetesimal in the heliocentric frame (the frame with the primary star at center) is

$$\frac{d^2\mathbf{r}_j}{dt^2} = -\frac{GM_1}{|\mathbf{r}_j|^3}\mathbf{r}_j + \frac{GM_2}{|\mathbf{R}-\mathbf{r}_j|^3}(\mathbf{R}-\mathbf{r}_j) - \frac{GM_2}{|\mathbf{R}|^3}\mathbf{R}, \tag{1}$$

where M_1 and M_2 are masses of the primary and the passing stars, $\mathbf{r}_j$ and $\mathbf{R}$ are position vectors of the planetesimal j and the passing star. The first term in the r. h. s. is force to produce Kepler motion around the primary star, and the second and third terms are direct and indirect perturbing forces of the passing star.

We scale length by pericenter distance D of the stellar encounter, mass by the primary star mass M_1, and time by $\Omega_{\rm kep}^{-1}$ where $\Omega_{\rm kep}$ is Keplerian frequency at $a = D$ given by $\sqrt{GM_1/D^3}$. Equation (1) is then transformed to

$$\frac{d^2\tilde{\mathbf{r}}_j}{d\tilde{t}^2} = -\frac{\tilde{\mathbf{r}}_j}{|\tilde{\mathbf{r}}_j|^3} - \frac{M_*(\tilde{\mathbf{r}}_j-\tilde{R})}{|\tilde{\mathbf{r}}_j-\tilde{R}|^3} - \frac{M_*\tilde{R}}{|\tilde{R}|^3}, \tag{2}$$

where $M_* = M_2/M_1$, $\tilde{\mathbf{r}}_j = \mathbf{r}_j/D$, $\tilde{\mathbf{R}} = \mathbf{R}/D$, and $\tilde{t} = \Omega_{\rm kep}t$. Thus the parameters of encounters are inclination (i_*) relative to the initial planetesimal disk, eccentricity (e_*), and argument of perihelion (ω_*) of orbit of the passing star, and the scaled passing star mass (M_*). The encounter geometry is illustrated

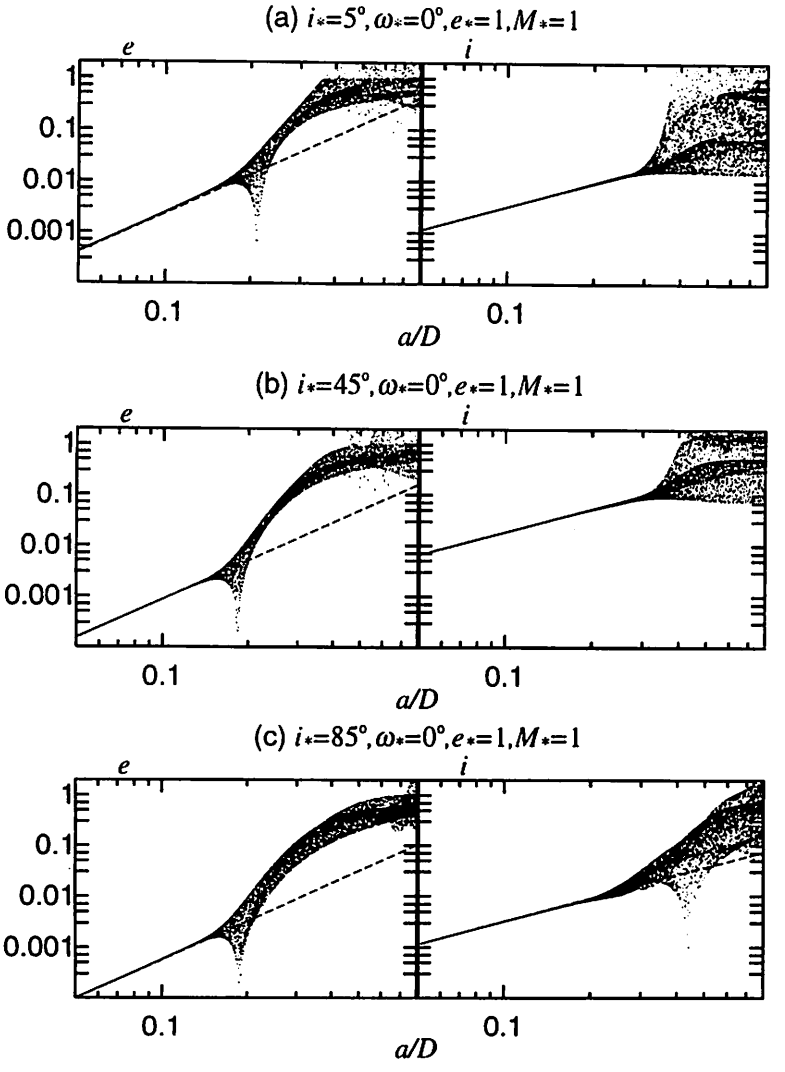

Figure 2: Orbital eccentricity e and inclination i of particles pumped-up by a passing star, as a function of scaled semimajor axis a/D, in the case with $\omega_* = 0°$, $e_* = 1$ and $M_* = 1$. Orbital inclination of the passing star is (a) 5°, (b) 45° and (c) 85°. Dashed lines express analytical expression derived in Eqs. (28) and (29) in Section 4. The dashed lines are almost distinguishable from the numerical results.

in Fig. 1. We calculate changes in e and i of the planetesimal according to Eq. (1) or (2) with various encounter parameters, through orbital integrations and analytical estimations.

3 Numerical Integration

Regarding the method of numerical integration, we follow (Ida *et al.* 2000). We integrated orbits of 10,000 particles with surface number density $n_s \propto a^{-3/2}$. The particles are distributed in the region $a/D = 0.05 - 0.8$. Since we neglect mutual gravity and collisions of planetesimals, the particular choice of a-dependence of n_s and outer and inner edges of the disk does not affect the results. The initial e and i of particles are 0. We integrated Eq. (2), using a fourth order predictor-corrector scheme. Many variations of encounter geometry, encounter velocity, and passing star mass were examined.

Figures 2 show the dependence of i_*, in the case with $\omega_* = 0°$, $e_* = 1$ and $M_* = 1$. i_* are 5° (Fig. 2a), 45° (Fig. 2b), 85° (Fig. 2c). The numerical results show i is strongly dependent on i_* like $\propto \sin 2i_*$ in the inner region. Comparison between i_* as well as ω_*. Analytical results are also plotted. In the inner region, $e = e_0(a/D)^{5/2}$ and $i = i_0(a/D)^{3/2}$. We investigate the dependence of e_0 and i_0 on ω_* and i_*, in the case with $e_* = 1$ and $M_* = 1$.

We next show the range of the power-law inner region is regulated by $\Omega_{\rm kep}$ and Ω_*, where $\Omega_{\rm kep} =$

$\sqrt{GM_1/a^3}$ and $\Omega_* = \sqrt{G(M_1+M_2)(1+e_*)/D^3}$ are the Keplerian frequency of a planetesimal with semimajor axis a and the angular velocity of the passing star at pericenter. Figure 2 show that if $\Omega_{\rm kep} \gtrsim 5\Omega_*$ ($a/D \lesssim 0.2$ in case with $e_* = 1$ and $M_* = 1$), ϵ is in proportion to $(a/D)^{2.5}$. If $\Omega_* \lesssim \Omega_{\rm kep} \lesssim 5\Omega_*$ ($0.2 \lesssim a/D \lesssim 0.3$ in case with $e_* = 1$ and $M_* = 1$), ϵ is pumped up most steeply. In this region, resonant interactions are important (Ostriker 1994). The condition of $n:1$ commensurability is $\Omega_*/\Omega_{\rm kep} = (a/D)^{3/2}\sqrt{(1+M_*)(1+e_*)} = 1/n$. For example, the 5:1, 4:1 and 3:1 resonances are at $a/D \simeq 0.21$, 0.25 and 0.30 in the case with $e_* = 1$, $M_* = 1$ (Fig. 2). The resonances lower than 5:1 dominate non-resonant effects in this case. Numerical simulations suggest that the boundary between the inner and outer regions is at the 5:1 commensurability, $a/D \simeq [(1+M_*)(1+e_*)]^{-1/3}(1/5)^{2/3}$, in the case of prograde encounters and at the 3:1, $a/D \simeq [(1+M_*)(1+e_*)]^{-1/3}(1/3)^{2/3}$, in the case of retrograde encounters. Ostriker (1994) analytically derived consistent conditions. If $\Omega_{\rm kep} \lesssim \Omega_*$ ($a/D \gtrsim 0.63$ in case with $e_* = 1$ and $M_* = 1$), there is no Lindblad resonance, so that a-gradient is less steep than that in the resonant region.

In the outer and outermost regions, pumped-up e and i depend not only on initial radial position but also on azimuthal position of planetesimals. In the case of a prograde encounter, particles in the near side of the disk at pericenter passage are affected by resonances while ones in the far side are hardly affected. In these region, $\Omega_{\rm kep}$ is not large enough compared with Ω_*, so that such asymmetry remains. In the case of a retrograde encounter, only far-side planetesimals are affected.

Such strong encounters would have many interesting features as mentioned in Section 1. However, in order to discuss the effects on planet accretion, the regimes of e, $i \sim 0.01$ are important (section 5). The pumped-up e and i in such regimes are near the inner region. Hence, analytical linear calculations would well predict the effects on planet accretion.

4 Analytical Solution

We derive analytical formulae of pumped-up e and i in the inner region. Orbital integrations show that in that region, $e = e_0(a/D)^{5/2}$ and $i = i_0(a/D)^{3/2}$. The analytical formulae explain these dependence on (a/D) as well as dependence of e_0 and i_0 on M_*, i_*, ω_* and e_*.

We adopt the following approximations to derive pumped-up e and i in the inner region.

(i) $\Delta a/a$ is neglected, since $\Delta a/a \ll e, i$,

(ii) orbital averaging is applied for planetesimal orbits, since $\Omega_{\rm Kep} \gg \Omega_*$,

(iii) e, i, $a/D \ll 1$ (the inner region).

In the equation of motion of a planetesimal given by Eq. (1), the second and third terms in the r. h. s. stand for the perturbation forces of the passing star. We define

$$\mathbf{F}_{\rm perturb} = \frac{GM_2}{|\,\mathbf{R}-\mathbf{r}\,|^3}(\mathbf{R}-\mathbf{r}) - \frac{GM_2}{|\,\mathbf{R}\,|^3}\mathbf{R}. \tag{3}$$

We divide the perturbation force into r, θ, and z components,

$$\mathbf{F}_{\rm perturb} = \bar{R}\mathbf{e}_r + \bar{T}\mathbf{e}_\theta + \bar{N}\mathbf{e}_z, \tag{4}$$

where $\mathbf{e}_r$ ($= \mathbf{r}/|\,\mathbf{r}\,|$), $\mathbf{e}_\theta$ and $\mathbf{e}_z$ are unit vectors in the radial, tangential, and normal components in initial orbital plane of the planetesimal disk, respectively. We define $h = e\sin(\omega+\varphi), k = e\cos(\omega+\varphi), p = \sin i \sin\varphi$ and $q = \sin i\cos\varphi$, where ω and φ are the argument of pericenter and longitude of ascending node of a planetesimal. The equation of motion with these orbital elements in $h, k, p, q \ll 1$ ($e, i \ll 1$: assumption (iii)) are (Brouwer & Clemence 1961)

$$\frac{dh}{dt} \simeq \sqrt{\frac{a}{GM_1}}(-\bar{R}\cos\theta + 2\bar{T}\sin\theta), \tag{5}$$

$$\frac{dk}{dt} \simeq \sqrt{\frac{a}{GM_1}}(\bar{R}\sin\theta + 2\bar{T}\cos\theta), \tag{6}$$

$$\frac{dp}{dt} \simeq \sqrt{\frac{a}{GM_1}}\bar{N}\sin\theta, \tag{7}$$

$$\frac{dq}{dt} \simeq \sqrt{\frac{a}{GM_1}}\bar{N}\cos\theta, \tag{8}$$

where $\theta = f + \omega + \varphi$ (f is true anomaly) and we retained the lowest order terms of e and i in the right hand side. $\mathbf{F}_{\rm perturb}$ defined by Eq. (3) is expanded as a series of a/D up to the order $(a/D)^2$:

$$\mathbf{F}_{\rm perturb} \simeq \frac{GM_2}{R^3}\left[\left(3\frac{\mathbf{R}\cdot\mathbf{e}_r}{R}\mathbf{R} - R\mathbf{e}_r\right)\left(\frac{a}{R}\right) + \left\{\left(\frac{15}{2}\frac{(\mathbf{R}\cdot\mathbf{e}_r)^2}{R^2} - \frac{3}{2}\right)\mathbf{R} - 3(\mathbf{R}\cdot\mathbf{e}_r)\mathbf{e}_r\right\}\left(\frac{a}{R}\right)^2\right], \quad (9)$$

where $R = \mid \mathbf{R} \mid$ and $\mathbf{e}_r = \mathbf{r}/a$. We denote $\mathbf{F}_{\rm perturb} = \bar{R}\mathbf{e}_r + \bar{T}\mathbf{e}_\theta + \bar{N}\mathbf{e}_z$, where $\mathbf{e}_\theta$ and $\mathbf{e}_z$ are unit vectors in the tangential and vertical directions. We denote that $\mathbf{e}_r = (\cos\theta, \sin\theta, 0)$ and $\mathbf{R} = (R_x, R_y, R_z)$ in the Cartesian coordinates where the initial planetesimal disk is on the x-y plane and the x-axis is directed to ascending node of the passing star's orbit. The components, $\bar{R}, \bar{T}$ and $\bar{N}$ are

$$\begin{aligned}
\bar{R} &\simeq \frac{GM_2}{R^3}\left[\left(3\frac{(R_x\cos\theta + R_y\sin\theta)^2}{R} - R\right)\left(\frac{a}{R}\right)\right. \\
&\left. + \left\{\left(\frac{15}{2}\frac{(R_x\cos\theta + R_y\sin\theta)^2}{R^2} - \frac{9}{2}\right)(R_x\cos\theta + R_y\sin\theta)\right\}\left(\frac{a}{R}\right)^2\right], \quad (10)\\
\bar{T} &\simeq \frac{GM_2}{R^3}\left[3\frac{(R_x\cos\theta + R_y\sin\theta)}{R}(-R_x\sin\theta + R_y\cos\theta)\left(\frac{a}{R}\right)\right. \\
&\left. + \left\{\left(\frac{15}{2}\frac{(R_x\cos\theta + R_y\sin\theta)^2}{R^2} - \frac{3}{2}\right)(-R_x\sin\theta + R_y\cos\theta)\right\}\left(\frac{a}{R}\right)^2\right], \quad (11)\\
\bar{N} &\simeq \frac{GM_2}{R^3}\left[3\frac{(R_x\cos\theta + R_y\sin\theta)}{R}R_z\left(\frac{a}{R}\right)\right. \\
&\left. + \left(\frac{15}{2}\frac{(R_x\cos\theta + R_y\sin\theta)^2}{R^2} - \frac{3}{2}\right)R_z\left(\frac{a}{R}\right)^2\right]. \quad (12)
\end{aligned}$$

We take orbit averaging, e.g.,

$$\left\langle\frac{dh}{dt}\right\rangle = \frac{\int_0^{2\pi}(dh/dt)d\theta}{2\pi}. \quad (13)$$

Substituting Eqs. (10), (12), and (11) into Eqs. (5), (6), (7) and (8) and taking the orbit averaging, we obtain

$$\left\langle\frac{dh}{dt}\right\rangle \simeq -\frac{GM_2}{R^3}\sqrt{\frac{a}{GM_1}}R_x\left[\frac{75}{16}\frac{R_x^2+R_y^2}{R^2} - \frac{15}{4}\right]\left(\frac{a}{R}\right)^2, \quad (14)$$

$$\left\langle\frac{dk}{dt}\right\rangle \simeq \frac{GM_2}{R^3}\sqrt{\frac{a}{GM_1}}R_y\left[\frac{75}{16}\frac{R_x^2+R_y^2}{R^2} - \frac{15}{4}\right]\left(\frac{a}{R}\right)^2, \quad (15)$$

$$\left\langle\frac{dp}{dt}\right\rangle \simeq \frac{GM_2}{R^3}\sqrt{\frac{a}{GM_1}}R_y\left[\frac{3}{2}\frac{R_z}{R}\right]\left(\frac{a}{R}\right), \quad (16)$$

$$\left\langle\frac{dq}{dt}\right\rangle \simeq \frac{GM_2}{R^3}\sqrt{\frac{a}{GM_1}}R_x\left[\frac{3}{2}\frac{R_z}{R}\right]\left(\frac{a}{R}\right), \quad (17)$$

where "$<\ >$" means the orbit averaging. Note that this averaging eliminate (a/R)-term of (14) and (15 because of the dependance on θ.

Finally, we integrate them along the trajectory of the passing star:

$$\begin{pmatrix} R_x \\ R_y \\ R_z \end{pmatrix} = \begin{pmatrix} R\cos(f_* + \omega_*) \\ R\sin(f_* + \omega_*)\cos i_* \\ R\sin(f_* + \omega_*)\sin i_* \end{pmatrix}, \quad (18)$$

where f_* is the true anomaly of the passing star. We integrate Eqs. (5) to (8) over time t from $-\infty$ to ∞.

$df_*/dt = \sqrt{G(M_1+M_2)(e_*+1)D}/R^2$ and $R = (e_*+1)D/(1+e_*\cos f_*)$. We integrate $\langle< dh/dt\rangle >$, $\langle< dk/dt\rangle >$, $\langle< dp/dt\rangle >$ and $\langle< dq/dt\rangle >$ by f_* instead of by t,

$$\begin{aligned}
\Delta h &\simeq -\frac{15}{4(e_*+1)^{5/2}}\frac{M_*}{\sqrt{M_*+1}}\left(\frac{a}{D}\right)^{5/2} \\
&\int_{-\gamma}^{\gamma}\left[\frac{5}{4}(\cos^2(f_*+\omega_*) + \sin^2(f_*+\omega_*)\cos^2 i_* - 1\right] \quad (19)\\
&\times \cos(f_*+\omega_*)(1+e_*\cos f_*)^2 df_*, \quad (20)
\end{aligned}$$

$$\Delta k \simeq -\frac{15}{4(1+e_*)^{5/2}}\frac{M_*}{\sqrt{M_*+1}}\left(\frac{a}{D}\right)^{5/2} \int_{-\gamma}^{\gamma}\left[\frac{5}{4}\{\cos^2(f_*+\omega_*)+\sin^2(f_*+\omega_*)\cos^2 i_*\}-1\right] \times \sin(f_*+\omega_*)\cos i_*(1+e_*\cos f_*)^2 df_*, \quad (21)$$

$$\Delta p \simeq \frac{3}{8(1+e_*)^{3/2}}\frac{M_*}{\sqrt{M_*+1}}\left(\frac{a}{D}\right)^{3/2}\sin 2i_* \int_{-\gamma}^{\gamma}\{1-\cos 2(f_*+\omega_*)\}(1+e_*\cos f_*)df_*, \quad (22)$$

$$\Delta p \simeq \frac{3}{4(1+e_*)^{3/2}}\frac{M_*}{\sqrt{M_*+1}}\left(\frac{a}{D}\right)^{3/2}\sin i_* \int_{-\gamma}^{\gamma}\sin 2(f_*+\omega_*)(1+e_*\cos f_*)df_*, \quad (23)$$

where γ is $\cos^{-1}(-1/e_*)$. The results of integration are

$$\Delta h \simeq -\frac{15}{4(e_*+1)^{5/2}}\frac{M_*}{\sqrt{M_*+1}}\left(\frac{a}{D}\right)^{5/2}\cos\omega_* \left[\frac{1}{8}\gamma e_*^4(5\cos^2 i_*-1)+\sqrt{e_*^2-1}\left\{\frac{e_*2}{6}(1+2e_*^2) -\frac{1}{24}(2+e_*^2+12e_*^4)\sin^2 i_*+\frac{1}{6}(e_*^2-1)^2\cos 2\omega_*\sin^2 i_*\right\}\right], \quad (24)$$

$$\Delta k \simeq \frac{15}{4(e_*+1)^{5/2}}\frac{M_*}{\sqrt{M_*+1}}\left(\frac{a}{D}\right)^{5/2}\sin\omega_*\cos i_* \left[\frac{1}{8}\gamma e_*^4(15\cos^2 i_*-11)+\sqrt{e_*^2-1}\left\{\frac{e_*2}{6}(1+2e_*^2) -\frac{1}{24}(-2+19e_*^2+28e_*^4)\sin^2 i_*+\frac{1}{6}(e_*^2-1)^2\cos 2\omega_*\sin^2 i_*\right\}\right], \quad (25)$$

$$\Delta p \simeq \frac{3}{8(e_*+1)^{3/2}}\frac{M_*}{\sqrt{M_*+1}}\left(\frac{a}{D}\right)^{3/2}\sin 2i_* \left[2\gamma+\frac{2}{3}e_*\sqrt{1-e_*^{-2}}\{(e_*^{-2}-1)\cos 2\omega_*+3\}\right], \quad (26)$$

$$\Delta q \simeq \frac{e_*}{2}\left(\frac{1-e_*^{-2}}{e_*+1}\right)^{5/2}\frac{M_*}{\sqrt{M_*+1}}\left(\frac{a}{D}\right)^{3/2}\sin i_*\sin 2\omega_*. \quad (27)$$

Since we start with $h,k,p,q=0$, the changes are equal to final h, k, p and q of the planetesimals. Using $e=\sqrt{h^2+k^2}=\sqrt{(\Delta h)^2+(\Delta k)^2}$ and $i=\sqrt{p^2+q^2}=\sqrt{(\Delta p)^2+(\Delta q)^2}$, the pumped-up e and i are calculated. Especially, the results of parabolic encounter ($e_*=1$) are

$$e \simeq \frac{15\pi}{128\sqrt{2}}\frac{M_*}{\sqrt{1+M_*}}\left(\frac{a}{D}\right)^{\frac{5}{2}} \left[\cos^2\omega_*\left\{5\cos^2 i_*-1\right\}^2+\sin^2\omega_*\cos^2 i_*\left\{15\cos^2 i_*-11\right\}^2\right]^{\frac{1}{2}}, \quad (28)$$

$$i \simeq \frac{3\alpha}{8\sqrt{2}}\frac{M_*}{\sqrt{1+M_*}}\left(\frac{a}{D}\right)^{\frac{3}{2}}\sin 2i_*. \quad (29)$$

5 Size of a Planet Forming Region

In the last section, we have derived analytical expressions for e and i pumped up by a passing stellar encounter. The expressions perfectly agree with numerical calculations in the region $e \lesssim 0.01$. In this section, we estimate the size of planet forming region in a protoplanetary disk, using these analytical expressions.

If velocity dispersion $v_{\rm d}$ of planetesimals exceeds surface escape velocity $v_{\rm esc}$ of the colliding planetesimals, the collision results in disruption rather than accretion. The velocity dispersion $v_{\rm d}$ is $\sim \sqrt{e^2+i}\ v_{\rm kep}$ (e.g., Safronov 1969; Lissauer & Stewart 1993; Ohtsuki *et al.* 1993). In many cases around $(e^2+i^2)^{1/2}\sim 0.01$, $e \gtrsim i$. Pumped-up i does not necessarily produce velocity dispersion directly, because the planetesimals with pumped-up i tend to have similar orbital planes. Thus we use e instead of

$(\epsilon^2 + i^2)^{1/2}$ to evaluate v_d. The condition $v_d > v_{esc}$ is equivalent to

$$\epsilon > 0.01 \left(\frac{m}{10^{22}\mathrm{g}}\right)^{\frac{1}{3}} \left(\frac{\rho}{1\mathrm{g/cm}^3}\right)^{\frac{1}{6}} \left(\frac{a}{10\mathrm{AU}}\right)^{\frac{1}{2}}, \tag{30}$$

where the nominal value of $m \sim 10^{22}$ g corresponds to typical mass of Kuiper belt objects and ρ is internal density of the planetesimal. Equation (30) shows that e as small as 0.01 significantly affects planetary accretion.

As shown in sections 3 and 4, the radial gradient of e is so steep that there is a sharp boundary of the disk that divides the planet forming region and the disruptive region where planet formation is inhibited. Here we derive the radius of the boundary as a function of physical parameters of the stellar cluster which the host star of the planetary system belonged to.

In the case with $e \gtrsim 0.01$, the analytical expressions slightly underestimate the pumped-up e, since resonant effects are also important in this case. However, we can use them to estimate the boundary radius, because the radial gradient of e is so steep that the underestimation hardly changes the estimation of the boundary radius.

We are mostly concerned with parabolic encounters ($e_* = 1$), since for encounters we are interested in, e_* is not far from 1, as follows. The specific angular momentum (l_*) and specific energy (E_*) of the passing star orbit relative to the primary star are $\sim v_* D \sim \sqrt{v_{*\mathrm{d}}^2 + [v_{\mathrm{kep}}(D)]^2} \times D$ and $v_{*\mathrm{d}}^2/2$, respectively, where $v_{*\mathrm{d}}$ is velocity dispersion of stars in a cluster. Thereby, $e_* = \sqrt{1 + 2l_*^2 E_*/G^2(M_1 + M_2)^2} \sim \sqrt{1 + (v_{*\mathrm{d}}/v_{\mathrm{kep}})^2[1 + (v_{*\mathrm{d}}/v_{\mathrm{kep}})]^2}$. Since $v_{*\mathrm{d}}$ is $\sim$ 1 km/s (Binney & Tremaine 1987) and $v_{\mathrm{kep}}(D)$ is larger than 1 km/s for $D \lesssim$ 1000AU, which we are interested in, e_* is ~ 1.

Substituting Eq. (28) which is taken the average with i_* and ω_* into Eq. (30), we obtain the boundary radius a_{planet} as

$$a_{\mathrm{planet}} \sim 40 \left(\frac{m}{10^{22}\mathrm{g}}\right)^{\frac{1}{6}} \left(\frac{A}{2}\right)^{\frac{1}{4}} \left(\frac{D}{150\mathrm{AU}}\right)^{\frac{5}{4}} \mathrm{AU}, \tag{31}$$

where $A = M_* + 1/M_*^2$. If M_* is 1, A is 2. The factor $(A/2)^{1/4}$ cannot significantly deviate from 1. The dependence of m on a_{planet} is very weak. Therefore, a_{planet} depends almost only on D. A stellar encounter with $D \sim$ 150-200AU restricts the disk radius of a planetary system (the disk radius of planet forming region) to 40-60AU.

Considering evaporation process of a stellar cluster, Adams and Laghlin (2001) estimated effective D before the evaporation as

$$D \sim 200 \left(\frac{R_{\mathrm{cluster}}}{2\mathrm{pc}}\right) \left(\frac{N}{2000}\right)^{-1} \mathrm{AU}, \tag{32}$$

where N is number of stars in a stellar cluster and R_{cluster} is size of the cluster. For the Trapezium cluster in Orion, $N \sim 2300$ and $R_{\mathrm{cluster}} \sim 2$ pc. In a dense cluster like Orion Trapezium, D is as small as 200AU, so that $a_{\mathrm{planet}} \sim$ 40-60AU. Ida *et al.* (2000) demonstrated that the high eccentricity and inclination of objects in the outer Kuiper Belt may be explained by the stellar encounter with $D \sim$ 150-200AU, which may suggest the Sun was born in a dense stellar cluster.

So far, we have only considered passing of a single star, however, passing of binary stars would also be important. Laughlin and Adams (1998) and Adams and Laghlin (2001) (also see the next section) suggested that passing binary encounters are more disruptive than passing single-star encounters. If we take into account the effects of passing binary encounters, a_{planet} may smaller tha Eq. (31).

We should investigate distribution of D (not only an effective value) as well as the effects of passing binary encounters, to discuss diversity of sizes of planetary systems in more detail.

6 Conclusion and Discussion

We have investigated the effects of a passing stellar encounter on a planetesimal disk through orbital integrations and analytical calculations. Since stars are generally born as members of a cluster and would stay in the cluster on timescales more than 10^8 years (Kroupa 1995;1998), a relatively close encounter, e.g., one with distance $\sim$ 200AU is likely to occur during formation age of a planetary system.

We considered that a disk of massless particles (planetesimals) orbiting a primary star encounters a passing single star. Encounter parameters are pericenter distance of the encounter (D), the argument of perihelion (ω_*), eccentricity (e_*) and inclination (i_*) of the orbit of the passing star, and the mass ratio (M_*) of the passing star's mass to the primary one. We showed that the pumped-up orbital eccentricities e and inclinations i of planetesimals have steep radial gradient. In the inner region at semimajor axis $a \lesssim \alpha\,[(1+M_*)/2]^{1/3}\,[(1+e_*)/2]^{1/3}\,D$, ($\alpha \simeq 0.2$ for a prograde encounter and $\alpha \sim 0.3$ for a retrograde

encounter) $e \propto (a/D)^{5/2}$ and $i \propto (a/D)^{3/2}$, independent of the encounter parameters. The result is also independent of initial azimuthal position of planetesimals, because orbital period of planetesimals is much shorter than passing time scale.

In the outer region $a \gtrsim \alpha\,[(1+M_*)/2]^{1/3}\,[(1+e_*)/2]^{1/3}\,D$, the radial gradient is steeper, but is not expressed by a single power-law. In this region, resonant effects are more important (Ostriker 1994).

The stellar perturbations significantly affect the outer part of a planetesimal disk. Even in the inner disk, e and i that are pumped up to $\gtrsim 0.01$ inhibit further planetesimal accretion. Because the velocity dispersion corresponding to $e, i \gtrsim 0.01$ exceeds the surface escape velocity of planetesimals, collisions between planetesimals should be disruptive. We investigate the relatively weakly perturbed region with $e, i \sim 0.01$ to study the effects on planetesimal accretion. Since a number of encounter parameters is rather large, numerical orbital integrations hardly cover entire phase space. We have derived analytical expressions of e and i in the power-law inner region.

In the derivation, we approximated the semimajor axis a of a planetesimal as a constant value, because the relative change of a is much smaller than the change of e and i during a stellar encounter. Since orbital period of planetesimals in the inner region is much shorter than the passing time scale, we apply orbit averaging of planetesimals' motion. As a result, we derived analytical expressions of the pumped-up e and i (Eqs. (28) and (29)) in the case with a parabolic encounter as

$$e \simeq \frac{15\pi}{32\sqrt{2}} \frac{M_*}{\sqrt{M_*+1}} \left(\frac{a}{D}\right)^{5/2} \times \left[\cos^2\omega_* \left(1-\frac{5}{4}\sin^2 i_*\right)^2 + \sin^2\omega_* \cos^2 i_* \left(1-\frac{15}{4}\sin^2 i_*\right)^2\right]^{1/2}, \tag{33}$$

$$i \simeq \frac{3\pi}{8\sqrt{2}} \frac{M_*}{\sqrt{M_*+1}} \left(\frac{a}{D}\right)^{3/2} \sin 2i_*. \tag{34}$$

Note that the dependence on ω_* is weak in both expressions (almost more for i_*) and that on i_* is also weak in the former expression. The analytical formulae agree with the numerical results within a factor 2. We also calculated e and i in the case with a hyperbolic encounter in Section 4.

Since the radial gradient of e is so steep that there is a sharp boundary in the disk that divides the planet forming region and the disruptive region where planet formation is inhibited. Planetesimal orbits are significantly modified beyond the boundary, while they are almost intact inside the boundary. We derived the boundary radius ($a_{\rm planet}$) by the condition that the pumped-up velocity dispersion of planetesimals is equal to their surface escape velocity (Eq.(31)):

$$a_{\rm planet} \sim 40 \left(\frac{m}{10^{22}{\rm g}}\right)^{\frac{1}{6}} \left(\frac{A}{2}\right)^{\frac{1}{4}} \left(\frac{D}{150{\rm AU}}\right)^{\frac{5}{4}} {\rm AU}, \tag{35}$$

where $A \simeq M_* + 1/M_*^2$ and m is planetesimal mass. The variation of $(A/2)^{1/4}$ is small. The dependence of $a_{\rm planet}$ on m is very weak. Thereby $a_{\rm planet}$ depends almost only on D. In a dense cluster like Orion Trapezium, D is as small as 200AU (Adams & Laughlin 2001). Such a stellar encounter with 150-200AU restricts the disk radius of a planetary system (the disk radius of planet forming region) to 40-60AU.

In the Solar system, there would be no planetary-sized object beyond Neptune at 30AU. Kuiper-belt objects beyond Neptune have velocity dispersion considerably larger than their surface escape velocity. These might be accounted for by a stellar encounter in a dense stellar (Ida *et al.* 2000; Adams & Laughlin 2001). Our Solar system may have belonged to a dense stellar in the formation age.

In a dense stellar cluster, planetary systems cannot be significantly larger than the size of the planetary region of our Solar system ($\sim$ 30-40AU). To discuss diversity of sizes of planetary systems in detail, we will need to investigate distribution of D (not only an effective value). In the present paper, we have only considered passing of a single star, however, passing of binary stars would also be important. Laughlin & Adams (1998;2000) suggested that passing binary encounters are more disruptive than passing single-star encounters. We performed several runs of passing close binary stars. The results show that the encounter of close binary stars is similar to a single stellar encounter, except that e is pumped up more highly at some resonant positions corresponding to the binary frequency even in the inner region. If we take into account the effects of passing binary encounters, $a_{\rm planet}$ may become smaller.

The effects of cumulative distant (large D) encounters may be neglected compared with a few closest encounters.The successive distant encounters change h, k, p, q defined in section 4 constructively or destructively, so that their averages would be zero. Their dispersions depend on D with large negative power-indexes (< -3), so that the cumulative effects integrated by $2\pi DdD$ would quickly vanish with D.

Disruptive collisions at $a > a_{\rm planet}$ would produce dust materials, which might form dust-debris disks around Vega-like stars. Although radiative pressure and pointing Robertson effect would cause migration

of the dust materials (Artymowicz 1997; Backman & Paresce 1993), $a_{\rm planet}$ may be closely related with the radius of inner holes of dust-debris disks. The radii of the observed inner holes around ϵ Eridani (Greaves *et al.* 1999), HD 14156 (Andrillat *et al.* 1990; Augereau *et al.* 1999; Weinverger *et al.* 1999;2000) HD 207129 (Jourdain de Muizon *et al.* 1999) and HR 4796A (Jura *et al.* 1995;Fajardo-Acosta *et al.* 1998) are 30-100AU, which are comparable to $a_{\rm planet}$ in the case of relatively dense clusters. We need more detailed analysis of distribution of $a_{\rm planet}$ as a function of environment parameters of stellar clusters, combined with discussions of collision outcomes and migration processes of dust materials, to discuss the diversity of inner holes of dust-debris disks.

REFERENCE

Adams, F. C., and G. Laughlin 2001. preprint

Andrillat, Y., M. Jaschek, and C. Jaschek 1990. *Astron. Astrophys.* **233**, 474-476.

Artymowicz, P. 1997. *Annu. Rev. Earth Planet. Sci.* **25**, 175-219.

Augereau, J. C., A. M. Lagrange, D. Mouillet, and F. Mnard 1999. *Astron. Astrophys.* **350**, L51-L54.

Backman, D. E., and F. Paresce 1993. In *Protostars and planets III* (E. H. Levy and J. Lunine, Eds.), pp. 1253-1304. Univ. of Arizona Press, Tucson.

Beckwith,S. V. W., and A. I. Sargent 1996. *Nature* **383**, 139-144.

Binney, J., and S. Tremaine 1987. *Galactic Dynamics.* Princeton Univ. Press, Princeton.

Bodenheimer, P., and J. B. Pollack 1986. *Icarus*, **67**, 391-408.

Brouwer, D., and G. M. Clemence, 1961. *Methods of Celestial Mechanics.* Academic Press, New York.

Fajardo-Acosta, S. B., C. M. Telesco, C. M., and R. F. Knacke 1998. *Astron. J.* **115**, 2101-2121.

Goldreich, P., and W. R. Ward 1973. *Astrophys. J.* **183**, 1051-1062

Greaves, J. S., and 10 colleagues, 1998. *Astrophys. J.* **506**, L133-L137.

Greenberg, R., W. K. Hartmann, C. R. Chapman, and J. F. Wacker, 1978. *Icarus* **35**, 1-26.

Hayashi, C. 1981. *Prog. Theor. Phys. Suppl.* **70**, 35-53.

Hayashi, C., K. Nakazawa, and Y. Nakagawa 1985. In *Protostars and Planets II* (D. C. Black and M. S. Matthews, Eds.), pp. 1100-1153. Univ. of Arizona Press, Tucson.

Ida, S., J. Larwood, and A. Burkert 2000. *Astrophys. J.* **528**, 351-356.

Ikoma, M., K. Nakazawa, and H. Emori 2000. *Astrophys. J.* **537**, 1013-1025.

Jayawardhana, R., S. Fisher, L. Hartmann, C. Telesco, R. Pina, and G. Fazio 1998. *Astrophys. J.* **503**, L79-L82.

Jura, M., A. M. Ghez,R. J. White, D. W. McCarthy, R. C. Smith, and P. G. Martin 1995. *Astrophys. J.* **455**, 451-456.

Jourdain de Muizon, M., and 10 colleagues, 1999. *Astron. Astrophys.* **350**, 875-882.

Kroupa, P. 1995. *Mon. Not. R. Astron. Soc.* **277** 1507-1521.

Kroupa, P. 1998. *Mon. Not. R. Astron. Soc.* **298**, 231-242.

Larwood, J. D., and P. G. Kalas 2001. *Mon. Not. R. Astron. Soc.* **323**, 402-416.

Laughlin G., and F. C. Adams 1998. *Astrophys. J.* **508**, L171-L174.

Laughlin G., and F. C. Adams 2000. *Icarus*, **145**, 614-627.

Lissauer, J. J., and G. R. Stewart, 1993. In *Protostars and planets III* (E. H. Levy and J. Lunine, Eds.), pp. 1061-1088. Univ. of Arizona Press, Tucson.

Mizuno, H. 1980. *Prog. Theor. Phys.* **64**, 544-557.

Ohtsuki, K., S. Ida, Y. Nakagawa, and K. Nakazawa 1993. In *Protostars and Planets III* (E. H. Levy & J. Lunine Eds.), pp. 1089-1107. Univ. Arizona Press, Tucson.

Ohtsuki, K. 1993. *Icarus* **106**, 228-246.

Ostriker, E. C. 1994. *Astrophys. J.* **424**, 292-318.

Safronov, V. S. 1969. *Evolution of the Protoplanetary Cloud and Formation of the Earth and Planets.* Nauka Press, Moscow.

Weidenschilling, S. J., and J. N. Cuzzi 1993. In *Protostars and Planets III* (E. H. Levy and J. I. Lunine Eds.), pp. 1031-1060. Univ. of Arizona Press, Tucson.

Weinberger, A. J., E. E. Becklin, G. Schneider, B. A. Smith, P. J. Lowrance, M. D. Silverstone, B. Zuckerman, and R. J. Terrile 1999. *Astrophys. J.* **525**, L53-L56.

Weinberger, A. J., R. M. Rich, E. E. Becklin, B. Zuckerman, and K. Matthews 2000. *Astrophys. J.* **544**, 937-943.

Wetherill, G. W. 1980. *Annu. Rev. Astron. Astrophys.* **18**, 77-113.

The Formation of Planetesimals through the Fragmentation of a Dust Layer — The Initial Masses of Planetesimals —

Izumi Furuya
Graduate School of Science and Technology, Kobe University
Rokkodai-cho, Nada, Kobe, 657-8501, Japan
E-mail: furuya@jet.planet.sci.kobe-u.ac.jp

Yoshitsugu Nakagawa
Faculty of Science, Kobe University
Rokkodai-cho, Nada, Kobe, 657-8501, Japan
E-mail: yoshi@whynot.phys.kobe-u.ac.jp

Abstract

We investigate how planetesimals are formed with how mach of thier initial masses through the gravitational instability of dust layer, by performing local N-body simulations. According to the linear perturbation theory for axisymmetric mode, the dust layer formed in the mid-plane of the solar nebula is broken into ring-shaped fragments. The mass of planetesimals is estimated by assuming that these fragments are broken into sub-fragments having the same size both in the azimuthal and radial directions. However, in our simulations, such ring-shaped fragments are not formed during the process of planetesimal formation. Instead, we find this process can be classified into three stages — non-axisymmetric wake-like structure formation, initial clump formation, growth of initial clumps through mutual accretion. The masses of initial clumps and finally formed clumps are about 0.1 and 2-5 times as large as the analytic estimate.

1 Introduction

Two prevailing processes of planetesimal formation are proposed. The first is the gravitational fragmentation of a dust layer (e.g., Safronov 1969, Hayashi 1972, Goldreich and Ward 1973). The second is the growth through mutual sticking of dust particles(Weidenschilling and Cuzzi 1993, Stepinski and Valageas 1996, 1997). In this study, we pay attention to the first process and investigate how planetesimals are formed and how much their initial masses are.

The solar nebula is considered to be turbulent more or less at early stages. After such turbulent motion has decayed, dust particles settle toward the central plane of the nebula and accumulate into a thin layer around the central plane — a dust layer (Weidenschilling 1980, Nakagawa et al. 1981). When the density in the dust layer exceeds the Roche density, the layer becomes gravitationally unstable to fragment into a number of planetesimals (Hayashi 1972, Goldreich and Ward 1973). The sizes of the resulting fragments are estimated by the linear perturbation theory for axisymmetric mode (e.g., Toomre 1964), in terms of the critical wavelength given by

$$\lambda_{\rm crit} = \frac{4\pi^2 G\Sigma}{{\Omega_{\rm K}}^2}, \tag{1}$$

where Ω_K is the Keprerian angular velocity, G is the gravitational constant, and Σ is the surface density of the layer. The condition for gravitational instability of the layer is given by Toomre's parameter Q as

$$Q \equiv \frac{\sigma_r \Omega_K}{3.36 G \Sigma} < 1, \tag{2}$$

where σ_r is the radial velocity dispersion. If the above condition is met, the dust layer is unstable to perturbations of wavelengths around the critical wavelength λ_{crit} and broken into ring-shaped fragments. The mass of a planetesimal is estimated as $\pi \Sigma \lambda_{crit}^2$ by assuming that ring-shaped fragments are broken into sub-fragments having the same size both in the azimuthal and radial directions. The mass has not been evaluated by numerical simulations. In the present study, we reproduce the gravitational fragmentation by local N-body numerical simulations and compare the process of gravitational fragmentation and the obtained mass of a fragment with the analytic ones.

2 Simulation Method

We follow the motions of dust particles in a cell of a square $L \times L$ present in a narrow ring which is a part of the dust layer. We then apply a local N-body method which was first applied to the study of a dense ring system by Wisdom and Tremaine (1988) and then used by Salo (1991, 1992a, 1992b, 1995), Richardson (1993, 1994) and Daisaka and Ida (1999). In this study, we assume that all particles have the same radius r_p and mass m. We take only the mutual forces and inelastic collisions of the particles into account, but we leave the disruption, sticking of the particles and drag by nebular gas out of consideration.

The equations of motion can be written in non-dimensional forms independent of mass and the heliocentric distance a_0, if we scale the time by Ω_0^{-1}, the length by $ha_0 = r_H$ and the mass by $h^3 M_\odot$ (Hill 1878, Nakazawa 1988) :

$$\begin{aligned} \tilde{t} &= \Omega_0 t, \\ \tilde{r} &= (\tilde{x}, \tilde{y}, \tilde{z}) = \frac{(x, y, z)}{h a_0}, \\ \tilde{m} &= \frac{m}{h^3 M_\odot} = \frac{3}{2}, \end{aligned} \tag{3}$$

where h is the reduced Hill radius defined by

$$h = \left(\frac{2m}{3M_\odot}\right)^{\frac{1}{3}}. \tag{4}$$

With the above scaling, the equation of motion for particle i are

$$\begin{aligned} \ddot{\tilde{x}}_i - 2\dot{\tilde{y}}_i &= 3\tilde{x}_i + \frac{3}{2} \sum_{j=1, i \neq j}^{N} \frac{1}{\tilde{r_{ij}}^3} (\tilde{x_j} - \tilde{x_i}), \\ \ddot{\tilde{y}}_i + 2\dot{\tilde{x}}_i &= +\frac{3}{2} \sum_{j=1, i \neq j}^{N} \frac{1}{\tilde{r_{ij}}^3} (\tilde{y_j} - \tilde{y_i}), \\ \ddot{\tilde{z}}_i &= -\tilde{x}_i + \frac{3}{2} \sum_{j=1, i \neq j}^{N} \frac{\tilde{1}}{\tilde{r_{ij}}^3} (\tilde{z_j} - \tilde{z_i}). \end{aligned} \tag{5}$$

where N is the number of particles, m_j is the mass of particles j and r_{ij} is the distance between particles i and j.

We apply the initial conditions that the x and y coordinates of particles are chosen at random, avoiding overlapping of particles, and uniformly distributed across the unit cell. The vertical distribution is also taken to be uniform up to a distance of h above and below the equatorial plane. The position of pairs of particles are chosen symmetrically so that the center of mass will lie at the center of the unit cell. The velocities except for the shear velocity of individual particles $3\tilde{x}_i/2$ are chosen randomly so that the initial random velocity becomes large enough to achieve $Q > 2$, since Salo (1995) and Daisaka (1999) showed that $Q \simeq 2$ in the equilibrium state.

The calculated system is characterized by two non-dimensional parameters; the dynamical optical depth τ and the ratio $r_h/2r_p$. Having scaled the time by Ω_0^{-1} and the length by r_h, if we obtain one solution, we can use it as solutions for any arbitrary m and a_0. The number of particles whose centers lie in the unit cell is constant and is denoted by N. Thus the dynamical optical depth is given by

$$\tau \equiv \frac{N\pi r_p^2}{L_x L_y}. \tag{6}$$

The other parameter, the ratio $r_{\rm H}/2r_{\rm p}$, is

$$\frac{r_h}{2r_p} = 105.6\,(\frac{\rho}{2{\rm g/cm}^3})^{1/3}(\frac{a_0}{1{\rm AU}}), \tag{7}$$

where Sun's mass $M_\odot = 2.0 \times 10^{33}$g, and ρ is the material density of particles. According to Ohtsuki (1993), which carried out three-body trajectory integration, the possibility of accretion is determined by the ratio $r_{\rm H}/2r_{\rm p}$. Accretion is possible even inside the Roche limit. The capture probability decreases abruptly for $r_{\rm H}/2r_{\rm p} \leq \frac{3}{2}$, where the target body protrudes out of the Hill sphere.

In our simulations, we adopt a smooth inelastic hard sphere collision model that has been commonly used in previous simulations (Wisdom and Tremaine 1988, Salo 1991, 1992a, 1992b, 1995, Richardson 1994, Daisaka and Ida 1999). A collision changes only the impact velocity in normal direction depending on restitution coefficient $\epsilon_n (0 \leq \epsilon_n \leq 1)$. The change of tangential component is neglected, by assuming tangential restitution coefficient $\epsilon_t = 1$, in order to exclude the effects of the spins of particles. Hereinbelow ϵ denotes ϵ_n for simplicity. The relative velocity $\boldsymbol{v}'_{ij}$ after collision is given by

$$\boldsymbol{v}'_{ij} = \boldsymbol{v}_{ij} - (1+\epsilon)\frac{\boldsymbol{r}_{ij}\cdot\boldsymbol{v}_{ij}}{r_{ij}}\frac{\boldsymbol{r}_{ij}}{r_{ij}}, \tag{8}$$

where $\boldsymbol{v}_{ij}$ and $\boldsymbol{r}_{ij}$ are the relative velocity and the relative position of two colliding particles i and j. We treat ϵ as a parameter.

Ideally, a collision should be detected the instant it occurs. However, such operation is impractical, and hence a certain amount of penetration or temporary overlap is unavoidable. When two or more particles approach and overlap each other, we consider that they collide.

3 Results and Discussion

We study in detail how planetesimals are formed. In this study, we perform the simulation in the case of $r_{\rm H}/2r_{\rm p} = 2.05$ and $\tau = 0.1$. We set the size of calculation region $L = 2.44, 4.15$ and 6.00, where the total particle numbers are $N = 3200, 9248$ and 20884, respectively. We find that planetesimals are formed over three stages (see Figs.1). In the first stage ($t = 0.76T_{\rm K}$ in Figs.1), vague non-axisymmetric wake-like structure is formed. In the second stage ($t = 2.86T_{\rm K}$ in Figs.1), many particles accrete together at the same time to form initial clumps from place to place. In the third stage ($t = 18.15T_{\rm K}$ in Figs.1), these initial clumps grow through accreting

together and two large clumps are finally formed. These planetesimal formation stages are distinguished by the number of clumps evolution shown in Figs.2.

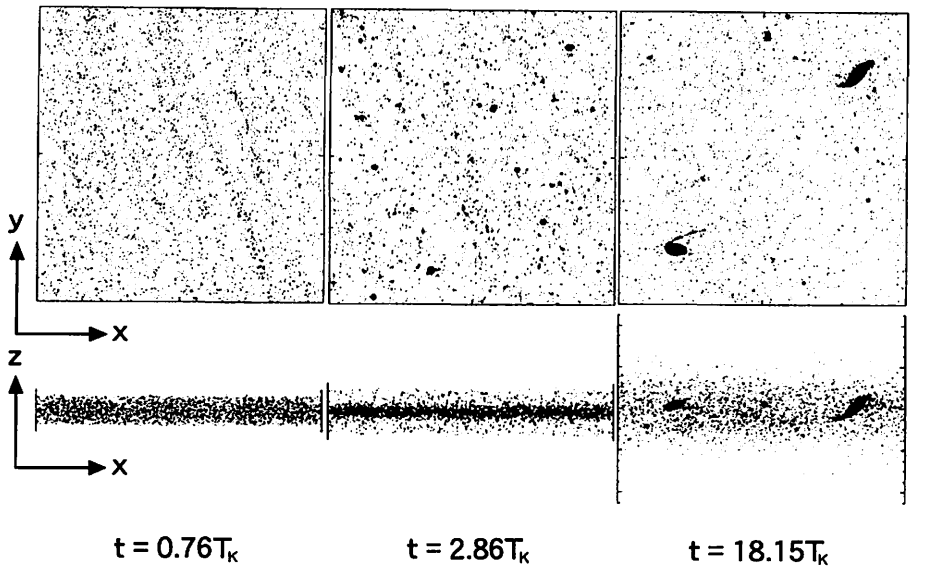

Figure 1: The evolution of perticle distribution in the case of $L/\lambda_{\rm crit} = 4.15$.

The left figure in Figs.2 shows that the number of clumps increases until a few Keplererian times (second stage), and decreases after that (third stage). The number of clumps reaches a maximum just when the Q-value becomes a minimum at $t = 2.86T_{\rm K}$ (see Figs.2). Here, we define a clump as an aggregate consisting of more than ten particles positioned at distances between each other of smaller than $1.5 \times 2r_{\rm p}$. In all these stages, ring-shaped fragments as the linear perturbation theory suggests are not formed. Thus, the process of planetesimal formation is defferent from that suggested by the linear perturbation theory. These results are common to all the simulations performed by us.

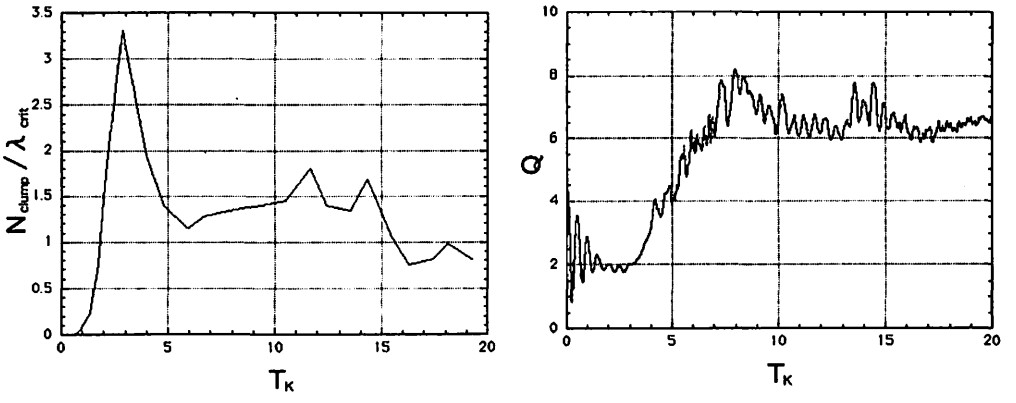

Figure 2: The evolution of the number of clumps in a unit area (i.e. ${\lambda_{\rm crit}}^2$) (left) and that of Q-value (right) in the case of $L/\lambda_{\rm crit} = 4.15$.

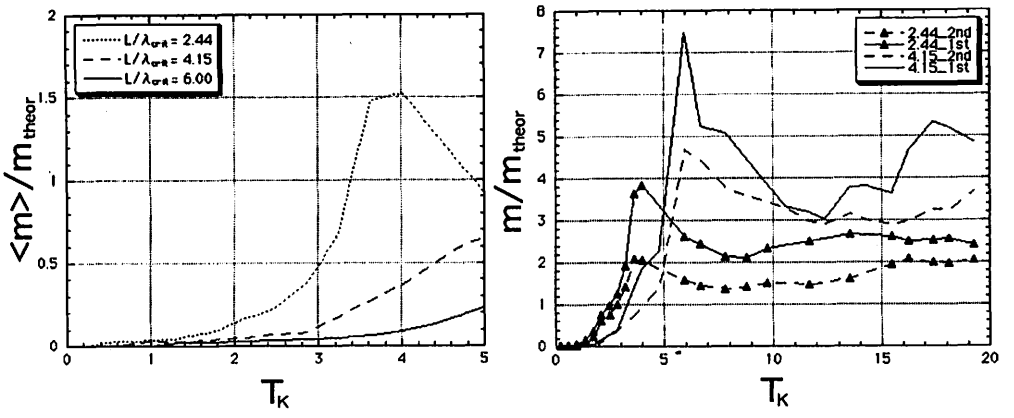

Figure 3: The evolution of mean mass of clumps (left) and two maximum clumps (right). The $m_{\rm theor}$ is 450 times of one particle mass.

Finally, we check the mass of clumps. The initial clumps have a mean mass (e.g. $t = 1.72, 2.86$ and $4.01T_K$ in the case of $L = 2.44, 4.15$ and 6.00, respectively.) of about $0.1m_{\rm theor}$ (see Fig.3), which is independent of the size of calculation area L. On the other hand, the clumps formed through mutual accretion of the initial clumps and the finally formed two large clumps have masses dependent of L and falling into the range $2\text{-}5m_{\rm theor}$, according to our simulations until now (see Fig.3). The finally formed clumps can be regarded as planetesimals and the obtained masses nearly agree with analytic estimate.

References

[1] Daisaka, H., and S. Ida, 1999. Spatial structure and coherent motion in dense planetary ring induced by self-gravitating instability. *Earth , Planet and Space*, **51**, 1195-1213.

[2] Goldreich, P., and W. R. Ward, 1973. The formation of planetesimals. *Astrophys. J.*, **183**, 1051-1061.

[3] Hayashi, C. 1972. Origin of the solar system. *In Proc. 5th Lunar Planetary Symposium, eds. K. Takayanagi and M. Shimizu (Tokyo:Inst. Space Aeronautical Sci.)*, pp.13-18.

[4] Hill, G. W., 1878. Researches in the lunar theory. *Amer. J. Math.*, **1**, 5-26, 129-147, 245-260.

[5] Nakagawa, Y. , Nakazawa, K. , and Hayashi, C., 1981. Growth and sedimentation of dust grains in the primordial solar nebula. *Icarus* **45**, 517-528.

[6] Nakazawa, K. and S. Ida, 1988. Hill's approximation in the three-body problem. *Prog. Theor. Phys. Suppl.*, **96**, 167-174.

[7] Ohtsuki, K. 1993. Capture probability of colliding planetesimals : Dynamical constraints in accretion of planets, satellites, and ring particles. *Icarus*, **106**, 228-246.

[8] Richardson, D. C., 1993. A new tree code method for simulation of planetesimal dynamics. *Mon. Not. R. Astron. Soc.*, **261**, 396-414.

[9] Richardson, D. C., 1994. Tree code simulations of planetary rings. *Mon. Not. R. Astron. Soc.*, **269**, 493-511.

[10] Safronov, V. S. 1969. Evolution of the Protoplanetary Cloud and Formation of the Earth and Planets. *NASA TTF-677*

[11] Salo, H. 1991. Numerical simulations of dense collisional systems. *Icarus*, **90**, 254-270.

[12] Salo, H. 1992a. Numerical simulations of dense collisional systems. II. Extended distribution of particle sizes. *Icarus*, **96**, 85-106.

[13] Salo, H. 1992b. Gravitational wakes in saturn's rings. *Nature*, **395**, 619-621.

[14] Salo, H. 1995. Simulation if dense planetary rings III. Self-gravitating identical particles. *Icarus*, **117**, 287-312.

[15] Stepinski, T. F. and Valageas, P. 1996. Global evolution of solid matter in turbulent protoplanetary disks. I. Aerodynamics of solid particles. *Astron. Astrophys.* **309**, 301-312.

[16] Stepinski, T. F. and Valageas, P. 1997. Global evolution of solid matter in turbulent protoplanetary disks. II. Development of icy planetesimals. *Astron. Astrophys.* **319**, 1007-1019.

[17] Toomre, A. 1964. On the gravitational stability of a disk of stars. *Astrophys. J.*, **139**, 1217-1238.

[18] Weidenschilling, S. J. 1980. Dust to planetesimals: Settling and coagulation in the solar nebula. *Icarus*, **44**, 172-189.

[19] Weidenschilling, S. J. and Cuzzi, J. N. 1993. Formation of planetesimals in the solar nebula. In *Protostars and Planets III* (Levy, E. H. and Lunine, J. L. , Eds), pp. 1031-1060. Univ. of Arizona Press, Tucson.

[20] Wisdom, J. and S. Tremaine, 1988. Local simulations of planetary rings. *Astron. J.*, **95**, 925-940.

Stability of a planet in a binary system; MACHO-97-BLG-41

Kazumasa Moriwaki
Graduate School of Science and Technology, Kobe University
Rokkodai-cho, Nada, Kobe, 657-8501, Japan
E-mail: moriwaki@jet.planet.sci.kobe-u.ac.jp

Abstract

This paper estimates an upper limit of binary eccentricity in the extrasolar planetary system, MACHO-97-BLG-41 lens system. This system is considered to be the first observed example of a planet orbiting around a binary star. Existence of a planet gives constraints on binary eccentricity. I performed long-term numerical integration of planetary orbital motions with various initial conditions of binary eccentricities, planet semimajor axis, planet eccentricity, and angle variables to see which kind of initial configuration produces the stable orbits during the integration (10^6 binary periods). The numerical results show that the upper limit of binary eccentricity in this system is 0.4 under the assumption of the initial circular orbit of the planet. In addition, I find that planetary orbits become unstable in shorter time scale when the planet eccentricity is higher. The numerical results show that the upper limit of the initial planetary eccentricity is 0.3. More over, I find that planetary retrograde orbit is more stable than prograde one.

Key words: binary: general - celestial mechanics - planetary system

1 Introduction

Among the 50 discovered extrasolar planets orbiting main sequence solar type stars only a few are confirmed to be in a binary star system. However, the majority of stars seem to form in binary or even multiple stellar systems. Therefore, an understanding of the stability of planets orbiting binary system is very important.

Orbits in binary systems have been traditionally separated into three categories. Following the designations of Dvorak (1986), the first includes planetary or P-type orbits. These are well outside the binary, where the planet essentially orbits the center of mass of the stars. The second type refers to the satellite or S-type orbits (such as 16Cyg B, 55 Cnc, τ Boo). These are orbits around one of the stars, with the second star considered to be a perturber. The third type refers to orbits near the L_4 or L_5 triangular Lagrangian points, which however are not normally of interest for binary systems because the mass ratio of the binary must be less than $\mu = m_2/(m_1 + m_2) \approx 0.04$ for the orbits to be linearly stable.

In this study, P-type orbits is examined. Recently, a quite suitable example for the dynamical test of stability was found - the planet orbiting the MACHO-97-BLG-41 lens systems (Bennett *et al* 1999). Gravitational microlensing events are observed via the time-varying magnification of the images as the lens system passes in front of the background source star. The separation of the images is too small to observe with current instruments. A planet orbiting the lens star

can be detected by a deviation of the microlensing light curve from the normal single lens light curve.

In this system, a planet of about $3M_J$ is orbiting a binary stellar system, which consist of a late-K dwarf and an M dwarf. The stars are separated by ~ 1.8 AU, and the planet orbits at a distance of about 7 AU (see Fig.1). The mass fractions of the three masses are 0.7870, 0.2086 and 0.0044. But binary eccentricity is unknown.

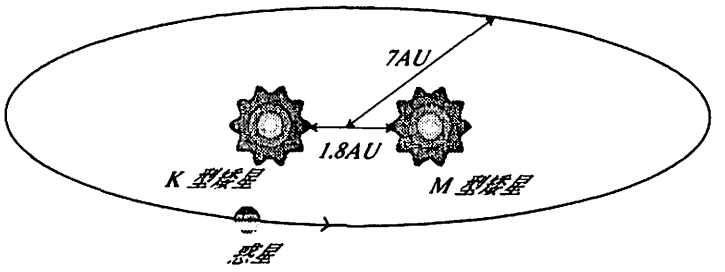

Figure 1: MACHO-97-BLG-41 lens system

The purpose of this study is to estimate the upper limit of the binary and planetary eccentricity by numerical integrations. It is estimated by the following procedure:

1. In the binary star system, the planet's future behavior is quite sensitive to initial conditions, especially binary eccentricity and mass ratio (Holman & Wiegert 1999).

2. The planetary orbit become unstable in a shorter time scale when the binary eccentricity is higher. (Dvorak 1986, Holman & Wiegert 1999)

3. It is natural to consider that existing planetary systems have been kept dynamically stable at least within the host star's age.

Given the binary eccentricity, planetary orbital motions are calculated by long term numerical integrations to find out whether the orbit is stable. If it become unstable within the host star's age, the assumed binary eccentricity is not suited for this system. In this way, I can estimate the binary and initial planetary eccentricity, which the planet is stable for a long time. In addition, I found that the planetary orbit become to be unstable in a short time when the planet eccentricity is higher. Then finally, the upper limit of the planet eccentricity is estimated.

In the first part of this paper, I estimate the upper limit of binary eccentricity of MACHO-97-BLG-41 lens system assuming a circular planet orbit. In the second part, I estimate the upper limit of planet eccentricity assuming a elliptic planet orbit. In the third part, I consider about the planetary retrograde orbit.

2 Calculation Method

This study investigates orbital stability numerically as a elliptic restricted three-body problem, in which a planet is modeled as a test particle moving in the gravitational field of a pair of stars on fixed eccentric orbits about each other. An approach first used by Dvorak (1986) is adopted, first, binary eccentricity, mass ratio and initial orbital longitude for the stars are chosen, and then a test particle on orbits near the binary is started.

For the orbital integrations, the symplectic mapping method of Yoshida (1990) is used. The time step of the integration is 1×10^{-2} of the binary period.

2.1 Initial Conditions

I adopt the binary mass ratio estimated from the microlensing observation. The mass ratio is $\mu = m_2/(m_1 + m_2) = 0.2086/0.9956$, in which m_1 and m_2 are the mass of the stars. Binary eccentricity in the range $0.0 \leq e \leq 0.7$ is examined. The initial phase of the binary orbit is another free parameter. The two extremes are examined: the binary initially at periapse and initially at apapse.

A test particle is initially on circular (or elliptic), prograde orbits (or retrograde) in the plane of the binary, is centered on the barycenter of binary. A semimajor axis of the test particle range from $1.5a_b$ to $5.0a_b$ (a_b is the binary semimajor axis). For each case of semimajor axis, eight cases of initial orbital longitudes: 0°, 45°, 90°, 135°, 180°, 225°, 270°, 315° are examined. The integration is performed for 10^6 binary periods, which corresponds to 2.8 Myr. The initial conditions of simulations are summarized in Table 1.

Table 1: Initial conditions for the binaries and test particles

Binaries	
semimajor axis	$a_b = 1.0$
mass ratio	$\mu = m_2/(m_1 + m_2) = 0.2086/0.9956$
eccentricity	$0.0 \leq e \leq 0.7, \Delta e = 0.1$
binary phase	periapse or apapse
Test particles (planets)	
orbital orientation	prograde or retrograde
semimajor axis	$1.5a_b \leq a \leq 5.0a_b, \Delta a_b = 0.1$
eccentricity	$0.0 \leq e_p \leq 0.4, \Delta e_p = 0.1$
eccentric anomaly	$0° \leq u \leq 360°, \Delta u = 45°$
	$i = \Omega = \omega = 0.0$*

*– A initial inclination of a test particle relative to the binary plane i, longitude of the ascending node Ω, and argument of perihelion ω are all set to be 0.0. The integration is performed for 46080 cases in total.

2.2 Determination of the stability limit

Given the initial conditions of the binary system and the test particle, the system is numerically integrated. During the course of the integration, escape orbits and close encounters between the test particles and stars are checked. If a test particle falls into one of the stars or escape from the system, integration is terminated. If the semimajor axis is large enough, test particle is stable. On the other hand, if semimajor axis is too short, a test particle is unstable. The critical semimajor axis is determined in the following way. At the end of the integrations, it is determined that the shortest semimajor axis at which the test particles at all initial longitudes survived the full integration time. I call this the upper critical semimajor axis (UCS). The critical semimajor axis determines the stability limit on the timescale of the numerical integration. On the other hand, the longest semimajor axis at which the test particles couldn't survive the full integration time is determined. I call this the lower critical semimajor axis (LCS).

3 Results

First, UCSs and LCSs are obtained as a function of binary eccentricity in the range of $0.0 \leq e \leq 0.7$, assuming that the planet is on initial circular (or elliptic) orbit. The result is organized in the following way: In § 3.1, the planet is on initial circular orbit (planetary eccentricity $e_p = 0.0$). In § 3.2, that is on initial elliptic orbit ($e_p = 0.1 - 0.4$). In § 3.3, that is on retrograde orbit.

3.1 initially circular orbit

For each values of e, the critical semimajor axis (UCSs and LCSs) is determined. Via least-squares fit to the data

$$a_{\rm UCS} = 2.19 + 6.64e - 5.42e^2, \tag{1}$$

$$a_{\rm LCS} = 1.72 + 4.49e - 2.32e^2, \tag{2}$$

Fig.2 shows the dependence of the initial semimajor axis of the planet on the binary eccentricity. One can see rather complicated structure of the grey region between the UCS and the LCS.

My results are very similar to those obtained by Holman & Wiegert (1999) even though my simulation are 100 times longer. They found the critical semimajor axis, (which corresponds to my 'Upper critical semimajor axis') is essentially independent of μ (mass ratio) and e, and provided the following equation.

$$\begin{aligned} a_{\rm c} &= (1.60 \pm 0.04) + (5.10 \pm 0.05)e \\ &+ (-2.22 \pm 0.11)e^2 + (4.12 \pm 0.09)\mu \\ &+ (-4.27 \pm 0.17)e\mu + (-5.09 \pm 0.11)\mu^2 \\ &+ (4.61 \pm 0.36)e^2\mu^2. \end{aligned} \tag{3}$$

In this system ($\mu = 0.2086/0.9956$), equation (3) is

$$a_{\rm c'} = 2.24 + 4.21e - 2.018e^2. \tag{4}$$

In Fig.3, my results are compared with Holman & Wiegert (1999). They concluded that an integration time of 10^4 binary periods was adequate to determine the stability boundary. Here it is seen that my data points follow the same general trend as those of Holman & Wiegert (1999), but typically at slightly larger values. This result indicates that, the stable region dose

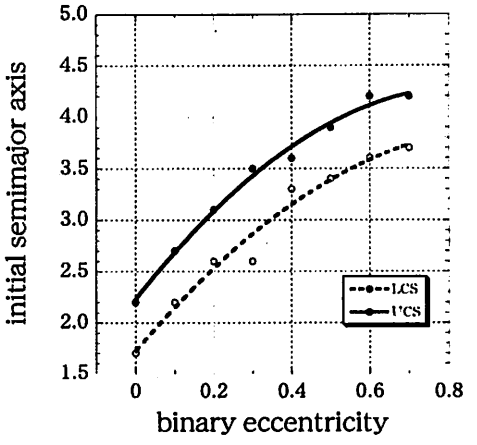

Figure 2: Critical semimajor axis as a function of eccentricity. The open circles show the UCS and the closed circles the LCS. The two lines represent the UCS and LCS given by a least square fit.

erode as the integration is extended, at least at higher binary eccentricities, but stable region was not shifted significantly by extending the integration to 10^6 periods. (A total of integration time 10^6 binary periods is still short compared with the ages of binary systems; therefore, it is possible that longer term instabilities will arise.)

In MACHO-97-BLG-41 lens system, the planet is separated from the stellar system centre of mass by 3.9 times the binary star separation, in the plane perpendicular to the line of sight. In Fig.2, most integrations with $e \geq 0.4$ become unstable within 10^6 binary period. When $e \leq 0.4$, all integrations are stable. Although the number of integrations may still not be enough to derive definite stastical conclusions, the upper limit of binary eccentricity of MACHO-97-BLG -41 lens system is estimated $e \leq 0.4$ assuming a circular planet orbit.

3.2 initially elliptic orbit

In this section, I study the effects of nonzero initial eccentricities of a planet. For each value e and e_p, UCS and LCS are determined. From the numerical results, an empirical expression of the critical semimajor axis can be derived as a function of e and e_p. The least-squares fit to the data (10^6 binary periods, $e_p = 0.0 - 0.3$) gives

$$\begin{aligned} a_{\rm UCS} &= 2.37 + 5.63e + (-1.13e_p) \\ &+ (-4.54e^2) + 17.2{e_p}^2 + (-2.04ee_p), \end{aligned} \tag{5}$$

$$\begin{aligned} a_{\rm LCS} &= 1.74 + 4.92e + (-2.23e_p) \\ &+ (-3.29e^2) + 22.8{e_p}^2 + (-4.51ee_p). \end{aligned} \tag{6}$$

In Fig.4 the dependence of the initial semimajor axis of the planet on the binary eccentricity is shown for four datasets ($e_p = 0.0 - 0.3$). It is seen that the stable region dose erode and unstable region expand as e_p increases, and the most of region is unstable when e_p is 0.4.

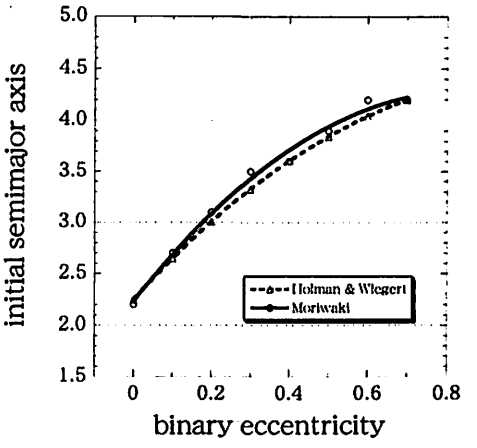

Figure 3: Critical semimajor axis as a function of eccentricity. The open circles are my results; the open triangles, those of Holman & Wiegert (1999). My least-squares fit is shown by the solid line; that of Holman & Wiegert, by dashed line. Our simulations were run 100 times longer (10^6 binary periods) than Holman & Wiegert (1999).

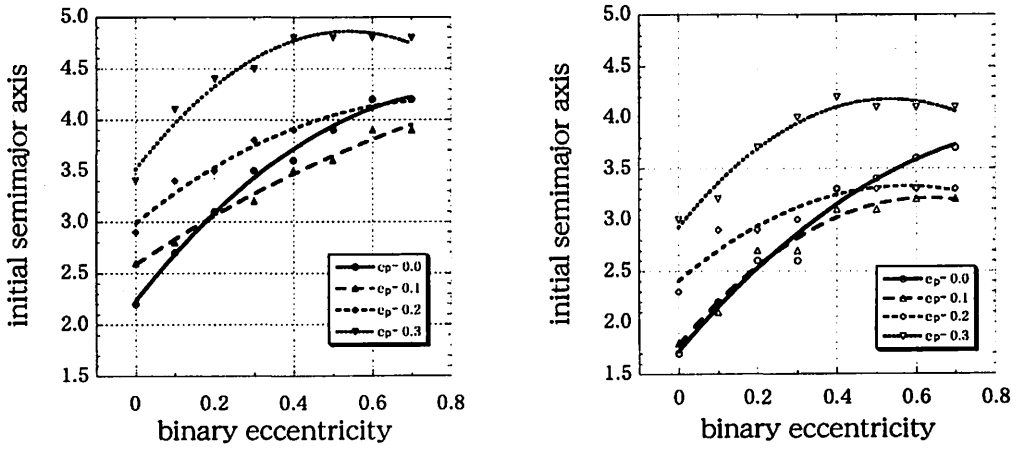

Figure 4: UCS(left) and LCS(right) as a function of eccentricity. Numerical integrations of 10^6 binary period is performed. The circle data points are $e_p = 0.0$; the triangles, $e_p = 0.1$; the squares,$e_p = 0.2$; the white triangles, $e_p = 0.3$.

In MACHO-97-BLG-41 lens system, the planet is separated from the stellar system centre of mass by 3.9 times the binary star separation. For each case of planet eccentricity e_p, I determine the upper limit of the binary eccentricity in the same way, § 3.1. The most of integrations with $e_p \geq 0.4$ become unstable within 10^6 binary periods. So, the upper limit planetary eccentricity of MACHO-97-BLG-41 lens system is estimated to be $e_p = 0.3$.

3.3 retrograde orbit

In this section, I study the effects of retrograde orbit of a planet, but it is mainly of theoretical interest. For each value e_p, UCS are determined. In Fig.5, the dependence of the initial semimajor axis of the planet on the binary eccentricity is shown for four datasets ($e_p = 0.0 - 0.3$).

I found that retrograde orbit is more stable than prograde. Wiegert & Holman(1988) also investigated the stability of planets in the α Cen system (binary eccentricity e is 0.52, mass ratio μ is 0.45). They only explored the case of zero planetary eccentricity and consider for non-zero inclinations. They found that retrograde orbit is stable outside $2.8a_b$. This is similar to my results (UCS is $2.8a_b$ when e is 0.5 and e_p is 0.4). Although the mass ratio of α Cen system is different from one of MACHO-97-BLG-41 lens system, UCSs do not depend on the mass ratio very much unless it changes by orders of magnitude (Szebehely(1980), Holamn & Wiegert(1999)).

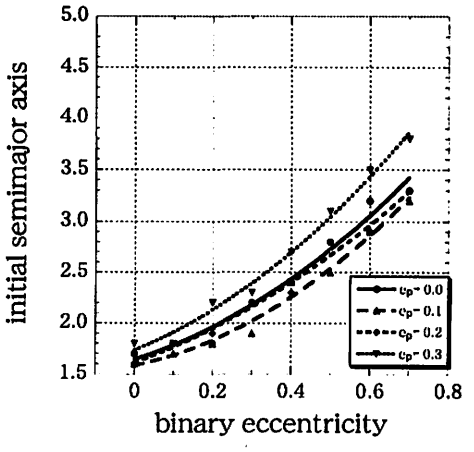

Figure 5: retrograde; (10^6 binary periods)

4 Conclusion

I have numerically estimated the upper limit of binary and planet eccentricity in MACHO-97-BLG-41 lens system. The binary eccentricity is $e \leq 0.4$ assuming a circular planet orbit. The planetary orbit becomes unstable in a short time scale when planet eccentricity is higher. When planet eccentricity is $e_p = 0.4$, there is not stable region in this system. Therefore, the upper limit of planet eccentricity is $e_p \leq 0.3$. In addition, I found that planetary retrograde orbit is stable than prograde one.

A test particle is integrated for 10^6 binary periods or approximately 2.8Myr. This is in fact very short time in comparison with the life time of the planetary system; therefore, it is possible that longer term instabilities will arise. Although the integration time of my calculations is significantly longer than Holman & Wiegert (1999), my results are mostly consistent with theirs. So, my result is a reasonable estimation.

References

[1] Benest, D. 1988. *Astron. Astrophys.* **206,** 143.

[2] — 1989. *Astron. Astrophys.* **223,** 361.

[3] — 1996. *Astron. Astrophys.* **314,** 983.

[4] Bennett, D. P.*et al.* 1999. *Nature* **402,** 57-59.

[5] Dvorak, R. 1986. *Astron. Astrophys.* **167,** 379-386.

[6] Dvorak, R., Froeschle, Ch., & Froeschle, Cl. 1989. *Astron. Astrophys.* **226,** 335-342.

[7] Holman, M. J. & Wiegert, P. A. 1999. *Astoron J,* **117,** 621-628.

[8] Szebehely, V., 1980. *Celest. Mech,* **22,** 7-12.

[9] Szebehely, V., & McKenzie, R. 1981. *Celest. Mech,* **23,** 3-7.

[10] Wiegert, P. A., & Holman, M. J. 1997. *Astron J,* **113,** 1445-1450.

[11] Yoshida H. 1990. *Phys. Lett. A,* **150,** 262.

Sweeping Secular Resonances in Extrasolar Planetary Systems

Makiko NAGASAWA, Shigeru IDA

Department of Earth and Planetary Sciences, Tokyo Institute of Technology, Meguro-ku, Tokyo 152-8551, Japan
E-mail:nagasawa@geo.titech.ac.jp

and

D. N. C. LIN

Board of Studies in Astronomy and Astrophysics, University of California, Santa Cruz, CA 95064

Abstract

We apply the sweeping secular resonances to the extrasolar planetary system. We analyze the evolution of planetary eccentricities of Upsilon Andromedae and HD168443 system during protoplanetary disk depletion. We found that the protoplanetary disk depletion changes the eccentricities of planets. On the other hand, the amplitudes of the periastron libration among the planets are not so changed. The origin of high eccentricities of the largest planet in Upsilon Andromedae system and the inner planet of HD168443 can be accounted by the sweeping secular resonance.

1. Introduction

Two multi-planet planetary systems were recently discovered. One is the three-planet system around Upsilon Andromedae, and another is the two-planet system around HD168443. The planets were detected using Doppler effects of light of host star due to a reflex motion of the planetary revolutions. Planets in these systems are thought to have larger masses than Jupiter. The variation in radial velocity of Upsilon Andromeda is nicely fitted with a model containing three planets. Butler et al. (1999) have determined orbits of these three planets. Inferred orbital elements of the Upsilon Andromedae planets are shown in Table 2(a) (http://exoplanets.org/esp/upsandb/upsandb.html). The variation in radial velocity of HD168443 is nicely fitted with a model containing two planets (Marcy et al. 2001). The best-fit orbital elements are shown in Table 2(b). The semi-major axis, the eccentricity, the longitude of periastron and mass of the planet are denoted by a, e, ω and M, respectively.

The most curious feature is the relation between orbital eccentricities and their masses of planet c and planet d in the Upsilon Andromedae system. The mass of planet d is about two times larger than that of planet c, while the eccentricity of planet d ($e_{\rm d}$) is about two times larger than that of planet c ($e_{\rm c}$). The orbital excitation caused by some kind of gravitational scatterings usually leads to inverse relation between the eccentricities and the masses from the conservation of energy and angular momentum, i.e., the eccentricity of a smaller planet is excited more than that of a larger planet. Long-term distant perturbations can pump up eccentricities of the three planets highly enough to start orbit crossing (e.g., Chambers et al. 1996). Suppose that orbit of planet b becomes comet-like one. If pericenter distance is

(a) Upsilon Andromedae system

	a(AU)	e	ω(rad)	$M \sin i(M_J)$	$T_{\rm peri}$
planet b	0.059	0.01	5.522	0.69	2450000.6383
planet c	0.827	0.23	4.314	2.06	2450399.0
planet d	2.56	0.35	4.374	4.10	2451348.9

Mass of Upsilon Andromeda is $1.3M_\odot$

(b) HD168443 system

	a(AU)	e	ω(rad)	$M \sin i(M_J)$	$T_{\rm peri}$
planet b	0.259	0.53	3.018	7.73	2450047.58
planet c	2.87	0.20	1.098	17.15	2450250.6

Mass of HD168443 is $1.01M_\odot$

Table 1: Orbital elements of the multi-planetary extra solar planets. The unit of mass is Jovian mass. i is the obliquity of the planetary system. $T_{\rm peri}$ is periastron time (JD) (a)Latest orbital parameters of Upsilon Andromedae planets (http://exoplanets.org /esp/upsandb/upsandb.html). (b)The best-fit orbital parameters of HD168443 planets (Marcy et al. 2001).

$\lesssim$0.05AU, the orbit is tidally circularized within 10^9 years (Rasio et al. 1996) and become isolated from the other planets (Rasio & Ford 1996). However, angular momentum exchange during orbit crossing usually results in smaller eccentricity for a more massive planet. It may be hard to explain the origin of eccentricity of planet d. Another curious feature is the coincidence of the longitude of periastrons of planet c ($\tilde{\omega}_{\rm c}$) and planet d ($\tilde{\omega}_{\rm d}$). The orbital evolution of planets c and d is shown in Figure 1a. The orbits are integrated over 2×10^5years started from the orbital elements of $e_{\rm c}/e_{\rm d} = 0.64$, $\tilde{\omega}_{\rm c} - \tilde{\omega}_{\rm d} \sim -0.44$ radian. The longitudes of periastrons are always close to each other.

When the planets are in closed track in (e-ω) diagram, the planetary system is stable for a long time. The stabilities of this system are well investigated (Rivera & Lissauer 2000, Ito & Tanikawa 2000), while the origin of the orbital configuration has not been studied.

Contrary to Upsilon Andromedae system, in the case of HD168443 system, the eccentricity of smaller planet b is always larger than the eccentricity of massive planet c. The eccentricity of planet b, however, is too large to get during the accretion. The planets are in open track in (e-ω) diagram. The orbital evolution of planets b and c is shown in Figure 1b. The orbits are integrated over 2.5×10^4 years started from the orbital elements of $e_{\rm b}/e_{\rm c} = 2.65$, $\tilde{\omega}_{\rm b} - \tilde{\omega}_{\rm c} \sim 1.92$ radian. $\omega_{\rm b} - \omega_{\rm c}$ changes from $-\pi$ to π in a period of about 7500 years.

The giant gas planets are formed before the depletion of protoplanetary disks, which are commonly observed around young stellar objects. Since the protoplanetary disk has already been depleted, planets in the Upsilon Andromedae and HD168443 system experienced the stage of protoplanetary disk depletion. When the disk is depleted, the gravitational potential of the system (disk potential) changes. This leads migration of the secular resonances. The importance of the sweeping secular resonances was first suggested by Ward et al. (1976).

In this paper, we apply the sweeping secular resonances to the Upsilon Andromedae and HD168443 system to explain the strange features of these extrasolar systems. We analyze

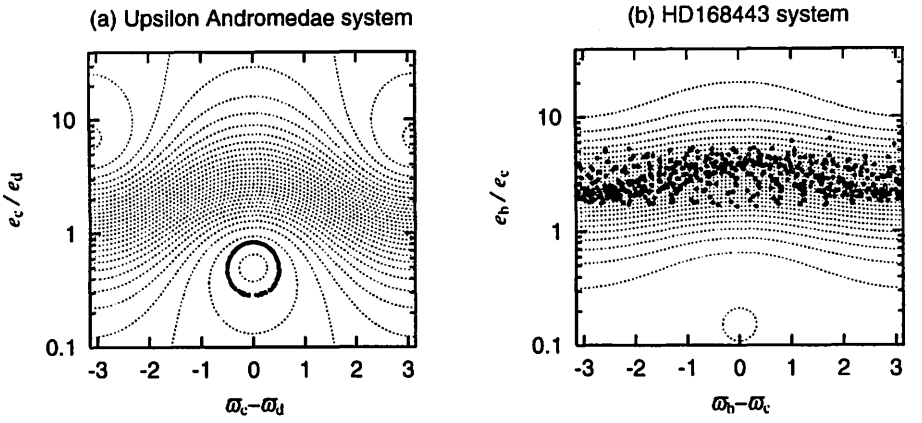

Figure 1: The orbital evolutions of extra solar planets. Points show the orbits obtained from numerical simulations. The dotted lines are the equi-Hamiltonian contours of the planetary system. The intervals of the contours are constant. (a) The orbital evolution of planets c and d (points) of Upsilon Andromedae system. Orbits are integrated for 2×10^5years started from present orbital elements. One period of the revolution is about 6500 years. (b) The orbital evolution of planets b and c (points) of HD168443 system. Orbits are integrated for 2.5×10^4years. $\omega_b - \omega_c$ changes from $-\pi$ to π with a period of about 7500 years.

the evolution of planetary eccentricities of these systems during protoplanetary disk depletion. We found that the protoplanetary disk depletion change the eccentricities, however, the amplitudes of the periastron libration among the planets are not so changed.

In Sec.2, we explain a model we used and methods to analyze the evolution of sweeping secular resonances. In Sec.3, we show results of calculations. We see the evolution of equi-Hamiltonian map during depletion of the protoplanetary disk, and see the results of numerical calculations. We give conclusions in Sec.4, and consider the system condition prior to the disk depletion.

2. Model and Methods

We consider a system of planets and the protoplanetary disk extended outside an outer planet. The tidal disturbance of sufficiently massive protoplanets may lead to the formation of gaps in the gas disk (e.g., Goldreich & Tremaine 1980, Lin & Papaloizou 1985, 1993). As planets in the Upsilon Andromedae and HD168443 system are very massive, it would be reasonable to assume that the protoplanetary disk inside planets is quickly removed and nebula outside planets is gradually cleared (e.g., Takeuchi et al. 1996). Since the outer planet is more massive than that of inner planet, and since the gas disk is more effective for near planet than inner planet, the depletion of this center-holed protoplanetary disk promise that a secular resonance passes the planetary system.

We consider a planer planetary system consists of two planets. In the case of Upsilon Andromedae system, we are concerned with planet c and d. In our consideration, we neglect planet b since its semi-major axis is very small to affects the other planets. The mutual gravity between planets c and d is included, however, we consider that they do not affect

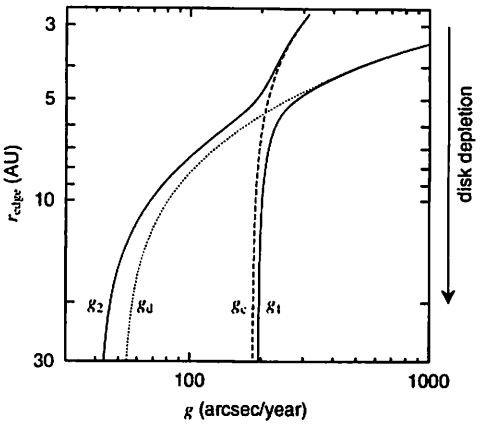

Figure 2: The location of the nebula edge ($r_{\rm edge}$) and the the eigenfrequencies of Upsilon Andromedae system.

protoplanetary disk. The only effect of the disk taken into account is its contribution to the axisymmetric component of the potential. We consider that the disk is depleted inside out way, i.e., the location of nebula inner edge ($r_{\rm edge}$) migrates from inside to outside. Mutual inclinations between the two planets and between the planet and the disk are neglected. The obliquity of the system is denoted by i. We take surface density of the disk as $5 \times \sin i$ times as much as the minimum mass solar nebula model (Hayashi 1981). The surface density profile of the protoplanetary disk is $\sigma = \sigma_0 (r/r_0)^{-3/2}$, where σ_0 is surface density at a reference value r_0. The occurrence of the sweeping of secular resonance itself does not depend on the detailed way of depletion or the structure of protoplanetary disk.

When the planetary orbital plane coincides with the disk mid-plane and the distance to the disk edge is farther than its scale height, the approximation that the disk is a thin planer one is sufficient to know the evolution of the planetary eccentricities. According to Ward (1981), the disk potential is

$$V(r) = 2\pi G \sigma_0 r \left(\frac{r_0}{r}\right)^{3/2} \sum_{n=0}^{\infty} \left(\frac{A_n}{2n+1/2}\right) \left(\frac{r}{r_{\rm edge}}\right)^{2n+1/2}, \qquad (1)$$

where periasteric distance is given as r, and G is the gravitational constant and $A_n = \{(2n)!/2^{2n}(n!)^2\}^2$. We assume the disk is extended to the infinite, and the semi-major axes of planets do not change. Expanding this potential by eccentricity and average it over an orbital period, we obtain the disturbing function due to the disk potential as follows:

$$< R_{\rm disk} >= e^2 \cdot \pi G \sigma_0 a \left(\frac{a_0}{a}\right)^{3/2} \sum_{n=1}^{\infty} A_n \frac{2n(2n+1)}{4n+1} \left(\frac{a}{r_{\rm edge}}\right)^{2n+1/2}. \qquad (2)$$

The secular resonance between two planets occurs when two eigenfrequencies of the system become nearly equal. The precession speeds of longitudes of periastrons of planets c and d in the present Upsilon Andromedae system are the same because one of the eigenfrequencies

is dominant for both planets. At present, however, the two eigenfrequencies are not close with each other, the planets are not in the secular resonance (Kinoshita & Nakai 1999). In Figure 2 shows the eigenfrequencies (g_1, g_2) versus the location of the disk edge ($r_{\rm edge}$). The eigenfrequencies are calculated according to Nagasawa et al. (2000). In a rough symbolic explanation, one of the frequencies ($g_{\rm c}$) is given as the summation of the frequency of planet c due to planet d ($g_{\rm c,d}$) and the frequency due to disk ($g_{\rm c,disk}$), i.e., $g_{\rm c} = g_{\rm c,d} + g_{\rm c,disk}$. Another frequency $g_{\rm d}$ is given as the summation of the frequency of planet d due to planet c ($g_{\rm d,c}$) and the frequency due to disk ($g_{\rm d,disk}$), i.e., $g_{\rm d} = g_{\rm d,c} + g_{\rm d,disk}$. Because planet d is more massive than planet c, $g_{\rm d,c} < g_{\rm c,d}$. Then, $g_2 \sim g_{\rm d} < g_1 \sim g_{\rm c}$ at present. Because planet d is nearer to the disk than planet c $g_{\rm c,disk} < g_{\rm d,disk}$. Before disk depletion, $g_2 \sim g_{\rm c} < g_1 \sim g_{\rm d}$, since the effect of disk potential is dominant. The secular resonance occurs when $g_{\rm c} = g_{\rm c,d} + g_{\rm c,disk} = g_{\rm d,c} + g_{\rm d,disk} = g_{\rm d}$. On the way of disk depletion, g_2 and g_1 approach with each other and the secular resonance occurs.

The Hamiltonian $H = N^2a^2/2 + R$ is calculated semi-analytically using the disturbing functions of planets (e.g., Brouwer & Clemence 1961) and Eq. (2), expanding to the second order of the eccentricities. N is mean motion. If we assume that the periastron of perturber precesses with constant velocity g' and take new variable $\omega_{\rm c} - \omega_{\rm d}$ as a new canonical variable, the new Hamiltonian becomes $\bar{H} = N^2a^2/2 + R - g'Na^2e^2/2$.

The orbits can be directly integrated in the numerical simulations using following gravitational force from the disk:

$$F = \frac{dV}{dr} = 2\pi G\sigma(r) \sum_{n=0} \frac{4n}{4n+1} A_n \left(\frac{r}{r_{\rm edge}} \right)^{2n+1/2} . \tag{3}$$

Except for small deviation due to non-linear effects, the contours in the equi-Hamiltonian map almost coincide with the numerically obtained orbits.

3. Result

Using the equi-Hamiltonian map, we see how the planets c and d evolve during disk depletion. Figure 3 shows the time evolution of the equi-Hamiltonian map of Upsilon Andromedae system. The mass ratio $M_{\rm c}/M_{\rm d} = 0.502$ is assumed. The nebula edge migrates from inside to outside (from panel (1) to panel (5)). When the nebula edge is at 4.2AU (panel (1)), the orbits is stable around ($e_{\rm c}/e_{\rm d} = 10$, $\tilde{\omega}_{\rm c} - \tilde{\omega}_{\rm d} = 0$) or ($e_{\rm c}/e_{\rm d} = 0.4$, $\tilde{\omega}_{\rm c} - \tilde{\omega}_{\rm d} = \pm\pi$). The precession speed of longitude of periastron of planet c is slower than that of planet d except for occasional regressions. The present orbital configuration is not on the closed track in this case. When the nebula edge is at 5AU (panel (2)), the two eigenfrequencies of the system are close to each other. The eccentricities of planets evolve with large amplitudes. The $e_{\rm c}/e_{\rm d}$ of center of the closed track where $\tilde{\omega}_{\rm c} - \tilde{\omega}_{\rm d} = 0$ is about 2. At $r_{\rm edge} = 5.5$AU, the secular resonance occurs (panel (3)). The precession frequencies of longitudes of periastrons can coincide with each other ($\dot{\tilde{\omega}}_{\rm c} \sim \dot{\tilde{\omega}}_{\rm d}$). Then, $\tilde{\omega}_{\rm c} - \tilde{\omega}_{\rm d}$ =constant, and only the eccentricities can change largely. The equi-Hamiltonian map is symmetric for the lines $\tilde{\omega}_{\rm c} - \tilde{\omega}_{\rm d} = -\pi$, $-\pi/2$, 0, $\pi/2$ and π or $e_{\rm c}/e_{\rm d} \sim 2$ in this case. When the nebula edge is beyond 5.5AU, the precession speed

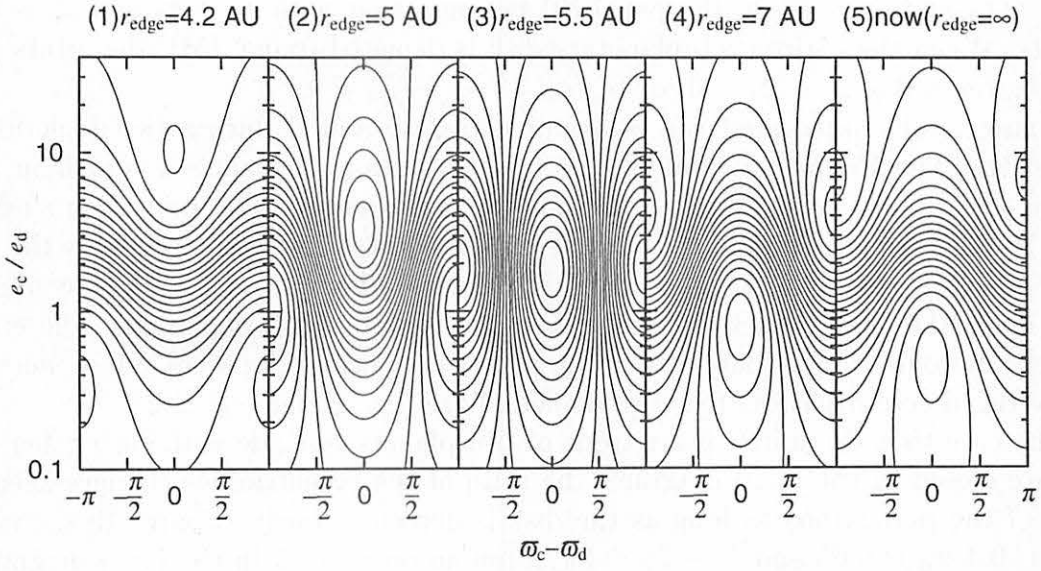

Figure 3: The equi-Hamiltonian contours of Upsilon Andromeda planetary system in (e_c/e_d-($\tilde{\omega}_c - \tilde{\omega}_d$)) diagram. The nebula depletion goes on from panel (1) to (5). The nebula edge is at (1) 4.2AU, (2) 5AU, (3) 5.5AU, (4) 6AU and (5) infinity (present planetary system).

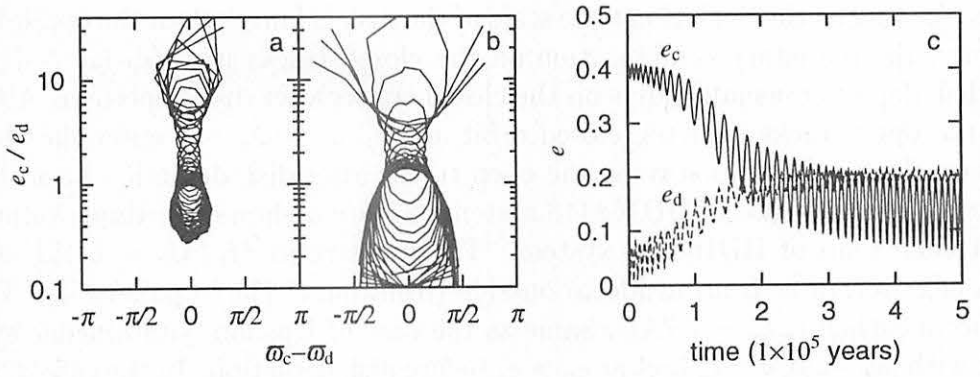

Figure 4: Orbital evolutions of planets during the depletion of the protoplanetary disk. (a) An example that planets initially in closed tracks on (e-$\tilde{\omega}$) diagram stay on closed track with high e_d after protoplanetary disk depletion. $e_c/e_d = 8$ and $\tilde{\omega}_c - \tilde{\omega}_d = \pi/4$ before disk depletion. (b) An example that planets initially on open tracks in (e-$\tilde{\omega}$) diagram enter on closed track after the disk depletion. $e_c = 0.4$, $e_d = 0.05$ and $\tilde{\omega}_c - \tilde{\omega}_d = 3\pi/2$ before disk depletion. (c) The evolution of the eccentricities in the cases of (a). The solid and dashed lines show the eccentricity of planet c and d, respectively. The migration speed of nebula edge is 10^{-5}(AU/y), and the nebula edge is 4.2 AU at $t = 0$.

of longitude of periastron of planet c is faster than that of planet d (except for occasional regressions). The panel (4) shows the case that the nebula edge is 6AU. The centers of closed tracks are reversed from the situation of the panel (1) and (2). The planetary configuration with $e_c > e_d$ and $\tilde{\omega}_c \sim \tilde{\omega}_d$ in the panel (2) becomes that with $e_c < e_d$ and $\tilde{\omega}_c \sim \tilde{\omega}_d$ in the panel (4). When the entire protoplanetary disk is depleted (panel (5)), the orbits are stable around ($e_c/e_d = 0.5$, $\tilde{\omega}_c - \tilde{\omega}_d = 0$) or ($e_c/e_d = 7$, $\tilde{\omega}_c - \tilde{\omega}_d = \pm\pi$).

We numerically integrated the orbits of planets c and d during the depletion of disk (Figures 4). The Figures 4a and b shows the evolution of planets c and d in the (e-$\tilde{\omega}$) diagram, and Figure 4c shows the evolution of eccentricities. The migration speed of disk edge is 10^{-5}AU/year. Initially we put the disk edge at 4.2AU. Figures 4a is the case that $e_c/e_d = 8$, and $\tilde{\omega}_c - \tilde{\omega}_d = \pi/4$ (closed track in the (e-$\tilde{\omega}$) diagram) in the initial condition. The planets enter the closed tracks in the (e-$\tilde{\omega}$) diagram after disk depletion. The eccentricity of planet c becomes lower than that of the planet d owing to the secular resonance passage. Time averaged eccentricities after disk depletion are $\langle e_c \rangle \simeq$ and $\langle e_d \rangle \simeq 0.2$.

In the case that the initial periastrons of two planets coincide with each other and their tracks are closed in the (e-$\tilde{\omega}$) diagram, the ratio of the eccentricities changes keeping coincidence of the periastrons as long as the disk is depleted slowly. Figure 4b shows the case that $e_c = 0.4$, $e_d = 0.05$ and $\tilde{\omega}_c - \tilde{\omega}_d = 3\pi/2$ (on an open track in the (e-$\tilde{\omega}$) diagram) in the initial conditions. In this case, planets enter a closed track in the (e-$\tilde{\omega}$) diagram. The mean eccentricities after disk depletion are the same as the case of panel (a), since the eccentricities are determined from the conservation of angular momentum. If initial planetary configuration is on an open track sufficiently distant from closed track, it enters a closed track during disk depletion and goes out of it later.

From the numerical calculations, we found that the orbits of planets evolve according to the evolution of e_c/e_d-($\tilde{\omega}_c - \tilde{\omega}_d$) diagram as long as the disk is slowly depleted because the change is adiabatic. As long as the depletion time scale of the disk is longer than the oscillation period of eccentricity, the planetary configuration on the closed tracks in e_c/e_d-($\tilde{\omega}_c - \tilde{\omega}_d$) diagram before the disk depletion usually stays on the closed tracks after disk depletion. Although the planets on the open tracks near the closed orbit around $\tilde{\omega}_c - \tilde{\omega}_d = 0$ enter the closed orbit, the planets on the open tracks stay on the open tracks after disk depletion basically.

Next we explain the case of HD168443 system. Figure 5 shows the time evolution of the equi-Hamiltonian map of HD168443 system. The mass ratio $M_b/M_c = 0.451$ is assumed. The nebula edge migrates from inside to outside (from panel (1) to panel (5)). The secular resonance occurs when $r_{edge} = 7.7$AU. Same as the case of Upsilon Andromedae system, the closed orbit with $|\omega_b - \omega_c| < \pi/2$ lays at $e_b > e_c$ before disk depletion. In the case of HD168443 system, the area in closed track is small. Outside the condition of the secular resonance, the changes of eccentricities are small, since two planets are separated with each other than the case of Upsilon Andromedae system. When $M_b/M_c(a_b/a_c)^{1/2}$ is small, the area in open track is large. Although when the mass of the disk is near the condition of secular resonance, the tracks are closed, this situation is short in time. In many cases, the track is open. The closed track area with $|\omega_b - \omega_c| < \pi/2$ moves downward in the Hamiltonian map as disk depletion is going on. If planets of HD168443 are in open track before disk depletion, they are also in open track after disk depletion.

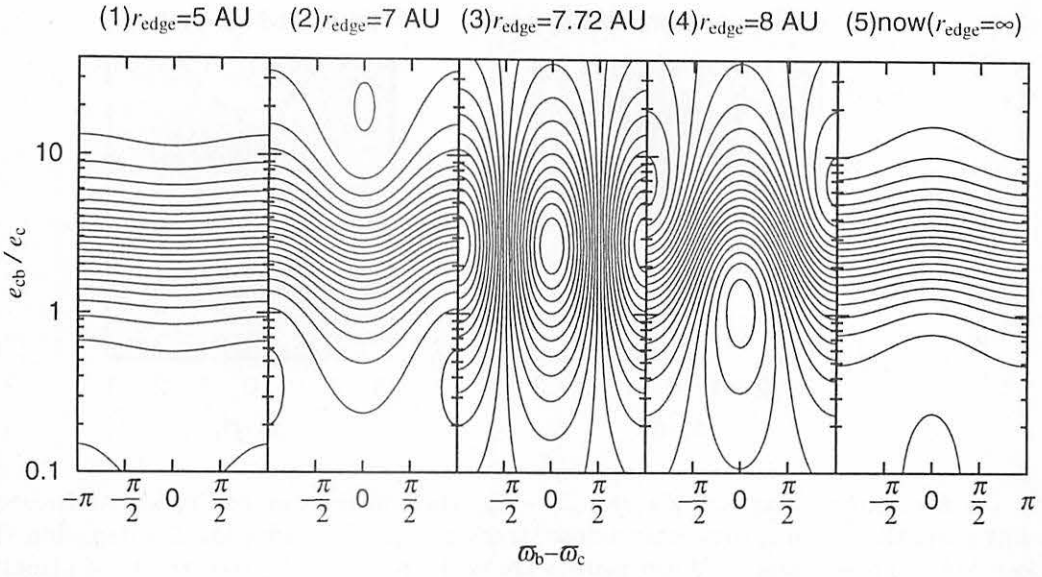

Figure 5: The equi-Hamiltonian contours of HD168443 planetary system in (e_b/e_c-($\tilde{\omega}_b - \tilde{\omega}_c$)) diagram. The nebula depletion goes on from panel (1) to (5). The nebula edge is at (1) 5AU, (2) 7AU, (3) 7.72AU (secular resonance) (4) 8AU and (5) infinity (present planetary system).

4. Conclusions and Discussions

In the present Upsilon Andromedae system, orbital configuration of planets c and d is on a closed track and the ratio of the mean eccentricities e_c/e_d are about 0.5 (see Figure 1). The absolute values of eccentricities are determined from the initial eccentricities. From the conservation of angular momentum, a relation

$$M_c n_c a_c^2 \sqrt{1-e_c^2} + M_d n_d a_d^2 \sqrt{1-e_d^2} = \text{const.} \tag{4}$$

holds if their orbital planets are not inclined from each other. Let the initial eccentricities of planets c and d be e_c' and e_d', and assume constant semi-major axes, the above equation means

$$\frac{e_d'^2 - e_d^2}{e_c^2 - e_c'^2} = \frac{M_c \sin i \sqrt{a_c}}{M_d \sin i \sqrt{a_d}} \sim 0.286. \tag{5}$$

Here, we take the eccentricities up to the second order term. The numerical results of Figure 4 satisfy this relation. If the eccentricities of planets satisfy the relation and the planets are on a closed track before disk depletion, the orbits of planets c and d become very similar to the present ones. The interesting thing is that the closed track at $|\omega_c - \omega_d| < \pi/2$ lays at $e_c > e_d$ when the disk exists. From the Figure 3, we found that to make the present-like orbits the planets need to be on closed track, i.e., the relation of $e_c > e_d$, which is a natural planetary configuration, is required before disk depletion. Therefore, the area, which is $e_c > e_d$ along the line of Eq. (5), is expected as the origin of the present-like orbits. The planets of a closed

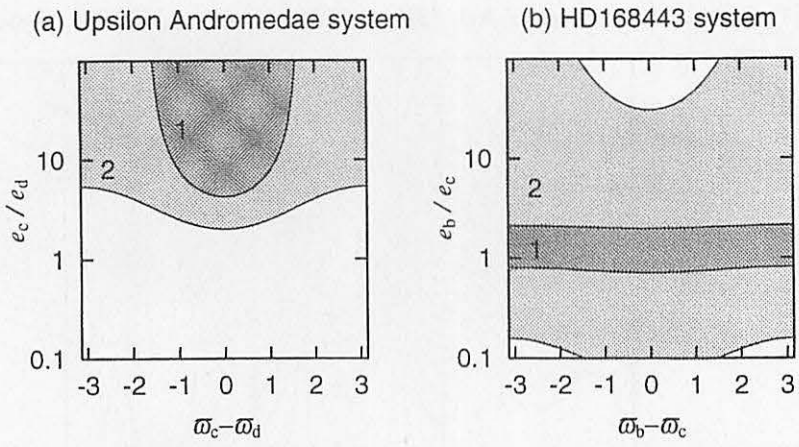

Figure 6: (a) A schematic diagram of e_c/e_d-$(\tilde{\omega}_c - \tilde{\omega}_d)$ plane in the case of Upsilon Andromedae system. When planets are in the region 1, they enter a closed track in $(e$-$\tilde{\omega})$ plane after the disk depletion. Their orbits become close one to present orbits. When planets are in the region 2, the eccentricity of planet d becomes larger than that of planet c after the nebula depletion. (b) A schematic diagram of e_b/e_c-$(\tilde{\omega}_b - \tilde{\omega}_c)$ plane in the case of HD 168443 system. When planets are in the region 2, they enter a open track in $(e$-$\tilde{\omega})$ plane after the disk depletion. The orbits of the planets in the region 1 become close ones to present orbits.

track in this area enter the present-like orbit, and the planets of an open track in this area enter the other (open) track.

In Figure 6, we show the initial condition to make the present-like Upsilon Andromedae system (panel a) in a schematic diagram of e_c/e_d-$(\tilde{\omega}_c - \tilde{\omega}_d)$ plane. When planets are in the region 1 before disk depletion, they evolve keeping their periastron coincidence during the disk depletion. They enter a closed track in $(e$-$\tilde{\omega})$ plane after the disk depletion. Their orbits become quite close to present ones. When planets are in the region 2 (and 1), the eccentricity of planet d becomes larger than that of planet c after the nebula depletion. The planets in the boundary between region 1 and region 2 would enter a closed track. The planets in the region 2 far from the region 1 enter an open track after disk depletion. The planets in the region of $e_c/e_d < 2$ can not enter an present-like track. Therefore, if the planets initially have orbital elements in the region 1 and $e_c \gtrsim 0.35$, the secular resonance sweeping results in planetary sytem like the present Upsilon Andromedae. This condition would be easy to be satisfied, since it is easy to pump up the eccentricity of planet c during orbit crossings as mentioned before.

In the case of HD168443 planets, the present track of is open. In Figure 6b, we show the initial condition to make the present-like HD168443 system in a schematic diagram of e_b/e_c-$(\tilde{\omega}_b - \tilde{\omega}_c)$ plane. When the planets are in the region 2, they would enter an open track after disk depletion. The condition to be present orbit is shown as region 1. The planets in region 1 enter present-like orbits as the eccentricity of planet c decrease a little and the eccentricity of planet b increase.

We know one more multi-planetary system. That is our solar system. Jupiter is more massive than Saturn. Their longitudes of perihelia do not coincide with each other. The ratio

of the Jovian eccentricity to the Saturnian eccentricity (e_J/e_S) varies from 0.3 to 5 with time. Since the inner planet is more massive than the outer one, the secular resonance for Jupiter and Saturn does not occur during depletion of the protoplanetary disk. Therefore, the initial orbits when Jupiter and Saturn are formed would not change before and after disk depletion. The sweeping secular resonances caused by the center-holed protoplanetary disk can explain consistently the origin of the orbit of presently known three multi-planet planetary systems.

We need to mind that the eccentricities of extrasolar planets are not the original eccentricities at the time of the planetary completion in the protoplanetary disk. The eccentricities of planet would change during the depletion of the protoplanetary disk though the angler momentum changes due to the secular resonances.

Acknowledgements

I would like to acknowledge H. Kinoshita, K. Nakazawa and H. Emori for fruitful discussions and for their advice. I also thank E. Kokubo and T. Ito for their helpful suggestions. I used the parallel computer (Silicon Graphics Origin 2000) of Earthquake Information Center of Earthquake Research Institute, University of Tokyo.

References

Brouwer, D., & Clemence, G. M. 1961, in Methods of Celestial Mechanics (Academic Press, New York)
Butler, R. P., Marcy, G. W., Fischer, D. A., Brown, T. M., Contos, A. R., Korzennik, S. G., Nisenson, P., & Noyes, R. W. 1999, ApJ, 526, 916
Chambers, J. E., Wetherill, G. W., & Boss, A. P. 1996, Icarus, 119, 261
Goldreich, P., & Tremaine, S. 1980, ApJ, 241, 425
Hayashi, C. 1981, Prog. Theor. Phys. Suppl., 70, 35
Ito, T., & Tanikawa, K. 2000, Icarus, submitted
Kinoshita, H., & Nakai, H. 1999, Planetary Systems in the Universe: Observation, Formation and Evolution ASP Conference Series, Vol. 3×10^8, edited by A. J. Penny, P. Artumowicz, A. -M. Lagrange, and S. S. Russell
Lin, D. N. C., & Papaloizou, J. C. B. 1985, in Protostars and Planets II, edited by D. C. Black and M. S. Matthews (Univ. of Arizona Press, Tucson), p.981
Lin, D. N. C., & Papaloizou, J. C. B. 1993, in Protostars and Planets III, edited by E. H. Levy and J. I. Lunine (Univ. of Arizona Press, Tucson), p.749
Nagasawa, M., Tanaka, H., & Ida, S. 2000, AJ, 119, 1480
Rasio, F. A., & Ford, E. B. 1996, Science, 274, 954
Rasio, F. A., Tout, C. A., Lubow, S. H., & Livio, M. 1996, ApJ, 470, 1187
Rivera, E. J., & Lissauer, J. J. 2000, ApJ, 530, 454
Takeuchi, T., Miyama, S. M., & Lin, D. N. C. 1996, AJ, 460, 832
Ward, W. R. 1981, Icarus, 47, 234

Does a Secular Resonance Take Place for a Planetary System?

Hiroshi Kinoshita
National Astronomical Observatory
2-21-1 Osawa, Mitaka, Tokyo, Japan
e-mail: Kinoshita@nao.ac.jp

Abstract

For a planetary system a secular resonance with a mixed secular term does not take place. For a planetary system which is composed of planets with same order mass, the enhancement of the amplitudes due to the closeness of two eigen frequencies is not large. When there is large deviation in planeatry mass distribution, the amplitude of a planet with small mass is largely enhanced, which we can call a secular resonance.

Corotaion of pericenters of outer two planets of υ Andromedae is not a secular resonance and the alignment of the pericenters is due to that the amplitude corresponding to one eigen frequencies is dominant for both planets.

1 Introduction

A small body such as an asteroid and a comet is usually treated as a mass less particle approximation. The solution for e(eccentricity) and ϖ(longitude of pericenter) in the linear secular perturbation theory is expressed in the following form (Brouwer and Clemence, 1961):

$$h = e\sin\varpi = \nu\sin(gt+\beta) + \sum_{j=1}^{n} \frac{\nu_j}{g-g_j}\sin(g_j t+\beta_j), \tag{1}$$

$$k = e\cos\varpi = \nu\cos(gt+\beta) + \sum_{j=1}^{n} \frac{\nu_j}{g-g_j}\cos(g_j t+\beta_j), \tag{2}$$

where g is an eigen frequency for the small body, which depends on the masses of the disturbing planets and the semi-major axis of the small body and planets. The g_j are eigen frequencies for the disturbing planets. When g is equal to one of the eigen frequencies

$(g = g_k)$, the form of the solution takes the following form:

$$h = \nu \sin(gt + \beta) + \sum_{j=1, j\neq k}^{n} \frac{\nu_j}{g - g_j} \sin(g_j t + \beta_j) + \nu_k t \sin(g_k t + \beta_k) \tag{3}$$

$$k = \nu \cos(gt + \beta) + \sum_{j=1, j\neq k}^{n} \frac{\nu_j}{g - g_j} \cos(g_j t + \beta_j) - \nu_k t \sin(g_k t + \beta_k). \tag{4}$$

The last term of (3) and (4) is a mixed secular term, of which amplitude increases with time. We can call the appearance of a mixed secular term a secular resonance.

When g is close to one of the eigen frequencies, g_k, in the form of (1) and (2), the amplitudes corresponding to g_k become large. We call this enhancement of the amplitude also a secular resonance.

Now a question arises in the following:
Does a secular resonance take place for a planetary system, in which all planets are mutually disturbed?

2 Linear Secular Perturbation Theory for a Planetary System

The solution of the secular perturbation for a planetary system takes the following form (Brouwer and Clemence, 1961):

$$e_i \sin \varpi_i = \sum_{j=1}^{n} M_{ij} \sin \theta_j, \tag{5}$$

$$e_i \cos \varpi_i = \sum_{j=1}^{n} M_{ij} \cos \theta_j, \tag{6}$$

where $\theta_j = g_j t + \beta_j$. In the above expressions g_j are the eigen frequencies, which are obtained from the following secular determinant:

$$|A - gI| = 0, \tag{7}$$

where A is a matrix of $n \times n$, of which element A_{ij} is a function of only the semi-major axes and masses of n planets, the matrix A is symmetric, and I is a unit matrix.

The coefficients M_{ij} is a function of the initial values of e and ϖ and eigen vectors for (7). Here we implicitly assume that the secular determinant (7) does not have equal roots. The nonexistence of multiple roots has not been ascertained except for $n = 2$ and $n = 3$. The nonexistence for multiple roots for $n = 2$ is easily proved from non-zero of the determinant

of the second-order equation derived from (7). Seeliger (1879) proved the nonexistence for equal roots for the case of $n = 3$. Darboux (1888) showed that there may be equal roots.

When the secular determinant (7) has r-multiple roots ($r \geq 2$), in general the solution (5) and (6) has the mixed secular term, t^{r-1}. However, according to the theory of linear differential equations with constant coefficients (for example: Coddington and Levinson, 1955), when the matrix A in the secular determinant (7) is symmetric, the solution (5) and (6) does not have the mixed secular terms.

Now we have to investigate the behavior of the amplitudes for the case where one eigen frequency is close to another eigen frequency. It is quite difficult to give the explicit functional form of the amplitudes,M_{ij} in (5) and (6), since we have to solve an algebraic equation with n-th order ($n \geq 3$). In the next section we discuss this problem with numerical method.

3 Numerical Investigation for Three Planets Case

In this section we study the behavior of the amplitudes for the case where one eigen frequency is very close to another eigen frequency. We choose three planets which elements are shown in Table 1. The orbital elements of Planet 1 and 2 are those for Jupiter and Saturn. The eccentricity and the longitude of the perihelion of Planet 3 are those for Mars. The mass and the semi-major axis of Planet 3 are parameters in the following discussion.

	Planet1	Planet 2	Planet 3
$M(M_{sun})$	9.5479×10^{-4}	2.859×10^{-4}	–
a(AU)	5.2026	9.5549	–
e	0.0485	0.0555	0.0934
ϖ	14.225	93.065	336.067

Table 1: Orbital Parameters

Fig 1-1 shows the three eigen frequencies with $m_3 = 10^{-6}$ for $1 < a < 2$. At near $a = 1.84$, the secular determinant seems to have equal roots. Fig 1-2 shows the enlargement around $a = 1.84$ and it is clear the two eigen frequencies are separated, as Seeliger (1879) showed the non-existence of equal eigen freequencies i the case of three planets. The distance between these close eigen frequencies depend on the mass of Planet 3. As m_3 decreases, the two eigen frequencies become closer. Fig. 1-3 shows the case for $m_3 = 10^{-4}$, which is comparable to m_1 and m_2 and shows the two eigen frequencies are well separated. We compute the amplitudes corresponding to 3 eigen frequencies for three planets and show them in Fig. 2 and 3. Fig. 2 show the case for $m_3 = 10^{-6}$. For larger planet 2 and 3, the

Fig. 1 − 1

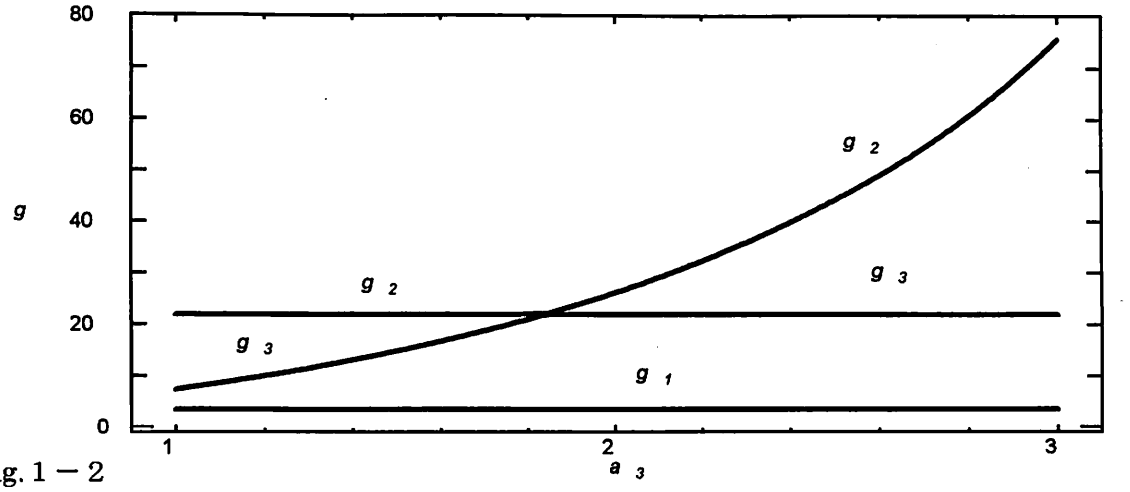

Fig. 1 − 2

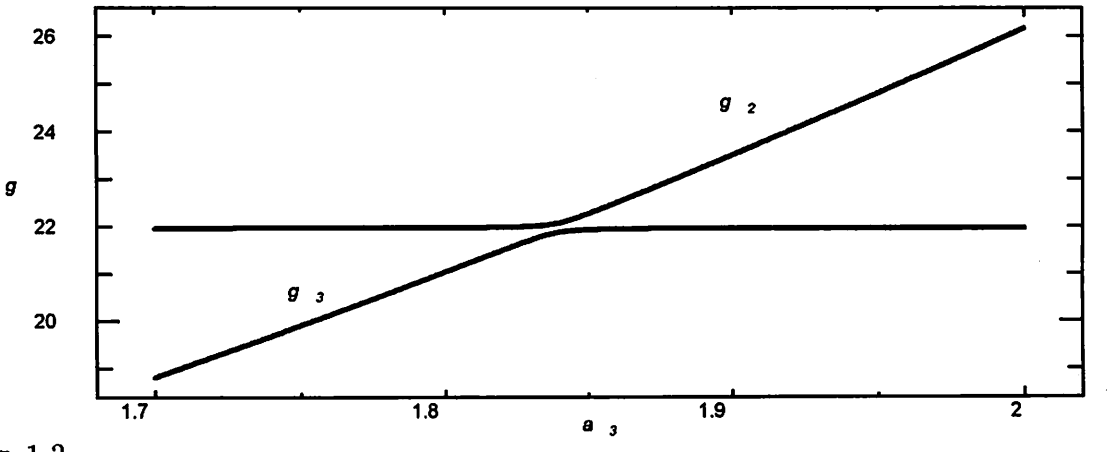

Fig. 1-3

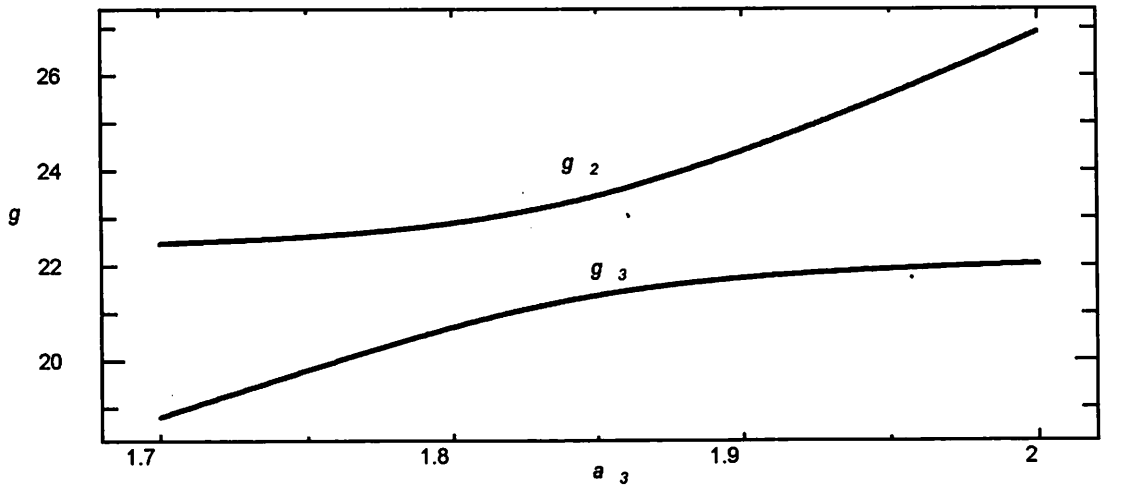

Figure 1: Eigen values for three planets in Table 1: 1-1)eigen values in the case of $m_1 = 10^{-6}$ for 1 AU< a_3 <2 AU 1-2)the enlargement of Fig1-1 for 1.7 AU< a_3 <2 AU, 1-3) eigen values in the case of $m_1 = 10^{-4}$ for 1.7 AU< a_3 <2 AU

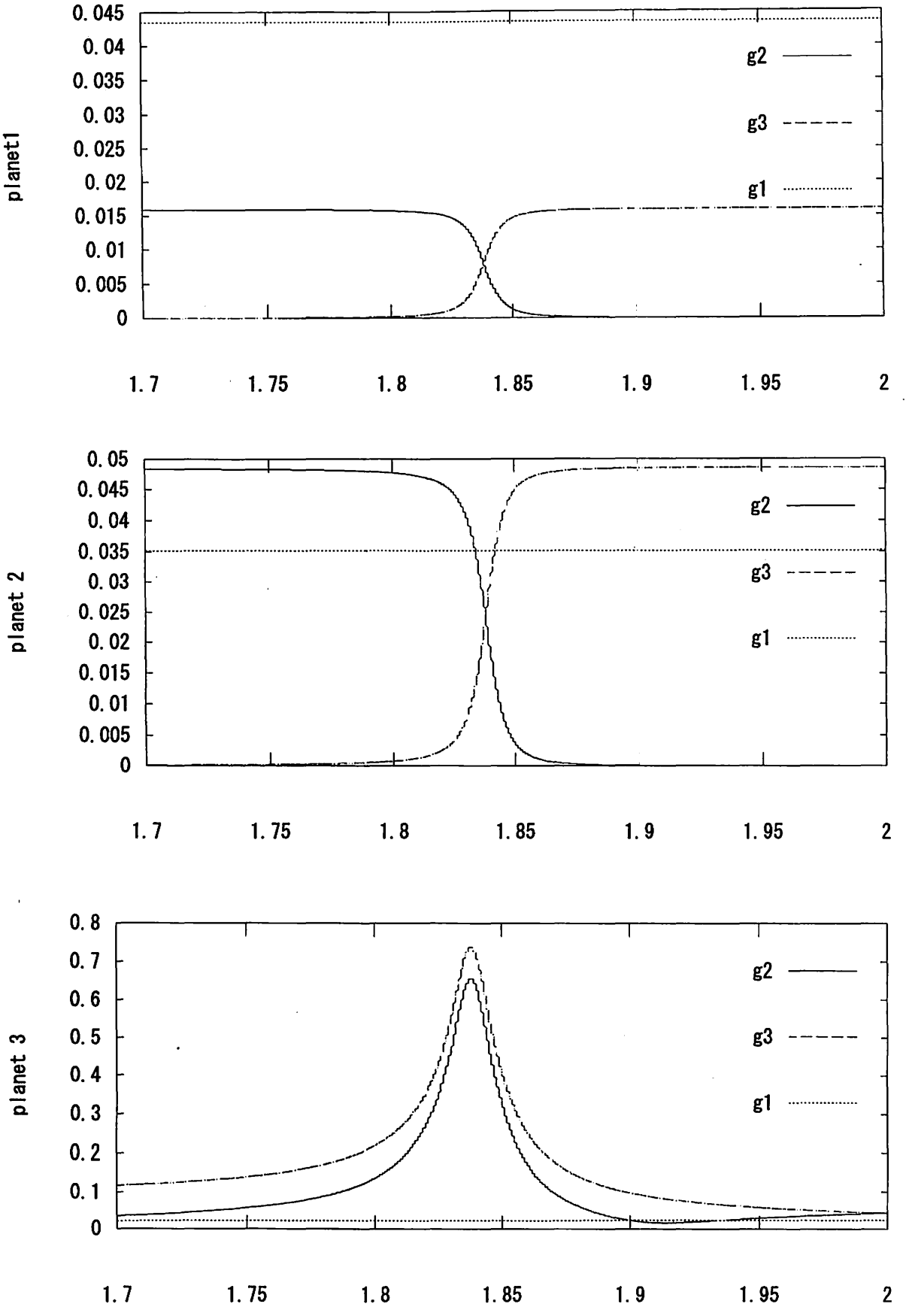

Figure 2: Amplitudes corresponding to each eigen frequencies g_1, g_2, and g_3 in the case of $m_1 = 10^{-6}$ for the range of 1.7 AU< a_3 <2 AU

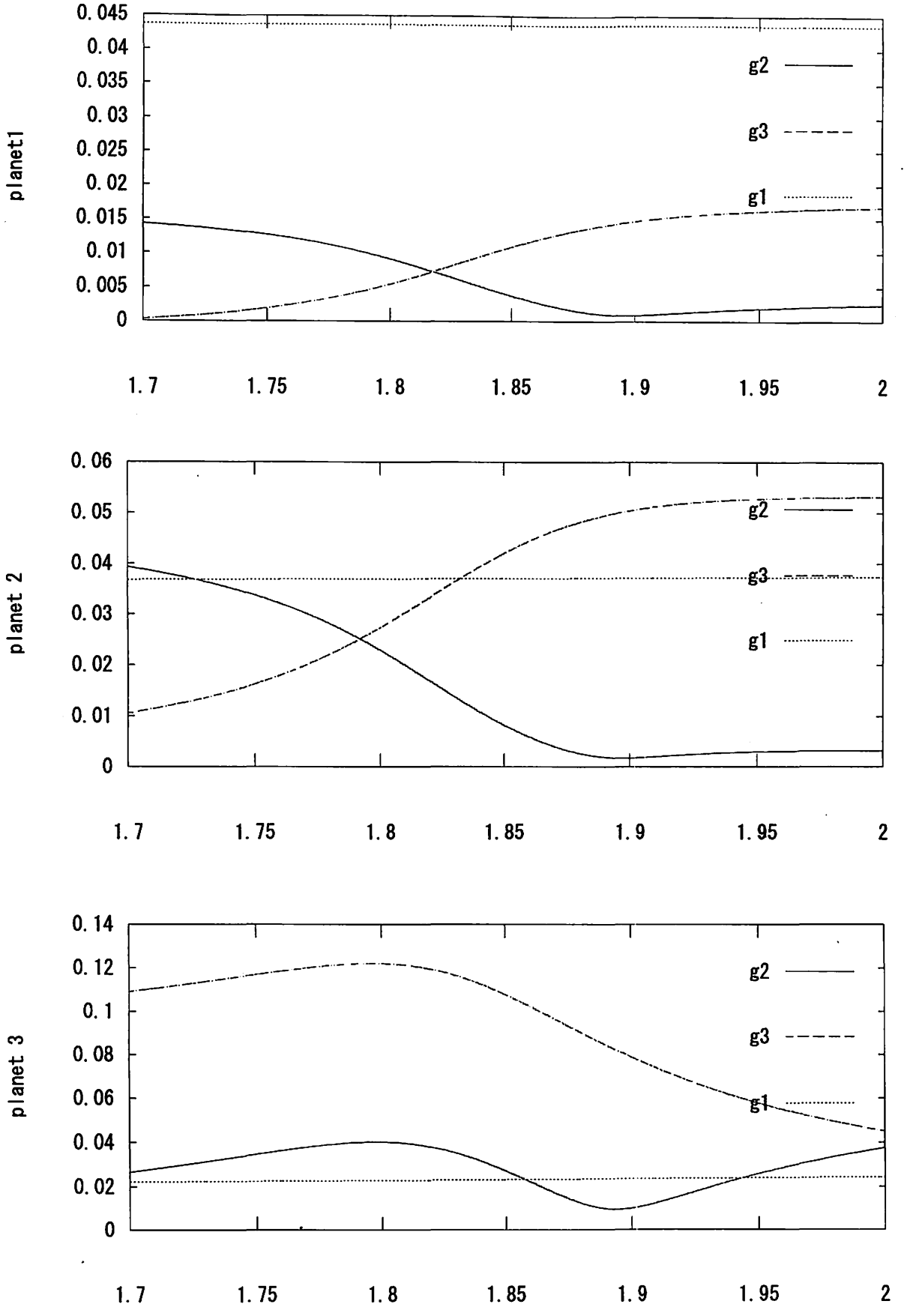

Figure 3: Amplitudes corresponding to each eigen frequencies g_1, g_2, and g_3 in the case of $m_1 = 10^{-4}$ 1.7 AU< a_3 <2 AU

enhancement of the amplitudes corresponding to eigen frequencies, g_2 and g_2, is small near at $a = 1.84$, where g_2 becomes close to g_3. On the other hand, the enhancement for Planet 3 is quite large. We can call this enhancement a secular resonance. Fig. 3 show the case for $m_3 = 10^{-4}$, in which the masses of three planets are comparable. Even if g_2 becomes close to g_3 near $a = 1.84$, there is no enhancement of the amplitudes for all planets.

When a planetary system is composed of large mass planets and ssmall mass planets and two eigen frequencies become close, a secular resonance take place for small mass planets When a planetary system is composed of planets whose mass is of same order, a secular resonance does not appear.

4 Corotation of Pericenters

The pericenters of outer two planets of υ Andoromedae planetary system is corotating and this alignment of the pericenters makes υ Andromedae planetary system stable. If this alignment is destroyed, the planetary system becomes unstable. This alignment of the pericenters are frequently called a secular resonance in the literature. We analyze this alignment with use of linear secular perturbation theory (Kinoshita and Nakai, 2000). Eigen frequencies for outer 2 planets of υ Andromedae are $g_1 = 30".59/y, g_2 = 200".35/y$. These two eigen frequencies are well separated and not close. Solutions for the initial values: $e_{10} = 0.22, \varpi_{10} = 219.°2, e_{20} = 0.44, \varpi_{20} = 245.°9$ (Butler et al. (1999)) are

$$e_1 \cos \varpi_1 = 0.1928 \cos \theta_1 + 0.0955 \cos \theta_2, e_1 \sin \varpi_1 = 0.1928 \sin \theta_1 + 0.0955 \sin \theta_2, \quad (8)$$

$$e_2 \cos \varpi_2 = 0.4404 \cos \theta_1 - 0.0078 \cos \theta_2, e_2 \sin \varpi_2 = 0.4404 \sin \theta_1 - 0.0078 \sin \theta_2, \quad (9)$$

where $\theta_1 = g_1 t + 244.°9, \theta_2 = g_2 t + 158.°2$.

Since the component of the eigen frequency g_1 is dominant for both planets, the pericenter longitudes take the following form

$$\varpi_1 = \theta_1 + (\text{periodic}), \varpi_2 = \theta_1 + (\text{periodic}), \quad (10)$$

and

$$\varpi_1 - \varpi_2 = (\text{periodic}), \quad (11)$$

which means that the pericenters are corotaing. Since the eigen frequencies are not close, this corotation is not a secular resonance.

The above discussions is easily extended to corotation of r planets of a planetary system composed of n planets ($r \leq n$). If one of the amplitudes corresponding to eigen freequency g_1 is dominant such as

$$|M_{i1} > \sum_{j=2}^{n} |M_{ij}| (i = 1, 2, ..., r), \quad (12)$$

the pericenters of r planets corotates.

This study was supported by the Grant-in-Aid of the Ministry of Education, Scence, Sports and Culture of Japan (12640241).

References

Brouwer, D. and Clemence, G.M., 1961,Methods of Celestial Mechanics, Academic Press, New York.

Butler, R. P., Marcy, G. W., Fischer, D. A., Brown, T. M., Contos, A. R., Korzennik, S. G., Nisenson, P.,& Noyes, R. W., 1999, ApJ, 526,916.

Coddington,E.A. and Levinson, N.,1955, Theory of Ordinary Differential Equations, McGraw Hill, New York.

Darboux,G., 1888, Oeuvres de Lagrange, XI, Gauthier-Villars, Paris, 492, note 8.

Kinoshita,H. and Nakai,H., 2000,in Proc. IAU Symposium No. 201, in press.

Rivera, E. J., & Lissauer, J. J., 2000, ApJ, **530**, 454.

Seeliger, H., 1879, Astro. Nachr., **93**, 353.

Stability Mechanism of GJ876 Planetary System

Hiroshi Kinoshita and Hiroshi Nakai
National Astronomical Observatory
2-21-1 Osawa, Mitaka, Tokyo, Japan
e-mail: Kinoshita@nao.ac.jp

Abstract

The newly discovered planetary system of GJ876 is stabilized by a 2:1 mean motion resonance. We carried out numerical simulations of the GJ876 planetary system for several sets of initial epochs and investigate their stability, since this planetary system is very sensitive for an initial epoch because of the large difference between the osculating elements and the mean elements.

1 Introduction

From precise Doppler measurements during 6 years from the Lick and Keck observatories, Marcy et al.(2001) found two planets orbiting GJ876 (M4V). The orbital parameters determined by Marcy et al.(2001) are given in Table1. In this paper Marcy et al.(2001). already performed numerical simulations of the dynamical evolutions of the GJ876 planetary system. They chose planet masses to be their minimum values and carried out about two dozen different values of the initial epoch of the integration. Many of these system self-destructed within 4 million years and two systems remain stable after over 500 million years, in which a 2:1 mean motion resonance is maintained.

In this paper we carried out numerical simulations with different initial epochs other than Marcy et al. chose and two more simulations with different planetary masses, which are discussed in Section 2.3.

Parameter	Inner	Outer
Orbital Period P(d)	30.12(0.02)	61.02(0.03)
Eccentricity	0.27(0.04)	0.10(0.02)
ϖ(deg)	330(12)	333(12)
Periastron Time(JD)	2450031.4 (1.2)	2450106.2(1.9)
$M \sin i$	0.56 (0.09)	1.89 (0.3)
a(AU)	0.130	0.208

Table 1: Orbital Parameters from Mercy et al. (2001)

2 Numerical Simulation

We assume that planet masses are their minimum as Marcy et al.(2001) did, which means two planets move in a same plane. We carried out numerical simulations for the following three sets of the orbital parameters with use of an extrapolation method as an integrator.

2.1 Change of the Initial Mean Anomaly

We put the planet 2(outer planet) on its pericenter at the initial epoch and changed the initial mean anomaly of the planet 1 (inner planet) from 0 degree to 360 degrees for every 30 degrees and integrated their orbits for 10^4 years. Among 12 cases, the cases of $l_1 = 0, 30, 60, 330$ degrees are stable for this period. The case for $l_1 = 60$ degrees becomes unstable after about 16000 years. Figures 1 and 2 show the case $l_1 = 0$ and Figures 3, 4, 5, 6 show the cases for $l_1 = 30$, 60, 300,and 330 degrees, respectively. We found the orbit with the initial mean anomaly $-60° < l_1 < 60°$ is stable and the planetary system for these initial mean anomaly of the planet 1 is in a stable 2:1 mean motion resonance.

The critical argument for this mean motion resonance is $\theta_c = \lambda_1 - 2\lambda_2 + \varpi_1$, which librates around 0° (see Figures from 1 to 6) . The initial critical argument for the stable system is about $-30° < \theta_c(0) < 30°$. The figures 1 to 6 shows not only the orbital elements and the critical argument but also the difference between the pericenter longitudes of the planets. At the initial epoch the pericenter of the planet 1 is very close to that of the planet 2. However the pericenters of the two planets move independently and are not corotating, as the planetary system υ Andoromedae where outer two planet's pericenter are in alignment.

In this 2:1 mean motion resonance the pericenter of the inner planet is always retrograde, which also occur in the asteroid of 2:1 mean motion resonance with Jupiter. The direction of the pericenter motion of the outer planet depends on l_1: prograde for $-60° < l_1 < -12°$ and $22° < l_1 < 60°$ and retrograde for $-11° < l_1 < 21°$.

2.2 Change of the Initial Epoch

The observed period which were used to determine the orbital parameters is from November 23, 1994 to December 22, 2000. For this period we searched the time at which the critical argument is zero: 2451362.7JD (July 3, 1999). From this epoch we started to integrate the equations of motion and found the planetary system for this initial epoch is stable and the 2:1 mean motion resonance is maintained. Then we chose another initial epoch near this epoch and studied the stability of the corresponding planetary systems. The planetary systems corresponding to the initial epoch, which is around t1=2451166 JD (December 18, 1998) to t2=2451559 JD (January 15, 2000), is stable and the 2:1 mean motion resonance is maintained. For the period from t1 to t2 , the critical argument calculated from the orbital elements from Table 1 varies from around $-30°$ to 30°, which is consistent with the result of Section 2.1.

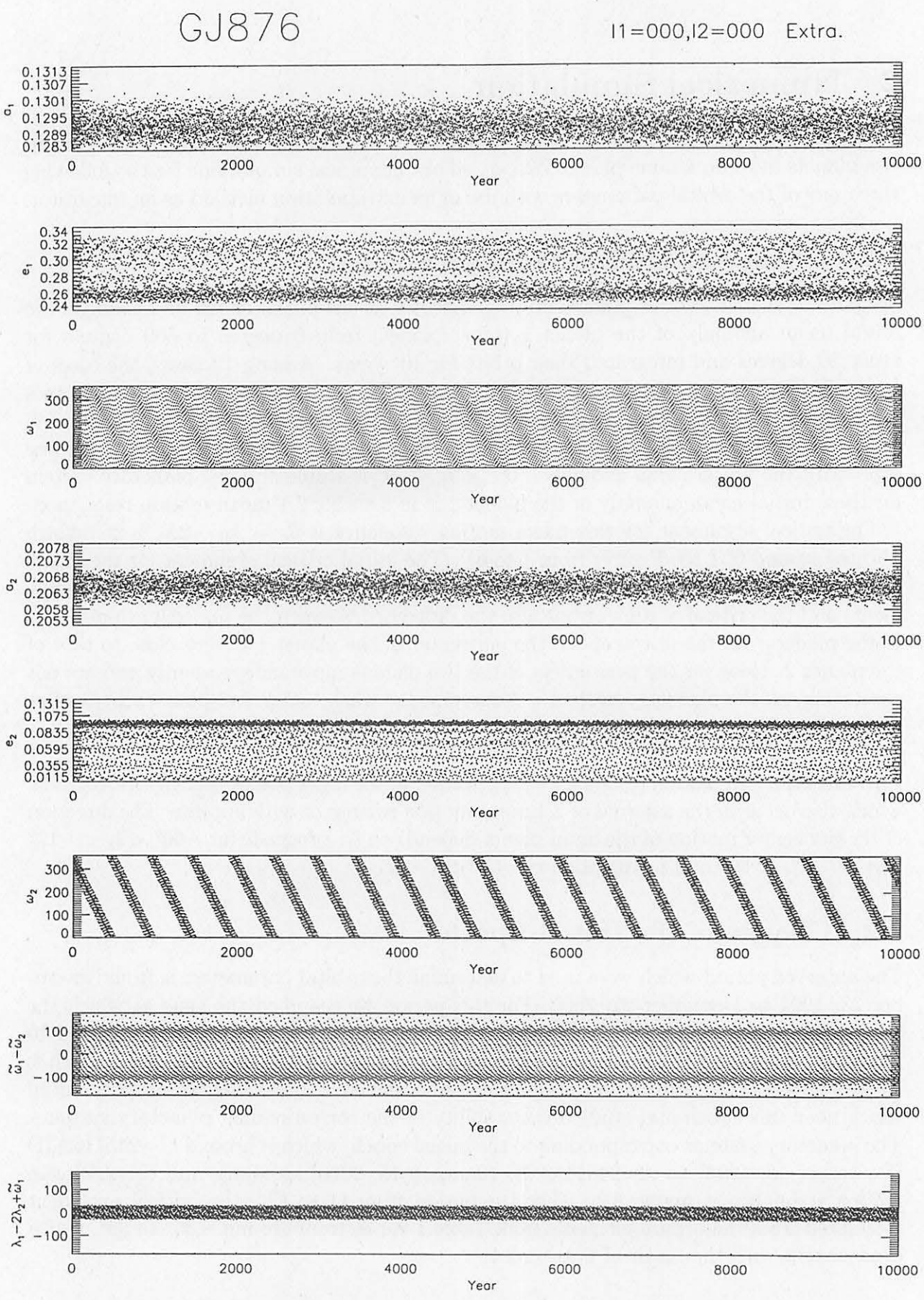

Figure 1: Orbital elements of two planets, the critical argument, and the difference between the pericenter longitudes:$l_1 = 0$ degree,$T = 10000$ years

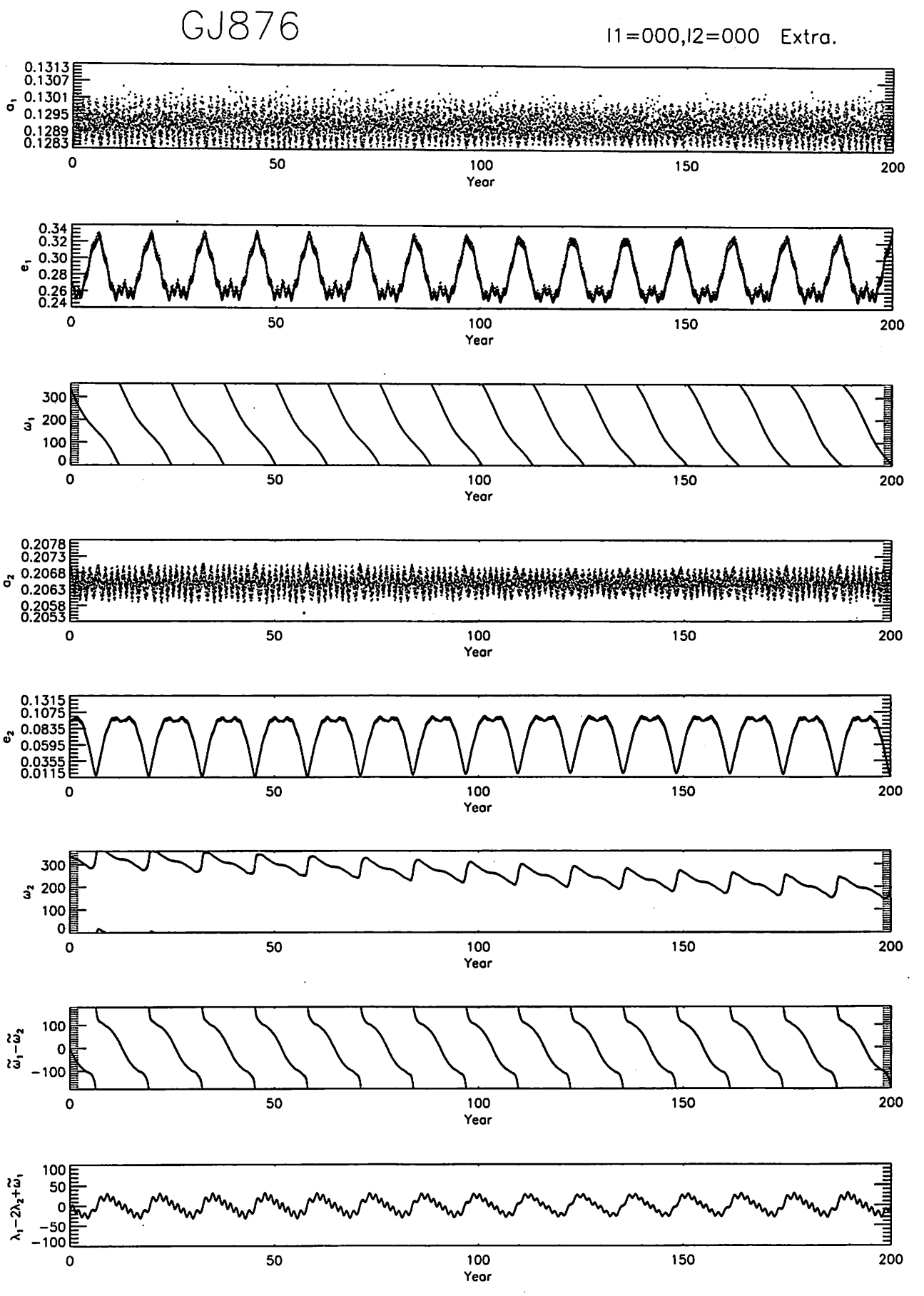

Figure 2: Orbital elements of two planets, the critical argument, and the difference between the pericenter longitudes:$l_1 = 0$ degree, $T = 200$ years

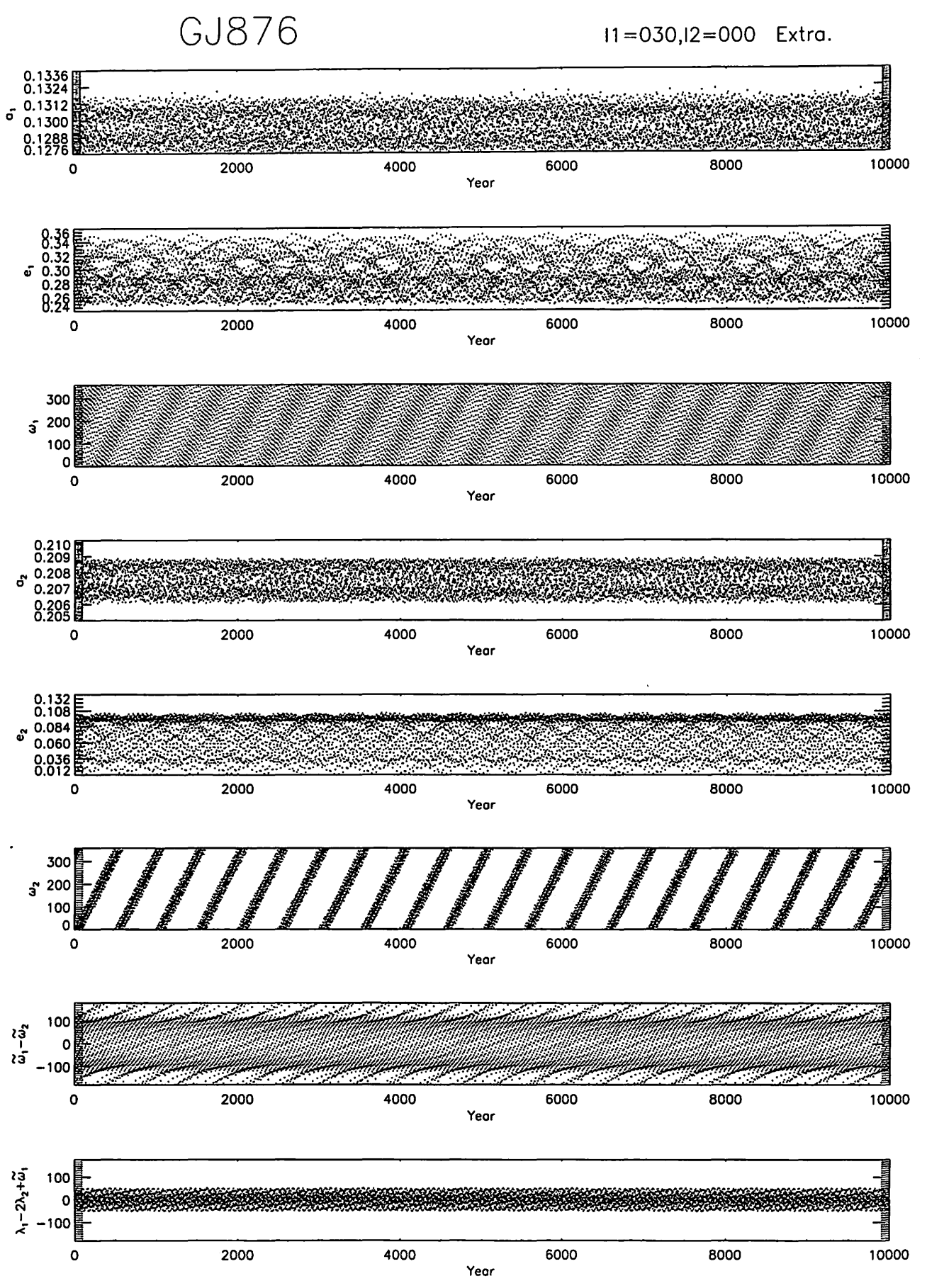

Figure 3: Orbital elements of two planets, the critical argument, and the difference between the pericenter longitudes:$l_1 = 30$ degrees, $T = 10000$ years

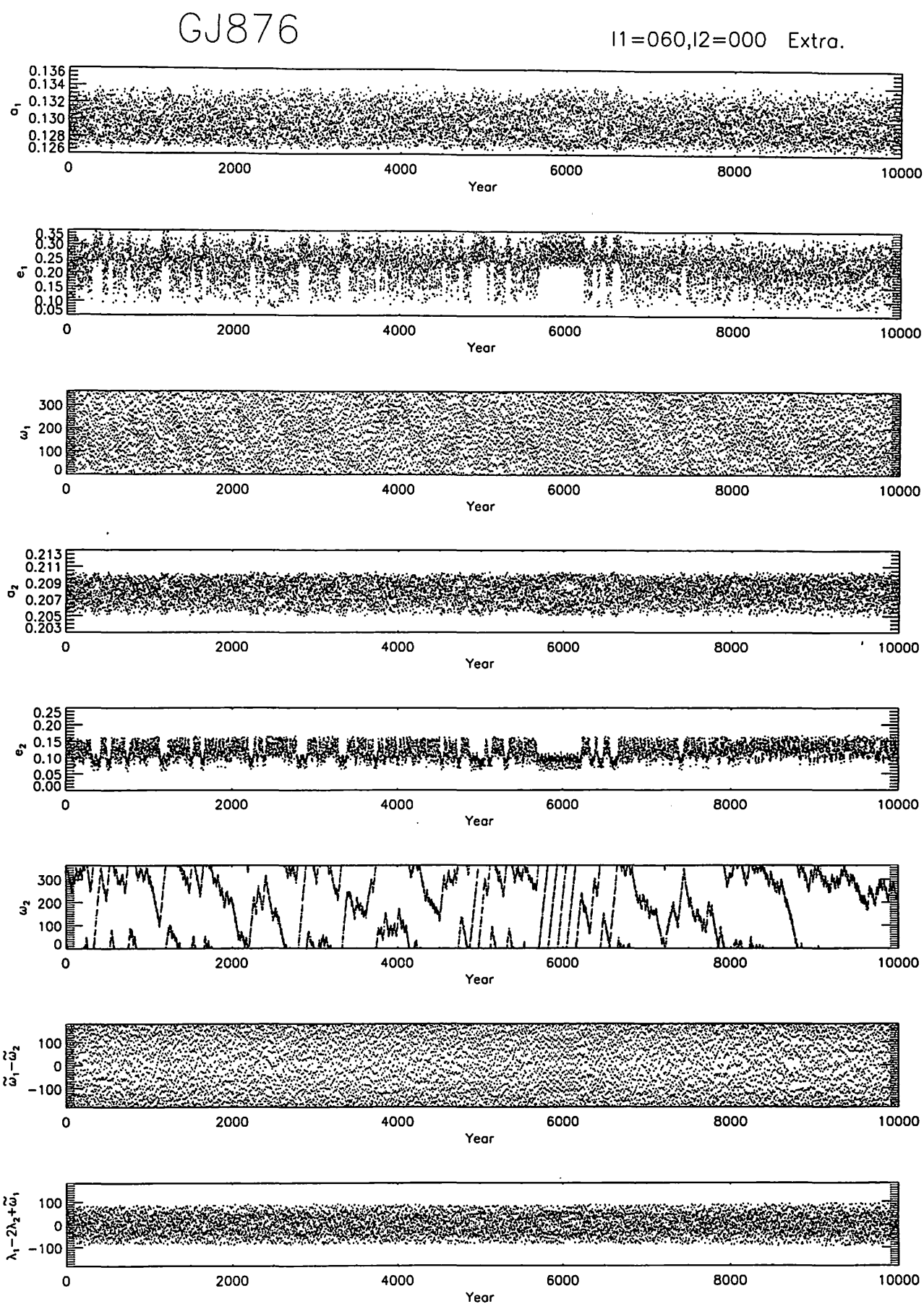

Figure 4: Orbital elements of two planets, the critical argument, and the difference between the pericenter longitudes:$I_1 = 60$ degrees, $T = 10000$ years

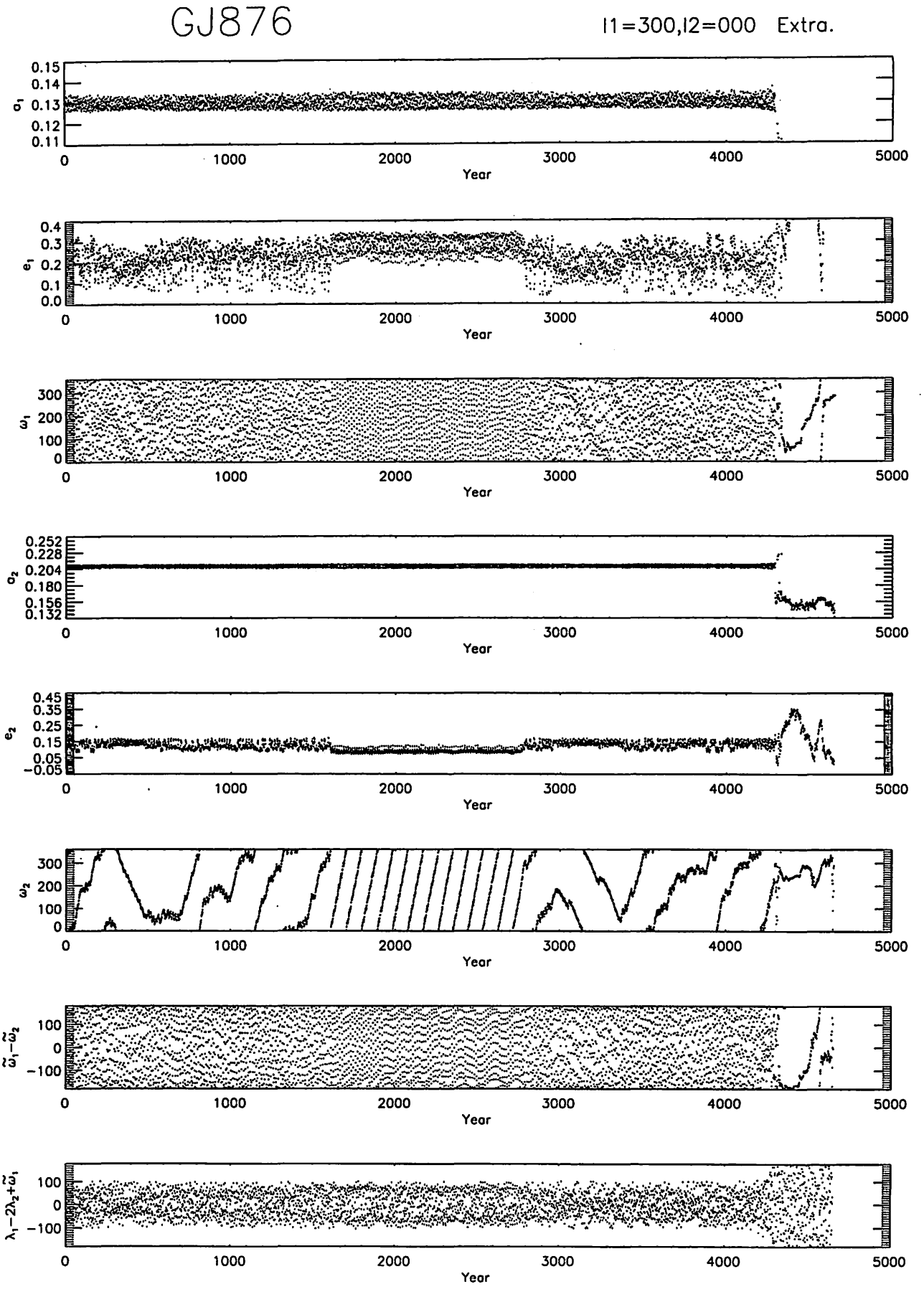

Figure 5: Orbital elements of two planets, the critical argument, and the difference between the pericenter longitudes:$l_1 = 300$ degrees, $T = 5000$ years

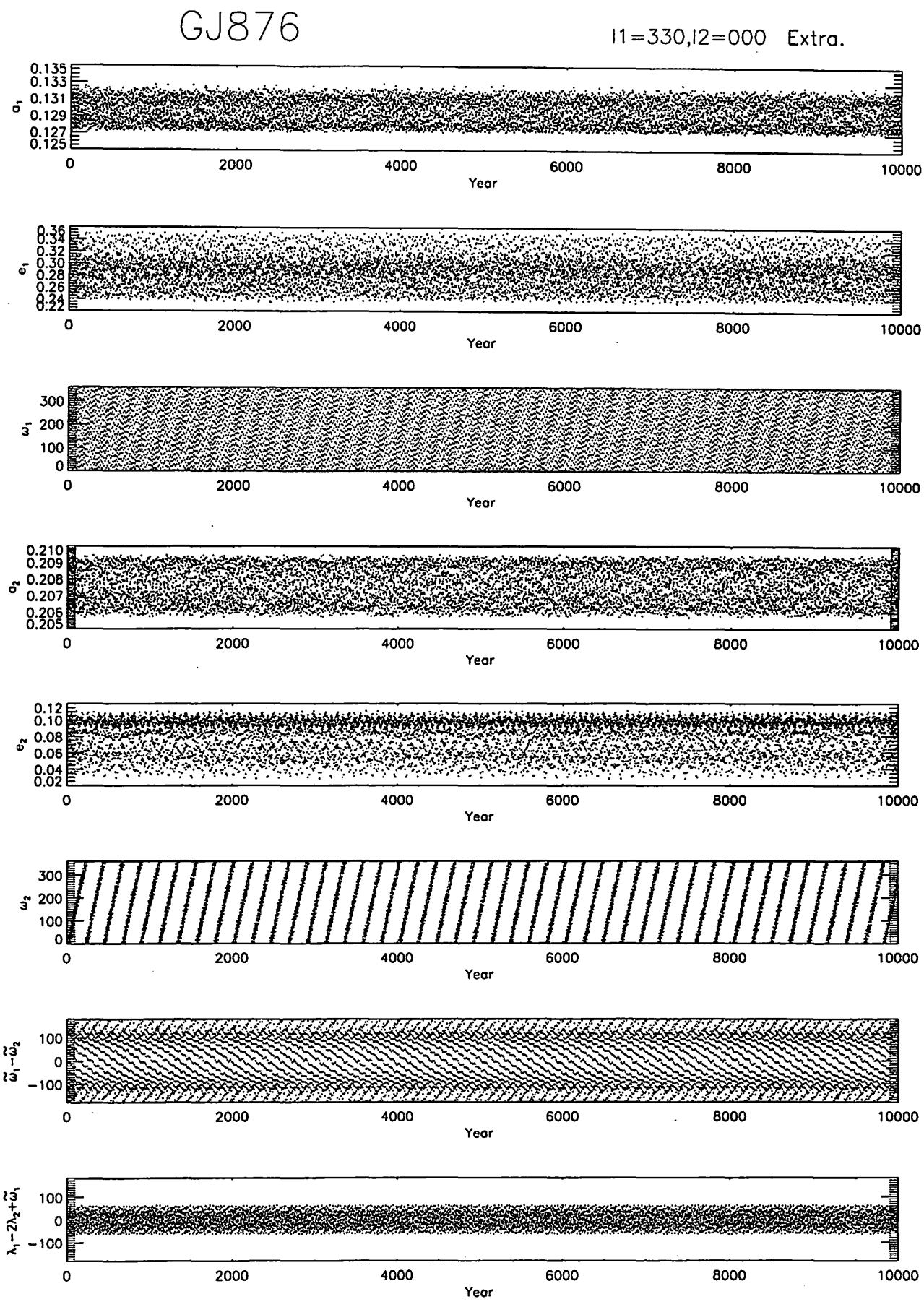

Figure 6: Orbital elements of two planets, the critical argument, and the difference between the pericenter longitudes:$l_1 = 330$ degrees, $T = 10000$ years

2.3 Change of Planetary Mass

Here we carried out two type of simulations:1)exchange the mass of two planets 2)reduce the inner planet mass to be zero.

1)We exchange the masses of the two planets: $m_1 = 1.89 M_J$ and $m_2 = 0.56 M_J$ and we performed a similar numerical simulations in Section 2.1.

The stable planetary system does exist around $l_1 = 60°$. The planetary system with other l_1 is unstable. When $l_1 = 50°$, for the first 200 years the planetary system is trapped in 2:1 mean motion resonance and stable and this resonance is very fragile. After the mean motion resonance is destroyed, the system becomes unstable. The critical argument for the stable mean motion resonance is $\theta_c = \lambda_1 - 2\lambda_2 + \varpi_1$, which is the same as that in the case of Section 2.1, and not $\theta_c = \lambda_1 - 2\lambda_2 + \varpi_2$.

2)We assume the small inner planet mass be zero, which means the outer planet is not disturbed by the inner planet and this system is an elliptic restricted three-body problem. We put the both planets on their pericenters at the initial epoch. The planetary system is trapped in a 2:1 mean motion resonance and the amplitude of the critical argument $\theta_c = \lambda_1 - 2\lambda_2 + \varpi_1$ is about 60 degrees, which is twice of the finite mass case. The planetary system, however, is stable like the case in Section 2.1. This system is stable at least for one million years and the orbital elements do not show any indications for irregular motions. Then we carried out the similar simulations as Section 2.1 and got similar results. The stable cases in Section 2.1 are also stable for the case of $m_1 = 0$ and the unstable cases in Section 2.1 are also unstable. The only diference is that the survival time for unstable cases for $m_1 = 0$ is longer than that for $m_1 \neq 0$. Figures 7 and 8 show the orbital elements for the stable ($l_1 = 0°$) and unstable ($l_1 = 60°$) cases, respectively.

In the solar system the region 2:1 mean motion resonance is a gap in the distribution of asteroids, which is called Hecuba gap. Even if this zone is unstable region, several asteroids such as Griqua (1362), Pala (1921), and Zulu (1922) exists, which is stabilized by a 2:1 mean motion resonance. The dynamical difference in the stability between the actual GJ876 system and the hypothetical GJ876 system, in which the mass of the inner planet is zero, should be investigated.

3 Discussion

The stability of the newly discovered planetary system of GJ876 is very sensitive for the value of the initial epoch. If we choose the initial epoch, at which the critical argument of a 2:1 mean motion resonance ($\theta_c = \lambda_1 - 2\lambda_2 + \varpi_1$) is within about 30 degrees, the planetary system is stable. The reason that the stability of the planetary system depends on the initial epoch is that the orbital elements derived from the Doppler observations (Marcy et al. 2001) are not osculating elements but the mean elements, in which determination the mutual perturbations were not taken into account. In order to study the long-term stability of the planetary system of GJ876 , we definitely need the osculating elements in which the mutual perturbations are considered. Recently Laughlin and Chambers (2001) tried to determine the osculating elements which include the mutual perturbations and obtained two sets of the preliminary values of the osculating elements by two methods.

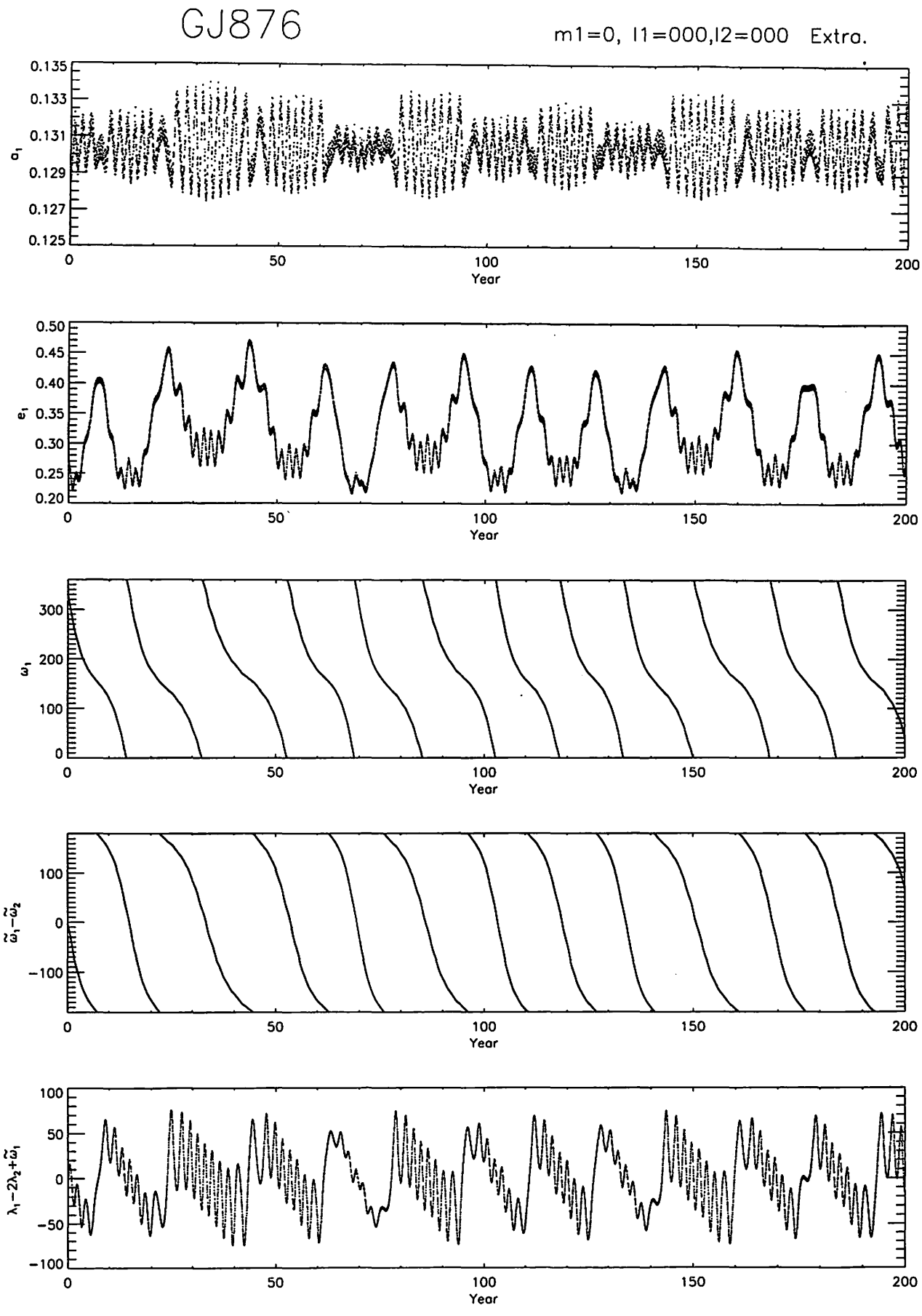

Figure 7: Orbital elements of the inner planet ($m_1 = 0$) , the critical argument, and the difference between the pericenter longitudes:$l_1 = 0$ degrees, $T = 200$ years

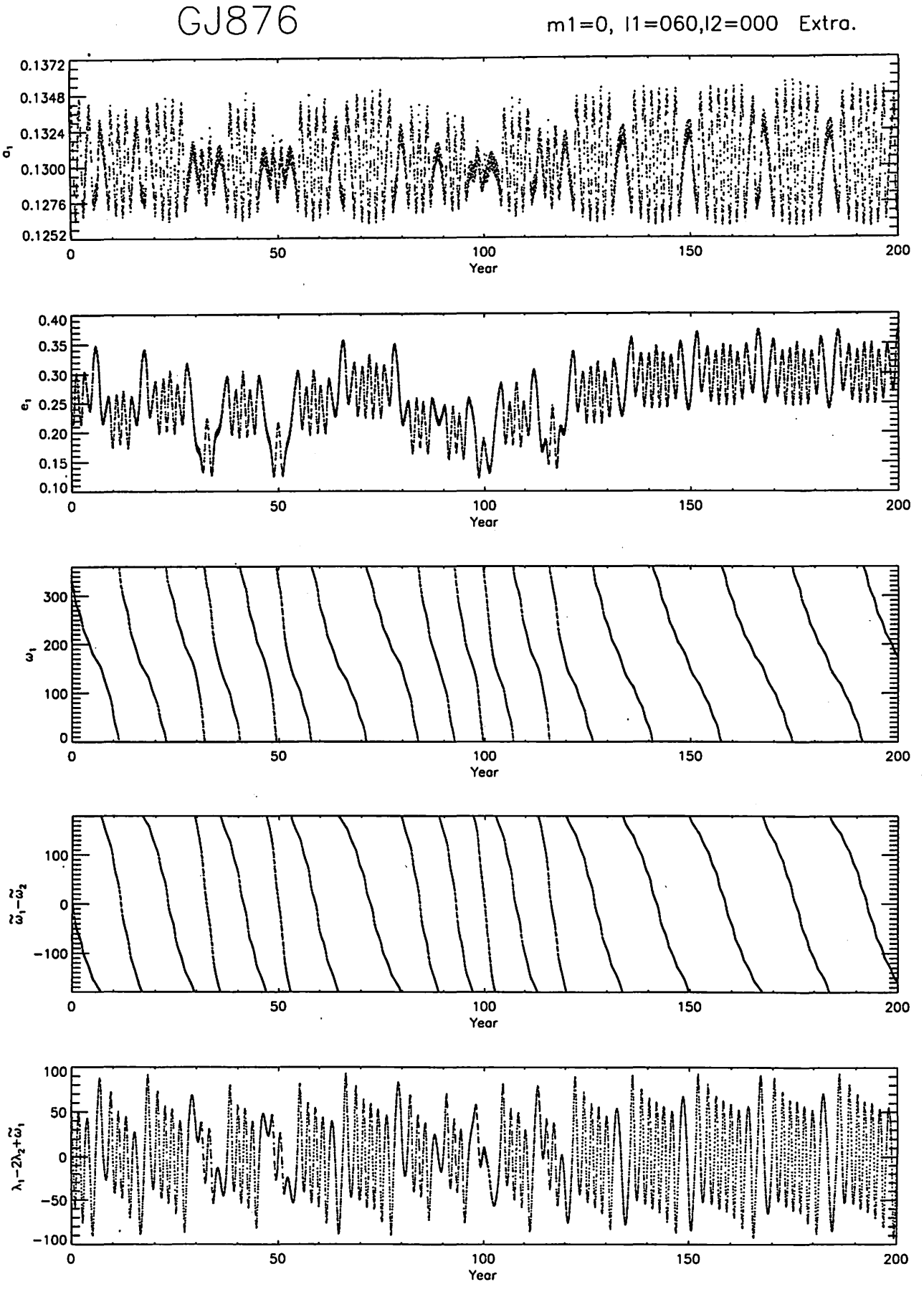

Figure 8: Orbital elements of the inner planet ($m_1 = 0$) , the critical argument, and the difference between the pericenter longitudes:$l_1 = 60$ degrees, $T = 200$ years

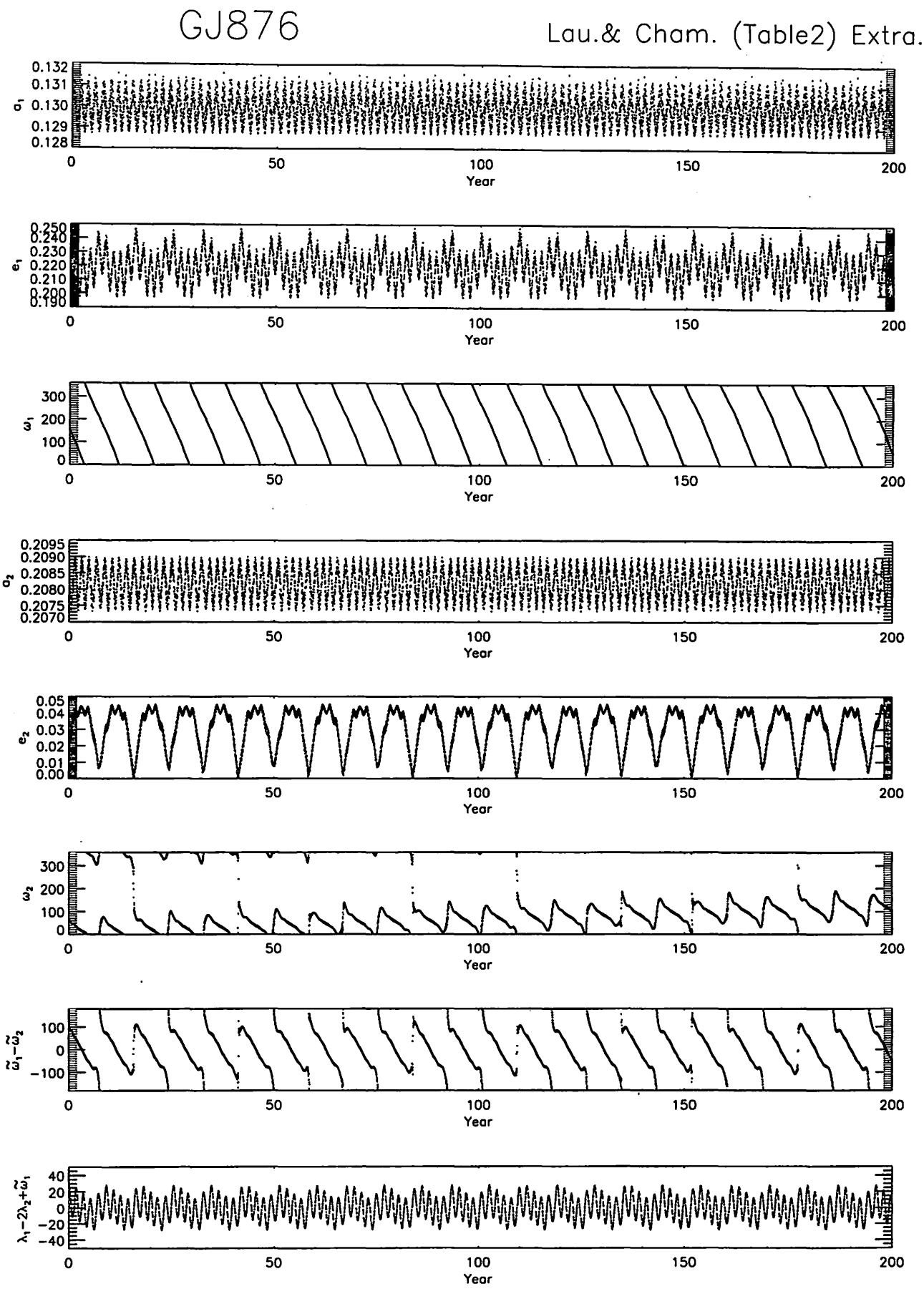

Figure 9: Orbital elements of two planets, the critical argument, and the difference between the pericenter longitudes:Initial orbital elements are taken from Laughlin and Chambers(2001),$T = 200$ years

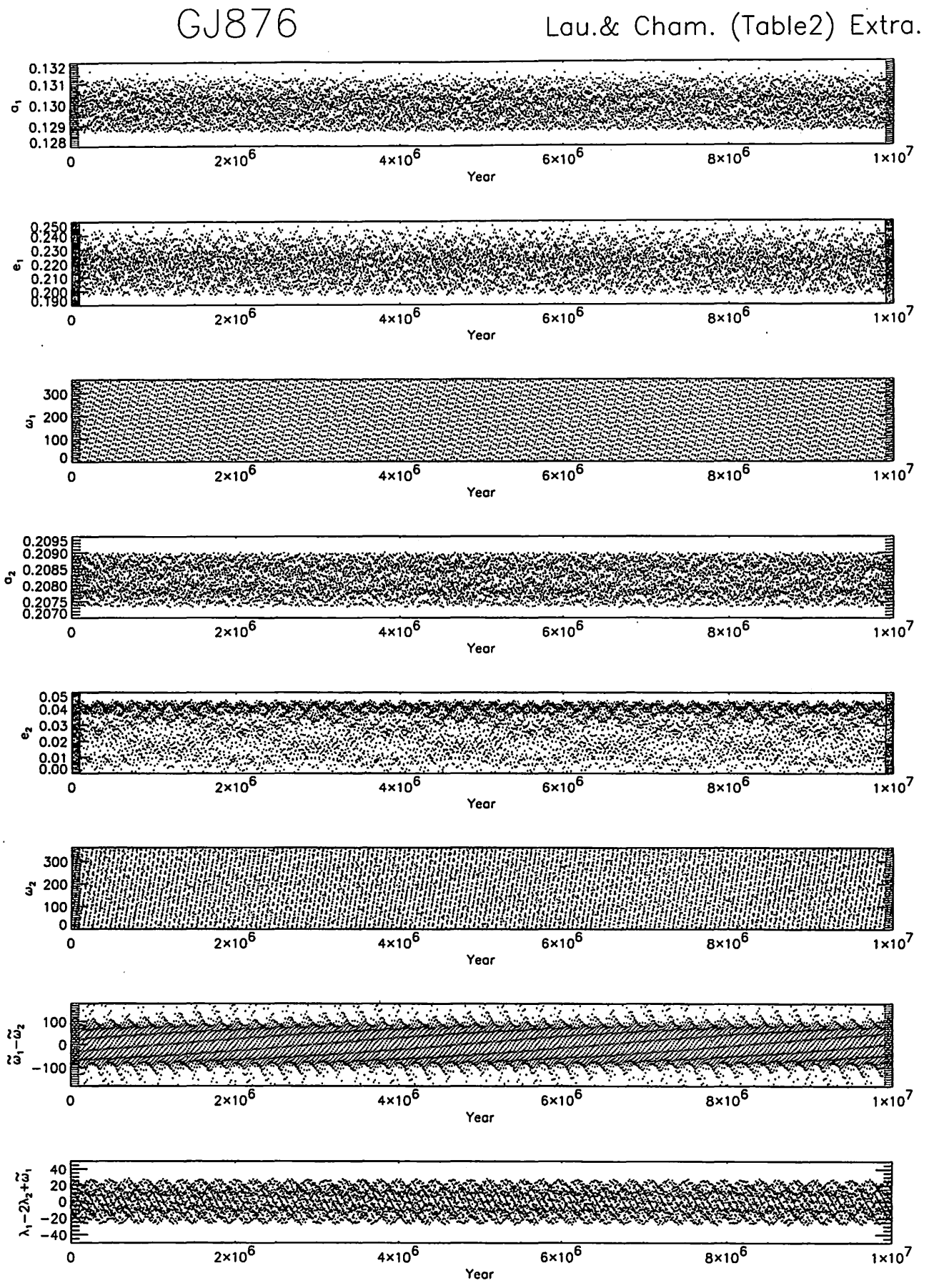

Figure 10: Orbital elements of two planets, the critical argument, and the difference between the pericenter longitudes:Initial orbital elements are taken from Laughlin and Chambers(2001),$T = 10^7$ years

We integrated the planetary system with one of osculating elements, which was derived by using Levenberg-Marquardt scheme, and found this planetary system is stable by a 2:1 mean motion resonance (see Figures 9 and 10). The methods proposed by Laughlin and Chambers (2001) can probably determine the true masses of the planets by eliminating the $\sin i$ degeneracy, since the mutual perturbations do depend on the $\sin i$.

This study was supported by the Grant-in-Aid of the Ministry of Education, Science, Sports and Culture of Japan (12640241).

References

Laughlin, G. and Chambers, J. E., 2001, ApJ, Submitted.

Marcy, G. W., Butler, R. P., Fischer, D., Vogt, S. S., Lissauer, J. J., & Rivera, E. J., 2001, ApJ, Submitted.

近点の連動と惑星軌道の安定性
The relation between apparent alignment of the major axes and stability of the planetary system

中井宏、木下宙（国立天文台）
H. Nakai and H. Kinoshita
National Astronomical Observatory

Abstract

We investigate the stability of the planetary system in which the pericenters of the two planets are corotating. In this paper, we assume that two planets move in a same plane and are not in a stable of mean motion resonance. Using the semi-analytical theory, we study the range of two planet's eccentricities for aligning their longitudes of pericenter. In the systems with the these eccentricities for two planets, the alignment of planet's longitudes of pericenter prevents close approaches between them. This alignment enhances the stability of the system.

1. はじめに

最近発見された*υ Andromedae*惑星系では、３個の惑星が確認されている(Butler et al. 1999)。２．２億年の数値シミュレーションの結果では、惑星系が安定な場合は全て外側の２惑星の近星点が連動していて、近星点経度の差が６０度以下であった。この惑星系では、近星点の連動が安定性に重要な働きをしている（中井、木下,2000)。仮想惑星系で２惑星の近星点が連動するための離心率の範囲を調べ、近星点が連動する場合と、そうでない場合の２惑星の最接近距離の変化と軌道の安定との関係を検討した。

2.1 摂動関数

惑星２におよぼす惑星１の摂動は

$$R_{21} = k^2 m_1 (\frac{1}{\Delta} - \frac{r_2}{r_1^2}\cos H),$$

惑星１におよぼす惑星２の摂動は

$$R_{12} = k^2 m_2 (\frac{1}{\Delta} - \frac{r_1}{r_2^2}\cos H)$$

となる。但し、Δ は２惑星間の距離、kはガウスの定数、m_1, m_2 は惑星の質量、r_1, r_2 は主星から惑星までの距離である。ここで、

$$\begin{aligned}
\Delta^2 &= r_1^2 - 2r_1 r_2 \cos H + r_2^2, \\
\cos H &= \cos(f_1+\varpi_1)\cos(f_2+\varpi_2) + \cos J \sin(f_1+\varpi_1)\sin(f_2+\varpi_2) \\
&= \cos(f_1 - f_2 + \varpi_1 - \varpi_2) - 2\sin^2\frac{J}{2}\sin(f_1+\varpi_1)\sin(f_2+\varpi_2)
\end{aligned}$$

$f_1, f_2, \varpi_1, \varpi_2$ はそれぞれ各惑星の真近点離角と近星点経度、J は惑星相互の軌道傾斜角、Hはr_1, r_2 間の角である。惑星１，２は同一平面内を運動すると仮定すると、

$$\cos H = \cos(f_1 - f_2 + \varpi_1 - \varpi_2)$$

となり、真近点離角は短周期であるので、平均操作により消去すると、摂動関数Rはe_1, e_2, $\varpi_1 - \varpi_2$ だけの関数となる。全角運動量θを決めると等エネルギーカーブから$\varpi_1 - \varpi_2$とe_1または$\varpi_1 - \varpi_2$とe_2の関係が分かる。ここで、

$$\begin{aligned}\theta &= \Theta_1\sqrt{1-e_1^2} + \Theta_2\sqrt{1-e_2^2},\\ \Theta_1 &= m_1\sqrt{k^2(1+m_1)a_1},\\ \Theta_2 &= m_2\sqrt{k^2(1+m_2)a_2}.\end{aligned}$$

但し、e_1, e_2は各惑星の離心率a_1, a_2は軌道長半径である。

2.2 等エネルギーカーブ

現在の木星、土星の軌道長半径を用い($a_{Jupiter} = 5.2AU$, $a_{Saturn} = 9.6AU$)、２惑星の平均近点離角 ($l_{Jupiter} = 0, 30, \cdots, 330$, $l_{Saturn} = 0$) を変化させ、近日点が連動するための２惑星の離心率の範囲を調べた。平均近点離角の差 ($\Delta l = l_{Jupiter} - l_{Saturn}$) が９０度または２７０度付近で２惑星は５：２平均運動共鳴 ($\theta_c = 2\lambda_J - 5\lambda_S + 3\varpi_s$) の関係になり、近日点経度の差 ($\varpi_J - \varpi_S$) は逆行から順行に変化した。平均運動共鳴の境界付近では、近日点経度の差は回転したり、秤動したりを繰り返し、安定な運動をしないので、近日点の連動と離心率の関係が明確でなくなる。そのため、今回は仮想惑星系を考え、２惑星が平均運動共鳴にならないように軌道長半径を選んだ。仮想２惑星は同一平面上を運動し、その軌道要素は $a_1 = 5AU$, $a_2 = 10AU$, $m_1 = M_{Jupiter}$, $m_2 = M_{Saturn}$ の一定とした。離心率、近星点経度、平均近点離角を変化させ、近星点の連動と離心率の関係を調べた。

図１は 仮想惑星系で$\theta = 5.23 \times 10^{-5}$ の場合の等エネルギーカーブで図1a,1bはそれぞれ惑星１，２の近星点経度の差($\varpi_1 - \varpi_2$) と離心率の関係である。近星点の運動は、お互いの近星点が連動する領域、近星点経度の差が回転する領域、近星点と遠星点が連動する領域の３部分に分かれる。図中の点は惑星の近星点が連動するように初期値 ($e_1 = 0.03, \varpi_1 = 0°, l_1 = 0°$, $e_2 = 0.05, \varpi_2 = 0°, l_2 = 0°$) を選んだ１００万年の数値積分の結果である。一つの角運動量θが決まると、一つの等エネルギーカーブが描け、近星点経度の差が連動する最大の離心率(e_u)、近星点経度の差が秤動する中心の離心率(e_c)、連動する最小の離心率(e_d) が求まる。

θ が与えられたとき、それぞれの惑星のとりうる最大の離心率は

$$\begin{aligned}e_{1m} &= \sqrt{1-((\theta-\Theta_2)/\Theta_1)^2},\\ e_{2m} &= \sqrt{1-((\theta-\Theta_1)/\Theta_2)^2}\end{aligned}$$

で決まる。添字１，２は惑星を表す。図１から分かるように、それぞれの離心率の間には$\Theta_1 > \Theta_2$の場合（図１)、

$$e_{1c} > e_{2c}, \quad e_{1u} = e_{1m}, \quad e_{2d} = 0$$

の関係がある。

$\Theta_1 < \Theta_2$ の場合は惑星の役割が入れ替わり、

$$e_{1c} < e_{2c}, \quad e_{2u} = e_{2m}, \quad e_{1d} = 0$$

の関係になる。（近点経度の差が１８０度の場合は Θ_1 と Θ_2 の関係が逆になる。）

3.1 近星点が連動する離心率の範囲

２惑星の近星点が完全に重なっている場合、２惑星の近星点経度の差はつねに０度であり、短周期成分を無視すれば、２惑星の離心率はそれぞれ一定値 e_{1c}, e_{2c} となる。e_{1c}, e_{2c} の大きさは、各惑星の角運動量の大きさにより $\Theta_1 > \Theta_2$ なら $e_{1c} > e_{2c}$ であり、$\Theta_1 < \Theta_2$ なら $e_{1c} < e_{2c}$ となる。

２惑星の近星点経度の差が $\pm\Delta\varpi$ で秤動する場合、２惑星の近星点が重なった時は、惑星１の離心率が $e_{1d} < e_1 < e_{1c}$ であれば、惑星２の離心率は $e_{2u} > e_2 > e_{2c}$ の範囲になる。逆に、惑星１の離心率が $e_{1c} < e_1 < e_{1u}$ であれば、惑星２の離心率は $e_{2c} > e_2 > e_{2d}$ の範囲になる。e_1, e_2 のとり得る値は e_{1c}, e_{2c} を中心とする範囲を変動し、その変動幅は近星点経度の差の秤動の振幅 $(\pm\varpi)$ によって変化する。

近星点経度の差の秤動の振幅が大きくなり、近星点が連動するか、回転するかの限界になると、２惑星の近星点が重なった時の２惑星の離心率は e_{1d}, e_{2u} または e_{1u}, e_{2d} となり、e_1, e_2 はその間を変動する。２惑星の離心率 (e_1, e_2) と角運動量 (θ) の間には、つねに $\theta = \Theta_1\sqrt{1-e_1^2} + \Theta_2\sqrt{1-e_2^2}$ の関係がある。

２惑星の近星点経度の差 $(\varpi_1 - \varpi_2)$ が０度になったとき、θ によって近星点経度の差が秤動する境界の離心率 (e_u, e_d) の範囲と、中心の離心率 (e_c) がどのように変化するかを図２に示す。図２ａ、２ｂはそれぞれ、惑星１，２の結果である。この例では $\Theta_1 = 3.67 \times 10^{-5}$, $\Theta_2 = 1.55 \times 10^{-5}$ となり、惑星１の角運動量が惑星２の角運動量より大きいので、近星点経度の差が秤動するための惑星１の離心率の範囲は大きな方に、惑星２の離心率の範囲は小さい方に現れている。

3.2 最接近距離

簡単化し、２惑星の最接近距離を $D = a_2(1 \pm e_2) - a_1(1 \pm a_1)$ とする。角運動量 θ に対して次の５つの場合に相当する各惑星の離心率を求める。

ケース１．(e_{1c}, e_{2c}) ２惑星の近星点が完全に重なって運動する。$(\varpi_1 - \varpi_2 = 0°)$
ケース２．　近星点経度の差が０度の回りを秤動する。$(\varpi_1 - \varpi_2 = \pm\Delta\varpi)$
ケース３．(e_{1u}, e_{2d}) 近星点経度の差が秤動と回転の境界になる。
ケース４．(e_{1d}, e_{2u}) 近星点経度の差が秤動と回転の境界になる。
ケース５．　近星点と他の惑星の遠星点が重なって運動する。$(\varpi_1 - \varpi_2 = 180°)$

５ケースについて、θ を変化させながら２惑星の最接近距離を求めたのが図３である。（実際の軌道要素はお互いの摂動で短周期の変動をしていて、最接近距離も、上の式とは一致しない。）$\theta = 4.2 \times 10^{-5}$ のとき、ケース１では惑星１，２の離心率が０．６６，０．３９と比較的大きいにもかかわらず２惑星は４．４ＡＵ以下には近づくことが無い。実際、１１００万年間の数値シミュレーションの結果でも２惑星の最接近距離は４．４２ＡＵであった。同じ角運動量で惑星１，２の離心率をそれぞれ０．６９，０．１９としたケース２では、数値シミュレーションでの最接近距離は２．１２ＡＵとなり、計算から求まる値 $(D = 3.5AU)$ より小さくなっていた。近星点経度の差の秤動の振幅が大きくなると最接

近距離は小さくなり軌道も不安定になる。近星点の連動（0度の回りの近星点経度の差の秤動）の振幅が小さい程2惑星の大接近は回避される。

3.3 数値積分

上記5ケースについて、θ がそれぞれ、4.2×10^{-5}, 4.6×10^{-5}, 5.0×10^{-5}, 5.2×10^{-5} に対応する離心率を初期値とし、１１００万年（惑星1の１００万公転に相当）数値シミュレーションを行い、軌道の安定性を調べた。離心率以外の初期の軌道要素は $a_1 = 5AU, \varpi_1 = 0°, l_1 = 0°$, $a_2 = 10AU, \varpi_2 = 0°, l_2 = 0°$ の一定とした。積分法は係数対称線形多段法(Quinlan and Tremaine, 1990) を用い、固定キザミ幅4日とした。図3には角運動量 θ と5ケースの離心率で求まる最接近距離の位置に数値シミュレーションの結果を重ねている。１１００万年間、軌道が安定（離心率が1以下）であった場合は○、軌道が不安定（離心率が1以上）になった場合は × で図示している。軌道が不安定になった場合は全て2惑星の近星点の連動は崩れていた。

図4は2惑星の初期の離心率をそれぞれ、０．０５から０．９まで変化させ、１１００万年数値シミュレーションを行った結果である。軌道が安定な場合は○、短期間で不安定になる場合は × で表している。５００万年以上安定で、その後不安定になった場合は △ で表している。図には2惑星の近星点が重なって運動する（ケース1）場所、秤動と回転の境界（ケース3，ケース4）の場所も示している。また、角運動量が等しい点は点線で示している。2惑星の近星点が連動すれば、軌道は安定になる。特に、離心率が大きな（角運動量の小さな）系では近星点が連動し、その秤動する振幅も小さいことが惑星系の安定性に重要である。近星点が重なっている系（$\varpi_1 - \varpi_2 = 0°$）では惑星1，2の離心率がそれぞれ、０．８，０．４でも軌道は安定であった。

4. 結論

2惑星の近星点の連動により最接近距離は大きくなり、2惑星の大接近は回避され、軌道の安定性が増す。2惑星の初期の離心率が秤動中心に近いと、2惑星の近星点経度の差（$\varpi_1 - \varpi_2$）の振幅は小さく、離心率が相当大きくても（$e_1 = 0.8, e_2 = 0.4$）軌道は安定である。初期の離心率が秤動中心から離れ、2惑星の近星点が連動するか回転するかの境界に近づくと2惑星の運動はカオス的になり、惑星系は不安定になる。近星点の連動が崩れた状態では2惑星の離心率が小さい場合以外は惑星系は不安定である。

5. おわりに

今後は、角運動量の異なる様々な惑星系で角運動量と近星点が連動する離心率の関係を調べ、実際に観測されている惑星系のデータと比較する。今回は、2惑星が同一平面上、平均運動共鳴関係にない場合を仮定したが、一般的な惑星系で平均運動共鳴にある場合とない場合で近星点の連動する離心率の範囲がどう変化するか検討する。これらを明らかにし、様々な共鳴と軌道の安定性の関係を調べることが今後の課題である。

6. 参考文献

Brouwer D. and Clemence G.M. : 1961, Methods of Celestial Mechanics, *Academic Press*, pp.465-466.

Butler R.P.,Marcy G.W.,Fischer D.A.,Brown T.W.,Contos A.R.,Korzennik S.G., Nisenson P. and Noyes R.W. : 1999, Evidence for Multiple Companions to υ Andromedae, *Astrophys. J.*,**526**,pp.916-927.

Kozai,Y : 1983, Secular Perturbations of Asteroids with Commensurable Mean Motions, Celestial Mechanics of the International Symposium G. LEMAITRE, Louvain-la-Neuve, Belgique, pp.1-20.

中井宏、木下宙 : 2000, υ Andromedae 惑星系の安定性, 第３２回天体力学研究会集録, pp.206-215.

Quinlan G.D. and Tremaine S. : 1990, Symmetric Multistep Methods for the Numerical Integration of Planetary Orbits, *Astron. J.*, **100**, pp.1694-1700.

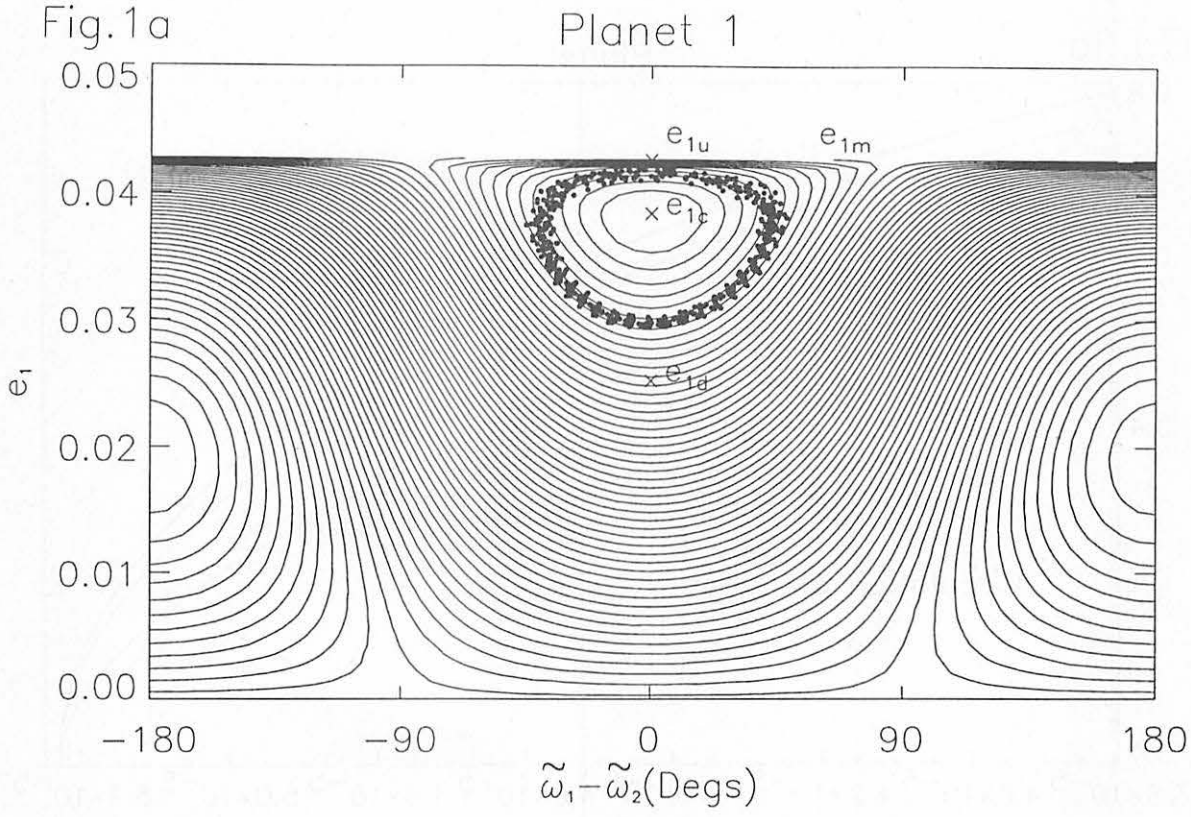

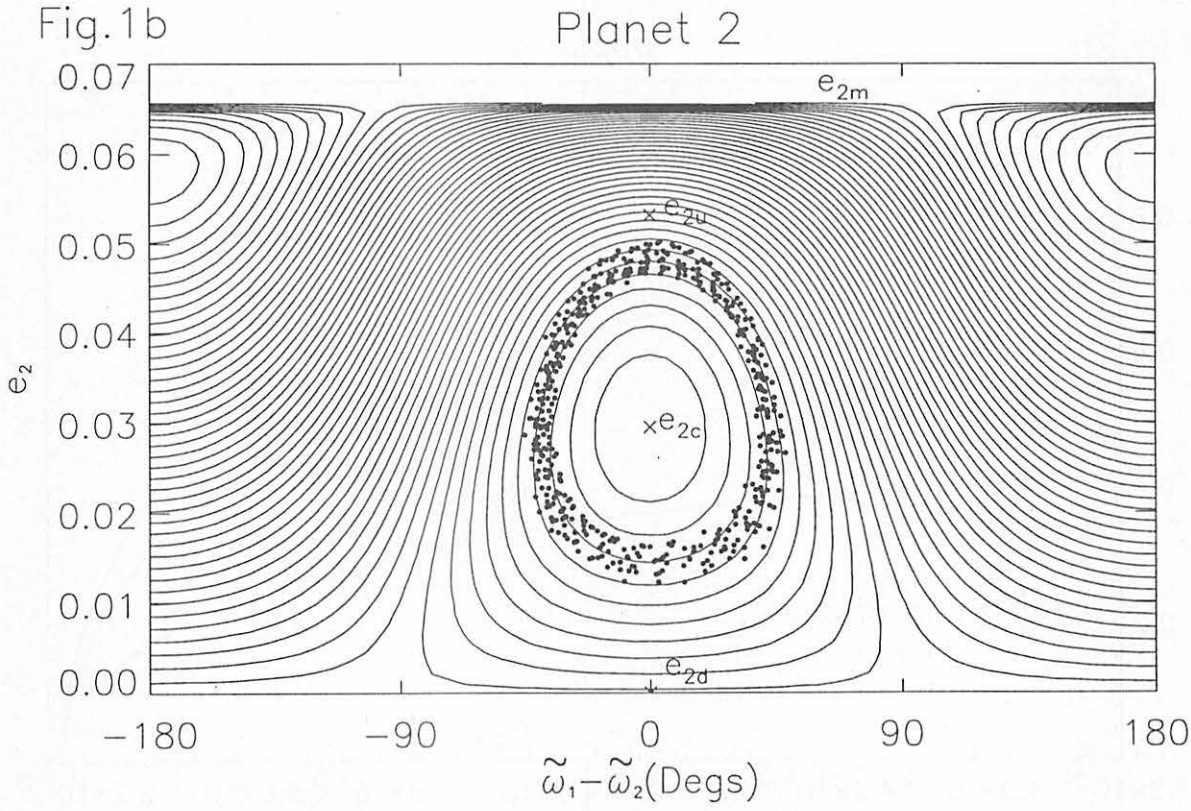

Figure 1. Equi-potential curves of the planets 1 and 2.
($\theta = 5.23 \times 10^{-5}$, $a_1 = 5AU, m_1 = M_{Jupiter}, a_2 = 10AU, m_2 = M_{Saturn}$.)
e_u is the maximum eccentricity, e_c is the eccentricity of the libration center, e_d is the minimum eccentricity at $\varpi_1 = \varpi_2$. The dots show the solutions by numerical integration.

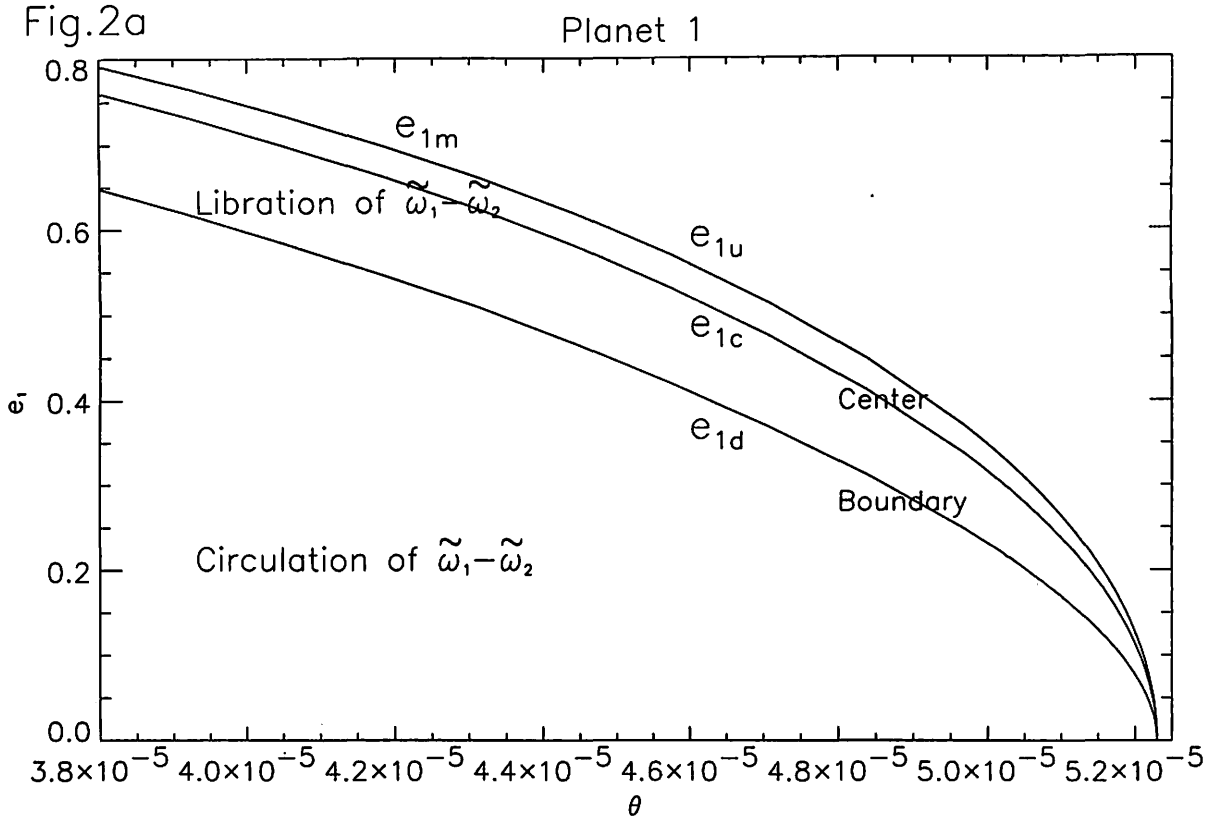

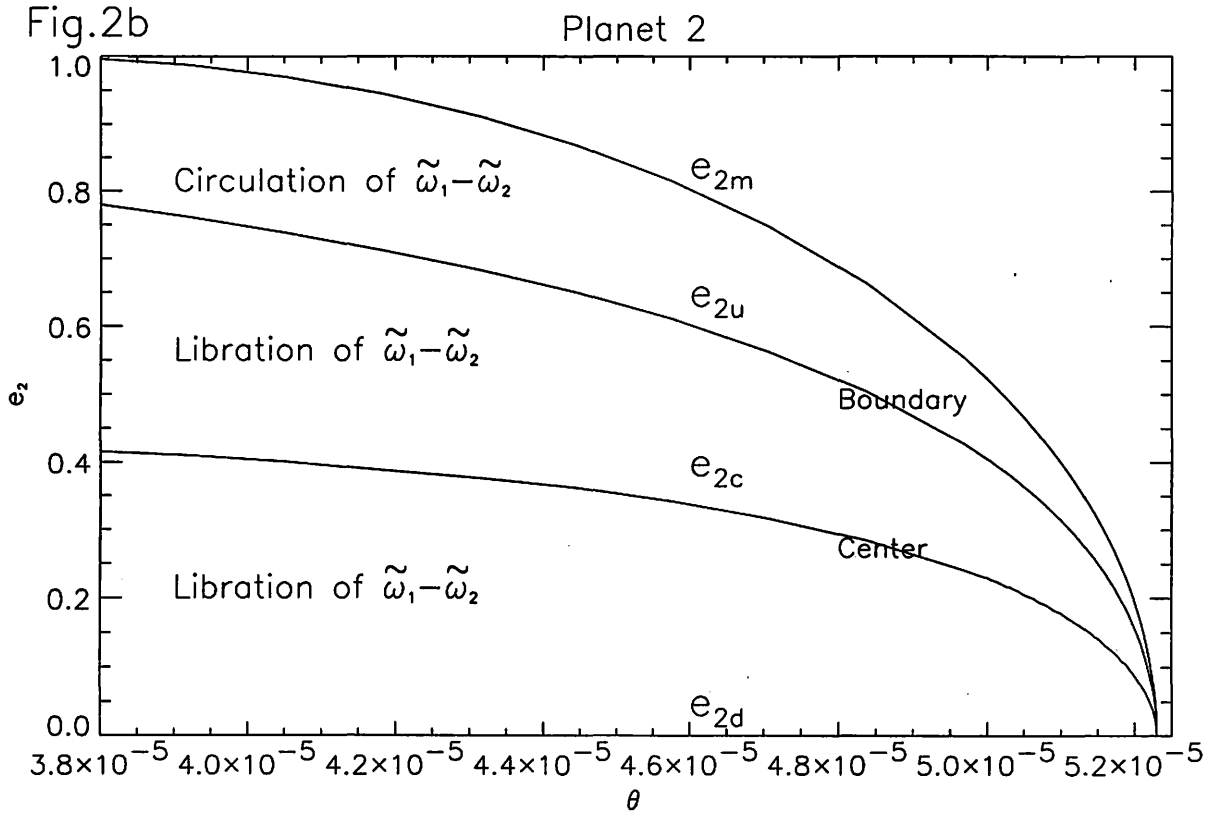

Figure 2. The e_u, e_c, e_d and e_m at $\varpi_1 = \varpi_2$.
Horizontal axis express angular momentum,
$\theta = m_1\sqrt{k^2(1+m_1)a_1(1-e_1^2)} + m_2\sqrt{k^2(1+m_2)a_2(1-e_2^2)}$.

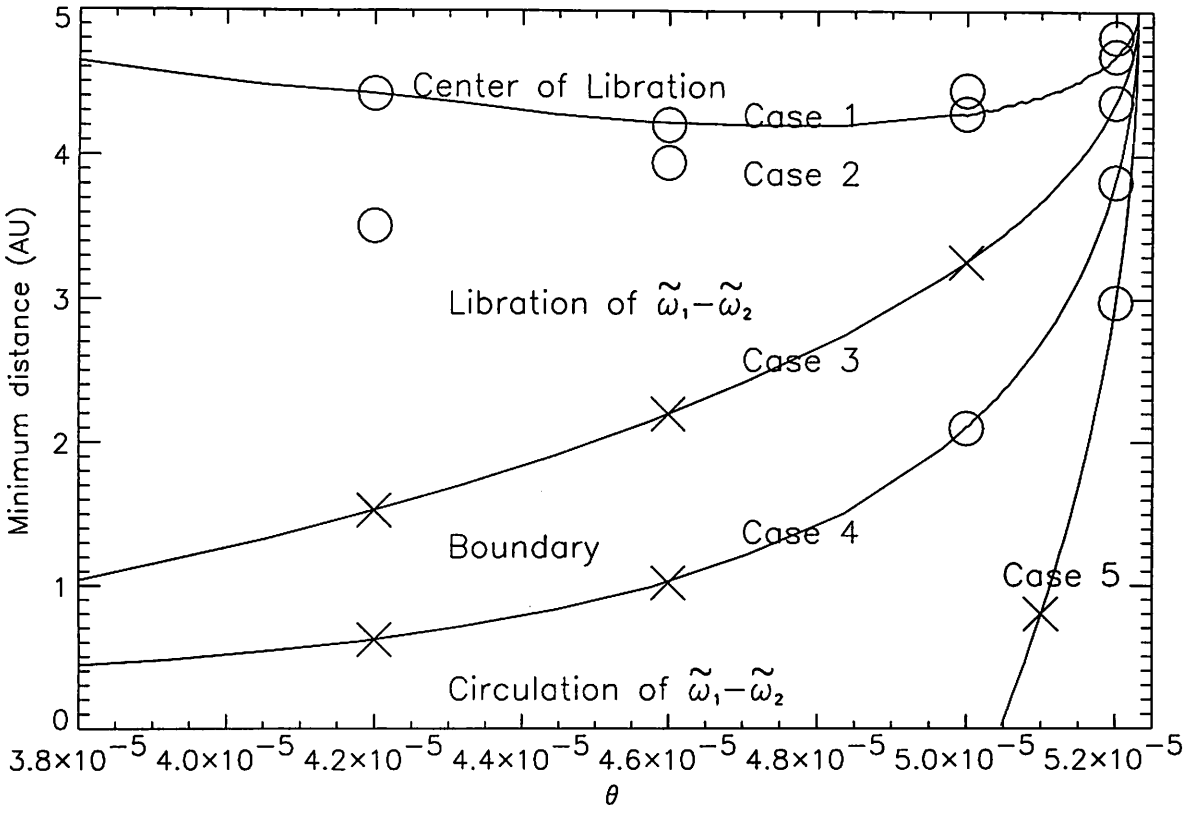

Figure 3. The minimum distance between two planets.
Horizontal axis express angular momentum (θ) and vertical axis express minimum distance(D), $D = a_2(1 \pm e_2) - a_1(1 \pm e_1)$. The open circles(○) mean the systems are still stable until 11 million years (about 10^6 revolutions for planet 1). The crosses(×) indicate unstable orbit($e > 0.99$) for a short time.

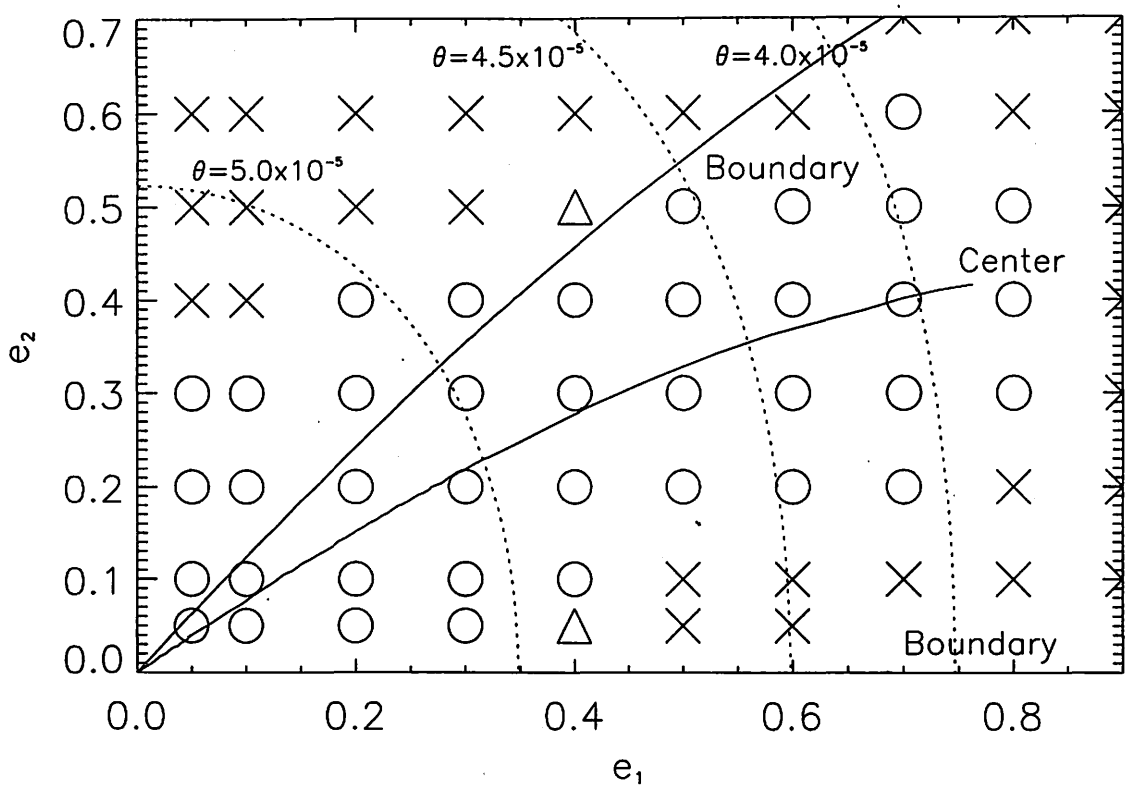

Figure 4. The stability of planetary system at $e_1 : e_2$ space.
The orbital parameters are $a_1 = 5AU, m_1 = M_{Jupiter}, \varpi_1 = 0, l_1 = 0,\ a_2 = 10AU, m_2 = M_{Saturn}, \varpi_2 = 0, l_2 = 0,$ and e_1, e_2 take the values of x,y coordinates. The open circles(○) mean the systems are still stable until 11 million years (about 10^6 revolutions for planet 1). The crosses(×) indicate unstable orbit($e > 0.99$) for a short time. The triangles(△) indicate stable orbits until 5 million years, but the orbits become unstable within 11 million years. The solid lines show center of libration and boundaries of $\varpi_1 - \varpi_2$. The dotted lines show equi-angular momentum curves at $\theta = 4.0 \times 10^{-5}, 4.5 \times 10^{-5}, 5.0 \times 10^{-5}$.

Construction of Analytical Expressions of Nereid's Motion Perturbed by Triton - (I) Planar Problem -

Yoshimitsu MASAKI[1] and Hiroshi KINOSHITA[2]

[1] The Graduate University for Advanced Studies (National Astronomical Observatory, Japan)
yoshimitsu.masaki@nao.ac.jp
2-21-1, Osawa, Mitaka, Tokyo, 181-8588, Japan

[2] National Astronomical Observatory, Japan
Kinoshita@nao.ac.jp
2-21-1, Osawa, Mitaka, Tokyo, 181-8588, Japan

ABSTRACT

The second satellite of Neptune, Nereid, moves on a highly eccentric ($e = 0.75$) orbit. A perturbation on Nereid is mainly caused by the Sun, but one from Triton is not negligible when we construct a precise ephemeride for Nereid. Ultimately, we aim to build an analytical ephemeride of Nereid.

In this paper, we simplify the problem into a planar model, i.e., Nereid and Triton revolve around Neptune on a common plane and Triton moves on a circular orbit. To derive analytical expressions of motion, Hori's canonical perturbation method is used. We compare with numerical results to check accuracy of our analytical ones.

We show that it requires many terms of a perturbing function of Triton or generating functions to obtain an accurate theory of motion, due to a close-approaching configuration of the system.

1 Introduction

1.1 Ephemerides of Nereid

Nereid, a satellite of Neptune, moves on the most eccentric orbit of known satellites in the Solar system. It is discovered by Kuiper in 1949 as the second satellite of Neptune. Its orbital period is nearly one year.

Before the investigation by the spacecraft Voyager II, only two satellites are known for Neptune. Triton, the first discovered one by Lassell in 1846, orbits on a nearly circular but retrograde orbit once in six days.

In the Voyager II mission, six satellites are newly found. All of them are in the vicinity of Neptune, their semimajor axes are spread from 1.94 to 4.75 in radius of Neptune, since Voyager II passed through Neptune in a close distance.

After the discovery of Nereid, many astronomers reported its osculating elements, such as van Biesbroeck (1951,1957), Rose(1974) and Veillet(1982). Due to its long orbital period (nearly 1 year), astrometric observations for a long span are required to obtain osculating elements accurately. Besides, its faintness (19th magnitude) has obstructed to get clear images of Nereid from the ground-based telescopes.

Mignard (1975) firstly studied the motion of Nereid, and built an ephemeride (1981) analytically. He used canonical transformations and took only the solar perturbation (P_2 and P_3 terms) into account.

For the Voyager II mission, it is required to get precise ephemerides of satellites for its flight program, Jacobson(1990, 1991) constructed a precise numerical ephemeride of Neptunian satellites.

In analytical approach, Oberti (1990) showed periodic and the secular perturbation terms of Nereid with use of a canonical perturbation method of Deprit type. In this work, the solar perturbation (P_2 to P_4 terms) and Triton's one (P_2 and P_3 terms) were included in his Hamiltonian and set the origin at Neptune-Triton barycenter. Segerman and Richardson (1997) also studied motion of Nereid. They took the solar perturbation (P_2 and P_3 terms) ,Triton's one (P_2 and P_3 terms) and J_2 effect of Neptune into consideration.

Saad(2000) studied the motion of Nereid with use of a canonical perturbation method of Hori type. He considered only the solar perturbation (P_2 term only). The secular perturbation is solved analytically, based on the Kinoshita and Nakai(1999)'s work.

2 Formulation of the planar restricted problem

In this section, we deal with a three-body problem such that Neptune, Triton and Nereid are moving on a common plane and suppose that Triton moves on a circular orbit.

2.1 A general expression of the problem

After here, we designate masses of Neptune, Triton and Nereid by M, m_{Tri}, m, respectively. Orbital elements of Triton are referred to the Neptune-centric coordinate system, and ones of Nereid are to the Neptune-Triton barycentric system. The subscript Tri is for a quantity of Triton, and no subscript (except M) is for one of Nereid. The universal gravity constant is written by k^2.

In general, a force function of three-body problem is expressed as follows:

$$U_0 = k^2 \left[\frac{M m_{Tri}}{r_{Neptune-Triton}} + \frac{m_{Tri} m}{r_{Triton-Nereid}} + \frac{mM}{r_{Nereid-Neptune}} \right]$$

where r is a mutual distance of two bodies of the set declared in the subscript.

From the definition written above, radii of orbits are

$$\begin{aligned} r_{Tri} &\equiv r_{Neptune-Triton} \\ r &\equiv r_{(Barycenter\,of\,Neptune\,and\,Triton)-Nereid}. \end{aligned}$$

So we can rewrite U_0 as

$$U_0 = k^2 \left[\frac{M m_{Tri}}{r_{Tri}} \right.$$

$$
\begin{aligned}
&+\frac{m_{Tri}m}{r}\left\{1+\frac{M}{M+m_{Tri}}(\frac{r_{Tri}}{r})P_1(\cos S)\right.\\
&\qquad+(\frac{M}{M+m_{Tri}})^2(\frac{r_{Tri}}{r})^2P_2(\cos S)\\
&\qquad\left.+(\frac{M}{M+m_{Tri}})^3(\frac{r_{Tri}}{r})^3P_3(\cos S)+\ldots\right\}\\
&+\frac{mM}{r}\left\{1-\frac{m_{Tri}}{M+m_{Tri}}(\frac{r_{Tri}}{r})P_1(\cos S)\right.\\
&\qquad-(\frac{m_{Tri}}{M+m_{Tri}})^2(\frac{r_{Tri}}{r})^2P_2(\cos S)\\
&\qquad\left.-(\frac{m_{Tri}}{M+m_{Tri}})^3(\frac{r_{Tri}}{r})^3P_3(\cos S)-\ldots\right\}\Bigg]\\
=\;& k^2\left[\frac{Mm_{Tri}}{r_{Tri}}\right.\\
&+\frac{(M+m_{Tri})m}{r}\\
&+\frac{Mm_{Tri}m}{M+m_{Tri}}\frac{1}{r}(\frac{r_{Tri}}{r})^2P_2(\cos S)\\
&\left.+\frac{Mm_{Tri}m(M-m_{Tri})}{(M+m_{Tri})^2}\frac{1}{r}(\frac{r_{Tri}}{r})^3P_3(\cos S)+\cdots\right],
\end{aligned}
$$

where S is the elongation between Triton and Nereid, and P_i is a Legendre polynomial of degree i.

For the motion of Nereid, a force function has to be multiplied by a mass factor, $\frac{M+m_{Tri}+m}{(M+m_{Tri})m}$, i.e.

$$U=\frac{M+m_{Tri}+m}{(M+m_{Tri})m}U_0.$$

The unperturbed hamiltonian of Nereid (i.e. Kepler motion) is expressed as

$$H_0=\frac{\mu}{2a}$$

where $\mu=k^2(M+m_{Tri}+m)$ and a is a semi-major axis of the orbit of Nereid.

A perturbation from Triton is adding on the system, a (perturbed) hamiltonian for Nereid becomes,

$$F=\mu\left[\frac{1}{2a}+\frac{Mm_{Tri}}{(M+m_{Tri})^2}\frac{r_{Tri}^2}{r^3}P_2(\cos S)+\frac{Mm_{Tri}(M-m_{Tri})}{(M+m_{Tri})^3}\frac{r_{Tri}^3}{r^4}P_3(\cos S)\right].$$

2.2 Simplification of the problem (Planar restricted problem)

After here, we simplify the problem (See Figure 1):

- All bodies are on a common plane.
- Triton moves on a circular orbit.
- Nereid's perturbation does not affect on the motion of Neptune or Triton (practically, it is equivalent that we neglect mass of Nereid, i.e. we study as a restricted problem).

Since observed Triton's eccentricity is very small, we can treat it as zero. After neglect of Triton's eccentricity, the hamiltonian is expressed easily:

$$F=\mu\left[\frac{1}{2a}+\frac{Mm_{Tri}}{(M+m_{Tri})^2}\frac{a^3}{r^3}\frac{a_{Tri}^2}{a^3}P_2(\cos S)+\frac{Mm_{Tri}(M-m_{Tri})}{(M+m_{Tri})^3}\frac{a^4}{r^4}\frac{a_{Tri}^3}{a^4}P_3(\cos S)+\ldots\right]$$

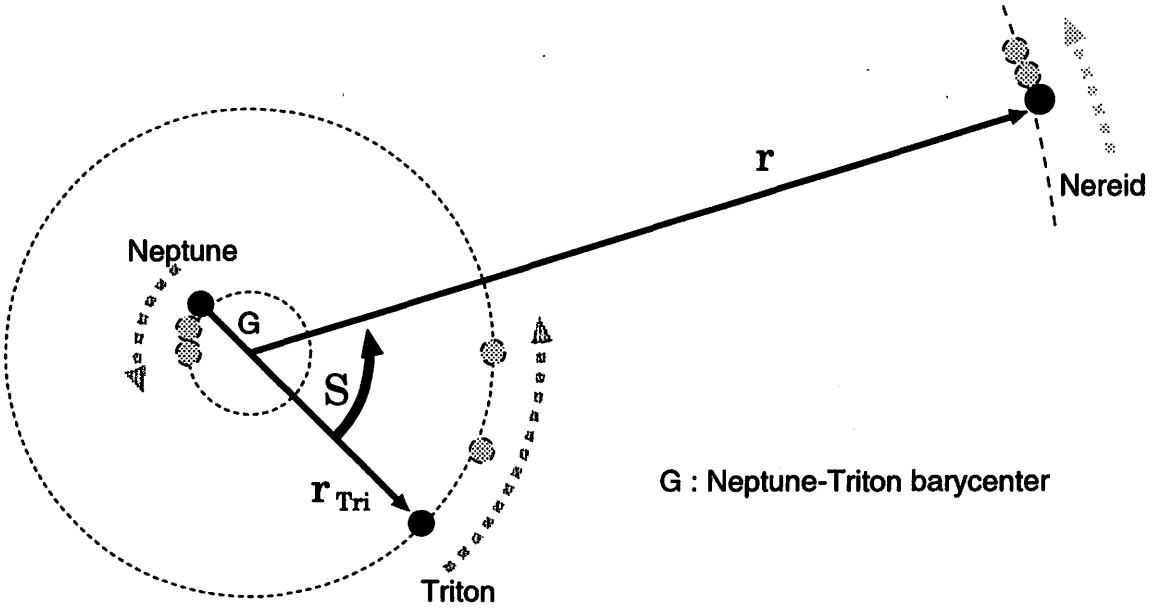

Figure 1: A schematically illustrated model of a planar restricted problem

An angular distance S is measured as an angle between Triton and Nereid at the Neptune-Triton barycenter. In a planar problem, S can be expressed as $f + \varpi - \lambda_{Tri}$, where ϖ is the longitude of the pericenter of Nereid, and λ_{Tri} is the longitude of Triton. Legendre polynomials P_is are expanded as follows:

$$\begin{aligned} P_2(\cos S) &= \frac{1}{4}(3\cos(2S)+1) \\ P_3(\cos S) &= \frac{1}{8}(5\cos(3S)+3\cos S). \end{aligned}$$

Then a hamiltonian becomes,

$$\begin{aligned} F &= \mu\left[\frac{1}{2a}\right. \\ &+\frac{Mm_{Tri}}{(M+m_{Tri})^2}\frac{a^3}{r^3}\frac{a_{Tri}^2}{a^3}\frac{1}{4}(3\cos(2(f+\varpi-\lambda_{Tri}))+1) \\ &\left.+\frac{Mm_{Tri}(M-m_{Tri})}{(M+m_{Tri})^3}\frac{a^4}{r^4}\frac{a_{Tri}^3}{a^4}\frac{1}{8}(5\cos(3(f+\varpi-\lambda_{Tri}))+3\cos(f+\varpi-\lambda_{Tri}))+\ldots\right]. \end{aligned}$$

2.3 Eliminate time from Hamiltonian and make new Hamiltonian expression

The hamiltonian includes a variable λ_{Tri}, which depends on time:

$$\lambda_{Tri} \equiv k = n_{Tri}t + const..$$

To make a hamiltonian independent of time, we introduce a canonical conjugate action variable, K. The term $-n_{Tri}K$ has to be added to the hamiltonian, then

$$F = \frac{\mu}{2a}$$

$$
\begin{aligned}
&-n_{Tri}K \\
&+\mu\frac{Mm_{Tri}}{(M+m_{Tri})^2}\frac{a^3}{r^3}\frac{a_{Tri}^2}{a^3}\frac{1}{4}(3\cos(2(f+\varpi-\lambda_{Tri}))+1) \\
&+\mu\frac{Mm_{Tri}(M-m_{Tri})}{(M+m_{Tri})^3}\frac{a^4}{r^4}\frac{a_{Tri}^3}{a^4}\frac{1}{8}(5\cos(3(f+\varpi-\lambda_{Tri}))+3\cos(f+\varpi-\lambda_{Tri}))+\ldots.
\end{aligned}
$$

In a planar problem, angular variables which are independent are two :

$$f \quad \text{and} \quad g+h-k$$

i.e. the degrees of freedom are two.

After a suitable canonical transformation, we can deduce the hamiltonian including only two sets of canonical variables, (y_1, x_1) and (y_2, x_2). Suppose the canonical transformation

$$F(l,g,h,k,L,G,H,K) \longrightarrow F(y_1,y_2,x_1,x_2).$$

This transformation is obtained when the condition below is satisfied :

$$Ll+Gg+Hh+Kk = x_1y_1+x_2y_2+x_3y_3+x_4y_4.$$

One of examples is :

$$
\begin{aligned}
y_1 &= l \\
y_2 &= g+h-k \\
y_3 &= h \\
y_4 &= k \\
x_1 &= L \\
x_2 &= G \\
x_3 &= H-G \\
x_4 &= K+G.
\end{aligned}
$$

Then the hamiltonian becomes

$$
\begin{aligned}
F &= \mu\frac{1}{2a} \\
&\quad -n_{Tri}(x_4-x_2) \\
&\quad +\mu\frac{Mm_{Tri}}{(M+m_{Tri})^2}\frac{a^3}{r^3}\frac{a_{Tri}^2}{a^3}\frac{1}{4}(3\cos(2(f+y_2))+1) \\
&\quad +\mu\frac{Mm_{Tri}(M-m_{Tri})}{(M+m_{Tri})^3}\frac{a^4}{r^4}\frac{a_{Tri}^3}{a^4}\frac{1}{8}(5\cos(3(f+y_2))+3\cos(f+y_2))+\ldots.
\end{aligned}
$$

The hamiltonian does not depend on y_4 anymore, we can eliminate x_4 from it. Finally, the hamiltonian is reduced to:

$$
\begin{aligned}
F &= \mu\frac{1}{2a} \\
&\quad +n_{Tri}x_2 \\
&\quad +\mu\frac{Mm_{Tri}}{(M+m_{Tri})^2}\frac{a^3}{r^3}\frac{a_{Tri}^2}{a^3}\frac{1}{4}(3\cos(2(f+y_2))+1) \\
&\quad +\mu\frac{Mm_{Tri}(M-m_{Tri})}{(M+m_{Tri})^3}\frac{a^4}{r^4}\frac{a_{Tri}^3}{a^4}\frac{1}{8}(5\cos(3(f+y_2))+3\cos(f+y_2))+\ldots.
\end{aligned}
$$

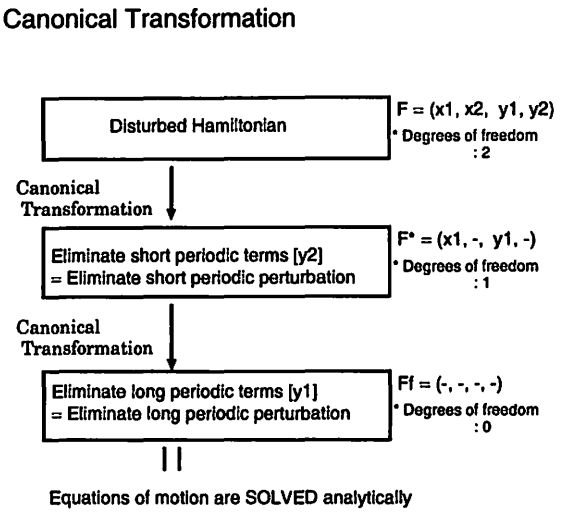

Figure 2: Flow chart of canonical transformations in the planar problem

This simplified hamiltonian expression is preferable to discussion hereafter.

3 Application of canonical transformations for the planar restricted problem

Afterhere, we decompose perturbations into three parts by their periodicities. They are:

- Short periodic perturbation (with periodicity of $\sim$ 6 days)
- Long periodic perturbation (with periodicity of $\sim$ 1 year)
- Secular perturbation .

Six-day perturbation is mainly caused by the revolution of Triton, and one-year one is by the revolution of Nereid. Removal each periodic contributions from the hamiltonian means decreasing degrees of freedom of the hamiltonian, and finally we can integrate equations of motion analytically.

After each periodic perturbation is separated, we deduce osculating elements from them.

This process is acomplished by Hori's canonical perturbation method. A briefly summmarized flowchart is seen in Figure 2.

In this section, for brevity, we consider up to P_2 term of Legendre polynomial of Triton's perturbation in the hamiltonian. The following discussion can be applied when higher terms of P_i are included in the hamiltonian.

3.1 Short periodic perturbation: Eliminate short periodic terms including y_2

First, we take a time-averaged hamiltonian over the short periodic variable, y_2, mainly explained by the revolution of Triton. Through this manipulation, we can obtain a new hamiltonian, $F^*(y_1, x_1)$,

which only contains one angular variable, y_1.

Now, we consider a canonical transformation

$$F(y_1, y_2, x_1, x_2) \longrightarrow F^*(y_1, x_1)$$

such that

$$\begin{aligned} \frac{dx^*}{dt^*} &= \frac{\partial F_0}{\partial y^*} \\ \frac{dy^*}{dt^*} &= -\frac{\partial F_0}{\partial x^*}, \end{aligned}$$

where F_0 is taken as the unperturbed hamiltonian.

From the second equation above, a fictious time increment dt^* is replaced by an angular variable dy^*

$$dt^* = \frac{dy^*}{(-\frac{\partial F_0}{\partial x^*})}.$$

The original hamiltonian (before transformation) is written by:

$$F = F_0 + F_1 + F_2$$

where,

$$\begin{aligned} F_0 &= n_{Tri} x_2 \\ F_1 &= \frac{\mu}{2a} \\ F_2 &= \mu \frac{M m_{Tri}}{(M + m_{Tri})^2} \frac{a^3}{r^3} \frac{a_{Tri}^2}{a^3} \frac{1}{4} (3\cos(2(f + y_2)) + 1). \end{aligned}$$

Subscripts are approximate orders of a small parameter $\frac{n}{n_{Tri}} \sim \frac{1}{60}$. However, seen in F_2, a mass coefficient $\frac{m}{M+m_{Tri}} \sim 2 \times 10^{-4}$ can be act as a more efficient small parameter. We continue to use subscripts for a small parameter $\frac{n}{n_{Tri}}$, but we sometimes truncate Poisson series by the orders of $\frac{m}{M+m_{Tri}}$, i.e., neglecting $(\frac{m}{M+m_{Tri}})^2$ or higher order terms.

We apply Hori's canonical perturbation method on F, a new hamiltonian $F^* = \sum_i F_i^*$ and a generating function $S = \sum_i S_i$ are:

$$\begin{aligned} F_0^* &= F_0(\text{UNPERTURBED}) \\ F_1^* &= [F_1]_{sec} \\ &= \frac{\mu^2}{2x_1^2} \\ S_1 &= \int [F_1]_{per} dt^* \\ &= 0 \\ F_2^* &= [\{F_1, S_1\} + F_2]_{sec} \\ &= \frac{1}{4} \mu \frac{M m_{Tri}}{(M + m_{Tri})^2} \frac{a^3}{r^3} \frac{a_{Tri}^2}{a^3} \\ S_2 &= \int [\{F_1, S_1\} + F_2]_{per} dt^* \\ &= -\frac{3}{8} \frac{\mu}{n_{Tri}} \frac{M m_{Tri}}{(M + m_{Tri})^2} \frac{a^3}{r^3} \frac{a_{Tri}^2}{a^3} \sin 2(f + y_2) \end{aligned}$$

$$
\begin{aligned}
F_3^* &= [\{F_1, S_2\}]_{sec} \\
&= 0 \\
S_3 &= \int [\{F_1, S_2\}]_{per} dt^* \\
F_4^* &= [\{F_1, S_3\}]_{sec} + O((\frac{m}{M + m_{Tri}})^2) \\
&= 0 \\
\cdots &= \cdots \\
F_i^* &= [\{F_1, S_{i-1}\}]_{sec} + O((\frac{m}{M + m_{Tri}})^2) \\
S_i &= \int [\{F_1, S_{i-1}\}]_{per} dt^* + O((\frac{m}{M + m_{Tri}})^2) \\
\cdots &= \cdots
\end{aligned}
$$

Here, $\{X, Y\}$ is an operation of Poisson bracket of X and Y. A conventional definition in the field of celestial mechanics, the hamiltonian is used to be reversed in its sign, therefore,

$$\{X, Y\} \equiv \sum_i \left[\frac{\partial X}{\partial x_i} \frac{\partial Y}{\partial y_i} - \frac{\partial X}{\partial y_i} \frac{\partial Y}{\partial x_i} \right].$$

An infinitesimal increment of time dt^* in indefinite integrals $\int \Box dt^*$ can be replaced by an angular variable, y_2, since F_0 depends only on x_2. This manipulation is equivalent to time-averaged quantity Q over y_2.

$$
\begin{aligned}
\int Q dt^* &= \int Q \frac{1}{(-\frac{\partial F_0}{\partial x_2^*})} dy_2^* \\
&= \int Q \frac{1}{-n_{Tri}} dy_2^*
\end{aligned}
$$

3.2 Long periodic perturbation: Eliminate long periodic terms including y_1

Next, we eliminate a long periodic angular variable y_1, which relates to the revolution of Nereid around Neptune. After a canonical transformation, we can eliminate all of angular variables y_i of the hamiltonian expression, which means the problem is solved analytically, equations of motion (canonical equations) are integrable.

A canonical transformation

$$F^*(y_1, x_1) \longrightarrow F^{**}$$

is defined by :

$$
\begin{aligned}
\frac{dx^{**}}{dt^{**}} &= \frac{\partial F_1^*}{\partial y^{**}} \\
\frac{dy^{**}}{dt^{**}} &= -\frac{\partial F_1^*}{\partial x^{**}}.
\end{aligned}
$$

A time increment dt^{**} is

$$dt^{**} = \frac{dy^{**}}{(-\frac{\partial F_1^*}{\partial x^{**}})}.$$

The hamiltonian (before transformation) is :

$$F^* = F_0^* + F_1^* + F_2^*$$

where,

$$\begin{aligned} F_0^* &= F_0 \\ F_1^* &= \frac{\mu^2}{2x_1^2} \\ F_2^* &= \frac{1}{4}\mu\frac{Mm_{Tri}}{(M+m_{Tri})^2}\frac{a^3}{r^3}\frac{a_{Tri}^2}{a^3}. \end{aligned}$$

Hori's canonical perturbation method is applied on this hamiltonian, neglecting $O((\frac{m}{M+m_{Tri}})^2)$, we obtain a new hamiltonan $F^{**} = \sum_i F_i^{**}$ and a generating function $S^* = \sum_i S_i^*$:

$$\begin{aligned} F_0^{**} &= F_0^* \\ F_1^{**} &= F_1^*(\text{UNPERTURBED}) \\ F_2^{**} &= [F_2^*]_{sec} \\ &= \frac{1}{4}\mu\frac{Mm_{Tri}}{(M+m_{Tri})^2}\frac{1}{\eta^3}\frac{a_{Tri}^2}{a^3} \\ S_1^* &= \int [F_2^*]_{per}\, dt^{**} \\ &= \frac{1}{4}\mu\frac{Mm_{Tri}}{(M+m_{Tri})^2}\frac{1}{n\eta^3}\frac{a_{Tri}^2}{a^3}(f + e\sin f - y_1) \\ F_2^{**} &= [\{F_2^*, S_1^*\}]_{sec} \\ &= O((\frac{m}{M+m_{Tri}})^2) \\ S_2^* &= \int [\{F_2^*, S_1^*\}]_{per}\, dt^{**} \\ &= O((\frac{m}{M+m_{Tri}})^2) \\ \ldots &= \ldots \end{aligned}$$

Here, an indefinite integral with t^{**} is replaced by

$$\begin{aligned} \int Q dt^{**} &= \int Q\frac{1}{(-\frac{\partial F_1^*}{\partial x_1^{**}})}dy_1^{**} \\ &= \int Q\frac{1}{n}dy_1^{**}. \end{aligned}$$

3.3 Secular perturbation

We have obtained a hamiltonian F^{**} which does not depend on any angular variables. We summarize again, it forms :

$$F^{**} = F_0^{**} + F_1^{**} + F_2^{**}$$

where,

$$\begin{aligned} F_0^{**} &= F_0^* \\ F_1^{**} &= F_1^* \\ F_2^{**} &= \frac{1}{4}\mu\frac{Mm_{Tri}}{(M+m_{Tri})^2}\frac{1}{\eta^3}\frac{a_{Tri}^2}{a^3}. \end{aligned}$$

This hamiltonian also satisfies canonical equations, i.e.:

$$\begin{aligned}\frac{dx^{**}}{dt} &= \frac{\partial F^{**}}{\partial y^{**}}(\equiv 0)\\ \frac{dy^{**}}{dt} &= -\frac{\partial F^{**}}{\partial x^{**}}\end{aligned}$$

From the first equation, we obtain

$$x^{**} = const.,$$

and from the second one,

$$y^{**} = (-\frac{\partial F^{**}}{\partial x^{**}})t + const..$$

If we calculate real values of $\frac{\partial F^{**}}{\partial x^{**}}$,

$$\begin{aligned}\frac{\partial F^{**}}{\partial x_1^{**}} &= -\frac{\mu^2}{x_1^3} - \frac{3}{4}\mu\frac{Mm_{Tri}}{(M+m_{Tri})^2}\frac{a_{Tri}^2}{na^5\eta^3}\\ &= -n - \frac{3}{4}\frac{n}{a^2}\frac{Mm_{Tri}}{(M+m_{Tri})^2}\frac{a_{Tri}^2}{\eta^3}\\ \frac{\partial F^{**}}{\partial x_2^{**}} &= n_{Tri} - \frac{3}{4}\mu\frac{Mm_{Tri}}{(M+m_{Tri})^2}\frac{a_{Tri}^2}{na^5\eta^4}\\ &= n_{Tri} - \frac{3}{4}\frac{n}{a^2}\frac{Mm_{Tri}}{(M+m_{Tri})^2}\frac{a_{Tri}^2}{\eta^4}\end{aligned}$$

and substitute values into them,

$$\begin{aligned}y_1^{**} &= (-\frac{\partial F^{**}}{\partial x_1^{**}})t + const.\\ y_2^{**} &= (-\frac{\partial F^{**}}{\partial x_2^{**}})t + const..\end{aligned}$$

In other words, action variables x^{**} be constants, and angular variables y^{**} increase (or decrease) linearly with time t. This means the action variables, or a semimajor axis a^{**} and an eccentricity e^{**}, does not have secular trends, while the angular variables, or a mean anomaly l^{**} and a longitude of perihelion ϖ^{**}, have secular trends linearly with time.

3.4 Mean elements

Orbital elements $a^{**}, e^{**}, l^{**}, \varpi^{**}$ deduced from x^{**} and y^{**} are mean orbital elements.

The real values of them are not obtained from dynamical theories, which only indicate the fact that these values are constants. We have to merge results of astrometrical positions to get real numerical values for Nereid.

But in this study, we do not identify these values.

3.5 Deriving osculating elements

Osculating elements E for canonical variables are summed up the following contributions:

- Mean elements E^{**}

- Contribution from long periodic perturbation δE^*
- Contribution from short periodic perturbation δE .

I.e., we firstly calculate

$$E^* = E^{**} + \delta E^*,$$

and after that, we evaluate

$$E = E^* + \delta E.$$

When we obtain a quantity of E^*, we have to evaluate δE^* with values of E^{**}. Similarly, a value E is calculated with E^* in the right hand side of the above equation.

From relationship on old and new variables of Hori's canonical perturbation method,

$$\begin{aligned}
\delta E^* &= \{E^*, S^*\} + \frac{1}{2}\{\{E^*, S^*\}, S^*\} + \dots \\
\delta E &= \{E, S\} + \frac{1}{2}\{\{E, S\}, S\} + \dots .
\end{aligned}$$

If we neglect $O((\frac{m}{M+m_{Tri}})^2)$ terms, all we have to do is taking Poisson bracket once, then,

$$\begin{aligned}
\delta E^* &= \{E^*, S^*\} \\
\delta E &= \{E, S\}.
\end{aligned}$$

These are equivalent the following operations.

$$\begin{aligned}
\delta x_i^* &= \{x_i^*, S^*\} \\
&= \frac{\partial S^*}{\partial y_i^*} \\
\delta y_i^* &= \{y_i^*, S^*\} \\
&= -\frac{\partial S^*}{\partial x_i^*} \\
\delta x_i &= \{x_i, S\} \\
&= \frac{\partial S}{\partial y_i} \\
\delta y_i &= \{y_i, S\} \\
&= -\frac{\partial S}{\partial x_i}
\end{aligned}$$

Deriving osculating elements expressed in orbital elements, we can use variational equations between orbital elements and canonical ones:

$$\begin{aligned}
\delta a &= \frac{2x_1}{\mu}\delta x_1 \\
\delta e &= -\frac{1}{e}\left[\frac{x_2}{(x_1)^2}\delta x_2 - \frac{(x_2)^2}{(x_1)^3}\delta x_1\right] \\
\delta l &= \delta y_1 \\
\delta \varpi &= \delta y_2.
\end{aligned}$$

The last equation is derived from $\delta \varpi = \delta y_2 + \delta k$ and k is not affected on Nereid's motion since $k \equiv n_{Tri}t + const.$ is supposed.

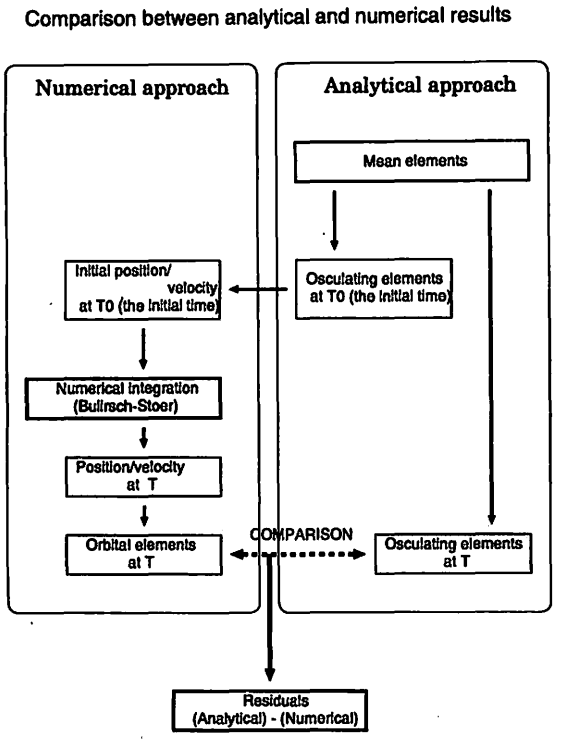

Figure 3: Flowchart for calculating residuals

Table 1: Mean elements for analytical calculation

Semimajor axis [Km]	5.5×10^6
Eccentricity	0.75
Angular variable y_1 [deg]	0.0
Angular variable y_2 [deg]	0.0
Longitude of Triton $\lambda_{Tri}[deg]$	0.0

4 Results and Discussions

4.1 General procedures and checking accuracy

Osculating elements calculated by an analytical theory are summations of many periodic terms (and some secular terms for angular variables) in final expressions. Any time is given, the theory provides osculating elements of the celestial body restrictly (except values deduced from integral constants). We calculate complicated arithmetics with the aid of MATHEMATICA ver.4.

We can assess our accuracy of analytical expression through comparing to numerical results, or calculating residuals in time sequence (See Figure 3). Numerical integration is performed by Bulirsch-Stoer ("extrapolation method") code in double-precision accuracy. This code provides high accuracy in results, suitable for our aim. We start integration with values which are converted the position and velocity into Cartesian coordinates from a set of analytical osculating elements at the initial time. Then, at a time

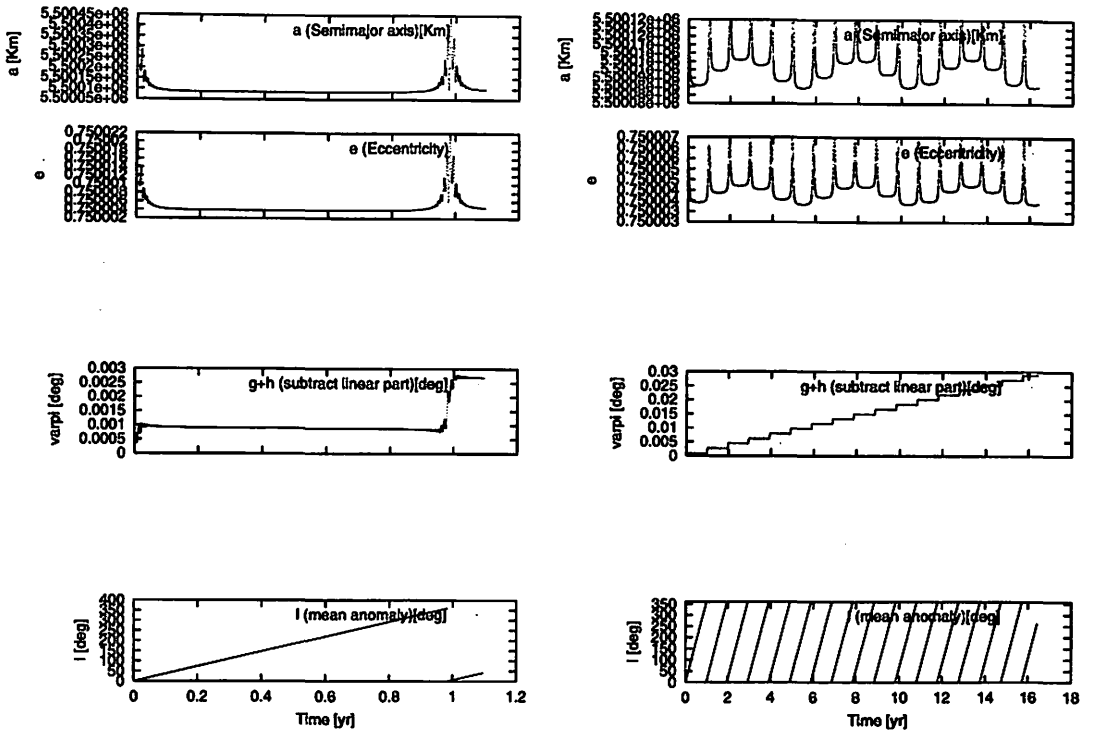

(a) (b)Trimmed for the vertical axis and zoomed up offsets

Figure 4: Numerical results (a)for one year (b)for 15 years (Note: for panel (b), the vertical axis is trimmed to easily find offsets in semimajor axis and eccentricity). The initial values for this calculation are used the mean elements instead of the initial osculating elements generated by an analytical theory. Secular trends of residuals in angular variables are subtracted.

T, residuals (analytical results minus numerically integrated ones) are calculated as:

$$\text{(Residuals)} = \text{(Analytical results)} - \text{(Numerical results)}.$$

When we calculate residuals in angular variables, y_1 and y_2, secular trends (the slopes of regression line for raw data) are subtracted, not to hide fine structures in residuals for output figures.

We set the values in Table 1 for the mean elements in analytical calculations. In here, $y_1 = l$ and $y_2 = \varpi - \lambda_{T\tau i}$.

4.2 Numerical Results

Figure 4 shows numerical results for one year and 15 years (Only these two panels are started calculation with initial conditions of mean elements, not osculating elements). In semimajor axis and eccentricity, they exhibit many rapid-changing variations with a period of six days, superposed on eminent bowl-shaped variations with a period of one-year. Amplitudes of the former variations grow larger with Nereid's approaching its pericenter.

It is noted that a bottom level of the latter variations are offset slightly to one of the next revolutional pereiods. This phenomenon is caused by the phase of Neptune-Triton system against its barycenter when

Table 2: Preliminary analytical models

Model Name	Hamiltonian expression (P_i of Legendre polynomials are considered)	Generating Function (S_i for short periodic terms are considered)	Direction of Triton's revolution
P2S2p	P_2	S_2	Prograde
P2S4p	P_2	S_2, S_3, S_4	Prograde
P3S2p	P_2, P_3	S_2	Prograde
P3S2r	P_2, P_3	S_2	Retrograde

Nereid passes through its pericenter. The pericentric distance of Nereid is $\sim 1.4 \times 10^6$ [Km] from the barycenter, which is only four times of the Triton's distance from the barycenter. In a planar problem, a configuration of close approach is occured, which often makes troubles in building accurate ephemerides.

4.3 Preliminary analytical results and residuals

We calculated residuals preliminarily, and they are shown in Figures 5 and 6. The analytical model we used are listed in Table 2.

Summarized speaking, there exist large discrepancies between analytical results and numerical ones. If we take up to smaller quantities (e.g. up to higher small parameter of generating functions or up to higher Legendre polynomials) into consideration in the analytical calculation, discrepancies become small, but unpleasantly, large residuals are still remained.

Comparing two models, whether Triton orbits in prograde or retrograde, we can see significant differences in residuals (see Figure 6). A retrograde model decreases its residuals drastically.

Afterhere, we use mainly progradely orbiting models. If we consider retrogradely orbiting ones, residuals are smaller than ones of prograde models.

4.4 Influence on residuals of truncation of Legendre polynomials

If we consider the problem perfectly, we have to deal with a full expression of the hamiltonian, i.e. infinite series of Legendre polynomials. However, we simplify the hamiltonian for convenience, which may cause discrepancies analytical results from numerical ones. To check the influence of truncation of Legendre polynomials,

(Full numerical results) − (Numerical results including up to P_i Legendre polynomials)

are calculated. The direction of Triton's revolution is prograde.

The full numerical calculation considers forces on Nereid from circular-orbiting Neptune and Triton, while a numerical calculation with truncated Legendre polynomials considers the model such that:

- a perturbing function is formulated into Cartesian coordinates. A P_2 potential is taking as an example:

$$F(P_2) = \mu \frac{M m_{Tri}}{(M + m_{Tri})^2} \frac{r_{Tri}^2}{r^3} \frac{1}{2} (3\cos^2 S - 1)$$

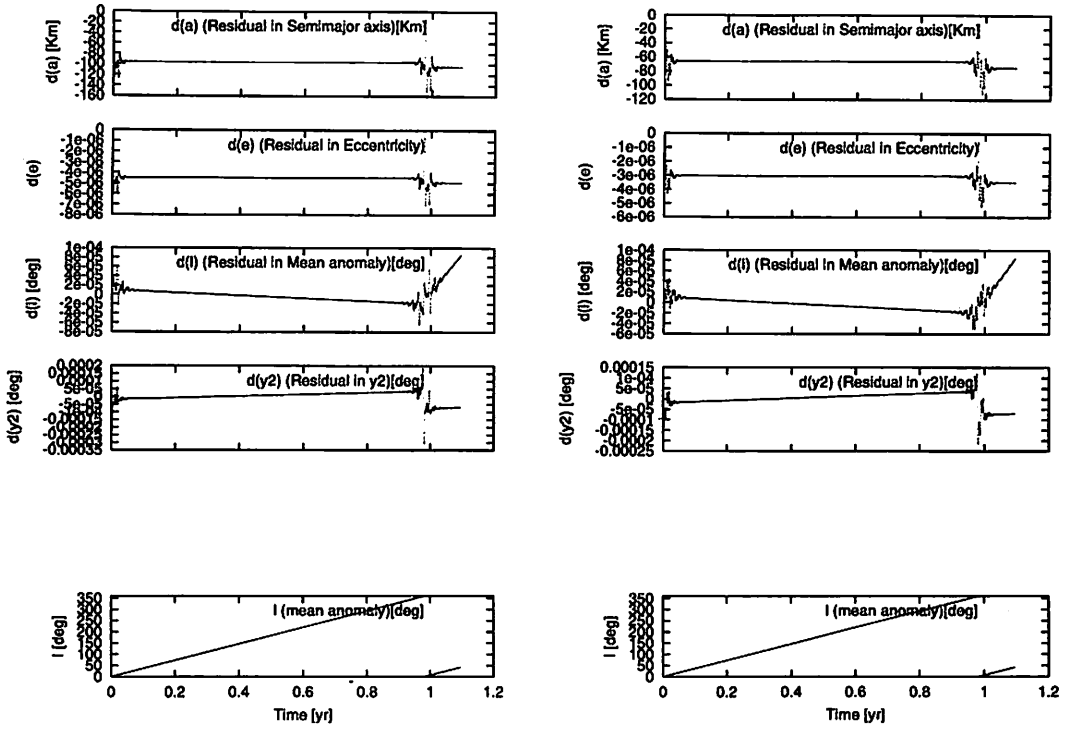

(a) (b)

Figure 5: Preliminary results. Residuals are shown for each model. (a)model P2S2p, (b)model P2S4p

$$= \frac{1}{2}\mu \frac{M m_{Tri}}{(M+m_{Tri})^2}\left[\frac{3}{r^5}(\boldsymbol{r}\cdot\boldsymbol{r}_{Tri})^2 - \frac{r_{Tri}^2}{r^3}\right],$$

where $(\mathrm{A}\cdot\mathrm{B})$ is an operation of inner product for A and B.

- acceleration is calculated through differentiating the potential.

These results are shown in Figure 7. If we expect to achieve accuracy of sub-Km in semimajor axis (in the case of Triton revoluting in prograde), we have to take terms up to P_5 in the hamiltonian into account.

4.5 Influence on residuals of truncation of generating functions

Next, we assess influence of truncational errors of short periodic generating functions S_i. The full expression of the short periodic generating function is

$$S = \sum_i^{\infty} S_i.$$

To check contribution from truncational effects, we introduce a hamiltonian, which includes only the P_n term of Legendre polynomial, for both numerical and analytical calculations. I.e.,

$$\left(\begin{array}{l}\text{Numerical results}\\ \text{including only } P_n\end{array}\right) - \left(\begin{array}{l}\text{Analytical results including only } P_n \text{ and}\\ \text{up to } S_i \text{ of generating functions for short periodic}\end{array}\right).$$

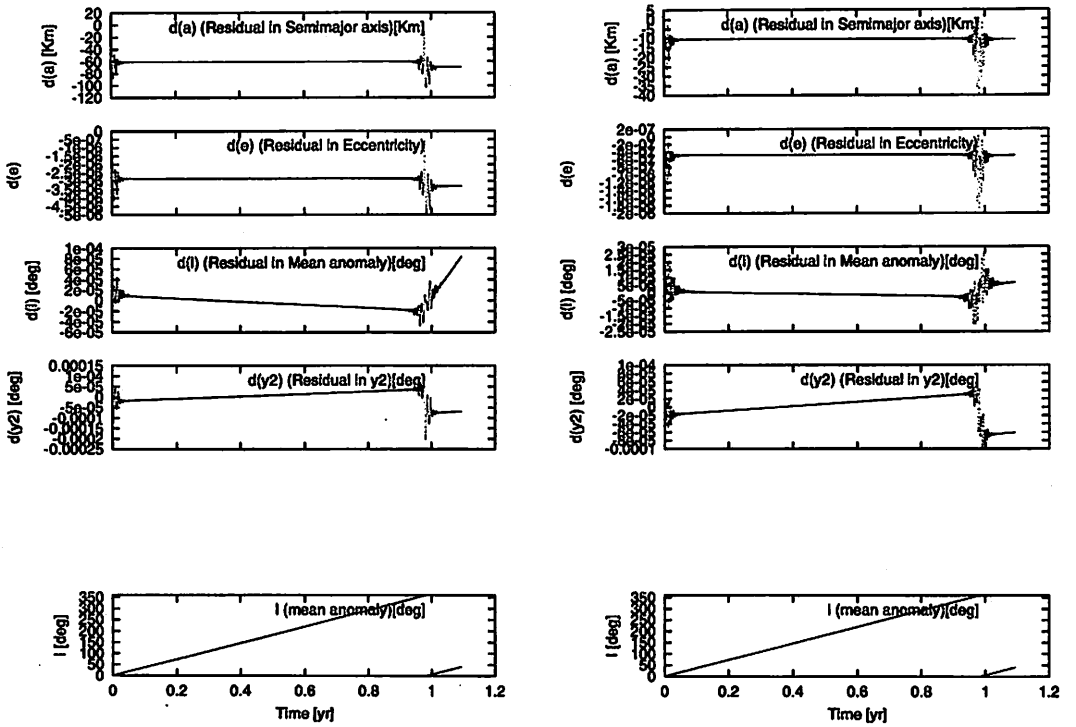

(a) (b)

Figure 6: Preliminary results (continued). Residuals are shown for each model. (a)model P3S2p, (b)model P3S2r

In this calculation, Triton revolves progradely.

Results are in Figures 8 and 9. In the case of P_2-limited problem, residuals are converged below sub-Km in semimajor axis when we take up to S_7 terms of a generating function into account. This means that it must be included up to higher orders of a small parameter, $\frac{n}{n_{Tri}}$, in calculations. This slow-converging property is reflected from a character of closely approaching problems. Since S_i is calculated as (neglecting $(\frac{m}{M+m_{Tri}})^2$):

$$\begin{aligned} S_i &= \int \{F_1, S_{i-1}\} dt^* \\ &= -\frac{n}{n_{Tri}} \int \frac{\partial S_{i-1}}{\partial y_1} dy_2, \end{aligned}$$

however $\frac{\partial S_{i-1}}{\partial y_1}$ are converted into

$$\frac{\partial S_{i-1}}{\partial y_1} = \frac{\partial f}{\partial y_1} \frac{\partial S_{i-1}}{\partial f},$$

a term

$$\begin{aligned} \frac{\partial f}{\partial y_1} &= \frac{(1+e\cos f)^2}{\eta^3} \\ &\sim 10.583 \text{(at the pericenter)} \end{aligned}$$

dilutes the converging factor of $\frac{n}{n_{Tri}} \sim \frac{1}{60}$ and prevents series of S_i from rapid convergence.

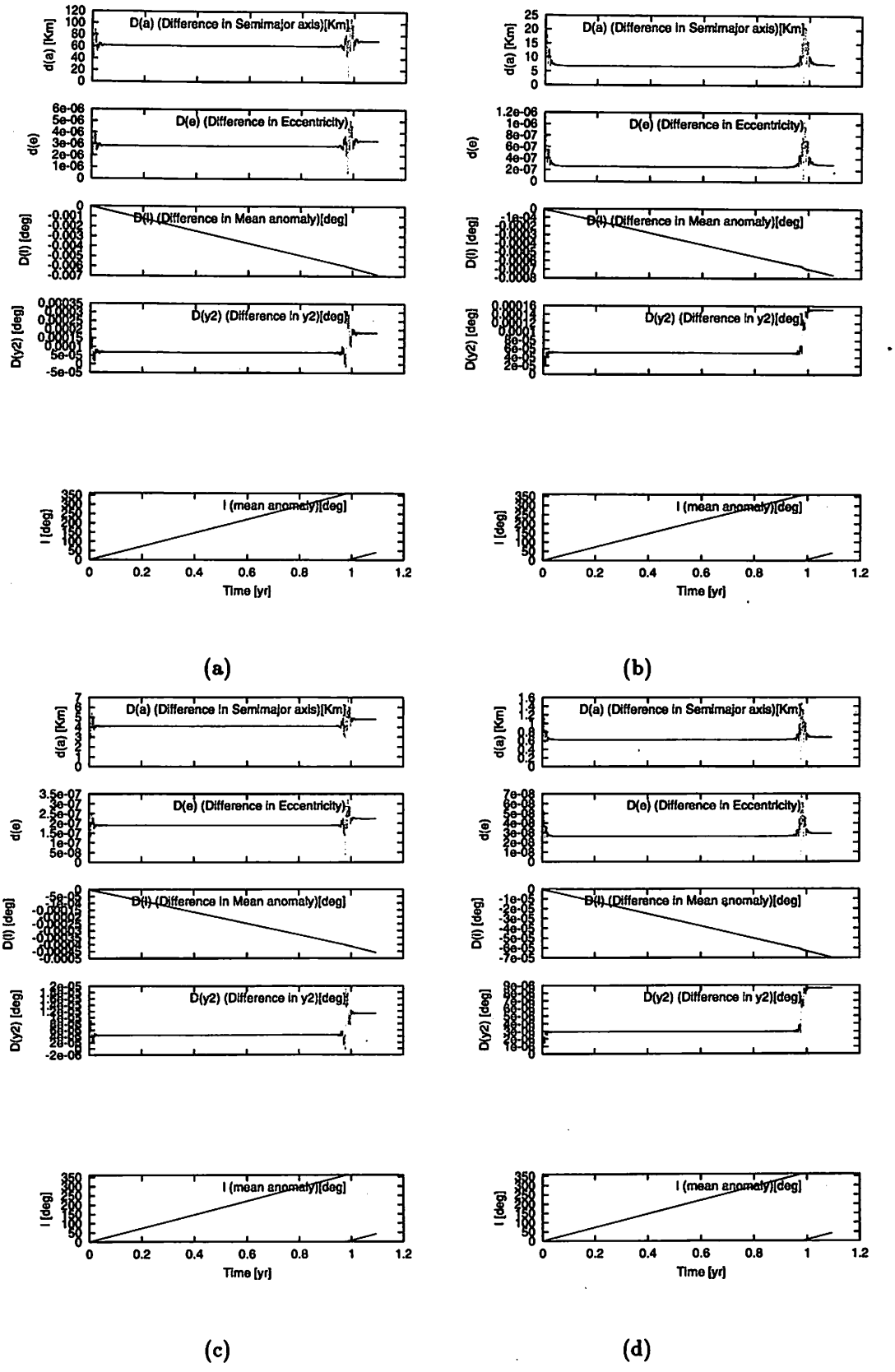

Figure 7: Residuals of full numerical results minus numerical results up to Legendre P_i terms in the hamiltonian. (a)up to P_2 term, (b)up to P_3 terms, (c)up to P_4 terms, (d)up to P_5 terms

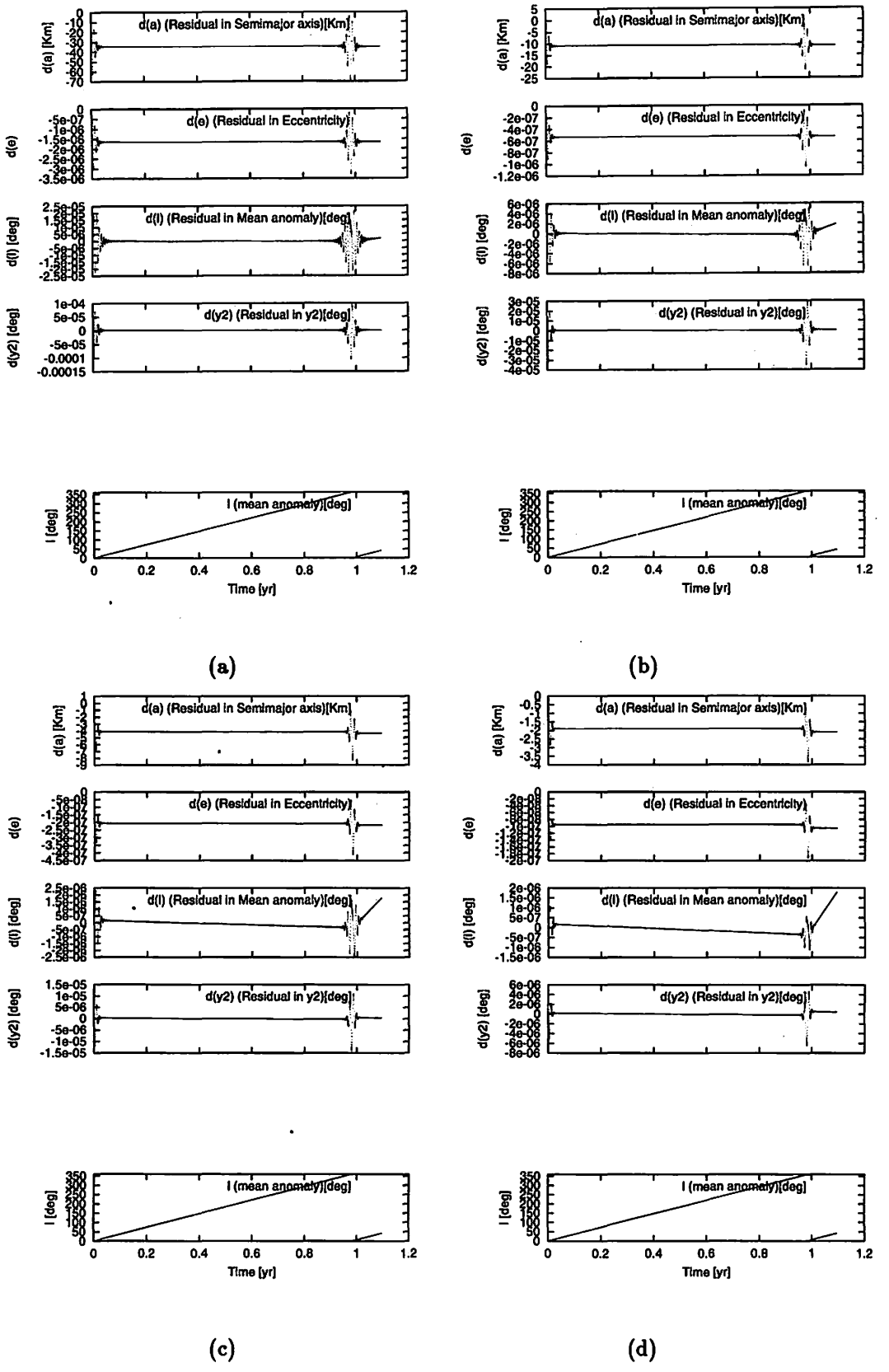

Figure 8: Residuals of numerical results minus truncated S_i results for a hamiltonian limited only Legendre P_2 contribution. Secular trends of residuals in angular variables are subtracted. (a)up to S_2 terms, (b)up to S_3 terms, (c)up to S_4 terms, (d)up to S_5 terms

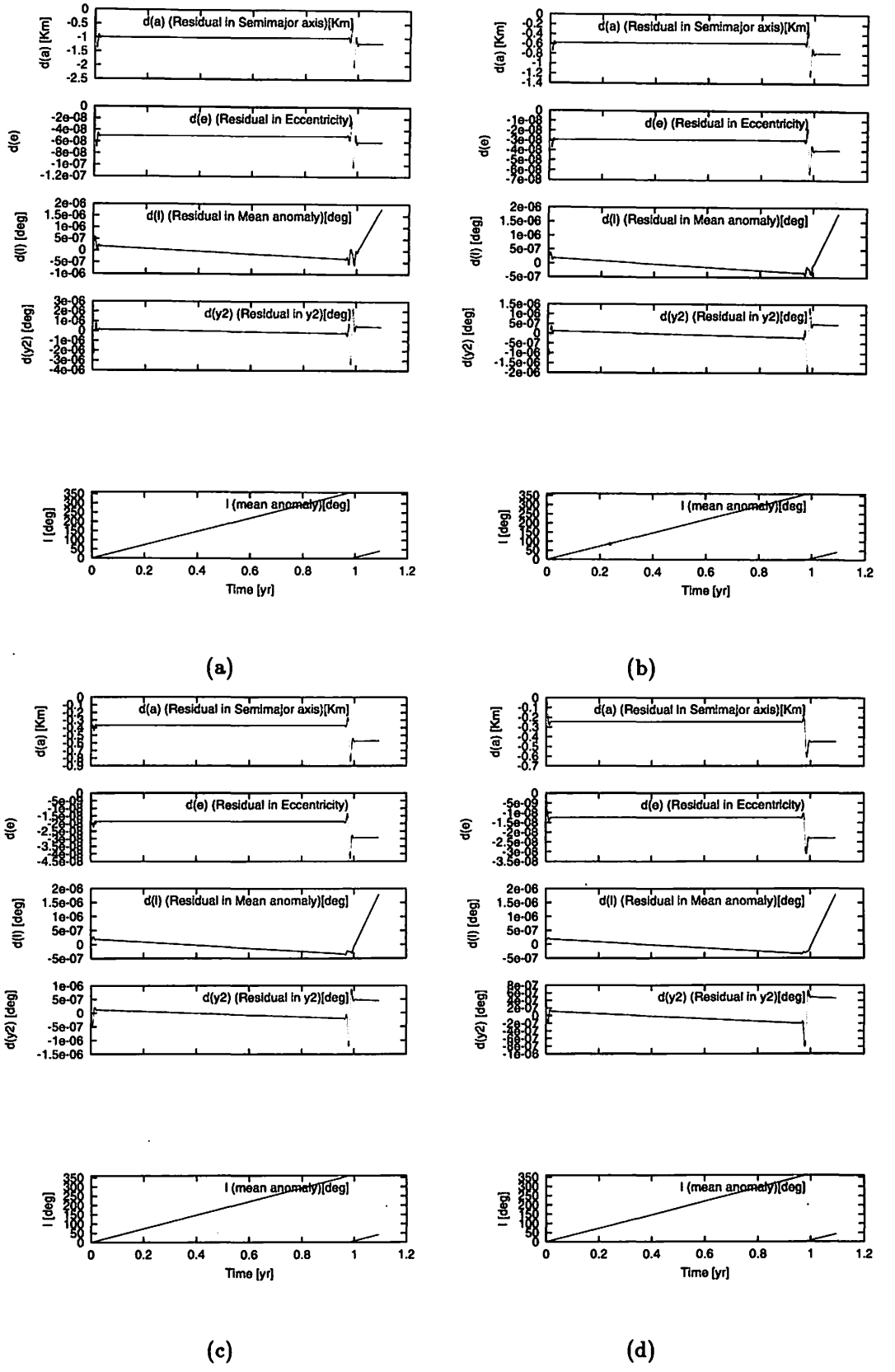

Figure 9: Residuals of numerical results minus truncated S_i results for a hamiltonian limited only Legendre P_2 contribution (continued). Secular trends of residuals in angular variables are subtracted. (a)up to S_6 terms, (b)up to S_7 terms, (c)up to S_8 terms, (d)up to S_9 terms

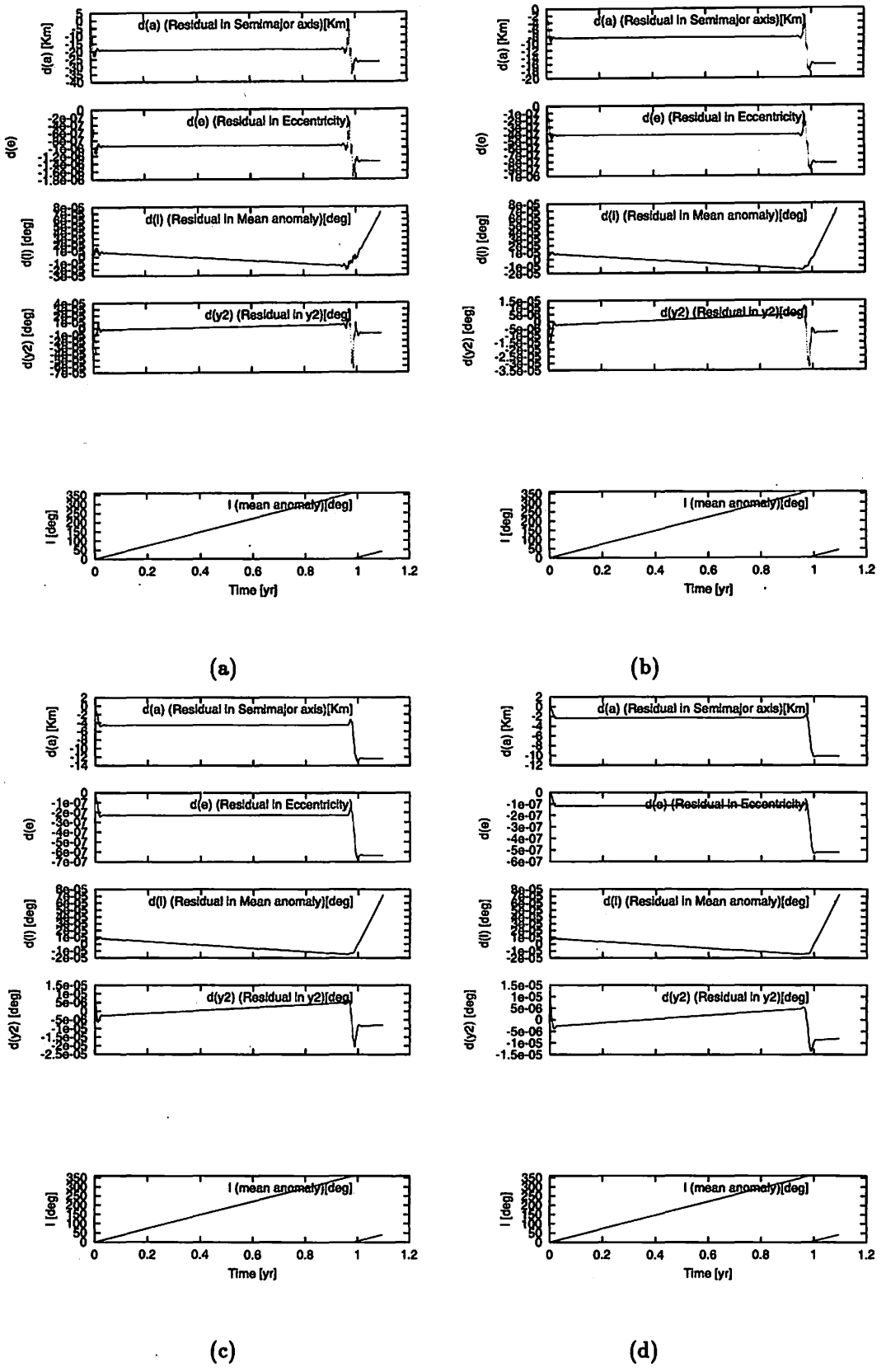

Figure 10: Residuals of numerical results minus truncated S_i results for a hamiltonian limited only Legendre P_3 contribution. Secular trends of residuals in angular variables are subtracted. (a)up to S_2 terms, (b)up to S_3 terms, (c)up to S_4 terms, (d)up to S_5 terms

Moreover, in the case of the P_3-limited problem, other phenomenon casts us troubles. It is shown in Figure 10. Eminent offsets in bottom level in semimajor axis or eccentricity are shown for each revolution of Nereid. These offsets are discussed in the section of Numerical results, caused by the longitude of Triton when Nereid passes through its pericenter. The offsets observed in the P_3-limited problem and the P_5-limited one are nearly comparable to the offset in numerical results, which means the offsets for each revolution of Nereid are mainly explained by contributions of P_3 and P_5 terms of Legendre polynomials in the hamiltonian.

If Triton orbits in retrograde, residuals are decreased.

In any case, eminent discrepancies between analytical and numerical results when Nereid approaches near its pericenter are observed, especially in low degrees of S_i. This phenomenon seems to be caused by (1)a slowly varying frequency with time near the pericenter, and (2)approximations in trigonometic functions of an offset function .

Near the point of close approaching Nereid with Neptune (or Triton), its synodic period between them is continuously varying, which means a time-variation profile of orbital elements cannot descript in a single frequency of trigonometric series. A compound expression of trigonometric functions with many frequencies is required.

In fact, shown in Figures, time-series profiles of residuals are more simple and smooth when we take higher S_is into account. They are shown in the Appendix, the number of trigonometric terms are increasing for higher S_is.

5 Conclusions

Analytical expressions of the planar Neptune-Triton-Nereid problem is required to consider higher Legendre polynomials P_i in the hamiltonian and with higher generating functions S_i in canonical transformations. In other words, it is a challenging problem for building analytical theory. The large eccentricity of Nereid and a close approaching with Triton prevent analytical expressions from simplicity.

There still remain problems to be accounted for: why residuals are improved when Triton orbits retrogradely; why larger offsets are observed when we deal a hamiltonian of odd-degree Legendre polynomials.

In this paper, we simplified the model as a planar restricted problem. In order to apply an analytical theory to the actual system of Nereid, we have to develop a new analytical theory for an inclined problem. When we discuss an inclined problem, a close-approach distance is larger than one for the planar problem, it will ease difficulties of building analytical theory.

6 References

Brouwer,D. and Clemence,G.M., 1961, Methods of Celestial Mechanics, Academic Press.

Deprit,A., 1968, Canonical Transformations Depending on a Small Parameter, *Cele.Mech.Dyn.Astron.*, **1**, 12.

Hori,G., 1966, Theory of General Perturbations with Unspecified Canonical Variables, *Publ.Astron.Soc.Japan*, **18**, 287.

Jacobson,R.A., 1990, The orbits of the satellites of Neptune, *Astron.Astrophys.*, **231**, 241.

Jacobson,R.A., 1991, Triton and Nereid astrographic observations from Voyager 2, *Astron.Astrophys.Suppl.Ser.*, **90**, 541.

Kinoshita,H. and Nakai,H., 1999, Analytical Solution of the Kozai Resonance and its Application, *Cele.Mech.Dyn.Astron.*, **75**, 125.

Mignard,F., 1975, Satellite à forte excentricité. Application à Néréide, *Astron.Astrophys*, **43**, 359.

Mignard,F., 1981, The Mean Elements of Nereid, *Astron.J.*, **86**, 1728.

Oberti,P., 1990, An accurate solution for Nereid's motion I. Analytical modeling, *Astron.Astrophys.*, **239**, 381.

Rose,L.E., 1974, Orbit of Nereid and the mass of Neptune, *Astron.J.*, **79**, 489.

Saad,A.S., 2000, The Theory of Motion and Ephemerides of the Second Neptunian Satellite Nereid, Ph.D. thesis, The Graduate University for Advanced Studies.

Segerman,A.M. and Richardson,D.L., 1997, An Analytical Theory for the Orbit of Nereid, *Cele.Mech.Dyn.Astron.*, **66**, 321.

van Biesbroeck, 1951, The Orbit of Nereid, Neptune's Second Satellite, *Astron.J.*, **56**, 110.

van Biesbroeck, 1957, The Mass of Neptune from a New Orbit of its Second Satellite Nereid, *Astron.J.*, **62**, 272.

Veillet,C., 1982, Orbital Elements of Nereid from New Observations, *Astron.Astrophys.*, **112**, 277.

7 Analytical expressions

We use the following descriptions in this paper.

M	Mass of Neptune
m_{Tri}	Mass of Triton
m	($\equiv 0$) Mass of Nereid
μ	$k^2(M+m_{Tri}+m) \equiv n^2a^3$
a	Semimajor axis of Nereid
a_{Tri}	Semimajor axis of Triton
n	Mean motion of Nereid
n_{Tri}	Mean motion of Triton
e	Eccentricity of Nereid
η	$\sqrt{1-e^2}$
f	True anomaly of Nereid
r	Radius of Nereid
ϖ	Longitude of pericenter of Nereid
λ_{Tri}	Longitude of Triton
y_2	$\varpi - \lambda_{Tri}$

$$C_2 \equiv \frac{Mm_{Tri}}{(M+m_{Tri})^2}$$
$$C_3 \equiv \frac{Mm_{Tri}(M^2-m_{Tri}^2)}{(M+m_{Tri})^4}$$

Afterhere, we neglect terms of $O((\frac{m}{M+m_{Tri}})^2)$.

7.1 Hamiltonians

Original hamiltonian

$$\begin{aligned} F &= n_{Tri}x_2 + \frac{\mu^2}{2x_1^2} \\ &\quad +\mu C_2 \frac{a_{Tri}^2}{a^3}(\frac{a}{r})^3 \frac{1}{4}[1 + 3\cos(2f + 2y_2)] \\ &\quad +\mu C_3 \frac{a_{Tri}^3}{a^4}(\frac{a}{r})^4 \frac{1}{8}[5\cos(3f + 3y_2) + 3\cos(f + y_2)] \\ &\quad +\ldots \end{aligned}$$

Hamiltonians F^* and F^{**}

$$\begin{aligned} F^* &= n_{Tri}x_2 + \frac{\mu^2}{2x_1^2} + \frac{1}{4}\mu C_2 \frac{a_{Tri}^2}{r^3} + \ldots \\ F^{**} &= n_{Tri}x_2 + \frac{\mu^2}{2x_1^2} + \frac{1}{4}\mu C_2 \frac{a_{Tri}^2}{a^3\eta^3} + \ldots \end{aligned}$$

7.2 P_2-limited generating functions

For short periodic terms

$$\begin{aligned} S_1 &= 0 \\ S_2 &= -\frac{3}{8}\mu C_2 \frac{1}{n_{Tri}} \frac{a_{Tri}^2}{r^3} \sin(2f + 2y_2) \\ S_3 &= -\frac{3}{32}\mu C_2 \frac{na}{\eta n_{Tri}^2} \frac{a_{Tri}^2}{r^4} \\ &\quad [-e\sin(f + 2y_2) \\ &\quad +4\sin(2f + 2y_2) \\ &\quad +5e\sin(3f + 2y_2)] \\ S_4 &= -\frac{3}{128}\mu C_2 \frac{(na)^2}{\eta^2 n_{Tri}^3} \frac{a_{Tri}^2}{r^5} \\ &\quad [+3e^2\sin(2y_2) \\ &\quad -10e\sin(f + 2y_2) \\ &\quad +(16 - 10e^2)\sin(2f + 2y_2) \\ &\quad +54e\sin(3f + 2y_2) \\ &\quad +35e^2\sin(4f + 2y_2)] \\ S_5 &= -\frac{3}{512}\mu C_2 \frac{(na)^3}{\eta^3 n_{Tri}^4} \frac{a_{Tri}^2}{r^6} \\ &\quad [+15e^3\sin(f - 2y_2) \\ &\quad +40e^2\sin(2y_2) \\ &\quad +(-68e + 45e^3)\sin(f + 2y_2) \\ &\quad +(64 - 208e^2)\sin(2f + 2y_2) \\ &\quad +(436e - 105e^3)\sin(3f + 2y_2) \\ &\quad +712e^2\sin(4f + 2y_2) \end{aligned}$$

$$+315e^3\sin(5f+2y_2)]$$

$$S_6 = -\frac{3}{2048}\mu C_2\frac{(na)^4}{\eta^4 n_{Tri}^5}\frac{a_{Tri}^2}{r^7}$$
$$[-105e^4\sin(2f-2y_2)$$
$$+210e^3\sin(f-2y_2)$$
$$+(340e^2-300e^4)\sin(2y_2)$$
$$+(-392e+1162e^3)\sin(f+2y_2)$$
$$+(256-2616e^2+630e^4)\sin(2f+2y_2)$$
$$+(3128e-3718e^3)\sin(3f+2y_2)$$
$$+(9620e^2-1260e^4)\sin(4f+2y_2)$$
$$+10270e^3\sin(5f+2y_2)$$
$$+3465e^4\sin(6f+2y_2)]$$

$$S_7 = -\frac{3}{8192}\mu C_2\frac{(na)^5}{\eta^5 n_{Tri}^6}\frac{a_{Tri}^2}{r^8}$$
$$[+945e^5\sin(3f-2y_2)$$
$$-1260e^4\sin(2f-2y_2)$$
$$+(1960e^3-2625e^5)\sin(f-2y_2)$$
$$+(2352e^2-8232e^4)\sin(2y_2)$$
$$+(-2064e+17784e^3-5250e^5)\sin(f+2y_2)$$
$$+(1024-26112e^2+26688e^4)\sin(2f+2y_2)$$
$$+(21072e-74712e^3+9450e^5)\sin(3f+2y_2)$$
$$+(108240e^2-67800e^4)\sin(4f+2y_2)$$
$$+(208520e^3-17325e^5)\sin(5f+2y_2)$$
$$+164820e^4\sin(6f+2y_2)$$
$$+45045e^5\sin(7f+2y_2)]$$

$$S_8 = -\frac{3}{32768}\mu C_2\frac{(na)^6}{\eta^6 n_{Tri}^7}\frac{a_{Tri}^2}{r^9}$$
$$[-10395e^6\sin(4f-2y_2)$$
$$+6930e^5\sin(3f-2y_2)$$
$$+(-12600e^4+28350e^6)\sin(2f-2y_2)$$
$$+(14896e^3-68166e^5)\sin(f-2y_2)$$
$$+(14448e^2-138208e^4+55125e^6)\sin(2y_2)$$
$$+(-10272e+211056e^3-236484e^5)\sin(f+2y_2)$$
$$+(4096-228384e^2+640368e^4-94500e^6)\sin(2f+2y_2)$$
$$+(136672e-1142352e^3+594780e^5)\sin(3f+2y_2)$$
$$+(1097712e^2-1989792e^4+155925e^6)\sin(4f+2y_2)$$
$$+(3384080e^3-1316490e^5)\sin(5f+2y_2)$$
$$+(4688600e^4-270270e^6)\sin(6f+2y_2)$$

$$
\begin{aligned}
&+2938110e^5\sin(7f+2y_2)\\
&+675675e^6\sin(8f+2y_2)]\\
S_9 \;=\; &-\frac{3}{131072}\mu C_2\frac{(na)^7}{\eta^7 n_{Tri}^8}\frac{a_{Tri}^2}{r^{10}}\\
&[+135135e^7\sin(5f-2y_2)\\
&+(97020e^5-363825e^7)\sin(3f-2y_2)\\
&+(-98560e^4+609840e^6)\sin(2f-2y_2)\\
&+(100240e^3-1195740e^5+694575e^7)\sin(f-2y_2)\\
&+(82176e^2-1807616e^4+2437200e^6)\sin(2y_2)\\
&+(-49216e+2150832e^3-6199416e^5+1157625e^7)\sin(f+2y_2)\\
&+(16384-1836288e^2+11526144e^4-6311520e^6)\sin(2f+2y_2)\\
&+(865088e-14854896e^3+20561688e^5-1819125e^7)\sin(3f+2y_2)\\
&+(10421760e^2-43162880e^4+13650720e^6)\sin(4f+2y_2)\\
&+(48111056e^3-53097996e^5+2837835e^7)\sin(5f+2y_2)\\
&+(103640320e^4-27550320e^6)\sin(6f+2y_2)\\
&+(111462540e^5-4729725e^7)\sin(7f+2y_2)\\
&+57820560e^6\sin(8f+2y_2)\\
&+11486475e^7\sin(9f+2y_2)]
\end{aligned}
$$

For long periodic terms

$$
\begin{aligned}
S_1^* &= \frac{1}{4}\mu C_2\frac{a_{Tri}^2}{a^3}\frac{1}{\eta^3 n}(f-y_1+e\sin f)\\
S_2^* &= O((\frac{m}{M+m_{Tri}})^2)
\end{aligned}
$$

7.3 P_3-limited generating functions

For short periodic terms

$$
\begin{aligned}
S_1 &= 0\\
S_2 &= -\frac{1}{24}\mu C_3\frac{1}{n_{Tri}}\frac{a_{Tri}^3}{r^4}\\
&\quad [+9\sin(f+y_2)\\
&\quad +5\sin(3f+3y_2)]\\
S_3 &= -\frac{1}{144}\mu C_3\frac{na}{\eta n_{Tri}^2}\frac{a_{Tri}^3}{r^5}\\
&\quad [-81e\sin(y_2)\\
&\quad +54\sin(f+y_2)\\
&\quad +135e\sin(2f+y_2)\\
&\quad -5e\sin(2f+3y_2)
\end{aligned}
$$

$$
\begin{aligned}
&+30\sin(3f+3y_2)\\
&+35e\sin(4f+3y_2)]
\end{aligned}
$$

$$
S_4 = -\frac{1}{864}\mu C_3\frac{(na)^2}{\eta^2 n_{Tri}^3}\frac{a_{Tri}^3}{r^6}
$$

$$
\begin{aligned}
&[-1215e^2\sin(f-y_2)\\
&-648e\sin(y_2)\\
&+(324-2430e^2)\sin(f+y_2)\\
&+2592e\sin(2f+y_2)\\
&+2835e^2\sin(3f+y_2)\\
&+15e^2\sin(f+3y_2)\\
&-80e\sin(2f+3y_2)\\
&+(180-70e^2)\sin(3f+3y_2)\\
&+520e\sin(4f+3y_2)\\
&+315e^2\sin(5f+3y_2)]
\end{aligned}
$$

$$
S_5 = -\frac{1}{5184}\mu C_3\frac{(na)^3}{\eta^3 n_{Tri}^4}\frac{a_{Tri}^3}{r^7}
$$

$$
\begin{aligned}
&[+25515e^3\sin(2f-y_2)\\
&-4374e^2\sin(f-y_2)\\
&+(-4860e+54675e^3)\sin(y_2)\\
&+(1944-57348e^2)\sin(f+y_2)\\
&+(37908e-76545e^3)\sin(2f+y_2)\\
&+113238e^2\sin(3f+y_2)\\
&+76545e^3\sin(4f+y_2)\\
&-75e^3\sin(3y_2)\\
&+350e^2\sin(f+3y_2)\\
&+(-860e+315e^3)\sin(2f+3y_2)\\
&+(1080-2100e^2)\sin(3f+3y_2)\\
&+(5780e-945e^3)\sin(4f+3y_2)\\
&+8350e^2\sin(5f+3y_2)\\
&+3465e^3\sin(6f+3y_2)]
\end{aligned}
$$

$$
S_6 = -\frac{1}{31104}\mu C_3\frac{(na)^4}{\eta^4 n_{Tri}^5}\frac{a_{Tri}^3}{r^8}
$$

$$
\begin{aligned}
&[-688905e^4\sin(3f-y_2)\\
&-201204e^3\sin(2f-y_2)\\
&+(-75816e^2+1530900e^4)\sin(f-y_2)\\
&+(-34992e+1110996e^3)\sin(y_2)\\
&+(11664-1014768e^2+2296350e^4)\sin(f+y_2)\\
&+(501552e-3653748e^3)\sin(2f+y_2)
\end{aligned}
$$

$$
\begin{aligned}
&+(3061800e^2 - 2755620e^4)\sin(3f + y_2) \\
&+5234220e^3 \sin(4f + y_2) \\
&+2525985e^4 \sin(5f + y_2) \\
&-525e^4 \sin(f - 3y_2) \\
&-2100e^3 \sin(3y_2) \\
&+(5000e^2 - 2100e^4)\sin(f + 3y_2) \\
&+(-7760e + 12460e^3)\sin(2f + 3y_2) \\
&+(6480 - 37680e^2 + 5670e^4)\sin(3f + 3y_2) \\
&+(57040e - 45260e^3)\sin(4f + 3y_2) \\
&+(147080e^2 - 13860e^4)\sin(5f + 3y_2) \\
&+141780e^3 \sin(6f + 3y_2) \\
&+45045e^4 \sin(7f + 3y_2)
\end{aligned}
$$

$$
\begin{aligned}
S_7 \;=\; & -\frac{1}{186624}\mu C_3 \frac{(na)^5}{\eta^5 n_{Tri}^6}\frac{a_{Tri}^3}{r^9} \\
&[+22733865e^5 \sin(4f - y_2) \\
&+18436410e^4 \sin(3f - y_2) \\
&+(4461480e^3 - 51667875e^5)\sin(2f - y_2) \\
&+(-384912e^2 + 13856832e^4)\sin(f - y_2) \\
&+(-244944e + 22902264e^3 - 80372250e^5)\sin(y_2) \\
&+(69984 - 15956352e^2 + 106209468e^4)\sin(f + y_2) \\
&+(6333552e - 117170712e^3 + 103335750e^5)\sin(2f + y_2) \\
&+(70158960e^2 - 222024240e^4)\sin(3f + y_2) \\
&+(226660680e^3 - 113669325e^5)\sin(4f + y_2) \\
&+264211470e^4 \sin(5f + y_2) \\
&+98513415e^5 \sin(6f + y_2) \\
&+4725e^5 \sin(2f - 3y_2) \\
&-15750e^4 \sin(f - 3y_2) \\
&+(-35000e^3 + 18375e^5)\sin(3y_2) \\
&+(56560e^2 - 95760e^4)\sin(f + 3y_2) \\
&+(-63440e + 283240e^3 - 47250e^5)\sin(2f + 3y_2) \\
&+(38880 - 531840e^2 + 339660e^4)\sin(3f + 3y_2) \\
&+(527600e - 1217800e^3 + 103950e^5)\sin(4f + 3y_2) \\
&+(2155280e^2 - 965280e^4)\sin(5f + 3y_2) \\
&+(3613400e^3 - 225225e^5)\sin(6f + 3y_2) \\
&+2615550e^4 \sin(7f + 3y_2) \\
&+675675e^5 \sin(8f + 3y_2)]
\end{aligned}
$$

$$
\begin{aligned}
S_8 \;=\; & -\frac{1}{1119744}\mu C_3 \frac{(na)^6}{\eta^6 n_{Tri}^7}\frac{a_{Tri}^3}{r^{10}} \\
& [-886620735e^6\sin(5f-y_2) \\
& -1209323520e^5\sin(4f-y_2) \\
& +(-479084220e^4+2046047850e^6)\sin(3f-y_2) \\
& +(-41990400e^3+536164920e^5)\sin(2f-y_2) \\
& +(-4304016e^2+628911216e^4-3255076125e^6)\sin(f-y_2) \\
& +(-1679616e+392190336e^3-2881591200e^5)\sin(y_2) \\
& +(419904-235356192e^2+3716202888e^4-4340101500e^6)\sin(f+y_2) \\
& +(78102144e-3147600384e^3+8422749360e^5)\sin(2f+y_2) \\
& +(1471868496e^2-11262980016e^4+5115119625e^6)\sin(3f+y_2) \\
& +(7965578880e^3-13891474080e^5)\sin(4f+y_2) \\
& +(16766110620e^4-5319724410e^6)\sin(5f+y_2) \\
& +14643364680e^5\sin(6f+y_2) \\
& +4433103675e^6\sin(7f+y_2) \\
& -51975e^6\sin(3f-3y_2) \\
& +138600e^5\sin(2f-3y_2) \\
& +(-283500e^4+198450e^6)\sin(f-3y_2) \\
& +(-452480e^3+892080e^5)\sin(3y_2) \\
& +(557200e^2-2489200e^4+496125e^6)\sin(f+3y_2) \\
& +(-487040e+4889600e^3-3184560e^5)\sin(2f+3y_2) \\
& +(233280-6526880e^2+11242600e^4-1039500e^6)\sin(3f+3y_2) \\
& +(4687360e-24745600e^3+8768640e^5)\sin(4f+3y_2) \\
& +(28411600e^2-36324400e^4+2027025e^6)\sin(5f+3y_2) \\
& +(73534720e^3-21447720e^5)\sin(6f+3y_2) \\
& +(90818700e^4-4054050e^6)\sin(7f+3y_2) \\
& +52659600e^5\sin(8f+3y_2) \\
& +11486475e^6\sin(9f+3y_2)]
\end{aligned}
$$

For long periodic terms

$$S^* = 0$$

Extension of Cassini's Laws

Sébastien Bouquillon
National Astronomical Observatory
Tokyo to Mitaka shi Osawa 3-5-2
JAPAN

Abstract. We have found a new type of Cassini's laws which describe the rotational motion in a 1:1 spin-orbit resonance. In the rotational motion which follows the conventional Cassini's laws, the figure axis coincides with the angular momentum axis. In the rotational motion described by the new type of Cassini's laws, the angle between the figure axis and the angular momentum axis is constant, which is not zero, and the precession of the angular momentum plane is equal to the mean motion of the argument of pericenter of the rotating body. The new type of a rotaional motion is only possible when the orbital eccentricty of the rotationg body is not zero.

1 Introduction

In this note, we show easy analytical relations which define the stationary points of the rotational Hamiltonian of rigid bodies and determine which ones correspond to the real motion of the Moon.

The starting point of this study is naturally the Cassini's Laws (1693) which describes the rotational motion of the Moon. The laws could be written like that:

- The Moon rotates in the counterclockwise with an uniform motion around an axis fixed with respect to her surface; the period of rotation is the same as the sideral revolution period of the Moon around the Earth.

- The angle between the rotation axis and the ecliptic pole is constant which is about $1^o35'$.

- The ecliptic pole, the axis normal to the Moon orbit and her rotation axis are always in a same plane.

Several works have been carried out to generalize these laws to others celestial bodies. The first law could be seen as a minimum of a simplified Hamiltonian of the rotation of celestial body which is reached by the tidal effects (see Goldreich and Peale (1966)). The second and third laws could be seen as the maximum of rotational Hamiltonian when the first law is assumed to be satisfied and the obliquity is not zero (see Colombo (1966)).

But all these works take place in a special case when the angle between the angular momentum and the axis of figure is zero ($J = 0$). that is to say, that these works assume that the sentence of Cassini "The Moon rotate... around an axis fixed with respect to her surface..." is true. In this note, we don't assume this and so we could define two new laws for the libration center of the Moon. These laws are :

- The angular momentum does not concide with the figure axis. The period of the complet rotation of the angular momentum around the axis of figure is equal to the period of ω, the perigee of the earth (measured from the ascending node of the orbital plane of the Earth with respect of ecliptic plane). That is to say a period of 6.00 years.

- The angle between the angular momentum and the axis is constant. This angle is $J \simeq 100$"arc seconds for the Moon.

In the section 2 we definie the variables used in this paper and we give the general form of the rotational Hamiltonian of rigid body with use of these variables. In the section 3 we present our theoretical study to obtained the analytical relations corresponding to the two new laws described just before: the method consists in the determination of stationary points of Hamiltonian of rotation. One of these points correspond to this extension of the Cassini's laws; we will call it the "Cassini's states". In the section 4 we determine the "observed" libration center of the Moon with the help the Moons solution (1981) adjusted to the Lunar Laser data. The differences between the results of this section and section 3 are discussed.

2 Andoyer's variables and Hamiltonian

We limit our study to two celestial bodies. A body S (the Moon) which is a satellite of a body P (the Earth). We study the rotation of the body S taking into account of the perturbation of body P. We use the Andoyer's variables to determine the relative position of the systeme $R_S = \{O, \vec{Ox}, \vec{Oy}, \vec{Oz}\}$ (link to S) from a reference systeme $R_P = \{O, O\vec{D}', \vec{N} \times O\vec{D}', \vec{N}\}$ (link to the orbital plane of P). R_S is formed by the principal axis of inertia of S in increase order. Principal moments of inertia are $A < B < C$. Variables of Andoyer are defined like that:

• h is the longitude of the ascending node Γ of the plane perpendicular to the angular momentum with respect to the orbital plane of P. The origine of the longitude is the point D' defined in the following.

• g is the angle between Γ and the ascending node Γ' of the equatorial plane with respect to the plane perpendicular to the angular momentum.

• l is the angle between Γ' and the axis of minimum moment of inertia A.

• H is the component of the angular momentum along the vector $\vec{N}$ normal to the orbital plane of P.

• G is the norm of total angular momentum of S.

• L is the component of the angular momentum along the vector $\vec{Oz}$ (axis of figure).

H, G and L are the respectif canonical conjugated momentum of h, g and l. We can write $H = G\cos I$ and $L = G\cos J$ where I is the obliquity of S and J is the angle between the angular momentum and the axis of figure.

Remark : The Obliquity I is different from the common obliquity which is usually measured with respect to the ecliptic plane (like one used by Colombo (1966)).For example, if we write down I_C as this usual obliquity, the Moon's obliquities have the relation : $I = I_C + i \simeq 6.7^o$.

To describe the orbital motion of P in an inertial system $R_I = \left\{O, \vec{OX}, \vec{OY}, \vec{OZ}\right\}$, we use the following variables:

- Ω is the longitude of the ascending node N of the orbital plane with respect to the plane $(\vec{OX}, \vec{OY})$ of reference system R_I. The origine of Ω is the point D. The point D' is defined as it is on the orbital plane of P and as it is $\bar{D'N} = \bar{DN}$.

- ω is the angle along the orbital plane between N and the perigee of P.

- M is the mean anomaly of P.

We consider that these angles are linear with respect to time : $M = n * t$; $\omega = \dot{\omega} * t + \omega_0$; $\Omega = \dot{\Omega} * t + \Omega_0$ where n is the mean motion of P. In order that Hamiltonian does not depend on time explicitly, we need to add to our Hamiltonian K the terms : $+n\Lambda_M + \dot{\omega}\Lambda_\omega + \dot{\Omega}\Lambda_\Omega$ where Λ_M, Λ_ω and Λ_Ω are respectively the conjugate momentum of M, ω and Ω.

e is the eccentricity of the orbit of P, i is the inclination of the orbit of P with respect to the plane $(\vec{OX}, \vec{OY})$ and $\lambda = \Omega + \omega + M$ is the mean longitude of P.(We regard e and i as constant of time.)

The geometrical meaning of these variables are summarised in the figures 1.

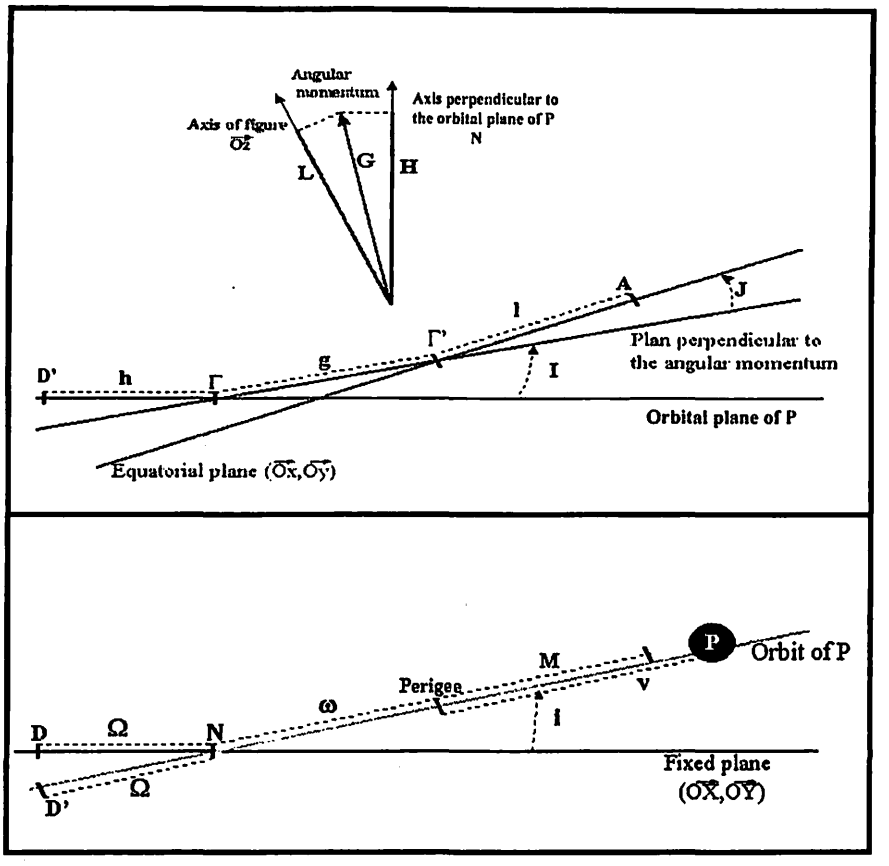

Figure 1: Andoyer's variables of S and orbital variables of P

The Hamiltonians of this paper are obtained from the complet Hamiltonian K of a rotating rigid body (Kinoshita, 1977). The general form of K could be written like that:

$$K = F + E + U_P + n\Lambda_M + \dot{\omega}\Lambda_\omega + \dot{\Omega}\Lambda_\Omega \tag{1}$$

where

$$\begin{aligned}
F &= \frac{G^2}{C}\left[\gamma_1 + \gamma_2 \cos^2 J + \gamma_3 \sin^2 J \cos(2l)\right] \\
E &= G \sin I \dot{\Omega} \sin i \cos(h - \Omega) + G \cos I (1 - \cos i)\dot{\Omega} \\
U_P &= U_1 + U_2 \\
U_1 &= \frac{\kappa^2 M_P}{r^3}\left[\frac{2C - A - B}{2} P_2(\sin\delta_p) + \frac{A - B}{4} P_2^2(\sin\delta_p)\cos(2\alpha_p)\right] \\
U_2 &= \sum_{\eta \geq 3} \frac{\kappa^2 M_P M_S R^\eta}{r^{\eta+1}}\left[J_\eta P_\eta(\sin\delta_p) - \sum_{m \leq \eta} P_\eta^m(\sin\delta_p)\left(C_{\eta,m}\cos(m\alpha_p) + S_{\eta,m}\sin(m\alpha_p)\right)\right]
\end{aligned}$$

F is the Hamiltonian for a free motion. In the expression of F, γ_1, γ_2 and γ_3 are three parameters only depended on the principal moment of inertia $A \leq B \leq C$ of body S ($\gamma_1 = 1/4(C/A + C/B)$, $\gamma_2 = 1/2 - \gamma_1$ and $\gamma_3 = 1/4(C/B - C/A)$).

U_P is the disturbing potential due to the disruptive body P represented by its expansion in spherical harmonics. κ^2 is the gravitational constant, M_P and M_S are respectively the mass of P and S, R is the mean equatorial radius of S, r is the distance between the barycenter of S and the barycenter of P, α_p and δ_p are longitude and latitude of the disturbing body P in the frame whose origin is the barycenter of S and axis the principal axis of S, and J_η, $C_{\eta,m}$ and $S_{\eta,m}$ are the coefficients of the potential of S. This part of the Hamiltonian K can be express with Andoyer's variables with the help of modified Jacobi polynomials (we limit our study to the effect of order 3 of this expansion : the modified Jacobi polynomials until the order 3 could be found in Kinoshita 1977).

E is a complementary term due to the fact that our reference plane is the orbital plane of the body P which is precessing and is not an inertial plane.

3 New type of Cassini's state

In this section we determinate the stationary point of the rotational Hamiltonian K of rigid body S. So we solve the following canonical equations:

$$\begin{aligned}
\dot{l}_i &= \frac{\partial K}{\partial L_i} = 0 \\
\dot{L}_i &= -\frac{\partial K}{\partial l_i} = 0
\end{aligned}$$

where (l_i, L_i) (with $i = [1, 2, 3]$) are linear combinations of the Andoyer's variables and orbit variables. One of these stationary points corresponds to the real libration center of the body (see Colombo 1966). We will call this the Cassini's state.

* * *

In this section, the angular momentum of the Moon and the axis of figure of the Moon are different($J \neq 0$) (see figure 2). But we suppose that the Moon is in a double resonance: the first one corresponds to the 1/1 spin-orbit resonance ($h + g + l - \lambda = 0$) and the second one is that the precession of the orbital plane is equal to that of the plane perpendicular to the angular momentum ($h - \Omega = 180^o$).This double resonance correspond to the conventional Cassini's Laws.

To have these resonances the norm of angular momentum G and the obliquity I must verified conditions determined by Colombo (1966) or peale (1969). All the conditions that the rotation variables of the Moon have to satisfied, have been summing up in following C_2:

$$(C_2) \qquad \left\{ \begin{array}{rcll} \theta_\lambda & = & h+g+l-\lambda = 0 & \\ G & = & \dot{\lambda} & \\ \theta_\Omega & = & h-\Omega+180^o = 0 & \\ \dfrac{\dot{\Omega}}{\dot{\lambda}} & = & \dfrac{3}{2}\dfrac{\sin(I)}{\sin(I-i)}\left[\beta' - \cos I(\alpha'-\beta')\right] & i.e. \qquad I = 6^o.6746 \end{array} \right\}$$

$$with \qquad \beta' = \frac{\beta}{C(\dot{\lambda}^2)} = -\left(\frac{1}{1+\mu}\right) f_2(e)\frac{A-B}{4C} \qquad \alpha' = \frac{\alpha}{C(\dot{\lambda}^2)}\left(\frac{1}{1+\mu}\right) f_1(e)\frac{2C-A-B}{2C}$$

And where μ is M_S divide by M_P, the function f_1 is equal to $1/\left(1-e^2\right)^{3/2}$ and the function f_2 is equal to $\left(1-\frac{5}{2}e^2+\frac{13}{16}e^4-\frac{35}{288}e^6+O(e^8)\right)$.

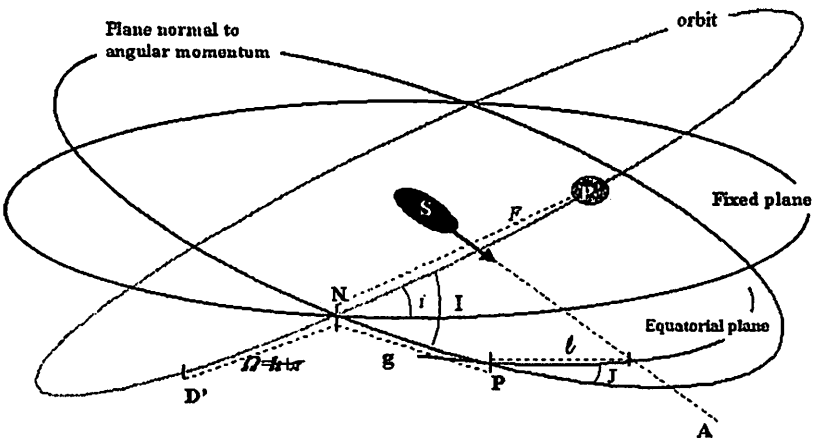

Figure 2: Variables in the Case where J is different of zero.

We make the following canonical transformation where the Andoyer's variable l is transformed into $\theta_\omega = l - \omega$.

$$\left\{ \begin{array}{cc} h & H \\ g & G \\ l & L \\ & \\ \Omega & \Lambda_\Omega \\ \omega & \Lambda_\omega \\ M & \Lambda_M \end{array} \right\} \dashrightarrow \left\{ \begin{array}{cc} X_1 = \theta_\Omega & Y_1 = H - G \\ X_2 = \theta_\lambda & Y_2 = G \\ X_3 = \theta_\omega & Y_3 = L - G \\ & \\ \Omega & \Lambda^*_\Omega = \Lambda_\Omega + H \\ \omega & \Lambda^*_\omega = \Lambda_\omega + L \\ M & \Lambda^*_M = \Lambda_M + G \end{array} \right\} \qquad (2)$$

In the following we will forget the asterisk on these variables. We obtain the averaged disturbing potential (named U_l) by integrating by M the expression (1). So U_l is written like that:

$$
\begin{aligned}
U_l \;=\; & \alpha\left[-\frac{1}{32}\,(1+3\cos 2J)\,(1+3\cos 2I)-\frac{3}{4}\sin^2 J\cos^4\left(\frac{I}{2}\right)\cos 2(\theta_\lambda-\theta_\omega-\omega)\right.\\
& \left.-\frac{3}{4}e\sin 2J\cos^3\left(\frac{I}{2}\right)\sin\left(\frac{I}{2}\right)\cos\left(\theta_\lambda+\theta_\Omega-\theta_\omega-2\omega\right)-\frac{9}{16}e\sin 2J\sin 2I\cos\left(\theta_\lambda-\theta_\Omega-\theta_\omega\right)\right]\\
+\; & \beta\left[3\cos^4\frac{J}{2}\cos^4\left(\frac{I}{2}\right)\cos 2\theta_\lambda+\frac{3}{8}\sin^2 J\,(1+3\cos 2I)\cos 2(\theta_\omega+\omega)\right.\\
& +3\sin^4\frac{J}{2}\cos^4\left(\frac{I}{2}\right)\cos 2(\theta_\lambda-2(\theta_\omega+\omega))\\
& -\frac{3}{2}e\cos^3\frac{J}{2}\sin\frac{J}{2}\sin I\left[6\cos I\cos\left(\theta_\lambda-\theta_\Omega+\theta_\omega+2\omega\right)+(1+\cos I)\cos\left(\theta_\lambda+\theta_\Omega+\theta_\omega\right)\right]\\
& \left.+\frac{3}{2}e\cos\frac{J}{2}\sin^3\frac{J}{2}\sin I\left[6\cos I\cos\left(\theta_\lambda-\theta_\Omega-3\theta_\omega-2\omega\right)+(1+\cos I)\cos\left(\theta_\lambda+\theta_\Omega-3\theta_\omega-4\omega\right)\right]\right]
\end{aligned}
\tag{3}
$$

To obtain the Hamiltonian total we have to add to U_L the kinetic energy corresponding to the free motion and the other terms determined in the before sections (see relation (1)).

$$
\begin{aligned}
K_l \;=\; & U_l+\frac{G^2}{C}\left[\gamma_1+\gamma_2\cos^2 J+\gamma_3\sin^2 J\cos 2\left(\theta_\omega+\omega\right)\right]+E\\
& +n\left(\Lambda_M-G\right)+\dot{\omega}\left(\Lambda_\omega-G\cos J\right)+\dot{\Omega}\left(\Lambda_\Omega-G\cos I\right)
\end{aligned}
\tag{4}
$$

We now assume that the celestial body S is exactly at the double resonance described by the condition (C_2). So we put $\theta_\lambda = 0$ and $\theta_\Omega = 0$ in the relation (4).

In this case, the Hamiltonian K_l depends of two angles θ_ω and ω.

When there is no disturbing perturbation ($U_l = 0$), the Hamiltonian K_l depends only on one angle ($\theta_\omega + \omega = l$). This Hamiltonian corresponds to the free rotation of S.

An other particular case is when there is a gravitational perturbation by a body P whose eccentricity is zero. In this case, Hamiltonian K_l depends also on only one angle : Andoyer's variable l.

We draw the section map of this Hamiltonian in the Moon's case to find the Cassini's state when J is different from zero (see graphs 3). To obtain these graphs we integrate numerically the canonical equations $\dot{Y}_3 = -\partial K_l/\partial X_3$ and $\dot{X}_3 = \partial K_l/\partial Y_3$ when θ_Ω and θ_λ are equal to zero. We plot a point in the plane ($\theta_\omega \times J$) each time that ω increased of 2π radians.

The upper figure is the section map of these equations in the case of the free rotation (no perturbation by an external body). We know in this case that it is an integrable system and so the section map is equivalent to the phase space ($l \times J$) drawn by Deprit (1967), with two distincts areas: one is a rotation area whom corresponds to a rotation of the angular momentum of S around the axis of figure of S and the other one is a libration area which corresponds to a rotation of the angular momentum of S around the axis of minimum moment of inertia OA of S (the axis of intermediar moment of inertia is an unstable position for the angular momentum). The minimum of this Hamiltonian in the case of the free motion is for $J = 0$: the angular momentum and the axis of figure are a same axis. The maximum: the case where the angular momentum and the axis of minimum moment of inertia are a same axis. The case where the angular momentum and the axis of intermediar moment of inertia are a same axis is also a stationary point but an hyperbolic point.

In the second graph, we now add the effect of a external body P but whose eccentricity is zero. It is a one degree freedom problem. We see, by comparison with the first figure, how the solution curves are modified by the presence of the body P. On the contrary, we see that the position of the stationary points are not modified by the disturbing body P. In particulary the minimum of this Hamiltonian is always for $J = 0$.

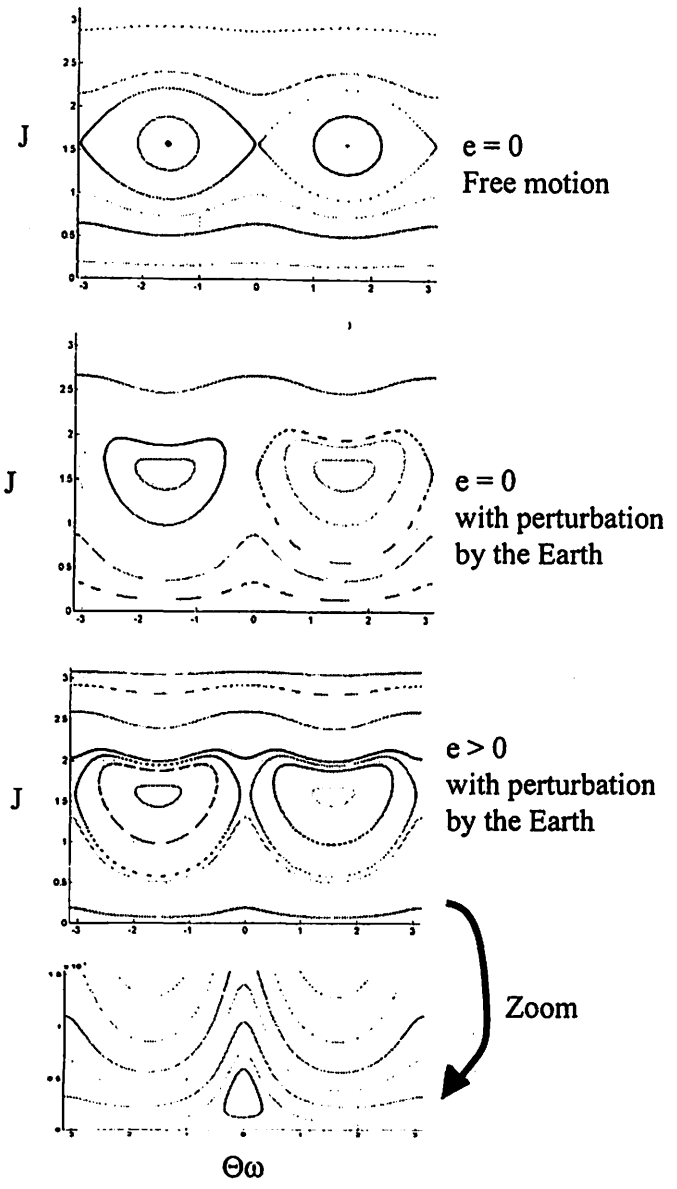

Figure 3: Poincarre map for the Moon for $\omega = 0$

In the two last graphs, we suppose now the eccentricity of the orbit of P is the real value of the eccentricity of the orbit of the Earth around the Moon. In this case, it is really a two degrees freedom problem, but no chaotic area seems appear in the stroboscopic map. We remark in particular that the minimum of the zero eccenticity Hamiltonian (for $J = 0$) moves into a stationary point of the section map of not zero eccentricity Hamiltonian (for which $J \neq 0$) which corresponds to the resonance $\theta_\omega = 0$ ($l = \omega$).

Remark: The stationary points of these section maps are not only the solutions of $\partial K_l/\partial X_3 = 0$ and $\partial K_l/\partial Y_3 = 0$. Indeed, the components (X_3, Y_3) of these stationary points correspond to periodic functions of same period that ω (named ω-periodic function). Of course, in the case of perturbation equal to zero ($U_l = 0$) or eccentricity equal to zero, the stationary points of the section map ($\theta_\omega \times J$) are the solutions of $\partial K_l/\partial l = 0$ and $\partial K_l/\partial L = 0$.

To determine precisely the position of the stationary points of this section map, we must study the equations $\dfrac{\partial K_l}{\partial X_3}$ and $\dfrac{\partial K_l}{\partial Y_3}$. They are written like that:

$$-\dot{Y}_3 = \frac{\partial K_l}{\partial X3} = \sin^2 J \left[\frac{3}{2}\alpha\cos^4\left(\frac{I}{2}\right) - \frac{3}{4}\beta(1+3\cos 2I) - 2\gamma_3\frac{G^2}{C}\right]\sin 2(\theta_\omega+\omega) \quad (5)$$
$$-12\beta\sin^4\left(\frac{J}{2}\right)\cos^4\left(\frac{I}{2}\right)\sin 4(\theta_\omega+\omega))$$
$$+e\sin J\left[\frac{3}{4}\sin I\left[\alpha\cos J\cos^2\left(\frac{I}{2}\right)+6\beta\cos I\cos^2\left(\frac{J}{2}\right)\right]\sin(\theta_\omega+2\omega)\right.$$
$$+\frac{3}{4}\sin I\left[3\alpha\cos J\cos I+\frac{1}{2}\beta(1+\cos J)(1+\cos I)\right]\sin(\theta_\omega)$$
$$\left.-\frac{9}{4}\beta\sin^2\left(\frac{J}{2}\right)\sin I\left[6\cos I\sin(3\theta_\omega+2\omega)+(1+\cos I)\sin(3\theta_\omega+4\omega)\right]\right]$$

and

$$\dot{X}_3 = \frac{\partial K_l}{\partial Y3} = -\frac{1}{G\sin J}\frac{\partial K_l}{\partial J} \quad (6)$$
$$= \left[-\dot{\omega}+2\frac{G}{C}\gamma_2\cos J-\frac{3}{8}\frac{\alpha}{G}\cos J(1+3\cos 2I)\right]$$
$$+\cos J\left[-2\frac{G}{C}\gamma_3+\frac{3}{2}\frac{\alpha}{G}\cos^4\left(\frac{I}{2}\right)-\frac{3}{4}\frac{\beta}{G}(1+3\cos 2I)\right]\cos 2(\theta_\omega+\omega)$$
$$+\frac{3}{2}\frac{\beta}{G}\cos J\cos^4\left(\frac{I}{2}\right)[1+\cos 4(\theta_\omega+\omega)]+\frac{3}{2}\frac{\beta}{G}\cos^4\left(\frac{I}{2}\right)[1-\cos 4(\theta_\omega+\omega)]$$
$$+\frac{e}{\sin J}*\left[\frac{3}{8}\sin I\left[\frac{\alpha}{G}\cos 2J(\cos I+1)-\frac{\beta}{G}\left(9\sin^2 J-12\cos^4\left(\frac{J}{2}\right)\right)\cos I\right]\cos(\theta_\omega+2\omega)\right.$$
$$+\frac{3}{4}\sin I\left[3\frac{\alpha}{G}\cos 2J\cos I-\frac{\beta}{G}\left(\frac{3}{4}\sin^2 J-\cos^4\left(\frac{J}{2}\right)\right)(\cos I+1)\right]\cos(\theta_\omega)$$
$$-\frac{3}{4}\frac{\beta}{G}\left(3\sin^2 J-4\sin^4\left(\frac{J}{2}\right)\right)\cos^3\left(\frac{I}{2}\right)\sin\left(\frac{I}{2}\right)\cos(3\theta_\omega+4\omega)$$
$$\left.-\frac{9}{16}\frac{\beta}{G}\left(3\sin^2 J-4\sin^4\left(\frac{J}{2}\right)\right)\sin 2I\cos(3\theta_\omega+2\omega)\right]$$

We are more particulary interested by the stationary point for which J is close to zero. When the eccentricity is not zero, we see this point on the last graph of the figure 3 which corresponds to the resonance case ($\theta_\omega = 0$). To determine precisely the relation that the components of this point must verified we simplify again the Hamiltonian K_l by remove all periodic terms except the term with only θ_ω and θ_Ω as argument. We named this new Hamiltonian K_l'. With this Hamiltonian, the components of looking for point verified the relations $\partial K_l'/\partial X_3 = 0$ and $\partial K_l'/\partial Y_3 = 0$. The first relation ($\partial K_l'/\partial X_3 = 0$) is verified for ($\theta_\omega = 0$). So by introduce ($\theta_\omega = 0$) in the second relation ($\partial K_l'/\partial Y_3 = 0$) we obtain the following relation for the stationary point :

$$\dot{\theta}_\omega = 0 = \frac{\partial K_l'}{\partial Y_3} = -\dot{\omega}+3\frac{\beta}{G}\cos^2\left(\frac{J}{2}\right)\cos^4\left(\frac{I}{2}\right)-\frac{3}{8}\frac{\alpha}{G}\cos J(1+3\cos(2I))+2G\gamma_2\cos J \quad (7)$$
$$+e\left[\frac{3}{4}\frac{\beta}{G}\left[4\frac{\cos^4(J/2)}{\sin J}-3\sin J\right]\cos^3\left(\frac{I}{2}\right)\sin\left(\frac{I}{2}\right)+\frac{9}{8}\frac{\alpha}{G}\frac{\cos 2J}{\sin J}\sin 2I\right]$$

In the case of the Moon we have to remark that the fourth condition C_2 which define the obliquity I (determined by Colombo (1966)) is modified due to the fact that the value of J is not zero. In fact to obtain a precise value of this stationary point of the Moon we have to determine I and J by using the two following canonical equations of the hamiltonian K_l':

$$\frac{\partial K_l'}{\partial Y_1} = 0 \qquad \textit{and} \qquad \frac{\partial K_l'}{\partial Y_3} = 0$$

And their explicit expressions are:

$$
\begin{aligned}
[\sin(I-i)]\,\dot{\Omega} &= 3\frac{\beta}{G}\cos^4\frac{J}{2}\cos^2\frac{I}{2}\sin I+\frac{3}{8}\frac{\alpha}{G}\left(1-3\cos^2 J\right)\sin 2I \\
&\quad +e\left[3\frac{\beta}{G}\cos^3\frac{J}{2}\sin\frac{J}{2}\left(2\cos I-1\right)\cos^2\frac{I}{2}+\frac{9}{8}\frac{\alpha}{G}\cos 2I\sin 2J\right] \qquad (8)\\
&\quad -\left[\frac{3}{8}\frac{\alpha_\odot}{G}\left(1-e_\odot\right)^{-3/2}\sin 2(I-i)\left(3\cos^2 J-1\right)\right]_{(Sun)} \\
&\quad -\frac{\alpha}{GJ_2}\frac{R}{a}\left[\frac{3}{16}\left(11-10\cos I-45\cos^2(I)\right)C_{3,1}+\frac{45}{8}\left(1+\cos I\right)^2 C_{3,3}\right] \\
\dot{\omega} &= 3\frac{\beta}{G}\cos^2\frac{J}{2}\cos^4\frac{I}{2}-\frac{3}{8}\frac{\alpha}{G}\cos J\left(1+3\cos(2I)\right)+2G\gamma_2\cos J \\
&\quad +e\left[\frac{3}{4}\frac{\beta}{G}\left[4\frac{\cos^4(J/2)}{\sin J}-3\sin J\right]\cos^3\frac{I}{2}\sin\frac{I}{2}+\frac{9}{8}\frac{\alpha}{G}\frac{\cos 2J}{\sin J}\sin 2I\right] \\
&\quad -\left[\frac{3}{8}\frac{\alpha_\odot}{G}\left(1-e_\odot\right)^{-3/2}\left(1+3\cos 2(I-i)\right)\cos J\right]_{(Sun)} \qquad (9)
\end{aligned}
$$

In these equations we add the effect of the Sun and the effect of the sub-harmonic of order 3 of the potential of the Moon with $\alpha_\odot = \frac{n_\odot^2}{1+\mu_\odot} J_2 M_S R^2$ ($n_\odot$ is the mean motion of the Sun around the Earth, $\mu_\odot$ is the sum of the mass of the Earth and the Moon divide by the mass of the Sun and $e_\odot$ is eccentricity of the orbit of the Sun around the Earth).

Remark: we show that the first relations (8) is not sensitive to the variations of J when J is small whereas the second one (9) is very sensitive to its variations. So firstly we determine the approximate value of I with the help of the equation (8) with $J = 0$. Then, we determine the approximate value of J with the help of the equation (9). We begin again this process until the required precision.

The values obtained by this way, without take into accound the little effect of the Sun and of the potential of order 3, are the following values:

$$I = 6^o.6740$$
$$J = 100''.6218$$

if we add the effect of the Sun and of the potential of P of order 3 these values become:

$$I = 6^o.6762$$
$$J = 100''.6225$$

The values used for the parameters of the Moon are listed in the table 1.

Remark: We have studied especially the stationary point for which the value of J is close to zero. Indeed we know that the internal friction inside the body S (in a non-rigid case) lead to minimize this angle J (see Harris 1994).

4 "Observed" librations of the Moon

With the use of more accurate observationnal method to measure the distance between the Earth and the Moon (Lunar laser), the theories of orbit and rotation of the Moon had been greatly improved in the last 40 years. This works has been done for the libration of the Moon in particular by Moons (1981). Her method consists to find an appropriate canonical transformation to convert a mean solution in a oscultating solution with the use of the Lie methods. To initialise her solution, Moons has supposed that the mean solution of the libration of the Moon is close of the position defined by the Cassini's law, so she has slightly modified this one in ajusting some constant determined with the Hamiltonian of rotation of Moon truncated to the first order with respect of variables I, J. By this way, the mean value of the angle J is zero (J and l are not present in her Hamiltonian).

On the contrary, when we study the final libration series of the Moon obtained by Moons, we see that the mean value of J is different from zero.

Moons solution are given as Fourrier series with coefficients half-analytical/half-numerical and with arguments which are linear combination of 4 angular variables. The analytical part of the coefficients depends of the geophysical parameters of Moon (J_2, $C_{2,2}$, C/MR^2,...). These parameters have been adjusted to the observations of Lunar laser ranging and doppler tracking data from a lunar satellite (Ferrari et al, 1980).

The Moons solution are three series which correspond to P_1, P_2 (the components of the unit vector pointing toward the pole of the mean ecliptic of the date along the two equatorial principal axes of inertia of the Moons) and τ the longitude libration. By using these three series and their derivatives with respect of time, we are able to compute numerically the corresponded values of the 6 Andoyer's variables with respect of time.

On the figure 4, we show the variations of Andoyer's variables l and J obtained by this way: $\theta_\omega = (l - \omega)$ with respect of time on the upper graph, J with respect of time on the middle graph and J with respect of θ_ω on the last graph. We get similar graphs for the other Andoyer's variables G, g, I and h.

We can fit a polynomial of first degree in time to the Angular Andoyer's variables h and l: $h \simeq n_h * t + h_0$ and $l \simeq n_l * t + l_0$. In the same way, we fit a constant to the action-type Andoyer's variables I and J: $I \simeq I_0$ et $J \simeq J_0$. The obtained values are :

$$\begin{aligned} I_0 &= 6^o.6837 \pm 0.0001 \\ n_h &= \dot{\Omega} = -337.6(rad/1000years) \\ h_0 &\simeq \Omega_0 + 180^o \pm 0.006 \end{aligned}$$

$$\begin{aligned} J_0 &= 103''.9582 \pm 0.7 \\ n_l &= \dot{\omega} = 1047.7(rad/1000years) \end{aligned}$$

The mean motion of Ω and ω are taken from Chapront-Touzé and Chapront (1988). The values for the variables h and I_0 correspond to the Cassini's laws. The values for the variables J and l correspond to the new type of Cassini's laws. A representation of this motion is drawn on the figure 5.

From these manipulations we can make severals remarks:

Remark 1: The mean value of J is not zero: 1/200 smaller than the obliquity I for the Moon (about 800 meters on the surface of the Moon).

Remark 3: For the Moon, the mean frequency of l is equal to the mean frequency of ω.

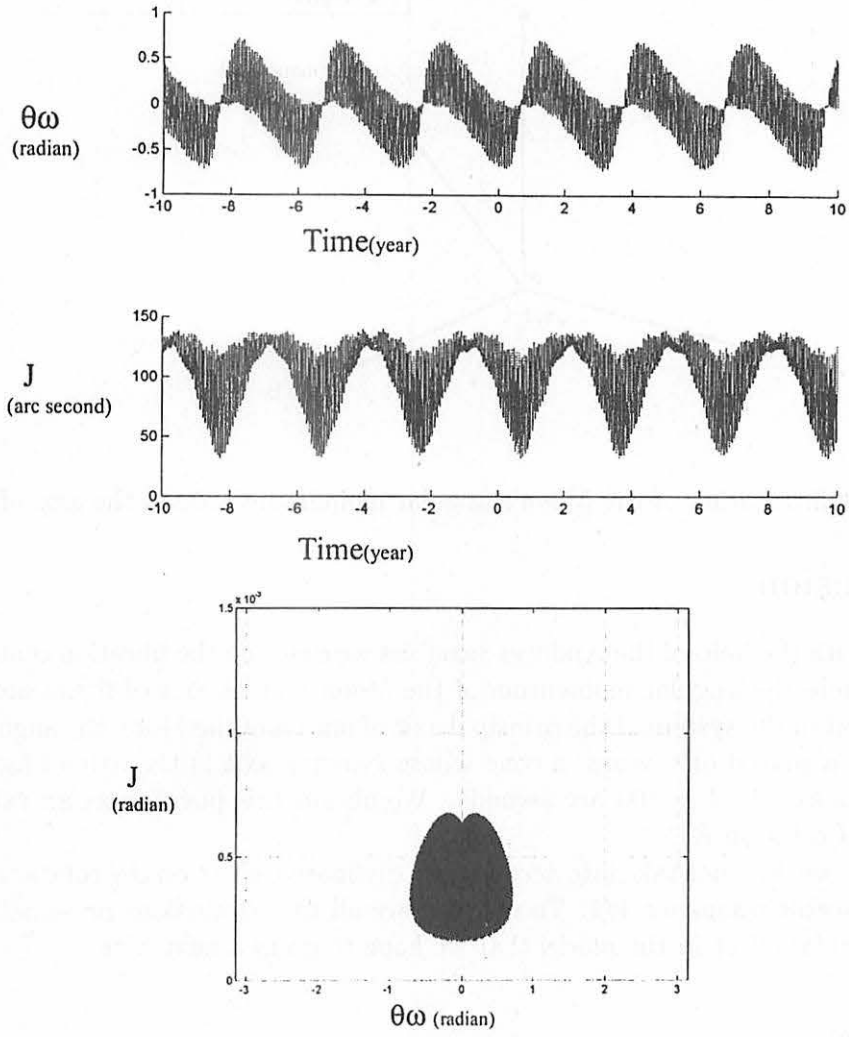

Figure 4: Moon's Libration obtain by Moons : Variables θ_ω and J

If we compare Lunar coordinates ($I = 6^o.6740, J = 100''.6218$) determinated in section 3 and which correspond to the stationary point of the equations (8) and (9) with the real values obtained in the section 4 ($I_0 = 6^o.6837, J_0 = 103''.9582$) we see a good agreement. The difference for obliquity is around 40 arc seconds (equivalent to 300 meters on the surface of the Moon), and the difference for J angle is around 3 arc seconds (equivalent to 20 meters on the surface of the Moon). This agreement is improve if we take into accound of the effect of the Sun ($I_a = 6^o.6762, J_a = 100''.6225$). The difference for obliquity is reducted to 20 arc seconds.

The relative important difference for obliquity can be explain by the use of mean inclination of the orbit of the Moon different to the Moons value. Moreover the mean value of the Andoyer variables determined in the section 4 are only approximation of the stationary point that we determine in the section 3.

The resuls of section 3 for the Moon may be probably generalized to other bodies in resonance spin-orbit 1/1.

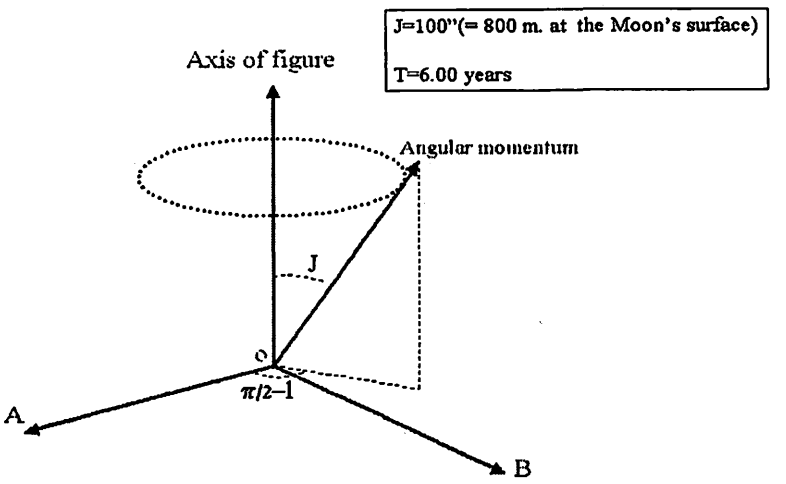

Figure 5: rotation of the Moon's angular momentum around the axis of figure

5 Conclusion

In this note, with the help of the Andoyer variables we describe the libration center of the Moon in the case where the angular momentum of the Moon and its axis of figure are different. We have shown that in the system of the principal axis of inertia of the Moon the angular momentum describe, with a period of 6 years, a cone whose symetry axis is the axis of figure and whose angle with this axis is $J \simeq 100$ arc seconds. We obtain this position as an extremum of the Hamiltonian of rotation K_l.

In this note we does not take into account of a dissipative effect on the rotation of the celestial bodies in spin-orbit resonance 1/1. To really prove all the conclusions presented here we must introduce the tidal effect in the model that we hope to do in a next note.

References

[1] Cassini, G.D., 1693 *Traité de l'origine et du progrès de l'astronomie*, Paris.

[2] Chapront-Touzé, M. and Chapront, J.: 1988, *Astron. Astrophys.* **190**, 342.

[3] Colombo, G.: 1966,*Astron. J.* **71**, 891.

[4] Deprit, A.: 1967,*Am. J. Phys.* **35**, 424.

[5] Ferrari, A.J. & al.: 1980, *J.Geophys.Res.* **85**, 3939.

[6] Goldreich, P. and Peale, S.: 1966, *Astron. J.* **71**, 425.

[7] Harris A.W.: 1994, *Icarus* **107**, 209.

[8] Kinoshita, H.: 1977, *Celest. Mech.* **15** 423.

[9] Moons, M.:1981,*thèse de doctorat*, Facultés Universitaires Notre-Dame de la Paix, Namur.

[10] Peale, S.: 1969, *Astron. J.* **74**, 483.

Name	Values for The Moon (Source)
$\mu = \frac{M_L}{M_T}$	$0.012150568^{(1)}$
$J_2 = -C_{(2,0)}$	$0.00020409^{(1)}$
$C_{(2,2)}$	$0.00002250^{(1)}$
$\frac{MR^2}{C}$	$\frac{1}{0.394}$ (1)
$\frac{2C-A-B}{2C} = J_2 \frac{MR^2}{C}$	$0.00051742^{(1)}$
$\frac{A-B}{4C} = -C_{(2,2)} \frac{MR^2}{C}$	-0.000056971 (1)
$\frac{\alpha}{C} = (\dot{\lambda})^2 \frac{1}{1+\mu} \left(\frac{2C-A-B}{2C}\right)$	$2.7036E-5(rad/day^2)$
$\frac{\beta}{C} = (\dot{\lambda})^2 \frac{1}{1+\mu} \left(\frac{A-B}{4C}\right)$	$-2.9768E-6(rad/day^2)$
$\gamma_2 = \left(\frac{1}{2} - \frac{1}{4}\left(\frac{C}{A} + \frac{C}{B}\right)\right)$	-0.0002589
$\gamma_3 = \frac{1}{4}\left[\frac{C}{B} - \frac{C}{A}\right]$	-0.00005703
e	$0.054879905^{(2)}$
i	$5^o.1298350639^{(2)}$
n	0.2280271 (rad/day)$^{(2)}$
n_Ω	-0.00092422 (rad/day)$^{(2)}$
n_ω	0.0028686 (rad/day)$^{(2)}$
$\dot{\lambda}$	0.2299715 (rad/day)
$n_\Omega/\dot{\lambda}$	$-4.019 * 10^{-2}$
I	$6^o.6715^{(3)}$
J	$100''.182^{(3)}$

Table 1: *values for the Moon*

[1]Numerical values uses in this Moon ephemeride DE-245 of the JPL.
[2]Chapront and Chapront-Touzé (1988)
[3]This article.

Precession, Nutation, and Variation of UT1 due to Sun's post-Newtonian Torque

Toshio Fukushima
National Astronomical Observatory
(E-mail) Toshio.Fukushima@nao.ac.jp

ABSTRACT

We derived the post-Newtonian transformation laws of the coordinate velocity and the coordinate acceleration between a global and a body-centric coordinate systems, which are related to each other by a kinematically non-rotating coordinate transformation. Next, by using the latter transformation, we obtained an explicit expression of the post-Newtonian tidal acceleration. Then, by conducting a spacial volume integral of torque element on an equal body-centric coordinate time hypersurface, we computed the post-Newtonian form of the gravitational torque. Finally, by integrating the Poisson approximation of the post-Newtonian extension of the Eulerian equation of rotational motion of the Earth moving along an elliptic orbit around the Sun and suffering the Sun's torque only, we evaluated post-Newtonian corrections to the precession, the nutation, and the variation of UT1. Except the geodesic precession and the geodesic nutation (Fukushima 1991), the largest effects are those related to the rotation angle of the Earth, UT1, as much as $\Delta\mathrm{UT1} = 10.50 \sin \ell' + 0.09 \sin 2\ell'$. where the unit is millisecond and ℓ' denotes the mean anomaly of the Sun. The associated variation of the angular velocity of the Earth rotation becomes $\Delta\Omega = 2.4 \cos \ell'$ in the unit of 10^{-14} rad/s. These are comparable with the tidal effects due to the nonrigidity of the Earth.

Subject headings: astrometry—Earth: rotation—ephemerides—reference systems

1. Introduction

The rotational dynamics and the orbital dynamics are two major subjects of the celestial mechanics. In the general relativitivistic framework, however, the former is not so well established as the latter is. Even in the first post-Newtonian approximation of the general relativity, the situation is the same. The Einstein-Infeld-Hoffmann formalism has been the base of the modern ephemerides and the analysis of high precision orbital data such as obtained in the space techniques such as SLR, LLR, VLBI, and GPS.

On the other hand, the largest general relativistic effect in the view point of rotational dynamics is the geodesic rotation in the wider sense, or the so-called effect of dragging of inertial

frame. In the case of the Earth rotation, its effect is well-known (de Sitter 1916). Actually it appear as corrections to the precession and the nutation of the Earth. The correction to the precession constant, named *geodesic precession*, amounts to

$$\Delta_g p = 1.919\ ''/\text{century} \tag{1}$$

and the correction to the nutation series, called *geodesic nutation*, becomes

$$\Delta_g \psi = 0.153 \sin \ell' + 0.002 \sin 2\ell' \tag{2}$$

where the coefficients are expressed in the unit of mas (Fukushima 1991). Both the above effects are to be *subtracted* from the Newtonian formula. Note that the geodesic rotation appears only in the precession/nutation in longitude and neither in the precession/nutation in obliquity nor in the variation of UT1. See also the more extensive studies (Bizouard *et al.* 1992; Brumberg *et al.* 1993; Bois and Vokrouhlicky 1995). In the case of the Moon, the same effect appears in a little different manner and one must add 29 mas/century to $\Delta_g p$ and add a monthly term of magnitude of 0.03 mas to $\Delta_g \psi$ (Vokrouhlicky 1995).

Fortunately, the so-called DSX formalism (Damour *et al.* 1991, 1992, 1993) has revealed the nature of the proper treatment of the rotational dynamics in the first post-Newtonian approximation (Klioner and Soffel 1998). However, from the author's point of view, there seems to remain some effects which has not been remarked so far. In fact, all the existing studies claimed that the post-Newtonian torque is in proportion to the dynamical flattening of the spinning body. Namely, they argued that the spinning body will suffer no torque when it is spherically symmetric in the Newtonian approximation. Unfortunately, there does exist the post-Newtonian correction, more specifically speaking the Lense-Thirring effect, to the acceleration of a test particle moving around a spinning central body;

$$\Delta_{LT}\vec{a} = \frac{\gamma+1}{2c^2}\vec{v}\times\vec{H}, \qquad \vec{H} = -\nabla\times\left(\frac{2G\vec{L}\times\vec{x}}{r^3}\right) = \frac{G}{r^3}\left[\vec{L} - \frac{3\left(\vec{x}\cdot\vec{L}\right)}{r^2}\vec{x}\right] \tag{3}$$

where $\vec{L}$ is the spin angular momentum of the central body, $r = |\vec{x}|$. This post-Newtonian effect remains even if the central body is spherically symmetric in the Newtonian sense. Since there must be a reaction to any action[1] , which is also true in the post-Newtonian framework in some sense, we think that there should be an anti-acceleration corresponding to the above gravito-magnetic acceleration which the spinnin body acting on the external body. In fact, the variation of orbital angular momentum vector associated with the above correction to the orbital acceleration becomes

$$\Delta_{LT}J = M\vec{x}\times\Delta_{LT}\vec{a} = -\left(\frac{\gamma+1}{2}\right)\frac{GM}{c^2r^3}\left[\left(\vec{x}\cdot\vec{L}\right)\left\{2\vec{v} - \frac{3\left(\vec{x}\cdot\vec{v}\right)}{r^2}\vec{x}\right\} + \left(\vec{x}\cdot\vec{v}\right)\vec{L}\right]. \tag{4}$$

[1] It must be stated properly as an anti-acceleration exists for any acceleration.

The conservation of the total angular momentum requires[2] a sort of change of the spin angular momentum of the same order of magnitude. In other words, we believe in a kind of post-Newtonian torque casued by an external body on a spinning body even if the spinning body is spherically symmetric. This situation is quite the same as that the lunar torque on the Earth exists as an anti-acceleration of the orbital acceleration of the Moon caused by the non-sphericity of the Earth.

In order to explore such possibility, we will examine the procedure of evaluation of post-Newtonian torque from the basics. As will be shown later, we found a significant effect not on the precession/nutation but on the variation of Earth rotation angle, UT1.

2. Post-Newtonian Torque

2.1. Equation of Rotational Motion

According to the DSX formalism (Damour *et al.* 1993), the post-Newtonian equation of rotational motion of a spinning body looks quite alike the Newtonian one;

$$\frac{\mathrm{d}\vec{L}}{\mathrm{dT}} = \vec{N}, \tag{5}$$

where T is the body-centric coordinate time,

$$\vec{L} \equiv \int_T \rho\, \vec{X} \times \vec{V}\, \mathrm{d}^3\vec{X}, \tag{6}$$

and

$$\vec{N} \equiv \int_T \rho\, \vec{X} \times \vec{A}\, \mathrm{d}^3\vec{X}, \tag{7}$$

are the post-Newtonian spin angular momentum and torque, respectively, Here ρ, $\vec{X}$, $\vec{V} \equiv \mathrm{d}\vec{X}/\mathrm{dT}$, and $\vec{A} \equiv \mathrm{d}^2\vec{X}/\mathrm{dT}^2$ are the density distribution, the coordinate position, the coordinate velocity, and the coordinate acceleration in the body-centric coordinate system, respectively.

The largest difference from the Newtonian form is in the coordinate system used. The coordinate system in the above formulation is the so-called body-centric one, namely the coordinate system attached to and moving with the spinning body under consideration. For example, the independent variable T is not the Barycentric Coordinate Time (TCB) but the Geocentric Coordinate Time (TCG) when the spinning body is the Earth. The above integration

---

[2] Strictly speaking, the corresponding variation $\Delta\vec{L}$ is not exactly equal to $-\Delta\vec{J}_{LT}$ since these two vectors are defined in different reference frame.

is done on the equal-T hypersurface. Thus, in order to evaluate the torque explicitly, we need to know the functional forms of the density distribution and the coordinate acceleration in the body-centric coordinate system as $\rho\left(T,\vec{X},\vec{V}\right)$ and $\vec{A}\left(T,\vec{X},\vec{V}\right)$.

However, as will be shown later, the $\vec{X}$- and $\vec{V}$-dependence of the post-Newtonian correction to the density distribution is of the quadratic and higher order. Then the resulting contribution in the integrand of the post-Newtonian correction to the torque is of the quartic and higher order with respect to $\vec{X}$ and/or $\vec{V}$. Thus we may neglect the post-Newtonian effects of ρ.

2.2. Post-Newtonian Corrections

In order to discuss the effect of post-Newtonian correction of ρ clearly, let us express ρ, $\vec{A}$, and $\vec{N}$ as the sum of the Newtonian part and the post-Newtonian correction;

$$\rho = \rho^{(N)} + \Delta\rho, \qquad \vec{A} = \vec{A}^{(N)} + \Delta\vec{A}, \qquad \vec{N} = \vec{N}^{(N)} + \Delta\vec{N}, \tag{8}$$

where the superfix (N) denotes the Newtonian part and Δ denotes the post-Newtonian correction. Then the Newtonian torque becomes

$$\vec{N}^{(N)} = \int_T \rho^{(N)}\, \vec{X} \times \vec{A}^{(N)}\, \mathrm{d}^3\vec{X}, \tag{9}$$

and the post-Newtonian correction to the torque is expressed as

$$\Delta\vec{N} = \Delta_\rho\vec{N} + \Delta_A\vec{N}, \tag{10}$$

where

$$\Delta_\rho\vec{N} = \int_T \Delta\rho\, \vec{X} \times \vec{A}^{(N)}\, \mathrm{d}^3\vec{X}, \qquad \Delta_A\vec{N} = \int_T \rho^{(N)}\, \vec{X} \times \Delta\vec{A}\, \mathrm{d}^3\vec{X}. \tag{11}$$

Now, the post-Newtonian correction of the density distribution is given as

$$\Delta\rho = \frac{\rho^{(N)}}{c^2}\left[\Pi(\vec{X}) + (3\gamma - 1)\Phi(T,\vec{X}) + \frac{\vec{V}^2}{2}\right], \tag{12}$$

where Π is the internal energy including the gravitational self energy contribution, and γ is one of the PPN parameters reducing to 1 in Einstein's general theory of relativity. Note that Π depends on the body-centric position only. Here Φ is the Newtonian tidal force function[3] written in the body-centric coordinates as

$$\Phi\left(T,\vec{X}\right) = \phi\left(t,\vec{x}_O + \vec{X}\right) - \phi\left(t,\vec{x}_O\right) - \left(\frac{\partial\phi}{\partial\vec{x}}\right)_O \vec{X}, \tag{13}$$

[3] The term *force function* means the negative gravitational potential.

where ϕ is the Newtonian gravitational force function expressed in the global coordinates.

The effect of $\vec{X}$-dependence in $\Delta\rho$ is easily absorbed by readjsting the functional form of $\rho^{(N)}$ since the $\vec{X}$-dependence of $\rho^{(N)}$ is not known precisely anyway. Therefore we ignore the contribution of Π. As a result, $\Delta\rho$ is expanded as a second and higher moments of $\vec{X}$ and $\vec{V}$ as

$$\Delta\rho\left(T,\vec{X},\vec{V}\right)=\frac{\rho^{(N)}}{2c^2}\left[(3\gamma-1)\vec{X}\cdot\left\{\left(\frac{\partial^2\phi}{\partial\vec{x}\partial\vec{x}}\right)_O\vec{X}\right\}+\vec{V}^2+\cdots\right]. \tag{14}$$

Negligiblly small are the effects of these second and higher order terms. In fact, the main term of the Newtonian tidal acceleration is linear with respect to $\vec{X}$, which implies that the main term of the post-Newtonian correction of the tidal acceleration is also linear[4] with respect to $\vec{X}$. Therefore, we will neglect $\Delta_\rho\vec{N}$ hereafter and concentrate ourselves on $\Delta_A\vec{N}$.

2.3. Coordinate Transformation

Since we saw that the post-Newtonian effects of ρ is negligiblly small, we will focus on $\vec{A}$ hereafter. In general, there are two ways to derive the explicit form of $\vec{A}$. The one is to derive the metric tensor in the body-centric coordinate system first and to obtain the coordinate acceleration by evaluating the associated Christoffel symbols. The other is to start from the coordinate transformation connecting the global and the body-centric coordinate systems and to differentiate it twice to calculate the coordinate acceleration. We adopt the latter approach since it is more general in the sense being capable with the non-gravitational force.

Let us begin with the coordinate transformation connecting the global and the body-centric coordinate systems. Its general form is given in an expansion with respect to the body-centric coordinate position as

$$x^\mu\left(x^{\hat{\alpha}}\right)=x^\mu_O\left(x^{\hat{0}}\right)+\sum_{j=1}^{3}\left(e^\mu_{\hat{j}}\right)_O\left(x^{\hat{0}}\right)x^{\hat{j}}+O\left(\left\{x^{\hat{j}}\right\}\right),\qquad(\mu=0,1,2,3) \tag{15}$$

where x^μ and $x^{\hat{\alpha}}$ are the global and the body-centric spacetime coordinates, respectively, and the suffix O means that the values are evaluated at at the origin of the body-centric coordinate system, namely at the barycenter of the spinning body. Since the second and higher order terms with respect to $x^{\hat{j}}$ in the right hand side are practically small in the post-Newtonian approximation, we ignore them and write the coordinate transformation in a vector form being linear with respect to $\vec{X}\equiv\left(x^{\hat{1}},x^{\hat{2}},x^{\hat{3}}\right)^{\mathrm{T}}$ as

$$t=t_O+\frac{T_1}{c^2},\qquad\vec{x}=\vec{x}_O+\vec{X}-\frac{1}{c^2}\left(X_X\vec{X}+X_v\vec{v}_O\right). \tag{16}$$

[4] Actually, it is also linear with respect to $\vec{V}$.

Here $t \equiv x^0/c$, $\vec{x} \equiv (x^1, x^2, x^3)^{\mathrm{T}}$, and

$$T_1 \equiv T_1\left(T, \vec{X}\right) = \vec{v}_O \cdot \vec{X}, \tag{17}$$

$$X_X \equiv X_X(T) = \gamma \phi_O, \tag{18}$$

$$X_v \equiv X_v\left(T, \vec{X}\right) = \frac{-\left(\vec{v}_O \cdot \vec{X}\right)}{2}. \tag{19}$$

Also, t_O, $\vec{x}_O$, and $\vec{v}_O$ are the coordinate time, the coordinate position, and the coordinate velocity of the barycenter of the spinning body in the global coordinate system, respectively, and ϕ_O is the Newtonian gravitational potential which the body feels. Those with suffix O are the functions of $T \equiv x^{\hat{0}}/c$ by way of t_O. Namely, we should read them as

$$\phi_O = \phi_O\left(t_O(T)\right), \quad \vec{x}_O = \vec{x}_O\left(t_O(T)\right), \quad \vec{v}_O = \vec{v}_O\left(t_O(T)\right) \equiv \left(\frac{\mathrm{d}\vec{x}_O(t)}{\mathrm{dt}}\right)_{t=t_O(T)}. \tag{20}$$

The functional form of $t_O(T)$ is denoted as a time ephemeris of the Earth when the spinning body is the Earth (Fukushima 1995; Irwin and Fukushima 1999).

We set the spatial part of the post-Newtonian correction in Eq.(16) in a symmetric form with respect to $\vec{X}$. This means that we adopted the kinematical non-rotating convention in defining the body-centric coordinate system such as the IAU did to define the Geocentric Celestial Reference System (GCRS) (IAU 2001). In other words, thus-defined body-centric coordinate system never suffers the so-called dragging of the inertial frame. Namely, the torque expression in this coodrinate system must include the effect of de Sitter's geodesic rotation, especially in the form of Coriolis force. Later, we will confirm it. This fact will support the correctness of our approach.

2.4. Transformation Law of Coordinate Velocity

Next, let us compute the T-derivatives of the global coordinates, $(t, \vec{x})$. The post-Newtonian equation of time dilatation along the world line of the barycenter of the spinning body (Fukushima 1995) is

$$\frac{\mathrm{d}t_O}{\mathrm{dT}} = 1 + \frac{\varphi_O}{c^2}, \qquad \text{where} \qquad \varphi_O \equiv \phi_O + \frac{\vec{v}_O^2}{2}. \tag{21}$$

By using this, we evaluate the T-derivatives of t and $\vec{x}$ in the post-Newtonian approximation as

$$\frac{\mathrm{d}t}{\mathrm{dT}} = \frac{\mathrm{d}t_O}{\mathrm{dT}} + \frac{1}{c^2}\left(\frac{\mathrm{d}T_1}{\mathrm{dT}}\right) = 1 + \frac{1}{c^2}\left[\varphi_O + \left(\frac{\mathrm{d}T_1}{\mathrm{dT}}\right)\right], \tag{22}$$

$$\frac{\mathrm{d}\vec{x}}{\mathrm{dT}} = \left(\frac{\mathrm{d}t_O}{\mathrm{dT}}\right)\vec{v}_O + \vec{V} - \frac{1}{c^2}\left[\left(\frac{\mathrm{d}X_X}{\mathrm{dT}}\right)\vec{X} + X_X\vec{V} + \left(\frac{\mathrm{d}X_v}{\mathrm{dT}}\right)\vec{v}_O + X_v\vec{a}_O\right], \tag{23}$$

where

$$\vec{a}_O \equiv \vec{a}_O\left(t_O(T)\right) = \left(\frac{\mathrm{d}\vec{v}_O(t)}{\mathrm{dt}}\right)_{t=t_O(T)} \tag{24}$$

is the body's coordinate acceleration in the global coordinate system. By taking the ratio of these two T-derivatives and ignoring the second and higher order terms with respect to v^2/c^2, we obtain the post-Newtonian transformation law of the coordinate velocity as

$$\vec{v} \equiv \frac{\mathrm{d}\vec{x}}{\mathrm{dt}} = \left(\frac{\mathrm{d}\vec{x}}{\mathrm{dT}}\right)\Big/\left(\frac{\mathrm{dt}}{\mathrm{dT}}\right) = \vec{v}_O + \vec{V} - \frac{1}{c^2}\left(V_X\vec{X} + V_V\vec{V} + V_v\vec{v}_O + V_a\vec{a}_O\right). \tag{25}$$

Here

$$V_X \equiv V_X(T) = \frac{\mathrm{d}X_X}{\mathrm{dT}} = \gamma\dot{\phi}_O, \tag{26}$$

$$V_V \equiv V_V\left(T,\vec{X},\vec{V}\right) = X_X + \varphi_O + \frac{\mathrm{d}T_1}{\mathrm{dT}} = (\gamma+1)\phi_O + \frac{\vec{v}_O^2}{2} + \vec{a}_O\cdot\vec{X} + \vec{v}_O\cdot\vec{V}, \tag{27}$$

$$V_v \equiv V_v\left(T,\vec{X},\vec{V}\right) = \frac{\mathrm{d}X_v}{\mathrm{dT}} + \frac{\mathrm{d}T_1}{\mathrm{dT}} = \frac{1}{2}\left(\vec{a}_O\cdot\vec{X} + \vec{v}_O\cdot\vec{V}\right), \tag{28}$$

$$V_a \equiv V_a\left(T,\vec{X}\right) = X_v = \frac{-1}{2}\left(\vec{v}_O\cdot\vec{X}\right), \tag{29}$$

where

$$\dot{\phi}_O \equiv \dot{\phi}_O\left(t_O(T)\right) = \left(\frac{\mathrm{d}\phi_O(t)}{\mathrm{dt}}\right)_{t=t_O(T)}. \tag{30}$$

2.5. Transformation Law of Coordinate Acceleration

Third, we evaluate the T-derivative of the global coordinate velocity $\vec{v}$, Eq.(25), as

$$\frac{\mathrm{d}\vec{v}}{\mathrm{dT}} = \left(\frac{\mathrm{d}t_O}{\mathrm{dT}}\right)\vec{a}_O + \vec{A}$$

$$-\frac{1}{c^2}\left[\left(\frac{\mathrm{d}V_X}{\mathrm{dT}}\right)\vec{X} + \left(V_X + \frac{\mathrm{d}V_V}{\mathrm{dT}}\right)\vec{V} + V_V\vec{A} + \left(\frac{\mathrm{d}V_v}{\mathrm{dT}}\right)\vec{v}_O + \left(V_v + \frac{\mathrm{d}V_a}{\mathrm{dT}}\right)\vec{a}_O + V_a\vec{j}_O\right], \tag{31}$$

where

$$\vec{j}_O = \vec{j}_O\left(t_O(T)\right) \equiv \left(\frac{\mathrm{d}\vec{a}_O(t)}{\mathrm{dt}}\right)_{t=t_O(T)} \tag{32}$$

is the body's coordinate jerk[5] in the global coordinate system.

By taking the ratio of this and $\mathrm{d}t/\mathrm{dT}$, we derive the transformation law of the coordinate acceleration as

$$\vec{a} \equiv \frac{\mathrm{d}\vec{v}}{\mathrm{dt}} = \left(\frac{\mathrm{d}\vec{v}}{\mathrm{dT}}\right) \Big/ \left(\frac{dt}{\mathrm{dT}}\right)$$

$$= \vec{a}_O + \vec{A} - \frac{1}{c^2}\left(A_X\vec{X} + A_V\vec{V} + A_A\vec{A} + A_v\vec{v}_O + A_a\vec{a}_O + A_j\vec{j}_O\right), \tag{33}$$

where

$$A_X \equiv A_X(T) = \frac{\mathrm{d}V_X}{\mathrm{dT}} = \gamma\left(\frac{\mathrm{d}^2\phi_O}{\mathrm{dt}^2}\right), \tag{34}$$

$$A_V \equiv A_V\left(T, \vec{X}, \vec{V}, \vec{A}\right) = V_X + \frac{\mathrm{d}V_V}{\mathrm{dT}} = (2\gamma+1)\dot{\phi}_O + \vec{v}_O\cdot\vec{a}_O + \vec{j}_O\cdot\vec{X} + 2\vec{a}_O\cdot\vec{V} + \vec{v}_O\cdot\vec{A}, \tag{35}$$

$$A_A \equiv A_A\left(T, \vec{X}, \vec{V}\right) = V_V + \varphi_O + \frac{\mathrm{d}T_1}{\mathrm{dT}} = (\gamma+2)\phi_O + \vec{v}_O^2 + 2\vec{a}_O\cdot\vec{X} + 2\vec{v}_O\cdot\vec{V}, \tag{36}$$

$$A_v \equiv A_v\left(T, \vec{X}, \vec{V}, \vec{A}\right) = \frac{\mathrm{d}V_v}{\mathrm{dT}} = \frac{1}{2}\left(\vec{j}_O\cdot\vec{X} + 2\vec{a}_O\cdot\vec{V} + \vec{v}_O\cdot\vec{A}\right), \tag{37}$$

$$A_a \equiv A_a\left(T, \vec{X}, \vec{V}\right) = V_v + \frac{\mathrm{d}V_a}{\mathrm{dT}} + \frac{\mathrm{d}T_1}{\mathrm{dT}} = \vec{a}_O\cdot\vec{X} + \vec{v}_O\cdot\vec{V}, \tag{38}$$

$$A_j \equiv A_j\left(T, \vec{X}\right) = V_a = \frac{-1}{2}\left(\vec{v}_O\cdot\vec{X}\right). \tag{39}$$

2.6. Body-Centric Coordinate Acceleration

Fourth, let us obtain the explicit expression of the body-centric coordinate acceleration $\vec{A}$ in terms of the body-centric coordinate time T, the body-centric coordinate position $\vec{X}$, and the

[5] The word *jerk* is used to denote the third time derivative of the position vector.

body-centric coordinate velocity $\vec{V}$ as $\vec{A} = \vec{A}\left(T, \vec{X}, \vec{V}\right)$. To do this, we solve the transformation law of the coordinate acceleration, Eq.(33), with respect to $\vec{A}$.

In general the global coordinate acceleration $\vec{a}$ is expanded around its value at the coordinate origin of the body-centric coordinate system, $\vec{a}_O \equiv \vec{a}\left(t_O, \vec{x}_O, \vec{v}_O\right)$, in terms of the global coordinate quantities $(t, \vec{x}, \vec{v})$ as

$$\vec{a} - \vec{a}_O = \left(\frac{\partial \vec{a}}{\partial t}\right)_O (t - t_O) + \left(\frac{\partial \vec{a}}{\partial \vec{x}}\right)_O (\vec{x} - \vec{x}_O) + \left(\frac{\partial \vec{a}}{\partial \vec{v}}\right)_O (\vec{v} - \vec{v}_O) + \cdots . \tag{40}$$

If we subsitute the coordinate transformations, Eqs (16) and (25), to $t - t_O$, $\vec{x} - \vec{x}_O$, and $\vec{v} - \vec{v}_O$, then

$$\vec{a} - \vec{a}_O = \left(\frac{\partial \vec{a}}{\partial \vec{x}}\right)_O \vec{X} + \left(\frac{\partial \vec{a}}{\partial \vec{v}}\right)_O \vec{V} + \cdots + \frac{1}{c^2}\left[T_1 \left(\frac{\partial \vec{a}}{\partial t}\right)_O - \left(\frac{\partial \vec{a}}{\partial \vec{x}}\right)_O \left(X_X \vec{X} + X_v \vec{v}_O\right)\right.$$

$$\left. - \left(\frac{\partial \vec{a}}{\partial \vec{v}}\right)_O \left(V_X \vec{X} + V_V \vec{V} + V_v \vec{v}_O + V_a \vec{a}_O\right)\right] . \tag{41}$$

The post-Newtonian coordinate acceleration in the global coordinate system, $\vec{a}$, is also expressed as the sum of the Newtonian part, $\vec{a}^{(N)}$, and the post-Newtonian correction, $\Delta\vec{a}$;

$$\vec{a}\left(t, \vec{x}, \vec{v}\right) = \vec{a}^{(N)}\left(t, \vec{x}, \vec{v}\right) + \Delta\vec{a}\left(t, \vec{x}, \vec{v}\right) . \tag{42}$$

By combining Eqs (41) and (42) and ignoring the second order effects, we obtain

$$\vec{a} = \vec{a}_O + \left(\frac{\partial \vec{a}^{(N)}}{\partial \vec{x}}\right)_O \vec{X} + \left(\frac{\partial \vec{a}^{(N)}}{\partial \vec{v}}\right)_O \vec{V} + \left(\frac{\partial \Delta\vec{a}}{\partial \vec{x}}\right)_O \vec{X} + \left(\frac{\partial \Delta\vec{a}}{\partial \vec{v}}\right)_O \vec{V} + \cdots$$

$$+ \frac{1}{c^2}\left[T_1 \left(\frac{\partial \vec{a}^{(N)}}{\partial t}\right)_O - \left(\frac{\partial \vec{a}^{(N)}}{\partial \vec{x}}\right)_O \left(X_X \vec{X} + X_v \vec{v}_O\right)\right.$$

$$\left. - \left(\frac{\partial \vec{a}^{(N)}}{\partial \vec{v}}\right)_O \left(V_X \vec{X} + V_V \vec{V} + V_v \vec{v}_O + V_a \vec{a}_O^{(N)}\right)\right] . \tag{43}$$

By substituting the expression Eq (33) into the above, and solving the resulting expression with respect to $\vec{A}$, we obtain the explicit expression of $\vec{A}$. If we split the obtained expression in the form, $\vec{A} = \vec{A}^{(N)} + \Delta\vec{A}$, and note that the Newtonian part is given as

$$\vec{A}^{(N)}\left(T, \vec{X}, \vec{V}\right) = \left(\frac{\partial \vec{a}^{(N)}}{\partial \vec{x}}\right)_O \vec{X} + \left(\frac{\partial \vec{a}^{(N)}}{\partial \vec{v}}\right)_O \vec{V} + \cdots , \tag{44}$$

then we obtain the expression of the post-Newtonian correction explicitly as

$$\Delta\vec{A}\left(T,\vec{X},\vec{V}\right) = \left[\left(\frac{\partial\Delta\vec{a}}{\partial\vec{x}}\right)_O + \frac{1}{c^2}\left\{A_X + (A_{AO} - X_X)\left(\frac{\partial\vec{a}^{(N)}}{\partial\vec{x}}\right)_O - V_X\left(\frac{\partial\vec{a}^{(N)}}{\partial\vec{v}}\right)_O\right\}\right]\vec{X}$$

$$+\left[\left(\frac{\partial\Delta\vec{a}}{\partial\vec{v}}\right)_O + \frac{1}{c^2}\left\{A_{VO} + (A_{AO} - V_{VO})\left(\frac{\partial\vec{a}^{(N)}}{\partial\vec{v}}\right)_O\right\}\right]\vec{V} + \frac{T_1}{c^2}\left(\frac{\partial\vec{a}^{(N)}}{\partial t}\right)_O$$

$$+\frac{1}{c^2}\left[A_v - X_v\left(\frac{\partial\vec{a}^{(N)}}{\partial\vec{x}}\right)_O - V_v\left(\frac{\partial\vec{a}^{(N)}}{\partial\vec{v}}\right)_O\right]\vec{v}_O + \frac{1}{c^2}\left[A_a - V_a\left(\frac{\partial\vec{a}^{(N)}}{\partial\vec{v}}\right)_O\right]\vec{a}_O$$

$$+\left(\frac{A_j}{c^2}\right)\vec{j}_O + \cdots, \tag{45}$$

where

$$A_{AO} \equiv (A_A)_{\vec{X}=\vec{V}=0} = (\gamma+2)\phi_O + \vec{v}_O^2, \tag{46}$$

$$A_{VO} \equiv (A_V)_{\vec{X}=\vec{V}=\vec{A}=0} = (2\gamma+1)\dot{\phi}_O + \vec{v}_O\cdot\vec{a}_O, \tag{47}$$

$$V_{VO} \equiv (V_V)_{\vec{X}=\vec{V}=0} = (\gamma+1)\phi_O + \frac{\vec{v}_O^2}{2}. \tag{48}$$

Here we assumed that negligiblly small are the contributions of the second and higher order terms with respect to $\vec{X}$ and $\vec{V}$. In the Newtonian framework, this assumption is equivalent with the ignorance of the torques due to the couplings of the external gravitating bodies and the J_3 and higher order of gravitational potentials of the spinning body. One has only to consider the Newtonian contribution when evaluating $\Delta\vec{A}$. Thus one may replace the embedded $\vec{A}$ by $\vec{A}^{(N)}$ when evaluating A_v.

Usually the Newtonian acceleration does not depend on the coordinate velocity as in the purely gravitational N-body problem. In such cases, the above expressions, Eqs (44) and (45), are simplified as

$$\vec{A}^{(N)}\left(T,\vec{X}\right) = \left(\frac{\partial\vec{a}^{(N)}}{\partial\vec{x}}\right)_O\vec{X}, \tag{49}$$

and

$$\Delta\vec{A}\left(T,\vec{X},\vec{V}\right) = \left[\left(\frac{\partial\Delta\vec{a}}{\partial\vec{x}}\right)_O + \frac{1}{c^2}\left\{A_X + (A_{AO} - X_X)\left(\frac{\partial\vec{a}^{(N)}}{\partial\vec{x}}\right)_O\right\}\right]\vec{X}$$

$$+\left[\left(\frac{\partial\Delta\vec{a}}{\partial\vec{v}}\right)_O+\frac{A_{VO}}{c^2}\right]\vec{V}+\frac{T_1}{c^2}\left(\frac{\partial\vec{a}^{(N)}}{\partial t}\right)_O+\frac{1}{c^2}\left[A_v-X_v\left(\frac{\partial\vec{a}^{(N)}}{\partial\vec{x}}\right)_O\right]\vec{v}_O$$

$$+\left(\frac{A_a}{c^2}\right)\vec{a}_O+\left(\frac{A_j}{c^2}\right)\vec{j}_O. \tag{50}$$

3. Keplerian Motion

In order to obtain a further explicit expression of $\vec{A}$, we must specify the form of global coordinate acceleration. As a simple case, we assume that the spinning body, of which mass we ignore, moves on a Keplerian orbit around a gravitating central body. In this section, we call the spinning body the Earth, E, and the gravitating body the Sun, S, respectively.

3.1. Body-Centric Coordinate Acceleration

The basic quantities to express the transformation laws are specified[6] as

$$\phi_E=\frac{\mu_S}{r_E}, \tag{51}$$

$$\vec{a}_E^{(N)}=-\left(\frac{\mu_S}{r_E^3}\right)\vec{x}_E, \tag{52}$$

$$\vec{j}_E=-\left(\frac{\mu_S}{r_E^3}\right)\left[\vec{v}_E-3\left(\frac{\vec{x}_E\cdot\vec{v}_E}{r_E^2}\right)\vec{x}_E\right], \tag{53}$$

$$\phi=\frac{\mu_S}{r}, \tag{54}$$

$$\vec{a}^{(N)}=-\left(\frac{\mu_S}{r^3}\right)\vec{x}, \tag{55}$$

$$\Delta\vec{a}=\left(\frac{\mu_S}{c^2r^3}\right)\left[\left\{2(\beta+\gamma)\phi-\gamma\vec{v}^2\right\}\vec{x}+2(\gamma+1)\,(\vec{x}\cdot\vec{v})\,\vec{v}\right], \tag{56}$$

where $\mu_S\equiv GM_S$, $r\equiv|\vec{x}|$, and $r_E\equiv|\vec{x}_E|$. The coordinate origin of the global coordinate system is the Sun.

---

[6] Note the change of the subscript O to E.

By using these, we obtain the necessary partial derivatives and the associated quantities to evaluate $\Delta\vec{A}$ as

$$\left(\frac{\partial\vec{a}^{(N)}}{\partial t}\right)_E = \left(\frac{\partial\vec{a}^{(N)}}{\partial\vec{v}}\right)_E = 0, \tag{57}$$

$$\vec{A}^{(N)} = \left(\frac{\partial\vec{a}^{(N)}}{\partial\vec{x}}\right)_E \vec{X} = -\left(\frac{\mu_S}{r_E^3}\right)\left[\vec{X} - \left(\frac{3}{r_E^2}\right)\left(\vec{x}_E\cdot\vec{X}\right)\vec{x}_E\right], \tag{58}$$

$$\left(\frac{\partial\Delta\vec{a}}{\partial\vec{x}}\right)_E \vec{X} = \left(\frac{\mu_S}{c^2 r_E^3}\right)\left[\left\{\frac{2(\beta+\gamma)\mu_S}{r_E} - \gamma\vec{v}_E^2\right\}\vec{X} - \left(\frac{8(\beta+\gamma)\mu_S}{r_E^3} - \frac{3\gamma\vec{v}_E^2}{r_E^2}\right)\left(\vec{x}_E\cdot\vec{X}\right)\vec{x}_E\right.$$

$$\left. +2(\gamma+1)\left(\vec{v}_E\cdot\vec{X}\right)\vec{v}_E - \left(\frac{6(\gamma+1)\left(\vec{x}_E\cdot\vec{v}_E\right)}{r_E^2}\right)\left(\vec{x}_E\cdot\vec{X}\right)\vec{v}_E\right], \tag{59}$$

$$\left(\frac{\partial\vec{a}^{(N)}}{\partial\vec{x}}\right)_E \vec{v}_E = -\left(\frac{\mu_S}{r_E^3}\right)\left[\vec{v}_E - 3\left(\frac{\vec{x}_E\cdot\vec{v}_E}{r_E^2}\right)\vec{x}_E\right], \tag{60}$$

$$\left(\frac{\partial\Delta\vec{a}}{\partial\vec{v}}\right)_E \vec{V} = 2\left(\frac{\mu_S}{c^2 r_E^3}\right)\left[(\gamma+1)\left\{\left(\vec{x}_E\cdot\vec{v}_E\right)\vec{V} + \left(\vec{x}_E\cdot\vec{V}\right)\vec{v}_E\right\} - \gamma\left(\vec{v}_E\cdot\vec{V}\right)\vec{x}_E\right], \tag{61}$$

$$A_X = \gamma\left(\frac{\mu_S}{r_E^3}\right)\left[\frac{\mu_S}{r_E} - \vec{v}_E^2 + 3\left(\frac{\vec{x}_E\cdot\vec{v}_E}{r_E}\right)^2\right], \tag{62}$$

$$A_{VE} = -2(\gamma+2)\left(\frac{\mu_S}{r_E^3}\right)\left(\vec{x}_E\cdot\vec{v}_E\right), \tag{63}$$

$$A_{AE} = (\gamma+2)\left(\frac{\mu_S}{r_E}\right) + \vec{v}_E^2, \tag{64}$$

$$X_X = \gamma\left(\frac{\mu_S}{r_E}\right), \tag{65}$$

$$A_v = -\left(\frac{\mu_S}{r_E^3}\right)\left[\vec{v}_E\cdot\vec{X} + \vec{x}_E\cdot\vec{V} - \frac{3}{r_E^2}\left(\vec{x}_E\cdot\vec{X}\right)\left(\vec{x}_E\cdot\vec{v}_E\right)\right], \tag{66}$$

$$X_v = A_j = \frac{-1}{2}\left(\vec{v}_E\cdot\vec{X}\right), \tag{67}$$

$$A_a = -\left(\frac{\mu_S}{r_E^3}\right)\left(\vec{x}_E \cdot \vec{X}\right) + \vec{v}_E \cdot \vec{V}. \tag{68}$$

Then $\Delta\vec{A}$ is evaluated as

$$\begin{aligned}\Delta\vec{A}\left(T, \vec{X}, \vec{V}\right) = \left(\frac{\mu_S}{c^2 r_E^3}\right)\Bigg[&\left\{(2\beta+3\gamma-2)\left(\frac{\mu_S}{r_E}\right) - (2\gamma+1)\vec{v}_E^2 + 3\gamma\left(\frac{\vec{x}_E\cdot\vec{v}_E}{r_E}\right)^2\right\}\vec{X} \\ &-2\left(\vec{x}_E\cdot\vec{v}_E\right)\vec{V} - \frac{1}{r_E^2}\left\{(8\beta+8\gamma-7)\left(\frac{\mu_S}{r_E}\right) + 3(\gamma-1)\vec{v}_E^2\right\}\left(\vec{x}_E\cdot\vec{X}\right)\vec{x}_E \\ &+(2\gamma+1)\left(\vec{v}_E\cdot\vec{X}\right)\vec{v}_E - 3(2\gamma+1)\left(\frac{\vec{x}_E\cdot\vec{v}_E}{r_E^2}\right)\left(\vec{x}_E\cdot\vec{X}\right)\vec{v}_E \\ &-(2\gamma+1)\left(\vec{v}_E\cdot\vec{V}\right)\vec{x}_E + (2\gamma+1)\left(\vec{x}_E\cdot\vec{V}\right)\vec{v}_E\Bigg].\end{aligned} \tag{69}$$

The last two terms are rewritten as a Coriolis acceleration as

$$\Delta_g\vec{A} = 2\vec{\Omega}_g \times \vec{V} \tag{70}$$

where

$$\vec{\Omega}_g \equiv \frac{1}{c^2}\left(\gamma + \frac{1}{2}\right)\vec{v}_E \times \vec{a}_E^{(N)} \tag{71}$$

is the angular velocity vector of de Sitter's geodesic rotation (Fukushima 1991). Namely this term appears because we adopted the kinematic non-rotation convention in defining the body-centric coordinates. Since its effect has been studied extensively, we will put the term outside of our scope hereafter.

3.2. Torque

By substituting the remaining acceleration into the definition of torque, Eq.(11), we obtain the follwing explicit expression of the post-Newtonian correction to the torque:

$$\Delta_A\vec{N} - \Delta_g\vec{N} = \Delta_L\vec{N} + \Delta_x\vec{N} + \Delta_v\vec{N} + \Delta_{xv}\vec{N} \tag{72}$$

where $\Delta_g\vec{N}$ is the torque corresponding to $\Delta_g\vec{A}$, the Coriolis acceleration casued by the geodesic rotation, and the other are

$$\Delta_L\vec{N} = -2\left(\frac{\mu_S}{c^2 r_E^3}\right)\left(\vec{x}_E\cdot\vec{v}_E\right)\vec{L}^{(N)}, \tag{73}$$

$$\Delta_x \vec{N} = -\left[(8\beta + 14\gamma - 13) - 3(\gamma - 1)\left(\frac{r_E}{a_E}\right)\right]\left(\frac{\mu_S^2}{c^2 r_E^6}\right)\left\{\vec{x}_E \times \left(\mathcal{I}^{(N)}\vec{x}_E\right)\right\}, \tag{74}$$

$$\Delta_v \vec{N} = (2\gamma + 1)\left(\frac{\mu_S}{c^2 r_E^3}\right)\left\{\vec{v}_E \times \left(\mathcal{I}^{(N)}\vec{v}_E\right)\right\}, \tag{75}$$

$$\Delta_{xv}\vec{N} = -3\left(\gamma + \frac{1}{2}\right)\left(\frac{\mu_S}{c^2 r_E^5}\right)(\vec{x}_E \cdot \vec{v}_E)\left[\mathcal{I}^{(N)}\{\vec{x}_E \times \vec{v}_E\}\right.$$

$$\left. + \vec{x}_E \times \left(\mathcal{I}^{(N)}\vec{v}_E\right) + \vec{v}_E \times \left(\mathcal{I}^{(N)}\vec{x}_E\right)\right]. \tag{76}$$

See Appendix for the derivation. Here a_E is the semi-major axis of the Keplerian orbit, $\vec{L}^{(N)}$ is the Newtonian spin angular momentum vector defined as

$$\vec{L}^{(N)} \equiv \int_T \rho^{(N)}\, \vec{X} \times \vec{V}\, \mathrm{d}^3\vec{X}, \tag{77}$$

and $\mathcal{I}^{(N)}$ is the moment of inertia tensor of the spinning body defined as

$$\mathcal{I}^{(N)} \equiv \int_T \rho^{(N)}\, \left[\left(\vec{X}\right)^2 \mathcal{E} - \vec{X} \otimes \vec{X}\right]\, \mathrm{d}^3\vec{X}, \tag{78}$$

where $\mathcal{E}$ is the unit tensor and $\otimes$ denotes the direct product. In the above derivation, we used the energy integral of the Keplerian motion

$$\frac{\vec{v}_E^2}{2} - \frac{\mu_S}{r_E} = \frac{-\mu_S}{2a_E}. \tag{79}$$

3.3. Approximate Solution for $\Delta_L \vec{N}$

Let us obtain an approximate time-dependence of the post-Newtonian torque by expanding them in terms of the eccentricity of the Keplerian orbit, which is usually small as

$$e_E = 0.01670862 \tag{80}$$

for the case of the Earth around the Sun[7] .

[7] Actually, we approximate the body moving around the Sun not as the Earth but as the Earth-Moon Barycenter (EMB)

First of all, let us examine the term $\Delta_L \vec{N}$. This vector is proportional to $\vec{L}^{(N)}$, the Newtonian spin angular momentum vector. If we ignore the differences among three axes, the angular momentum axis, the angular velocity axis, and the figure axis, then this torque is approximately parallel with the z-axis. This means that it hardly disturbes the axis of rotation but affects the speed of rotation. Namely it has negiligible effects on the precession and nutation but causes a variation of Earth's angular velocity as

$$\frac{\mathrm{d}\Delta_L \Omega}{\mathrm{dt}} = -2\Omega_0 \left(\frac{\mu_S}{c^2 r_E^3} \right) (\vec{x}_E \cdot \vec{v}_E) \tag{81}$$

where

$$\Omega_0 = (7.2921150 \pm 0.0000001) \times 10^{-5} \text{ rad/s} \tag{82}$$

is the mean angular velocity of the Earth rotation (Groten 2000). This is easily integrated as

$$\Delta_L \Omega = \Omega_L \left(\frac{e_E + \cos f_E}{1 - e_E^2} \right) = \Omega_L \left(\cos \ell_E + e_E \cos 2\ell_E + \cdots \right), \tag{83}$$

where f_E and ℓ_E are the true and the mean[8] anomalies of the EMB, respectively. We added an integration constant such that the time average be zero since its contribution will be embedded in the uncertainty of Ω_0. Here the coefficient is expressed as

$$\Omega_L = 2\Omega_0 \left(\frac{\mu_S}{c^2 a_E} \right) e_E. \tag{84}$$

Noting that the factor of general relativistic effect for the case of the EMB's orbit around the Sun is evaluated (Fukushima 1991) as

$$\frac{\mu_S}{c^2 a_E} = 9.870647451 \times 10^{-9}, \tag{85}$$

we evaluate the coefficient Ω_L as

$$\Omega_L = 2.4053026 \times 10^{-14} \text{ rad/s}. \tag{86}$$

This amplitude is significantly large in the sense that it is roughly the same as that of the annual term of the Newtonian tidal variation (Yoder *et al.* 1981). As a result, we express Eq.(83) more explicitly as

$$\Delta_L \Omega = 2.405 \cos \ell_E + 0.040 \cos 2\ell_E, \tag{87}$$

---

[8] This is the same as the so-called mean anomaly of the Sun, ℓ', in terms of Delauney angles.

where the unit is 10^{-14} rad/s.

If we integrate Eq.(83) once again with respect to time, we obtain the perturbation of UT1 as

$$\Delta_L \mathrm{UT1} = U_L \sin u_E = U_L \left(\sin \ell_E + \frac{e_E}{2} \sin 2\ell_E + \cdots \right) \tag{88}$$

where u_E is the eccentric anomaly of the EMB's orbit. Here the coefficient is expressed as

$$U_L = 86400 \left(\frac{\Omega_L}{n_E} \right) = 10.437964 \text{ ms} \tag{89}$$

where

$$n_E \equiv \sqrt{\frac{\mu_S}{a_E^3}} = 6.2830662 \text{ rad/Julian year} = 1.9909835 \times 10^{-7} \text{ rad/s} \tag{90}$$

is the mean motion of the EMB's orbit. The resulting explicit expression is

$$\Delta_L \mathrm{UT1} = 10.4380 \sin \ell_E + 0.0872 \sin 2\ell_E \tag{91}$$

where the unit is ms. This is also significant.

In summary, this term causes an appreciable effect in the LOD measurement and must be taken into account in the precision UT1 analysis.

3.4. Approximate Solution for $\Delta_x \vec{N}$

Next, consider the second term $\vec{N}_x$. Before doing so, we note that the Newtonian torque is expressed in this approximation as

$$\vec{N}^{(N)} = 3 \left(\frac{\mu_S}{r_E^5} \right) \left[\vec{x}_E \times (\mathcal{I} \vec{x}_E) \right]. \tag{92}$$

Namely $\Delta_x \vec{N}$ is simply proportional to $\vec{N}^{(N)}$ with an almost constant ratio

$$-\left(\frac{1}{3} \right) \left[(8\beta + 14\gamma - 13) \left(\frac{a_E}{r_E} \right) - 3(\gamma - 1) \right] \left(\frac{\mu_S}{c^2 a_E} \right) \approx -3 \left(\frac{\mu_S}{c^2 a_E} \right) (1 + e_E \cos \ell_E + \cdots) \tag{93}$$

where we approximated the PPN parameters as $\beta = \gamma = 1$, which is the case of Einstein's general theory of relativity. Thus the constant offset results simply the modification of the Newtonian amplitudes of the solar part of the precession and nutation. In the acutual process of data

analysis, such effects will be mostly absorbed by readjusting the magnitude of the moments of inertia, which is a solve-for parameter. In other words, one must take this effect into account when estimating precisely the value of dynamical flattening of the Earth. On the other hand, it is easily conjectured that the small annual term in the above ratio mainly results in the modification of the annual term of the nutation in longitude.

To be more specific, we express the quantities in the mean equatorial coordinates[9] and ignore the second and higher order effects of the eccentricity, e_E. Also we assume that $\mathcal{I}^{(N)}$ is axially symmetric. Then the resulting expressions of basic quantities become

$$\vec{x}_E = a_E \begin{pmatrix} \xi_E \\ \eta_E \cos\varepsilon \\ \eta_E \sin\varepsilon \end{pmatrix}, \qquad \frac{a_E}{r_E} = 1 + e_E \cos\ell_E, \qquad \mathcal{I}^{(N)} = \begin{pmatrix} A & 0 & 0 \\ 0 & A & 0 \\ 0 & 0 & C \end{pmatrix}. \tag{94}$$

Here ξ_E and η_E are the ecliptic cordinates of $\vec{x}_E$ divided by a_E. They are expanded as

$$\xi_E = \cos L_E - \frac{3e_E}{2}\cos\omega_E + \frac{e_E}{2}\cos\left(L_E + \ell_E\right), \tag{95}$$

$$\eta_E = \sin L_E - \frac{3e_E}{2}\sin\omega_E + \frac{e_E}{2}\sin\left(L_E + \ell_E\right), \tag{96}$$

where ω_E is the argument of perihelion of the EMB, $L_E \equiv \ell_E + \omega_E$ is the mean longitude of the EMB[10] , A and C are the smaller and the larger principal moments of inertia, respectively.

These lead to[11] the expression of $\vec{N}_x$ as

$$\vec{N}_x = -9\left(\frac{\mu_S^2}{c^2 r_E^6}\right)\left[\vec{x}_E \times \left(\mathcal{I}^{(N)}\vec{x}_E\right)\right] = -\left(\frac{\mu_S}{c^2 a_E}\right)\left(\frac{9(C-A)\mu_S \sin\varepsilon}{2a_E^3}\right)$$

---

[9] This is the coodrinate system such that its z-axis is in the direction of the North pole and its x-axis is in the direction of mean equinox.

[10] This is 180° offset the so-called mean longitude of the Sun. In terms of Delauney angles, it is expressed as $L_E \equiv L' + 180° = F + \Omega - D + 180°$.

[11] The same approximation leads to the Newtonian torques as

$$\vec{N}^{(N)} = 3\left(\frac{\mu_S}{r_E^5}\right)\left[\vec{x}_E \times (\mathcal{I}\vec{x}_E)\right] = \frac{3(C-A)\mu_S \sin\varepsilon}{2a_E^3}$$

$$\times \begin{pmatrix} \cos\varepsilon\left[1 - \cos 2L_E + 3e_E\cos\ell_E + (e_E/2)\cos\left(2L_E - \ell_E\right) - (7e_E/2)\cos\left(2L_E + \ell_E\right)\right] \\ -\sin 2L_E + (e_E/2)\sin\left(2L_E - \ell_E\right) - (7e_E/2)\sin\left(2L_E + \ell_E\right) \\ 0 \end{pmatrix}. \tag{97}$$

Note the similarity and/or difference between this and the expression of $\vec{N}_x$.

$$\times \begin{pmatrix} \cos\varepsilon\,[1-\cos 2L_E+4e_E\cos\ell_E-4e_E\cos(2L_E+\ell_E)] \\ -\sin 2L_E-4e_E\sin(2L_E+\ell_E) \\ 0 \end{pmatrix}. \tag{98}$$

Clearly it has no effect on the speed of Earth rotation nor on the variation of UT1. By using the so-called Poisson approximation[12] , we have an approximate equation of time development of the corresponding correction to the precession/nutation angles as

$$\sin\varepsilon\frac{\mathrm{d}\Delta_x\psi}{\mathrm{dt}}=\frac{\left(\vec{N}_x\right)_X}{\Omega_0 C}, \qquad \frac{\mathrm{d}\Delta_x\varepsilon}{\mathrm{dt}}=\frac{\left(\vec{N}_x\right)_Y}{\Omega_0 C}. \tag{99}$$

This is easily integrated as

$$\Delta_x\psi=-3q\cos\varepsilon\left[n_E t-\frac{1}{2}\sin 2L_E+4e_E\sin\ell_E-\frac{4e_E}{3}\sin(2L_E+\ell_E)\right], \tag{100}$$

$$\Delta_x\varepsilon=-3q\sin\varepsilon\left[\frac{1}{2}\cos 2L_E+\frac{4e_E}{3}\cos(2L_E+\ell_E)\right], \tag{101}$$

where the common factor q is expressed as

$$q\equiv\frac{3}{2}\left(\frac{\mu_S}{c^2 a_E}\right)\left(\frac{C-A}{C}\right)\left(\frac{n_E}{\Omega_0}\right) \tag{102}$$

Let us prepare the numerical values needed to evaluate these solutions. In the case of the Earth, the best estimate of the dynamical flattening (Shirai and Fukushima 2000) is

$$\frac{C-A}{C}=0.0032737914. \tag{103}$$

Also the latest best estimate of the obliquity of the ecliptic (Fukushima 2001) is

$$\varepsilon=(84381.4059\pm 0.0003)''. \tag{104}$$

The important constant factors are its sine and cosine;

$$\sin\varepsilon=0.397776969, \qquad \cos\varepsilon=0.917482143. \tag{105}$$

---

[12] This means the ignorance of the time derivative of smaller components of the spin angular velocity, $\mathrm{d}\Omega_A/\mathrm{dt}$ and $\mathrm{d}\Omega_B/\mathrm{dt}$, in the Eulerian equation of rotational motion.

Then the common factor is evaluated as

$$q = 1.32340997 \times 10^{-13} \tag{106}$$

Then the corresponding correction to the precession constant becomes

$$\Delta_x p = -3qn_E \cos\varepsilon = -47.2\ \mu\text{as/century}. \tag{107}$$

This is marginally meaningful when compared with the latest estimates of the correction to the IAU 1976 value of the general precession constant (e.g. Shirai and Fukushima 2001) such as

$$\Delta p = -0.29856 \pm 0.00030\ ''\text{/century}. \tag{108}$$

On the other hand, the corrections to the nutation are rewritten more explicitly as

$$\Delta_x \psi = 37.6 \sin 2L_E - 5.0 \sin \ell_E + 1.7 \sin (2L_E + \ell_E)\,, \tag{109}$$

$$\Delta_x \varepsilon = -16.3 \cos 2L_E - 0.7 \cos (2L_E + \ell_E)\,, \tag{110}$$

where the unit is nano arcseccond. These are quite small when compared with the precision of recent and near-future VLBI nutation observation, say 10 μas.

In summary, only the correction to the precession constant will be marginally meaningful.

3.5. Approximate Solution for $\Delta_v \vec{N}$

Third, $\Delta_v \vec{N}$ is quite alike $\Delta_x \vec{N}$. The major difference is the appearance of $\vec{v}_E$ in place of $\vec{x}_E$. Roughly speaking, apart from the magnitude difference of the factor 3, the constant terms of these two torques, $\Delta_x \vec{N}$ and $\Delta_v \vec{N}$, are the same while their main periodic terms, the semi-annual term, are mostly in the reverse sense.

To be more specific, we follow the same approximation in the previous subsection and express the orbital velocity as

$$\vec{v}_E = n_E a_E \begin{pmatrix} -\sin L_E - e_E \sin (L_E + \ell_E) \\ \cos\varepsilon\,[\cos L_E + e_E \cos (L_E + \ell_E)] \\ \sin\varepsilon\,[\cos L_E + e_E \cos (L_E + \ell_E)] \end{pmatrix}. \tag{111}$$

Then the torque is expressed as

$$\Delta_v \vec{N} = \left(\frac{\mu_S}{c^2 a_E}\right) \left(\frac{3(C-A)\mu_S \sin\varepsilon}{2a_E^3}\right) \begin{pmatrix} \xi'_E \cos\varepsilon \\ -\eta'_E \\ 0 \end{pmatrix}, \tag{112}$$

where

$$\xi'_E \equiv 1 + \cos 2L_E + 5e_E \cos \ell_E + (3e_E/2)\cos(2L_E - \ell_E) + (7e_E/2)\cos(2L_E + \ell_E)\,, \tag{113}$$

$$\eta'_E \equiv \sin 2L_E + (3e_E/2)\sin(2L_E - \ell_E) + (7e_E/2)\sin(2L_E + \ell_E)\,, \tag{114}$$

and we approximated $\gamma = 1$. Similarly in the previous subsection, the speed and angle of of Earth rotation are not affected.

By using the Poisson approximation again, we integrate the corresponding correction to the Euler's equation as

$$\Delta_v \psi = q\cos\varepsilon \int \xi'_E \mathrm{d}\ell_E$$

$$= q\cos\varepsilon \left[n_E t + \frac{1}{2}\sin 2L_E + 5e_E \sin \ell_E + \frac{3e_E}{2}\sin(2L_E - \ell_E) + \frac{7e_E}{6}\sin(2L_E + \ell_E) \right], \tag{115}$$

$$\Delta_v \varepsilon = -q\sin\varepsilon \int \eta'_E \mathrm{d}\ell_E$$

$$= q\sin\varepsilon \left[\frac{1}{2}\cos 2L_E + \frac{3e_E}{2}\cos(2L_E - \ell_E) + \frac{7e_E}{6}\cos(2L_E + \ell_E) \right]. \tag{116}$$

Then the corresponding correction to the precession constant becomes

$$\Delta_v p = q n_E \cos\varepsilon = \frac{-\Delta_x p}{3} = 15.7\ \mu\text{as/century}. \tag{117}$$

On the other hand, the corrections to the nutation measured in the unit of nano arcseccond are given as

$$\Delta_v \psi = 12.5\sin 2L_E + 2.1\sin \ell_E + 0.6\sin(2L_E - \ell_E) + 0.5\sin(2L_E + \ell_E)\,, \tag{118}$$

$$\Delta_v \varepsilon = 5.4\cos 2L_E + 0.3\cos(2L_E - \ell_E) + 0.2\cos(2L_E + \ell_E)\,. \tag{119}$$

Again, these are quite small.

3.6. Approximate Solution for $\Delta_{xv}\vec{N}$

Finally, just similarly to the case of $\Delta_L\vec{N}$, $\Delta_{xv}\vec{N}$ has a significant feature that it remains non-zero in the limit the moments of inertia is spherically symmetric, i.e. $A = C$. Actually it is approximated as

$$\Delta_{xv}\vec{N} = -3\left(\gamma+\frac{1}{2}\right)\left(\frac{\mu_S}{c^2 r_E^5}\right)(\vec{x}_E\cdot\vec{v}_E)\left[\mathcal{I}^{(N)}(\vec{x}_E\times\vec{v}_E)+\vec{x}_E\times\left(\mathcal{I}^{(N)}\vec{v}_E\right)+\vec{v}_E\times\left(\mathcal{I}^{(N)}\vec{x}_E\right)\right]$$

$$= \frac{9}{2}\left(\frac{\mu_S}{c^2 a_E}\right)e_E n_E^2 s_E\begin{pmatrix}(C-A)s_\psi\sin\varepsilon\cos\varepsilon\\ A\sin\varepsilon+(C-A)s_\varepsilon\sin\varepsilon\\ -C\cos\varepsilon\end{pmatrix}. \tag{120}$$

Here

$$s_E \equiv \left(\frac{a_E}{r_E}\right)^5\sin u_E = \sin\ell_E + 3e_E\sin 2\ell_E \tag{121}$$

$$s_\psi \equiv 2\eta_E\frac{\mathrm{d}\eta_E}{\mathrm{d}\ell_E} = \sin 2L_E - \frac{3e_E}{2}\sin(2L_E-\ell_E)+\frac{3e_E}{2}\sin(2L_E+\ell_E), \tag{122}$$

$$s_\varepsilon \equiv \xi_E\frac{\mathrm{d}\eta_E}{\mathrm{d}\ell_E}+\eta_E\frac{\mathrm{d}\xi_E}{\mathrm{d}\ell_E} = \cos 2L_E - \frac{3e_E}{2}\cos(2L_E-\ell_E)+\frac{3e_E}{2}\cos(2L_E+\ell_E), \tag{123}$$

and therefore

$$s_E s_\psi = \frac{1}{2}\cos(2L_E-\ell_E)-\frac{1}{2}\cos(2L_E+\ell_E)-\frac{9e_E}{4}\cos(2L_E+2\ell_E)$$

$$+\frac{3e_E}{2}\cos 2L_E+\frac{3e_E}{4}\cos 2\omega_E, \tag{124}$$

$$s_E s_\varepsilon = -\frac{1}{2}\sin(2L_E-\ell_E)+\frac{1}{2}\sin(2L_E+\ell_E)+\frac{9e_E}{4}\sin(2L_E+2\ell_E)$$

$$-\frac{3e_E}{2}\sin 2L_E-\frac{3e_E}{4}\sin 2\omega_E. \tag{125}$$

By using the Poisson approximation once again, we obtain the corresponding correction to the Euler's equation as

$$\frac{\mathrm{d}\Delta_{xv}\psi}{\mathrm{dt}} = 3\left(qn_E e_E\cos\varepsilon\right)s_E s_\psi, \tag{126}$$

$$\frac{\mathrm{d}\Delta_{xv}\varepsilon}{\mathrm{dt}} = 3\left(q' n_E e_E \sin\varepsilon\right) s_E + 3\left(q n_E e_E \sin\varepsilon\right) s_E s_\varepsilon, \tag{127}$$

$$\frac{\mathrm{d}\Delta_{xv}\Omega}{\mathrm{dt}} = -\Omega_{xv} n_E s_E, \tag{128}$$

where

$$q' = q''\left(\frac{A}{C}\right), \qquad q'' = \frac{3}{2}\left(\frac{\mu_S}{c^2 a_E}\right)\left(\frac{n_E}{\Omega_0}\right), \qquad \Omega_{xv} = \frac{9}{2}\left(\frac{\mu_S}{c^2 a_E}\right) e_E n_E \cos\varepsilon. \tag{129}$$

These are easily integrated as

$$\Delta_{xv}\psi = (3qe_E\cos\varepsilon)\left[\frac{3e_E}{4}(\cos 2\omega_E)\, n_E t + \frac{1}{2}\sin(2L_E - \ell_E) - \frac{1}{6}\sin(2L_E + \ell_E)\right.$$

$$\left. -\frac{9e_E}{16}\sin(2L_E + 2\ell_E) + \frac{3e_E}{4}\sin 2L_E\right], \tag{130}$$

$$\Delta_{xv}\varepsilon = -(3q' e_E \sin\varepsilon)\left[\cos\ell_E + \frac{3e_E}{2}\cos 2\ell_E\right] + (3qe_E\sin\varepsilon)\left[-\frac{3e_E}{4}(\sin 2\omega_E)\, t\right.$$

$$\left. +\frac{1}{2}\cos(2L_E - \ell_E) - \frac{1}{6}\cos(2L_E + \ell_E) - \frac{9e_E}{16}\cos(2L_E + 2\ell_E) + \frac{3e_E}{4}\cos 2L_E\right], \tag{131}$$

$$\Delta_{xv}\Omega = \Omega_{xv}\left(\cos\ell_E + \frac{3e_E}{2}\cos 2\ell_E\right). \tag{132}$$

The basic quantities are numerically estimated as

$$q'' = 4.0425095 \times 10^{-11}, \qquad q' = 4.0292752 \times 10^{-11} \tag{133}$$

$$3qe_E\cos\varepsilon = 6.086307 \times 10^{-15}, \qquad 3qe_E\sin\varepsilon = 2.638736 \times 10^{-15}, \tag{134}$$

$$3q' e_E \sin\varepsilon = 8.0339366 \times 10^{-13}, \qquad 3q'' e_E \cos\varepsilon = 1.859133 \times 10^{-12}. \tag{135}$$

$$\Omega_{xv} = 1.355701 \times 10^{-16}\ \mathrm{rad/s} \tag{136}$$

Then, we numerically evaluate the secular component[13] in the unit of nano arcsec/century as

$$\Delta_{xv}p = \frac{9}{4} q e_E^2 n_E \cos 2\omega_E \cos\varepsilon = 9.884449\,(\cos 2\omega_E), \tag{137}$$

---

[13] Actually, this term will be a very long periodic term, the term of the period of one circulation of ω_E.

$$\Delta_{xv}\dot{\varepsilon} = \frac{9}{4} q e_E^2 n_E \sin 2\omega_E \sin\varepsilon = 4.285431\,(\sin 2\omega_E)\,. \tag{138}$$

Unfortunately these are negligiblly small.

On the other hand, we evaluate the nutation in the units of nano arcsec as

$$\Delta_{xv}\psi = 0.6\sin(2L_E - \ell_E) - 0.2\sin(2L_E + \ell_E)\,, \tag{139}$$

$$\Delta_{xv}\varepsilon = -165.7\cos\ell_E - 4.2\cos 2\ell_E + 0.3\cos(2L_E - \ell_E) - 0.1\cos(2L_E + \ell_E)\,. \tag{140}$$

Again, even the largest term, the annual term of $\Delta\varepsilon$ is still small.

While the variation of the angular velocity is evaluated in the unit of 10^{-14} rad/s as

$$\Delta_{xv}\Omega = 0.014\cos\ell_E \tag{141}$$

This is once more integrated with respect to time and evaluated in the unit of ms as

$$\Delta_{xv}\mathrm{UT1} = U_{xv}\sin\ell_E = 0.0588\sin\ell_E \tag{142}$$

where

$$U_{xv} = 86400\left(\frac{\Omega_{xv}}{n_E}\right) = 0.0588 \text{ ms.} \tag{143}$$

This is marginally significant.

3.7. Summary of Approximate Solutions

Here we sum up the obtained solutions of the post-Newtonian corrections.

First, the correction to the precession constant is

$$\Delta_{pN}p = \Delta_x p + \Delta_y p + \Delta_{xv}p = -31.5\ \mu\text{as/century.} \tag{144}$$

Clearly the contribution to the drift of obliquity of the ecliptic is negligible.

Next the correction to the nutation in the unit of nano arcsec become

$$\Delta_{pN}\psi = \Delta_x\psi + \Delta_v\psi + \Delta_{xv}\psi$$

$$= 50.1\sin 2L_E - 2.9\sin\ell_E + 2.0\sin(2L_E + \ell_E) + 1.2\sin(2L_E - \ell_E)\,, \tag{145}$$

$$\Delta_{pN}\varepsilon = \Delta_x\varepsilon + \Delta_v\varepsilon + \Delta_{xv}\varepsilon$$

$$= -165.7\cos\ell_E - 10.9\cos 2L_E - 4.2\cos 2\ell_E - 0.6\cos(2L_E + \ell_E) + 0.6\cos(2L_E - \ell_E)\,. \quad (146)$$

While the variation of the angular velocity is evaluated in the unit of 10^{-14} rad/s as

$$\Delta_{pN}\Omega = \Delta_L\Omega + \Delta_{xv}\Omega = 2.415\cos\ell_E + 0.040\cos 2\ell_E, \quad (147)$$

and that of UT1 in the unit of ms becomes

$$\Delta_{pN}\mathrm{UT1} = \Delta_L\mathrm{UT1} + \Delta_{xv}\mathrm{UT1} = 10.4968\sin\ell_E + 0.0872\sin 2\ell_E. \quad (148)$$

If we compare these results with the latest precision of nutation and UT1 observations by using space techniques, we know that significant are the effects on the speed of Earth rotation and the variation of UT1, namely Eqs (147) and (148). Also marginally meaningful is the additional correction to the precession constant, -31.5 μas/century.

4. Conclusion

Triggered by the development of recent and near-future precision observations, especially by the recent progress in VLBI observation, we reconsidered the rotational motion of the Earth in the post-Newtonian framework. First, we derived the post-Newtonian transformation laws of the coordinate velocity and of the coordinate acceleration between the solar-system-barycentric and the terrestrial coordinate systems. The latter formula lead us to an explicit expression of the torque in the post-Newtonian framework. Next, by assuming the so-called Poisson approximation, we integrated the post-Newtonian extension of the Eulerian equation of rotational motion of the Earth for the Sun's torque as the simplest case. Then, we derived a post-Newtonian correction to the precession and nutation and the variation of UT1 caused by the Sun.

Apart from the so-called geodesic precession and nutation, the most significant effects are those related to the rotation angle; the variation of the angular velocity of Earth rotation in the unit of 10^{-14} rad/s as $\Delta\Omega = 2.4\cos\ell'$ and the variation of UT1 in the unit of ms as $\Delta\mathrm{UT1} = 10.50\sin\ell' + 0.09\sin 2\ell'$ where ℓ' denotes the mean anomaly of the Sun, which is one of Delauney's angles. These are significant in the sense being comparable with the non-rigid tidal effects in the Newtonian framework.

In the current study, we concentrated ourselves to the effects of Sun's direct torque acting on the Earth. Naturally, the next target will be the contribution of the Moon.

REFERENCES

Bizouard C., Schastok, J., Soffel, M., and Souchay, J. 1992, Proc. Journees Systems de Reference Spatio-Temporels, 1992, 76

Bois, E., and Vokrouhlicky, D. 1995, A&A, 300, 559

Brumberg, V.A., Bretagnon, P., and Francou, G. 1993, A&A, 275, 651

Damour, T., Soffel, M., and Xu, C. 1991, Phys. Rev., D, 43, 3273

Damour, T., Soffel, M., and Xu, C. 1992, Phys. Rev., D, 45, 1017

Damour, T., Soffel, M., and Xu, C. 1993, Phys. Rev., D, 47, 3124

de Sitter, W. 1916, Mon. Not. R. Astron. Soc., 77, 155

Fukushima, T. 1991, A&A, 244, L11

Fukushima, T. 1995, A&A, 294, 895

Fukushima, T. 2001, Highlights of Astronomy, 12, in printing

Groten, E. 2000, Proc. IAU Colloq. 180, 337

IAU 2001, Transactions of IAU, 25A, in printing

Irwin, A., and Fukushima, T. 1999, A&A, A&A, 348, 642

Klioner, S.A., and Soffel, M. 1998, Highlights of Astronomy, 11A, 173

Shirai, T., and Fukushima, T. 2001, AJ, 121, vol.6, in printing

Voinov, A.V. 1988, Celest. Mech., 42, 293

Vokrouhlicky, D. 1996, Phys. Rev. D 52, 6894

APPENDIX

This preprint was prepared with the AAS LaTeX macros v4.0.

A. Derivation of Integral Form of Torque

Consider an integral of the type;

$$\vec{J} \equiv \int_T \rho\left(\vec{X}\right)\left(\vec{X}\cdot\vec{P}\right)\vec{X}\times\vec{Q}\,\mathrm{d}^3\vec{X}, \tag{A1}$$

where $\vec{P} \equiv (P_X, P_Y, P_Z)$ and $\vec{Q} \equiv (Q_X, Q_Y, Q_Z)$ are constant with respect to $\vec{X} \equiv (X, Y, Z)$.

By using the coordinate expressions of vectors in the integrand, the integral is rewritten more explicitly as

$$\vec{J} = \int_T \rho\left(\vec{X}\right)(XP_X + YP_Y + ZP_Z)\begin{pmatrix} YQ_Z - ZQ_Y \\ ZQ_X - XQ_Z \\ XQ_Y - YQ_X \end{pmatrix}\mathrm{d}^3\vec{X} \tag{A2}$$

By taking the principal axes of the moment of oinertia ellipsoid as the coordinate axes, we can nullify the moment products as

$$0 = \int_T \rho\left(\vec{X}\right)XY\,\mathrm{d}^3\vec{X} = \int_T \rho\left(\vec{X}\right)YZ\,\mathrm{d}^3\vec{X} = \int_T \rho\left(\vec{X}\right)ZX\,\mathrm{d}^3\vec{X}. \tag{A3}$$

Then, the resulting expression becomes

$$\vec{J} = \int_T \rho\left(\vec{X}\right)\begin{pmatrix} Y^2P_YQ_Z - Z^2P_ZQ_Y \\ Z^2P_ZQ_X - X^2P_XQ_Z \\ X^2P_XQ_Y - Y^2P_YQ_X \end{pmatrix}\mathrm{d}^3\vec{X}$$

$$= \begin{pmatrix} P_YQ_Z\int_T \rho\left(\vec{X}\right)Y^2\,\mathrm{d}^3\vec{X} - P_ZQ_Y\int_T \rho\left(\vec{X}\right)Z^2\,\mathrm{d}^3\vec{X} \\ P_ZQ_X\int_T \rho\left(\vec{X}\right)Z^2\,\mathrm{d}^3\vec{X} - P_XQ_Z\int_T \rho\left(\vec{X}\right)X^2\,\mathrm{d}^3\vec{X} \\ P_XQ_Y\int_T \rho\left(\vec{X}\right)X^2\,\mathrm{d}^3\vec{X} - P_YQ_X\int_T \rho\left(\vec{X}\right)Y^2\,\mathrm{d}^3\vec{X} \end{pmatrix}. \tag{A4}$$

Since the principal moments of inertia are expressed as

$$A \equiv \int_T \rho\left(\vec{X}\right)\left(Y^2+Z^2\right)\,\mathrm{d}^3\vec{X},\quad B \equiv \int_T \rho\left(\vec{X}\right)\left(Z^2+X^2\right)\,\mathrm{d}^3\vec{X},$$

$$C \equiv \int_T \rho\left(\vec{X}\right)\left(X^2+Y^2\right)\,\mathrm{d}^3\vec{X}, \tag{A5}$$

we have the relations as

$$\int_T \rho\left(\vec{X}\right)X^2\,\mathrm{d}^3\vec{X} = \frac{B+C-A}{2},\quad \int_T \rho\left(\vec{X}\right)Y^2\,\mathrm{d}^3\vec{X} = \frac{C+A-B}{2},$$

$$\int_T \rho\left(\vec{X}\right) Z^2 \, \mathrm{d}^3\vec{X} = \frac{A+B-C}{2}, \tag{A6}$$

Thus, we rewrite the above expression in the form as

$$\vec{J} = \frac{1}{2}\begin{pmatrix} (C+A-B)P_Y Q_Z - (A+B-C)P_Z Q_Y \\ (A+B-C)P_Z Q_X - (B+C-A)P_X Q_Z \\ (B+C-A)P_X Q_Y - (C+A-B)P_Y Q_X \end{pmatrix}$$

$$= \frac{1}{2}\begin{pmatrix} A\,(P_Y Q_Z - P_Z Q_Y) + [P_Y\,(CQ_Z) - P_Z\,(BQ_Y)] + [Q_Y\,(CP_Z) - Q_Z\,(BP_Y)] \\ B\,(P_Z Q_X - P_X Q_Z) + [P_Z\,(AQ_X) - P_X\,(CQ_Z)] + [Q_Z\,(AP_X) - Q_X\,(CP_Z)] \\ C\,(P_X Q_Y - P_Y Q_X) + [P_X\,(BQ_Y) - P_Y\,(AQ_X)] + [Q_X\,(BP_Y) - Q_Y\,(AP_X)] \end{pmatrix}$$

$$= \frac{1}{2}\left[\mathcal{I}\left\{\vec{P}\times\vec{Q}\right\} + \vec{P}\times\left(\mathcal{I}\vec{Q}\right) + \vec{Q}\times\left(\mathcal{I}\vec{P}\right)\right]. \tag{A7}$$

In the special case when $\vec{P}$ is parallel with $\vec{Q}$ such as $\vec{P} = k\vec{Q}$, then the above expression is simplified as

$$\vec{J} = \vec{P}\times\left(\mathcal{I}\vec{Q}\right). \tag{A8}$$

Orbital stability of Lagrange equilibrium point of Sun and Earth-Moon barycenter system

Hideyoshi Arakida

Department of Astronomical Science, Graduate University for Advanced Studies, 2-21-1, Osawa, Mitaka, Tokyo 181-8588 JAPAN

h.arakida@nao.ac.jp

Toshio Fukushima

National Astronomical Observatory of Japan, 2-21-1, Osawa, Mitaka, Tokyo 181-8588 JAPAN

Toshio.Fukushima@nao.ac.jp

ABSTRACT

We investigated the stability of Lagrangian triangular equilibrium point of Sun and Earth-Moon barycentric system. We took into account the realistic perturbations from Mercury to Pluto, and Moon and examined the difference from the restricted three body problem. We will show that both the short and long periods around the equilibrium point are the almost same as in the restrict and realistic cases, while there are some difference in the behaviors. In the case of restricted three body problem, the motion around the equilibrium point depends on the initial disposition, on the other hand, it is concerned in the a placement of the perturbers in the realistic case.

Subject headings: celestial mechanics — Lagrangian equilibrium point — orbital stability : method — numerical

1. Introduction

Lagrangian equilibrium Points from L_1 to L_5 are stable regions where the net of gravitational force vanishes. In the most works about Lagrangian points, the stability was discussed in the framework of restricted three body problem by both the mathematical and the astronomical interests. It is advantageous for the space missions to launch the spacecrafts into these stable regions because of making the steady station keeping easily. In fact, the some missions were carried out at Lagrangian point ; the solar observation satellite ISEE-3 (later ICE), and SOHO by NASA and ESA at L_1, and the several missions are planed ; the CMB observation satellite MAP, 8m-size space telescope NGST by NASA, the space Astrometry satellite GAIA by ESA, the infrared satellite SPICA by

ISAS at L_2, and the gravitational wave detecting project at the triangular equilibrium point of Sun-Earth system. So far, the researches of stability of Lagrangian points, especially L_4 and L_5 were mostly investigated in terms of the three body problem according to circumstances including the effect of solar radiation pressure or the perturbation from giant planet for study of the asteroids at triangular equilibrium point, and interests are payed attention to the long term stability of Sun-planet triangular equilibrium point such as the Trojan of Jupiter, or the possibility and existence of Saturn's Trojan group, the escape time from these stable regions, the populations of asteroids, and so on. However, the stability of satellites in the space mission at Lagrangian points hardly be examined until now since the short lifetime of satellite. In a little studies done before, the stability and satellite transfer into Lagrangian point are generally treated in the simple physical model, the restricted three body problem, and stability and orbital transfer into the Halo orbit are mainly examined by both of the analytical and the numerical.
See the textbooks of Gòmez, Llibre, Martìnez, and Simò (2000) and its bibliography about the study of Lagrangian equilibrium points.

Nevertheless, it seems that in the realistic problems it is important to take into account the perturbations from another planets for L_4 and L_5, and Earth's J_2 effect for L_1 and L_2. In this paper we will discuss the stability of triangular equilibrium points L_4 and L_5 of Sun and Earth-Moon barycentric system with paying attention to the perturbations from Mercury to Pluto. and Moon, and investigate the orbital evolution, and the difference from the restricted three body problem by the numerical integration.

2. Numerical Experiments

Let us investigate the stability of Lagrangian equilibrium points L_4 and L_4 of Sun and Earth-Moon barycentric system. We examine the stability and the orbital evolution when the initial condition of satellite is slightly shifted from the proper throwing point, that is, the complete Lagrangian point. And we compare with the results of restricted three body problem. We deal with the restricted perturbed two body problem, regarding the satellite as the test particle and including the perturbations from Mercury to Pluto, and Moon interacting under the Newtonian gravitational force. The positions and velocities of perturbers were taken from JPL's DE 405 package. Though we consider the Sun and Earth-Moon barycentric system, the perturbations of Earth and Moon were separated. We note that there was no difference even if we regarded the Earth-Noon barycentric system as the One point mass. We adopted the KS element approach for the equation of motion (Arakida and Fukushima 2001) because the KS approach reduce the numerical integration error dramatically (Arakida and Fukushima 2000, 2001). As the numerical integrator we applied the 8th order Adams-Bashforth method. Fig. ?? indicates the coordinate system used in this work. Here, the xy plane is the corotational coordinate system and the scale of this coordinate system is normalized by the real distance between Sun and Earth-Moon barycentric system r_e because of the

ecliptic orbit of Earth-Moon barycentric system. Hence in the xy plane, the distance between Sun and Earth-Moon barycenter is always unity. The XY plane is to rotate xy plane 60 degree towards counterclockwise and the origin of coordinate is transfered into the Lagrangian point. Table 1 represents the initial condition of satellite at the epoch. In order to investigate the orbital stability in the neighborhood of Lagrangian point, the initial conditions are chosen as the point on the radius a from the Lagrangian point and the angle, Φ is per 5 degree over $0 \leq \Phi < 360$ degree.

From now on, we express the numerical results. Fig. 2 and Fig. 3 show the time variation of Y axis of the realistic calculation (hereafter Full) and the restricted one (hereafter Restrict) for 10 years in the case of $\Phi = 45$ (deg.), respectively. Fig. 4 and Fig. ?? are the same as Fig. 2 and Fig. 3 but $\Phi = 90$ (deg.). Figs. 6-9 are the same as Figs. 2-?? but for 300 years. From these results, we find that both the short and long periods of orbital variation do not almost change even in the Full calculation, while the behavior is different. In spite of the same initial condition, in the case of Full the orbits are toward to the plus direction of Y axis, while in the case of Restrict these are toward to the minus direction. The most remarkable difference is found when $\Phi = 90$ (deg.). In the case of Full, the trajectories are similar to the case of $\Phi = 45$ (deg.). On the other hand, the motions on Y axis are oscillating. At that time the orbits are nearly circular around the Lagrangian point in the case of Restrict.

Figs. 12 and 11 illustrate the Φ dependence of the maximum values of Y axis for 300 years in the cases of Full and Restrict, respectively, and Figs. 13 and 13 are the same as Figs. 12 and 11 but for X axis. From these figures, there is obvious difference between the Full and Restrict. In the case of Restrict, the maximum values of Y axis becomes the minimum at almost $\Phi = 90$ and 270 degree where the orbit is nearly circular around the equilibrium point. While in the case of Full. the maximum value at $\Phi = 90$ degree is the greatest and it is the least at $\Phi = 270$ degree for $a = 0.1, 1.0, 10.0, 100.0$ km. However this feature is transformed and then the range between $\Phi = 180$ degree and 345 degree begin to protrudes when $a = 1000.0$ km and finally the point at $\Phi = 270$ degree is the greatest point when $a = 10000.0$ km.

This difference of orbit between Full and Restrict is almost due to the perturbations from Jupiter, Saturn, and Venus. Table 2 lists the ratio of tidal force between Earth-Moon barycenter

Table 1. Initial Conditions of Numerical Integration

Radius a	$a = 0.1, 1, 0, 10.0, 100.0, 1000.0, 10000.0$ [km]
Angle Φ	$0.0 \leq \Phi < 360.0$ [deg.] per 5.0 [deg.]

Note. — The initial conditions are given by the point on the circle with the radius a km and per 5 degree around the Lagrangian point.

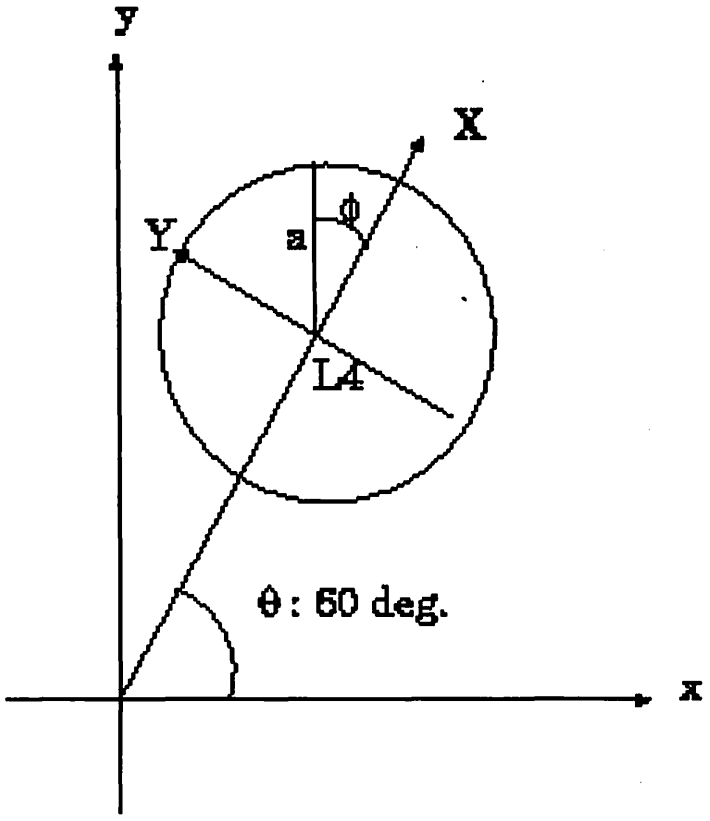

Fig. 1.— Relation of coordinate system. xy plane is the corotational coordinate system and the scale of this coordinate system is normalized by the real distance between Sun and Earth-Moon barycentric system r_e because of the ecliptic orbit of Earth-Moon barycentric system. Hence in the xy plane, the distance between Sun and Earth-Moon barycenter is always unity. The XY plane is to rotate xy plane 60 degree towards counterclockwise and the origin of coordinate is transfered into the Lagrangian point.

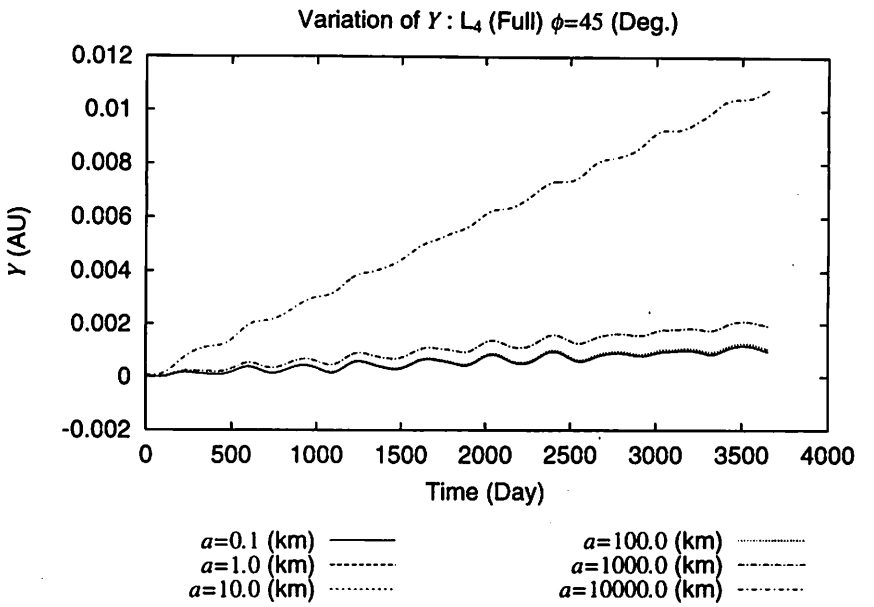

Fig. 2.— Variation of Y axis of Realistic Calculation for 10 years (Full) :
This figure shows the variations of Y axis at $a = 0.1, 1.0, 10.0, 100.01000.0, and 10000.0$ km and $\phi = 45$ degree with respect to time.

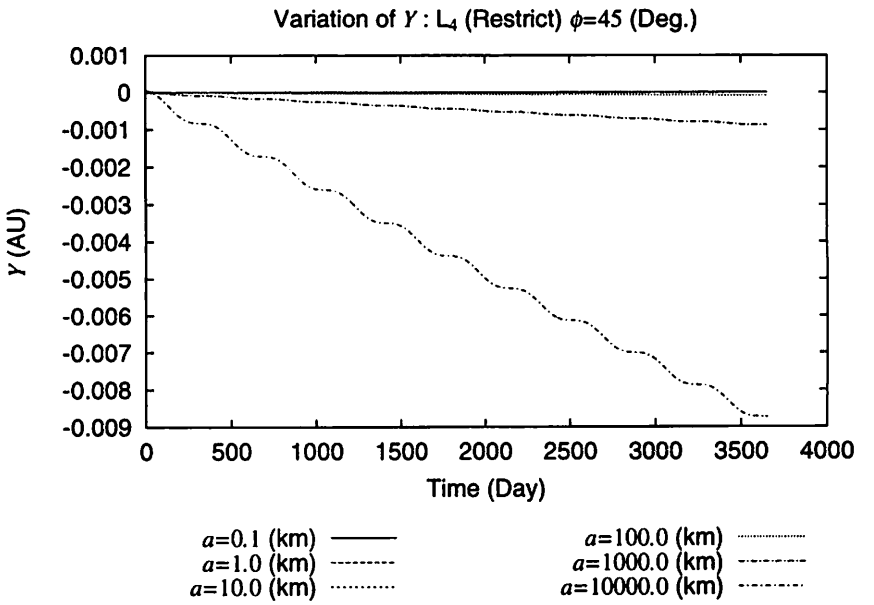

Fig. 3.— Variation of Y axis of Restrict Calculation for 10 years (Restrict) :
This figure is the same as Fig. 2 but in the case of Restrict.

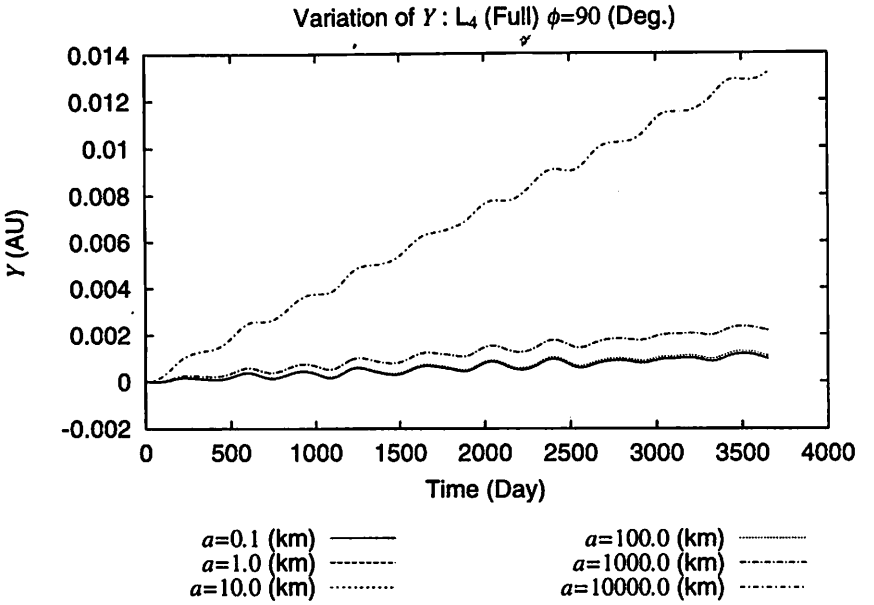

Fig. 4.— Variation of Y axis of Realistic Calculation for 10 years (Full) : This figure is the same as Fig. 2 but at $\Phi = 90$ degree.

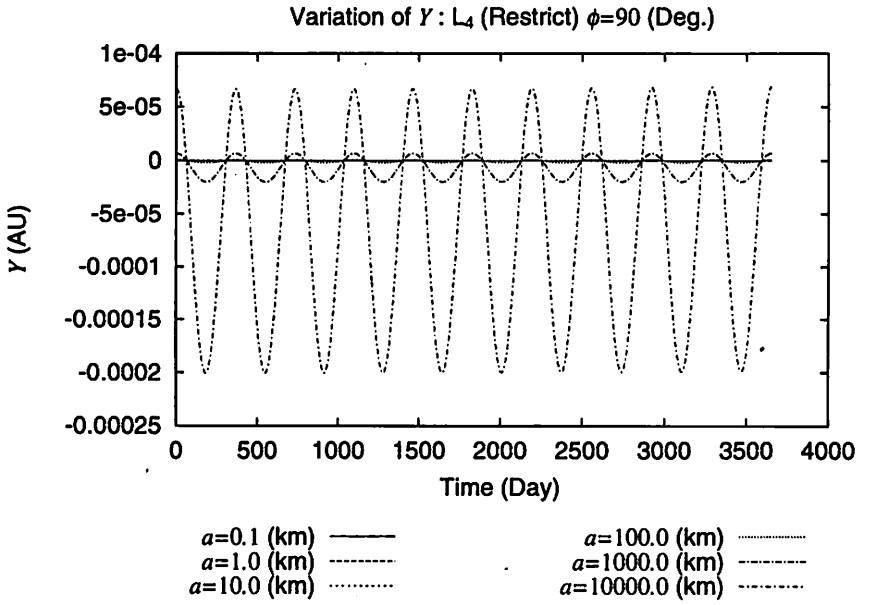

Fig. 5.— Variation of Y axis of Restrict Calculation for 10 years (Restrict) : This figure is the same as Fig. 3 but at $\Phi = 90$ degree.

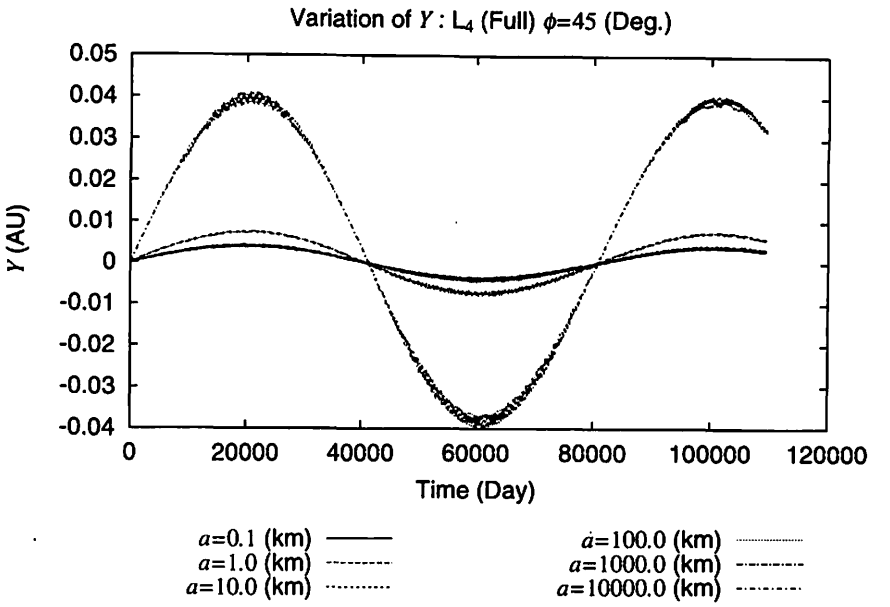

Fig. 6.— Variation of Y axis of Realistic Calculation for 300 years (Full) : This figure is the same as Fig. 2 but for 300 years.

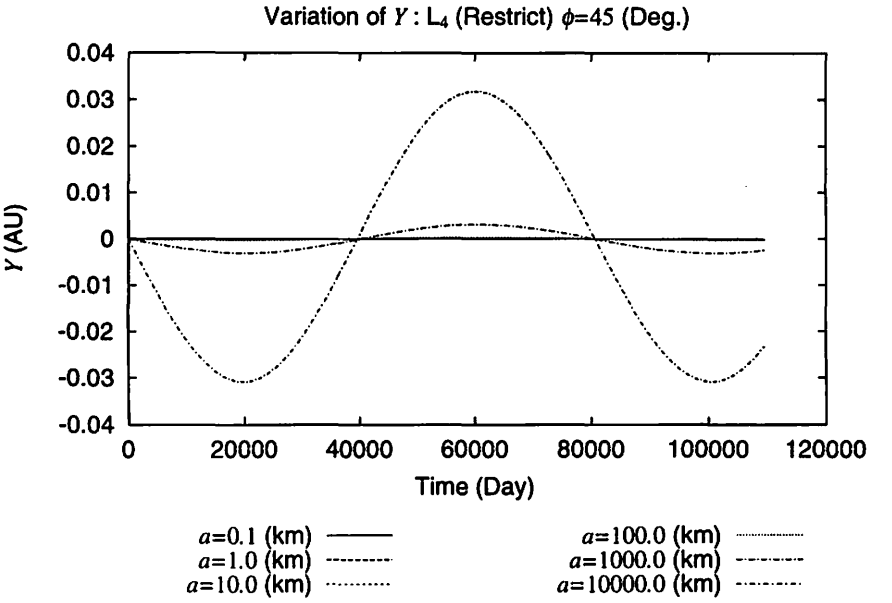

Fig. 7.— Variation of Y axis of Restrict Calculation for 300 years (Restrict) : This figure is the same as Fig. 3 but for 300 years.

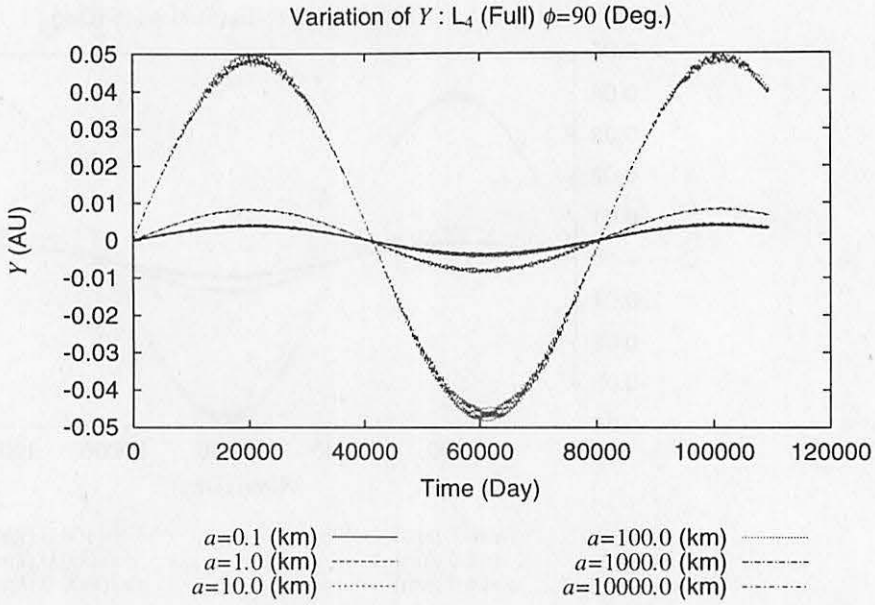

Fig. 8.— Variation of Y axis of Realistic Calculation for 300 years (Full) : This figure is the same as 6 but at $\Phi = 90$ degree.

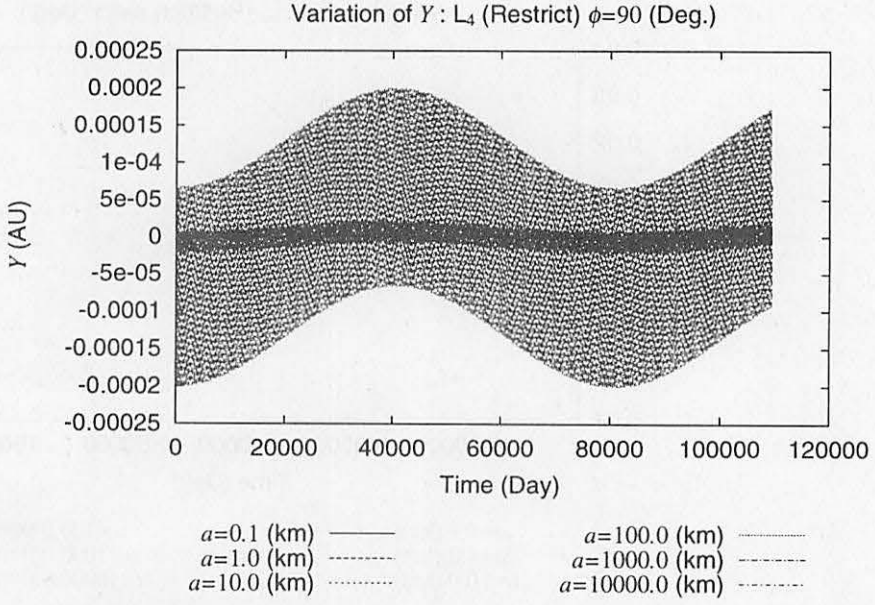

Fig. 9.— Variation of Y axis of Restrict Calculation for 300 years (Restrict) : This figure is the same as Fig. but at $\Phi = 90$ degree.

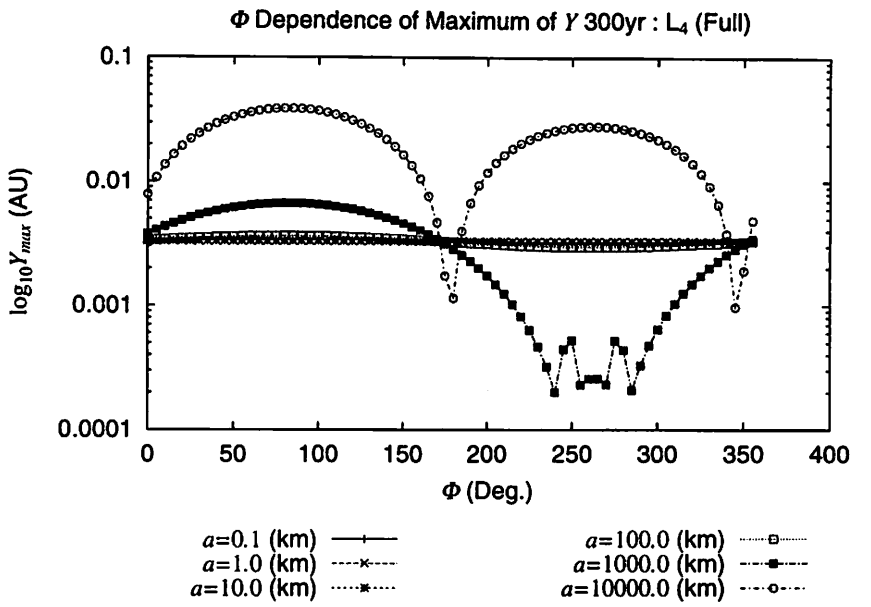

Fig. 10.— Φ Dependence of Maximum Values of Y Axis for 300 years (Full) :
This figure illustrates the Φ dependence of The maximum value of Y axis for a = 0.1, 1.0, 10.0, 100.0, 1000.0, *and*10000.0 km in the case of Full.

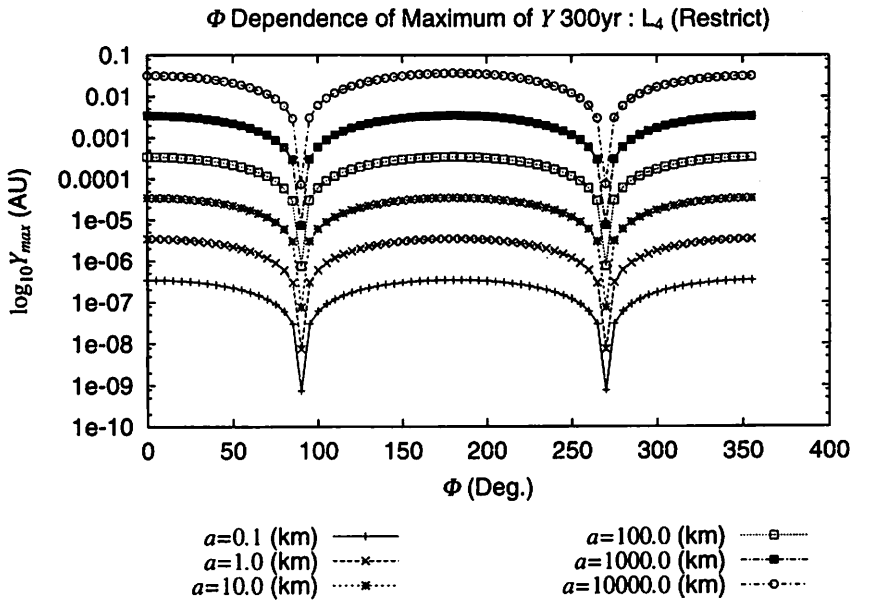

Fig. 11.— Φ Dependence of Maximum Values of Y Axis for 300 years (Restrict) :
This figure is the same as Fig. 12 but in the case of Restrict.

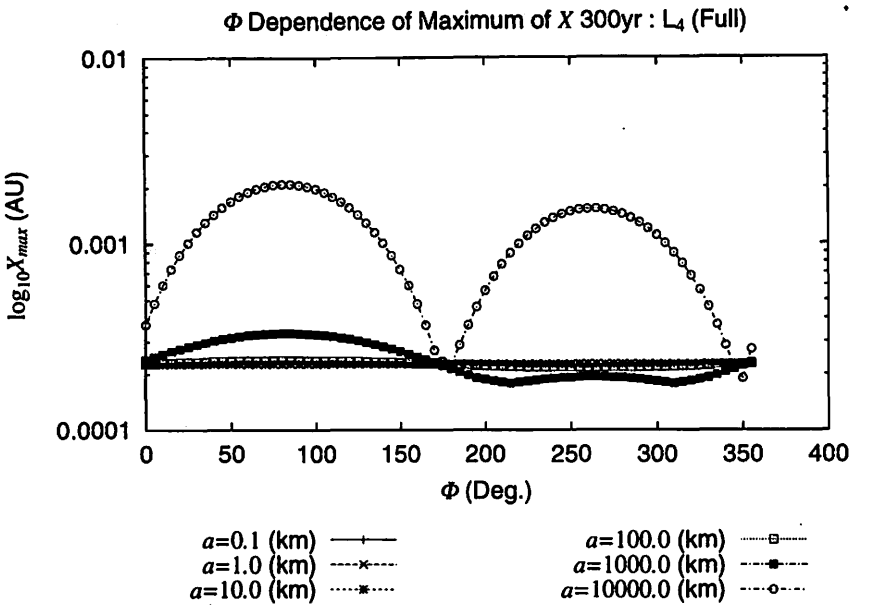

Fig. 12.— Φ Dependence of Maximum Values of X Axis for 300 years (Full) : This figure is the same as but plotted are X axis.

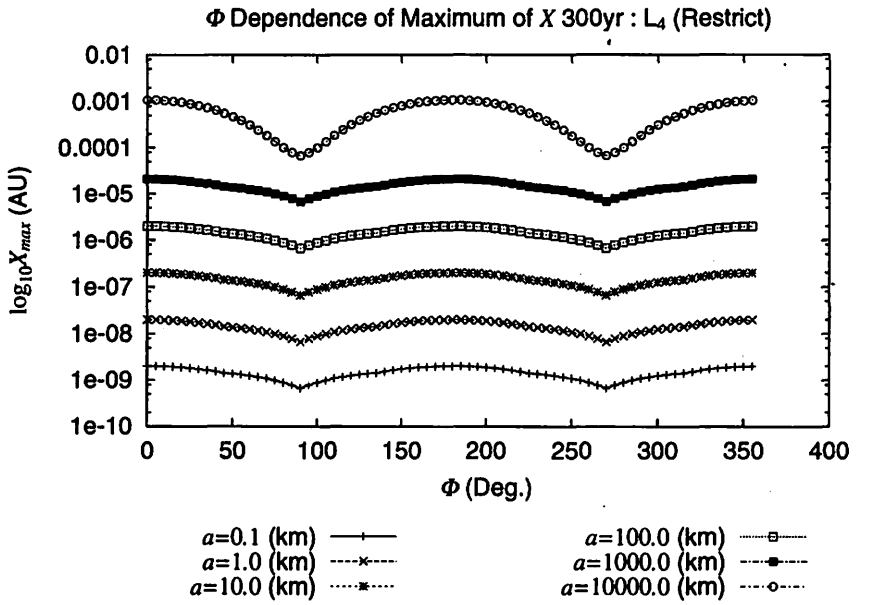

Fig. 13.— Φ Dependence of Maximum Values of X Axis for 300 years (Restrict) : This figure is the same as Fig. but in the case of Restrict.

and other planets onto the satellite at equilibrium point.

3. Conclusions

We investigated the orbital stability of the Lagrangian triangular equilibrium points of Sun and Earth-Moon system. We took into account the perturbations from Mercury to Pluto, and Moon and compared with the restricted three body problem. Our numerical experiments showed that the short and long periods of the orbital variation did not change even if perturbations of more than 4 bodies are included. However, the motion in the XY plane is different mainly due to the perturbations of Jupiter, Saturn and Venus. In the case of restricted three body problem, the difference of the orbital evolution depends on the initial condition at epoch, while in the realistic case this difference relies on the disposition of the perturbing planets rather than the initial condition. Therefore it seems that it is important to include , at least, the effect of perturbations from Jupiter, Saturn, and Venus for the Lagrangian triangular equilibrium points of Sun and Earth-Moon barycentric system and it may be principal for the triangular equilibrium points of another planets such as Saturn to care about the disturbing forces from more than the 4 planets. Though we did not deal with the collinear equilibrium point in this paper, the effect of Earth's J_2, solar radiation pressure, and eccentricity of orbit of Earth-Moon system may play a vital role for the stability and steady station keeping at L_1 and L_2.

REFERENCES

Arakida, H., and Fukushima, T., 2000, AJ, 120, 3333

Arakida, H., and Fukushima, T., 2001, AJ, 121, 1764

Gòmez G., Llibre J., Martìnez R., and Simò C, 2000, Dynamics and Mission Design Near Libration Points Vol. I, II, III, and IV, World Scientific

Table 2. Ratio of Tidal Force between Planets and Earth-Moon barycentric system

Planet	Ratio of Tidal Force
Mercury	0.148
Venus	10.395
Mars	0.329
Jupiter	18.018
Saturn	1.302
Uranus	0.043
Neptune	0.020
Pluto	1.552×10^{-6}

Note. — This table represents the ratio of tidal force onto the Lagrangian points between planets and Earth-Moon barycentric system. We regarded the orbit of planets as the circular in these evaluations.

Sub-km Main Belt Asteroids Survey (SMBAS) using SUBARU telescope

-The Estimation Methods of Size Distributions-

Fumi Yoshida
National Astronomical Observatory of Japan,
Mitaka, Tokyo, 181-8588 Japan
Graduate School of Science and Technology, Kobe University,
Nada, Kobe 657-8501, Japan
E-mail fumiy@komadori.planet.sci.kobe-u.ac.jp

Tsuko Nakamura
National Astronomical Observatory of Japan,
Mitaka, Tokyo, 181-8588 Japan
E-mail tsuko@cc.nao.ac.jp

Abstract

We have attempted to estimate the size distribution of the sub-km Main Belt Asteroids (MBAs), using large telescopes such as SUBARU telescope, for study of the collisional process among MBAs. However we cannot make the precise orbit determination by the successive follow-up observations, because of the limited observing times of large telescopes. So we are interested in estimating the orbital elements of the asteroids with the short observational arc (e.g. one day).

We have shown that the semimajor axis (a) and inclination (I) of MBAs can be statistically estimated from apparent motion vectors projected on the celestial sphere. However it is impossible to determine actually the eccentricity (e) of the asteroid without follow-up observations. The uncertainty of the e influences the estimation of the a for each asteroid and it also affects the size distribution of MBAs through translating the brightness of the asteroid into the size. So it is necessary to evaluate the error of a caused by the uncertainty of e and the resulting error on the size distribution of MBAs.

In this paper we used various orbital distributions of asteroids generated by the Monte Carlo simulations to evaluate the error of the a estimated from an apparent motion vector for individual asteroids. The simulations produced for three sets of orbital distributions, nine cases of size distributions respectively. Each case includes 5000 asteroids. In order to estimate quantitatively the error of a, we calculated the motion vectors of asteroids from orbits generated in the above simulations, by Bowell's equations which assumed $e = 0$, and estimated the a' for each asteroid (hereafter we express the semimajor axis calculated by Bowell's equations; a'). And the a' of the asteroid was compared with the true a. The difference between the a' and a corresponds to the error of the a which includes the uncertainty of its e.

Next in all orbital distributions, we constructed the size distributions based on the a' and the a respectively. Then we obtained the corresponding two slopes of the cumulative size distribution for each orbital distribution.

Finally we found that the differences of the two slopes was less than ± 0.1 in all. This means that if there is a difference in the observed cases slope larger than 0.1 for sub-km MBAs and km-sized MBAs, the difference will be detected by the method mentioned above. A preliminary analysis of our Sub-km Main Belt Asteroids Survey (SMBAS), which was performed on Feb. 21 and 24, 2001, seems to suggest that the size distribution for sub-km MBAs is appreciably different from that for larger ones.

1 Introduction

In the origin of the solar system, the study on the origin and the evolution of the MBAs is a very important issue. Especially, it is worth knowing their collisional process to estimate the relative velocities or the material strength of MBAs. The size distribution of the current MBAs reflects direct results caused by the mutual collisions among the MBAs. The size distribution of the MBAs down to a few km in diameter has been determined from the Palomar-Leiden survey (PLS : van Houten et al. 1970), and the Spacewatch survey (Jedicke and Metcalfe 1998). On the other hand, sub-km asteroids have never been observed systematically in the past because of their faintness.

However, the Suprime-cam, which is a wide-field mosaic CCD camera, attached to the prime focus of the 8.2m SUBARU telescope, allows us to detect the MBAs with about 150-300m in diameter at the center of main belt (a = 2.7AU). Now we can examine the size distribution of sub-km MBAs which anybody has never explored before.

Even if the motion of an asteroid was observed only one night, the orbit can be determined in principle from the three measured positions of the asteroid. However the orbit determined with this method can include large errors. The IAU has adopted currently the rule that if a new asteroid was observed more than three nights, the asteroid is given a temporary number and after a few more observations at opposition, it can be numbered. Practically it is impossible to follow-up the faint asteroids discovered by SUBARU on other days or with other 8-10m large telescopes, because of the restriction of the telescope's allocated times. So it is probably impossible to determine the precise orbital elements for those faint asteroids. But we noticed that the approximate a and I of an MBA can be statistically estimated from its motion vector without follow-up observations (Nakamura 1997, Yoshida 1999 master thesis), thanks to the special geometry in near-opposition observations. Moreover, the inferred a and I of many asteroids allow us to calculate the statistical errors of their a and I. Fortunately it is expected to detect a large number of sub-km MBAs in the SMBAS using SUBARU telescope (Yoshida and Nakamura 2000).

The goal of our paper is to determine the difference between the simulated size distribution of MBAs and that calculated from the a based on the apparent motion

vector of each asteroid. This is to infer the true size distribution of the MBAs from SMBAS with the short observational arcs. We argue the difference between the true a and the a' calculated by Bowell's equations for individual asteroids (section 2). In section 3 we investigate the influence of the error of the a' on the size distribution of the MBAs. Finally we refer to the correct values on the slope of the cumulative size distribution for sub-km MBAs.

2 a and I estimated from motion vector

First, by generating various orbital elements with the Monte Carlo simulations, we made the orbital distributions of various objects in the solar system and calculated their daily motions using a two-body ephemeris generator, under the condition that they locate at oppositions. Fig.1 represents a correlation diagram between a and daily motion for various objects in the solar system. From this figure, it seems that we can distinguish the a estimated from their motion vector for inner MBAs from ones for outer MBAs. However, for quantitative analysis, we need a more mathematical procedure.

In 1990, Bowell et al. proposed a method to derive an approximate a and I of an asteroid from the sky motion vector, assuming that its $e = 0$. They showed that a and I of the asteroid are represented by the following equations from the apparent motion vector of the asteroid:

$$a' = \frac{1}{2\gamma}\left(\gamma - 2k\lambda \pm \sqrt{|\kappa|}\right)$$

$$\tan I' = \frac{|\beta|}{\lambda + \dfrac{k}{a'-1}}$$

$$\gamma = \lambda^2 + \beta^2$$

$$\kappa = \gamma^2 - 4k\lambda\gamma - 4k^2\beta^2,$$

where λ is the component in longitude of motion vector, β is the latitude component and k is Gauss constant. Note that these equations are valid only for near-opposition and near-ecliptic observations. We call these "Bowell's equations" and express the semimajor axis calculated by Bowell's equations as " a' " to distinguish from true a determined by traditional orbit determination in our paper. What must be careful in applying Bowell's equations is that the value of a' are calculated as $e = 0$. Generally, it is difficult to determine the e of an asteroid without the follow-up observations. It is the same in our SMBAS because of the short observational arc. So we must assume $e = 0$ and estimate the a from the motion vector only. However, actually the e distribution of MBAs ranges from 0 to 0.4. Therefore the a' of one asteroid includes the uncertainty of its e.

In an orbital distribution of asteroids generated by the Monte Carlo simulation, we

compared the a for each asteroid, which we defined as the true a, with the a' calculated by Bowell's equations from the motion vector of the asteroid. As seen in fig.2, individual a' can considerably be different from the corresponding true a. However one can see that the averaged a' over many asteroids has no systematic deviation from the true a. We divided the main belt into three regions, i.e. inner, middle and outer regions and examined the difference between the a' and a (see table 1). It is found that the averaged difference is nearly equal to or less than 0.1AU over the main belt (2.1-3.3AU). Therefore, we can regard that the error of the a' derived from the uncertainty of its e is about 0.1 AU for each region.

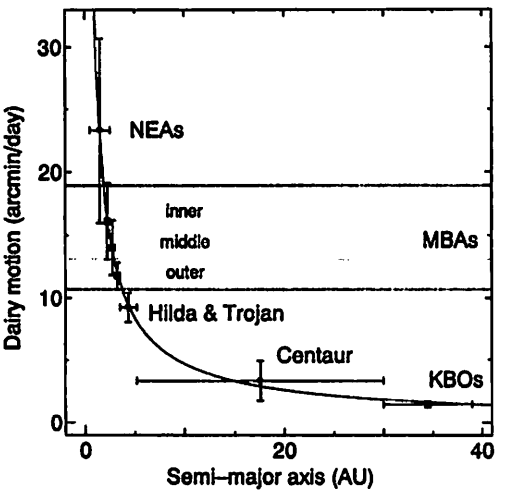

Fig.1 a vs. daily motion for various objects in the solar system.

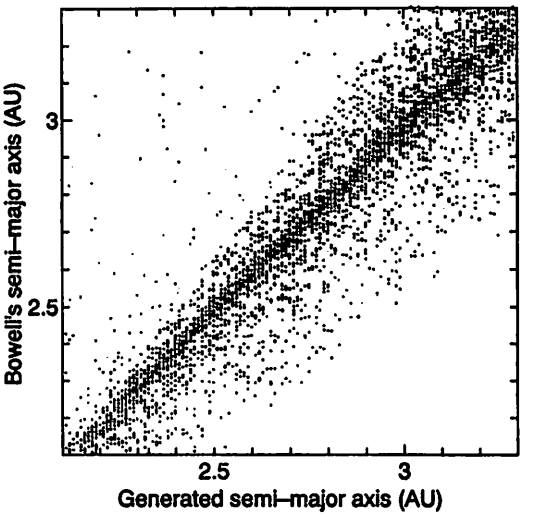

Fig.2 Generated a vs. Bowell's a' plot for members of an orbital distribution generated by the simulation.

The horizontal axis: the value of a generated in a computer run. The vertical axis: the value of a' from Bowell orbit. The a' of each asteroid is considerably averaged different from it's a. The difference between a' and a is about 0.1 AU.

Table 1 The differences between the a' and a in three belt regions.

a	ave($a-a'$)
inner belt $2.1 \leqq a \leqq 2.5$	0.094
middle belt $2.5 < a \leqq 2.9$	0.102
outer belt $2.9 < a \leqq 3.3$	0.113

3 Estimation of size distribution based on a'

We found out in section 2 that the error of the a' estimated from the apparent motion vector only is about 0.1 AU. We now examine in this section how the a' error affects the size distribution inferred from our SMBAS. For this purpose, we carried out simulations by the following procedure.

1. Generate three likely orbital distributions with Monte Carlo simulation (see table 2). We produced nine parent populations with different size distribution slopes, each population with 5000 members of asteroids. Individual asteroids of each parent population have various a, I and e within the range designated in table 2. Therefore, we made 27 orbital distributions in total.

2. Pick up asteroids in an observational window assumed for observations by our SMBAS, for each distribution.

3. Calculate apparent motion velocities in longitude and in latitude, with a two-body ephemeris generator, for each asteroid picked up.

4. Calculate a' and I' of each asteroid using Bowell's equations from the apparent motion vector of the asteroid.

5. Assume that the heliocentric distance (r) of each asteroid is equal to its a', and calculate the absolute magnitude (H) of the asteroid by the following equation,

$$H = V - 5 \log \{a'(a' - 1)\} \quad \text{.....(1)},$$

where V is apparent magnitude of the asteroid.

6. Assume an albedo of the asteroid, and translate the H to the radius (R) of the asteroid with the following equation,

$$H \propto -2.5 \log (AR^2) \quad \text{.....(2)},$$

where A is the albedo.

7. Produce the size distribution from various R of asteroids for every population and get the slope (b') of the cumulative size distribution by a least squares method.

8. Compare the slope (b) of the original cumulative size distribution generated in simulations with the b' estimated from a'.

Since we have no information at all on orbital distribution for the sub-km MBAs, we

assumed that the orbital distributions for sub-km MBAs are similar to those for currently known MBAs. Among those distributions, we selected in table 2 three typically likely combinations of a, I, and e-range. For those likely three kinds of the populations generated in the simulations, we calculated the slopes of the cumulative size distribution in each case, following the procedure mentioned before.

Next we investigated whether or not the b' inferred from a' using Bowell's equations can reproduce properly the original b, in comparison of the b' with the b for each population. We adopted the nine kinds of b = 1.0, 1.5, 1.6, 1.7, 1.75, 1.8, 1.9, 2.0 and 2.5, for each original orbital distribution. Fig.4(a)-(c) show log$N$ vs. H plot for the three cases (Ⅰ , Ⅱ and Ⅲ in table 2) with b = 1.75 whose value was determined by the PLS. N is the cumulative number of asteroids as a function of their H. The solid line represents the slope (α) as a function of H, namely 0.35. Because H and the size (or R) are connected by the equation (2), we can find immediately the following relation, $b = 5\alpha$. In fig.4(a)-(c), open circles show the original cumulative H-distribution generated by the simulations and filled circles show the cumulative H-distribution derived from Bowell's equations. The open circles and filled circles are linearly fitted by a least squares method, respectively. The obtained b's for each case are listed in table 3, along with α 's. Due to the observational bias that the field observed by our SMBAS is very small compared with the whole sky, the slope of the H-distribution represented by open circles is different slightly from the original one (α = 0.35) generated by the simulation.

The true size distribution of asteroids that will be detected in the SMBAS is regarded as that (b) expressed by open circles in fig.4 (a)-(c), on the other hand, the size distribution that we will obtain from the analysis of SMBAS data corresponds to the distribution (b') expressed by filled circles in fig. 4(a)-(c), which is estimated from the apparent motion vector for each asteroid. Therefore, we attempt to determine the correction value for the b' by calculating the difference between b' and b. When the correction value is applied to the size distribution derived from a's, we will obtain the true size distribution of MBAs.

Table 2 Adopted orbital populations

Ⅰ : It is most similar to the orbital distribution of currently known MBAs.

Ⅱ : It is slightly wider in range than the orbital distribution of currently known MBAs.

Ⅲ : It corresponds to the FWHM of the orbital distribution for currently known MBAs.

Case	Ⅰ	Ⅱ	Ⅲ
a	2.6±0.5	2.7±0.6	2.7±0.6
i	10±10	15±15	7.5±5
e	0.2±0.1	0.2±0.2	0.175±0.08
limiting mag	25mag	25mag	25mag

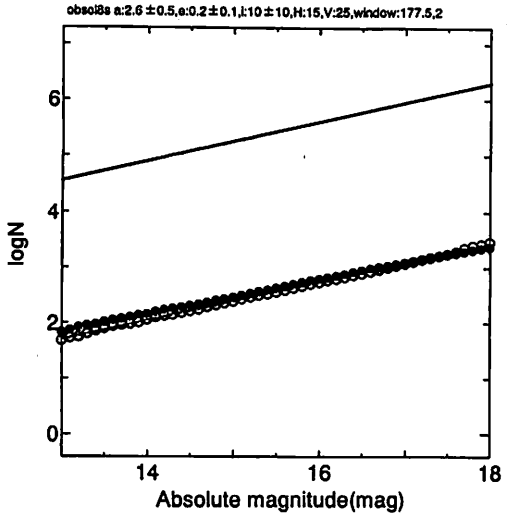

Fig.4 (a) log$N$ vs. H based on Case Ⅰ.

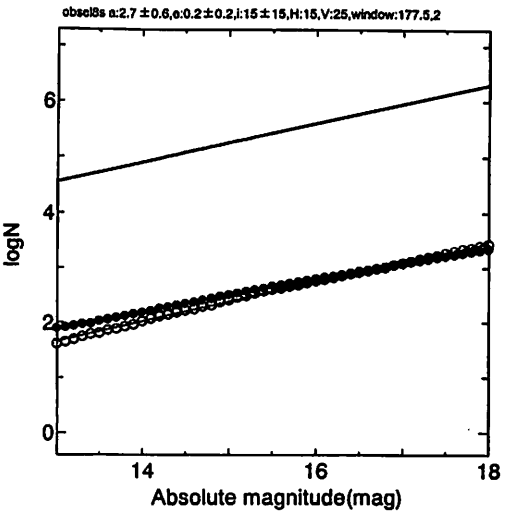

Fig.4 (b) log$N$ vs. H based on Case Ⅱ.

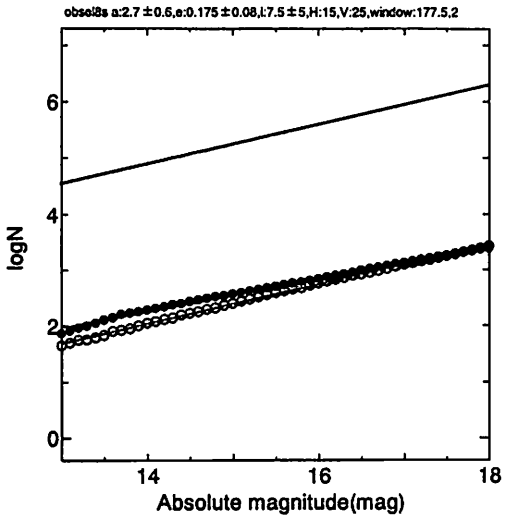

Fig.4 (c) log$N$ vs. H based on CaseⅢ.

Table 3 The slopes of the size distributions

	Ⅰ	Ⅱ	Ⅲ
Generated α	0.347	0.361	0.353
Bowell's α'	0.309	0.297	0.292
Generated b	1.735	1.805	1.765
Bowell's b'	1.545	1.485	1.460
$\Delta b=b-b'$	0.190	0.320	0.305
Δb-average of Δb	-0.082	0.048	0.033

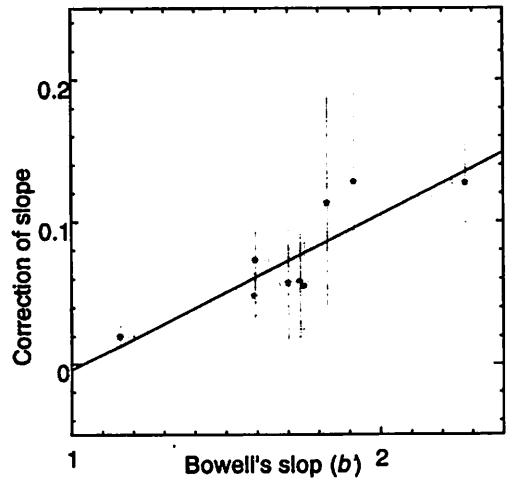

Fig.5 The correction value of b'.

Fig.5 shows the correction values calculated for each parent orbital distribution with the various b's. For the data points on this graph, we draw a straight line coming as close as possible to all the data points in a least-squares sense. The error bars for each data point correspond to the standard deviation of the b' (error bar of x) and $b - b'$ (error bar of y), both of which are derived from the three variations of the parent orbital distributions. Note that all the correction values are less than ± 0.1 in all cases.

This means that if there is a difference of slope larger than 0.1 between the size distribution for sub-km MBAs and that for km-sized MBAs, one can expect that the difference will be detected using our statistical method as mentioned above. Our SMBAS was performed on Feb. 21 and 24, 2001. According to the preliminary analysis, it actually seems likely that the size distribution for sub-km MBAs is appreciably different from that for larger ones. Furthermore, a more simplified analysis of only several tens of sub-km MBAs observed with SUBARU on June 12, 2000 also seems to support the conclusion discussed above (Yoshida et al. 2001).

References

- Bowell, E., Skiff, B. A., Wasserman, L. H. and Russell, K. S. (1990): Orbital information from asteroid motion vectors, ACM-Ⅲ, Uppsala Univ. pp.19-24.
- Jedicke, R. and Metcalfe, T. S. (1998): The orbital and absolute magnitude distributions of main belt asteroids, Icarus, **131**, pp.245-260.
- Nakamura, T. (1997): Statistical survey observations of faint belt asteroid with SUBARU-class telescopes, Proc. of the 29th Sympo. on Celestial Mechanics, Tokyo, pp.274-278 (in Japanese).
- Van Houten, C. J., Van Houten-Groeneveld, I., Herget, P., Gehrels, T., (1970): The Palomar-Leiden survey of faint minor planets, Astr. Astrophys. Suppl. **2**, pp.339-448.
- Yoshida, F. (1999): Master Thesis (in Japanese), Fukuoka Univ. of Education.
- Yoshida, F., Nakamura, T. (2000): SUBARU Sub-km Main Belt Asteroid Survey Plan -Statistical Estimation of Size Distribution-, Proc. of the 33rd ISAS Lunar and Planetary Symposium pp.21-24.
- Yoshida, F., Nakamura, T., Fuse, T., Komiyama, Y., Yagi, M., Miyazaki, S., Okamura, S., Ouchi, M. and Miyazaki, M.: First Subaru Observations of Sub-km Main Belt Asteroids (submitted to PASJ).

火星探査機「のぞみ」の軌道決定における諸問題
Problems in the orbital determination for NOZOMI spacecraft

吉川真、加藤隆ニ、市川勉、山川宏、川口淳一郎（宇宙研）
石橋史朗、佐藤耕一、大西隆史、野田明、篠崎憲次、黒須勝仁（富士通）

Makoto Yoshikawa, Takaji Kato, Tsutomu Ichikawa,
Hiroshi Yamakawa, Jun'ichiro Kawaguchi
Institute of Space and Astronautical Science (ISAS)
3-1-1 Yoshinodai, Sagamihara, Kanagawa 229-8510, JAPAN

Shiro Ishibashi, Kouichi Sato, Takafumi Ohnishi, Akira Noda,
Kenji Shinozaki, Katsutoshi Kurosu
Fujitsu Limited
3-9-1 Nakase, Mihama-ku, Chiba-shi, Chiba 261-8588, JAPAN

ABSTRACT
After the launch on July 3, 1998 from Kagoshima Space Center (KSC), NOZOMI spacecraft is now on going to Mars in the interplanetary space. The orbital determination group of ISAS has been carrying out not only the works of orbital determination using the radiometric data taken in Usuda Deep Space Center (UDSC) but also the accuracy analysis by the methods such as comparing the results from Jet Propulsion Laboratory (JPL) or others. In this paper, we overview the present status of the orbital determination and summarize the technical difficulties.

概要
火星探査機「のぞみ」は、1998年7月3日に打ち上げられ、現在は、惑星間空間を飛行中である。宇宙科学研究所の軌道決定グループでは、臼田局で取得された追跡データを使用して軌道決定運用を行うとともに、JPLとの比較を含む軌道決定解析をおこなってきた。ここでは、現在までの各軌道フェーズにおける軌道決定の状況について概観するとともに、軌道決定における技術的な課題について整理する。

1. はじめに

火星探査機「のぞみ」(Fig.1)は、日本が打ち上げた最初の火星探査機である。宇宙科学研究所では、すでに「さきがけ」や「すいせい」などの探査機を惑星間空間に打ち上げているが、軌道決定の立場から見ると、軌道決定精度の要求において、「のぞみ」はこれらの以前の探査機とはかなり異なるものになっている。それは、「のぞみ」の場合、月や地球によるスイングバイや火星周回軌道投入のために、より高い軌道決定精度が要求されているためであ

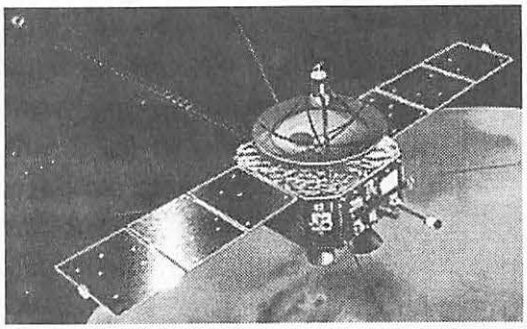

Fig.1 Nozomi Spacecraft

る。宇宙研の軌道決定グループでは、1998年の打ち上げ以来、軌道決定精度の向上を目指してきた。ここでは、「のぞみ」の軌道決定作業の現状を紹介し、その困難な点についてまとめてみることにする。

2.「のぞみ」の軌道

ここでは、「のぞみ」の今までの経過について整理してみることにする。まず、軌道決定に影響のあるイベントをまとめてみると次のようになる。

（表1） 軌道決定に影響のあるイベント

日付（世界時）	イベント
1998年7月3日	：打ち上げ
1998年12月19日	：第2月スイングバイ
1998年12月20日	：地球スイングバイ（火星遷移軌道投入）
1999年3月まで	：多数の軌道修正マヌーバー(ΔVA1～ΔV10)
1999年5月2日	：微少のガスリーク（日本時間では、7月4日）
1998年9月24日	：第1月スイングバイ
1999年7月5日	：Sバンドのダウンリンクの停止
2000年6月22-23日	：軌道修正のマヌーバー(ΔV11)

当初の予定では、1999年10月には火星に到着する予定であったのだが、1998年12月の地球スイングバイの時に不具合が発生して、急遽、軌道計画を変更することになった。最初の軌道計画と変更後の軌道について、Fig.2に概念図を示す。

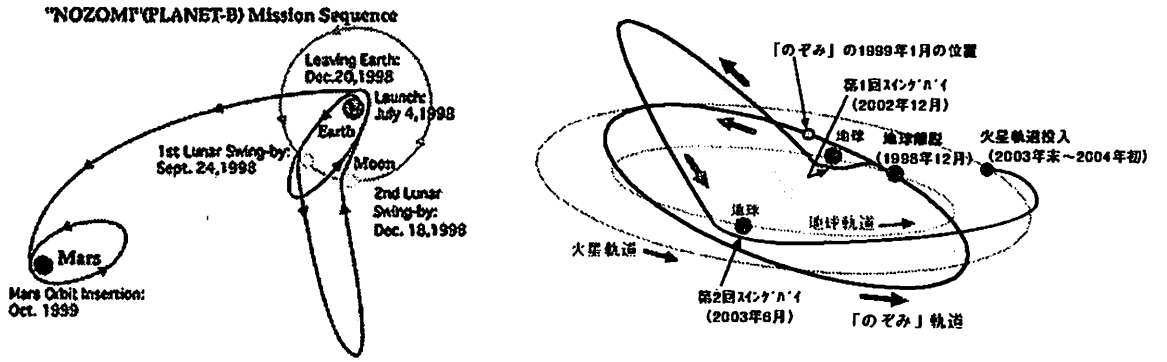

Fig. 2 The Orbit of Nozomi spacecraft.
The left figure shows the original plan, and the right figure shows the new plan.

さて、表1に上げたイベントのほとんどは、探査機の運動に直接影響を及ぼすもので、現在宇宙研で用いている軌道決定ソフトウエアでは、これらのイベントをまたいで軌道決定を行うことは難しい。したがって、これらのイベントは、軌道決定の期間を区分するものとなっている。実際の軌道決定では、必要に応じて軌道決定を行う期間をさらに分割して作業を行っている。なお、表1でSバンドのダウンリンクの停止という項目があるが、これは直接

的には軌道運動には影響しない。ただし、これ以降、探査機のダウンリンクがXバンドで行われるようになり、そのために頻繁に姿勢制御がなされることになった。後述するように姿勢制御に伴って微小な推力が発生してしまうため、軌道決定に大きな影響を及ぼしている。

Fig.3 には、「のぞみ」と地球との距離の変化の様子を示す。打ち上げ直後から3ヶ月くらいの間は、「のぞみ」は地球を周回しており、このときの地球からの距離は最大で 5×10^5 km 程度であった。その後、一度 1.7×10^6km くらいまで離れたあと、地球スイングバイを経て惑星間空間に飛び出していき、最大で 3×10^8 km 程度まで地球から離れる。したがって、このくらいの距離にある探査機の位置・速度を正確に求めることが課題となるわけである。

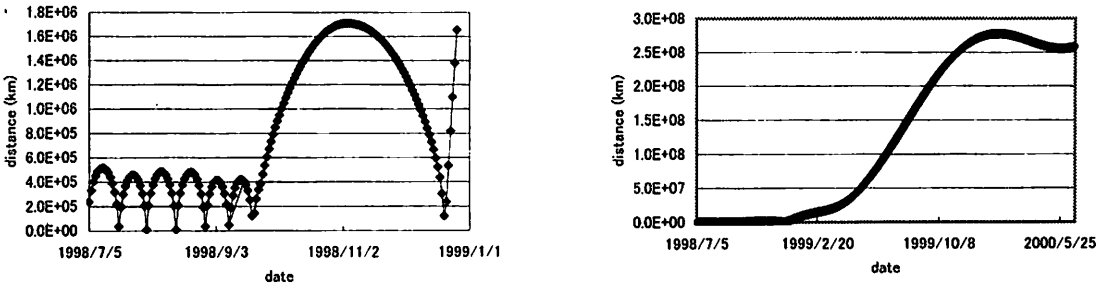

Fig.3 Distance between NOZOMI spacecraft and the earth.
The left figure shows for near-earth phase and right one shows for the whole period.

3．軌道決定の方法

宇宙研では、ISSOP (ISAS Orbit Determination Program) と呼ばれる軌道決定ソフトウエアを15年以上前から開発してきた。このソフトウエアは、1985年にハレー彗星に向けて打ち上げられた「さきがけ」や「すいせい」探査機の軌道決定にまず用いられた。そして、1990年に打ち上げられた「ひてん」の軌道決定でも改良されたものが使われている。それ以降も、宇宙研が打ち上げている地球周回の衛星から深宇宙の探査機まで、それらの軌道決定にISSOPが用いられている（参考文献 [1],[2]）。

ここでは、軌道決定ソフトウエアISSOPについて、ごく簡単に紹介する。このソフトウエアでは、追跡データであるレンジとレンジレートを用いて、探査機の軌道を決定する。データとしては、探査機の高度・方位角といった角度データも用いることがあるが、精度があまりよくない。特に深宇宙探査機の場合では、角度データは打ち上げ初期に使われるだけで、通常はレンジとレンジレートが使われる。力学モデルとしては、太陽、月、惑星（水星から土星）の摂動、惑星の周りでは引力の非球状成分、太陽輻射圧、大気抵抗を考慮している。また、たとえばガスリークのような微小な力も考慮する。また、探査機の軌道決定には、最小自乗法を用いている。

「のぞみ」探査機については、より精度の高い軌道決定をするために、このISSOPをいくつかの点において改良した。以下では、軌道決定精度や軌道決定における問題点についてまとめる。

4．軌道決定精度

探査機の軌道決定において最も難しい点は、真の軌道が決してわからないため、軌道決定を行ってもその結果がどのくらい正しいものなのか知ることができないということである。ここでは、軌道決定の精度がどのくらいあるのかを評価するために、次のような方法を用いることにした。

(a) O-C をチェックする（O:観測値, C:計算値）
(b) 自己矛盾がないことをチェックする
(c) 別のソフトウエアを使った軌道決定結果と比較する
(d) 別のグループが行った軌道決定結果と比較する

(a)については、もし O-C が 0 の値のまわりにランダムに分布していれば、軌道決定の精度はよいと考える。ランダムの分布は、観測のノイズに相当することになる。(b)については、軌道決定は特定の期間ごとに行われるが、連続する期間のそれぞれの軌道決定値を同じ時刻で比較することを行う。もし、軌道がよく決まっているとすれば、比較した場合にそのずれが小さくなる。このずれが大きければ、軌道がよく決まっているとは言えないことになる。(c)については、現在は ISSOP に匹敵するようなソフトウエアが別にはないために完全に独立な軌道決定を行って比較することはできないが、ISSOP による軌道決定結果をできる範囲でいろいろな方面から確認をすることを試みている。最後に(d)については、アメリカのジェット推進研究所（JPL）で「のぞみ」の軌道決定を行う場合が時々あるが、そのときに結果を比較することを行っている。

ここでは、「のぞみ」のこれまでの軌道決定における精度について簡単に紹介する。まず、Fig.4 には、打ち上げ（1998 年 7 月）から 1999 年 3 月までの期間について、軌道決定の期間の境目での位置と速度の接続差（自己矛盾性）を示してある。また、Fig.5 には、同じ期間について、宇宙研の軌道決定値と JPL の軌道決定値の差を示した。この期間は、「のぞみ」が地球からはまだそう遠くまでは離れておらず、地球と「のぞみ」の距離は 2×10^7 km よりは小さい。この期間では、これらの図より、軌道決定精度（1σ）は、位置で 1km から 100km、速度で 1cm/s から 10cm/s 程度であることが分かる。精度がばらついているのは、軌道のフェーズによって決定精度が異なるためである。大きな傾向としては、地球からの距離が大きくなるほど軌道決定の誤差が大きくなる。また、これらの図でスパイク的に軌道決定精度が悪くなっているように見える部分があるが、そのような部分の多くは軌道修正がなされたときに対応している。

次に、Fig.6 に、2000 年の 1 月から 6 月までについて、レンジとレンジレートの O-C のグラフを示す。この期間では、「のぞみ」の地球からの距離は 2.6×10^8 km とかなり遠くなっている。Fig.6 より、レンジの O-C は±400 m 程度の幅で、周期的な変動成分がある。レンジレートの O-C については、±5 mm/s 程度で振れている。したがって、この軌道決定にはまだ改善すべき点があることになる。

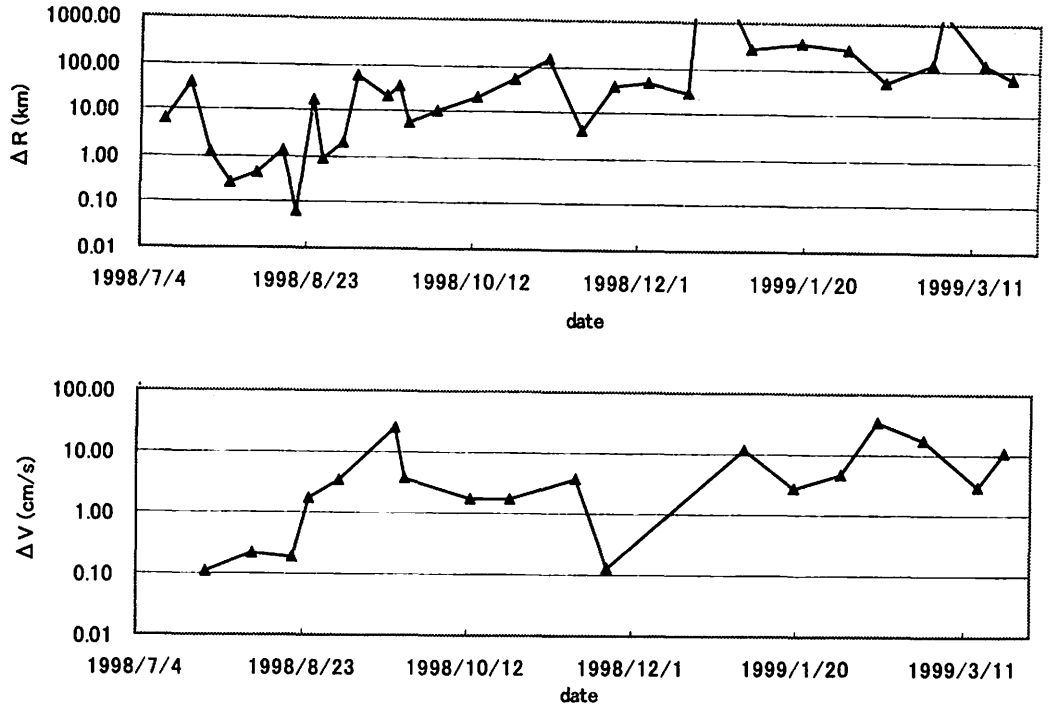

Fig.4 Self-consistency check.
These graphs show the difference of the determined values between the successive periods. (ΔR:range, ΔV:range-rate)

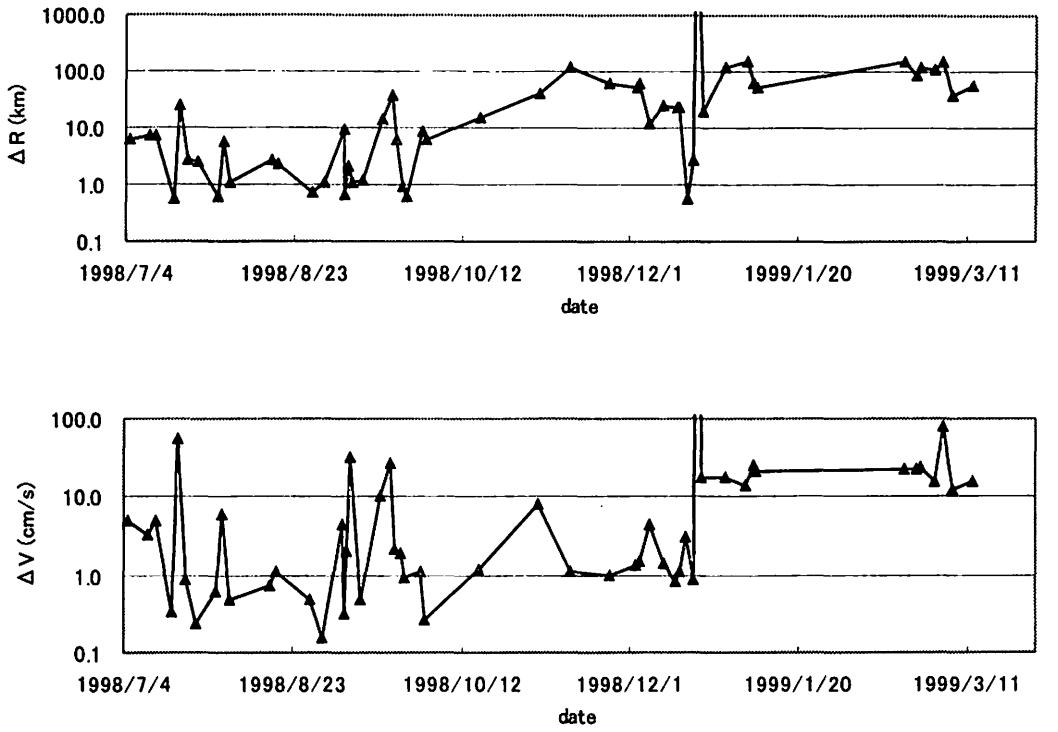

Fig.5 Comparison between the results of ISAS and that of JPL.
These graphs show the difference of the determined values by ISAS and JPL. (ΔR:range, ΔV:range-rate)

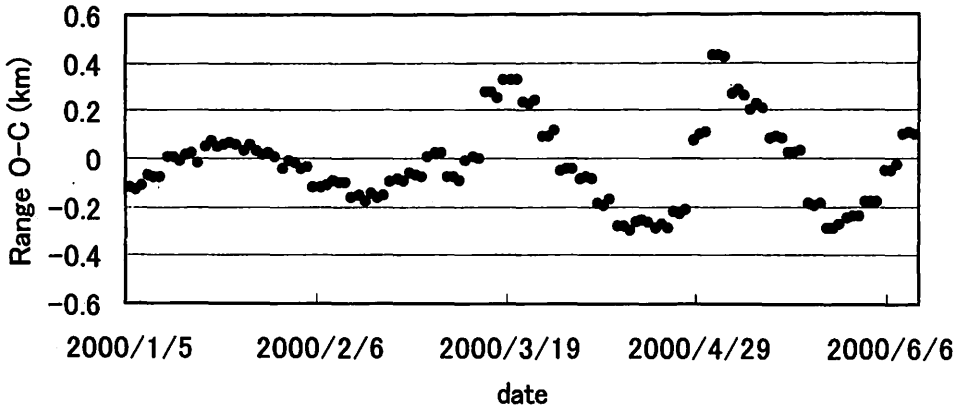

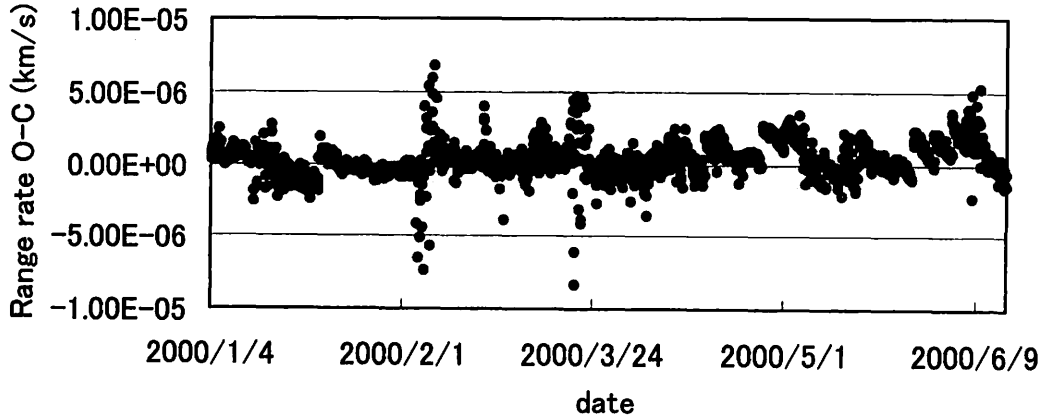

Fig.6 O-C of range and range-rate in the interplanetary phase.

5．問題点

以上述べてきた「のぞみ」の軌道決定を行う過程で、主要な問題点が 4 つあったが、それらは次のようなものである。

(a) スピンによるモジュレーション
(b) 太陽輻射圧
(c) 姿勢制御に伴って発生する加速度
(d) 「合」による影響

「のぞみ」の場合、1 分間に約 7 回転スピンしている。このスピンが、レンジやレンジレートの観測値に影響を及ぼす。より精度の高い軌道決定をするためには、このスピンの影響を除去する必要がある。ここでは、簡単な関数でスピンを模擬することでスピンの影響を取り除くことを行った。その結果、わずかではあるが、軌道決定精度が向上している。

太陽輻射圧については、今までの ISSOP のモデルを大幅に改良することを行った。今までの太陽輻射圧モデルは非常に簡単なもので、探査機としては単純な平板を考えて、輻射によって受ける力の方向は反太陽方向としていた。改良したモデルでは、探査機の形状を考慮し、太陽光の反射・吸収・透過やスピンの影響も考慮した輻射圧の計算を行っている。このより精密なモデルを導入することによって、軌道の決定精度はかなり向上した。しかし、まだ完全とは言えず、更なる改良が必要である。

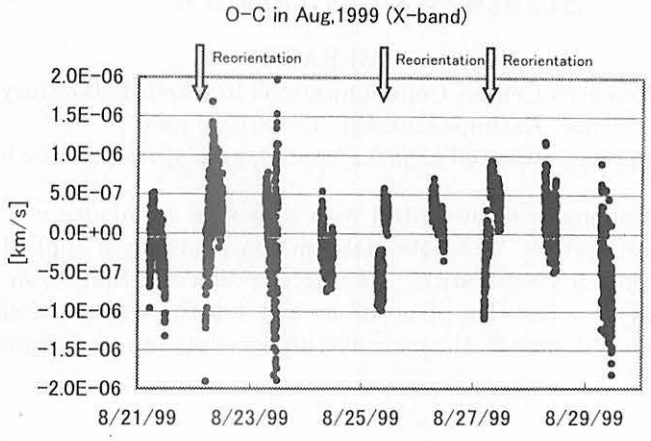

Fig.7　Unexpected acceleration at reorientation maneuvers

姿勢制御に伴って発生する加速度については、これが最も取り扱いの難しい問題である。実際のところ、姿勢制御に伴って加速度が発生するとは予期されていなかった。「のぞみ」では、姿勢制御はスラスターによってなされるが、スラスターは対称的に配置されており、かつ、推力がキャンセルされるように動作させる。したがって、姿勢制御のときには、ほとんど軌道運動に対して加速度は生じないはずだったのであるが、実際には 1mm/s 程度の加速が姿勢制御のときに発生している。この加速の大きさは、姿勢制御を行うときにレンジレートを取得することによって分かった（Fig.7)。さらに都合の悪いことに、S バンドによるダウンリンクが停止して代わりに X バンドを使わざるを得なくなったため、姿勢制御がより頻繁になされるようになってしまった。この姿勢制御による加速度については、それを推定する試みを行っているが、まだ満足する結果は得られていない。

最後に 2000 年末から 2001 年 1 月にかけては、「のぞみ」が太陽と合となり、レンジやレンジレートの観測データに大きな影響があった。この「合」の影響については、今後解析を行う予定である。

「のぞみ」は、火星周回軌道に投入（2004 年初めの予定）されるときはもちろんのこと、これから 2 度の地球スイングバイ（2002 年 12 月と 2003 年 6 月）のときにも、高精度の軌道決定が要求される。今後も、より精密な軌道決定に向けて、作業を進めていく必要がある。

参考文献

[1] T.Nishimura, T.Kato, and A.Ushikoshi : Tracking of Sakigake and Suisei and Development of Software package ISSOP for Orbit Determination. *ISAS report* NO.42, 1986.

[2] T.Nishimura, T.Ichikawa, A.Ushikoshi, H.Kosaka : Tracking of MUSES-A 'HITEN' and description of software package ISSOP for orbit determination. *ISAS report* NO.70, 1991.

Intelligent Co-location System of Many Artificial Satellites — Strategy of Guidance

Hiroaki UMEHARA
Kashima Space Research Center, Communications Research Laboratory (CRL)
Hirai, Kashima, Ibaraki, 314-0012, Japan
ume@crl.go.jp, http://www.crl.go.jp/ka/control/people/ume/index-e.html

Abstract: A strategy of autonomous orbit-control with near-miss avoidance is considered in the co-located many artificial-satellite system. The potential-function guidance is applied to the autonomous formation-keeping of the eccentricity separation. The acceleration resulting from the continuous and throttled thrust is formulated as a function of positions and velocities of all satellites. If these state variables are measured by on-board sensors, the maneuvering schedule can be computed for each satellite.

1 Introduction

Increased use of the geostationary orbit has led to intensive study of co-location methods. Dynamical features and optimal control of cluster-satellite systems have been studied in the Communications Research Laboratory (CRL) [1]. The ultimate goal of this study is to realize *autonomous uncooperative co-location*, i.e., ths satellites can be co-located without monitoring even if various organizations put satellites into orbit without considering the locations of other satellites. As a preliminary step, autonomous *cooperative* co-location is developed in this paper.

Here, technical terms in the astrodynamics field are explained as follows [2].

constellation. In a satellite communications, a number of satellites with approximately equal spacing aroud an orbit, or orbits, designed to provide maximum coverage of the Earth.

co-location. A term used to express a similarity in position of two or more satellites in geostationary orbit, such that satellites in the same nominal orbital position are said to be 'co-located'.

Moreover, we define *cooperative* as the state that every satellite recognizes dynamical infomations of the other satellites.

We already have some established formations of cooperative co-location [3]. The eccentricity separation (hereafter, e-separation) is one of the well-known formations [4]. The satellite orbits are controlled so that the drift rates are equal to each other and the directions of eccentricity vectors are separated from each other. As a result, near-miss is avoided. However, control strategies of co-location should be still studied in order to lower the fuel consumption and the operational efforts [5],[6]. Moreover, on-board autonomous control is considered to be preferable if the co-located satellites are increased, since controlling satellites individually from a ground station may be complex and expensive [7].

McInnes [7] considered autonomous constellation-keeping in a planar many-satellite system. He used the potential-function guidance which is the extention of Lyapunov's Second Method. Kalman and Bertram [8],[9] have described this method as:

> *If* $\mathrm{d}E(\boldsymbol{x})/\mathrm{d}t$ *of the energy* $E(\boldsymbol{x})$ *of an isolated physical system is negative for every possible state* $\boldsymbol{x}$*, except for a single equilibrium state* $\boldsymbol{x}_e$*, then the energy will continually decrease until it finally assumes its minimum value* $E(\boldsymbol{x}_e)$.

In McInnes's model, continuous and throttled thrust is exerted in the longitudinal and the radial directions as if repulsive interactions with frictional forces were applied to the satellites. The desired constellation thus corresponds to the equilibrium state of a potential energy defined by McInnes. The system leads to the equilibrium state, i.e., the system is guided so that the satellites revolve at regular intervals around the Earth.

McQuade [10] modified the formula of the guidance for the circular ring formation in a co-located many-satellite system. The satellites revolve at regular intervals around a nominal point in the rotating coordinates system.

In this paper, the potential-function guidance is applied to the e-separation of satellites with the continuous thrust in all directions. In order to maintain the e-separation, the potential-function guidance was used for the eccentricity vectors [5]. The maneuvers were assumed to be impulsive and restricted to the longitudinal direction. Here, let the model of each satellite be the same as the one in the works of McInnes and McQuade. This paper is based on Umehara [11].

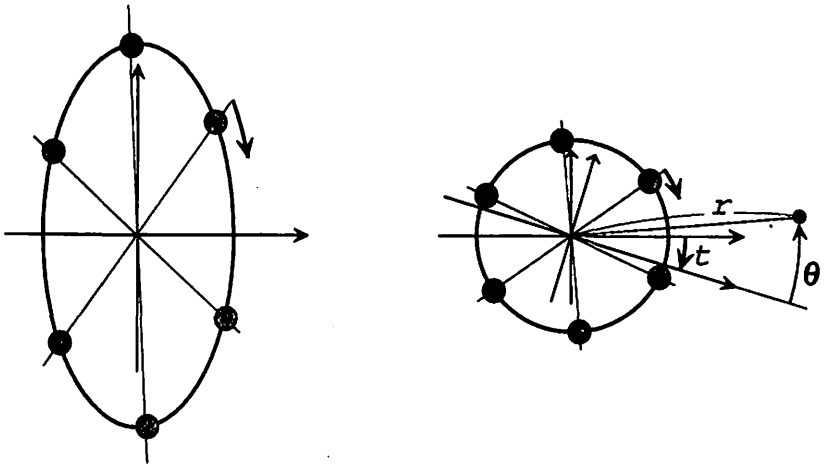

(a) (b)

Figure 1: The configuration of satellites corresponding to the e-separation solution. (a) The (R_i, L_i)-space before the variable transformation. The gravity of the Earth works from the left direction. (b) The $(r_i \cos\theta_i, r_i \sin\theta_i)$-space as a result of the variable transformation.

2 Orbit-control method

The state of the e-separation will be defined as the only one equilibrium state of the system with the artificial potential. The system will lead to the equilibrium state by the Lyapunov's theorem.

The dynamics of the planar co-located n-satellite system is considered around a nominal point on the geostationary ring. The satellites are located on the same plane of the equator. The equations of motion without perturbations are given by

$$\ddot{R}_i - 2\dot{L}_i - 3R_i = a_{Ri}, \quad \ddot{L}_i + 2\dot{R}_i = a_{Li}, \tag{1}$$

where (R_i, L_i) means the position of the i-th satellite ($i = 1, 2, \ldots, n$). The variables R_i and L_i are the radial and the longitudinal components, respectively. A dot represents the time derivative ($\dot{} := \mathrm{d}/\mathrm{d}t$). The time-dependent values $a_{Ri}(t)$ and $a_{Li}(t)$ are defined as continuous-thrust accelerations in the radial and the longitudinal directions, respectively. While $a_{Ri} = a_{Li} = 0$, the general solution $(R_i(t), L_i(t))$ includes a particular solution $(\tilde{R}_i(t), \tilde{L}_i(t))$ given by:

$$\tilde{R}_i(t) = A\cos\{(2\pi i/N) + t - B\}, \quad \tilde{L}_i(t) = -2A\sin\{(2\pi i/N) + t - B\}, \tag{2}$$

where A and B are constant numbers. This solution corresponds to the e-separation since the drift rates for all satellites are equal to zero and the directions of the eccentricity vectors are separated from each other. The above solution is periodic for time, and all distances between satellites does not vanish. A tilde ($\tilde{}$) is added for any variables which corresponds to the above e-separation solution. Figure 1(a) shows the e-separation solution on the (R_i, L_i)-space in the six-satellite system.

The variables are transformed from (R_i, L_i) into (r_i, θ_i) by the following relation:

$$R_i = r_i\cos(\theta_i - t), \quad L_i = 2r_i\sin(\theta_i - t). \tag{3}$$

Then, the e-separation solution is obtained by

$$\tilde{r}_i = 1, \quad \tilde{\theta}_i - \tilde{\theta}_j = -\frac{2\pi(i-j)}{N}, \quad \frac{\mathrm{d}\tilde{\theta}_i}{\mathrm{d}t} = 0. \tag{4}$$

Figure 1(b) represents the transformed configurations on the $(r_i\cos\theta_i, r_i\sin\theta_i)$-space. There is also an e-separation solution if $\tilde{r}_i$ is any positive constant number for all i. However, the solution can be limited to $\tilde{r}_i = 1$ without loss of generality since normalization is possible if necessary. The equations of motion are expressed as

$$\begin{aligned} &\{\ddot{r}_i - r_i\dot{\theta}_i(\dot{\theta}_i + 2)\}\cos(\theta_i - t) - \{r_i\ddot{\theta}_i + 2\dot{r}_i(\dot{\theta}_i + 1)\}\sin(\theta_i - t) = a_{Ri}, \\ &2\{r_i\ddot{\theta}_i + \dot{r}_i(2\dot{\theta}_i - 1)\}\cos(\theta_i - t) + 2\{\ddot{r}_i - r_i\dot{\theta}_i(\dot{\theta}_i - 1)\}\sin(\theta_i - t) = a_{Li}. \end{aligned} \tag{5}$$

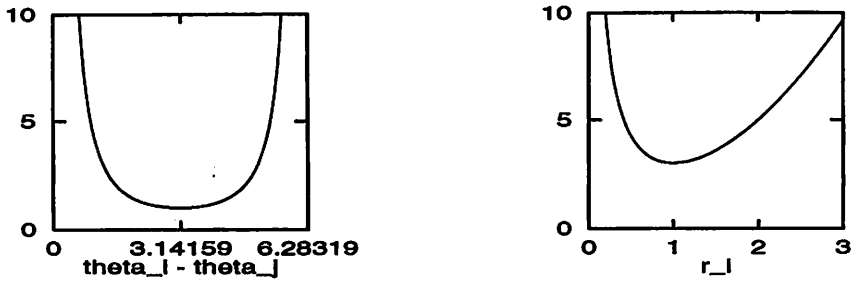

(a) (b)

Figure 2: A part of the potential function. (a) The function $1/\cos^2\theta_{ij}$ of θ_{ij}. (b) $r_i^2 + 2/r_i$ of r_i.

Let bold character $\boldsymbol{x}$ be $(x_1, x_2, \ldots, x_n)$ for variables x_i. The potential function $E(\boldsymbol{r}, \boldsymbol{\theta}, \dot{\boldsymbol{r}}, \dot{\boldsymbol{\theta}})$ guiding the system to the e-separation is defined as

$$\begin{aligned} E &= \frac{1}{2}\sum_{i=1}^{N}(\dot{r}_i^2 + \dot{\theta}_i^2) + \frac{1}{2}(\alpha U(\boldsymbol{r}) + \beta V(\boldsymbol{\theta})), \\ U(\boldsymbol{r}) &= \sum_{i=1}^{N} r_i^2 + \frac{2}{r_i},\ V(\boldsymbol{\theta}) = \sum_{i=1}^{N}\sum_{j\neq i}^{N}\frac{1}{\cos^2\theta_{ij}},\quad \theta_{ij} = \frac{1}{2}(\theta_i - \theta_j + \pi), \end{aligned} \tag{6}$$

where α and β are positive parameters that should be chosen adequately. Then, E has a minimum value if and only if $(r_i, \theta_i, \dot{r}_i, \dot{\theta}_i) = (\tilde{r}_i, \tilde{\theta}_i, \mathrm{d}\tilde{\theta}_i/\mathrm{d}t)$. The function $V(\boldsymbol{\theta})$ was introduced by McInnes [7] for the first time. This function is convenient for both the isotropic formation and the collision avoidance since E is minimum when $\theta_{i+1} - \theta_i = 2\pi/n$ and $E \to \infty$ as $\theta_i \to \theta_j$ $(j \neq i)$. See Fig. 2(a). The graph satisfies the above two conditions. The guidance of $\boldsymbol{r}$ is carried out by the function $U(\boldsymbol{r})$. McInnes [7] did not consider this guidance. The function $U(\boldsymbol{r})$ should satisfy the following two conditions: (a) U has a minimum value at $r_i = \tilde{r}_i = 1$ for any i, and (b) $U \to \infty$ as $r_i \to 0$. The condition (b) is necessary for collision avoidance. See Fig. 2(b) satisfying the above two conditions.

The configuration is formed into the desired solution if $\dot{E}$ is always negative except at the desired solution. To do this, we should have the following equation as a result:

$$\dot{E} = -\zeta\sum_{i=1}^{N}\dot{r}_i^2 - \eta\sum_{i=1}^{N}\dot{\theta}_i^2, \tag{7}$$

where ζ and η are parameters that should be chosen adequately. This is realized by the following controls of $\ddot{r}_i$ and $\ddot{\theta}_i$:

$$\ddot{r}_i = -\alpha\frac{r_i^3 - 1}{r_i^2} - \zeta\dot{r}_i,\quad \ddot{\theta}_i = -\beta\sum_{j\neq i}^{N}\frac{\sin\theta_{ij}}{\cos^3\theta_{ij}} - \eta\dot{\theta}_i. \tag{8}$$

The above relations are given by differentiating E and using the identity

$$\sin\theta_{ij}/\cos\theta_{ij}^3 = -\sin\theta_{ji}/\cos\theta_{ji}^3. \tag{9}$$

The desired accelerations $a_{Ri}(\boldsymbol{R}, \boldsymbol{L}, \dot{\boldsymbol{R}}, \dot{\boldsymbol{L}}, t)$ and $a_{Li}(\boldsymbol{R}, \boldsymbol{L}, \dot{\boldsymbol{R}}, \dot{\boldsymbol{L}}, t)$ are evaluated by replacing $(\ddot{r}_i, \ddot{\theta}_i)$ with $(r_i, \theta_i, \dot{r}_i, \dot{\theta}_i)$ in Eq. (5) and by using the inverse transformation of Eq. (3).

3 Numerical experiments

It is necessary to confirm the validity of the guidance obtained in the preceding section. Equation (1) is solved numerically in the six-geostationary-satellite system ($n = 6$). The fourth-order Runge-Kutta integration is used with a time-step $\delta t = \pi \times 10^{-3}$. Let the time unit 1 [T] and the length unit 1 [L] be $86164/2\pi$ [sec] and 1 [km], respectively. The size of the desired e-separation is defined as $\tilde{r}_i = 1$ [L], i.e., A in Eq. (3) is equal to 1 [km]. Let the initial values be

$$R_i(0) = 1,\ L_i(0) = 5\left(\frac{i}{n} - \frac{1}{2}\right),\quad \dot{R}_i(0) = 0,\ \dot{L}_i(0) = -\frac{3}{4}R_i(0), \tag{10}$$

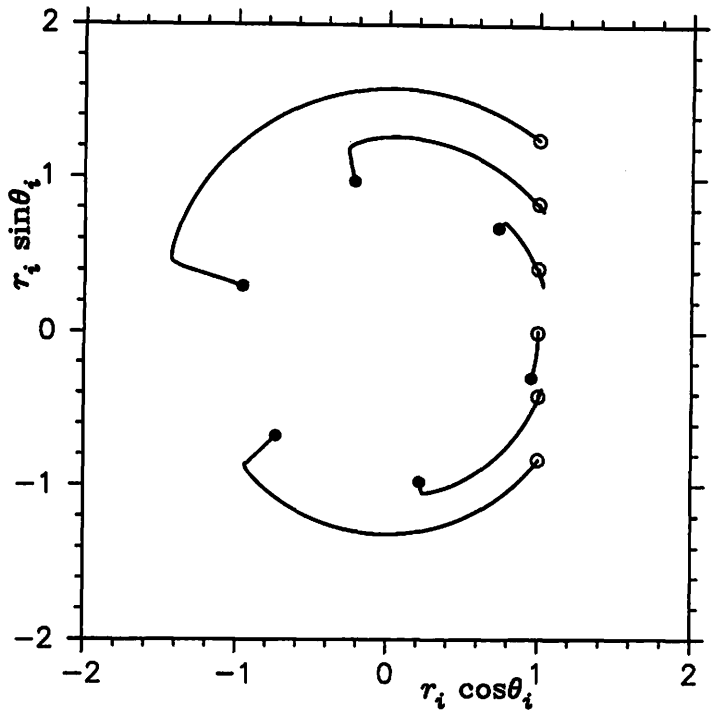

Figure 3: Trajectories of $(r_i(t)\cos\theta_i(t), r_i(t)\sin\theta_i(t))$, $i = 1, 2, \ldots, 6$.

which correspond to the formation with longitude separation [3]. The parameters in Eqs. (7) and (8) are chosen as

$$\alpha = \beta = 1, \quad \zeta = \eta = 10. \tag{11}$$

While continuous thrust is exerted by Eqs. (5), (7), and (8), the configuration tends to be the e-separation given by Eq. (4). The trajectories of $(r_i\cos\theta_i, r_i\sin\theta_i)$ are drawn for the respective satellites in Fig. 3. An open circle represents initial positions of the respective trajectories. A filled circle stands for the positions at the time $t = 6\pi$ corresponding to three sidereal days. Without any near-miss, the configuration forms a regular hexagon on the $(r\cos\theta, r\sin\theta)$-plane. This is indicated on the e-separation state.

Figure 4 shows the time-dependent distance between satellites. A near-miss is avoided. The abscissa is the time. The unit is 1 sidereal hour. The ordinate is the distance [km]. Each curve represents the distance D_i between the neighbor satellites, i.e., $D_i = \sqrt{(R_i - R_{i-1})^2 + (L_i - L_{i-1})^2}$, $i = 1, 2, \ldots, n$, $(R_0, L_0) = (R_n, L_n)$. Six curves converge to three periodic curves after one day. The distances continue to satisfy that $D_1(t) = D_4(t)$, $D_2(t) = D_5(t)$, and $D_3(t) = D_6(t)$. All distances fluctuate between 1 [km] and 2 [km]. This shows that the system results in the e-separation in a day.

The fuel consumption will now be investigated. The time-dependent total velocity-change $\delta v(t)$ and the time-integral individual velocity-change Δv_i are defined as

$$\delta v(t) = \sum_{i=1}^{n}(|a_{Ri}(t)| + |a_{Li}(t)|)\delta t, \quad \Delta v_i = \int_0^\infty (|a_{Ri}(t)| + |a_{Li}(t)|)\mathrm{d}t. \tag{12}$$

Figure 5 shows $\delta v(t)$. The time-dependent fuel-consumption decreases as the configuration forms the e-separation. Although the e-separation is accomplished quickly, the fuel consumption is large. Each Δv_i [m/sec] is evaluated as

$$\Delta v_1 = 3.33, \ \Delta v_2 = 2.78, \ \Delta v_3 = 0.919, \ \Delta v_4 = 2.43, \ \Delta v_5 = 3.58, \ \Delta v_6 = 5.97. \tag{13}$$

Finding a way to decrease these costs is for future work. The formulation of the potential function and the selection of the parameters will lower the amount of thrust fuel expended.

4 Discussion

The use of the potential-function guidance achieved autonomous e-separation with continuous thrust. The potential function was formulated as Eq. (6); therefore, the continuous thrust was obtained as Eqs.

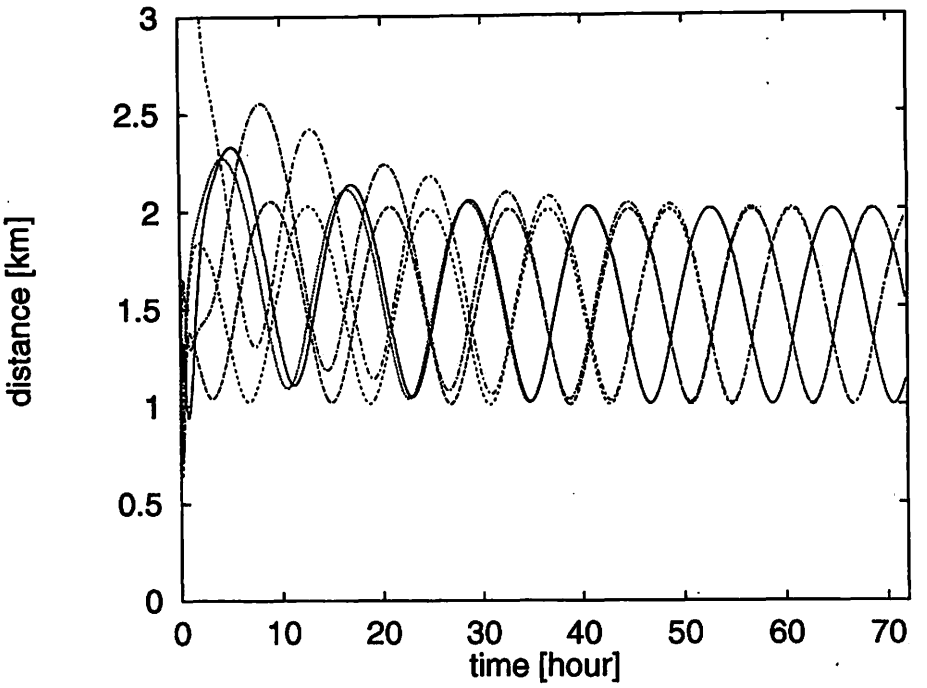

Figure 4: The distances between neighboring satellites for three sidereal days.

(5), (7), and (8). The numerical simulation validates the co-located six-satellite system where initial values and the parameters are given by Eqs. (10) and (11).

However, the fuel consumption is very high. As McQuade [10] said, it is necessary to use the natural drift in the movement of satellites. Umehara [5] considered this natural drift in the impulsive autonomous e-separation since the maneuvers are restricted to the longitudinal direction in his model. This still does not result in reduction of costs. Only the configuration space with the linear transformation is investigated in this paper. The potential-function guidance should be considered on various spaces. Moreover, the work by Nakato and Aizawa [12] implies that geodesic flow should be analyzed in order to make full use of the natural drift.

Acknowledgments

The author thanks Dr. S. Kawase and Dr. F. McQuade for their valuable discussions.

References

[1] Sawada, F. and Kawase, S., "Near-miss analysis for uncoordinatedly co-located geosynchronous satellites", *Proceedings of the 12th International Symposium on "Space Flight Dynamics"*, ESOC, Darmstadt, Germany, 1997, pp.65-69.

[2] Williamson,M.: "The Cambridge Dictionary of Space Technology", Cambridge University Press, 2001.

[3] Soop,E.M.: Section 5.6 of "Handbook of Geostationary Orbits", Kluwer, 1994.

[4] Härting, A., Rajasingh, C. K., Eckstein, M. C., Leibold, A. F., and Srinivasamurthy, K. N.: "On the collision hazard of colocated geostationary satellites", AIAA/AAS Astrodynamics Conference, Minneapolis, MN, 1988, pp. 204-212.

[5] Umehara, H.: "Eccentricity separation of geostationary satellites using imaginary-interaction guidance", *Journal of the Japan Society for Aeronautical and Space Sciences*, **48**, pp. 118-121, 2000 (in Japanese), or "Improvement of eccentricity-inclination separation using imaginary-interaction guidance", *Proceedings of the 15th International Symposium on "Space Flight Dynamics"*, Biarritz, France, 2000, MS00/40.

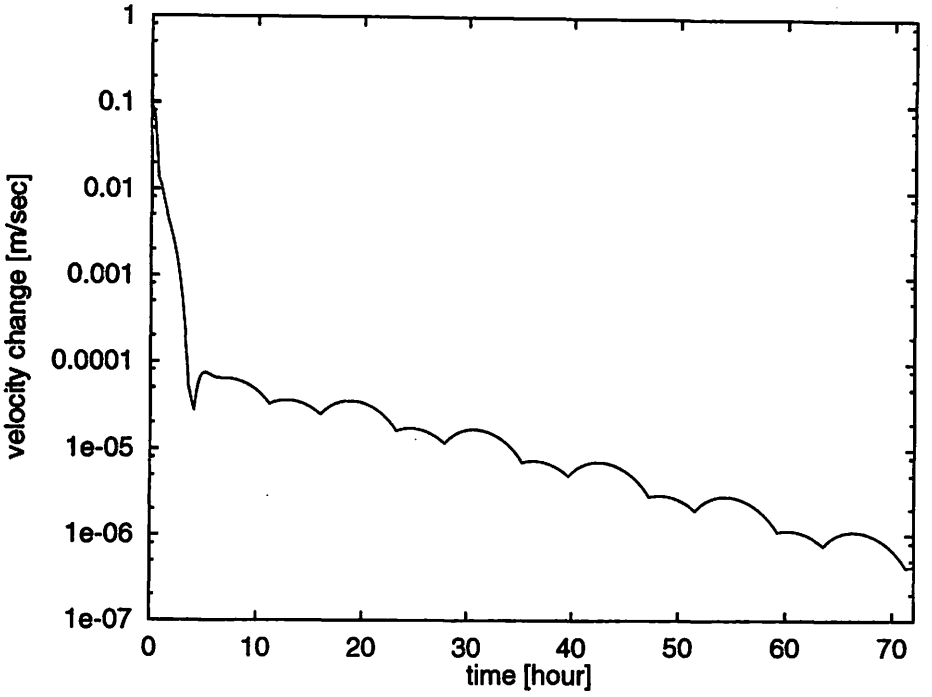

Figure 5: The time-dependent total velocity-change $\delta v(t)$.

[6] Wauthier, P., Bischops, E., Francken, P., Hooghe, M., and Laroche, H.: "On the co-location of eight ASTRA satellites", *Proceedings of the 15th International Symposium on "Space Flight Dynamics"*, Biarritz, France, 2000, MS00/41.

[7] McInnes, R. C.: "Autonomous ring formation for a planar constellation of satellites", *Journal of Guidance, Control, and Dynamics*, **18**, 1215-1217, 1995.

[8] Kalman, R. E. and Bertram, J. E.: "Control system analysis & design via the second method of Lyapunov Part I: Continuous systems", *Trans. ASME*, **82**, pp.371-393, June 1960.

[9] Kalman, R. E. and Bertram, J. E.: "Control system analysis & design via the second method of Lyapunov Part II: Discrete systems", *Trans. ASME*, **82**, pp.394-400, June 1960.

[10] McQuade, F., Ward, R., and McInnes, R. C.: "The autonomous configuration of satellite formations using a generic potential function", *Proceedings of the 15th International Symposium on "Space Flight Dynamics"*, Biarritz, France, 2000, MS00/P26.

[11] Umehara, H.: "Potential-function guidance forming eccentricity separation of satellites with continuous thrust" *Transactions of the Japan Society for Aeronautical and Space Sciences* , 2001 (in press).

[12] Nakato, M. and Aizawa, Y.: "Clustering motions in N-body systems – free-fall motions in the Gaussian three-body problem", *Chaos, Solitons and Fractals*, **11**, 171-185, 2000.

「Le Verrier 中間軌道」の正しい把捉
True Features of "the Le Verier's Intermediary Orbit"

井上　猛　（京都産業大学）
T. Inoue
Kyoto Sangyo University

Abstract. A special orbit is introduced (Inoue, 1992) in order to express what Le Verrier treated for the purpose of including the influences due to the planet Venus (Le Verrier, 1859). "The Le Verrier's intermediary orbit" is one of orbits which retrograde 43 seconds of arc per century, if one compares this orbit with a fixed ellipse.
The study aims to verify the fact that "the Le Verrier's orbit" is given by the solution of a Hamilton-Jacobi's partial-differential equation. In the previous studies, the momenta corresponding to the coordinates, radius vector & longitude are not explicitely introduced in 'the energy integral'.

1．水星の運動に及ぼす金星の影響を、Le Verrierは、初発の零次軌道の中に巧みに取り込んだ。彼の"取り扱い"が齎らす処のものを端的に示す目的で、二個の'離心率'を有する『中間軌道』なるものを提示したのであった(Inoue, 1992)。これには一寸した修正が必要であった。以下に、正しい表式を列挙して置く(Inoue, 1994)。

(1)　$u - e_M \sin u = M$,　$M = \int_{t0}^{t} n\,dt + \chi$;

(2)　$n \equiv \sqrt{\{\mu / a^3\}}$,　$\mu = G(m_{太陽} + m_{水星})$;

(3)　$\tan(f/2) = \sqrt{\{(1+e_M)/(1-e_M)\}} \cdot \tan(u/2)$;

(4)　$r = a(1 - e_r \cos u)$,

(5)　$\phi = \varpi + f$;

(6)　$\Delta e \equiv e_r - e_M \equiv +1.53\ 8156 \times 10^{-8}$.

此処で、a、e_M ; ϖ及びχは、長半径、離心率、近日点黄経及び元期に於ける平均近点離角に類似の定数を、M、u及びfは平均近点離角、離心近点離角及び真近点離角に類似の変数を表わすものとする。変数r及びϕは、極座標としての、動径及び黄経を表わして居る。

此の軌道に関して、既に、次の様な扱いをして来た(Inoue, 1992 ; 井上、1998)。
① 上記軌道が有する'エネルギー積分'を計算。
② これを Hamilton 函数として、要素変化の式を解く。
その結果、"当該軌道が、一世紀当り43秒角、近日点黄経ϖに後退の永年変化を包含して居ると云うのが明らかになった"として来たのであった。

本小論の目的は、"只今の'エネルギー積分'を Hamilton 函数と見做して、要素変化の式を解く"と云うのが、果たして、的を射たものであったか否かを知る事である。これに答えるには、極座標の動径r及び黄経ϕに共軛な運動量として導入した、p_r及びp_ϕが適切なものであったか否かを確認すれば良い。そこでは、運動量p_r及びp_ϕが、次式で与えられるとしたのであった（井上、2000）。

(7)　　$p_r \equiv \dot{r} = n a e_r \sin u/(1-e_M \cos u)$　,

(8)　　$p_\phi \equiv r^2\dot{\phi} = n r^2 \sin f/\{\sin u\,(1-e_M \cos u)\}$　.

以下に於ては、煩瑣を避ける為に量 e_Mを単にｅと表記する事にする。座標 ：ｒ、φ及び速度 ：$\dot{r}$、$r\dot{\phi}$ を考慮する時は 「Le Verrier 中間軌道」なるもの次の形の‘エネルギー積分’を有する。

(9)　　$-\mu/(2a) = \{(\dot{r}^2 + r^2\dot{\phi}^2)/2\} - \{\mu/r + \varepsilon R\}$　,

(10)　　$\varepsilon R \equiv \mu(Ae/e)\{-1/a+3/r-a/r^2-ap/r^3\}$　;

此処で、ｐなる表記は、運動量と紛らわしいが、以下の量を略記したものである。

(11)　　$p \equiv a\eta^2$　,　　$\eta \equiv \sqrt{\{1-e^2\}}$　.

我々は、只今の(9)式(10)式に依る表式が、(7)式(8)式を通じて、次の形の Hamilton 函数 Ｈ を与えると捉えたのであった。

(12)　$H \equiv H(r,\phi\ ;\ p_r, p_\phi) = \{(p_r^2+p_\phi^2/r^2)/2\} - \{\mu/r + \varepsilon R\}$　.

此の事の正当性を吟味する目的で、此の表式を基に、Hamilton-Jacobi の偏微分方程式を立てて、これを解いてみる。上記の 「Le Verrier 中間軌道」が得られるならば、我々のこれ迄の取り扱いは、総て正しかったと云う事になる。

２．以下に於ては、一連の計算を列挙して行く事にする。

Hamilton-Jacobi の偏微分方程式 ：

(13)　　$\partial W/\partial t + H(r,\phi\ ;\ \partial W/\partial r, \partial W/\partial \phi) = 0$　,

(14)　　$W = W(r,\phi\ ;\ \alpha_r, \alpha_\phi\ ;\ t)$　.

此処に、α_r, α_ϕ は、積分定数である。

運動量 ：p_r、p_ϕが、未知函数 Ｗ に依って、次の様に与えられるのであった。

(15)　　$p_r = \partial W/\partial r$,　$p_\phi = \partial W/\partial \phi$　.

更に、解表式は、新たな積分定数をβ_r, β_ϕ とする時、次の形を取る。

(16)　　$\beta_r = \partial W/\partial \alpha_r$,　$\beta_\phi = \partial W/\partial \alpha_\phi$　.

常套手段に訴えて、求める未知函数 Ｗ に次の形を要請する。

(17)　　$W \equiv -\alpha_r t + \alpha_\phi\phi + W_1(r,-\ ;\ \alpha_r, \alpha_\phi)$　.

此の $W_1(r,-\ ;\ \alpha_r, \alpha_\phi)$ に対しては、次の積分表示が得られる。

(18)　$W_1 = \int_{r0}^{r} \sqrt{\{-\alpha_\phi^2/s^2+2\mu/s+2\alpha_r+2\mu Ae(-1/a+3/s-a/s^2-ap/s^3)/e\}}\,ds$　.

これは、積分変数 ｓ を、以下の様に選ぶ時は、容易に解く事の出来るものである。

(19) $\quad s \equiv a^*(1-e^*\cos u^*) = p^*/(1+e^*\cos f^*)$;

(20) $\quad s = r_0 = a^*(1-e^*)$; $(u^*=0,\ f^*=0)$.

此処に、星印 *の付いた量は、以下の様に与えられるものである。

(21) $\quad \mu^* p^* \equiv \alpha_\phi^2 + 6\mu p \Delta e/(e\eta^2)$,

(22) $\quad \mu^* \equiv \mu(1+4\Delta e/e)$,

(23) $\quad \mu^*/a^* \equiv -2\alpha_r + 2\mu\Delta e/(ae)$,

(24) $\quad a^* = a(1+2\Delta e/e)$,

(25) $\quad e^* = e(1-3\Delta e/e)$.

平均運動 n*は、次の関係を満たす。

(26) $\quad n^* \equiv \sqrt{\{\mu^*/a^{*3}\}} = \sqrt{\{\mu/a^3\}}\cdot(1-\Delta e/e) = n\cdot(1-\Delta e/e)$.

以上の準備の基に、解表式を書き出して行く。

(27) $\quad \beta_r = \partial W/\partial\alpha_r = -t + \partial W_1/\partial\alpha_r$.

これは、次の形に書く事が出来る :

(28)
$$\begin{cases} n^*(t+\beta_r) = \{1+\Delta e(1+e^{*2})/e^{*3}\}\cdot(u^*-e^*\sin u^*) + \\ +\{\Delta e(2e^{*2}-3)/e^{*3}\}u^* + \Delta e(1-3e^{*2})/(e^{*3}\eta^*)\cdot(2f^*+e^*\sin f^*) . \end{cases}$$

(29) $\quad \beta_\phi = \partial W/\partial\alpha_\phi = +\phi + \partial W_1/\partial\alpha_\phi$.

これを、次の形に書くのは容易な事である :

(30)
$$\begin{cases} \phi = \beta_\phi + f^* + \Delta e\{-4/(e^*\eta^{*2})\}\cdot f^* + \\ +\Delta e\{\eta^*/e^{*3}\}\cdot(M^*-3u^*) + \{\Delta e/(e^{*3}\eta^{*2})\cdot(2f^*+e^*\sin f^*) . \end{cases}$$

以上で Hamilton-Jacobiの偏微分方程式を解くと云う計算は、総て為し終えた事になる。残るは、これが、所望の「Le Verrier中間軌道」を表わして居るか否かを確かめるのみである。

3．先ず初めに、(5)式の経度φと、(30)式の経度φとが同一であると云う事を要請して変数 f と変数 f* との間の関係を導いて行く。

(31)
$$\begin{cases} f = f^* + \Delta e\{-4/(e^*\eta^{*2})\}\cdot f^* + \\ +\Delta e\{\eta^*/e^{*3}\}\cdot(M^*-3u^*) + \{\Delta e/(e^{*3}\eta^{*2})\cdot(2f^*+e^*\sin f^*) . \end{cases}$$

これで、変数 f* に依って「Le Verrier中間軌道」が、余す処なく表わされ得るのが確認された事になる。
次には「Kepler方程式」に相当の(1)式が、(28)式から導かれ得るか否かを見て行く事にする。(28)式には変数 f* が含まれて居るので、これを変数 u* に書き換えて行く必要がある。次の近似表式は、此の目的の為に有用なものとなる。

(32)　　$f^* = u^* + e^* \sin u^* \ , \quad f = u + e \sin u \ .$

先ず、(31)式の関係を(28)式に代入し、続いて、これに只今の(32)式を考慮すれば、次の表式に到達する。

(33)
$$\left| \begin{array}{l} n^*(t+\beta_r) = u^* - e^* \sin u^* + \\ \quad + \Delta e\{(4/\eta^* - 5)/e^*\}\cdot(u^* + e^* \sin u^*) + \\ + (1-3e^{*2})\eta^*\cdot\{(u + e \sin u) - (u^* + e^* \sin u^*)\} + \\ \quad + \Delta e\{(3-12/\eta^*)/e^*\}\cdot(u^* + e^* \sin u^*)\cdot e^{*2} + \\ \qquad + \Delta e(3/e^*)\cdot u^*\cdot e^{*2} \ . \end{array} \right.$$

此の件に関しての Le Verrier の扱いに合わせて、上記表式中の、e^{*2}を係数に持つ項を無視する。勿論、量η^*は1に置き換える。そうすれば、(33)式は次の様に簡単になる。

(34)
$$\left| \begin{array}{l} n^*(t+\beta_r) = u^* - e^* \sin u^* + \\ \quad - (\Delta e/e^*)\cdot(u^* + e^* \sin u^*) + \\ \quad + (u + e \sin u) - (u^* + e^* \sin u^*) \ . \end{array} \right.$$

微小量 Δeを係数に持つ項では、uと u^*および e と e^*とを混同しても構わないであろう。これを考慮した表式を書いて置く。

(35)
$$\left| \begin{array}{l} n^*(t+\beta_r) = u^* - e^* \sin u^* + \\ + (1 - \Delta e/e)\cdot(u + e \sin u) + \\ \qquad - u^* - e^* \sin u^* \ . \end{array} \right.$$

此処で、次の関係の成立は、その導入から明らかである。

(36)　　$M^* = n^*(t+\beta_r) = u^* - e^* \sin u^* \ .$

斯くして、我々は、(28)式を次の形に書き換える事が出来る処まで来た。

(37)
$$\left| \begin{array}{l} 0 = (1 - \Delta e/e)\cdot(u + e \sin u) + \\ \quad - \{M^* + e^* \sin u^*\} - e^* \sin u^* \ . \end{array} \right.$$

更に、(26)式に遡って考えるならば、次の等式の成立する事に気付く。序でに、(25)式も再掲して置く。

(38)　　$(1 + \Delta e/e)\cdot M^* = (1 + \Delta e/e)\cdot n^*(t+\beta_r) = M \ .$

(25)　：　$e^* = e(1 - 3\Delta e/e) \ .$

これらを(37)式に考慮すれば、次の表式に到達する。

(39)　　$M = u + e \sin u - 2e(1 - 2\Delta e/e)\cdot \sin u^* \ .$

此処で、「Le Verrier中間軌道」の表式(1)式を書き出す。

(40) $$M = u - e_M \sin u \quad .$$

先に(8)式の直ぐ下で述べた処であるが、此処でのｅは、量e_Mを略記したものである。従って、変数ｕ* と変数ｕとの間に、次の関係を要求するのは「自然な事」と言うべきであろう。

(41) $$(1 - 2\Delta e/e)\cdot\sin u^* \equiv \sin u \quad .$$

これは、(31)式を勘案する時、ｆ*＝０ に対して ｆ＝０ が成立しなければならないのが知れ、(32)式を通じて、ｕ*＝０ の時は ｕ＝０ でなければならない事とも矛盾しない。上の関係は、次の等式の成立を促す。

(42) $$\begin{cases} (1 + 2\Delta e/e)\cdot\cos u = \cos u^* + 2\Delta e/(e\cdot\cos u^*) \ , \\ (1 + 2\Delta e/e)\cdot\sin u = \sin u^* \quad . \end{cases}$$

これに伴って動径ｒはどの様に表わされるのであろう？「Le Verrier中間軌道」に於ては(4)式で見た様に、次の形に表わされるのであった。

(43) $$r = a(1 - e_r \cos u) \quad .$$

此処で、量:ａ、e_r、ｕを、只今の量:ａ*、ｅ*、ｕ*に結び付ける為に、(24)式及び(6)式と(25)式の関係から、次の形の等式を導いて置く。

(44) $$a = a^*(1 - 2\Delta e/e) \ , \quad e_r = e(1 + \Delta e/e) = e^*(1 + 4\Delta e/e) \ .$$

これらに依って、所望の動径ｒの表式が次の様に与えられるのが知れた。

(45) $$\begin{cases} r = a(1 - e_r \cos u) = \\ \qquad = a^*(1 - e^* \cos u^*) - 2a^*\Delta e\{1/e + 1/(\cos u^*)\} \ . \end{cases}$$

これは、充分に、受容可能なものと考えられる。変数ｕ* が、 $\pi/2$ に近い値を取る時の不都合は、改めて考えるものとする。

４．以上から、(12)式を Hamilton 函数とする正準方程式系の解に依って、我々が主張して来た「Le Verrier中間軌道」が、余す処なく表わされ得ると云うのが明らかとなった。斯くして、第25回天体力学研究会で述べて以来、一貫して論じて来た『水星近日点黄経に於ける余剰の永年変化の問題』に対する我々の理解は、『総てが正しかった』と云うのが判明した事になる。

参考文献

1. Inoue, T. : 1992, *Proceedings of the Twenty-Fifth Symposium on Celestial Mechanics.*
2. Inoue, T. : 1994, *Proceedings of the Twenty-Sixth Symposium on Celestial Mechanics.*
3. 井上　猛 : 1998, 第３０回天体力学研究会集録.
4. 井上　猛 : 2000, 第３２回天体力学研究会集録.
5. Le Verrier, U. J. : 1859, *Annales de l'Observatoire Impérial de Paris, V.*

(01503J)

Time-logarithmic transformations near a resonant hyperbolic equilibrium point

Patrick BONCKAERT
Limburgs Universitair Centrum, 3590 Diepenbeek, Belgium
patrick.bonckaert@luc.ac.be
Vincent NAUDOT
The National Astronomical Observatory, Mitaka, Tokyo, Japan
vincntnu@cc.nao.ac.jp
Jiazhong YANG
Institute of Mathematics, Peking University,
Beijing, 100871, China yang@sxx0.math.pku.edu.cn

Abstract: In this paper we develop an explicit normal form conjugacy procedure, *Time-Logarithmic normalization*, to study linearization of a smooth vector field in a neighborhood of a hyperbolic equilibrium point with resonant eigenvalues. We give an asymptotic expression for such a linearization in terms of functions of Logarithmic Mourtada type.

1 Introduction and Main Result

Let $\mathcal{X}$ be a smooth vector field defined in a vicinity of a hyperbolic equilibrium point in an n-dimensional C-manifold, which will be assumed to be $\mathbf{C}^n$, as our discussion is completely local We also assume that the equilibrium point is fixed at the origin O. This means that in terms of ordinary differential equation $\mathcal{X}$ can be written in the following form.

$$\dot{X} = (A+N)\cdot X + F(X,\bar{X}), \tag{1}$$

where $X \in \mathbf{C}^n$, $\bar{X} \in \mathbf{C}^n$ are X's complexly conjugated variables, A and N are $n \times n$ matrices, A is diagonal and N nilpotent, and F is a smooth function that consists of non-linear terms only, i.e., $\|F(X,\bar{X})\| = \mathcal{O}(\|(X,\bar{X})\|^2)$, where $\|.\|$ represents any norm on $\mathbf{C}^{2n}$. We rewrite (1) with the conjugated variables

$$\mathcal{X}: \quad \begin{cases} \dot{X} &= (A+N)X + F(X,\bar{X}) \\ \dot{\bar{X}} &= (\bar{A}+\bar{N})\bar{X} + \bar{F}(X,\bar{X}) \end{cases} \tag{2}$$

and consider its associated linear vector field $\mathcal{X}_l$

$$\mathcal{X}_l: \quad \begin{cases} \dot{X} &= (A+N)X \\ \dot{\bar{X}} &= (A+N)\bar{X}. \end{cases} \tag{3}$$

We say that $\mathcal{X}_l$ and $\mathcal{X}$ are C^r $(r \geq 0)$ conjugated if there exists a C^r diffeomorphism h such that $h^*\mathcal{X} = \mathcal{X}_l$.

¿From Poincaré's works, we know how to construct a normal form procedure that enables us to write formally a conjugacy between (2) and (3) as long as the spectrum of A does not possess any resonance. This latter assumption is generic. Sternberg in [8, 9] elaborated the Poincaré result in the real case and showed under the same assumption that $\mathcal{X}$ can always be C^∞ linearized. Namely, $\mathcal{X}$ is C^∞ conjugated to $\mathcal{X}_l$. In a general context, Hartman and Grobman (see [5]) proved that $\mathcal{X}$ is always C^0 linearizable. The proof of this result, however, is not based on normal form procedure but obtained by showing the existence of a contraction in a Banach space. Therefore, it does not give further information about the transformation itself. We note that much work also has already been done for finitely differentiable families of vector field, see [1, 2, 3, 4, 6] and some others. For instance, Hartman in [4] shows that in the 2-dimensional case, one can always find a C^1 linearization. The aim of this paper is to develop a more explicit normal form conjugacy procedure, "*Time-Logarithmic normalization*", to present an asymptotic expression of such a linearization. It turns out that the results obtained here essentially generalize the known ones and the methods developed here are ideally suited to studyinging related conjugacy problems.

Let us consider the following illustrative examples.

Example 1 *Consider the 2-dimensional ODE*

$$\dot{x} = x \qquad \dot{y} = -y + xy^2.$$

As shown in [7], this vector field is not C^2 linearizable. However, it admits an explicit C^1 linearizing conjugacy

$$x = x_1, \qquad y = \frac{y_1}{1 + x_1 y_1 \log|y_1|}.$$

We remark the presence of a logarithmic function, and therefore a function of the Mourtada type (see definition further on).

In the above example, we present the linearizing conjugacy in an explicit way. Note that, however, in general it is not trivial to find an explicit linearizing transformation. Consider the following example.

Example 2 *Take the vector field*

$$\dot{x} = 2x \qquad \dot{y} = y + xz \qquad \dot{z} = -z.$$

It is known that this vector field is not C^1 linearizable (see [4]). Moreover, it is not obvious to describe explicitly the linearizing transformation. Yet the results of the paper imply that such a linearization consists of functions of the Mourtada type.

We refer the reader to [2] for more examples concerning the presence of logarithmic functions. We now introduce a definition.

Definition 1 *Let $\mathcal{U} \subset \mathbf{C}^n$ be a neighbourhood of 0 and f be a continuous function. We say that $f : \mathcal{U} \to \mathbf{C}$ is a Logarithmic Mourtada type function if there*

exist a positive integer l, a neighbourhood of 0, $\mathcal{V}_l \subset \mathbf{C}^{n(l+1)}$, and a C^∞ function $\mathbf{F} : \mathcal{V}_l \to \mathbf{C}$ such that

$$f(z) = \mathbf{F}(\{z_i T^j\},\ i = 1, \ldots, n,\ j = 0, \ldots, l),$$

where

$$T = \log \sum_{i=1}^{n} a_i (z_i \bar{z}_i)^{n_i}, \quad a_i \in \mathbf{R}^+, \quad n_i \in \mathbf{N}.$$

A map $\Phi : \mathbf{C}^n \to \mathbf{C}^n$ is called a Logarithmic Mouratda type homeomorphism if each component of the map Φ is a Logarithmic Mouratda type function.

We now are in position to state the main theorem of this paper.

Theorem 1 *Let $\mathcal{X}$ be a smooth vector field defined in a neighborhood $\mathcal{U} \in \mathbf{C}^n$ of the hyperbolic equilibrium point 0. Suppose that $\mathcal{X}_l$, the linear part of $\mathcal{X}$, at 0 is semi-simple (i.e. $N \equiv 0$). Then up to a C^∞ change of coordinates there exist $\mathcal{V} \subset \mathcal{U}$ and a Logarithmic Mourtada type homeomorphism Φ such that on $\mathcal{V}$*

$$\Phi^*(\mathcal{X}_l) = \mathcal{X}.$$

2 Preliminaries

In this section, we fix some notations and set some preliminaries.

2.1 Notations

Throughout the paper, we assume that, in terms of (2), the dimension of the stable manifold is p and that of the unstable manifold is q, $2n = p + q$. Denote by

$$\{\alpha_i\}_{1 \le i \le q} \quad \text{and} \quad \{-\beta_j\}_{1 \le j \le p},$$

respectively, the set of positive real part eigenvalues and the set of negative real part eigenvalues, i.e., both α_i and β_j have positive real part. We assume that they are ordered in the following way:

$$\mathcal{R}e(\beta_1) \le \mathcal{R}e(\beta_2) \le \cdots \le \mathcal{R}e(\beta_p) \tag{4}$$

and

$$\mathcal{R}e(\alpha_1) \le \mathcal{R}e(\alpha_2) \le \cdots \le \mathcal{R}e(\alpha_q). \tag{5}$$

Since (2) is written on $\mathbf{C}^{2n}$, for every odd integer $1 \le i \le q-1$, we can take

$$\alpha_{i+1} = \bar{\alpha}_i \quad \text{and} \quad x_{i+1} = \bar{x}_i,$$

where $\bar{\alpha}_i$ and $\bar{x}_i$ denote, respectively, α_i's and x_i's complex conjugate. In a similiar way, for every odd integer $1 \le j \le p-1$, we take

$$\beta_{j+1} = \bar{\beta}_j \quad \text{and} \quad y_{j+1} = \bar{y}_j.$$

It is clear that both q and p are even numbers.

Let

$$\vec{X} = (x_1, x_2, \ldots, x_q) \quad \text{and} \quad \vec{Y} = (y_1, y_2, \ldots, y_p).$$

Namely, $\vec{X}$ and $\vec{Y}$, respectively, represent the coordinates in the unstable and the stable manifolds of the equilibrium point. Each line

$$\mathcal{S}_{j_0} = \{y_j = 0,\ j \neq j_0\}, \quad 1 \leq j_0 \leq p,$$

is tangent to the eigenspace associated with the eigenvalue $-\beta_{j_0}$, whereas each line

$$\mathcal{U}_{i_0} = \{x_i = 0,\ i \neq i_0\}, \quad 1 \leq i_0 \leq q,$$

is tangent to the eigenspace associated with the eigenvalue α_{i_0}. With these notations, (3) can be rewritten as follows

$$\begin{cases} \dot{x}_i = \alpha_i x_i, & 1 \leq i \leq q, \\ \dot{y}_j = -\beta_j y_j, & 1 \leq j \leq p. \end{cases} \tag{6}$$

We use multi-index notations in the standard way, that is, if

$$\underline{\iota} = (\iota_1, \iota_2, \ldots, \iota_q) \in \mathbf{N}^q \quad \text{and} \quad \underline{\eta} = (\eta_1, \eta_2, \ldots, \eta_p) \in \mathbf{N}^p,$$

then

$$\vec{X}^{\underline{\iota}} = x_1^{\iota_1} x_2^{\iota_2} \cdots x_q^{\iota_q} \quad \text{and} \quad \vec{Y}^{\underline{\eta}} = y_1^{\eta_1} y_2^{\eta_2} \cdots y_p^{\eta_p}.$$

As usual, the order between multi-indices is defined as follows. Given two multi-indices $\underline{h} = (h_1, h_2, \ldots, h_r)$ and $\underline{n} = (n_1, n_2, \ldots, n_r)$, we say that $\underline{h} < \underline{n}$ if and only if $h_i < n_i$ for all integers $1 \leq i \leq r$.

We also employ the following notations

$$\vec{X}_\infty = (x_{1,\infty}, x_{2,\infty}, \ldots, x_{q,\infty}) \quad \text{and} \quad \vec{Y}_\infty = (y_{1,\infty}, y_{2,\infty}, \ldots, y_{p,\infty}),$$

where the precise meaning of $\{x_{i,\infty}\}$ and $\{y_{j,\infty}\}$ will be specified in Section 4.

We denote by

$$\mathbf{U}_{i,l} = x_i s^l, \quad \vec{\mathbf{U}} = \{\mathbf{U}_{i,l}\}_{1 \leq i \leq q,\ 1 \leq l \leq L},$$

$$\mathbf{V}_{j,l} = y_j t^l, \quad \vec{\mathbf{V}} = \{\mathbf{V}_{j,l}\}_{1 \leq j \leq p,\ 1 \leq l \leq L},$$

where L is an integer, t and s are real values. All of them will be defined in the forthcoming section. Finally, in a parallel way, we introduce the notations

$$\mathbf{U}_{i,l,\infty} = x_{i,\infty} s^l, \quad \vec{\mathbf{U}}_\infty = \{\mathbf{U}_{i,l,\infty}\}_{1 \leq i \leq q,\ 1 \leq l \leq L},$$

$$\mathbf{V}_{j,l,\infty} = y_{j,\infty} t^l, \quad \vec{\mathbf{V}}_\infty = \{\mathbf{V}_{j,l,\infty}\}_{1 \leq j \leq p,\ 1 \leq l \leq L}.$$

We end this subsection by giving the following

Definition 2 *A term $\vec{X}^{\underline{n}} \vec{Y}^{\underline{m}} \partial/\partial y_j$ is called a resonant monomial if*

$$\sum_{i=1}^{q} n_i \alpha_i - \sum_{l=1}^{p} m_l \beta_l = -\beta_j. \tag{7}$$

We call $|\underline{n}|$, $|\underline{m}|$ and $D := |\underline{n}| + |\underline{m}|$, respectively, the unstable order, the stable order and the total order (attached to y_j) of the monomial. It is called a bad resonant monomial if $m_j = 0$. In particular, if $|\underline{m}| = 1$, then it is called a bad

resonant monomial of stable order 1 attached to y_j. In a similar way, a term $\vec{X}^{\underline{n}}\vec{Y}^{\underline{m}}\partial/\partial x_k$ is called a resonant monomial if

$$\sum_{i=1}^{q} n_i\alpha_i - \sum_{l=1}^{p} m_l\beta_l = \alpha_k. \tag{8}$$

It is called a bad resonant monomial if $n_k = 0$. In particular, if $|\underline{n}| = 1$, then it is called a bad resonant monomial of unstable order 1 attached to x_k.

2.2 Resonant Monomials

2.2.1 Orders of resonant monomials

Given a resonant monomial $\vec{X}^{\underline{n}}\vec{Y}^{\underline{m}}\partial/\partial y_j$, due to the hyperbolicity of the equilibrium point, we know there exist positive numbers a, b, c and d such that for all the eigenvalues satisfy the inequalities

$$a \leq Re(\alpha_i) \leq b, \quad c \leq Re(\beta_k) \leq d.$$

It follows that

$$c|\underline{m}| \leq \sum_{k=1}^{p} m_k\beta_k \leq d|\underline{m}|.$$

On the other hand, from (7), we have

$$a|\underline{n}| + \beta_j \leq \sum_{k=1}^{p} m_k\beta_k \leq b|\underline{n}| + \beta_j.$$

Therefore we obtain an inequality $a|\underline{n}| < d|\underline{m}|$. Let $\tau = \frac{a}{d}$ and $E_1 = \frac{\tau}{1+\tau}$. Then, due to the hyperbolicity of the vector field, $E_1 \neq 0, 1$. Moreover, it is clear that $|\underline{m}| \geq E_1 D$.

Applying similar arguments to resonant monomials of the form $\vec{X}^{\underline{n}}\vec{Y}^{\underline{m}}\partial/\partial x_i$, we can find another number $E_2 < 1$ such that $|\underline{n}| \geq E_2 D$. Then we put $E = \min\{E_1, E_2\}$ (which is often called the eccentricity of the equilibrium point) and introduce the previously mentioned integer L, $L \geq \frac{1}{E} + 1$.

2.2.2 Resonant monomials with unstable orders at least 2

In what follows, we introduce the notion of "time logarithmic tags" and show how to arrange resonant monomials together with their time logarithmic tags. Take a resonant monomial whose unstable order is at least 2. First we prove the following statement.

Lemma 1 *Let $s \in \mathbf{R}$ and consider the "resonant tag" $x_{n_{i_0}}\vec{X}^{\underline{n}}\vec{Y}^{\underline{m}}s^h$, where $1 \leq n_{i_0} \leq q$, $|\underline{n}| > 0$ and $h \leq |\underline{m}| + |\underline{n}|$, then there exist $\bar{\underline{n}} \leq \underline{n}$ and $\underline{u} \in \mathbf{N}^{qL}$ such that*

$$x_{n_{i_0}}\vec{X}^{\underline{n}}s^h = x_{n_{i_0}}\vec{X}^{\bar{\underline{n}}}\vec{\mathbf{U}}^{\underline{u}}.$$

2.2.3 Resonant monomials with stable orders at least 2

Very similiar to the last subsection, we have a counterpart statement concerning resonant monomials with stable orders at least 2. More precisely, the following lemma holds.

Lemma 2 *Let $t \in \mathbf{R}$ and consider the following resonant tag*

$$y_{m_{j_0}} \overrightarrow{X}^{\underline{n}} \overrightarrow{Y}^{\underline{m}} t^h$$

where $1 \leq m_{j_0} \leq p$, $|\underline{m}| > 0$ and $h \leq |\underline{m}| + |\underline{n}|$, then there exist integers $\underline{\tilde{m}} \leq \underline{m}$ and $\underline{v} \in \mathbf{N}^{pL}$ such that

$$y_{m_{j_0}} \overrightarrow{Y}^{\underline{m}} t^h = y_{m_{j_0}} \overrightarrow{Y}^{\underline{\tilde{m}}} \overrightarrow{\mathbf{V}}^{\underline{v}}.$$

2.2.4 Resonant monomials with stable order 1

Consider a bad resonant monomial of stable order 1. Then the total order of the monomial $D = |\underline{n}| + 1$. Suppose that $\overrightarrow{X}^{\underline{n}} y_j \partial/\partial y_i$ is a bad resonant term, then from the order (4), we have $j > i$. This implies that the p-th component does not possess any j-th, $j < p$, bad resonance of stable order 1. Take $k \leq |\underline{n}|$. Then

$$\overrightarrow{X}^{\underline{n}} y_j t^k = \overrightarrow{X}^{\underline{n}} \mathbf{V}_{j,l},$$

where $l \leq L$.

2.2.5 Resonant monomials with unstable order 1

The total order of a bad resonant monomial with unstable order 1 is given by $D = |\underline{m}| + 1$. We suppose that $\overrightarrow{Y}^{\underline{m}} x_j \partial/\partial x_i$ is such a bad resonant term, then by the same arguments as used before we know that $j > i$. Take $k \leq |\underline{m}|$. Then

$$\overrightarrow{Y}^{\underline{n}} x_j s^k = \overrightarrow{Y}^{\underline{n}} \mathbf{U}_{j,l},$$

where $l \leq L$.

3 Some settings

We come back to the initial vector field $\mathcal{X}$. To prove the main theorem of this paper, we need only to consider the case that $\mathcal{X}$ possesses some resonant monomials. Therefore in what follows we shall assume that $\mathcal{X}$ is already written in its classical resonant normal form as this can always be done under a smooth change of coordinates. Write (2) in the following form

$$\begin{cases} \dot{x}_i = \alpha_i x_i + f_i(\overrightarrow{X}, \overrightarrow{Y}), & 1 \leq i \leq q, \\ \dot{y}_j = -\beta_j y_j + g_j(\overrightarrow{X}, \overrightarrow{Y}), & 1 \leq j \leq p, \end{cases} \tag{9}$$

where $\{f_i\}_{i=1,\ldots,q}$ and $\{g_j\}_{j=1,\ldots,p}$ are smooth functions of order at least 2, which means that

$$|f_i(\overrightarrow{X}, \overrightarrow{Y})| \leq \sum_{r=0}^{2} \mathcal{O}\Big(\|\overrightarrow{X}\|^{2-r} \|\overrightarrow{Y}\|^r \Big)$$

and

$$|g_j(\vec{X},\vec{Y})| \leq \sum_{r=0}^{2} \mathcal{O}\Big(\|\vec{X}\|^{2-r}\|\vec{Y}\|^r\Big).$$

In general, we will say that a function Φ is of order n if

$$|\Phi(\vec{X},\vec{Y})| \leq \sum_{r=0}^{n} \mathcal{O}\Big(\|\vec{X}\|^{n-r}\|\vec{Y}\|^r\Big).$$

It is easy to see that the functions $f_i(\vec{X},\vec{Y})$ and $g_j(\vec{X},\vec{Y})$ satisfy the following equalities.

$$\left[\mathcal{X}_l, f_i(\vec{X},\vec{Y})\frac{\partial}{\partial x_i}\right] = 0, \qquad \left[\mathcal{X}_l, g_j(\vec{X},\vec{Y})\frac{\partial}{\partial y_j}\right] = 0, \tag{10}$$

where $[\cdot\,,\cdot]$ denotes the Lie bracket of two vector fields, and $\mathcal{X}_l$ is given by (6). This moreover implies that

$$\begin{aligned} \mathcal{X}(f_i(\vec{X},\vec{Y})) &= \alpha_i f_i(\vec{X},\vec{Y}) + f_{i,2}(\vec{X},\vec{Y}) \\ \mathcal{X}(g_j(\vec{X},\vec{Y})) &= -\beta_j g_j(\vec{X},\vec{Y}) + g_{j,2}(\vec{X},\vec{Y}), \end{aligned} \tag{11}$$

where $f_{i,2}(\vec{X},\vec{Y})$ and $g_{j,2}(\vec{X},\vec{Y})$ are functions of order at least 3. Both of them satisfy property (10). In other words,

$$\left[\mathcal{X}_l, f_{i,2}(\vec{X},\vec{Y})\frac{\partial}{\partial x_i}\right] = 0, \qquad \left[\mathcal{X}_l, g_{j,2}(\vec{X},\vec{Y})\frac{\partial}{\partial y_j}\right] = 0, \tag{12}$$

which again implies that

$$\begin{aligned} \mathcal{X}(f_{i,2}(\vec{X},\vec{Y})) &= \alpha_i f_{i,2}(\vec{X},\vec{Y}) + f_{i,3}(\vec{X},\vec{Y}), \\ \mathcal{X}(g_{j,2}(\vec{X},\vec{Y})) &= -\beta_j g_{j,2}(\vec{X},\vec{Y}) + g_{j,3}(\vec{X},\vec{Y}), \end{aligned} \tag{13}$$

where once more $f_{i,3}(\vec{X},\vec{Y})$ and $g_{j,3}(\vec{X},\vec{Y})$ are functions of order at least 4 satisfying (10). For all integers $1 \leq i \leq q$ and $1 \leq j \leq p$, we then construct sequences of functions $\{f_{i,r}\}_{r\in\mathbf{N}}$ and $\{g_{j,r}\}_{r\in\mathbf{N}}$ which satisfy

$$|f_{i,r}(\vec{X},\vec{Y})| \leq \sum_{d=0}^{r+1} \mathcal{O}(\|\vec{X}\|^{r+1-d}\|\vec{Y}\|^d),$$

$$|g_{j,r}(\vec{X},\vec{Y})| \leq \sum_{d=0}^{r+1} \mathcal{O}(\|\vec{X}\|^{r+1-d}\|\vec{Y}\|^d),$$

and

$$\begin{aligned} \mathcal{X}\Big(f_{i,r}(\vec{X},\vec{Y})\Big) &= \alpha_i f_{i,r}(\vec{X},\vec{Y}) + f_{i,r+1}(\vec{X},\vec{Y}), \\ \mathcal{X}\Big(g_{j,r}(\vec{X},\vec{Y})\Big) &= -\beta_j g_{j,r}(\vec{X},\vec{Y}) + g_{j,r+1}(\vec{X},\vec{Y}). \end{aligned} \tag{14}$$

In the next section, we develop a sort of normal form procedure called "Time-Logarithmic Normal Form". The deduced changes of variables will enable us to "kill" the monomial terms by adding two "time variables".

4 Time-Logarithmic Normal Form

We consider again the initial equation, adding two variables s and t called time logarithmic tags or time variables.

$$\begin{cases} \dot{x}_i &= \alpha_i x_i + f_i(\vec{X},\vec{Y}), \quad 1 \le i \le q, \\ \dot{s} &= 1, \\ \dot{y}_j &= -\beta_j y_j + g_j(\vec{X},\vec{Y}), \quad 1 \le j \le p, \\ \dot{t} &= 1. \end{cases} \tag{15}$$

We put

$$\begin{cases} x_{i,1} &= x_i + \lambda_1 f_i(\vec{X},\vec{Y})s, \quad 1 \le i \le q, \\ y_{j,1} &= y_j + \mu_1 g_j(\vec{X},\vec{Y})t, \quad 1 \le j \le p, \end{cases} \tag{16}$$

where λ_1 and μ_1 are complex numbers to be determined in a moment. Then

$$\begin{aligned} \dot{x}_{i,1} &= \alpha_i(x_{i,1} - \lambda_1 f_i(\vec{X},\vec{Y})s) + f_i(\vec{X},\vec{Y}) \\ &+ \lambda_1 \mathcal{X}(f_i(\vec{X},\vec{Y}))s + \lambda_1 f_i(\vec{X},\vec{Y}), \quad 1 \le i \le q, \\ \dot{y}_{j,1} &= -\beta_j y_j(y_{i,1} - \mu_1 g_i(\vec{X},\vec{Y})t) + g_j(\vec{X},\vec{Y}) \\ &+ \mu_1 \mathcal{X}(g_j(\vec{X},\vec{Y}))t + \mu_1 g_j(\vec{X},\vec{Y}), \quad 1 \le j \le p, \end{aligned}$$

Recalling (11), we can write these equations into

$$\begin{aligned} \dot{x}_{i,1} &= \alpha_i x_{i,1} + f_i(\vec{X},\vec{Y}) + \lambda_1 f_{i,2}(\vec{X},\vec{Y})s + \lambda_1 f_i(\vec{X},\vec{Y}), \\ \dot{y}_{j,1} &= -\beta_j y_{j,1} + g_j(\vec{X},\vec{Y}) + \mu_1 g_{j,2}(\vec{X},\vec{Y})t + \mu_1 g_j(\vec{X},\vec{Y}). \end{aligned}$$

Putting $\lambda_1 = -1$ and $\mu_1 = -1$ in the above equations, we thus obtain

$$\begin{cases} \dot{x}_{i,1} &= \alpha_i x_{i,1} - f_{i,2}(\vec{X},\vec{Y})s, \quad 1 \le i \le q, \\ \dot{s} &= 1, \\ \dot{y}_{j,1} &= -\beta_j y_{j,1} - g_{j,2}(\vec{X},\vec{Y})t, \quad 1 \le j \le p, \\ \dot{t} &= 1. \end{cases} \tag{17}$$

By inductively introducing

$$x_{i,n+1} = x_{i,n} + \frac{(-1)^{n+1}}{(n+1)!} f_{i,n+1}(\vec{X},\vec{Y})s^{n+1} \tag{18}$$

$$y_{j,n+1} = y_{j,n} + \frac{(-1)^{n+1}}{(n+1)!} g_{j,n+1}(\vec{X},\vec{Y})t^{n+1}, \tag{19}$$

we can express $x_{i,n}$ and $y_{j,n}$ in terms of the $x_{i,k}$ and $y_{j,k}$, where $k < n$. Namely, we have the following equalities.

$$\begin{cases} x_{i,n} &= x_i + \sum_{k=1}^{n} \frac{(-1)^k}{k!} f_{i,k}(\vec{X}, \vec{Y}) s^k, \quad 1 \le i \le q, \\ y_{j,n} &= y_j + \sum_{k=1}^{n} \frac{(-1)^k}{k!} g_{j,k}(\vec{X}, \vec{Y}) t^k, \quad 1 \le j \le p, \end{cases} \tag{20}$$

where $f_{i,k}$ (as well as $g_{j,k}$) are functions of the form

$$f_{i,r+1}(\vec{X}, \vec{Y}) = \sum_{\underline{\iota} \in \mathcal{I}} \Gamma_{\underline{\iota}} \vec{X}^{\underline{k}} \vec{Y}^{\underline{u}},$$

where $\mathcal{I} \subset \mathbf{N}^{p+q}$ is a multi-index set, $\underline{\iota} = (k_1, \ldots, k_q, u_1, \ldots, u_p)$, $\Gamma_{\underline{\iota}}$'s are real numbers, and $|\underline{k}| + |\underline{u}| \ge r + 1$. Indeed the term $\vec{X}^{\underline{k}} \vec{Y}^{\underline{u}} \partial/\partial x_i$ is a resonant monomial, and t^r is the *tag* associated to it. In this coordinate system, we have

$$\begin{aligned} \dot{x}_{i,n} &= \alpha_i x_{i,n} + \frac{(-1)^n}{n!} f_{i,n+1}(\vec{X}, \vec{Y}) s^n, \\ \dot{y}_{j,n} &= -\beta_j y_{j,n} + \frac{(-1)^n}{n!} g_{j,n+1}(\vec{X}, \vec{Y}) t^n \end{aligned}$$

In the above discussion, one needs to understand the arguments in the formal category, i.e., we are working on the formal series level. Hence if necessary one can put a hat to each expression in (20) to clarify this point. By letting n tend to infinity in (20), we can obtain

$$\begin{cases} x_{i,\infty} &= x_i + \sum_{k=1}^{\infty} \frac{(-1)^k}{k!} f_{i,k}(\vec{X}, \vec{Y}) s^k, \quad 1 \le i \le q, \\ y_{j,\infty} &= y_j + \sum_{k=1}^{\infty} \frac{(-1)^k}{k!} g_{j,k}(\vec{X}, \vec{Y}) t^k, \quad 1 \le j \le p. \end{cases} \tag{21}$$

In the present coordinate system, the initial system is completely linear up to some flat terms depending on x, y, s and t. More precisely, we have

$$\begin{aligned} \dot{x}_{i,\infty} &= \alpha_i x_{i,\infty} + H_x(x, y, s), \quad 1 \le i \le q, \\ \dot{y}_{j,\infty} &= -\beta_i y_{j,\infty} + H_y(x, y, t), \quad 1 \le j \le p, \end{aligned} \tag{22}$$

where for any integers n and m we have

$$\begin{aligned} |H_x| &\le \mathcal{O}\Big(\|\vec{X}\|^{n+1} \|\vec{Y}\|^m s^r \Big), \quad r \le n + m, \\ |H_y| &\le \mathcal{O}\Big(\|\vec{X}\|^n \|\vec{Y}\|^{m+1} t^u \Big), \quad u \le n + m. \end{aligned} \tag{23}$$

The expression written in (21) in fact defines a *formal* change of variables. Certainly, by the Borel theorem, we know that in the vicinity of $\vec{X} = 0$, $\vec{Y} = 0$, $t = s = 0$, there exists a smooth diffeomorphism that maps the coordinates (X, Y) to $(\vec{X}_\infty, \vec{Y}_\infty)$, and therefore linearizes the vector field up to some flat terms. We will see, however, that t and s cannot be chosen to be close to 0. This is because they depend on $(\vec{X}_\infty, \vec{Y}_\infty)$ and tend to ∞ as $(\vec{X}_\infty, \vec{Y}_\infty)$ tend to 0.

In the next section we shall finish the proof of the theorem.

5 Proof of the theorem

¿From the previous section, we know that the expression written in (21) is formally equivalent to the following expression.

$$\begin{cases} x_{i,\infty} &= x_i + \sum_{k=i+1}^{q} \mathbf{U}_{k,l_k} \mathcal{B}_{i,k}(\vec{Y}) \\ &\quad + \sum_{k=1}^{q} x_k \mathcal{G}_{i,k}(\vec{X}, \vec{U}, \vec{Y}), \quad 1 \le i \le q \\ y_{j,\infty} &= y_j + \sum_{k=j+1}^{p} \mathbf{V}_{k,l_k} \mathcal{B}_{q+j,k}(\vec{X}) \\ &\quad + \sum_{k=1}^{p} y_k \mathcal{G}_{q+j,k}(\vec{X}, \vec{Y}, \vec{V}), \quad 1 \le j \le p \end{cases} \tag{24}$$

where $l_k \le L$, $\mathcal{G}_{i,k}$, $\mathcal{G}_{q+j,k}$, $\mathcal{B}_{q+j,k}$, $\mathcal{B}_{i,k}$ are smooth functions and $\mathcal{B}_{q,k} \equiv \mathcal{B}_{q+p,k} \equiv 0$.

In (24), we start from the q-th line and write it as follows.

$$x_{q,\infty} = x_q + \sum_{k=1}^{q} x_k \mathcal{G}_{q,k}(\vec{X}, \vec{U}, \vec{Y}). \tag{25}$$

Therefore, by multiplying s^l, where $l \le qL$, we obtain

$$\mathbf{U}_{q,l,\infty} = \mathbf{U}_{q,l} + \sum_{k=1}^{q} \mathbf{U}_{k,l} \mathcal{G}_{q,k}(\vec{X}, \vec{U}, \vec{Y}), \quad l \le qL. \tag{26}$$

Next we consider the $(q-1)$-th line in (24) and rewrite it in the form

$$x_{q-1,\infty} = x_{q-1} + \mathbf{U}_{q,l_q} \mathcal{B}_{q-1,q}(\vec{Y}) + \sum_{k=1}^{q} x_k \mathcal{G}_{q-1,k}(\vec{X}, \vec{U}, \vec{Y}). \tag{27}$$

We then multiply it by s^l, where $l \le (q-1)L$, and obtain

$$\mathbf{U}_{q-1,l,\infty} = \mathbf{U}_{q-1,l} + \mathbf{U}_{q,l+l_q} \mathcal{B}_{q-1,q}(\vec{Y}) + \sum_{k=1}^{q} \mathbf{U}_{k,l} \mathcal{G}_{q-1,k}(\vec{X}, \vec{U}, \vec{Y}). \tag{28}$$

More generally, for any integer $1 \le i \le q$, we can rewrite the i-th equation of (24) as follows.

$$x_{i,\infty} = x_i + \sum_{k=i+1}^{q} \mathbf{U}_{k,l_k} \mathcal{B}_{i,k}(\vec{Y}) + \sum_{k=1}^{q} x_k \mathcal{G}_{i,k}(\vec{X}, \vec{U}, \vec{Y}). \tag{29}$$

Then we multiply it by s^l, where $l \le iL$, and obtain

$$\mathbf{U}_{i,l,\infty} = \mathbf{U}_{i,l} + \sum_{k=i+1}^{q} \mathbf{U}_{k,l+l_k} \mathcal{B}_{i,k}(\vec{Y}) + \sum_{k=1}^{q} \mathbf{U}_{k,l} \mathcal{G}_{i,k}(\vec{X}, \vec{U}, \vec{Y}). \tag{30}$$

We can apply the above arguments in the same way to the stable coordinates. Namely, we start from considering the $(p+q)$-th equation of (24)

$$y_{p,\infty} = y_p + \sum_{k=1}^{p} y_k \mathcal{G}_{q+p,k}(\vec{X}, \vec{Y}, \vec{V}) \tag{31}$$

and multiply it by t^l, where $l \leq pL$. We obtain

$$\mathbf{V}_{p,l,\infty} = \mathbf{V}_{p,l} + \sum_{k=1}^{p} \mathbf{V}_{k,l}\mathcal{G}_{q+p,k}(\vec{X}, \vec{Y}, \vec{V}). \tag{32}$$

Next, rewrite the $(q+p-1)$-th equation of (24) in the form

$$y_{p-1,\infty} = y_{p-1} + \mathbf{V}_{p,l_p}\mathcal{B}_{q+p-1,p}(\vec{X}) + \sum_{k=1}^{p} y_k\mathcal{G}_{q+p,k}(\vec{X}, \vec{Y}, \vec{V})$$

and multiply it by t^l, where $l \leq (p-1)L$. We get

$$\mathbf{V}_{p-1,l,\infty} = \mathbf{V}_{p-1,l} + \mathbf{V}_{p,l+l_p}\mathcal{B}_{q+p-1,p}(\vec{X}) + \sum_{k=1}^{p} \mathbf{V}_{k,l}\mathcal{G}_{q+p,k}(\vec{X}, \vec{Y}, \vec{V}). \tag{33}$$

More generally, for any integer $1 \leq j \leq p$, from the $(q+j)$-th equation of (24)

$$y_{j,\infty} = y_j + \sum_{k=j+1}^{p} \mathbf{V}_{k,l_k}\mathcal{B}_{q+j,k}(\vec{X}) + \sum_{k=1}^{p} y_k\mathcal{G}_{q+j,k}(\vec{X}, \vec{Y}, \vec{V}), \tag{34}$$

we multiply it by t^l, where $l \leq jL$, and obtain

$$\mathbf{V}_{j,l,\infty} = \mathbf{V}_{j,l} + \sum_{k=j+1}^{p} \mathbf{V}_{k,l+l_k}\mathcal{B}_{q+j,k}(\vec{X}) + \sum_{k=1}^{p} \mathbf{V}_{k,l}\mathcal{G}_{q+j,k}(\vec{X}, \vec{Y}, \vec{V}). \tag{35}$$

Finally we put together (29), (30), (34) and (35) to form a system of equations

$$\begin{cases} x_{i,\infty} = x_i + \sum_{k=i+1}^{q} \mathbf{U}_{k,l_k}\mathcal{B}_{i,k}(\vec{Y}) + \sum_{k=1}^{q} x_k\mathcal{G}_{i,k}(\vec{X}, \vec{U}, \vec{Y}) \\ \mathbf{U}_{i,l,\infty} = \mathbf{U}_{i,l} + \sum_{k=i+1}^{q} \mathbf{U}_{k,l+l_k}\mathcal{B}_{i,k}(\vec{Y}) + \sum_{k=1}^{q} \mathbf{U}_{k,l}\mathcal{G}_{i,k}(\vec{X}, \vec{U}, \vec{Y}), \\ \qquad l \leq iL, \quad 1 \leq i \leq q \\ y_{j,\infty} = y_j + \sum_{k=j+1}^{p} \mathbf{V}_{k,l_k}\mathcal{B}_{q+j,k}(\vec{X}) + \sum_{k=1}^{p} y_k\mathcal{G}_{q+j,k}(\vec{X}, \vec{Y}, \vec{V}) \\ \mathbf{V}_{j,l,\infty} = \mathbf{V}_{j,l} + \sum_{k=j+1}^{p} \mathbf{V}_{k,l+l_k}\mathcal{B}_{q+j,k}(\vec{X}) \\ \qquad + \sum_{k=1}^{p} \mathbf{V}_{k,l}\mathcal{G}_{q+j,k}(\vec{X}, \vec{Y}, \vec{V}), \quad 1 \leq j \leq p. \end{cases} \tag{36}$$

Equation (36) defines a diffeomorphism $\Phi_{P,Q}$ on a neighbourhood of $0 \in \mathbf{C}^P \times \mathbf{C}^Q$ where

$$P = L\frac{p(p+1)}{2} + p \quad \text{and} \quad Q = L\frac{q(q+1)}{2} + q.$$

Therefore we can inverse the expression in (36) and get the following

$$\begin{cases} x_i &= x_{i,\infty} + \sum_{k=i+1}^{q} \mathbf{U}_{k,l_k,\infty} \tilde{B}_{i,k}(\overrightarrow{Y}_\infty) + \sum_{k=1}^{q} x_{k,\infty} \tilde{G}_{i,k}(\overrightarrow{X}_\infty, \overrightarrow{U}_\infty, \overrightarrow{Y}_\infty) \\ \mathbf{U}_{i,l} &= \mathbf{U}_{i,l,\infty} + \sum_{k=i+1}^{q} \mathbf{U}_{k,l+l_k,\infty} \tilde{B}_{i,k}(\overrightarrow{Y}_\infty) \\ &+ \sum_{k=1}^{q} \mathbf{U}_{k,l,\infty} \tilde{G}_{i,k}(\overrightarrow{X}_\infty, \overrightarrow{U}_\infty, \overrightarrow{Y}_\infty), \quad l \le iL, \ \ 1 \le i \le q \\ y_j &= y_{j,\infty} + \sum_{k=j+1}^{p} \mathbf{V}_{k,l_k,\infty} \tilde{B}_{q+j,k}(\overrightarrow{X}_\infty) \\ &+ \sum_{k=1}^{p} y_{k,\infty} \tilde{G}_{q+j,k}(\overrightarrow{X}_\infty, \overrightarrow{Y}_\infty, \overrightarrow{V}_\infty) \\ \mathbf{V}_{j,l} &= \mathbf{V}_{j,l,\infty} + \sum_{k=1}^{p} \mathbf{V}_{k,l,\infty} \tilde{G}_{q+j,k}(\overrightarrow{X}_\infty, \overrightarrow{Y}_\infty, \overrightarrow{V}_\infty) \\ &+ \sum_{k=j+1}^{p} \mathbf{V}_{k,l+l_k} \tilde{B}_{q+j,k}(\overrightarrow{X}_\infty), \quad l \le jL, \ \ 1 \le j \le p. \end{cases} \tag{37}$$

Now from (22) and (23) in the previous section we have that

$$\begin{cases} \dot{x}_{i,\infty} &= \alpha_i x_{i,\infty} + H_x(\overrightarrow{X}, \overrightarrow{Y}, s), \quad 1 \le i \le q \\ \dot{y}_{j,\infty} &= -\beta_i y_{j,\infty} + H_y(\overrightarrow{X}, \overrightarrow{Y}, t), \quad 1 \le j \le p, \end{cases} \tag{38}$$

where for all integers n and m we have

$$\begin{aligned} |H_x| &\le \mathcal{O}\Big(\|\overrightarrow{X}\|^{n+1} \|\overrightarrow{Y}\|^m s^r \Big), \quad r \le n+m \\ |H_y| &\le \mathcal{O}\Big(\|\overrightarrow{X}\|^{n} \|\overrightarrow{Y}\|^{m+1} t^u \Big), \quad u \le n+m. \end{aligned} \tag{39}$$

In other words, we have

$$\begin{cases} \dot{x}_{i,\infty} &= \alpha_i x_{i,\infty} + \sum_{k=1}^{q} x_k H_k(\overrightarrow{X}, \overrightarrow{Y}, \overrightarrow{U}), \quad 1 \le i \le q \\ \dot{y}_{j,\infty} &= -\beta_i y_{j,\infty} + \sum_{k=1}^{p} y_k H_{q+k}(\overrightarrow{X}, \overrightarrow{Y}, \overrightarrow{V}), \quad 1 \le j \le p, \end{cases} \tag{40}$$

where H_k and H_{q+k} are flat functions at $(\overrightarrow{X}, \overrightarrow{Y}, \overrightarrow{U}, \overrightarrow{V}) = 0$. But from the above equation one gets the following new ordinary differential equation

$$\begin{cases} \dot{\mathbf{U}}_{i,l,\infty} &= \alpha_i \mathbf{U}_{i,l,\infty} + l\mathbf{U}_{i,l-1,\infty} + \sum_{k=1}^{q} \mathbf{U}_{k,l,\infty} H_k(\overrightarrow{X}, \overrightarrow{Y}, \overrightarrow{U}), \\ & \quad l \le iL, \ .1 \le i \le q \\ \dot{\mathbf{V}}_{j,l,\infty} &= -\beta_i \mathbf{V}_{j,l,\infty} + l\mathbf{V}_{i,l-1,\infty} + \sum_{k=1}^{p} \mathbf{V}_{k,l,\infty} H_{q+k}(\overrightarrow{X}, \overrightarrow{Y}, \overrightarrow{V}), \\ & \quad l \le jL, \quad 1 \le j \le p. \end{cases} \tag{41}$$

This system is completely linear up to some flat terms. Using the Sternberg theorem, we know that there exists a diffeomorphism that is close to identity and erases the flat terms. Therefore those flat functions do not appear. In other

words, we have

$$\begin{cases} \dot{x}_{i,\infty} &= \alpha_i x_{i,\infty} \\ \dot{\mathbf{U}}_{i,l,\infty} &= \alpha_i \mathbf{U}_{i,l,\infty} + l\mathbf{U}_{i,l-1,\infty}, \quad l \le iL, \quad 1 \le i \le q \\ \dot{y}_{j,\infty} &= -\beta_j y_{j,\infty} \\ \dot{\mathbf{V}}_{j,l,\infty} &= -\beta_j \mathbf{V}_{j,l,\infty} + l\mathbf{V}_{i,l-1,\infty}, \quad l \le jL, \quad 1 \le j \le p. \end{cases} \tag{42}$$

We can now express the time variables as functions of $\vec{X}_\infty$ and $\vec{Y}_\infty$. Denote by

$$\pi_\beta = \prod_{k=0}^{\frac{p}{2}-1} \beta_{2k+1}\beta_{2k+2}, \quad \pi_\alpha = \prod_{k=o}^{\frac{q}{2}-1} \alpha_{2k+1}\alpha_{2k+2},$$

and define

$$\hat{\beta}_j = \frac{\pi_\beta}{\bar{\beta}_j \beta_j} \quad (j = 1, \ldots, p), \qquad \hat{\alpha}_k = \frac{\pi_\alpha}{\bar{\alpha}_k \alpha_k} \quad (k = 1, \ldots, q).$$

Then we put

$$t = -\frac{1}{2\pi_\beta} \log \left| \sum_{k=0}^{\frac{p}{2}-1} (y_{2k+1,\infty} y_{2k+2,\infty})^{\hat{\beta}_{2k+1}} \right|$$

and

$$s = \frac{1}{2\pi_\alpha} \log \left| \sum_{k=0}^{\frac{q}{2}-1} (x_{2k+1,\infty} x_{2k+2,\infty})^{\hat{\alpha}_{2k+1}} \right|.$$

We here recall that $\bar{y}_{2k+1,\infty} = \bar{y}_{2k+2,\infty}$ is the conjugated variable associated with $y_{2k+1,\infty}$. A straightforward computation shows that $\dot{t} = 1$ and $\dot{s} = 1$. Now by (36), we prove the theorem.

References

[1] G. BELITSKII, *Equivalence and normal forms of germs of smooth mappings*, Russ. Math. Surv. **33**, 1 (1978), 107-177.

[2] I. U. BRONSTEIN AND A. YA. KOPANSKII *Smooth invariant manifolds and normal forms*, World Scientific, Singapore, 1994.

[3] P. BONCKAERT *On the continuous dependence of the smooth change of coordinates in parametrized normal forms,* J. Diff. Eq. **106** (1993), 107-120.

[4] P. HARTMAN *On local homeomorphisms of Euclidean spaces*, Bol. Soc. Mat. Mexicana, **5** (1960), 220-241.

[5] M. HIRSCH, C. PUGH, M. SHUB *Invariant Manifolds*, Lect. Notes Math., Vol. 583, Springer-Verlag, 1977.

[6] V.S.SAMOVOL *Linearization of systems of ordinary differential equations in a neighbourhood of invariant toroidal manifolds*, Proc. Moscow Math. Soc. **38** (1979), 187-219.

[7] V.S.SAMOVOL *A necessary and sufficient condition of smooth linearization of autonomous planar systems in a neighborhood of a critical point,* Matematicheskie Zametki, **46** (1989), 67-77.

[8] S. STERNBERG *On the structure of local homomorphisms of euclidean n-space, I,* Am. J. Math. **80** (1958), 623-31.

[9] S. STERNBERG *On the structure of local homomorphisms of euclidean n-space, II,* Am. J. Math. **81** (1959), 578-605.

Forcing Relation of Symmetric Non-Birkhoff Periodic Points in Standard–like Mappings [1]

Kiyotaka TANIKAWA[1] and Yoshihiro YAMAGUCHI[2]

[1] National Astronomical Observatory, Mitaka, Tokyo 181–8588, Japan.
email: tanikawa@exodus.mtk.nao.ac.jp

[2] Teikyo Heisei University, Ichihara, Chiba 290–0193, Japan.

Abstract

We study the coexistence of symmetric non-Birkhoff periodic orbits of C^1 standard–like mappings on the cylinder. We prove the equivalence of the existence of non–Birkhoff periodic orbits and that of homoclinic intersection of stable and unstable manifolds of the fixed point. We derive the positional relation of symmetric Birkhoff and non–Birkhoff periodic orbits and obtain the forcing relation of symmetric non–Birkhoff periodic orbits. In the proof of various properties of the mappings, reversibility plays an essential role.

In the monotone twist mappings, the variational principle usually is the tool for finding periodic points. The principle does not give us locations of periodic points. Reversible monotone twist mappings have their dynamical origin in reversible Hamiltonian systems. (Reversible systems contain not only time-reversible systems but also time-irreversible systems like the restricted three-body problem.) Reversibility replaces the role of the variational principle and gives us more information. It allows us to locate symmetric periodic points to some extent. Another example is that the required smoothness is only C^1. Unimodality of the mapping function simplifies the discussion. Symmetric non-monotone(i.e., non-Birkhoff) periodic points are born through tangent bifurcation. This paper explores the forcing relation of these periodic points using geometrical method. An extension of the Sharkovskii order to two-dimensional mappings has been carried out.

[1] submitted to Chaos

1 Introduction

1.1 Statement of the results

Extensions of Sharkovskii's theorem on the coexistence of periodic points or the forcing relation of periodic points to two-dimensional mappings have been carried out in various settings[1–10]. We consider in this paper a forcing relation of symmetric non–Birkhoff (i.e., non–monotone) periodic points in reversible C^1 standard–like twist mappings T on the cylinder $S^1 \times \mathbf{R}$ (see [11,12] for non–Birkhoff points, [13] for examples of these points, and [14] for reversibility):

$$T : (x, y) \mapsto (x + y + af(x) (\mathrm{mod}\ 2\pi),\ y + af(x)) \tag{1}$$

where $a \geq 0$ is a parameter and $f(x)$ satisfies the following conditions.

(A1) $f(x)$ is a periodic C^1 function with period 2π;
(A2) $f(x) = -f(2\pi - x)$;
(A3) $f(0) = 0$, and $f(x) > 0$ for $0 < x < \pi$;
(A4) $\mathrm{d}f(x)/\mathrm{d}x (= f'(x))$ is strictly monotone decreasing in $0 < x < \pi$.

Property (A2) assures the reversibility. Due to (A3), there are only two fixed points $P = (0, 0)$ and $Q = (\pi, 0)$ where P is a saddle and Q is an elliptic point or a saddle with reflection.

Example. $f(x) = \sin(x - \epsilon \sin x)$[15]. $f'(x)$ is strictly monotone decreasing in $0 < x < \pi$ if $|\epsilon| < \epsilon_1$ where $\epsilon_1 = 0.31767....$ Otherwise, there appears a point where $f'(x)$ is not monotone decreasing.

Theorem 4.6 is our main result. It gives the order relations of symmetric non–Birkhoff periodic orbits.

Theorem 4.6: For the mapping (1), there is a forcing relation $\rightarrow$ of non–Birkhoff periodic points of rotation number $1/q, q \geq 3$ such that $n \rightarrow m$ means that the existence of periodic points of period n implies the existence of periodic points of period m. The relation gives the dynamical order of non–Birkhoff periodic points as given in the following diagram. (See §4 for the precise meaning of the notations.)

$$\begin{array}{lccccccccccc}
I_1\colon & 3 & \rightarrow & 4 & \rightarrow & 5 & \rightarrow & 6 & \rightarrow & 7 & \rightarrow & \cdots \\
 & \downarrow & & \downarrow & & \downarrow & & \downarrow & & \downarrow & & \\
I_2\colon & 5 & \rightarrow & 6 & \rightarrow & 7 & \rightarrow & 8 & \rightarrow & 9 & \rightarrow & \cdots \\
 & \downarrow & & \downarrow & & \downarrow & & \downarrow & & \downarrow & & \\
I_3\colon & 7 & \rightarrow & 8 & \rightarrow & 9 & \rightarrow & 10 & \rightarrow & 11 & \rightarrow & \cdots \\
 & \downarrow & & \downarrow & & \downarrow & & \downarrow & & \downarrow & & \\
\cdots & \cdots & & \cdots & & \cdots & & \cdots & & \cdots & & \cdots
\end{array}$$

The Poincaré–Birkhoff theorem for the existence of periodic points in twist mappings is most easily proved in our setting(Theorem 3.1). Lemma 4.4 gives some idea of the relative positions of the symmetric Birkhoff and symmetric non–Birkhoff

periodic orbits. Theorem 4.5 shows the equivalence of the existence of homoclinic intersections and that of symmetric non–Birkhoff periodic orbits.

In §1.2, we introduce the notations and definitions used in this paper. In §2, we derive some useful properties of stable and unstable manifolds of P. In §3, we consider the differences between Birkhoff and non–Birkhoff periodic orbits. In §4, we derive forcing relations.

1.2 Notation and definition

We mainly work on the universal cover $\mathbf{R}^2$. We consider that $(0,0)$ is a fixed point of the lift. Then the lift of T is uniquely determined. We consider here periodic orbits of rotation number $1/q$. Our working area in most cases is restricted to the fundamental domain $0 \leq x < 2\pi$ of the universal cover. We use the same notation T and (x,y), respectively, for mappings and coordinates on the cylinder and on its universal cover. This may cause no confusion.

Now let us summarize the notations and definitions used in this paper.

1) Reversibility and symmetry axes of reversibility[14]

Mapping T has reversibility, i.e., it can be decomposed into a product of two involutions:

$$T = R_2 R_1, \tag{2}$$

where $R_1^2 = R_2^2 = \mathrm{Id}$ and $\det R_1 = \det R_2 = -1$. The set of points invariant under these involutions is called a symmetry axis. There is an infinite number of symmetry axes in the universal cover. These are

$$\begin{array}{ll} S_1^k: & x = 2\pi k, \\ S_2^k: & x = 2\pi k + \pi, \\ S_3^k: & y = 2(x - 2k\pi), \\ S_4^k: & y = 2(x - (2k+1)\pi), \end{array} \tag{3}$$

with $-\infty < k < +\infty$. Here S_1^k and S_2^k are symmetry axes for R_1, whereas S_3^k and S_4^k are those for R_2. The positive (resp. negative) part of S_i^k will be denoted by S_{i+}^k (resp. S_{i-}^k). Symmetry axes of the reversibility contained in the fundamental domain $0 \leq x < 2\pi$ or having common points with it are

$$\begin{array}{ll} S_1^0 : x = 0, & S_2^0 : x = \pi, \\ S_3^k : y = 2(x - 2k\pi), & S_4^k : y = 2(x - (2k+1)\pi). \end{array} \tag{4}$$

In what follows we use $S_1 = S_1^0, S_2 = S_2^0, S_3 = S_3^0$, and $S_4 = S_4^0$(see Fig.1). The expressions for R_1 and R_2 with respect to these axes are

$$R_1 \begin{bmatrix} y \\ x \end{bmatrix} = \begin{bmatrix} y + af(x) \\ 2\pi - x \end{bmatrix}, \quad R_2 \begin{bmatrix} y \\ x \end{bmatrix} = \begin{bmatrix} y \\ y - x \end{bmatrix}. \tag{5}$$

2) Stable manifold W_s and unstable manifold W_u of saddle P

Figure 1: Schematic illustration of four symmetry axes and the stable (W_s) and unstable (W_s) manifolds.

In the universal cover, we denote by P' the copy of P at $(2\pi, 0)$. There are two branches of stable and unstable manifolds. Those initially go into the fundamental domain and with $y > 0$ will be denoted by W_u and W_s(see Fig.1), respectively. We introduce an order $\prec_+$ on W_u in such a way that if $p, q \in W_u$, and p is closer to P along W_u than q is, then we write $p \prec_+ q$. An arc on W_u is written as $[p, q]_{W_u}$ for $p \prec_+ q$. An open arc and a semi open arc are defined similarly. We introduce an order $\prec_-$ on W_s in such a way that if $p, q \in W_s$ and q is closer to P' along W_s than p is, then we write $p \prec_- q$. Arc $[p, q]_{W_s}$ on W_s is introduced.

The stable and unstable manifolds map each other under R_1 and R_2, that is,

$$R_1 W_{s,u} = W_{u,s}, \quad R_2 W_{s,u} = W_{u,s} \tag{6}$$

We express the slopes of W_u and W_s at p and q, respectively as $\xi_u(p)$ and $\xi_s(q)$. The slopes transform each other as

$$\xi_{s,u}(R_1 p) = R_1 \xi_{u,s}(p) = -\xi_{u,s}(p) - af'(x_p), \tag{7}$$

and

$$\xi_{s,u}(R_2 p) = R_2 \xi_{u,s}(p) = \frac{\xi_{u,s}(p)}{\xi_{u,s}(p) - 1} \tag{8}$$

with $p = (x_p, y_p)$.

3) Primary homoclinic points (PHP) and primary homoclinic lobes (PHL)[16]

Let $p \in (W_u \cap W_s) \backslash P$ be a homoclinic point. If the arc $(P,p)_{W_u} \cap (p,P')_{W_s} = \emptyset$, then p is called a primary homoclinic point. The image of a PHP is also a PHP. Let u and v ($u \prec_+ v$) be adjacent PHP's of W_u and W_s. Let $\gamma_1 = [u,v]_{W_u}$ and $\gamma_2 = [u,v]_{W_s}$. The open region bounded by γ_1 and γ_2 is called a primary homoclinic lobe (PHL). The image of a PHL is also a PHL.

4) Symmetric Birkhoff and non–Birkhoff periodic orbits (SBO and SNBO)

Let (x_k, y_k), $k \in \mathbf{Z}$, where $(x_{k+1}, y_{k+1}) = T(x_k, y_k)$, be an orbit with rotation number $1/\alpha, \alpha > 0$. The orbit is monotone or Birkhoff if $x_k < x_{k+1}$ for any k. If the orbit is non–monotone, $x_k \leq x_{k-1}$ for some k. In this case, we have $y_k \leq 0$. If $x_{k+q} = x_k + 2\pi$, $y_{k+q} = y_k$ for some $q > 1$, the orbit is periodic. The minimum q which satisfies this condition is called the period of the orbit. A periodic orbit which has points on different symmetry axes is called symmetric. There are three kinds of symmetric periodic orbits[14]. In our notation, these are a $2k$–periodic orbit starting in S_{1+} and having a point in S_2 at the k–th iterate, a $2k$–periodic orbit starting in S_{3+} and having a point in S_4 at the k–th iterate, and a $(2k+1)$–periodic orbit starting in S_{1+} (resp. S_{2+}) and having a point in S_4 (resp. S_3) at the $(k+1)$–st iterate.

An orbit which is symmetric, periodic, and monotone is called a symmetric Birkhoff periodic orbit (SBO). A point of an SBO is a symmetric Birkhoff periodic point(SBP). An orbit which is symmetric, periodic, and non–monotone is called a symmetric non–Birkhoff orbit (SNBO). A point of an SNBO is a symmetric non–Birkhoff periodic point (SNBP).

2 Some properties of W_u and W_s

We now discuss some initial behaviors of W_u and W_s. These will be useful in later sections. Let $D = \{(x,y) | 0 < x < \pi, y > 0\}$. Let $p \in \partial D$ be a point on W_u such that $(P,p)_{W_u} \subset D$ and such that there is a point q in any small neighborhood of p satisfying $q \notin \mathrm{clos}(D)$, $p \prec_+ q$ where $\mathrm{clos}(D)$ is the closure of D. We say W_u exits D if p exists. More precisely, we say W_u exits D at p through S_{2+} if $p \in S_{2+}$.

The following lemma is basic(see [17] for C^2 case).

Lemma 2.1. (i) W_u exits D at a point u through S_{2+}.

(ii) The slope of the graph of $[P,u]_{W_u}$ is strictly monotone decreasing and is positive in $\mathrm{clos}(D)$.

(iii) The graph of $[u,P']_{W_s}$ is unimodal and its slope is strictly monotone decreasing.

Proof. (i) We first show that u exists. The initial slope of W_u at P is positive and less than one as is easily confirmed by linear analysis. Let p be a point close to P on the initial arc of W_u. The x– and y–coordinates of its images under T increase and images are below $y = x$ as long as the preceding ones are in D. If the images do not exit D, they accumulate at a point, i.e. a fixed point in $\mathrm{clos}(D)$. But we do not have a fixed point with positive y. Thus W_u exits D.

Suppose W_u exits D through the x–axis at u. $T^{-1}u$ has a positive y–coordinate, which implies $f(x) < 0$ at $T^{-1}u$. This is impossible in D. So W_u exits D through S_{2+}.

(ii) We first show that the slope is strictly monotone decreasing. The mapping of the slope of W_u is given by

$$\xi(Tp) = \frac{\xi(p) + f'(x_p)}{1 + \xi(p) + f'(x_p)}, \tag{9}$$

where x_p is the x–coordinate of p. The slope changes continuously unless the denominator becomes zero. Let $w = u$ if the slope of the graph of $[P, u]_{W_u}$ is non–negative in clos(D) and let $w \in [P, u]_{W_u}$ be a point of a negative slope otherwise. We will show the slope is strictly monotone decreasing in $[P, w]_{W_u}$. Assume $\xi(p) \leq \xi(q)$ for some p and q, $p \prec_+ q \prec_+ w$ and derive a contradiction. Let $p_{-n} = T^{-n}p$ and $q_{-n} = T^{-n}q$. We obtain

$$\xi(q_{-1}) - \xi(p_{-1}) = \alpha(p, q)(\xi(q) - \xi(p)) - (f'(x_{q_{-1}}) - f'(x_{p_{-1}})) > 0 \tag{10}$$

with

$$\alpha(p, q) = (1 + \xi(q_{-1}) + f'(x_{q_{-1}}))(1 + \xi(p_{-1}) + f'(x_{p_{-1}})). \tag{11}$$

Repeating the procedure, we obtain

$$\xi(q_{-n}) - \xi(p_{-n}) \to \infty \quad \text{as} \quad n \to \infty. \tag{12}$$

This contradicts the fact that the slope of the graph of $[P, w]_{W_u}$ becomes constant near P.

Next, let us show that the slope is positive in $[P, u]_{W_u}$. Suppose the contrary, that the slope of $[P, u]_{W_u}$ becomes zero for the first time at some point $w \prec_+ u$. We have $(R_1 w, P']_{W_s} = R_1[P, w)_{W_u}$ and the slope is given by Eq.(7), i.e.,

$$\xi_s(R_1 p) = -\xi_u(p) - f'(x_p). \tag{13}$$

$\xi_s(R_1 p)$ is strictly monotone increasing with p since $\xi_u(p)$ and $f'(x_p)$ are strictly monotone decreasing. Therefore, the slope of W_s is strictly monotone decreasing from $R_1 w$ to P'. On the other hand, arc $(R_2 w, P']_{W_s} = R_2[P, w)_{W_u}$ has zero slope at $R_2 w$ which is closer to P' than $R_1 w$ is. The slope of W_s at $R_1 w$ is positive, i.e., $f'(x_w) < 0$(we can easily show that the slope of the graph of $[P, w]$ is positive if $f'(x_w) > 0$). This implies that between $(R_1 w, R_2 w)_{W_s}$ there should be negative slopes followed by a zero slope as x increases. This is a contradiction.

(iii) We have $[u, P']_{W_s} = R_1[P, u]_{W_u}$. The transformation of the derivative is given by Eq.(13). $\xi_s(R_1 p)$ is strictly monotone decreasing when $R_1 p$ moves from $u = R_1 u$ to P' because of (ii). If $\xi_s(u)$ is non–positive, then the y–coordinate decreases from u to P' along W_s. But this is impossible because $Tu \in (u, P')_{W_s}$ and Tu has the same y–coordinate as u. Therefore, we have $\xi_s(u) > 0$. This means that W_s has a peak between u and P'. □

Theorem 2.2: $W_u \cap W_s \neq \emptyset$ for any $a > 0$.

Proof: W_u and W_s pass through point u in Lemma 2.1(i). □

Let $v \in (u, P')_{W_s}$ be the point on S_{4+}. Symmetry R_2 assures that W_u passes v, and v is a PHP.

Lemma 2.3: The graph of $[P, v]_{W_u}$ is either monotone increasing or unimodal. Its slope is strictly monotone decreasing.

Proof: The slope of the graph of $[v, P']_{W_s}$ is transformed to the slope of the graph of $[P, v]_{W_u}$ by Eq.(8). The difference of slopes is transformed as

$$\xi_u(R_2 p) - \xi_u(R_2 q) = \frac{\xi_s(q) - \xi_s(p)}{(\xi_s(p) - 1)(\xi_s(q) - 1)}. \tag{14}$$

From this relation and Lemma 2.1(iii), the slope is strictly monotone decreasing along $[P, v]_{W_u}$ as long as $\xi_s(v) < 1$. We shall show that we always have $\xi_s(v) < 1$.

Let us assume the contrary, that $\xi_s(v) \geq 1$ for some parameter value a. Then $\xi_s(p) > 1$ for all $p \in [u, v)_{W_s}$. From Eq.(8), $\xi_u(R_2 p) > 0$ for $R_2 p \in (v, Tu]_{W_u}$. This implies that the x–coordinate of Tu is smaller than that of v. On the other hand, the x–coordinate of Tu should be larger than that of v because $Tu \in [v, P']_{W_s}$. This is a contradiction. □

Let $\Gamma_0 = [P, v]_{W_u} \cup [v, P']_{W_s}$ and let us denote by V the open region above Γ_0 in the fundamental domain. Similarly, U is the open region with positive y and below Γ_0. Further let $V \backslash S_{4+} = V_1 \cup V_2$ where V_1 is to the left of S_{4+}. Let $U \backslash S_{4+} = U_1 \cup U_2$ where U_1 is to the left of S_{4+}.

Proposition 2.4: $TV_1 \cap U_1 = \emptyset$, $T^{-1}V_2 \cap U_2 = \emptyset$.

Proof: We confirm the former relation. The latter relation is obtained from the former by reversibility. For the proof, it is sufficient to show that there is no point $p \in \partial V_1 = S_{1+} \cup [P, v]_{W_u} \cup \{\text{segment of } S_{4+} \text{ above } v\}$ such that $Tp \in U_1$ since both TV_1 and U_1 are open and arcwise connected.

Obviously $Tp \notin U_1$ for $p \in S_{1+}$ since we know that TS_{1+} is above $[P, v]_{W_u}$. Next, let $p = (x, y) \in S_{4+}$, $Tp = (x^*, y^*)$. In order that $Tp \in U_1$, it is necessary that $x^* < x$ and $0 < y^* < y$. But this is impossible. To have $x^* < x$, we need to have $y^* < 0$.

Let us consider the image of $[P, v]_{W_u}$. We divide the arc: $[P, v]_{W_u} = [P, v_{-1}]_{W_u} \cup [v_{-1}, u]_{W_u} \cup [u, v]_{W_u}$ where $v_{-1} = T^{-1}v$. So, $T[P, v]_{W_u} = [P, v]_{W_u} \cup [v, Tu]_{W_u} \cup [Tu, Tv]_{W_u}$. Obviously, $[P, v]_{W_u} \cap U_1 = \emptyset$. We have $R_2[v, Tu]_{W_u} = [u, v]_{W_s}$. We know that $[u, v]_{W_s} \cap S_{4+} = v$. This implies $[v, Tu]_{W_u} \cap S_{4+} = v$. Finally let us consider $T[u, v]_{W_u} = [Tu, Tv]_{W_u}$. This curve is contained in the area sandwiched between TS_{2+} and TS_{4+}. One observes that this area is below the half–line TS_{2+} or below the x–axis with $x \leq \pi$. This means $T[u, v]_{W_u}$ does not have points common with the boundary of U_1. □

3 Birkhoff and non–Birkhoff orbits

In this section, we consider the positional difference of Birkhoff and non–Birkhoff orbits.

The Poincaré–Birkhoff theorem on the existence of periodic points in twist mappings has been repeatedly proved[18–21,11]. In our setting, we can in addition specify the positions of these points to some extent using the reversibility. Here we prove the theorem for the points with rotation number $1/q, q > 0$.

Theorem 3.1: There are Birkhoff periodic points with rotation number $1/q(q > 0)$ in every symmetry axis for standard–like mappings.

Remark. There are at least two Birkhoff periodic points for every rotation number of the form $1/q$.

Proof. We only consider Birkhoff periodic orbits with rotation number $1/(2k)$, $k = 1, 2, \ldots$ and starting in S_{1+}. The proof is similar for odd periods or for orbits starting in other symmetry axes.

The future orbit of the SBP with rotation number $\frac{1}{2}$ is $(n\pi/, \pi), n = 1, 2, \ldots$. TS_{1+} is a half line starting from $(0, 0)$ and passing through (π, π). We know that W_u starting at P intersects S_{2+} at u for the first time. Let $\mathcal{F}$ be the region bounded by TS_{1+}, $[P, u]_{W_u}$, and S_{2+}. Any two $T^k S_{1+}$ and $T^{k+1} S_{1+}$ are disjoint except at $(0, 0)$ and all $T^k S_{1+}$, $k \geq 2$ are disjoint from $(P, u]_{W_u}$ and they pass through $(k\pi/2, \pi)$. So they exit $\mathcal{F}$ through S_{2+}, which implies the existence of a point of period $2k$ with rotation number $1/(2k)$.

We have $R_2 T^k S^0_{1+} = T^{-(k-1)} S^1_{1+}$ and $R_1 T^k S^0_{1+} = T^{-k} S^1_{1+}$. These relations allows us to show that each of $T^k S^0_{1+}, k = 2, 3, \ldots$ is monotone increasing in $\mathcal{F}$ as a graph. If this is shown, then periodic point p discovered in the former paragraph is monotone because all the arcs of $T^k S^0_{1+}$ between $(0, 0)$ and p are in $\mathcal{F}$, i.e., above the x–axis. We proceed by induction. For $k = 1$, our assertion is true that the graph of $T^k S^0_{1+}$ is monotone increasing in $\mathcal{F}$. Suppose that for $k < n$, the graph of $T^k S^0_{1+}$ is monotone increasing in $\mathcal{F}$ and that for $k = n$, $T^k S^0_{1+}$ has a point of zero slope in $\mathcal{F}$. Then relation $R_2 T^k S^0_{1+} = T^{-(k-1)} S^1_{1+}$ indicates that the graph of $T^{-(k-1)} S^1_{1+}$ has a point of zero slope to the right of S_{4+}. On the other hand, relation $R_1 T^{k-1} S^0_{1+} = T^{-(k-1)} S^1_{1+}$ together with the hypothesis of the induction indicates that the slope of $T^{-(k-1)} S^1_{1+}$ on S_{2+} is increasing, which implies at least two points of the zero slope of $T^{-(k-1)} S^1_{1+}$ for $\pi < x < 2\pi$. This contradicts the monotone increase of the graph of $T^{k-1} S^0_{1+}$ in $\mathcal{F}$. Thus the graph of $T^k S^0_{1+}, k = n$ is monotone increasing in $\mathcal{F}$.

Let us consider symmetric periodic orbits with rotation number $1/(2k)$ starting in S^0_{3+}. S^0_{3+} is contained in the region sandwiched between S^0_{1+} and TS^0_{1+}. T is a homeomorphism in the universal cover and the region has only one fixed point on its vertex $(0, 0)$. Then each $T^n S^0_{3+}$ is sandwiched between $T^n S^0_{1+}$ and $T^{n+1} S^0_{1+}$. This implies that each $T^n S^0_{3+}$ exits $\mathcal{F}$ through S_{2+} and before intersecting the x–axis if any, it intersects S^0_{4+}. This means that there is a symmetric periodic orbit with rotation number $1/(2k)$ which starts in S^0_{3+}. □

The location of a monotone periodic orbit has been specified to some extent in

the sense that two of its orbital points are on the symmetry axes. We want to specify the positions of the remaining orbital points. Let us consider the relative disposition of W_u and W_s. Let us assume that W_u and W_s have homoclinic intersections. We know that there are PHPs on S_{2+} and S_{4+}. We call these u and v, respectively(see §2). In many cases, u and v are adjacent. However, there are cases in which there is another PHP between them due to the bifurcation of homoclinic points u and/or v[15]. We cannot exclude the possibility of an infinite number of PHPs in $(u,v)_{W_u}$ when f is C^1.

Let $w_i, i = 1,2,\ldots,N$ be PHPs in $(u,v)_{W_u}$ satisfying $w_i \prec_+ w_{i+1}$. $N = 0$ or $N \to \infty$ is allowed. Arcs $(u,v)_{W_u}$ and $(u,v)_{W_s}$ are graphs. It is meaningful to say that one of their two subarcs is above or below the other according to the height of the points at the same x-coordinate. There are three cases(see Fig.2).

case 1) $N = 0$ and $(u,v)_{W_s}$ is above $(u,v)_{W_u}$.
case 2) $N = 0$ and $(u,v)_{W_s}$ is below $(u,v)_{W_u}$.
case 3) $N \neq 0$.

Let us carefully consider case 3). Let $(w_{k_i}, w_{k_i+1})_{W_s}$ be the arcs above $(w_{k_i}, w_{k_i+1})_{W_u}$ where $1 \leq k_i \leq N, i = 1,2,\ldots,N_h$ is an increasing sequence. Let $\hat{w}_i = R_2 w_i$, $i = 1,\ldots,N$. Then $\hat{w}_i$ are PHPs in $[v,Tu]_{W_u}$. We have $(\hat{w}_{k_i+1}, \hat{w}_{k_i})_{W_u} = R_2(w_{k_i}, w_{k_i+1})_{W_s}$. $(\hat{w}_{k_i+1}, \hat{w}_{k_i})_{W_u}$ is above $(\hat{w}_{k_i+1}, \hat{w}_{k_i})_{W_s}$.

Let us introduce curves dividing the cylinder into upper and lower components. Let

$$\begin{aligned} \Gamma_0 &= [P,v]_{W_u} \cup [v,P']_{W_s}, \\ \Gamma^{\text{out}} &= [P,u]_{W_u} \cup \gamma^{\text{out}} \cup [Tu,P']_{W_s}, \\ \Gamma^{\text{in}} &= [P,u]_{W_u} \cup \gamma^{\text{in}} \cup [Tu,P']_{W_s}, \end{aligned} \tag{15}$$

where

$$\gamma^{\text{out}} = \begin{cases} [u,v]_{W_s} \cup [v,Tu]_{W_u}, & \text{in case 1)} \\ [u,v]_{W_u} \cup [v,Tu]_{W_s}, & \text{in case 2)} \\ \gamma_1 \cup ([u,v]_{W_u} - \gamma_1^*) \cup \gamma_2 \cup ([v,Tu]_{W_s} - \gamma_2^*), & \text{in case 3)} \end{cases}$$
$$\gamma^{\text{in}} = \begin{cases} [u,v]_{W_u} \cup [v,Tu]_{W_s}, & \text{in case 1)} \\ [u,v]_{W_s} \cup [v,Tu]_{W_u}, & \text{in case 2)} \\ \gamma_1^* \cup ([u,v]_{W_s} - \gamma_1) \cup \gamma_2^* \cup ([v,Tu]_{W_u} - \gamma_2), & \text{in case 3)} \end{cases} \tag{16}$$

with

$$\begin{aligned} \gamma_1 &= \cup_{i=1}^{N_h} (w_{k_i}, w_{k_i+1})_{W_s}, \quad \gamma_2 = \cup_{i=1}^{N_h} (\hat{w}_{k_i+1}, \hat{w}_{k_i})_{W_u}, \\ \gamma_1^* &= \cup_{i=1}^{N_h} (w_{k_i}, w_{k_i+1})_{W_u}, \quad \gamma_2^* = \cup_{i=1}^{N_h} (\hat{w}_{k_i+1}, \hat{w}_{k_i})_{W_s}. \end{aligned} \tag{17}$$

Let $\mathcal{E}_0$, $\mathcal{E}^{\text{out}}$ and $\mathcal{E}^{\text{in}}$ be the lower components of the cylinder divided in turn by Γ_0, Γ^{out} and Γ^{in}. Let

$$\mathcal{H} = \mathcal{E}^{\text{out}} - \text{clos}(\mathcal{E}^{\text{in}}). \tag{18}$$

Then, $\mathcal{H}$ consists of PHLs. Let

$$\mathcal{H} = \mathcal{H}_s \cup \mathcal{H}_u, \tag{19}$$

Figure 2: Primary homoclinic lobes for cases 1), 2) and 3).

where $\mathcal{H}_s$ consists of PHLs whose upper boundary is composed of W_s, whereas $\mathcal{H}_u$ consists of PHLs whose upper boundary is composed of W_u. In cases 1) and 2), $\mathcal{H}_s$ consists of a unique component which is to the left in case 1) and to the right of S_{4+} in case 2). In case 3), $\mathcal{H}_s$ has more than one components, some of them being to the left of S_{4+} and others to the right. A well–known feature of $\mathcal{H}_s$ and $\mathcal{H}_u$ to be used here is that these or their iterates are sometimes contained in $\mathcal{E}_0$ and otherwise out of $\mathcal{E}_0$.

Cases 2) and 3) are not necessarily realized for all values of a. In fact, the slopes of W_u and W_s are related through Eq.(7). We have at u

$$\xi_s(u) + \xi_u(u) = -af'(\pi). \tag{20}$$

$\xi_s(u) < \xi_u(u) < 1$ in case 2) and part of case 3). We have in these cases

$$a < 2/|f'(\pi)|. \tag{21}$$

The remaining part of case 3) is not realized for large a, In fact, for large $a > 0$, the peak of the graph $[u, v]_{W_s}$ becomes large. The absolute values of slope of W_s at u and v should be large, whereas those of W_u are small. Intersections of W_u and W_s are impossible between u and v.

Proposition 3.2: All the points of any SBO with rotation number $1/q$ are above Γ^{out}.

Proof: We first show that all the points of any SBO are above Γ_0. At least one point of a given SBO exists above Γ_0 since the SBO has one of its points in S_{1+} or S_{3+}. Suppose that a point of the orbit $\{p_i\}$ of an SBO is below Γ_0. Then there exists an integer i such that $p_{i-1} \in V_1$ and $p_i \in U_1$ or $p_i \in U_2$. But by reversibility, if $p_i \in U_2$, then p_{q+2-i} is in U_1. Since we are considering the SBOs of rotation number $1/q$, this means that there exists j such that $p_j \in V_1$ and $p_{j+1} \in U_1$, which contradicts Proposition 2.4.

No points of the SBOs are in the homoclinic lobe $\mathcal{H}$. As we pointed out above, some forward or backward iterates of $\mathcal{H}$ fall below Γ_0. □

Franks[22] proved the following theorem. The theorem is adapted to our setting. Let $\mathcal{D}$ be the region bounded by the simple heteroclinic cycle P, P' and v, v' where v' is the primary homoclinic point obtained by rotating v by angle π with its center at Q.

Theorem 3.3[22]: Let p/q be a rational number between 0 and $\rho_P(Q, T)$, the total infinitesimal rotation number relative to P. Then $\mathcal{D}$ contains a periodic point x whose rotation number around Q is equal to p/q. The entire orbit of x lies in $\mathcal{D}$.

See [22] for the definition of the 'total infinitesimal rotation number'. We can slightly extend the result. Let $\mathcal{D}^{\text{in}}$ be the region bounded by Γ^{in} and the arc obtained by rotating Γ^{in} by angle π with center at Q. $\mathcal{D}^{\text{in}}$ is not bounded by a simple heteroclinic cycle.

Proposition 3.4: Let p/q be a rational number between 0 and $\rho_P(Q, T)$, the total infinitesimal rotation number relative to P. Then $\mathcal{D}^{\text{in}}$ contains a periodic point x whose rotation number around Q is equal to p/q. The entire orbit of x lies in $\mathcal{D}^{\text{in}}$.

Proof: We only have to show that the periodic orbit encircling Q does not have a point in homoclinic lobes. This is obvious because otherwise the orbit has a point above Γ_0 or below the lower boundary of $\mathcal{D}$. □

Propositions 3.2 and 3.4 give us information about the meaning and role of the homoclinic lobe $\mathcal{H}$. It turns out that $\mathcal{H}$ contains neither SBPs nor periodic points encircling fixed point Q. Periodic points contained in $\mathcal{H}$ are non–Birkhoff points of a non–zero rotation number. This is easily confirmed.

4 Forcing relation of non–Birkhoff orbits

We assume that W_u and W_s intersect transversely for $a > 0$. We introduced in §3 homoclinic lobe $\mathcal{H}$. This has at least two components. We introduced $\mathcal{H}_s$ and $\mathcal{H}_u$. One easily confirms that

$$\begin{array}{llll} \mathcal{H}_s \cap \mathcal{E}_0 = \emptyset, & \mathcal{H}_u \cap \mathcal{E}_0 = \emptyset, & T\mathcal{H}_s \subset \mathcal{E}_0, & \text{and } T^{-1}\mathcal{H}_u \subset \mathcal{E}_0 \quad \text{for case 1),} \\ \mathcal{H}_s \subset \mathcal{E}_0, & \mathcal{H}_u \subset \mathcal{E}_0, & T^{-1}\mathcal{H}_s \cap \mathcal{E}_0 = \emptyset, & \text{and } T\mathcal{H}_u \cap \mathcal{E}_0 = \emptyset \quad \text{for case 2).} \end{array} \tag{22}$$

In case 3), each $\mathcal{H}_i, i = s, u$ has components both to the left and right of S_{4+}. Let $\mathcal{H}_i = \mathcal{H}_i^l \cup \mathcal{H}_i^r, i = s, u$ where $\mathcal{H}_i^l$ and $\mathcal{H}_i^r$ are the left and right components, respectively. We have

$$\left.\begin{array}{llll} \mathcal{H}_s^l \cap \mathcal{E}_0 = \emptyset, & \mathcal{H}_u^r \cap \mathcal{E}_0 = \emptyset, & T\mathcal{H}_s^l \subset \mathcal{E}_0, & \text{and } T^{-1}\mathcal{H}_u^r \subset \mathcal{E}_0, \\ \mathcal{H}_s^r \subset \mathcal{E}_0, & \mathcal{H}_u^l \subset \mathcal{E}_0, & T^{-1}\mathcal{H}_s^r \cap \mathcal{E}_0 = \emptyset, & \text{and } T\mathcal{H}_u^l \cap \mathcal{E}_0 = \emptyset. \end{array}\right\} \text{for case 3)} \tag{23}$$

Let us formally write $\mathcal{H}_s = \mathcal{H}_s^l \cup \mathcal{H}_s^r$ also in cases 1) and 2). We have $\mathcal{H}_s^r = \emptyset$ in case 1) and $\mathcal{H}_s^l = \emptyset$ in case 2).

Proposition 4.1. W_u and W_s are assumed to have homoclinic intersections for $a > 0$. Then,

(i) $T^{-1}\mathcal{H}_s^r \cap S_1^+ = \emptyset$;

(ii) $T\mathcal{H}_s \cap S_{4-} \neq \emptyset$ for sufficient large $a > 0$;

(iii) $T^{-1}\mathcal{H}_s^l \cap S_{1+} \neq \emptyset$ for sufficient large $a > 0$;

(iv) For any $a > 0$, there exists $n > 0$ such that $T^{-n}\mathcal{H}_s \cap S_{1+} \neq \emptyset$; and

(v) For any $a > 0$, there exists $n > 0$ such that $T^n\mathcal{H}_s \cap S_{4-} \neq \emptyset$.

Proof. (i) $T^{-1}[v, Tu,]_{W_s} = R_1R_2[v, Tu]_{W_s} = R_1[u, v]_{W_u}$ is a graph in D(see §2) and region $T^{-1}\mathcal{H}_s^r$ is below this graph.

(ii) We only need to consider case 1) and show that $T[u, v]_{W_u} \cap S_{4-} \neq \emptyset$. In cases 2) and 3), parameter value a cannot be large.

Take a point $p = (x, y) \in [v_{-1}, u)_{W_u}$ and consider three points $R_1p = (x^*, y^*) \in (u, v]_{W_s}$, $w = (x^*, \tilde{y}) \in (u, v]_{W_u}$, and $Tw = (x^{**}, y^{**})$. We have

$$y^{**} = \tilde{y} - af(x), \quad x^{**} = 2\pi - x + y^{**} \tag{24}$$

Both x^{**} and y^{**} are negative for a large value of a since x and $\tilde{y}$ are of the order of 2π. Tw is near the line $y = x$, and hence above $y = 2(x - \pi)$. This means that $T[u, v]_{W_u} \cap S_{4-} \neq \emptyset$ for a sufficiently large $a > 0$.

(iii) For large $a > 0$, there are points in $[u, v]_{W_s}$ which are above $y = x$. The x–coordinates of images of these points under T^{-1} are negative.

(iv) and (v). Proof is trivial. We apply the lambda lemma[23] to the arc of W_s of $\mathcal{H}_s$ in (iv) and to the arc of W_u of $\mathcal{H}_s$ in (v). □

We introduce intervals

$$I_n = S_{1+} \cap T^{-n}\mathcal{H}_s, \quad n \geq 1. \tag{25}$$

Figure 3: Appearance of interval I_1 through the homoclinic tangency of W_u and W_s on S_1 when $f(x) = 2.922 \sin x$.

and critical parameter values

$$a_c(I_n) = \inf\{a > 0 | I_n \text{ is not empty}\}. \tag{26}$$

One easily confirms the following two relations from the twist property and Proposition 4.1(iv).

$$0 < \cdots < a_c(I_2) < a_c(I_1), \tag{27}$$

$$\lim_{n\to\infty} a_c(I_n) = 0 \text{ if } \mathrm{W_u} \text{ and } \mathrm{W_s} \text{ intersect transversely for } a > 0. \tag{28}$$

The appearance of I_1 is shown in Fig.3.

Proposition 4.2: (i) $T^{n+1}I_n \cap S_{4-} \neq \emptyset$ for any $n \geq 1$ and sufficiently large $a > 0$.
(ii) $T^{n+m}I_n \cap S_{4-} \neq \emptyset$ for any $a > 0, n \geq 1$ and sufficiently large $m > 0$.

Proof: (i) I_n divides region $T^{-n}\mathcal{H}_s$ into two, the left and right sides of this arc. The relative area of the right region decreases to zero as we increase a because the leftmost point of $T^{-n}\mathcal{H}_s$ tends to negative infinity. This means that arc $T^{n+1}I_n$ becomes closer and closer to $T[u,v]_{W_u}$ in $T\mathcal{H}_s$ as a increases. From Proposition 4.1(ii), $T[u,v]_{W_u}$ crosses S_{4-} for sufficient large $a > 0$. Then our assertion holds.

(ii) I_n divides region $T^{-n}\mathcal{H}_s$ into two, the left and right sides of this arc. The relative area of the right region is given for fixed a and n. From Proposition 4.1(v), for any $a > 0$, there exists $m > 0$ such that $T^m\mathcal{H}_s \cap S_{4-} \neq \emptyset$. By the lambda lemma, the area of $T^m\mathcal{H}_s$ which is to the left of S_{4-} increases as m increases. This means that arc $T^{n+m}I_n \in T^m\mathcal{H}_s$ crosses S_{4-} as m increases. □

Lemma 4.3: The minumum possible period of an SNBP in I_n $(n \geq 1)$ is $(2n+1)$. Its rotation number is $1/(2n+1)$.

Proof: From Proposition 4.2(i), $T^{n+1}I_n \cap S_{4-} \neq \emptyset$ for any $n \geq 1$ and sufficiently large $a > 0$. This means the existence of an SNBP of period $(2n+1)$ with rotation number $1/(2n+1)$. □

Let J_n be the arc of S_{1+} between I_n and I_{n+1}. The following lemma describes the vertical relative positions of SBPs and SNBPs of similar rotation numbers.

Lemma 4.4: (i) J_n contains SBPs with rotation number $1/(2n)$ and $1/(2n+1)$ for case 1).

(ii) J_n contains SBPs with rotation number $1/(2n-1)$ and $1/(2n)$ for case 2).

(iii) J_n contains SBPs with rotation number $1/(2n-1)$, $1/(2n)$, and $1/(2n+1)$ for case 3), provided that $S_{1+} \cap T^{-n}\mathcal{H}_s^l \neq \emptyset$ and $S_{1+} \cap T^{-n}\mathcal{H}_s^r \neq \emptyset$.

Proof: (i) Take I_n and I_{n+1}. $T^n I_n$ is in $\mathcal{H}_s$, whereas $T^n I_{n+1}$ is in D which is defined in the beginning of §2. Then $T^n J_n$ connecting $T^n I_n$ and $T^n I_{n+1}$ necessarily intersects S_{2+}. Therefore the intersection point is a $(2n)$–periodic point with rotation number $1/(2n)$. It is monotone since $T^k J_n, k = 1, 2, \ldots, n-1$ are contained in D.

$T^{n+1} I_n$ is to the right of S_{4+} and $T^{n+1} I_{n+1} \subset \mathcal{H}_s$. Therefore, $T^{n+1} J_n$ intersects S_{4+}. The intersection point is a $(2n+1)$–periodic point with rotation number $1/(2n+1)$.

(ii) The argument is almost the same. The difference is that $\mathcal{H}_s$ is to the right of S_{4+}.

(iii) Apply the argument of (i) and (ii). □

It is well known that non–integrability is equivalent with the existence of homoclinic intersections[24]. The following theorem says that the existence of homoclinic intersections is equivalent with the existence of SNBOs. The existence of SNBOs can be detected easier than that of a horseshoe in near–integrable cases. In addition, we may use SNBOs to measure the complexity of a given dynamical system[5].

Theorem 4.5: There are SNBOs with non-zero rotation numbers if and only if W_u and W_s have homoclinic intersections.

Proof: Sufficiency: An SNBO of rotation number $1/q, q \geq 3$ has a point above the x-axis and a point below the x-axis. The argument is similar for an SNBO with negative rotation number. This excludes the possibility of a smooth connection of W_u and W_s. By Theorem 2.2, W_u and W_s have homoclinic intersections.

Necessity: From Eq.(28) and Proposition 4.2(ii), there are SNBPs for any small $a > 0$. □

Finally we arrive at our main result. We consider symmetric non–Birkhoff periodic points in I_n. We define a forcing relation $\rightarrow$ in such a way that $m_{I_n} \rightarrow m'_{I_{n'}}$ if the existence of an SNBP of period m in I_n implies the existence of an SNBP of period m' in $I_{n'}$.

Theorem 4.6:

(i) $(2m+1)_{I_n} \rightarrow (2m+2)_{I_n}$ for $m \geq n \geq 1$.

(ii) $(2m+1)_{I_n} \rightarrow (2m+3)_{I_{n+1}}$ for $m \geq n \geq 1$.

(iii) $(2m)_{I_n} \rightarrow (2m+1)_{I_n}$ for $m \geq n+1 \geq 2$.

(iv) $(2m)_{I_n} \rightarrow (2m+2)_{I_{n+1}}$ for $m \geq n+1 \geq 2$.

These relations are combined into the following diagram.

$$
\begin{array}{lccccccccccc}
I_1\colon & 3 & \to & 4 & \to & 5 & \to & 6 & \to & 7 & \to & \dots \\
 & \downarrow & & \downarrow & & \downarrow & & \downarrow & & \downarrow & & \\
I_2\colon & 5 & \to & 6 & \to & 7 & \to & 8 & \to & 9 & \to & \dots \\
 & \downarrow & & \downarrow & & \downarrow & & \downarrow & & \downarrow & & \\
I_3\colon & 7 & \to & 8 & \to & 9 & \to & 10 & \to & 11 & \to & \dots \\
 & \downarrow & & \downarrow & & \downarrow & & \downarrow & & \downarrow & & \\
\dots & \dots & & \dots & & \dots & & \dots & & \dots & & \dots
\end{array}
$$

Proof. (i) By hypothesis, $T^{m+1}I_n \cap S_{4-} \neq \emptyset$. This implies $T^{m+1}I_n \cap S_{2-} \neq \emptyset$. I_n contains a $(2m+2)$–periodic point.

(ii) $T^{m+2}I_{n+1}$ and $T^{m+1}I_n$ are in the same iterate of $\mathcal{H}_s$. $T^{m+2}I_{n+1}$ is closer to the unstable arc of $\mathcal{H}_s$. Therefore $T^{m+1}I_n \cap S_{4-} \neq \emptyset$ implies $T^{m+2}I_{n+1} \cap S_{4-} \neq \emptyset$. I_{n+1} contains a $(2m+3)$–periodic point.

(iii) By hypothesis, $T^{m}I_n \cap S_{2-} \neq \emptyset$. Then $T^{m+1}I_n \cap S_{4-} \neq \emptyset$ by the twist property. I_n contains a $(2m+1)$–periodic point.

(iv) $T^{m+1}I_{n+1}$ and $T^{m}I_n$ are in the same iterate of $\mathcal{H}_s$. $T^{m+1}I_{n+1}$ is closer to the unstable arc of $\mathcal{H}_s$. This means $T^{m+1}I_{n+1} \cap S_{2-} \neq \emptyset$. I_{n+1} contains a $(2m+2)$–periodic point. □

Acknowledgments

The authors express their thanks to Dr. T. Matsuoka for discussions. They thanks Dr. V. Naudot for reading the manuscript. Yolande McLean has improved the English.

References

[1] T. Matsuoka, Braids of periodic points and a 2–dimensional analogue of Sharkovskii's ordering, World Sci. Adv. Ser. in Dynamical Systems **1** 58–72(1986).

[2] K. Tanikawa and Y. Yamaguchi, Coexistence of periodic points in reversible dynamical systems on a surface *Journ. Math. Phys.* **28** 921–928(1987).

[3] K. Tanikawa and Y. Yamaguchi, Coexistence of periodic points in the Standard Map *Journ. Math. Phys.* **30**, 608–616(1989).

[4] P. Boyland, An analog of Sharkovski's theorem *Contemporary Mathematics* **81**, 119–133(1988).

[5] P. Boyland, Topological methods in surface dynamics *Topology and Its Applications* **58** 223–298(1994).

[6] S. Baldwin, An extension of Sharkovskii's theorem to the n–od *Ergod. Th. & Dynami. Sys.* **11** 249–271(1991).

[7] S. Baldwin, Version of Sharkovskii's theorem on trees and dendrites *Topology proceedings* **18** 19–31(1993).

[8] T. Hall, The creation of horseshoes *Nonlinearity* **7** 861–924(1994).

[9] M. Handel, The forcing partial order on the three times punctured disk *Ergod. Th. & Dynami. Sys.* **17** 593–610(1997).

[10] J. Los, On the forcing relation for surface homeomorphisms *I.H.E.S.* 5–61(1997).

[11] A. Katok, Some remarks on Birkhoff and Mather twist map theorems *Ergod. Th. & Dynam. Sys.* **2** 185–194(1982).

[12] G.R. Hall, A topological version of a theorem of Mather on twist maps *Ergod. Th. & Dynam. Sys.* **4** 585–603(1984).

[13] Y. Yamaguchi and K. Tanikawa, Symmetrical non–Birkhoff period–3 orbits in standard–like mappings *Prog. Theor. Phys.* **104** 943–954(2000).

[14] R. DeVogelaere, On the structure of symmetric periodic solutions of conservative systems, with applications in *Contributions to the Theory of Oscillations Vol.IV Ann. Math. Studies* **No.41** Princeton University Press, 1953, p.53.

[15] K. Tanikawa and Y. Yamaguchi, Running homoclinic and periodic points in the Standard–like mappings *Prog. Theor. Phys.* **105**, 2001(in press).

[16] S. Wiggins, *Chaotic Transport in Dynamical Systems* Springer–Verlag, 1991.

[17] Y. Yamaguchi and K. Tanikawa, Homoclinic intersection in C^2 standard–like mappings *Prog. Theor. Phys.* **103** 1127–1136(2000).

[18] G.D. Birkhoff, Proof of Poincaré's geometric theorem *Trans. Amer. Math. Soc.* **14** 14–22(1913).

[19] G.D. Birkhoff, An extension of Poncaré's last geometric theorem *Acta Math.* **47** 297–311(1925).

[20] M. Brown and W.D. Neumann, Proof of the Poincaré–Birkhoff fixed point theorem *Michigan Math. J.* **24** 21–31(1977).

[21] J. Franks, A variation of the Poincaré–Birkhoff theorem *Contemporary Math.* **81** 111–116(1988).

[22] J. Franks, Periodic points and rotation numbers for area preserving diffeomorphisms of the plane *Publ. I.H.E.S.* **71** 105–120(1990).

[23] J. Palis, On Morse–Smale dynamical systems *Topology* **8** 385–405(1969).

[24] J. Moser, *Stable and random motions in dynamical systems* Princeton University Press Princeton New Jersey USA, 1973.

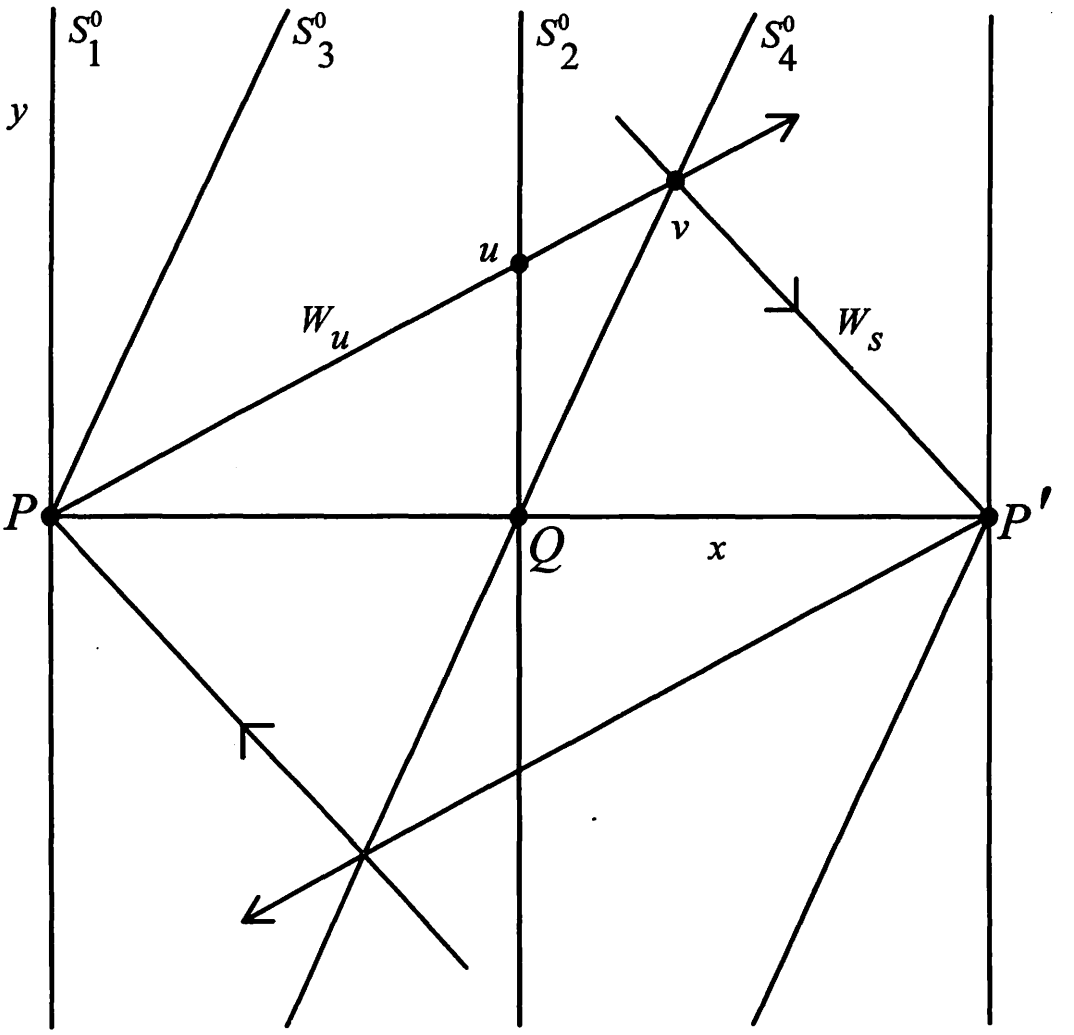

Fig. 1

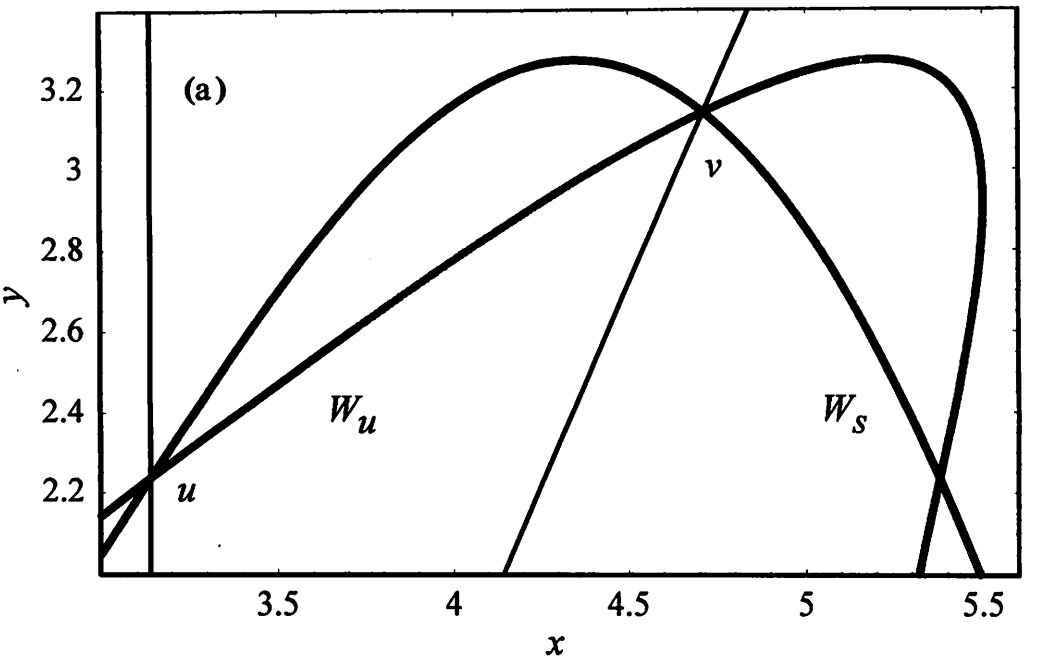

Fig. 9 a

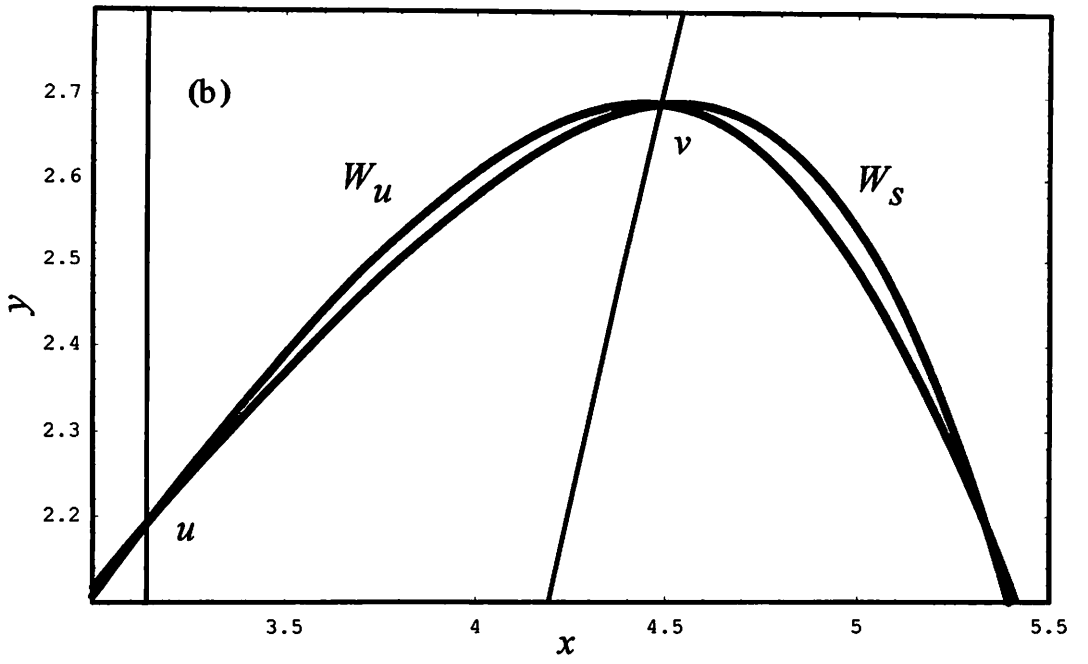

Fig. 26

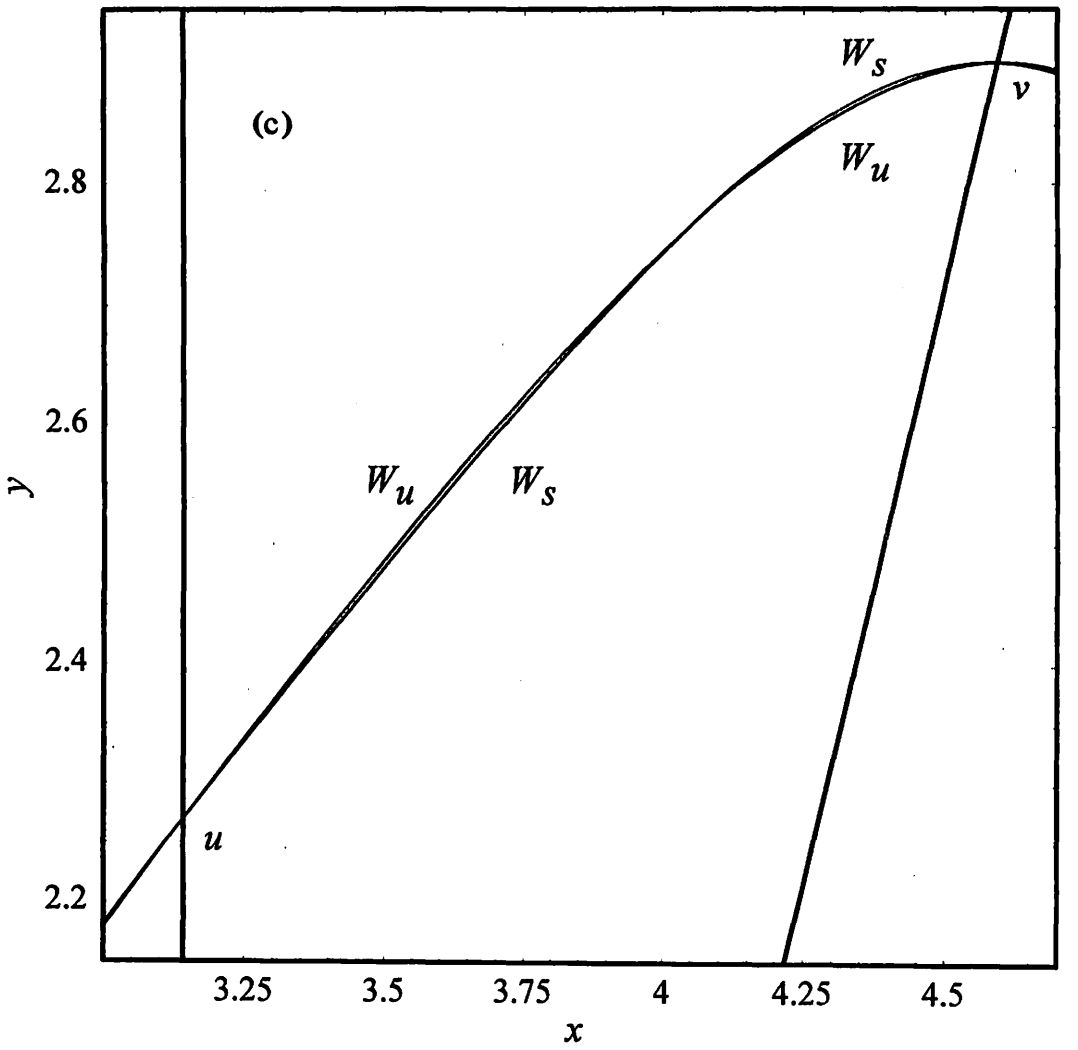

Fig. 2c

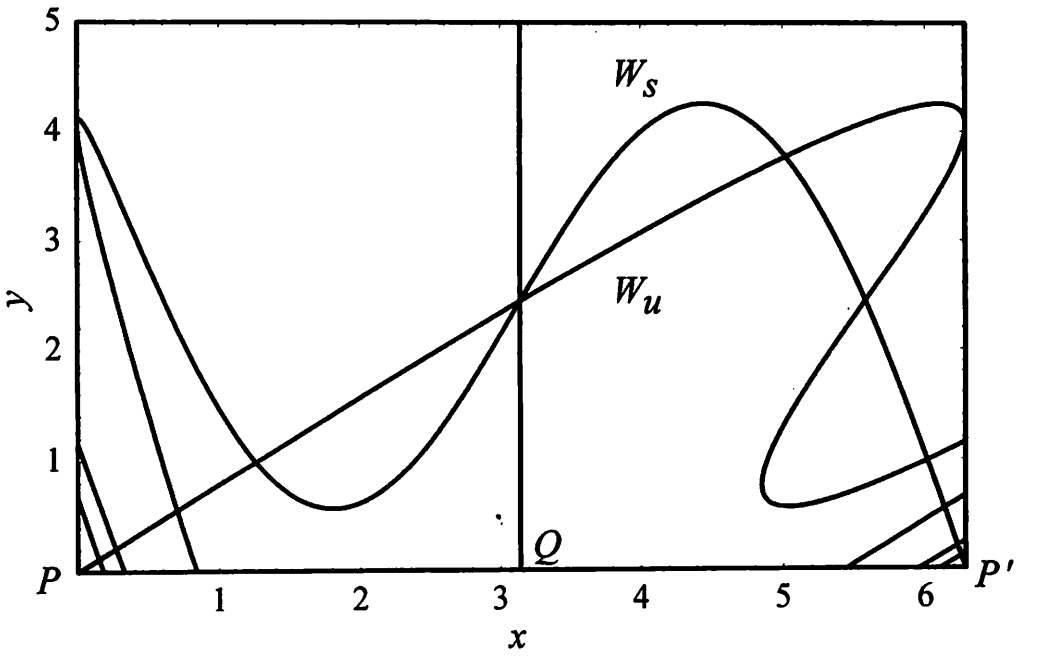

Fig. 3

Forcing Relation of Non–Birkhoff Periodic Orbits in Forced Pendulums

Yoshihiro YAMAGUCHI[1] and Kiyotaka TANIKAWA[2]

[1] *Teikyo Heisei University, Ichihara 290–0193, Japan*

[2] *National Astronomical Observatory, Mitaka 181–8588, Japan*

Abstract

Forced pendulums induce reversible non–montone twist mappings. Non–Birkhoff periodic orbits (NBO) are found in these mappings, hence in the pendulums. The existence of an NBO is equivalent with the non–integrability of the system. Two types of the forcing relation for NBOs are obtained.

1 Introduction

There are two types of periodic orbits encircling the cylinder $S^1 \times \mathbf{R}$ in the twist mappings.[1)] The first one preserves the cyclic order of the first coordinates of the orbital points. This is called a Birkhoff orbit (BO).[2)] The second one does not preserve the cyclic order. This is called a non–Birkhoff orbit (NBO).[3)] A notable characteristic of NBOs is the existence of turning points. NBOs appear due to the saddle–node bifurcation. We are interested in their appearance order, or the forcing relation. The well–known forcing relation is the Sharkovskii ordering in one–dimensional mappings.[4)] Several forcing relations were found in one–dimensional mappings.[5)] Extensions of the Sharkovskii ordering to two–dimensional mappings and to other systems have been done.[6–13)] Boyland[8),10)] proved a forcing relation of NBOs in twist mappings on the annulus. In standard–like mappings defined on the infinite cylinder, a different type of forcing relation of NBOs has been obtained.[13)]

For orbits (or solutions) of a system of ordinary differential equations, we can also define Birkhoff and non–Birkhoff orbits. In this paper, we consider the parametrically forced pendulum on the surface of the (infinite) cylinder ($-\pi \leq x < \pi, -\infty < y < \infty$):

$$\begin{aligned} \frac{dx}{dt} &= y, \\ \frac{dy}{dt} &= -(1+\epsilon\cos t)\sin x, \end{aligned} \tag{1}$$

where ϵ is a parameter. We assume a relatively weak perturbation ($|\epsilon| < 1$). There are two fixed points $P = (-\pi, 0)$ and $Q = (0, 0)$. Point P is a saddle for $|\epsilon| < 1$. In the situation with $|\epsilon| < 1$, the direction of vector field $(-(1+\epsilon\cos t)\sin x/y)$ does not strongly depend on t. The direction of the vector is to the upper–right in $-\pi < x < 0$, $y > 0$, it is to the lower–right in $0 < x < \pi$, $y > 0$, it is to the lower–left in $0 < x < \pi$, $y < 0$, and it is to the upper–left in $-\pi < x < 0$, $y < 0$.

Although BOs and NBOs are initially defined in two–dimensional mappings, We see here that these notions are clearer in the case of continuous time. In fact, motions described by equations (1) are roughly classified into three groups. The motion in the first group regularly encircles the cylinder. The motion will be called Birkhoff. The motion in

the second group both encircles the cylinder and fixed point Q. The motion will be called non–Birkhoff. The motion in the last group always encircles fixed point Q.

A rational rotation number $\nu = p/q$ is associated with a BO or an NBO. In our case, $2\pi q$ is the period during which the orbit revolves the cylinder p times. In this paper, we study NBOs with rotation number of the form $\nu = 1/q$.

In §2, we reduce the system of differential equations to a surface mapping. In §3, several notations are introduced and the fundamental properties of symmetric periodic points are obtained. In §4, three theorems on the forcing relations of symmetric periodic points are proved. We give several remarks in §5.

2 Reduction to Reversible Mappings

2.1 Symmetry of equations of motion

This system (1) of differential equations is invariant under the change of variables in two ways. One change is

$$x \longleftrightarrow -x, \quad y \longleftrightarrow y, \quad t \longleftrightarrow -t, \tag{2}$$

and the other change is

$$x \longleftrightarrow x, \quad y \longleftrightarrow -y, \quad t \longleftrightarrow -t. \tag{3}$$

Let us consider three different solutions for any possible x_0 and y_0.

$$\begin{array}{llllll} \varphi_0(t) = & (x_0(t),\ y_0(t)), & x_0(0) = & x_0, & y_0(0) = & y_0 \\ \varphi_1(t) = & (x_1(t),\ y_1(t)), & x_1(0) = & -x_0, & y_1(0) = & y_0 \\ \varphi_2(t) = & (x_2(t),\ y_2(t)), & x_2(0) = & x_0, & y_2(0) = & -y_0 \end{array} \tag{4}$$

Due to symmetries (2) and (3), we always have

$$\begin{cases} x_1(t) = -x_0(-t) \\ y_1(t) = y_0(-t) \end{cases} \quad \text{and} \quad \begin{cases} x_2(t) = x_0(-t) \\ y_2(t) = -y_0(-t) \end{cases} \tag{5}$$

We now introduce a Poincaré surface and the corresponding surface mapping. A solution to Eq.(1) describes a curve in the (t, x, y) space. Let us call this curve a trajectory. Due to the uniqueness of the solution of Eq.(1), trajectories do not intersect. The phase flow, that is, the set of all trajectories, is directed from the negative t–axis to the positive t–axis in this space. If we denote by Σ^τ the (x, y)–plane at $t = \tau$ in space (t, x, y),[15] any trajectory has unique representative point in this surface. Every trajectory intersects $\Sigma^{\tau+2n\pi}, n = 0, \pm1, \pm2, \ldots$. If we identify surface $\Sigma^{\tau+2n\pi}$ with Σ^τ for any n, we obtain a surface transformation, i.e., a transformation of Σ^τ onto itself. Let us denote the transformation by T. T is invertible and analytic. We also call T the Poincaré mapping.

Figure 1(a) is for the integrable case and Figure 1(b) is for $\epsilon = 0.08$ on the Poincaré surface Σ^0. We introduced BOs and NBOs in the introduction in the case of continuous time. In our surface, we define BOs and NBOs as the representative set of orbital points of the continuous solution. Later we will redefine NBOs on a rigorous base. In §2.2, let us briefly consider the basic property of T.

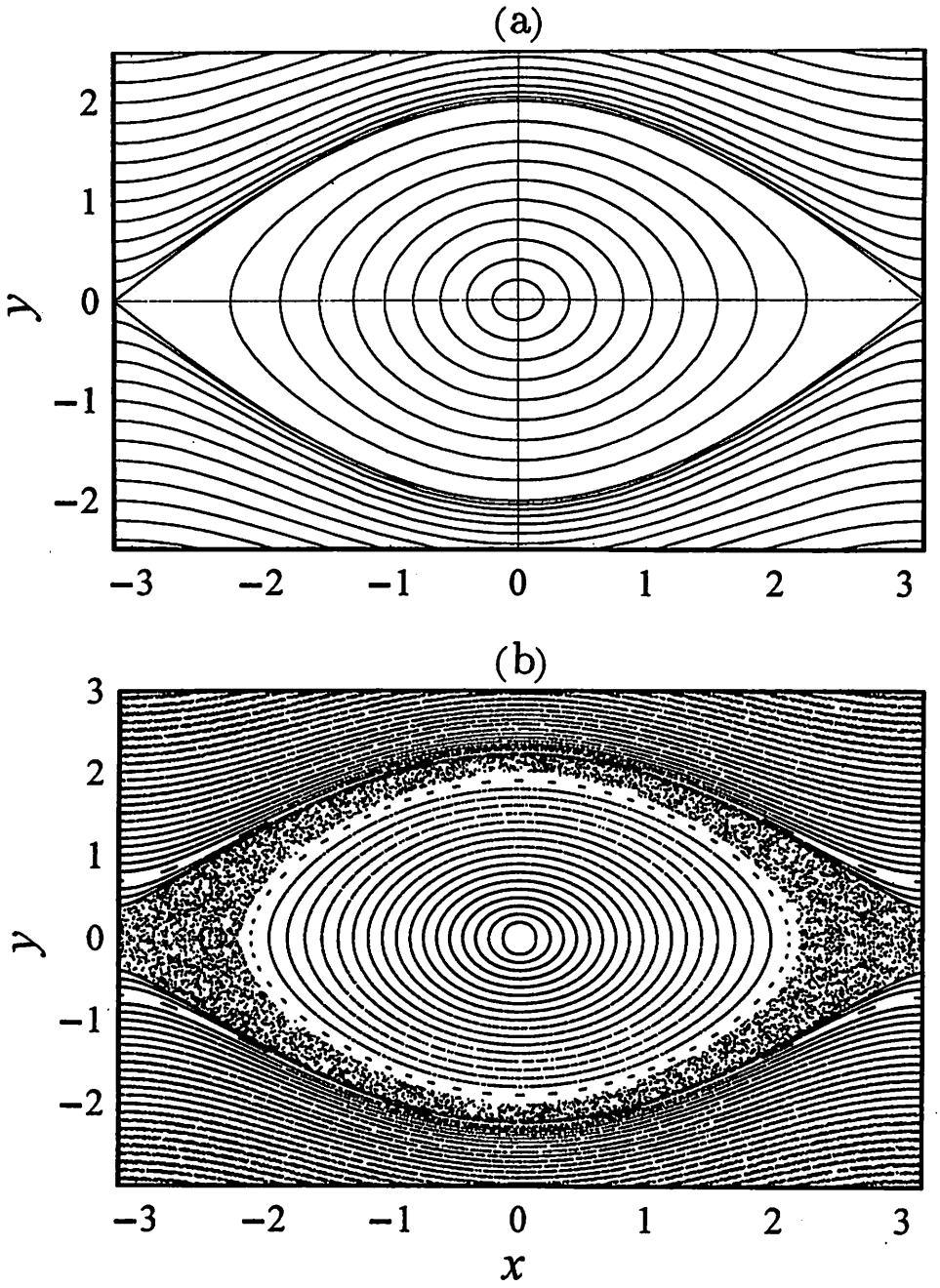

Fig.1 Surface portraits of the forced pendulum: (a) the integrable case, (b) a non-integrable case for $\epsilon = 0.08$ on the Poincaré surface Σ^0.

2.2 Double reversibility of the mapping

Take examples from Eq.(4). We put $p = (x_0, y_0)$. We define operators:

$$R_1 = \begin{pmatrix} -1 & 0 \\ 0 & 1 \end{pmatrix} \quad \text{and} \quad R_3 = \begin{pmatrix} 1 & 0 \\ 0 & -1 \end{pmatrix}. \tag{6}$$

Then, $(-x_0, y_0) = R_1 p$ and $(x_0, -y_0) = R_3 p$. By definition, $Tp = (x(2\pi), y(2\pi))$. Inserting $t = 2\pi$ in Eq.(5), we have

$$\begin{pmatrix} x_1(2\pi) \\ y_1(2\pi) \end{pmatrix} = T \begin{pmatrix} -x_0(0) \\ y_0(0) \end{pmatrix} = TR_1 p \tag{7}$$

On the other hand, we have

$$\begin{pmatrix} x_1(2\pi) \\ y_1(2\pi) \end{pmatrix} = \begin{pmatrix} -x_0(-2\pi) \\ y_0(-2\pi) \end{pmatrix} = R_1 \begin{pmatrix} x_0(-2\pi) \\ y_0(-2\pi) \end{pmatrix} = R_1 T^{-1} p \tag{8}$$

From these two, we obtain

$$TR_1 = R_1 T^{-1}. \tag{9}$$

Since $(TR_1)(TR_1) = TR_1 R_1 T^{-1} = I$, where I is the identity, TR_1 itself is an involution. Writing $TR_1 = R_2$, we find that T can be expressed as a product of two involutions as

$$T = R_2 R_1. \tag{10}$$

The expression of R_2 is unknown to us.

In a similar manner, we get an expression

$$T = R_4 R_3. \tag{11}$$

A mapping having the expression (10) or (11) is called reversible.[14] Our mapping T has two different expressions. This mapping is called doubly reversible.[7]

2.3 Axes of reversibility

The set of points invariant under an involution is called the symmetry axis corresponding to that particular involution. There are four kinds of symmetry axes in our maps because there are four involutions.

We mainly use the first expression (8). Thus we consider two symmetry axes. The symmetry axis of involution R_1 has a simple form: $x = -\pi$ and $x = 0$. In the universal cover, $x = n\pi, n = 0, \pm 1, \pm 2, \ldots$ are the symmetry axes for R_1. We want to know the form of the symmetry axis of R_2. However, it is obvious that the analytical expression cannot be obtained since otherwise an analytical expression of the mapping itself is obtained. So we will be content with getting qualitative form of the symmetry axis.

We know[14] that intersection points of the symmetry axes of R_1 and R_2 is fixed points. Conversely, fixed points are obtained as the cross points of these two axes. Therefore, the symmetry axis of R_2 passes through P and Q. The determining equation of the axis is

$$R_2 p = TR_1 p = p. \tag{12}$$

2.3.1 Integrable case

Let us first consider the integrable case. From Eq.(1),

$$\begin{aligned} \dot{x} &= y, \\ \dot{y} &= -\sin x, \end{aligned} \tag{13}$$

By quadrature, we obtain the energy relation

$$\frac{1}{2}y^2 = \cos x + h. \tag{14}$$

For the energy $h < -1$, the right hand side is always negative. No motion is possible on the cylinder for this range of energy. For $h = -1$, the motion is possible only for $x = 0, y = 0$, i.e., point Q. For $-1 < h < 1$, the motion is possible for $\cos x \geq -h$. We get a closed orbit in the (x, y) plane for each h. For $h = 1$, we get separatrices. Finally, for $h > 1$, the orbit is not any more closed. The phase portrait is seen in Fig. 1(a).

The equation to determine the period for a given $h, -1 < h < 1$ is

$$\text{Period} = 2\int_{-x_0}^{x_0} \frac{dx}{\sqrt{2(h+\cos x)}}, \tag{15}$$

where $\cos x_0 = -h$. The period is increasing together with h.[1)] The period approaches 2π as $h \to -1$ and it is infinite for $h = 1$. Let $h_{4\pi}$ be the energy for which the period of the motion is 4π, and $x_{4\pi} > 0$ be the intersection point of the equi-energy contour with the x-axis.

Now let us look for the form of the symmetry axis of R_2 based on above information. First we consider the component of the axis that contains $(0,0)$, and call it S_4. We take initial positions on the y-axis at $t = \pi$. We follow trajectories until $t = 2\pi$. Let p be the (x,y) coordinates of the moving point at $t = 2\pi$. Similarly, we trace back the trajectory until $t = 0$. Let q be the coordinates of the moving point at $t = 0$. Both p and q are on Σ^0. By the definition of the mapping, we have $p = Tq$. Taking into account that the starting x-coordinate is zero, we have $p = R_1 q$. Hence we have $p = TR_1 p$, i.e., $R_2 p = p$, that is, p is on the symmetry axis of R_2.

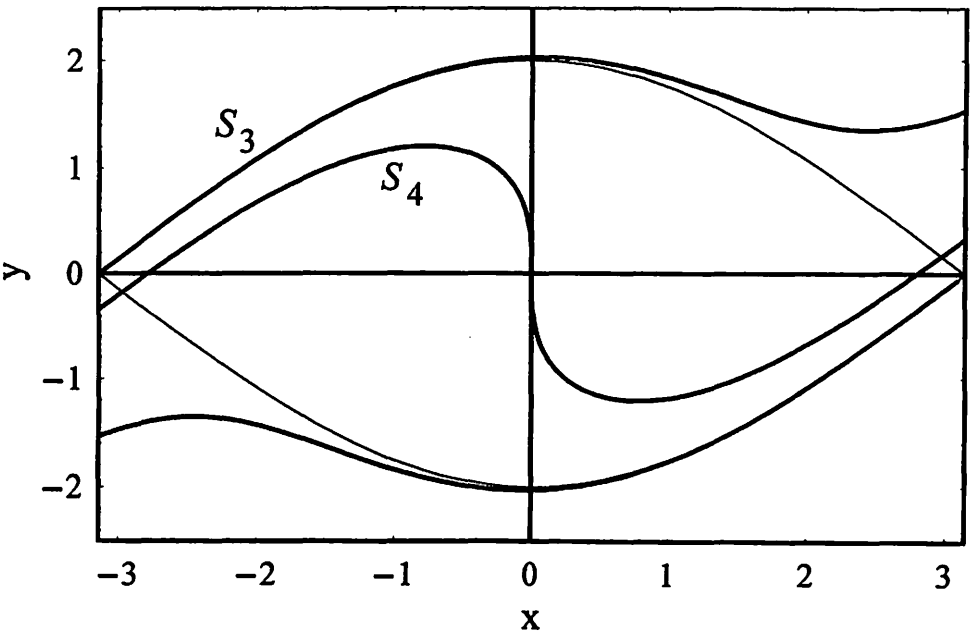

Fig. 2 Symmetry axes of R_1 and R_2 for the integrable pendulum.

Starting from $(0,0)$, let us choose initial positions going up the y-axis. Until the corresponding h arrive at $h_{4\pi}$, the period $\mathcal{T}$ of motion satisfies $2\pi < \mathcal{T} < 4\pi$. Consequently, point p at $t = 2\pi$ is in the fourth quadrant, that is, the symmetry axis starting at $(0,0)$ is in the fourth quadrant for these initial conditions. The symmetry axis is tangent to the y-axis at $(0,0)$ since $d\mathcal{T}/dh \to 0$ as $h \to -1$. At $h = h_{4\pi}$ for which $\mathcal{T} = 4\pi$, point p becomes on the x-axis. Period $\mathcal{T}$ increases up to infinity when we go up the y-axis until the separatrix. In this range of h, the symmetry axis is in the first quadrant.

Let us further extend S_4. Now, above the separatrix, trajectories on the (x,y)-plain flow from the left to the right, i.e., from the direction of the negative x to the direction of positive x not encircling Q since we are considering the integrable case. For the motion with $h > 1$, the trajectory is not closed and expressed as

$$y = \sqrt{2(\cos x + h)} > 0, \tag{16}$$

from Eq.(12). The time required to traverse the fundamental domain is given also by

$$\text{Traverse Time} = \int_{-\pi}^{\pi} \frac{dx}{\sqrt{2(\cos x + h)}}. \tag{17}$$

Let h_{cross} be the value of h such that the traverse time 2π. Let $y_{\text{cross}} = \sqrt{2(-1 + h_{\text{cross}})}$. Then S_4 crosses the line $x = \pi$ at (π, y_{cross}). Passing through this point, S_4 extends to the upper–right indefinitely since the velocity of the phase flow increase as we go up the y–axis.

The branch of S_4 extending from Q to the left is obtained from the above by rotating 180° around Q. Numerically obtained S_4 is shown in Fig. 2.

Next let us consider the symmetry axis passing through P. The procedure is similar. We start from the axis $x = -\pi$ at $t = \pi$. The position p of the moving point at $t = 2\pi$ is the position of the symmetry axis. Numerical results are shown in Fig. 2.

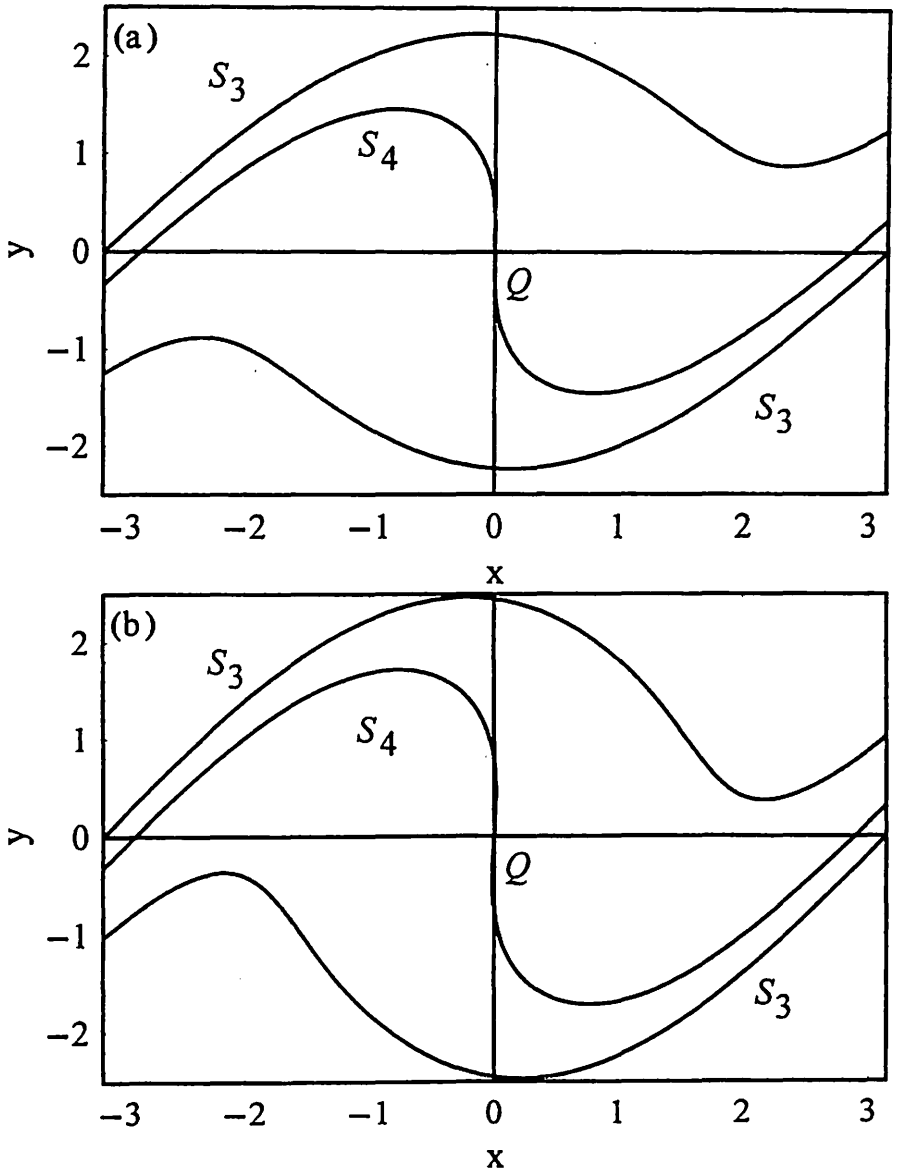

Fig. 3(a) and 3(b) Symmetry axes of R_2 for $\epsilon = 0.4$ (a) and 0.8 (b) on Σ^0.

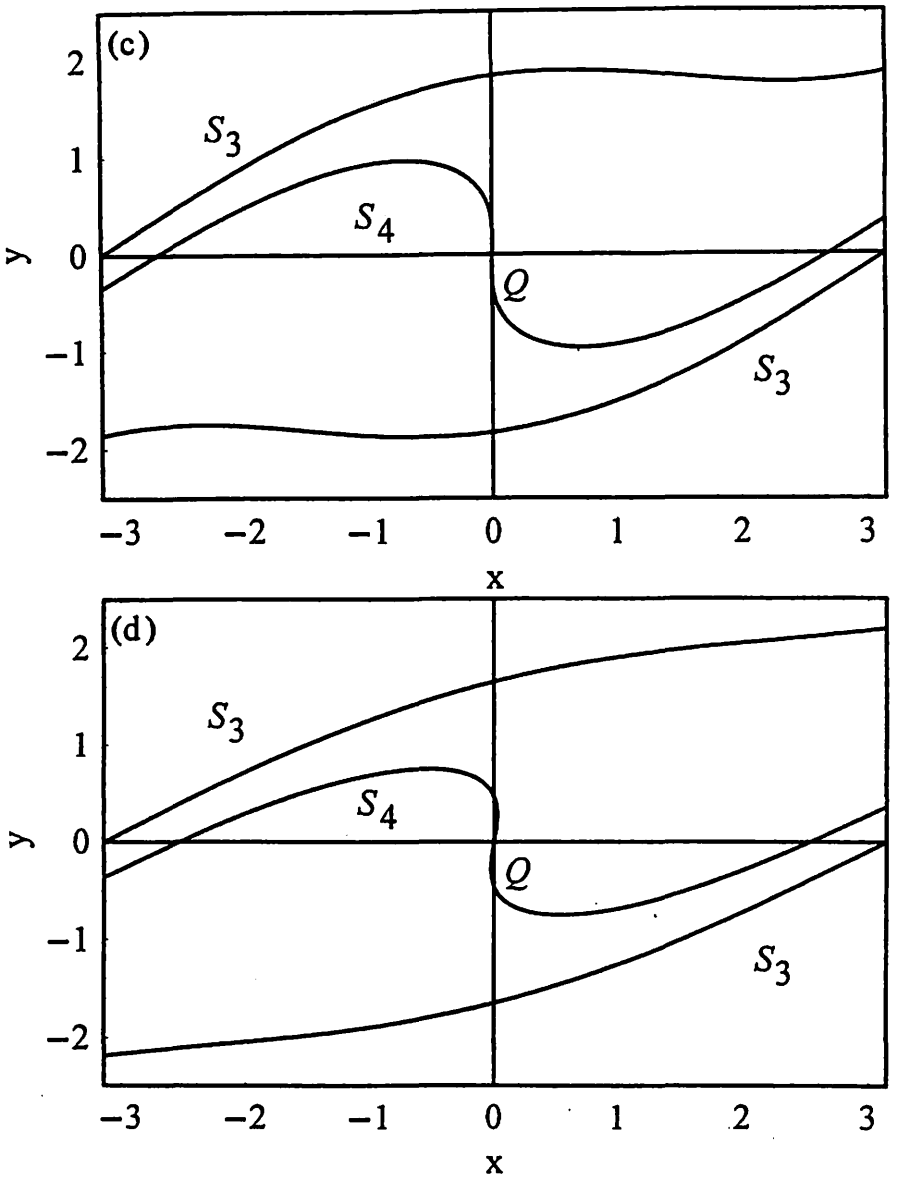

Fig. 3(c) and 3(d) Symmetry axes of R_2 for $\epsilon = 0.4$ (c) and 0.8 (d) on Σ^{π}.

2.3.2 Non–integrable case

Here the situation is different from the integrable case in the sense that we cannot use the energy relation such as Eq.(14). We start from the original equations of motion (1).

Let us first estimate the asymptotic period of infinitesimal motion around Q for $0 < \epsilon < 1$. In order to do this, we integrate the equations of motion (1) in a small neighborhood of Q. First, we combine two equations into one as

$$\ddot{x} = -f(t)\sin x, \quad \text{with} \quad f(t) = 1 + \epsilon\cos t. \tag{18}$$

We get

$$\frac{d}{dt}\left(\frac{1}{2}\dot{x}^2 - f(t)\cos x\right) = -\frac{df(t)}{dt}\cos x = \epsilon\sin t\cos x$$

Then we get

$$\dot{x}^2 - 2f(t)\cos x = 2\epsilon\int \sin t\cos x dt + h^*.$$

or approximating $\cos x \approx 1 - \frac{1}{2}x^2$

$$\dot{x}^2 + f(t)x^2 \approx 2\epsilon \cos t - \epsilon \int x^2 \sin t dt + h^*$$

Thus for small x, the trajectory in $(x, \dot{x})$–plane is on an ellipse of finite non–zero size at each instant of time. The radius of ellipse is changing. So the trajectory does not necessarily close itself. However, the motion is a revolution around Q. Let us estimate the angle of rotation during π. If the limiting angle Θ as (amplitude of motion) $\to 0$ satisfies $\pi \leq \Theta \leq 2\pi$, then the symmetry axis starting from Q tends downwards. We know that for $\epsilon = 0$ this holds. Thus by continuity this holds for small value of ϵ. We want to show that this holds for all $0 < \epsilon < 1$.

Similar to the integrable case, the symmetry axis passes through the x–axis from below at $0 < x < \pi$, crosses the stable manifold flowing into P' from the left, cut the symmetry line S_1^{r+}, and extends to infinity right–upwards. The form of the symmetry axis is depicted in Fig. 3 for $\epsilon = 0.4$ and 0.8 on Σ^0 and Σ^π.

Important character of the symmetry axis is that it divides the cylinder into two, the upper and lower components. In the universal cover, it divides $\mathbf{R}^2$ into two, the upper and lower components.

2.4 Non–monotonicity of the mapping

Non–monotonicity of the mapping is easily confirmed by mapping the positive y–axis. Near $(0, 0)$, mapped points have negative x–coordinates since the period of motion is greater than 2π and less than 4π. Points with large y–coordinates are mapped to the right. Therefore, at least near $(0, 0)$, monotonicity is violated. Figure 3 shows a numerical example.

If we take a Poincaré section every $\pi/2$, then the corresponding mapping is monotone twist. This means that our mapping is a finite composition of monotone twist mappings. This kind of mapping is called a tilt mapping by Mather.[15] The twist is not monotone but the property of the mapping is simple compared with general non–monotone twist mappings. We will not discuss this point further in this report.

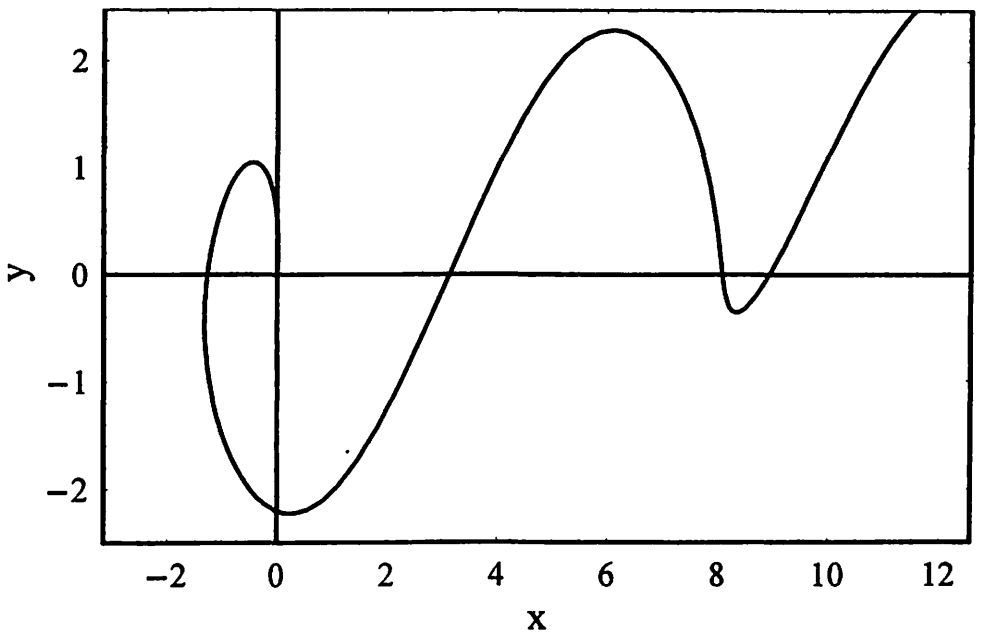

Fig. 4 Image of the positive y–axis for the non–integrable pendulum when $\epsilon = 0.5$. This shows the non–monotonicity of the mapping.

2.5 The second expression of reversibility

Let us consider briefly the second expression (11). Involution R_3 is a reflection with respect to the x–axis and hence its symmetry axis is the x–axis. We want to know the symmetry axis of R_4. The determining equations is

$$R_4 p = T R_3 p = p. \tag{19}$$

To get the axis, we start from the x–axis at $t = \pi$, and follow the trajectory backward to $t = 0$ and forward to $t = 2\pi$. Let q, p be the positions of the trajectory at these instants. Then by symmetry, we have $p = Tq = TR_3 p$, that is, p is on the symmetry axis of R_4. We depict the form of the symmetry axis for the integrable case in Fig. 5. For non–integrable cases, the symmetry axis is a little deformed.

We easily see that the axis is contained in the stable region of elliptic point Q. In fact, In order that point p is on the symmetry axis, the x–coordinates of $TR_3 p$ and p should coincide. If p is in the upper half plane, then $R_3 p$ is in the lower half plane. We know that the flow generally goes to the right in the upper half plane, and to the left in the lower half plane. Thus, if the flow does not turn around, Eq.(19) will never be satisfied. Rotational motion around a point on the x–axis is necessary for Eq.(19) to be true.

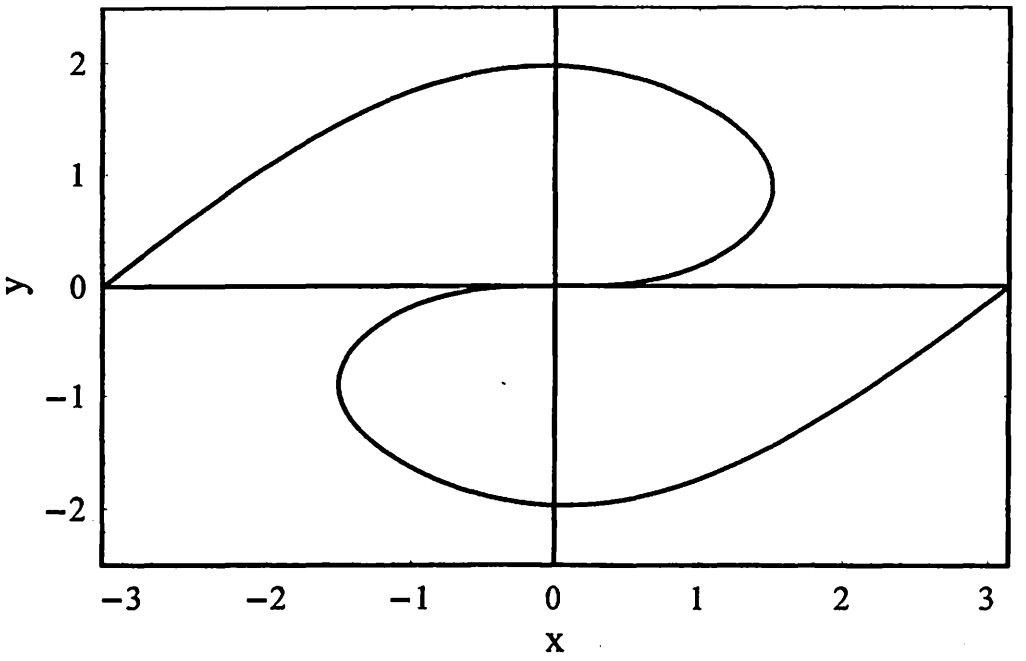

Fig. 5 Symmetry axes of R_3 and R_4 for the integrable pendulum.

2.6 Stable and unstable manifolds

The stable and unstable manifolds are two–dimensional surfaces in space (t, x, y). We consider the Poincaré surface Σ^τ. In this surface, the stable and unstable manifolds appear as one–dimensional manifolds. Let W_u^1 be the branch of the unstable manifold in Σ^τ starting at $(-\pi, 0)$ to the right as the time increases and W_s^1 be the branch of the stable manifold tending to $(\pi, 0)$ from the left. Let W_u^2 be the unstable manifold starting at $(\pi, 0)$ to the left, and W_s^2 be the stable manifold tending to $(-\pi, 0)$ from the right.

In the unperturbed situation at $\epsilon = 0$, there exists separatrices expressed by

$$y = \pm\sqrt{2(1 + \cos x)}. \tag{20}$$

It is well known that if a Melnikov function has a simple zero, the stable and unstable manifolds intersect transversely.[16),17)] The Melnikov function $M(\epsilon, t_0)$ for Eq.(1) is given by

$$\begin{aligned} M(\epsilon, t_0) &= -\epsilon \int_{-\infty}^{\infty} y_0(t) \sin x_0(t) \cos(t + t_0) dt, \\ &= \frac{2\epsilon\pi \sin t_0}{\sinh(\pi/2)} \end{aligned} \tag{21}$$

where t_0 means the phase of external force or the position of Poincaré surface, and the unperturbed solutions based at $x_0(0) = 0$ and $y_0(0) = 2$ on the separatrix at $y \geq 0$ are given by

$$\sin(x_0(t)/2) = \tanh(t), \tag{22}$$

$$y_0(t) = 2/\cosh(t). \tag{23}$$

Thus the existence of homoclinic intersection is obvious for $\epsilon \neq 0$. The Melnikov function has symmetries:

$$M(\epsilon, t_0) = -M(-\epsilon, t_0) = -M(\epsilon, t_0 + \pi). \tag{24}$$

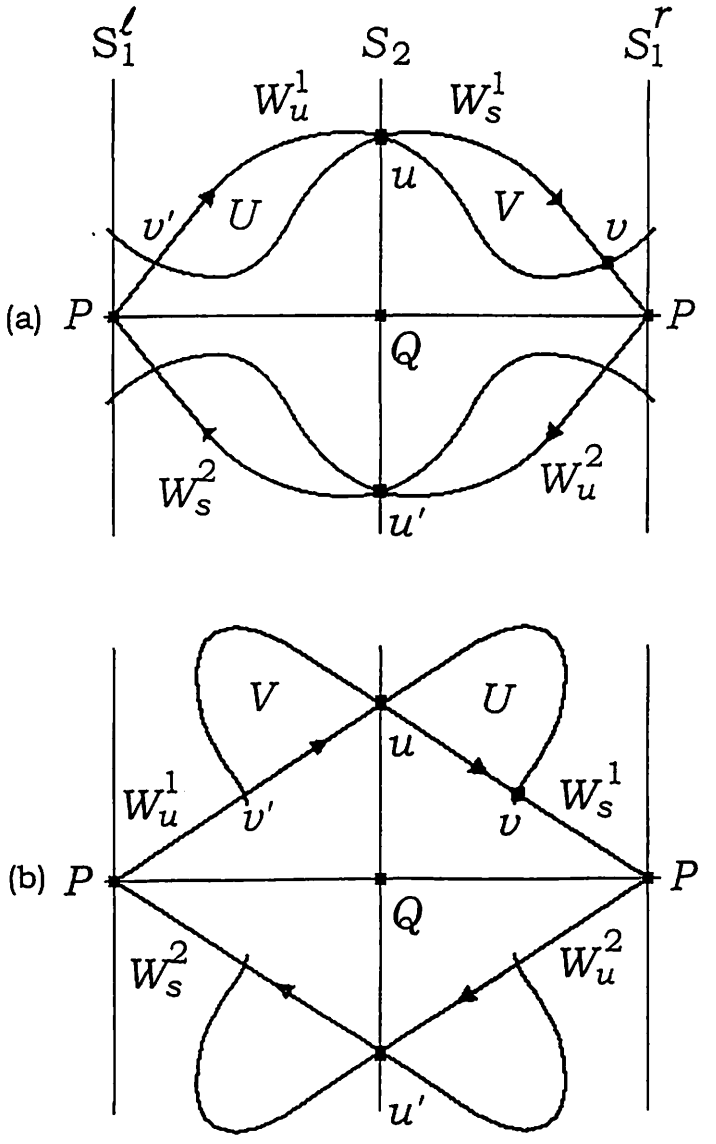

Fig. 6 Two configurations of stable and unstable manifolds.

Figure 6 illustrates the disposition of stable and unstable manifolds in the surfaces of section Σ^τ and $\Sigma^{\tau+\pi}$. Point u is the first intersection point of W_u^1 and S_2^+. According to the symmetry (4), W_s^1 also intersects S_2^+ at u and then u is a homoclinic intersection point. Let v (resp. v') be the primary homoclinic point next to (resp. precedent to) u along W_u^1. Similarly, u' is defined as the first intersection point of W_u^2 and S_2^-. In Fig. 6a, the slope of W_s^1 is taken to be larger than that of W_u^1 at u. The opposite case takes place on $\Sigma^{\tau+\pi}$, and is illustrated in Fig. 6b. To draw these figures, we used the fact that $W_{u,s}^1$ and $W_{u,s}^2$ are rotationally symmetric with respect to Q. Further, our system has a symmetry involving parameter ϵ. If Figure 6a shows the case with $\epsilon = \epsilon_0$ on Σ^τ, then Figure 6b is the case with $\epsilon = -\epsilon_0$ on Σ^τ. Therefore we consider the system with $0 < \epsilon < 1$ and use two Poincaré surfaces Σ^τ and $\Sigma^{\tau+\pi}$. The structure change of stable and unstable manifolds is confirmed in Fig. 7 obtained by numerical calculation. In the following, we take τ such that the situation exhibited in Fig. 6 is realized.

We denote by $[u, v]_{W_u}$ the closed arc on W_u with $u, v \in W_u$ as end points where u is closer to P along W_u. Similarly, we denote by $[u, v]_{W_s}$ the closed arc on W_s with $u, v \in W_s$ as end points where v is closer to P along W_s. Open and semi-open arcs are defined in a similar manner. Let us consider $\gamma_s = [u, P)_{W_s^1}$ (see Figs. 6a and 6b). We note that $\gamma_s \cap S_1^{\tau+} = \emptyset$. In fact, if $\gamma_s \cap S_1^{\tau+} \neq \emptyset$ holds, the unstable manifold also intersects $S_1^{\tau+}$ at the same points. Since the direction of vector field is right, the intersection points $\gamma_s \cap S_1^{\tau+}$ are mapped in the right side of $S_1^{\tau+}$ and then $T\gamma_s$ intersects $S_1^{\tau+}$. Therefore γ_s has infinitely many folded structure in the vicinity of P. This contradicts the fundamental property of stable manifold in the vicinity of P derived by the stable manifold theorem. Due to the symmetry, $(P, u]_{W_u^1}$ does not intersect S_1^{l+}.

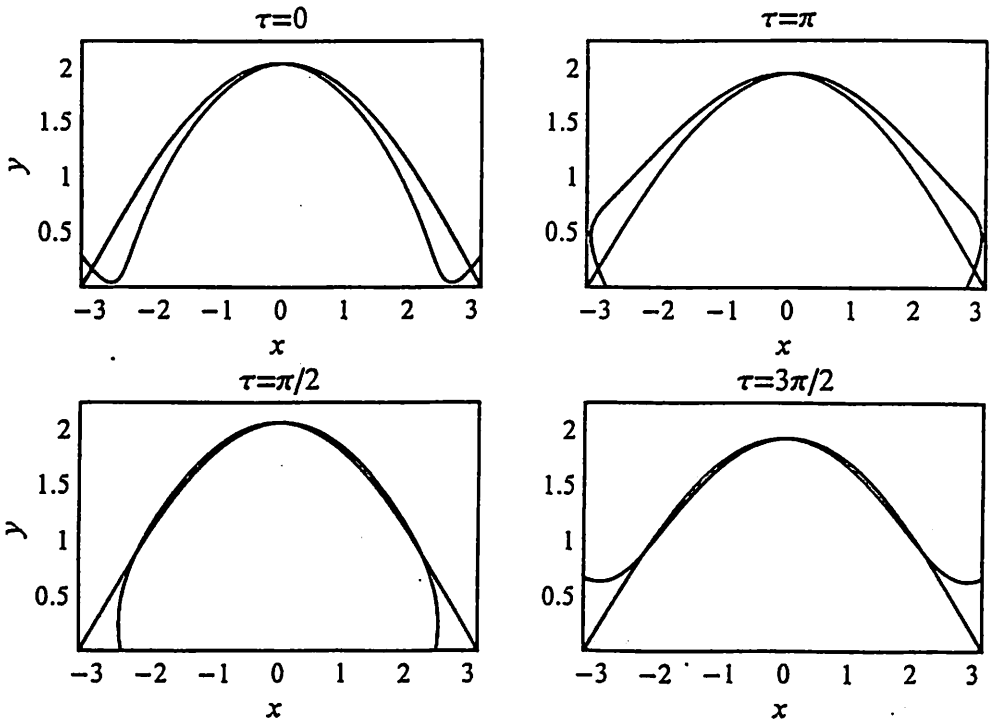

Fig. 7 Structure of stable and unstable manifolds of P on four Poincaré surfaces: (a)Σ^0, (b) $\Sigma^{\pi/2}$, (c) Σ^π and (d)$\Sigma^{3\pi/2}$ at $\epsilon = 0.1$.

2.7 Symmetry axes, stable and unstable manifolds

In analyzing the forcing relation of periodic points, primary homoclinic points and the intersection points of symmetry axes and invariant manifolds play an important role. In

this subsection, we consider the disposition of these axes and manifold.

The symmetry axis of R_2 which passes through P is obtained as a locus of orbital points at $t = 2\pi$ of S_1 starting at $t = \pi$. Of course, this axis is above W_u, the unstable manifold passing through P into the fundamental domain because W_u is invariant. On the other hand, the symmetry axis which passes through Q is obtained as a locus of orbital points at $t = 2\pi$ of S_2 starting at $t = \pi$. Let u be the primary homoclinic point on S_2^+ introduced before. The semi-infinite segment of S_2 below u is below W_u. Therefore, its image under T is also below W_u.

We have shown in the preceding section that stable and unstable manifolds of P (or P') intersect transversely. We have introduced two primary homoclinic points u and v(see Fig. 8).

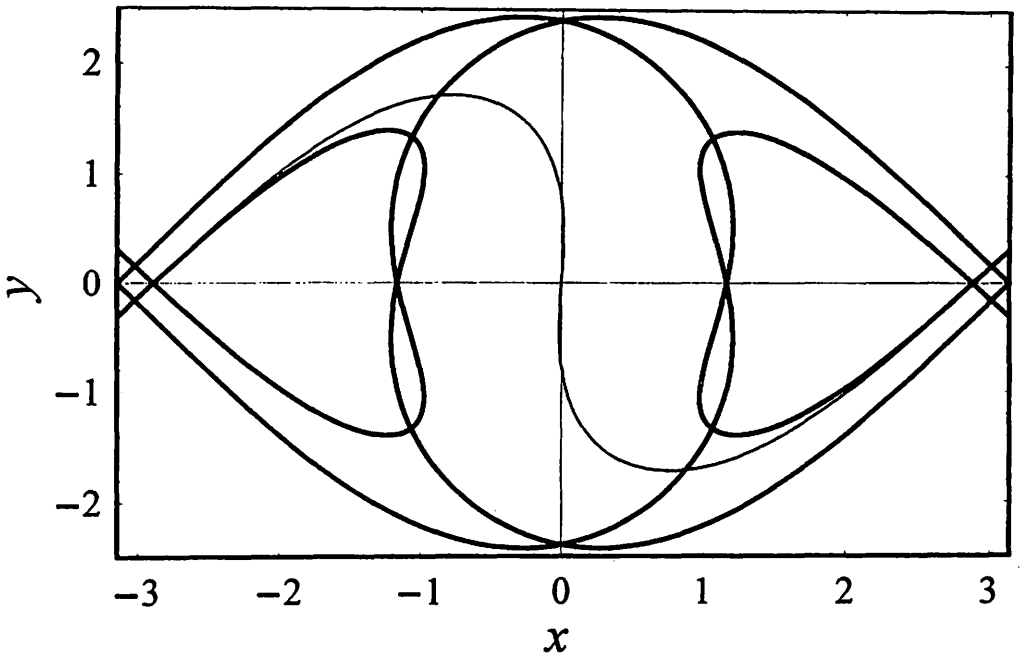

Fig. 8 Stable and unstable manifolds starting at P (P') and symmetry axes of R_2 on Σ^0 for the non-integrable pendulum when $\epsilon = 0.8$.

3 Symmetric periodic points

We work in the universal cover ($-\infty < x < \infty, \infty < y < \infty$) of the cylinder. We consider NBOs with $\nu = 1/q$. These orbits in time interval $0 \leq t < 2\pi q$ are confined in the fundamental domain E ($-\pi \leq x < \pi$ and $-\infty < y < \infty$) of the universal cover. One may not necessarily aware whether our working surface is the cylinder or its universal cover. We divide E into two open domains E^l ($-\pi \leq x < 0$ and $-\infty < y < \infty$) and E^r ($0 \leq x < \pi$ and $-\infty < y < \infty$).

3.1 Birkhoff and non–Birkhoff periodic orbits

In this subsection, we discuss the relation of symmetry axes and periodic orbits of period q. As we pointed out in §2.3, the involution R_1 has two symmetry lines ($x = -\pi$ and $x = 0$) in E and one additional symmetry line ($x = \pi$) on its right boundary. We call them S_1^l, S_2, and S_1^r. Let $S_i^+ (i = 1, 2)$ be the upper part ($y > 0$) of S_i, and S_i^- be the lower part ($y < 0$). The other involution R_2 has two symmetry axes S_3 and S_4. In the following discussion, we use only S_4 passing through Q. This has two branches defined

by $S_4^- = T_2 S_2^-$ and $S_4^+ = T_2 S_2^+$. T_2 means the mapping from a point on $\Sigma^{\tau+\pi}$ to a point on $\Sigma^{\tau+2\pi}$. In Figs. 3(a) and (c), S_4^- (resp. S_4^+) locates in the left (right) side of S_2. In Figs. 3(b) and (d), S_4^- (resp. S_4^+) penetrates into the right (left) side of S_2.

Now we discuss the relation of symmetry axes and periodic trajectory of period q. Assume that all points $p_i (0 \leq i \leq q)$ locate on Σ^τ. Let us consider the periodic trajectory starting from $p_0 = (-\pi, y_0) \in S_1^{l+}$ and arriving at $p_q = (\pi, y_0) \in S_1^{\tau+}$. We have [P1] and [P2] due to the symmetry by R_1 and have [P3] by R_2:

[P1] For even period $q = 2k (k \geq 1)$, $p_k \in S_2$.

[P2] For odd period $q = 2k+1 (k \geq 1)$, the trajectory passes through S_2 at $t = (2k+1)\pi$.

[P3] For odd period $q = 2k + 1 (k \geq 1)$, $p_{k+1} \in S_4$.

The symmetry of periodic trajectory gives the useful relation for any $q (\geq 2)$:

$$x_i + x_{q-i} = 2\pi \tag{25}$$

where $p_i = (x_i, y_i)$ on Σ^τ, $0 \leq i \leq q$ and $2\pi q$ is a period.

Here we define Birkhoff and non–Birkhoff orbits discussed in this paper.

Definition: An orbit is called a Birkhoff periodic orbit (BO) with rotation number $1/q$ if

[1] it starts from $(-\pi, y_0) \in S_1^{l+}$ at $t = 0$ and arrives at $(\pi, y_0) \in S_1^{\tau+}$ at $t = 2q\pi (q \geq 1)$, and

[2] its y–coordinate is positive in the time interval $(0, 2q\pi)$.

An orbit is called a non–Birkhoff periodic orbit (NBO) with rotation number $1/q$ if

[1] it starts from $(-\pi, y_0) \in S_1^{l+}$ at $t = 0$ and arrives at $(\pi, y_0) \in S_1^{\tau+}$ at $t = 2q\pi (q \geq 2)$, and

[2] its y–coordinate becomes negative at some t in the time interval $(0, 2q\pi)$.

There exist several types of NBO with large period, for example, NBO revolving Q $n (\geq 2)$–times during one period. Then we restrict our attention to NBOs satisfying the following restriction:

Restriction on NBO: NBO with $\nu = 1/q (q \geq 2)$ revolves around Q only once.

Due to Restriction, we have Property 1.

Property 1 The trajectory of an NBO with period q intersects S_2^- once at $t = q\pi$.

The turning back of the orbital point exists in an NBO but does not exist in a BO. If $x_{n+1} < x_n$ holds for some n, we can say that this orbit is an NBO. However the converse is not true. The relation $x_0 = -\pi < x_1 = 0 < x_2 = \pi$ always holds for an orbit with period 2 irrespective of Birkhoffness or non–Birkhoffness of the orbit. Therefore we need to check the value of y_1. If $y_1 < 0$ holds, this orbit is NBO.

We shall give the relations of periodic points and symmetry lines on the Poincaré surface Σ^τ. The points $T^k S_1^l \cap S_2 \neq \emptyset$ are the periodic points with $\nu = 1/(2k)$. We have to distinguish whether the periodic point found above is that of BO or NBO. Particularly, the points $T^k S_1^{l+} \cap S_2^- \neq \emptyset$ are the points of NBO with $\nu = 1/(2k)$. In this situation, $T^k S_1^l \cap S_2^+ \neq \emptyset$ holds. Using the direction of the vector field, this fact is shown.

Next we consider the orbits with odd period. The structure of S_4 is complicated compared with S_2. The trajectory passes through S_2^- at $t = (2k+1)\pi$ and arrives at S_4 at $t = 2(k+1)\pi$. Thus there exist three situations:

[1] $p_{k+1} \in S_4^-$,

[2] $p_{k+1} \in S_4^+ \cap E^l$, and

[3] $p_{k+1} \in S_4^+ \cap E^r$.

As shown in Fig. 3(b) and (d), there exists a situation satisfying $S_4^+ \cap E^l \neq \emptyset$. In the situation, p_2 locates in E^r and thus p_1 locates in E^l because of the symmetry with respect to S_2. The trajectory first intersects S_2^- at $0 < t < 2\pi$, passes the point $p_1 \in E^l$ at $t = 2\pi$, passes the point $p_2 \in E^r$ at $t = 4\pi$, intersects S_2^- at $4\pi < t < 6\pi$ and arrives at S_1^{r+} at $t = 6\pi$. Since this trajectory does not satisfy Property 1, we do not consider the third situation.

The relation of symmetry lines and period of NBO plays an essential role in the proofs of Theorems 1–3. Therefore we shall denote it as Property 2.

Property 2
[1] A point of NBO with $\nu = 1/(2k)(k \geq 1)$ exists in S_1^{l+} if $T^k S_1^{l+} \cap S_2^- \neq \emptyset$ holds.
[2] A point of NBO with $\nu = 1/(2k+1)(k \geq 1)$ exists in S_1^{l+} if $T^k S_1^{l+} \cap S_4^- \neq \emptyset$ holds or $T^k S_1^{l+} \cap (S_4^+ \cap E^l) \neq \emptyset$ holds.

3.2 Periodic points in homoclinic lobes

An arc of stable or unstable manifold will be called primary if the end points of the arc are neighboring primary homoclinic points. The region bounded by two primary arcs of stable and unstable manifolds is called a primary homoclinic lobe. Arcs $[u, v]_{W_u^1}$ and $[u, v]_{W_s^1}$ in Fig. 6(a) are primary. We denote by V the (primary) homoclinic lobe bounded by $[u, v]_{W_u^1}$ and $[u, v]_{W_s^1}$. Similarly, we denote by U the homoclinic lobe bounded by $[v', u]_{W_u^1}$ and $[v', u]_{W_s^1}$.

We now introduce four sequences of intervals I_k^l, I_k^r, J_k^l, and J_k^r, $k \geq 0$ by

$$I_k^l = T^{-k} V \cap S_1^{l+}, \tag{26}$$
$$I_k^r = T^k U \cap S_1^{r+}, \tag{27}$$
$$J_k^l = T^{-k} V \cap S_1^{l+}, \tag{28}$$
$$J_k^r = T^k U \cap S_1^{r+}. \tag{29}$$

I_0^l and I_0^r are empty as described in the last paragraph of the preceding subsection. I_k^l and I_k^r are on Σ^r, whereas J_k^l and J_k^r are on $\Sigma^{r+\pi}$. Note that $I_k^l = I_k^r$ and $J_k^l = J_k^r$ hold on the surface of cylinder. In the following, we omit suffices in unnecessary situations.

Here we shall give several properties.

Property 3
(i) The minimum possible period of NBOs starting from $I_k (k \geq 1)$ is $2k + 1$.
(ii) The minimum possible period of NBOs starting from $J_k (k \geq 0)$ is $2k + 2$.

Proof: It takes k iterations from I_k^l (resp. U) to V (resp. I_k^r) and one iteration from V to U. Thus (i) is proved.

Assume that a point of an NBO with period $(2k+1)$ exists in J_k. It takes k iterations from J_k^l (resp. U) to V (resp. J_k^r). Thus $TV \cap U \neq \emptyset$ holds. Decreasing the value of ϵ, we can construct the situation that the mapped image of $[v', u]_{W_u}$ is tangent to $[u, v]_{W_s}$. Let w be the tangential point. We construct a closed loop Γ by $[Tv', w]_{W_u^1}$ and $[Tv', w]_{W_s^1}$. Using the symmetry, we also have Γ' by using arcs of W_u^2 and W_s^2. Here Q locates in two closed curves Γ and Γ', and Γ' locates the symmetrical position with respect to Γ. These facts mean the intersection of W_u^1 and W_u^2. This is a contradiction. If $T^{k+1} J_k^l$ is tangent to S_2^-, $T^{-(k+1)} J_k^r$ is tangent to S_2^- at the same point. This is a point of NBO with period $(2k + 2)$. Then (ii) is proved.(Q.E.D.)

Here we summarize the structure of NBOs with $\nu = 1/q (q \geq 2)$ starting from I_k^l or J_k^l on the Poincaré surface. Property 4 gives the detailed structure of NBOs satisfying the restriction.

Property 4
(i) The point p_0 exists on S_1^{l+} and p_q locates on S_1^{r+}. The point p_{k+m} exists on S_2^-, the points $\{p_1, p_2, \cdots, p_{k-1}\}$ and $\{p_{k+m+1}, p_{k+m+2}, \cdots, p_{k+2m}\}$ locate in the region sandwiched by S_1^l and S_2, and the other points
$\{p_k, p_{k+1}, \cdots, p_{k+m-1}\}$ and $\{p_{k+2m+1}, p_{k+2m+2}, \cdots, p_{2k+2m-1}\}$ locate in the region sandwiched by S_2 and S_1^r where $q = 2k + 2m$, $m \geq 1$, $k \geq 1$ for I_k and $k \geq 0$ for J_k.
(ii) The point p_0 exists on S_1^{l+} and p_q locates on S_1^{r+}. The points
$\{p_1, p_2, \cdots, p_{k-1}\}$ and $\{p_{k+m+1}, p_{k+m+2}, \cdots, p_{k+2m+1}\}$ locate in the region sandwiched by S_1^l and S_2, and the other points $\{p_k, p_{k+1}, \cdots, p_{k+m}\}$ and $\{p_{k+2m+2}, p_{k+2m+3}, \cdots, p_{2k+2m}\}$ locate in the region sandwiched by S_2 and S_1^r where $q = 2k + 2m + 1$, $m \geq 1$, $k \geq 1$ for I_k and $k \geq 0$ for J_k.
Proof: Using Eq.(25) and Restriction on NBO, these are obtained.(Q.E.D.)

Property 5
(i) Let A and B be two ends of $I_k^l (k \geq 1)$. $T^i A$ and $T^i B (k - 1 \geq i \geq 0)$ locate in the left side of S_2^+, and $T^i A$ and $T^i B (i \geq k)$ locate in the right side of S_2^+.
(ii) Let A and B be two ends of $J_k^l (k \geq 0)$. $T^i A$ and $T^i B (k \geq i \geq 0)$ locate in the left side of S_2^+, and $T^i A$ and $T^i B (i \geq k + 1)$ locate in the right side of S_2^+.

Proof: Arc$T^k I_k$ exists in V and two points $T^i A$ and $T^i B$ for any i locate on W_s^1. Combining these facts and the definition of I_k, we have (i). The proof of (ii) is similar to that of (i).(Q.E.D.)

Property 6 The following forcing relation on I_k holds.

$$I_1 \to I_2 \to I_3 \to \cdots, \tag{30}$$

where $I_k \to I_{k+1}$ means that an interval I_{k+1} exists if I_k exists.

Let $\epsilon_c(I_k)$ be a critical value at which the interval I_k appears. Then two relations hold:

$$\epsilon_c(I_k) > \epsilon_c(I_{k+1}), \tag{31}$$

$$\lim_{k \to \infty} \epsilon_c(I_k) = 0. \tag{32}$$

Proof: Let A and B be two ends of I_k^l. According to the direction of the vector field, two points ($T^{-1}A$ and $T^{-1}B$) are mapped in the left side of S_1^{l+}. Due to the continuity of $T^{-(k+1)}V$, there exist the intersection points of $T^{-(k+1)}V$ and S_1^{l+}. This means the existence of I_{k+1}. Note that Eq.(30) is proved in terms of the lambda lemma.[18)]

We shall prove the order relations on parameters. Equation (30) gives the order relation $\epsilon_c(I_k) \geq \epsilon_c(I_{k+1})$. We deny the situation satisfying the equality. Fix ϵ at $\epsilon_c(I_k)$ where $T^{-k}V$ is tangent to S_1^{l+}. According to the direction of the vector field, the previous image of tangent point locates in the left side of S_1^{l+}. This gives that $T^{-(k+1)}V$ intersects S_1^{l+}. Under the assumption, $T^{-(k+1)}V$ is tangent to S_1^{l+} and it does not intersect S_1^{l+}. Thus the contradiction is derived.

Finally we prove Eq.(32) showing the accumulation of $\epsilon_c(I_k)$. Assume that Eq.(32) does not hold. Thus there is no intervals at some parameter region $0 < \epsilon < \delta$. But the homoclinic intersection exists at this parameter region due to Eq.(21). Using the lambda lemma, we can prove the existence of $I_k (k \geq k_0)$ where k_0 depends on ϵ. This is a contradiction.(Q.E.D.)

Similar properties hold for J_k. We omit the proof.

Property 7 The following forcing relation on J_k holds.

$$J_0 \to J_1 \to J_2 \to \cdots, \tag{33}$$

Let $\epsilon_c(J_k)$ be a critical value at which the interval J_k appears.

$$\epsilon_c(J_k) > \epsilon_c(J_{k+1}), \tag{34}$$

$$\lim_{k\to\infty} \epsilon_c(J_k) = 0. \tag{35}$$

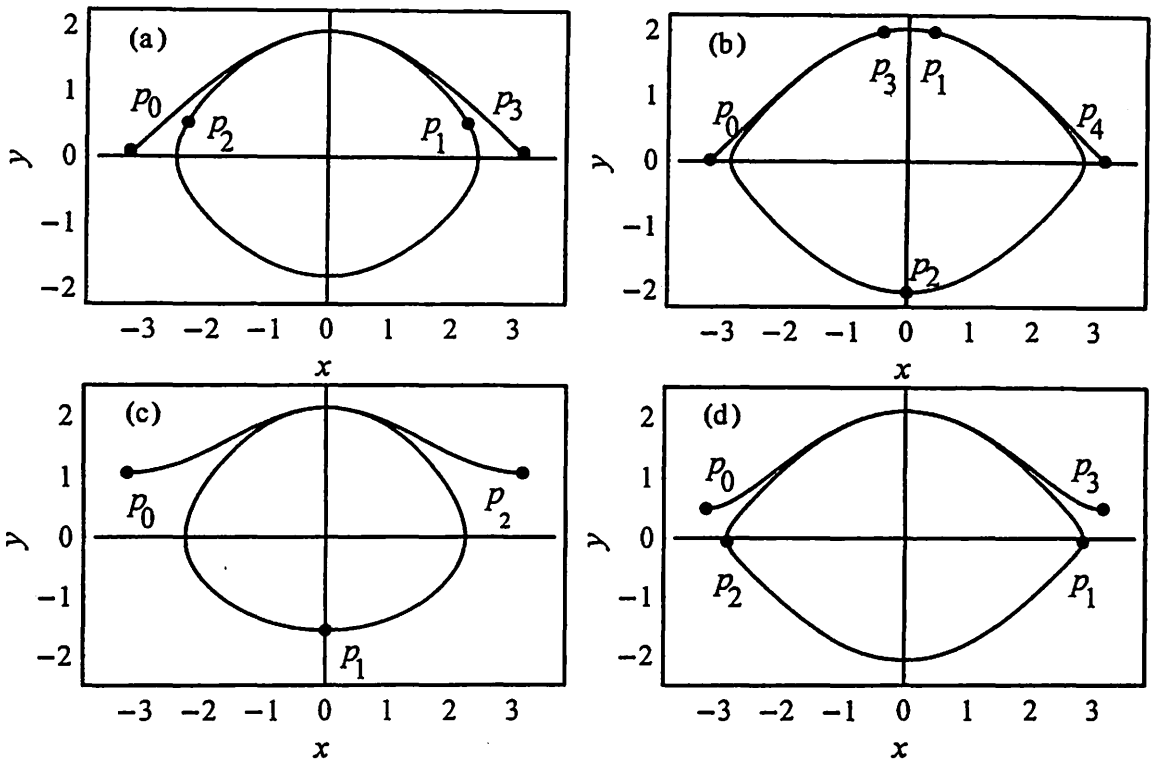

Fig. 9 Continuous curve is the projected trajectory of NBO and filled circles show the orbital points $\{p_n\}$ on the Poincaré surface. (a) $\nu = 1/3$ with $\epsilon = 0.1$ and (b) $\nu = 1/4$ with $\epsilon = 0.1$ on Σ^0. (c) $\nu = 1/2$ with $\epsilon = 0.47$ and (d) $\nu = 1/3$ with $\epsilon = 0.2$ on Σ^π.

3.3 Typical orbits of NBOs

We shall give numerical evidences of NBO with $\nu = 1/3$. NBO with $\nu = 1/3$ appears in I_1 when $\epsilon = 0.0742\cdots$ at which $T^3 I_1^l$ is tangent to interval I_1^r. This is certainly a tangent bifurcation, which gives rise to one saddle and one elliptic point. However we need to check whether the orbits are NBO with $\nu = 1/3$ or not. The orbits of NBO with $\nu = 1/3$ and $1/4$ are given in Figs. 9(a) and 9(b). In J_0, NBO with $\nu = 1/2$ appears. This orbit and NBO with $1/3$ are shown in Figs. 9(c) and 9(d). We observe the symmetry of orbit that p_1 locates at the symmetrical position of p_2 for NBO with $\nu = 1/3$, and p_1(resp. p_2) locates in S_2^- for NBO with $\nu = 1/2$(resp. $1/4$). Several critical values of NBOs are obtained in Table I.

Table I: Critical values of NBOs.

ν	Critical value	ν	Critical value
$1/3 \in I_1$	0.0742	$1/2 \in J_0$	0.468
$1/4 \in I_1$	0.00527	$1/3 \in J_0$	0.161

4 Main Results

4.1 Equivalence of an NBO and homoclinic intersection

Proposition 1 If a non–Birkhoff periodic orbit exists, the stable and unstable manifolds of P intersect and the intervals $I_k(k \geq k_0)$ and $J_{k'}(k' \geq k'_0)$ exist for some $k_0 > 0$ and $k'_0 > 0$.

Proof: In this system, the stable and unstable manifolds construct the separatrix at $\epsilon = 0$ and they have common points for $\epsilon \neq 0$. The situation with $W_u^{1,2} \cap W_s^{1,2} = \emptyset$ does not occur. The existence of NBO starting from S_1^l means that the orbit penetrates into the region satisfying $y < 0$. If the separatrix exists, this is inhibited since the starting point p_0 locates outside the region surrounded by two separatrices connecting saddles. Thus the statement on the existence of homoclinic intersection is proved. The existence of interval I_k and $J_{k'}$ is proved by the lambda lemma. Note k_0 and k'_0 depend on the parameter ϵ.(Q.E.D.)

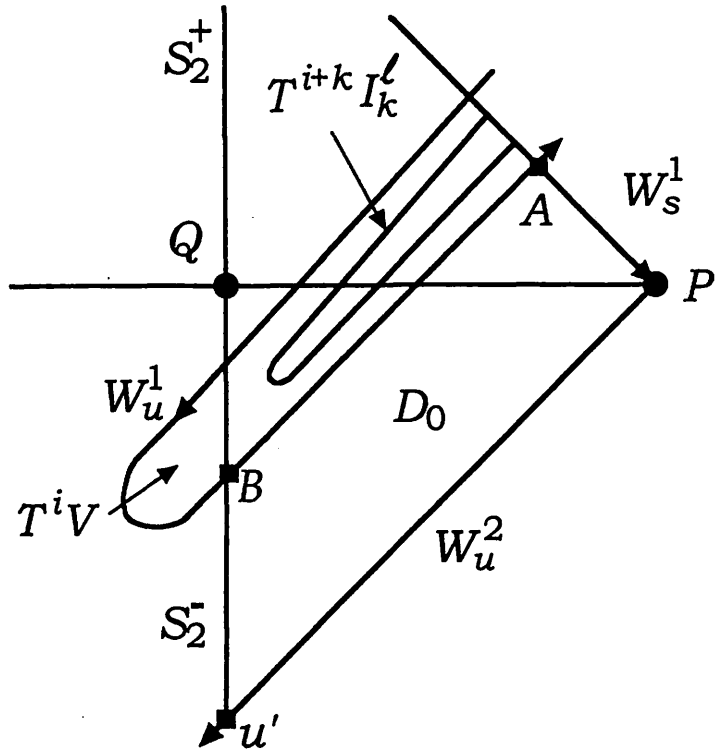

Fig. 10 Definition of the compact region D_0.

Proposition 2 If an interval $I_k(k \geq 1)$ exists, NBO passing through I_k exists. If an interval $J_{k'}(k' \geq 0)$ exists, NBO passing through $J_{k'}$ exists.

Proof: We shall give a proof for I_k. The proof for $J_{k'}$ is omitted. Using the lambda lemma, we can prove that there exists a positive integer i such that $T^i V \cap S_2^- \neq \emptyset$. The situation with $T^i V \cap S_2^- \neq \emptyset$ is shown in Fig. 10. Since the direction of the vector field on S_2^+ is right, $T^i V$ does not intersect S_2^+ before intersecting S_2^-. If $T^{k+i} I_k \cap S_2^- \neq \emptyset$ holds, this proposition is proved. Thus the situation showing $T^{k+i} I_k \cap S_2^- = \emptyset$ is illustrated in Fig. 10. We define the compact region D_0 surrounded by Arc$[A, B]$ of W_u^1, Arc$[B, u']$ of S_2^-, Arc$[u', P]$ of W_u^2 and Arc$[P, A]$ of W_s^1. Assume that $T^{j+k} I_k \cap S_2^- = \emptyset$ for all $j > i$. Thus all regions surrounded by $T^{j+k} I_k$ and W_s^1 exist in D_0. The relation $T^{j+k} I_k \cap T^{j'+k} I_k = \emptyset$ for $j \neq j'$ holds. In fact, the unstable manifold intersects itself if this relation does not hold. Thus the situation mentioned above contradicts the area preservation. Therefore,

there exists an integer $m(>k)$ such that $T^m I_k \cap S_2^- \neq \emptyset$. The intersection points are the points of NBO with $\nu = 1/(2m)$.(Q.E.D.)

Combining Propositions 1 and 2, we have Theorem 1.

Theorem 1 NBO exists if and only if the stable and unstable manifolds of P intersect.

4.2 Forcing relation

In order to state Theorems 2 and 3, we introduce the following notation:

$$\left(\frac{1}{m}\right)_i \to \left(\frac{1}{n}\right)_j \tag{36}$$

where m and n are integers satisfying $2 \leq m < n$. This notation means that NBO with $\nu = 1/n$ starting from I_j (reps. J_j) exists if NBO with $\nu = 1/m$ starting from I_i (reps. J_i) exists.

We also introduce the critical value $\epsilon_c(\nu|_i)$ at which points of NBO with ν appear in I_i or J_i.

Theorem 2 For NBOs in Eq.(1) on Σ^τ, (a) and (b) hold.

(a) $\left(\frac{1}{n}\right)_k \to \left(\frac{1}{n+1}\right)_k$, $\epsilon_c(1/n|_k) > \epsilon_c(1/(n+1)|_k)$,

where $n \geq 2k+1$, and $k \geq 1$.

(b) $\left(\frac{1}{n}\right)_k \to \left(\frac{1}{n+2}\right)_{k+1}$, $\epsilon_c(1/n|_k) > \epsilon_c(1/(n+2)|_{k+1})$,

where $n \geq 2k+1$ and $k \geq 1$.

Proof of (a): Consider the cases with $n = 2m(m \geq 2)$. $\left(\frac{1}{2m}\right)_k$ means $T^m I_k^l \cap S_2^- \neq \emptyset$ where $T^m I_k^l \subset \Sigma^\tau$. Let z be one of intersection points of $T^m I_k^l$ and S_2^-. The axis S_4 divides the fundamental domain E in two, namely, the upper and lower domains. Since $Tz = R_2 R_1 z = R_2 z$ holds, Tz locates in the upper (resp. lower) domain if z exists in the lower (resp. upper) domain. The trajectory starting from the point on S_2^- moves toward left. Combining these facts, we have $T^{m+1} I_k^l \cap (S_4^- \cup (S_4^+ \cap E^l)) \neq \emptyset$. Thus Property 2 gives that these are the points of NBO with $\nu = 1/(2m+1)$ starting from I_k^l.

Next consider the cases with $n = 2m+1(m \geq 1)$. $\left(\frac{1}{2m+1}\right)_k$ means $T^{m+1} I_k^l \cap (S_4^- \cup (S_4^+ \cap E^l)) \neq \emptyset$. According the direction of vetor fiels, we have $T^{m+1} I_k^l \cap S_2^- \neq \emptyset$. The intesections are the points of NBO with $\nu = 1/(2m+2)$ starting from I_k^l.

Consider the cases with $n = 2m(m \geq 2)$. The forcing relations give the order relations on parameters including the equality. We deny the situation satisfying $\epsilon_c(1/(2m)|_k) = \epsilon_c(1/(2m+1)|_k)$. Fix $\epsilon = \epsilon_c(1/(2m)|_k)$ at which $T^m I_k^l$ is tangent to S_2^-. Using the same method mentioned above, we can show that $T^{m+1} I_k^l$ intersects $(S_4^- \cup (S_4^+ \cap E^l))$ and S_2^-. The contradiction is derived. The proof for the cases with $n = 2m+1(m \geq 1)$ is similar. Then we omit it. (Q.E.D.)

Proof of (b): Consider the cases with $n = 2m(m \geq 2)$. $\left(\frac{1}{2m}\right)_k$ means $T^m I_k^l \cap S_2^- \neq \emptyset$. In Fig. 11b, two filled squares are the points of NBO with $\nu = 1/(2m)$. In Fig. 11a, the relation of I_k^l and TI_{k+1}^l is displayed. As shown in Fig. 11b, $T^{m+1} I_{k+1}^l$ locates outside $T^m I_k^l$. Two intersection points of S_2^- and $T^{m+1} I_{k+1}^l$ are displayed by two filled circles.

This fact gives the relation $T^{m+1}I^l_{k+1} \cap S^-_2 \neq \emptyset$. Using Property 2, the existence of NBO with $\nu = 1/(2m+2)$ starting from I_{k+1} is proved. This proof also gives the impossibility of situation satisfying $\epsilon_c(1/(2m)|_k) = \epsilon_c(1/(2m+2)|_{k+1})$.

The proof for the cases with $n = 2m+1 (m \geq 1)$ is similar. Then we omit it. (Q.E.D.)

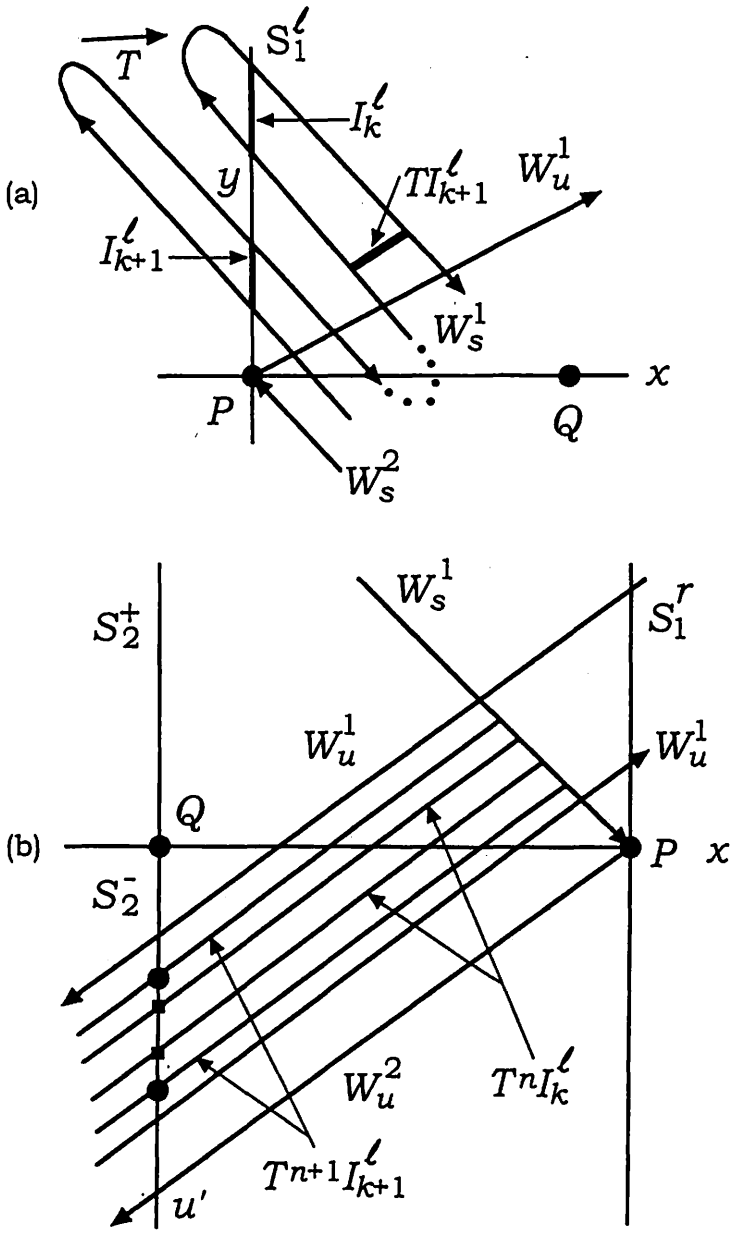

Fig. 11 (a) Relation of I_k and TI_{k+1} located in the left side of S_2. (b) Relation of T^nI_k and $T^{n+1}I_{k+1}$. Filled squares are the points of $\nu = 1/(2n)$ and filled circles show the points of $\nu = 1/(2n+2)$.

Schematic version of forcing relations stated in Theorem 2 is obtained in Table I where a symbol $\downarrow$ shows the forcing relation as same as the symbol $\rightarrow$.

Table I Forcing relation.

I_1	:	1/3	$\rightarrow$	1/4	$\rightarrow$	1/5	$\rightarrow$
		$\downarrow$		$\downarrow$		$\downarrow$	
I_2	:	1/5	$\rightarrow$	1/6	$\rightarrow$	1/7	$\rightarrow$
		$\downarrow$		$\downarrow$		$\downarrow$	
I_3	:	1/7	$\rightarrow$	1/8	$\rightarrow$	1/9	$\rightarrow$
		$\downarrow$		$\downarrow$		$\downarrow$	

Theorem 3 For NBOs in Eq.(1) on $\Sigma^{\tau+\pi}$, (a) and (b) hold.

(a) $\left(\frac{1}{n}\right)_k \rightarrow \left(\frac{1}{n+1}\right)_k$, $\epsilon_c(1/n|_k) > \epsilon_c(1/(n+1)|_k)$,

where $n \geq k+2$, and $k \geq 0$.

(b) $\left(\frac{1}{n}\right)_k \rightarrow \left(\frac{1}{n+2}\right)_{k+1}$, $\epsilon_c(1/(2n)|_k) > \epsilon_c(1/(2n+2)|_k)$,

where $n \geq k+2$ and $k \geq 0$.

Proof: The proofs are similar to those in Theorem 2. We omit them.(Q.E.D.)

Schematic version of forcing relations stated in Theorem 3 is illustrated in Table II.

Table II Forcing relation.

J_0	:	1/2	$\rightarrow$	1/3	$\rightarrow$	1/4	$\rightarrow$
		$\downarrow$		$\downarrow$		$\downarrow$	
J_1	:	1/4	$\rightarrow$	1/5	$\rightarrow$	1/6	$\rightarrow$
		$\downarrow$		$\downarrow$		$\downarrow$	
J_2	:	1/6	$\rightarrow$	1/7	$\rightarrow$	1/8	$\rightarrow$
		$\downarrow$		$\downarrow$		$\downarrow$	

Property 8 For NBOs stated in Theorems 2 and 3, the following relations hold:

$$\lim_{q\to\infty} \epsilon_c(1/q|_k) = \epsilon_c(I_k) \ (I_k \in \Sigma^{\tau}), \tag{37}$$

$$\lim_{q\to\infty} \epsilon_c(1/q|_k) = \epsilon_c(J_k) \ (J_k \in \Sigma^{\tau+\pi}). \tag{38}$$

Proof: We shall give a proof of Eq.(37). The proof of Eq.(38) is omitted. Assume that

$$\lim_{q\to\infty} \epsilon_c(1/q|_k) = \epsilon_d > \epsilon_c(I_k). \tag{39}$$

This fact means that there is no NBO in I_k at the parameter region with $\epsilon_d > \epsilon > \epsilon_c(I_k)$. This contradicts Proposition 2.(Q.E.D.)

5 Concluding remarks

The orbit outside ZI cannot penetrate into ZI and the orbit inside ZI cannot escape from ZI. Then Theorem 1 implies that all NBOs locate in ZI.

We think that Theorem 1 holds in all systems including the homoclinic intersection points of stable and unstable manifolds of fixed point. The proof for the systems not having the symmetry structure is not obtained.

Using our method, we cannot derive the forcing relation of NBOs with the same rotation number (for example, $1/6 \in I_1$ and $1/6 \in I_2$ in Table I). To define the order relation, we need the numerical calculation.

Theorems 2 is the same forcing relation obtained in standard-like mappings.[13] Theorems 2 and 3 may hold in many systems with the same symmetry axes in Eq.(1).

There exist other types of NBO not listed in Theorems 2 and 3, for example, NBOs revolving Q $n(n \geq 2)$-times, and NBOs with $\nu = p/q(p \geq 2)$. It is necessary to make clear the forcing relation among them. This is a future problem.

The order of $\{p_n\}$ for NBO with $\nu = 1/3$ shown in Figs. 9(a) and 9(d) is the same as that of standard-like mappings obtained in Ref. 19. Thus NBO with $\nu = 1/3$ has the braid type $\sigma_1\sigma_2^{-1}$ where σ_1 and σ_2^{-1} are generators of braid. The system including NBO with $\nu = 1/3$ has a positive topological entropy ($\geq \ln(3+\sqrt{5})/2$) and then is pseudo-Anosov.[20] The chaotic motion with this topological entropy exists in ZI. The detailed results on the braid type and the topological entropy are reported elsewhere.

Acknowledgments

The authors express their thanks to Dr.T.Matsuoka for useful comments.

References

1) K. R. Meyer and G. R. Hall, *Introduction to Hamiltonian Dynamical Systems and the N-Body Problem* (Springer, 1991).
2) G. D. Birkhoff, Acta. Math. **43** (1920), 44.
3) P. Boyland and G. R. Hall, Topology **26** (1987), 21.
4) A. Sharkovskii, Ukr. Mat. Z. **16** (1964), 61.
5) L. Alsedà, J. Llibre and M. Misiurewicz, *Combinatorial Dynamics and Entropy in Dimension One* (World Scientific, 1993).
6) T. Matsuoka, in *Dynamical Systems* **1** (World Scientific, 1986), p. 13.
7) K. Tanikawa and Y. Yamaguchi, J. Math. Phys. **28** (1987), 921: **30** (1989), 608.
8) P. Boyland, Comtemp. Math. **81** (1988), 119.
9) S. Baldwin, Ergod. Th. & Dynam. Sys. **11** (1991), 249.
10) P. Boyland, Topology and its Appl. **58** (1994), 223.
11) M. Handel, Ergod. Th. & Dynam. Sys. **17** (1997), 593.
12) J. Loss, I.H.E.S. (1997), 5.
13) K. Tanikawa and Y. Yamaguchi (Preprint, 2001).
14) R. DeVogelare, in *Contributions to the theory of Oscillations* Vol. IV Ann. Math. Studies No.41, Princeton University Press, 1953, p.53.
15) J. N. Mather, Journ. Amer. Math. Soc. **4**, 207–263(1991).
16) S. Wiggins, *Global bifurcation and chaos* (Springer, 1988).
17) V. K. Melnikov, Trans. Moscow Math. Soc. **12** (1963), 1.
18) J. Palis and W. de Melo, *Geometric Theory of Dynamical Systems* (Springer, 1982).
19) Y. Yamaguchi and K. Tanikawa, Prog. Theor. Phys. **104** (2000), 943.
20) A. J. Casson and S. A. Bleilerm *Automorphisms of Surface after Nielsen and Thurston* (Cambridge Univ. Press, 1988).

Relaxation Process of Modified Konishi-Kaneko Systems

QUNIBA Hideyasu(Nikon Corp.) and INAGAKI Shogo(Kyoto Univ.)

Abstract

We study the relaxation process of modified Konishi-Kaneko Systems to investigate its relaxation process. Our N-body simulations used 128 particles and 6th order symplectic integrator, then the total energy conserved within 10^{-9}% for whole integration periods. When the total energy of the system E was negative, we found that the disribution function $N(e)$ approached the equilibrium distribution and its time required became shorter as E approaches 0. But when the total energy of the system E was positive, the distribution function $N(e)$ did not appoach the equilibrium distribution within the period we calculated. We estimated Makino[5]'s relaxation time measure which was originally used for one-dimensional sheet model and found that the measure predicted by T_r was relatively appropriate when the total energy E was negative. However, when the total energy E was positive, it was not so.

1 Introduction

これまで1次元 sheet 系の緩和過程についてはよく調べられてきて (e.g. Tsuchiya *et al.* [1],[2],[3],[4], Makino [5]) 、その緩和過程の特異性が指摘されてきた。これは、1次元 sheet 系では、BBGKY 方程式から Fokker-Planck 方程式を導く際、2体相関関数の寄与による collision term が零になる (金森 [6], Eldridge and Feix [7] も参照のこと) ためと思われる。

Konishi-Kaneko 系は、初め、$(x_i, p_i) \mapsto (x_i', p_i')$ の discrete map,

$$p_i' = p_i + k\sum_{j\neq i}^{N} \sin[2\pi(x_j - x_i)], \qquad (1)$$

$$x_i' = x_i + p_i \qquad (\mathrm{mod}1) \qquad (2)$$

として定義され、そのカオス的性質が調べられた (Konishi and Kaneko [8])。しかし、その力学的性質を調べるには discrete map よりも、連続時間系の方が調べ易く、ハミルトニアン

$$H = \sum_{i=1}^{N}\left\{\frac{1}{2}p_i^2 - \frac{k}{4\pi}\sum_{j\neq i}^{N}\cos[2\pi(x_j - x_i)]\right\} \qquad (3)$$

定義される系の力学的安定性を Inagaki and Konishi [9]、熱力学的安定性を Inagaki [10] が調べ、その後も熱力学性質は調べ続けられている (*c.f.* Latora *et al.* [11]。ハミルトニアン (3) で定義される系は、1次元 sheet 系の Fourier 成分の first harmonic だけを取った系にもなっており、1次元 sheet 系より単純なため、その性質を調べておくのは意味があると思われる。また、1次元 sheet 系は relaxation time が非常に長いため、大きな粒子数を取れなかったが、上記のハミルトニアンで記述される系 (以下、modified Konishi-Kaneko 系と呼ぶ) には、蔵本変換 (Kuramoto [12]) が存在して、力の計算は通常の N 体のように N^2 に比例するのでなく、N に比例するように出来るため、粒子数を増やすのは容易であると思われる。また、modified Konishi-Kaneko 系には、clustered state と uniform state があるため (Inagaki [10] Fig. 1 参照)、緩和過程がどう違うか見るのは興味深い。

2 Initial Conditions

2.1 Cold の場合

初期条件はエネルギーが負となるように clustered initial condition を設定した。その distribution function は

$$f(x,p) = \frac{M}{2p_0}\left\{1 + \cos\left(\frac{\pi p}{p_0}\right)\right\}(1 - \cos 2\pi x) \qquad (4)$$

$$0 \le x \le 1, \quad -p_0 \le p \le p_0$$

$$p_0^2 = \frac{4}{M}\frac{1}{\frac{2}{3} - \frac{4}{\pi^2}}\left(E + \frac{kM^2}{16\pi}\right)$$

とした。ここで、M は total mass, E は total energy である。つまり、

$$M = \int_{-p_0}^{p_0}\int_0^1 f(x,p)dxdp \qquad (5)$$

$$E = \int_{-p_0}^{p_0}\int_0^1 \left\{\frac{1}{2}p^2 + \frac{1}{2}\psi(x)\right\} f(x,p)dxdp \qquad (6)$$

ただし、

$$\psi(x) = -\frac{k}{2\pi}\int_0^1\int_{-p_0}^{p_0}\cos[2\pi(x' - x)]f(x',p')dp'dx'$$

$$= \frac{kM}{4\pi}\cos 2\pi x \qquad (7)$$

そして、これを再現するよう、位相空間の $0 \leq x \leq 1$, $-p_0 \leq p \leq p_0$ の領域を $l \times m$ 個に分割し、各々の小領域の重心に粒子を置いた。

2.2 hot な場合

hot な初期条件の場合は密度を一様にした。つまり、

$$f(x,p) = \frac{M}{2p_0}\left\{1+\cos\left(\frac{\pi p}{p_0}\right)\right\} \tag{8}$$

と distribution function が x によらないようにした。

3 Numerical Simulations

3.1 運動方程式

ハミルトニアン (1) より、運動方程式

$$\frac{dx_i}{dt} = p_i \tag{9}$$

$$\frac{dp_i}{dt} = k\sum_{j\neq i}^{N}\sin[2\pi(x_j - x_i)] \tag{10}$$

を得る。蔵本変換は

$$R = \sum_{j=1}^{N}\exp(2\pi\sqrt{-1}\,x_j) \tag{11}$$

とした時、

$$f_i = k\mathcal{I}\left[\exp(-2\pi\sqrt{-1}\,x_i)R\right] \tag{12}$$

で定義され、(ここで $\mathcal{I}$ は複素数の虚部である)(10) 式の右辺と一致することが容易に示せるが、今回はあまり大きな粒子数まで計算しなかったので、用いなかった。用いた k の値は、$k = 1/N$ である。

4 N(e) の変化

エネルギーが e より小さい粒子の割合を $N(e)$ とした。つまり

$$N(e) = \int_{e'<e} f(x',p')dx'dp' \tag{13}$$

そしてシミュレーションの $N(e)$ を平衡状態と比較した。

4.1 $N = 128, E = -0.01025, T = 0.0559$ の場合

$N(e)$ の変化を図 1,2 に示した。ただし、実線は平衡分布関数で、熱力学的平衡状態の分布関数

$$f_0(x,p) = \frac{N\exp\left[-\beta\left(\frac{1}{2}p^2+\psi\right)\right]}{\sqrt{\frac{2\pi}{\beta}}\int_0^1\exp[-\beta\psi(x)]dx} \tag{14}$$

である。ここで、

$$\psi(x) = B\cos 2\pi x \tag{15}$$

で、β と B の間には

$$B = -\frac{kN}{2\pi}\frac{\int_0^1\cos 2\pi x\exp[-\beta\psi(x)]dx}{\int_0^1\exp[-\beta\psi(x)]dx} \tag{16}$$

の関係があり、total energy E を与えると、β と B は決まる (Inagaki [10])。

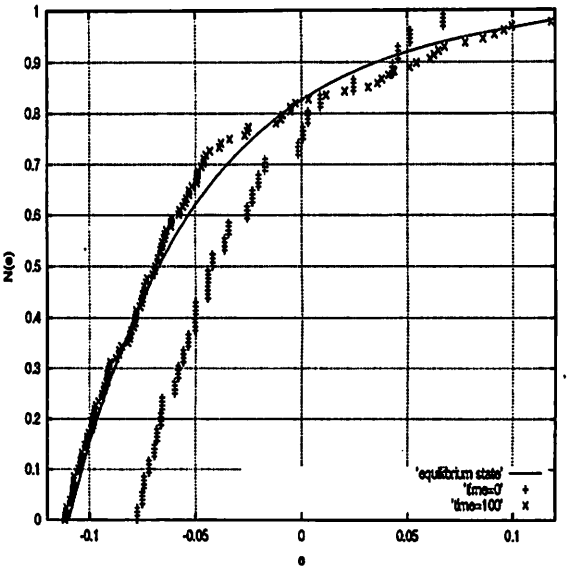

Figure 1: $N = 128,\ E = -0.01025,\ t = 0, 100$

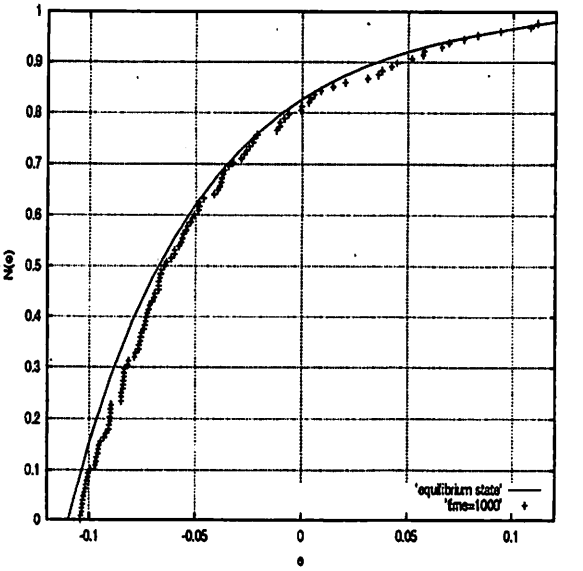

Figure 2: $N = 128,\ E = -0.01025,\ t = 1000$

$t = 1000$ 程度で、平衡分布関数に近づいていることが分かる。

4.2 $N = 128, E = -0.01674, T = 0.0521$ の場合

$N(e)$ の変化は図 3,4 に示した。$t = 10000$ 程度で、

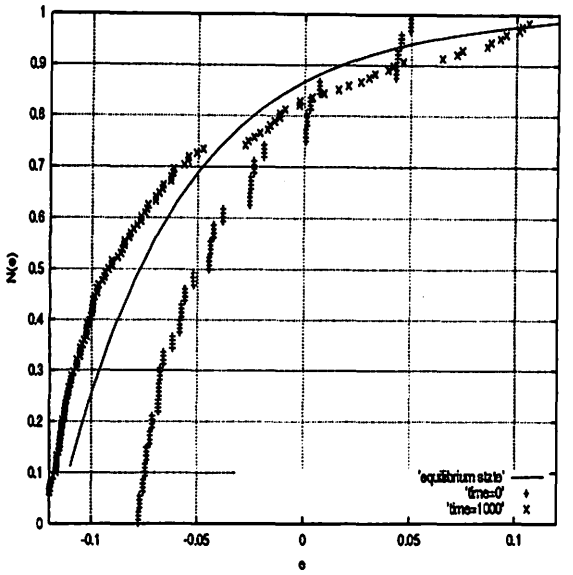

Figure 3: $N = 128,\ E = -0.01674,\ t = 0, 1000$

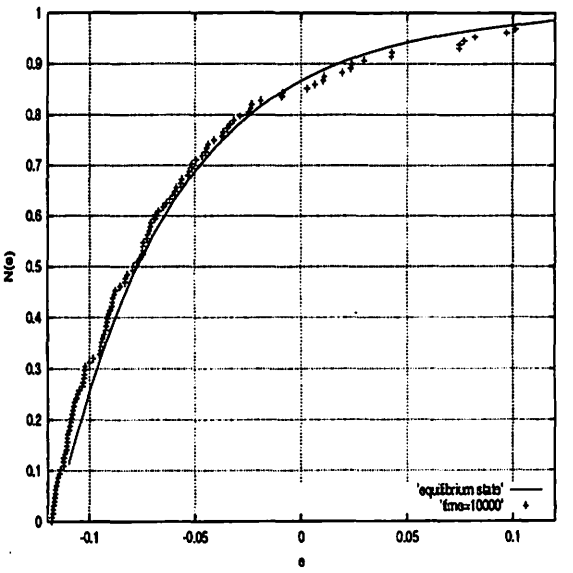

Figure 4: $N = 128,\ E = -0.01674,\ t = 10000$

平衡分布関数に近づいていることが分かる。

4.3 $N = 128, E = 0.0972, T = 0.194$ の場合

初期条件は密度一定である。time=100000 でも平衡分布関数 $N_0(e)$ には遠い。$N(e)$ の変化は図 5 に示した。

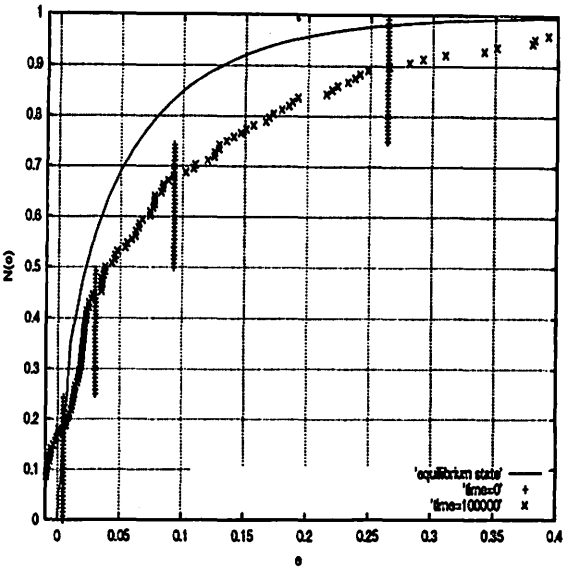

Figure 5: $N = 128,\ E = 0.0972,\ t = 0, 100000$

4.4 $N = 128, E = 0.484, T = 0.968$ の場合

初期条件は密度一定である。この場合も time=100000 でも $N_0(e)$ には遠い。$N(e)$ の変化は図 6 に示している。

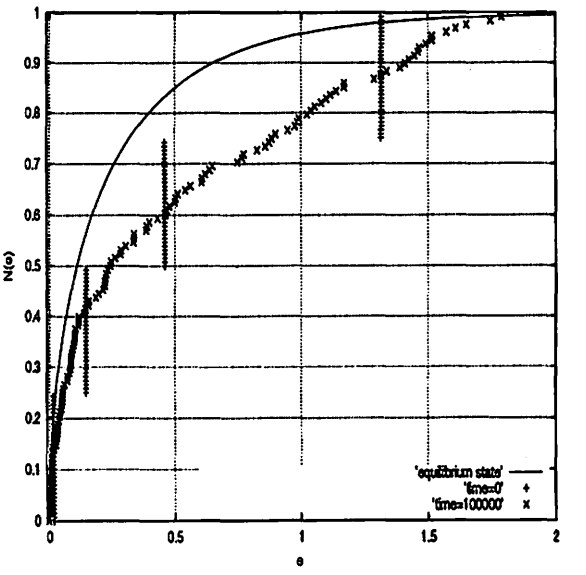

Figure 6: $N = 128,\ E = 0.484, t = 0, 100000$

5 Relaxation Timescale

平衡分布 $N_0(e)$ に近づく time scale と Makino [5] が用いた relaxation timescale

$$D_2 = \frac{<[\epsilon_i(t_0) - \epsilon_i(t_0 + \Delta t)]^2>}{\Delta t} \quad (17)$$

$$T_r = \frac{\epsilon^2}{D_2} \quad (18)$$

を比較するため Makino [5] の relaxation time を計算した。

ϵは一粒子あたりの energy で、$(k = 1/N, M = N)$

$$\epsilon_i = \frac{1}{2}p_i^2 - \frac{kM}{2\pi N}\sum_{i \neq j}\cos[2\pi(x_i - x_j)] \quad (19)$$

Makino [5] に従い $\Delta t = Nt_c$ とする。

図 7 に T_r/NT_c のグラフを示す。但し、$E > 0$ の系のシミュレーションは $t < 100000$ では relax しなかった。

図 7 から $e \simeq 0$ で T_r/NT_c が小さくなっている事が判る。$-0.1 < e < 0.1$ の領域が relax しやすいバンドだと考えられる。この領域に含まれる粒子の割合とシミュレーションで得られた T_r' の関係は表 (1) のようになる。 これより T_r は modified Konishi-Kaneko 系で $E < 0$ では relaxation time の比較的良い measure であるものの、$E > 0$ ではそうでない事が言える。

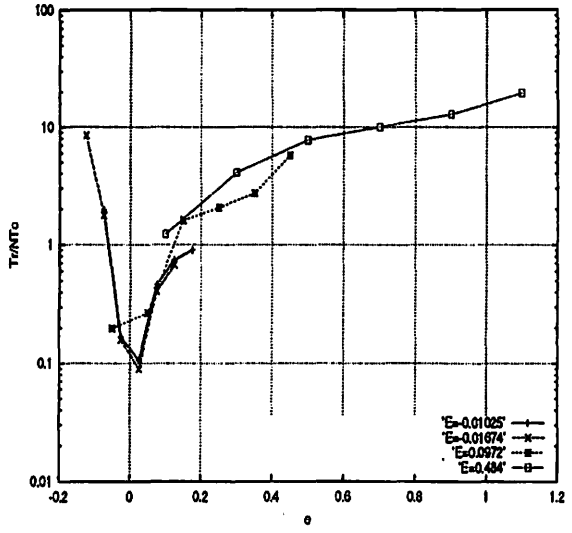

Figure 7: Tr/NTc

Table 1: E, populations in the relaxation band, T_r'

total energy E	$-0.1 < e < 0.1$	T_r'
-0.01674	70%	$\simeq 10000$
-0.01025	95%	$\simeq 1000$
0.0972	65%	> 100000
0.484	25%	> 100000

References

[1] T. Tsuchiya, T. Konishi, and N. Gouda, Phys. Rev. **E50** (1994), 2607.

[2] T. Tsuchiya, N. Gouda, and T. Konishi, Phys. Rev. **E53** (1996), 2210.

[3] T. Tsuchiya, N. Gouda, and T. Konishi, Ap. SS., **257** (1997), 319.

[4] T. Tsuchiya, and N. Gouda, Phys. Rev. **E61** (2000), 948.

[5] J. Makino, 天体力学N体力学研究会集録 (2000), 234.

[6] 金森洋一, 京都大学大学院理学研究科修士論文 (1995)

[7] O.C. Eldridge, and M. Feix, Phys. Fluids (1963), **6**, 398.

[8] T. Konishi, and K. Kaneko, J. Phys. (1992) **A25**, 6283.

[9] S. Inagaki, and T. Konishi, PASJ (1993) **45**, 733.

[10] S. Inagaki, Prog. Theor. Phys. (1993) **90**, 577.

[11] V. Latora, A. Rapisarda, and S. Ruffo, Physica (1998) **D131**, 38.

[12] Y. Kuramoto, Prog. Theor. Phys. Suppl. (1984) **49**, 223.

シンプレクティックマップに対するくりこみ群の方法

後藤振一郎 (S. GOTO) *　　野崎一洋 (K. NOZAKI)
名古屋大学　理学部・物理学教室　R研

Regulrized renormalization Group reduction of Symplectic maps †

Shin-itiro GOTO* and Kazuhiro NOZAKI
Department of Physics,Nagoya University,Nagoya 464-8602,Japan

abstract

By means of the perturbative renormalization group method, we study a long-time behaviour of some symplectic discrete maps near elliptic and hyperbolic fixed points. It is shown that a naive renormalization group (RG) map breaks the symplectic symmetry and fails to describe a long-time behaviour. In order to preserve the symplectic symmetry, we present a regularization procedure, which gives a regularized symplectic RG map describing an approximate long-time behaviour succesfully.

1 Introduction

ハミルトン系における時間大域的な フロー (flow) の様子は, 平均化法 (averaging method) や多重時間尺度法 (multiple-timescales method) などの様な特異摂動法 (singular perturbation method) による長い研究の歴史がある. ハミルトニアンフロー (Hamiltonian flow) はポアンカレマップ (Poincaré map) と呼ばれるシンプレクティックマップ (Symplectic map) に 簡約 (reduce) されうる. この場合, シンプレクティックマップを定義する相空間は元もとのフローを表現する相空間の次元よりも低い次元になっているので, 力学系研究者は高次元力学系を理解する為に勢力的に研究を行ってきた. しかしながら, 平均化法や多重時間尺度法は直ちにシンプレクティックマップ系へ適用する事はできない. だが, くりこみ群の方法 (Renormalizatin group metod; RG method) はフローの場合と同様に時間離散系に対して長時間後の振舞いを知る為の道具になりうる可能性がある. 元来, くりこみ群の方法は微分方程式に対する強力な特異摂動法の一つとして開発された方法 [CGO96] で, この方法では 正則摂動解 (naive perturbation solution) ‡ の永年項や発散項は非摂動項の積分定数にくりこむ事によって取り除かれる. このくりこみ群の方法は単純な くりこみ変換 (renormalization transformation) と リー群 (Lie group) を基礎にして再定式化された [GMN99].

*e-mail: sgoto@allegro.phys.nagoya-u.ac.jp
†reference: J. Phys. Soc. Jpn. vol 70. (2001), pp 49--54.
‡スモールパラメーターの自然数巾による摂動解.

このＲＧ法は離散系への適用が容易であり, 幾つかのカオス的離散系の 不安定多様体 (unstable manifold) の漸近展開 (asymptotic expansion) が構成された [GN01]. しかし, このＲＧ法をシンプレクティックマップ系へ適用できるかどうかは自明では無い. それはシンプレクティック性が, この論文で示すように素朴な ＲＧＥ (Renormalization Group Equation) では破れてしまうからである. これは, 時間連続系の場合, すなわち 正準方程式 (canonical equation) の場合 [YN98] と独立に考察しなければならない.

この論文の主な目的は シンプレシティー (Smplecity) を保存したくりこみ群の方法を提供する事である. この論文においてこの手続きは正則化されたくりこみ群の手続き (Regularized RG procedure) と呼ばれ, それは, 2つのステップから成る. 第一に再定式化されたくりこみ群の方法を使う [GMN99]. それにより, 楕円 (elliptic) 及び, 双曲 (hyperbolic) 型不動点近傍のＲＧマップを得る. この際得られるマップは近似的にしかシンプレクティック性を保存せず, 系の長時間の振舞いを記述する事はできない. 第2にシンプレシティーを回復する為にシンプレクティックマップをもたらす 指数化 (exponentiation) の手続きを導入する. 本論文ではこのプロセス, 及びこれにより得られるシンプレクティックＲＧマップをそれぞれＲＧの正則化 (regularization), 正則化されたくりこみ群マップ (regularized RG map) と呼ぶ事にする.

2 Linear Symplectic Map

ここでは導入として, 厳密に解ける系である線系シンプレクティックマップの正則摂動, またそのくりこみを考え, 厳密解と比較する事により問題点を指摘するとともに, 正則化くりこみの方法を述べ, その方法の有用性等を述べる. 問題を具体的にする為, 次のマップを考える. $\boldsymbol{R}^2 \ni (x_n, y_n) \mapsto (x_{n+1}, y_{n+1}) \in \boldsymbol{R}^2$:

$$\begin{aligned} x_{n+1} &= x_n + y_{n+1}, \\ y_{n+1} &= y_n - Jx_n + 2\epsilon J x_n, \end{aligned} \tag{1}$$

ここで $n(\in \boldsymbol{Z})$ は離散時間, ϵ はスモールパラメーターである. このマップ (1) 式 は パラメーター $0 < J < 2$ で原点に楕円型不動点を持つ. (1) 式から y 変数を消去する事により, 2階の差分方程式を得る :

$$Lx_n \equiv x_{n+1} - 2\cos(\theta)x_n + x_{n-1} = \epsilon 2 J x_n, \tag{2}$$

ここで $\cos\theta = 1 - J/2$, $0 < J < 2$ を仮定する. このマップ (2) 式 は次の厳密解 x_n^{exact} を有する :

$$\begin{aligned} x_n^{exact} &= A\exp\Big(i\arccos(\cos\theta + \epsilon J)n\Big) + \text{c.c.}, \\ &= A\exp\left[i\left(\theta + \epsilon\frac{-J}{\sin\theta} + \epsilon^2\frac{-\cos\theta}{2\sin\theta}\left(\frac{J}{\sin\theta}\right)^2 + \mathcal{O}(\epsilon^3)\right)n\right] + \text{c.c.}, \end{aligned} \tag{3}$$

ここで $A(\in \boldsymbol{C})$ は積分定数, c.c. はこの記号以前までの項の複素共役を表す.
ここでＲＧ法を使って小さな ϵ に対して (1) 式の時間大域的な解を構成する事を考える. 次の展開を代入する :

$$x_n = x_n^{(0)} + \epsilon x_n^{(1)} + \epsilon^2 x_n^{(2)} + \mathcal{O}(\epsilon^3), \tag{4}$$

これを Eq.(2) 式に代入し,

$$Lx_n^{(0)} = 0, \quad Lx_n^{(1)} = 2Jx_n^{(0)}, \quad Lx_n^{(2)} = 2Jx_n^{(1)}, \cdots.$$

$$x_n^{(0)} = A\exp(i\theta n) + \text{c.c.}, \tag{5}$$

$$x_n^{(1)} = -\frac{iJA}{\sin\theta} n\exp(i\theta n) + \text{c.c.}, \tag{6}$$

$$x_n^{(2)} = -\frac{J^2A}{2\sin^2\theta}\left(n^2 + i\frac{\cos\theta}{\sin\theta}n\right)\exp(i\theta n) + \text{c.c.}, \tag{7}$$

ここで $A(\in C)$ は非摂動問題 (5) 式から生じた積分定数で, 高次の摂動問題 (6),(7) 式で生じる斉次解の積分定数は初めから非摂動問題の積分定数 A に含まれているものとする. この正則摂動解から生じる永年項 ($\propto n, n^2$) を消去する為に, くりこみ変換 $A \mapsto \widetilde{A}(n)$ を導入する [GMN99]:

$$\widetilde{A}(n) \equiv A - \epsilon\frac{iJA}{\sin\theta}n + \epsilon^2\frac{-J^2A}{2\sin^2\theta}\left(n^2 + i\frac{\cos\theta}{\sin\theta}n\right) + \mathcal{O}(\epsilon^3), \tag{8}$$

くりこみ群方程式の離散版は丁度 $\widetilde{A}(n)$ が満たす 1 階の差分方程式である. その局所的な解は (8) 式で与えられる. (8) 式から,

$$\widetilde{A}(n+1) - \widetilde{A}(n) = \left(-i\epsilon\frac{J}{\sin\theta} - \epsilon^2\frac{J^2}{2\sin^2\theta}\left(2n+1+i\frac{\cos\theta}{\sin\theta}\right)\right)A + \mathcal{O}(\epsilon^3), \tag{9}$$

ここで A は $\widetilde{A}(n)$ で表すことができる. この事はくりこみ変換 (8) 式の逆をとる事によって成し遂げられる.

$$A = \left(1 + i\epsilon\frac{Jn}{\sin\theta} + \mathcal{O}(\epsilon^2)\right)\widetilde{A}(n). \tag{10}$$

(10) 式を (9) 式へ代入して, $\mathcal{O}(\epsilon^2)$ までのくりこみ群マップを得る.

$$\widetilde{A}(n+1) = \left(1 + \frac{-i\epsilon J}{\sin\theta} + \frac{1}{2!}\left(\frac{-i\epsilon J}{\sin\theta}\right)^2 - i\epsilon^2\frac{J^2\cos\theta}{2\sin^3\theta}\right)\widetilde{A}(n) + \mathcal{O}(\epsilon^3), \tag{11}$$

そしてその解は,

$$\widetilde{A}(n) = \left(1 + \frac{-i\epsilon J}{\sin\theta} + \frac{1}{2!}\left(\frac{-i\epsilon J}{\sin\theta}\right)^2 - i\epsilon^2\frac{J^2\cos\theta}{2\sin^3\theta} + \mathcal{O}(\epsilon^3)\right)^n\widetilde{A}(0). \tag{12}$$

その一方で, 厳密解 (3) 式から $\widetilde{A}(n)$ は厳密に次のように書けるであろう.

$$\widetilde{A}(n) = \widetilde{A}(0)\exp\left[i\left(\epsilon\frac{-J}{\sin\theta} - \epsilon^2\frac{\cos\theta}{2\sin\theta}\left(\frac{J}{\sin\theta}\right)^2 + \mathcal{O}(\epsilon^3)\right)n\right], \tag{13}$$

ここで注意するべき事は $|\widetilde{A}|^2$ が厳密に保存量となっている事である. しかし素朴な (=単純な, naive) くりこみ群マップ (11) 式では $|\widetilde{A}|^2$ は厳密な保存量では無い. シンプレクティック構造もまた, 単純なくりこみ群マップでは厳密に保存しない. $\mathcal{O}(\epsilon^k)$ までの近似でのくりこみ群マップにおいて以下が成立する,

$$d\widetilde{A}(n+1)\wedge d\widetilde{A}^*(n+1) - d\widetilde{A}(n)\wedge d\widetilde{A}^*(n) = \mathcal{O}(\epsilon^{(k+1)}) \neq 0,$$

ここで $k = 1, 2, \cdots$. $\widetilde{A}^*$ は $\widetilde{A}$ の複素共役を表し,$\widetilde{A}$ の正準共役な力学変数になるべきであろう§. この単純なＲＧマップの欠陥は ϵ が小さい極限で消失するが, その欠陥の様子を図 1 (Fig. 1) に示す.

§ハミルトニアンフローに関して, 単純なＲＧＥ (Renormalization Grouup Equation) は $\widetilde{A}(t)$ と $\widetilde{A}(t)^*$ が正準性をスモールパラメーター ϵ の各オーダー毎に保存し, 正準共役な力学変数になる. そして,$|\widetilde{A}|^2$ が運動の定数になる. Appendix 1 を参考.

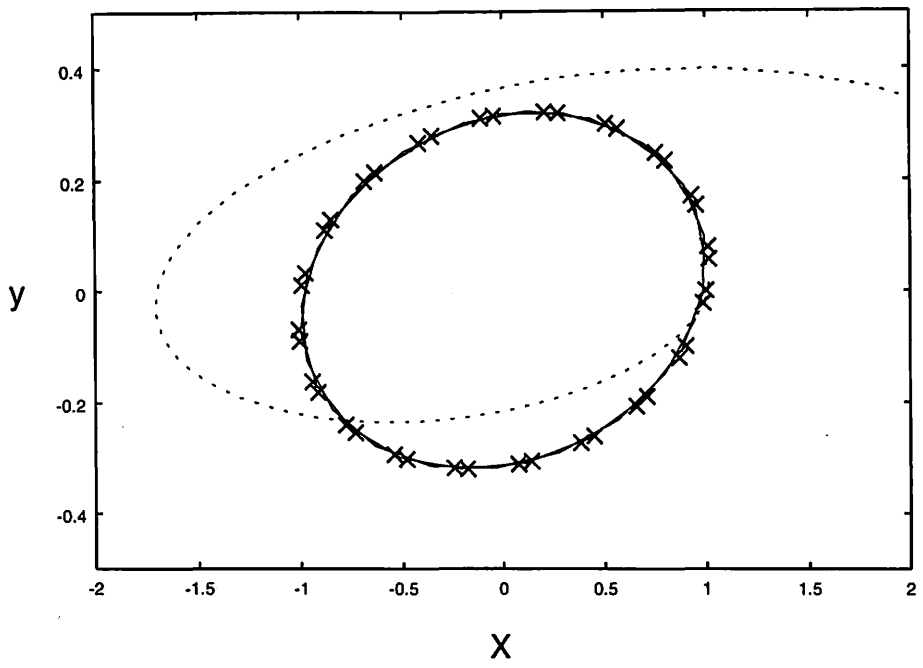

図 1: [Fig. 1] Trajectries constructed from the naive RG map (broken line), the regularized RG map(solid line) and an "exact" trajectry of the original map (1) (crosses) for $J = 0.2, \epsilon = 0.25$ and an initial condition $(x_0 = 1.0, y_0 = 0.0)$.

この様な欠陥を改善するために, 次の厳密解に於ける $\widetilde{A}(n)$ の係数に関する決定的な観察を利用する. すなわち, (11) 式は次の様に修正できる.

$$\begin{aligned} & 1 + \frac{-i\epsilon J}{\sin\theta} + \frac{1}{2!}\left(\frac{-i\epsilon J}{\sin\theta}\right)^2 - i\epsilon^2 \frac{J^2\cos\theta}{2\sin^3\theta} \\ = \quad & \exp\left(\frac{-i\epsilon J}{\sin\theta} - i\epsilon^2 \frac{J^2\cos\theta}{2\sin^3\theta}\right) + \mathcal{O}(\epsilon^3). \end{aligned}$$

修正された係数を用いる事により, 単純なＲＧマップのシンプレシティーは次の様に回復される.

$$\widetilde{A}(n+1) = \exp\left(\frac{-i\epsilon J}{\sin\theta} - i\epsilon^2 \frac{J^2\cos\theta}{2\sin^3\theta}\right)\widetilde{A}(n), \tag{14}$$

これは, 厳密な保存量 $|\widetilde{A}|$ を有する. このプロセスが $\widetilde{A}(n)$ の係数の "指数化" に他ならず, 本論文でＲＧマップの正則化と呼ぶものである. 簡単に確かめられる事は正則化ＲＧマップの解は厳密解 (13) 式の漸近展開に一致し, 系の長時間 $(n \sim \mathcal{O}(\epsilon^{-2}))$ の記述する事である. 図 1 において, 素朴なＲＧマップ ((11) 式) から構成された軌道と正則化ＲＧマップ ((14) 式) が系 ((1) 式) の "厳密な" 軌道と比較されている.

3 Two-dimensional Non-linear Symplectic Map

3.1 Elliptic Fixed Point

ここでは一般にカオスが生じる弱非線形シンプレクティックマップの解析を行う.
$R^2 \ni (x_n, y_n) \mapsto (x_{n+1}, y_{n+1}) \in R^2$:

$$\begin{aligned} x_{n+1} &= x_n + y_{n+1}, \\ y_{n+1} &= y_n - Jx_n + 2\epsilon J x_n^3, \end{aligned} \tag{15}$$

または,

$$Lx_n = \epsilon 2Jx_n^3, \tag{16}$$

ここで, ϵ はスモールパラメーターで, L は (2) 式で定義されている. また, (16) 式系が原点 (0,0) が楕円点になる様に $0 < J < 2$ を仮定する. 線形の場合と同様にまず, 正則摂動解を求めるために x_n を ϵ の巾で展開して,

$$x_n = x_n^{(0)} + \epsilon x_n^{(1)} + \epsilon^2 x_n^{(2)} + \mathcal{O}(\epsilon^3), \tag{17}$$

これにより, 以下を得る,

$$Lx_n^{(0)} = 0, \quad Lx_n^{(1)} = 2Jx_n^3, \quad Lx_n^{(2)} = 6Jx_n^{(0)}x_n^{(1)}, \cdots,$$

そしてその解は $\mathcal{O}(\epsilon^2)$ までで, 次の様に与えられる.

$$\begin{aligned} x_n^{(0)} &= A\exp(i\theta n) + \text{c.c.}, \\ x_n^{(1)} &= \alpha_1 A^3 \exp(3i\theta n) + i\alpha_{1R}|A|^2 An\exp(i\theta n) + \text{c.c.}, \\ x_n^{(2)} &= i\alpha_1\alpha_{1R}|A|^4 An\exp(i\theta n) - \frac{\alpha_{1R}^2}{2}|A|^4 A\left(n^2 + i\frac{\cos\theta}{\sin\theta}n\right)\exp(i\theta n) \\ &\quad +3i\alpha_1\alpha_{1R}|A|^2A^3\left(n - i\frac{\sin(3\theta)}{\cos 3\theta - \cos\theta}\right)\exp(3i\theta n) \\ &\quad +6\alpha_1^2|A|^2A^3\exp(3i\theta n) + \frac{3J\alpha_1 A^5}{\cos 5\theta - \cos\theta}\exp(5i\theta n) + \text{c.c.}, \end{aligned}$$

ここで,

$$\alpha_1 \equiv \frac{J}{\cos 3\theta - \cos\theta}, \quad \alpha_{1R} \equiv \frac{-3J}{\sin\theta},$$

そして, $A(\in C)$ は積分定数である. 基本振動数 (fundermental harmonic) $\exp(i\theta n)$ の係数の永年項を消去する為に, くりこみ変換 $A \mapsto \widetilde{A}(n)$ を導入する :

$$\widetilde{A}(n) = A + \epsilon(i\alpha_{1R}|A|^2An) + \epsilon^2\left(\frac{-\alpha_{1R}^2}{2}|A|^4A\left(n^2 + i\frac{\cos\theta}{\sin\theta}n\right) + i\alpha_1\alpha_{1R}|A|^4An\right). \tag{18}$$

前章と同様な手続きに従い, (18) 式から素朴なＲＧマップを導出すると,

$$\begin{aligned} \widetilde{A}(n+1) - \widetilde{A}(n) &= \epsilon i\alpha_{1R}|\widetilde{A}(n)|^2\widetilde{A}(n) \\ &\quad +\epsilon^2\left(\frac{-\alpha_{1R}^2}{2}|\widetilde{A}(n)|^4\widetilde{A}(n)\left(1 + i\frac{\cos\theta}{\sin\theta}\right) + i\alpha_1\alpha_{1R}|\widetilde{A}(n)|^4\widetilde{A}(n)\right), \end{aligned} \tag{19}$$

このマップはシンプレシティーを破っていて, 運動の定数を持たない. シンプレシティーを回復する為に, 単純なＲＧマップ (19) 式の正則化を $\widetilde{A}(n)$ の係数の "指数化" によって行う. すなわち,

$$\widetilde{A}(n+1) \quad = \quad \widetilde{A}(n)\exp\left(i\epsilon|\widetilde{A}(n)|^2\alpha_{1R}+i\epsilon^2|\widetilde{A}(n)|^4\left(\frac{-\cos\theta}{2\sin\theta}\alpha_{1R}^2+\alpha_1\alpha_{1R}\right)\right), \qquad (20)$$

この正則化ＲＧマップはもちろん (19) 式と $\mathcal{O}(\epsilon^2)$ までで一致する. また,

$$d\widetilde{A}(n+1)\wedge d\widetilde{A}^*(n+1)=d\widetilde{A}(n)\wedge d\widetilde{A}^*(n),$$

である事や, 運動の定数 $|\widetilde{A}|$ を持つ事は簡単にわかる. 極座標表示 $\widetilde{A}(n)=|\widetilde{A}(n)|\exp(i\widetilde{\phi}(n))$ を導入して, 正則化ＲＧマップは単純な以下で与えられるような位相方程式に簡約される.

$$\widetilde{\phi}(n+1) \quad = \quad \widetilde{\phi}(n)+\left(\epsilon|\widetilde{A}(0)|^2\alpha_{1R}+\epsilon^2|\widetilde{A}(0)|^4\left(\frac{-\cos\theta}{2\sin\theta}\alpha_{1R}^2+\alpha_1\alpha_{1R}\right)\right), \qquad (21)$$

それゆえ, 正則化ＲＧマップ (20) 式は厳密に解ける. この事は素朴なＲＧマップ (19) 式では保存量が存在しなかった事とは対照的である. また, 第３高調波 (the third harmonic), $\exp(3i\theta n)$ の前の永年項はくりこまれた変数 $\widetilde{A}_3(n)$ を次のように定義して, 処理されうる：

$$\epsilon\widetilde{A}_3(n) \quad \equiv \quad \epsilon\alpha_1A^3+\epsilon^2\left(3i\alpha_1\alpha_{1R}|A|^2A^3\left(n-\frac{i\sin3\theta}{\cos3\theta-\cos\theta}\right)+6\alpha_1^2|A|^2A^3\right). \qquad (22)$$

(18) 式で得られるくりこみ逆変換 ($=A$ を $\widetilde{A}(n)$ で表現した関係式) を (22) 式へ代入する事により微分方程式の場合と同様に消去される [GMN99] ¶.

この結果の応用として, 楕円点近傍の回転数の解析的表現を得る事ができる. 回転数 $\rho(x_0,y_0)$ の定義は以下で与えられる.

$$\rho(x_0,y_0)\equiv\lim_{N\to\infty}\frac{1}{2\pi N}\sum_{n=0}^{N}\phi_n,$$

ここで, ϕ_n は 相空間中のベクトル (x_n,y_n) と (x_{n+1},y_{n+1}) の間のなす角の事である [Ai*89]. 高振動数を無視した近似で, この (15) 式系での回転数 $\rho(x_0,y_0)$ は次で与えられる：

$$2\pi\rho(x_0,y_0)\approx\theta+\left(\epsilon|\widetilde{A}(0)|^2\alpha_{1R}+\epsilon^2|\widetilde{A}(0)|^4\left(\frac{-\cos\theta}{2\sin\theta}\alpha_{1R}^2+\alpha_1\alpha_{1R}\right)\right)+\widetilde{\phi}(0), \qquad (23)$$

ここで, 初期値 (x_0,y_0) は正則化ＲＧマップの初期値 $|\widetilde{A}(0)|$, $\widetilde{\phi}(0)$ と関係する. 図３において, (23) 式で与えられる回転数 $\rho(x_0,y_0)$ をプロットしてある. 図３で回転数の初期値 (x_0,y_0) は図２で示されている相空間中の線分 $0<x_0<0.8,\quad y_0=0$ 上にとってある. この結果は元もとのマップ (15) 式系の数値計算と正則化ＲＧによる回転数の解析的な表式とが強い共鳴が現れる $x_0\simeq0.6$ 辺りまで良い一致を示している.

¶[GMN99] の論文, または, Appendix 1 を参考の事.

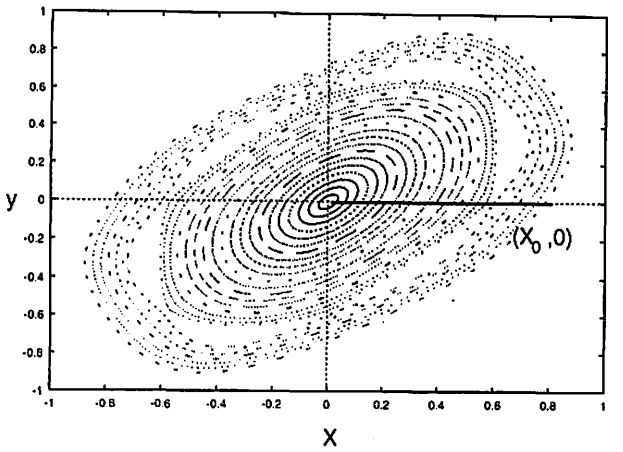

図 2: [Fig. 2]A phase portrait of the map (15) for $J = 1.2, \quad \epsilon = 0.25$. The solid half line represents initial phase points $0 < x_0 < 0.8, \quad y_0 = 0$ of the rotation number $\rho(x_0, y_0)$.

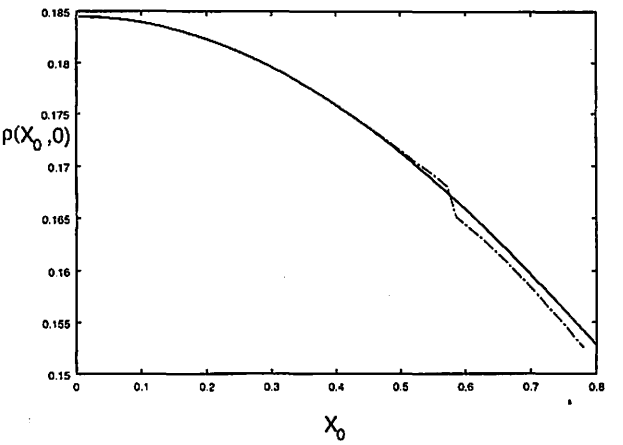

図 3: [Fig. 3]The rotation number $\rho(x_0, y_0)$ versus initial phase points $(x_0, 0)$ for $J = 1.2, \quad \epsilon = 0.25$. The solid curve represents the rotation number given by the regularized RG map (23), while the dashed curve is obtained by numerical calculations of the original map (15).

3.2 Hyperbolic Fixed Point

(15) 式において, $J<0$ の場合について考察する. この場合原点 $(0,0)$ が双曲型不動点で (16) 式は次の様になる.

$$Lx_n = \epsilon 2Jx_n^3, \tag{24}$$

ここで

$$Lx_n \equiv x_{n+1} - 2\cosh(\theta)x_n + x_{n-1}, \quad \cosh\theta = 1 - J/2 \quad (J<0),$$

そして $K \equiv \exp(\theta)$ は原点での線形化方程式の固有値の 1 つでである. すなわち,

$$K = \frac{1}{2}\left(2 - J + \sqrt{-4J+J^2}\right), \quad \text{or} \quad K = \frac{1}{2}\left(2 - J - \sqrt{-4J+J^2}\right).$$

x_n を (17) 式の様に展開して, 次の摂動解を得る.

$$\begin{aligned}
x_n^{(0)} &= A_+K^n + A_-K^{-n}, \\
x_n^{(1)} &= 2J\left(\frac{A_+^3K^{3n}}{D(K)} + \frac{A_-^3K^{-3n}}{D(K)} + \frac{3A_+^2A_-}{K-K^{-1}}nK^n + \frac{3A_+A_-^2}{K^{-1}-K}nK^{-n}\right), \\
x_n^{(2)} &= 12J^2\left(\frac{3A_+^3A_-^2}{2(K-K^{-1})^2}\left(n^2 - a(K)n\right) + \frac{A_+^3A_-^2}{(K-K^{-1})D(K)}\right)K^n \\
&\quad +12J^2\left(\frac{3A_-^3A_+^2}{2(K^{-1}-K)^2}\left(n^2 + a(K)n\right) + \frac{A_-^3A_+^2}{(K^{-1}-K)D(K)}\right)K^{-n} + \text{n.r.},
\end{aligned}$$

ここで,

$$\begin{aligned}
D(K) &\equiv K^3 - (K+K^{-1}) + K^{-3} = D(K^{-1}) \in \boldsymbol{R}, \\
a(K) &\equiv \frac{K+K^{-1}}{K-K^{-1}} = -a(K^{-1}) \in \boldsymbol{R}.
\end{aligned}$$

$A_+(\in \boldsymbol{R})$ と $A_-(\in \boldsymbol{R})$ は実数の積分定数で n.r. は永年項以外の項を表す. くりこみ変換 : $A_+ \mapsto \widetilde{A}_+(n)$ 及び, $A_- \mapsto \widetilde{A}_-(n)$ を導入して, K^n の係数の永年項を消去する. すると, 素朴な RG マップは :

$$\begin{aligned}
\widetilde{A}_+(n+1) &= \widetilde{A}_+(n) - 2\epsilon J\frac{3\widetilde{A}_+^2(n)\widetilde{A}_-(n)}{K-K^{-1}} \\
&\quad +12\epsilon^2J^2\left(\frac{3\widetilde{A}_+^3(n)\widetilde{A}_-^2(n)}{2(K-K^{-1})^2}\left(1 - a(K)\right) + \frac{\widetilde{A}_+^3(n)\widetilde{A}_-^2(n)}{(K-K^{-1})D(K)}\right), \qquad (25) \\
\widetilde{A}_-(n+1) &= \widetilde{A}_-(n) - 2\epsilon J\frac{3\widetilde{A}_-^2(n)\widetilde{A}_+(n)}{K^{-1}-K} \\
&\quad +12\epsilon^2J^2\left(\frac{3\widetilde{A}_-^3(n)\widetilde{A}_+^2(n)}{2(K^{-1}-K)^2}\left(1 + a(K)\right) + \frac{\widetilde{A}_-^3(n)\widetilde{A}_+^2(n)}{(K^{-1}-K)D(K)}\right). \qquad (26)
\end{aligned}$$

この系 (25) 式及び,(26) 式系はシンプレシティーを有さないが, 指数化の手続きにより, 正則化される.

$$\tilde{A}_+(n+1) = \tilde{A}_+(n)\exp\left\{\epsilon\frac{6J\tilde{A}_+(n)\tilde{A}_-(n)}{K-K^{-1}}\right.$$
$$\left.+\epsilon^2 12J^2\left(-a(K)\frac{3\tilde{A}_+^2(n)\tilde{A}_-^2(n)}{2(K-K^{-1})^2}+\frac{\tilde{A}_+(n)\tilde{A}_-(n)}{(K-K^{-})D(K)}\right)\right\}, \quad (27)$$

$$\tilde{A}_-(n+1) = \tilde{A}_-(n)\exp\left\{\epsilon\frac{6J\tilde{A}_-(n)\tilde{A}_+(n)}{K^{-1}-K}\right.$$
$$\left.+\epsilon^2 12J^2\left(+a(K)\frac{3\tilde{A}_-^2(n)\tilde{A}_+^2(n)}{2(K^{-1}-K)^2}+\frac{\tilde{A}_-(n)\tilde{A}_+(n)}{(K^{-1}-K)D(K)}\right)\right\}. \quad (28)$$

この正則化ＲＧマップは運動の定数 P を有する.

$$P \equiv \tilde{A}_+(n)\tilde{A}_-(n) = \tilde{A}_+(0)\tilde{A}_-(0),$$

そして, これもまた, 楕円型の場合同様に厳密に解く事ができる. P により, (27) 式及び (28) 式の一般解は次の様に与えられる.

$$\tilde{A}_+(n) = \tilde{A}_+(0)\exp\Big(Q(P;\epsilon)n\Big),$$
$$\tilde{A}_-(n) = \tilde{A}_-(0)\exp\Big(-Q(P;\epsilon)n\Big),$$

ここで, $Q(P;\epsilon)$ は P の多項式である:

$$Q(P;\epsilon) \equiv \epsilon\frac{6JP}{K-K^{-1}}+\epsilon^2 12J^2\left(\frac{-3a(K)P^2}{2(K-K^{-1})^2}+\frac{P}{(K-K^{-1})D(K)}\right).$$

4 Four-dimensional Symplectic Map

ここでは 2 つのシンプレクティックマップ (15) 式が結合した系を考察する.
$\boldsymbol{R}^4 \ni (x_n, y_n, x'_n, y'_n) \mapsto (x_{n+1}, y_{n+1}, x'_{n+1}, y'_{n+1}) \in \boldsymbol{R}^4$:

$$x_{n+1} = \frac{\partial F}{\partial y_{n+1}}, \quad y_n = \frac{\partial F}{\partial x_n}, \quad (29)$$
$$x'_{n+1} = \frac{\partial F}{\partial y'_{n+1}}, \quad y'_n = \frac{\partial F}{\partial x'_n}, \quad (30)$$

ここで F は母関数 (generating function),

$$F(x_n, y_{n+1}, x'_n, y'_{n+1}) = x_n y_{n+1} + x'_n y'_{n+1} + \frac{1}{2}(y_{n+1}^2 + y'^2_{n+1})$$
$$+\frac{1}{2}(Jx_n^2 + J'x'^2_n) - 2\epsilon\left(J\frac{x_n^4}{4} + J'\frac{x'^4_n}{4} + ax_n^2 x'^2_n\right).$$

原点 $(0,0,0,0)$ は $0 < J < 2$ と $0 < J' < 2$ において (29) ,(30) 式の楕円型不動点である. (29), (30) 式から y, y' 式を消去して. 連立 2 階差分方程式を得る :

$$x_{n+1} - 2\cos(\theta)x_n + x_{n-1} = 2\epsilon(Jx_n^3 + 2ax_n x'^2_n), \quad (31)$$
$$x'_{n+1} - 2\cos(\theta')x'_n + x'_{n-1} = 2\epsilon(J'x'^3_n + 2ax_n^2 x'_n), \quad (32)$$

ここで, $\cos\theta = 1 - J/2$, $\cos\theta' = 1 - J'/2$ である. 今, (31), (32) 式の非摂動解の周波数比 (i.e.θ/θ') を無理数の場合に限定する[‖]. これらの事により, 計算を行うと,(31) ,(32) 式の摂動解は,

$$\begin{aligned}
x_n^{(0)} &= A\exp(i\theta n) + \text{c.c.}, \\
x_n^{'(0)} &= B\exp(i\theta' n) + \text{c.c.}, \\
x_n^{(1)} &= \frac{-i}{\sin\theta}(3J|A|^2A + 4a|B|^2A)n\exp(in\theta) + \text{c.c.} + \text{n.r.}, \qquad (33) \\
x_n^{'(1)} &= \frac{-i}{\sin\theta'}(3J'|B|^2B + 4a|A|^2B)n\exp(in\theta') + \text{c.c.} + \text{n.r.}, \qquad (34)
\end{aligned}$$

ここで $A \in (C)$ and $B(\in C)$ は積分定数である. (33) や (34) 式での永年項を消去する為に, くりこみ変換 $A \mapsto \widetilde{A}(n), B \mapsto \widetilde{B}(n)$ を導入する:

$$\begin{aligned}
\widetilde{A}(n) &\equiv A + \epsilon\frac{-i}{\sin\theta}(3J|A|^2 + 4a|B|^2)An, \\
\widetilde{B}(n) &\equiv B + \epsilon\frac{-i}{\sin\theta'}(3J'|B|^2 + 4a|A|^2)Bn,
\end{aligned}$$

これにより素朴なＲＧマップは次のように得られる.

$$\begin{aligned}
\widetilde{A}(n+1) &= \widetilde{A}(n)\left\{1 + \epsilon\frac{-i}{\sin\theta}(3J|\widetilde{A}|^2 + 4a|\widetilde{B}|^2)\right\}, \\
\widetilde{B}(n+1) &= \widetilde{B}(n)\left\{1 + \epsilon\frac{-i}{\sin\theta'}(3J'|\widetilde{B}|^2 + 4a|\widetilde{A}|^2)\right\}.
\end{aligned}$$

これらを正則化する為に, くりこみ変数を次のようにスケールする,

$$\alpha(n) \equiv \frac{\widetilde{A}(n)}{\sqrt{\sin\theta'}}, \qquad \beta(n) \equiv \frac{\widetilde{B}(n)}{\sqrt{\sin\theta}},$$

ここで, $\sin\theta > 0$, $\sin\theta' > 0$. 結局, 素朴なくりこみマップを次のように "指数化" して,

$$\begin{aligned}
\alpha(n+1) &= \alpha(n)\exp\left\{\epsilon(-i)\left(3J\frac{\sin\theta'}{\sin\theta}|\alpha(n)|^2 + 4a|\beta(n)|^2\right)\right\}, \qquad (35) \\
\beta(n+1) &= \beta(n)\exp\left\{\epsilon(-i)\left(3J'\frac{\sin\theta}{\sin\theta'}|\beta(n)|^2 + 4a|\alpha(n)|^2\right)\right\}, \qquad (36)
\end{aligned}$$

(35), (36) 式がシンプレシティーを有す事,

$$d\alpha(n+1)\wedge d\alpha^*(n+1) + d\beta(n+1)\wedge d\beta^*(n+1) = d\alpha(n)\wedge d\alpha^*(n) + d\beta(n)\wedge d\beta^*(n),$$

や, 運動の定数, $|\alpha|^2$ と $|\beta|^2$ であるである事が簡単に示される.

5 Conclusion

この論文では幾つかのシンプレクティックマップの楕円型, 双曲型不動点まわりのシンプレシティーを保存したＲＧの手続きを与えた. 正則化は素朴なくりこみの簡単な指数化によって成し遂げられ, シンプレクティックマップを与える. これにより, 元の系の長時間の振舞いを定性的に正しく記述する事が可能になった. 正則化を施さなければ, 素朴なＲＧマップは系の長時間の運動の記述は失敗する. 更に, ここで挙げた正則化ＲＧマップは運動の定数を持っていて, 厳密に解くことが

[‖]有理数の場合は Appendix 2 にて議論を行う.

できる. これに対し, 正則化を行わない, 素朴なＲＧマップでは保存量が存在せず, また, 解析的に解けない. 正則化ＲＧマップの方法の応用として, 楕円型不動点近傍の回転数を近似的ではあるが解析的表式を与えた.

また, ここでの正則化ＲＧの方法はこの論文で挙げた例以外の, より一般な系, より高次元の系に対しても同様である事は明らかである.

Apendix 1：Lie-Group Approach to Perturbative Renormalization Group Method

ここでは, リー群の解釈に基づく漸近解析の道具としてのくりこみ群の方法の常微分方程式の部分について復習する [GMN99]. ここでの "くりこみ群の方法" とは漸近解析の道具の一種であり, 近年その数理構造の理解, 応用が理論物理の様々な分野でよく研究されている. たとえば, 力学系 [YN98], 量子力学 [Kun95], 反応拡散系 [MN01], 相対論的宇宙論 [Nam01] 等が挙げられる. なお, 偏微分方程式系に関するくりこみは [GMN99] や [MN01] に記述がある. また, この方法による離散時間力学系の不安定 (安定) 多様体の構成は [GN01] により研究されている.

Linear Problem

まず, 定数係数の線形常微分方程式を例にとりこの方法を説明する. ここでの例は厳密解が存在する系であるので, くりこみの結果と厳密解の比較が可能である.

$$\frac{d^2q}{dt^2}+\omega^2 q=-\epsilon q, \qquad (0<\epsilon\ll 1) \tag{37}$$

ここで, ϵ はスモールパラメーターである. この方程式はハミルトン系で,

$$\frac{dq}{dt}=p=\frac{\partial H}{\partial p}, \qquad \frac{dp}{dt}=-(\omega^2+\epsilon)q=-\frac{\partial H}{\partial q}, \qquad H(q,p)=\frac{p^2}{2}+\frac{(\omega^2+\epsilon)q^2}{2}.$$

また, この系は定数係数の線形の常微分方程式なので厳密解を有する.

$$\begin{aligned} q^{exact}(t) &= A\exp\left(i\omega t\sqrt{1+\frac{\epsilon}{\omega^2}}\right)+\text{c.c.} \\ &= A\exp\left\{i\left(\omega+\frac{\epsilon}{2\omega}-\frac{\epsilon^2}{8\omega^3}+\mathcal{O}(\epsilon^3)\right)t\right\}+\text{c.c.}, \end{aligned} \tag{38}$$

を持つ. また, $A(\in C)$ は積分定数である. この方程式系をあえて, 摂動で解いてみる. 正則摂動解は $q^{n.p.}(t)=q^{(0)}+\epsilon q^{(1)}+\epsilon^2 q^{(2)}+\mathcal{O}(\epsilon^3)$ を (37) 式へ代入して以下を得る.

$$\mathcal{O}(\epsilon^0) \qquad q^{(0)}(t)=A\exp(i\omega t)+\text{c.c.}, \tag{39}$$

$$\mathcal{O}(\epsilon^1) \qquad q^{(1)}(t)=\frac{itA}{2\omega}\exp(i\omega t)+\text{c.c.}, \tag{40}$$

$$\mathcal{O}(\epsilon^2) \qquad q^{(2)}(t)=\left(-\frac{At^2}{8\omega^2}-\frac{iAt}{8\omega^3}\right)\exp(i\omega t)+\text{c.c.}, \tag{41}$$

$$q^{n.p.}(t) = A\left\{1+\epsilon\frac{it}{2\omega}+\epsilon^2\left(-\frac{t^2}{8\omega^2}-\frac{it}{8\omega^3}\right)+\mathcal{O}(\epsilon^3)\right\}\exp(i\omega t)+\text{c.c.}, \tag{42}$$

ここで $A(\in C)$ は非摂動解から生じた積分定数である．また，高次 (摂動パラメーター ϵ の 1 次以上) の摂動問題の解は (40), (41) 式以外に斉次解を有するが，その斉次解から生じる積分定数は初めから非摂動解の積分定数 A に含まれているとする．この正則摂動解は $\propto t$ なる (混合型) 永年項が存在する為，時間が経過すればする程永年項が成長し，真の解から外れていく．これが通常の正則摂動論の限界である．近年までに開発されてきた種々の特異摂動論はこう言った正則摂動を超える摂動法である．くりこみ群の方法はこういった種々の方法を統一し，職人的な技巧を必要としない方法であるとされている点が利点とされている．

では，くりこみの方法をこの系に適用して，この方法の有用性をみてみる．この方法の考え方は，非摂動項の積分定数 $(=A)$ が摂動によって変化した $(=\widetilde{A}(t))$ と思い，積分定数の変化に対する微分方程式を構成し，それを解くことにより正則摂動解を改善しようという考え方である．その意味でこの方法は定数変化法に近いが，定数変化法と異るのは，ＲＧ法では正則摂動解の共鳴部分や発散項のみに注目する点である．具体的に一連の操作を見てみる:

$$\widetilde{A}(t) \equiv A\left\{1+\epsilon\frac{it}{2\omega}+\epsilon^2\left(-\frac{t^2}{8\omega^2}-\frac{it}{8\omega^3}\right)+\mathcal{O}(\epsilon^3)\right\}, \tag{43}$$

とくりこみ変換 $A \mapsto \widetilde{A}(t)$ を定義する．これは $\widetilde{A}(t)$ を永年項と非摂動問題から生じる積分定数 A とを含ませて定義されている．このくりこみ変数 $\widetilde{A}$ は時間 t が小さい間は正則摂動解をよく近似するという意味で意味をなす．この表式がくりこみ変数 $\widetilde{A}(t)$ の時刻 t 近傍での時間的に局所的情報を与える．くりこみ群方程式を構成する事とは，この多項式から t が小さい近傍で成立する微分方程式を構成する事に相当する．(43) 式からくりこみ逆変換 $A=\widetilde{A}(t)(1-it\epsilon/(2\omega)+\cdots)$ であることを用いると，

$$\begin{aligned}
\widetilde{A}(t+\tau) &= A\left\{1+\epsilon\frac{i(t+\tau)}{2\omega}+\epsilon^2\left(-\frac{t^2+2t\tau+\tau^2}{8\omega^2}-\frac{i(t+\tau)}{8\omega^3}\right)+\mathcal{O}(\epsilon^3)\right\} \\
&= \widetilde{A}(t)\left(1-\epsilon\frac{it}{2\omega}+\mathcal{O}(\epsilon^2)\right)\left(1+\epsilon\frac{i(t+\tau)}{2\omega}+\epsilon^2\left(-\frac{t^2+2t\tau+\tau^2}{8\omega^2}-\frac{i(t+\tau)}{8\omega^3}\right)+\mathcal{O}(\epsilon^3)\right) \\
&= \widetilde{A}(t)\left(1+\tau\left(\epsilon\frac{i}{2\omega}+\epsilon^2\frac{-i}{8\omega^3}+\mathcal{O}(\epsilon^3)\right)+\mathcal{O}(\tau^2)\right),
\end{aligned} \tag{44}$$

が成立する．これにより，$\widetilde{A}(t+\tau)$ を $\widetilde{A}(t)$ のみで閉じた関係式を構成する事ができた**．一方で，$\widetilde{A}(t)$ がテイラー展開可能であると仮定すると，

$$\begin{aligned}
\widetilde{A}(t+\tau) &= \exp(\tau\partial_t)\widetilde{A}(t) \\
&= \left(1+\tau\frac{d}{dt}+\tau^2\frac{d^2}{2!dt^2}+\mathcal{O}(\tau^3)\right)\widetilde{A}(t),
\end{aligned} \tag{45}$$

が成立する．(45) 式はくりこみ変数 $\widetilde{A}$ を時刻を t から $t+\tau$ までマップさせる演算を表している．その無限小変換を与える部分は τ の 1 次の部分である．この 2 つの独立な議論，すなわち，$\widetilde{A}(t)$ の定義から構成した関係式とテイラー展開の関係式を τ の 1 次で等値する．すると，(44) 式と，(45) 式から ϵ^2 までの近似で，

$$\frac{d\widetilde{A}}{dt}=i\left\{\epsilon\frac{1}{2\omega}-\epsilon^2\frac{1}{8\omega^3}\right\}\widetilde{A}, \tag{46}$$

**この計算は実は，$\widetilde{A}(t+\tau)-\widetilde{A}(t)$ を (43) 式から構成し，それにくりこみ逆変換を代入した方が計算量は少なくてすむ．この脚注で述べた方法でシンプレクティックマップのＲＧＥは計算されている．

これが求めるべき くりこみ群方程式（ＲＧＥ）である．なお，(46) 式の解は

$$\widetilde{A}(t) = \widetilde{A}(0)\exp\left\{i\left(\epsilon\frac{1}{2\omega} - \epsilon^2\frac{1}{8\omega^3}\right)t\right\},$$

となり，$|\widetilde{A}|^2$ が保存量になる．また，元の変数 q でくりこまれた解を観察するには，

$$\begin{aligned} q^{RG} &= \widetilde{A}(t)\exp(i\omega t) + \text{c.c.}, \\ &= \widetilde{A}(0)\exp\left\{i\left(\omega + \epsilon\frac{1}{2\omega} - \epsilon^2\frac{1}{8\omega^3}\right)t\right\} + \text{c.c.}, \end{aligned}$$

これは，厳密解 (38) 式と考察した摂動次数である ϵ^2 までで一致する．次にこの系のＲＧＥ (46) 式のハミルトン構造に注目してみる．$\widetilde{A}$ および $\widetilde{A}^*$ を正準共役な力学変数に選ぶと

$$\begin{aligned} \frac{d\widetilde{A}}{dt} &= i\left\{\epsilon\frac{1}{2\omega} - \epsilon^2\frac{1}{8\omega^3}\right\}\widetilde{A} = \frac{\partial H^{RG}}{\partial \widetilde{A}^*}, \\ \frac{d\widetilde{A}^*}{dt} &= -i\left\{\epsilon\frac{1}{2\omega} - \epsilon^2\frac{1}{8\omega^3}\right\}\widetilde{A}^* = -\frac{\partial H^{RG}}{\partial \widetilde{A}}, \\ H^{RG}(\widetilde{A},\widetilde{A}^*) &= i\left\{\epsilon\frac{1}{2\omega} - \epsilon^2\frac{1}{8\omega^3}\right\}|\widetilde{A}|^2, \end{aligned}$$

と書ける．

次に線形常微分方程式に関するくりこみ群方法の一般的な事がらについて議論する．結果を先に述べると，くりこみ変換と指数関数の間の関係が得られる．まず，くりこみ変換 $A \mapsto \widetilde{A}(t)$ が以下の様に求まったとする．

$$\widetilde{A}(t) \equiv A\cdot\left(1 + \sum_{n=1}\epsilon^n P_n(t)\right), \quad \frac{\partial P_n}{\partial A} = 0, \quad \text{(線形方程式より)}. \tag{47}$$

なお，先程の調和振動子の例では $P_1(t) = it/2\omega, P_2(t) = -t^2/8\omega^2 - it/8\omega^3$ である．また，くりこみ逆変換はくりこみ変換の定義である (47) 式から一般に

$$A = \frac{\widetilde{A}(t)}{1 + \sum_{n=1}\epsilon^n P_n(t)},$$

と求まる事に注意して，$\widetilde{A}(t+\tau)$ が $\widetilde{A}(t)$ を用いて以下のように表される，

$$\begin{aligned} \widetilde{A}(t+\tau) &= A\left(1 + \sum_{n=1}\epsilon^n\left(P_n(t+\tau) - P_n(t)\right)\right) \\ &= \frac{\widetilde{A}(t)}{1 + \sum_{n=1}\epsilon^n P_n(t)}\left(1 + \sum_{n=1}\epsilon^n\left(P_n(t+\tau) - P_n(t)\right)\right) \\ &= \frac{\widetilde{A}(t)}{1 + \sum_{n=1}\epsilon^n P_n(t)}\left(1 + \tau\sum_{n=1}\epsilon^n\dot{P}_n(t) + \mathcal{O}(\tau^2)\right) \\ &= \left(\frac{1 + \tau\sum_{n=1}\epsilon^n\dot{P}_n(t) + \mathcal{O}(\tau^2)}{1 + \sum_{n=1}\epsilon^n P_n(t)}\right)\widetilde{A}(t) \\ &= \left[1 + \epsilon\tau\left\{\dot{P}_1(t) + \epsilon\left(\dot{P}_2(t) - P_1(t)\dot{P}_1(t)\right)\right.\right. \\ &\qquad + \epsilon^2\left(\dot{P}_3(t) - P_1(t)\dot{P}_2(t) - \left(P_2(t) - P_1^2(t)\right)\dot{P}_1(t)\right) \\ &\qquad \left.\left. + \mathcal{O}(\epsilon^3)\right\} + \mathcal{O}(\tau^2)\right]\widetilde{A}(t), \end{aligned} \tag{48}$$

ここで $\dot{P}_n = dP_n/dt$. 一方, $\widetilde{A}(t)$ のテイラー展開から

$$\begin{aligned}\widetilde{A}(t+\tau) &= \exp(\tau\partial_t)\widetilde{A}(t) \\ &= \widetilde{A}(t) + \tau\frac{d\widetilde{A}(t)}{dt} + \mathcal{O}(\tau^2). \end{aligned} \tag{49}$$

調和振動子の例と同様に, 両者, すなわち (48) 式と (49) 式 $\mathcal{O}(\epsilon^3)$ を無視して, τ の 1 次で比較する事により,

$$\begin{aligned}\frac{d\widetilde{A}}{dt} &= \epsilon\left\{\dot{P}_1 + \epsilon\left(\dot{P}_2 - P_1\dot{P}_1\right) + \epsilon^2\left(\dot{P}_3 - P_1\dot{P}_2 - \left(P_2 - P_1^2\right)\dot{P}_1\right)\right\}\Bigg]\widetilde{A} \\ &= \epsilon\widetilde{A}\frac{d}{dt}\left\{P_1 + \epsilon\left(P_2 - \frac{P_1^2}{2}\right) + \epsilon^2\left(P_3 - P_1P_2 + \frac{P_1^3}{3}\right)\right\}, \end{aligned} \tag{50}$$

これがＲＧＥである. この方程式は変数分離法で解く事ができて,

$$\widetilde{A}(t) = \widetilde{A}(0)\exp\left(\epsilon P_1 + \epsilon^2\left(P_2 - \frac{P_1^2}{2}\right) + \epsilon^3\left(P_3 - P_1P_2 + \frac{P_1^3}{3}\right)\right), \tag{51}$$

となる. これは, くりこみ変換の定義 (47) 式を指数関数の形に書き直したものに他ならない.

Nonlinear Problem

ここでは非線形常微分方程式系でのくりこみを考える. くりこみ手順は線形の場合と全く同様である. ここでの非調和振動子で非線形項が摂動項となる問題である.

$$\frac{d^2q}{dt^2} + \omega^2 q = -\epsilon q^3, \tag{52}$$

ここで, ϵ は先程の線形問題と同様にスモールパラメーターである. この方程式はハミルトン系で,

$$\frac{dq}{dt} = p = \frac{\partial H}{\partial p}, \qquad \frac{dp}{dt} = -(\omega^2 q + \epsilon q^3) = -\frac{\partial H}{\partial q}, \qquad H(q,p) = \frac{p^2}{2} + \left(\frac{\omega^2 q^2}{2} + \frac{\epsilon q^4}{4}\right).$$

正則摂動問題は, $q^{n.p.} = q^{(0)} + \epsilon q^{(1)} + \epsilon^2 q^{(2)} + \mathcal{O}(\epsilon^3)$ を (52) 式へ代入して

$$\begin{aligned}
\mathcal{O}(\epsilon^0) \quad & q^{(0)} = A\exp(i\omega t) + \text{c.c.}, \\
\mathcal{O}(\epsilon^1) \quad & q^{(1)} = \frac{3i|A|^2A}{2\omega}t\exp(i\omega t) + \frac{A^3}{8\omega^2}\exp(3i\omega t), \\
\mathcal{O}(\epsilon^2) \quad & q^{(2)} = \left(-\frac{9}{8\omega^2}t^2 - \frac{15i}{16\omega^3}t\right)|A|^4A\exp(i\omega t) \\
& \qquad + \left(\frac{9i}{16\omega^3}t - \frac{21}{64\omega^4}\right)|A|^2A^3\exp(3i\omega t) + \frac{A^5}{64\omega^4}\exp(5i\omega t), \\
q^{n.p.}(t) = & \left\{A + \epsilon\frac{3i|A|^2A}{2\omega}t + \epsilon^2\left(-\frac{9}{8\omega^2}t^2 - \frac{15i}{16\omega^3}t\right)|A|^4A + \mathcal{O}(\epsilon^3)\right\}\exp(i\omega t) \\
& + \left\{\epsilon\frac{A^3}{8\omega^2} + \epsilon^2\left(\frac{9i}{16\omega^3}t - \frac{21}{64\omega^4}\right)|A|^2A^3 + \mathcal{O}(\epsilon^3)\right\}\exp(3i\omega t) \\
& + \left\{\epsilon^2\frac{A^5}{64\omega^4} + \mathcal{O}(\epsilon^3)\right\}\exp(5i\omega t) + \cdots + \text{c.c.}.
\end{aligned}$$

くりこみ変換を以下の様に定義する．すなわち，基本振動数の永年項を消去するようにくりこみ変換 $A \mapsto \widetilde{A}(t)$ を定義する．

$$\widetilde{A}(t) \equiv A + \epsilon \frac{3i|A|^2 A}{2\omega} t + \epsilon^2 \left(- \frac{9}{8\omega^2} t^2 - \frac{15i}{16\omega^3} t \right) |A|^4 A + \mathcal{O}(\epsilon^3), \tag{53}$$

このくりこみ変換 (53) 式と (45) 式により，今の場合のくりこみ逆変換が

$$A = \widetilde{A}(t) \left(1 - \epsilon \frac{3i|\widetilde{A}|^2 t}{2\omega} \right) + \mathcal{O}(\epsilon^2),$$

である事を用いると，$\mathcal{O}(\epsilon^2)$ までの近似で

$$\frac{d\widetilde{A}}{dt} = i \left\{ \epsilon \frac{3|\widetilde{A}|^2 \widetilde{A}}{2\omega} + \epsilon^2 \left(- \frac{15|\widetilde{A}|^4 \widetilde{A}}{16\omega^3} \right) \right\}, \tag{54}$$

が得られ，これがＲＧＥである．ＲＧＥ (54) 式の解は

$$\widetilde{A}(t) = \widetilde{A}(0) \exp \left\{ i \left(\epsilon \frac{3|\widetilde{A}|^2}{2\omega} + \epsilon^2 \frac{-15|\widetilde{A}|^4}{16\omega^3} \right) t \right\},$$

となり，$|\widetilde{A}|$ が保存量となる．この系の正準性はやはり，$\widetilde{A}$, $\widetilde{A}^*$ を正準共役な力学変数にとって，

$$\begin{aligned}
\frac{d\widetilde{A}}{dt} &= i \left\{ \epsilon \frac{3|\widetilde{A}|^2 \widetilde{A}}{2\omega} + \epsilon^2 \left(- \frac{15|\widetilde{A}|^4 \widetilde{A}}{16\omega^3} \right) \right\} = \frac{\partial H^{RG}}{\partial \widetilde{A}^*}, \\
\frac{d\widetilde{A}^*}{dt} &= -i \left\{ \epsilon \frac{3|\widetilde{A}|^2 \widetilde{A}}{2\omega} + \epsilon^2 \left(- \frac{15|\widetilde{A}|^4 \widetilde{A}}{16\omega^3} \right) \right\} = -\frac{\partial H^{RG}}{\partial \widetilde{A}}, \\
H(\widetilde{A}, \widetilde{A}^*) &= i \left\{ \epsilon \frac{3|\widetilde{A}|^4 \widetilde{A}}{4\omega} - \epsilon^2 \frac{5|\widetilde{A}|^6}{16\omega^3} \right\}.
\end{aligned}$$

また，第 3 高調波に生じる永年項は以下のように $\widetilde{A}$ を使って処理できる．

$$\begin{aligned}
\epsilon \widetilde{A}_3 &\equiv \epsilon \frac{A^3}{8\omega^2} + \epsilon^2 \left(\frac{9i}{16\omega^3} t - \frac{21}{64\omega^4} \right) |A|^2 A^3 \\
&= \epsilon \frac{\widetilde{A}^3}{8\omega^2} \left(1 - 3\epsilon \frac{3i|\widetilde{A}|^2 t}{2\omega} \right) + \epsilon^2 \left(\frac{9i}{16\omega^3} t - \frac{21}{64\omega^4} \right) |\widetilde{A}|^2 \widetilde{A}^3 \\
&= \epsilon \frac{\widetilde{A}^3}{8\omega^2} - \epsilon^2 \frac{21}{64\omega^4} |\widetilde{A}|^2 \widetilde{A}^3.
\end{aligned}$$

線形の場合と同様に元の変数で解を観察する場合には，

$$q^{RG}(t) = \widetilde{A}(t) \exp(i\omega t) + \epsilon \widetilde{A}_3(t) \exp(3i\omega t) + \epsilon^2 \frac{\widetilde{A}^5(t)}{64\omega^2} \exp(5i\omega t) + \text{c.c.},$$

とすれば良い．

Appendix 2 : When the θ/θ' is an rational number in § 4

ここでは，§ 4 で取り扱った 4 次元非線形マップ (29)–(30) 式の正則化くりこみについて，特に線形固有値が有理比である場合について考察する．結論から先に言えば，この様な場合には “指数化” による正則化，シンプレシティーの回復は不可能である．

問題を簡単にする為, $\theta = \theta'$(i.e, $J = J'$) という場合について計算を行う.
正則摂動解 $x_n = x_n^{(0)} + \epsilon x_n^{(1)} + \mathcal{O}(\epsilon^2)$, $x_n' = x_n'^{(0)} + \epsilon x_n'^{(1)} + \mathcal{O}(\epsilon^2)$ は,

$$
\begin{aligned}
x_n^{(0)} &= A\exp(i\theta n) + \text{c.c.}, \\
x_n'^{(0)} &= B\exp(i\theta n) + \text{c.c.}, \\
x_n^{(1)} &= -\frac{in}{\sin\theta}\left(3J|A|^2A + 2a(A|B|^2 + A^*B^2)\right)\exp(i\theta n) + \text{c.c.}, \\
x_n'^{(1)} &= -\frac{in}{\sin\theta}\left(3J|B|^2B + 2a(B|A|^2 + B^*A^2)\right)\exp(i\theta n) + \text{c.c.},
\end{aligned}
$$

と計算され, くりこみ変換 $A \mapsto \widetilde{A}(n)$, $B \mapsto \widetilde{B}(n)$ は,

$$
\begin{aligned}
\widetilde{A}(n) &\equiv A - \epsilon\frac{in}{\sin\theta}\left(3J|A|^2A + 2a(A|B|^2 + A^*B^2)\right), \\
\widetilde{B}(n) &\equiv B - \epsilon\frac{in}{\sin\theta}\left(3J|B|^2B + 2a(B|A|^2 + B^*A^2)\right).
\end{aligned}
$$

素朴なＲＧＥは差分のＲＧの一般論の下, 以下のように計算される.

$$
\widetilde{A}(n+1) = \widetilde{A}(n) - \epsilon\frac{in}{\sin\theta}\left(3J|\widetilde{A}|^2\widetilde{A} + 2a(\widetilde{A}|\widetilde{B}|^2 + \widetilde{A}^*\widetilde{B}^2)\right), \tag{55}
$$

$$
\widetilde{B}(n+1) = \widetilde{B}(n) - \epsilon\frac{in}{\sin\theta}\left(3J|\widetilde{B}|^2\widetilde{B} + 2a(\widetilde{B}|\widetilde{A}|^2 + \widetilde{B}^*\widetilde{A}^2)\right). \tag{56}
$$

"指数化" を行うと,

$$
\widetilde{A}(n+1) = \widetilde{A}(n)\exp\left[\epsilon\frac{-i}{\sin\theta}\left\{3J|\widetilde{A}(n)|^2 + 2a\left(2|\widetilde{B}(n)|^2 + \frac{\widetilde{A}(n)^*}{\widetilde{A}(n)}\widetilde{B}(n)^2\right)\right\}\right], \tag{57}
$$

$$
\widetilde{B}(n+1) = \widetilde{B}(n)\exp\left[\epsilon\frac{-i}{\sin\theta}\left\{3J|\widetilde{B}(n)|^2 + 2a\left(2|\widetilde{A}(n)|^2 + \frac{\widetilde{B}(n)^*}{\widetilde{B}(n)}\widetilde{A}(n)^2\right)\right\}\right]. \tag{58}
$$

このマップ系 (57),(58) 式はシンプレクティックマップになっていない事は単純な計算により示される.

References

[CGO96] L. Y. CHEN, N. GOLDENFELD and Y. OONO, *Renormalization group and sigular perturbations : Multiple scales, boundary layers, and reductive perturbation theory*, Phys. Rev. E. 54 (1996) 376.

[GMN99] S. GOTO, Y. MASUTOMI and K. NOZAKI, *Lie-Group Approach to Perturbative Renormalization Group Method*, Prog. Theo. Phys. 102-3 (1999) 471.

[GN01] S. GOTO and K. NOZAKI, *Asymptotic Expansions of Unstable and Stable Manifolds in Time-Discrete Systems*, Prog. Theo. Phys. 105-1 (2001) 99. or,
S. GOTO and K. NOZAKI, *Asymptotic expansions of unstable (stable) manifolds in time-discrete systems*, Proceedings of the 32nd Symposium on Celestical Mechanics pp.249–260, (in Japanese).

[YN98] Y. Y. YAMAGUCHI and Y. NAMBU, *Renormaization Group Equations and Integrability in Hamiltonian Systems*, Prog. Theo. Phys. 100-1 (1998) 199.

[KM98] T. KUNIHIRO and J. MATSUKIDAIRA, *Dynamical reduction of discrete systems based on the renormalization-group method*, Phys. Rev. E. 57 (1998) 4817.

[Ai*89] For example, Y. AIZAWA, Yasuhiro KIKUCHI, Takahisa HARAYAMA, Kenshi YAMAMOTO, Motonori OTA and Kenji TANAKA, *Stagnant Motions in Hamiltonian Systems*, Prog. Theo. Phys. Suppl. 98 (1989) 36.

[Kun95] T. KUNIHIRO, *A geometrical Formulation of the Renormalization Group Method for Global Analysis*, Phys. Rev. D. 57 (1998) 2035.

[MN01] Y. MASUTOMI and K. NOZAKI, *Derivation of Non-isotropic Phase Equations from a General Reaction-Difusion Equation*, Physica D. 151-1 (2001) 44.

[Nam01] Y. NAMBU, *Backreaction problem in the inflationary universe*, Phys. Rev. D. 63 (2001) 044013.

近可積分ハミルトン系における局所リャプノフ指数の振舞いについて

Local Lyapunov Exponents in Near-integrable Hamiltonian Systems

篠原 晋
早稲田大学理工学部応用物理学科
Susumu Shinohara
Department of Applied Physics, Waseda University
E-mail: ssusumu@mse.waseda.ac.jp

The stagnant motion around KAM tori in near-integrable Hamiltonian systems is studied by using the local Lyapunov exponents(LLE) for all the expanding and contracting directions in the tangent space. It is shown that the LLE is useful for describing the qualitative changes of motion in the mixed phase space, where chaos and tori coexist.

1 はじめに

近可積分ハミルトン系の相空間は、カオスとトーラスが複雑に混在した不均質なものである. そのような相空間を持つ系のカオス軌道は、単に乱雑な振舞いをするだけでなく、間欠的にトーラス近傍に捕らえられて一時的に規則的軌道のように振舞う「淀み運動」を行いつつ相空間を彷徨する [3, 4, 5]. そこで、近可積分系のカオス軌道の性質を理解するには、相空間の各領域がどのような不安定性を持つかという相空間の不均質性を捉えることが重要になる. 2 自由度系では、ポアンカレ断面をとることによって相空間を視覚化できるため、相空間構造を詳しく知ることが可能であるが、自由度が 3 以上の系では相空間が高次元になり、相空間の不均質性を捉えることは容易ではない. 本研究では、高次元相空間の不均質性を捉えるものとして、局所リャプノフ指数に注目した. ここで考える局所リャプノフ指数は、相空間の各点で定義され、軌道に沿って長時間平均をとったものがリャプノフ指数に一致するという性質をもつ [7]. ここでは、具体的な近可積分系として一次元振動子系を考え、初期にトーラス近傍に置かれた軌道が強カオス領域に遷移してゆく過程における局所リャプノフ指数の振舞いについて報告する.

2 非線形格子振動における誘導現象

隣接粒子が非線形のバネでつながれた $(N+2)$ 粒子からなる一次元系 (Fermi-Pasta-Ulam(FPU) モデル) を考える.

$$H = \sum_{i=1}^{N} \frac{p_i^2}{2} + \sum_{i=0}^{N} V(q_{i+1} - q_i), \qquad V(r) = \frac{1}{2}r^2 + \frac{\alpha}{3}r^3 + \frac{\beta}{4}r^4 \tag{1}$$

ここで、終端粒子は固定されているものとする. i.e., $q_0 = q_{N+1} = 0$. α と β はパラメータである. この系は $\alpha = \beta = 0$ のとき、基準座標 $(\boldsymbol{P}, \boldsymbol{Q})$ への正準変換によって、

$$H = \sum_{k=1}^{N} E_k, \qquad E_k = \frac{1}{2}(P_k^2 + \omega_k^2 Q_k^2), \tag{2}$$

と書ける．ここで $\omega_k = 2\sin(\pi k/2(N+1))$ である．$\alpha = \beta = 0$ のとき、$E_1, \cdots, E_N$ は運動の恒量になる．

FPU モデルでは、α と β が微小のとき、初期に単一のモード（基準振動）に与えたエネルギーが、ある時間を経た後、一斉に他のモードへ分配される「誘導現象」が起こる [6]．誘導現象は、軌道がトーラス近傍に一時的に留まることによって生じる現象であり、多自由度系の淀み運動と考えることができる．

図 1 は、$N = 15, \alpha = 0.5, \beta = 0$ の系で、初期に 11 番目のモードのみを励起したときの、E_9, E_{11}, E_{13} の時系列である．しばらくは 11 番目のモードにエネルギーが留まり、$t \approx 100$ で他のモードへのエネルギー分配が始まる．図 1 のモードエネルギーの振舞いからは、ある時点で弱カオス的運動から強カオス的運動へ遷移していることが分かるが、軌道の振舞いに関して、それ以上のことに言及することは難しい．以下では、局所リャプノフ指数によって誘導現象を調べ，軌道の振舞いについてより詳細な情報を得る．

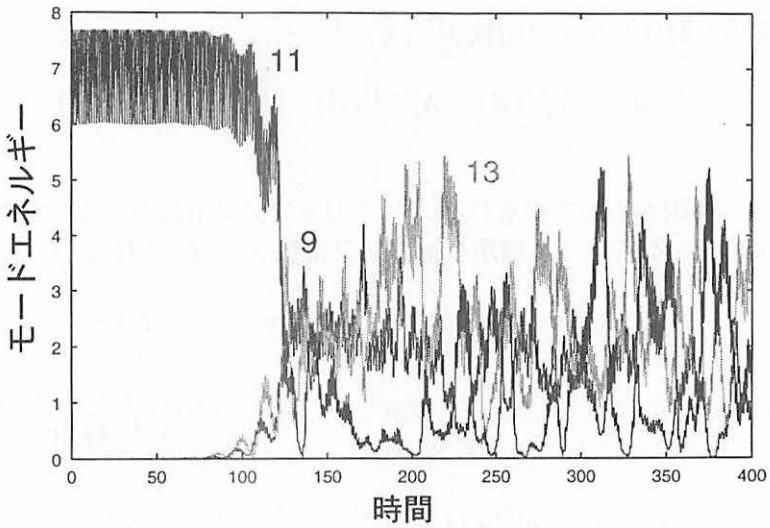

Fig.1 Plots of mode energies E_9, E_{11} and E_{13} versus time for the FPU model with $N = 15$.

3 局所リャプノフ指数

3.1 定義

$z_t \in \mathbf{R}^{2N}$ を N 自由度ハミルトニアン $H(z)$ の正準方程式の解とする．i.e.,

$$\frac{d}{dt}z_t = J\frac{\partial H}{\partial z}(z_t), \qquad J = \begin{pmatrix} 0 & Id \\ -Id & 0 \end{pmatrix} \tag{3}$$

局所リャプノフ指数の定義の準備として、相空間の点 $\boldsymbol{Z} \in \mathbf{R}^{2N}$ における**有限時間 (τ 時間) 平均リャプノフ指数** $\lambda_\tau^{(k)}(\boldsymbol{Z})$ $(k = 1, \cdots, 2N)$ を以下のようにして定義する [1, 2]：

(i) $\delta \boldsymbol{z}_{-\infty}^{(1)}, \cdots, \delta \boldsymbol{z}_{-\infty}^{(2N)} \in \mathbf{R}^{2N}$ を、接空間を張る $2N$ 個の一次独立なベクトルとし、正準方程式の変分方程式

$$\frac{d}{dt}\delta z_t = L(z_t)\delta z_t, \qquad L(z_t) = J\frac{\partial^2 H}{\partial z \partial z}(z_t) \tag{4}$$

のもとで時間発展させる. i.e.,

$$\delta z_0^{(k)} = \exp\left[\int_{-\infty}^{0} L(z_s)\,ds\right] \delta z_{-\infty}^{(k)} \tag{5}$$

ここで z_t は正準方程式の解で $z_0 = Z$ を満たすとする.

(ii) $\delta z_t^{(1)}, \cdots, \delta z_t^{(k)}$ を辺とする平行体の体積を $V_t^{(k)}$ とおき、時刻 $t=0$ における（すなわち点 Z における）$V_t^{(k)}$ の τ 時間平均指数的拡大率を $\Lambda_\tau^{(k)}(Z)$ とおく. i.e.,

$$V_t^{(k)} = \| \wedge_{i=1}^{k} \delta z_t^{(i)} \| \qquad (k = 1, \cdots, 2N) \tag{6}$$

$$\Lambda_\tau^{(k)}(Z) = \frac{1}{\tau} \ln \frac{V_\tau^{(k)}}{V_0^{(k)}} \qquad (k = 1, \cdots, 2N) \tag{7}$$

点 Z における τ 時間平均リャプノフ指数 $\lambda_\tau^{(k)}(Z)$ は、次式で定義される：

$$\lambda_\tau^{(k)}(Z) = \Lambda_\tau^{(k)}(Z) - \Lambda_\tau^{(k-1)}(Z) \qquad (k = 1, \cdots, 2N) \tag{8}$$

ただし $\Lambda_\tau^{(0)} = 0$ とおく.

平均時間 $\tau \to \infty$ の極限をとって得られる $\lambda_\infty^{(k)}$ が**リャプノフ指数**である. 一方、平均時間 $\tau \to 0$ の極限をとったものを点 Z における**局所リャプノフ指数** $\lambda_0^{(k)}(Z)$ と呼ぶ [7]. i.e.,

$$\lambda_0^{(k)}(Z) = \lim_{\tau \to 0} \lambda_\tau^{(k)}(Z) \qquad (k = 1, \cdots, 2N) \tag{9}$$

$\left\{\delta z_t^{(k)}\right\}_{k=1}^{2N}$ を Gram-Schmidt 法により正規直交化したものを $\left\{e_t^{(k)}\right\}_{k=1}^{2N}$ とおくと†、局所リャプノフ指数は次のように書くことができる [7, 8]：

$$\lambda_0^{(k)}(Z) = e_0^{(k)} \cdot L(Z)\, e_0^{(k)} \qquad (k = 1, \cdots, 2N) \tag{10}$$

3.2 局所リャプノフ指数の性質

(a) $\lambda_0^{(k)}(z_t)$ を長時間平均したものは、リャプノフ指数に一致する. i.e.,

$$\lambda_\infty^{(k)} = \lim_{\tau \to \infty} \frac{1}{\tau} \int_0^\tau \lambda_0^{(k)}(z_s)\,ds \qquad (k = 1, \cdots, 2N) \tag{11}$$

(b) N 自由度ハミルトン系では、

$$e_t^{(2N-k+1)} = J e_t^{(k)} \quad (k = 1, \cdots, N) \tag{12}$$

が成り立ち、その結果として、

$$\lambda_0^{(k)}(z_t) = -\lambda_0^{(2N-k+1)}(z_t) \quad (k = 1, \cdots, N) \tag{13}$$

が成り立つ.

---

† ベクトル $e_0^{(1)}$ の向きは点 Z における接空間の最大拡大方向に一致するが、$e_0^{(k)}$ $(k \neq 1)$ は必ずしも拡大方向あるいは縮小方向とは一致しない.

(c) 周期 T の不安定周期軌道の場合
z_{t_0} におけるモノドロミー行列

$$M = \exp\left[\int_{t_0}^{t_0+T} L(z_s)\,ds\right] \tag{14}$$

の固有値を $\chi_1 \geq \cdots \geq \chi_{2N}$ とし、対応する固有ベクトルを $\boldsymbol{v}_1, \cdots, \boldsymbol{v}_{2N}$ とすると、

$$\chi_k = \exp\left[\int_0^T \lambda_0^{(k)}(z_s)\,ds\right] \tag{15}$$

が成り立ち、$\{\boldsymbol{v}_k\}_{k=1}^{2N}$ を正規直交化したものは $\left\{e_{t_0}^{(k)}\right\}_{k=1}^{2N}$ に等しい.

4 N 自由度 FPU モデルに対する結果

4.1 $N = 2$ の場合

図 2 (a)(b) は、2 自由度 FPU モデル ($\alpha = 1, \beta = 0, E = 0.65$) のカオス軌道について求めた $\lambda_0^{(1)}(z_t)$ と $\lambda_0^{(2)}(z_t)$ の時間変化である[§]. 局所リャプノフ指数と相空間構造との対応を見る場合は、時系列そのものではなく、その積分値

$$I_k(t) = \int_0^t \lambda_0^{(k)}(z_s)\,ds \tag{16}$$

を調べるのが適している. $I_k(t)$ グラフの傾きは、リャプノフ指数に相当する. カオス軌道に対する I_1 と I_2 の時系列を図 3 に示す. ハミルトン系では一般に $\lambda_\infty^{(N)} = \lambda_\infty^{(N+1)} = 0$ が成り立つが [9]、この性質によって $I_2 \approx 0$ が成り立っている. 一方、I_1 の振舞いは、軌道がトーラスに間欠的に捕らえられることを反映して、傾きの変化が見られる. 図 3 において I_1 の傾きが一定と見なされる時間区間 (a)-(d) について、同一軌道のポアンカレ断面をとったものが図 4 (a)-(d) である. 軌道がトーラスに捕らえられる時間区間（図 4 (a)(c)）では、I_1 の傾きは極めて小さく、軌道がエルゴード的に振舞う時間区間（図 4 (b)(d)）では、I_1 の傾きは大きくなる. 図 4 (b) と図 4 (d) のカオス領域は同一なので、時間区間 (b) と (d) での I_1 の傾きは等しくなる.

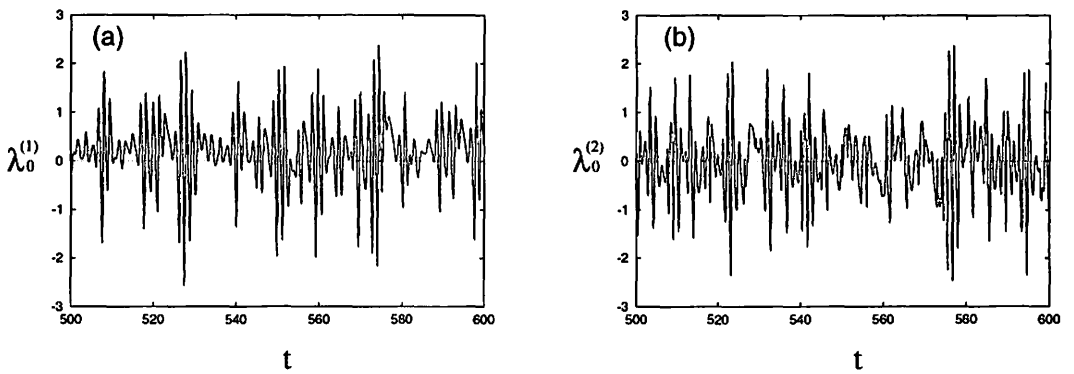

Fig.2 Plots of the local Lyapunov exponent $\lambda_0^{(k)}(z_t)$ versus time for a chaotic trajectory of the FPU model with $N = 2$. (a) $k = 1$, (b) $k = 2$.

[§]スペクトルの対称性（式 (13)）より、$\lambda_0^{(4)}(z_t) = -\lambda_0^{(1)}(z_t)$、$\lambda_0^{(3)}(z_t) = -\lambda_0^{(2)}(z_t)$ が成り立つ.

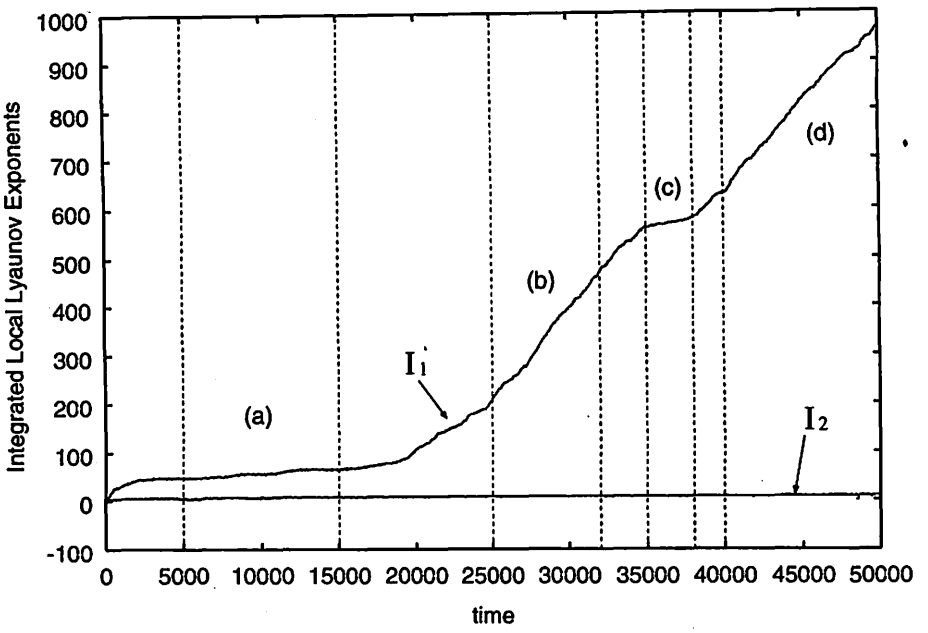

Fig.3 Cumulative functions of the local Lyapunov exponents $\lambda_0^{(1)}(z_t)$ *and* $\lambda_0^{(2)}(z_t)$ *for a chaotic trajectory of the FPU model with* $N = 2$.

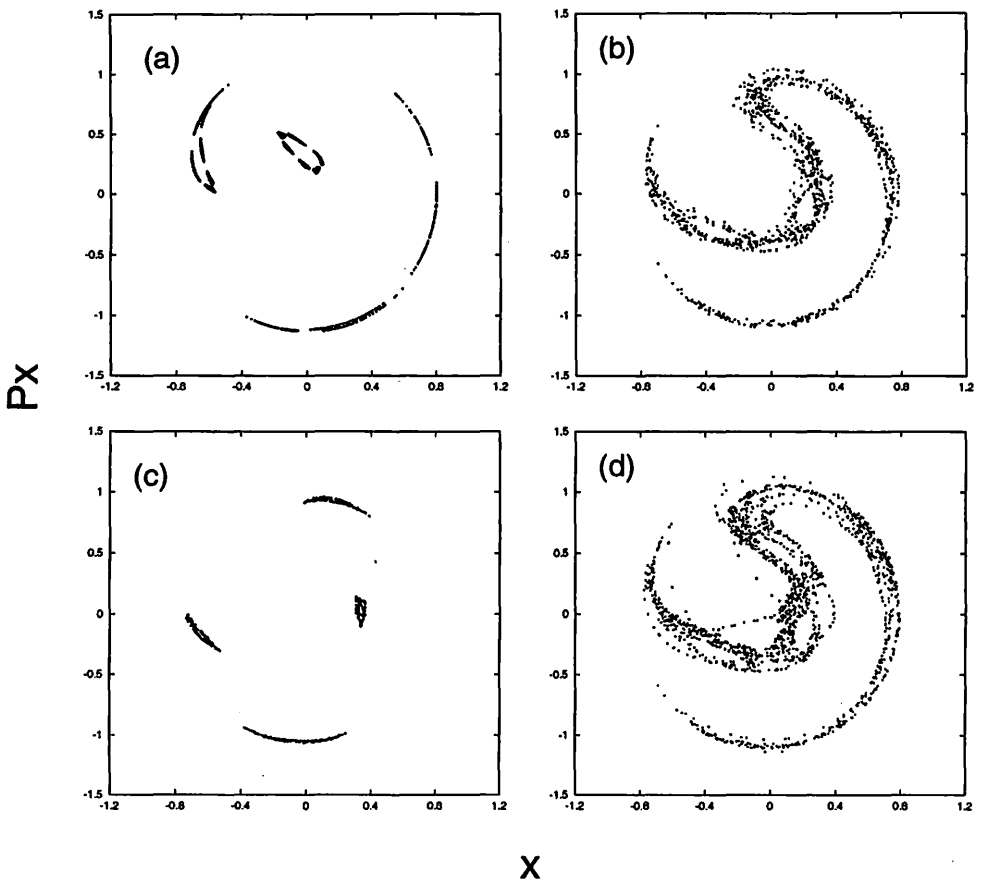

Fig.4 Poincaré sections($y = 0, P_y \geq 0$) *for the time intervals (a)-(d) indicated in Fig.3.*

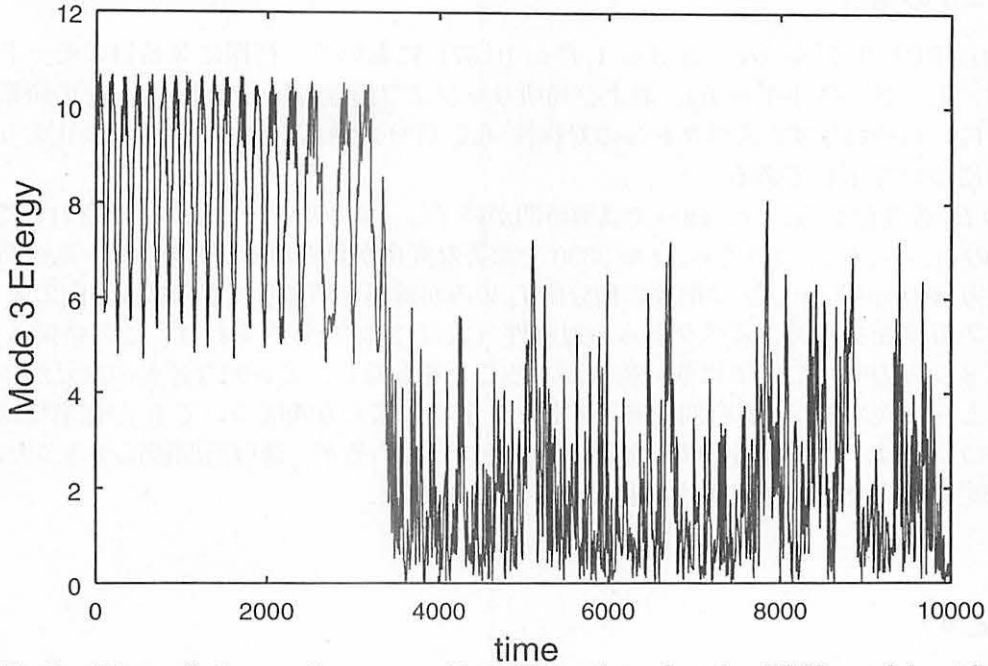

Fig.5 Plots of the mode energy E_3 versus time for the FPU model with $N = 5$.

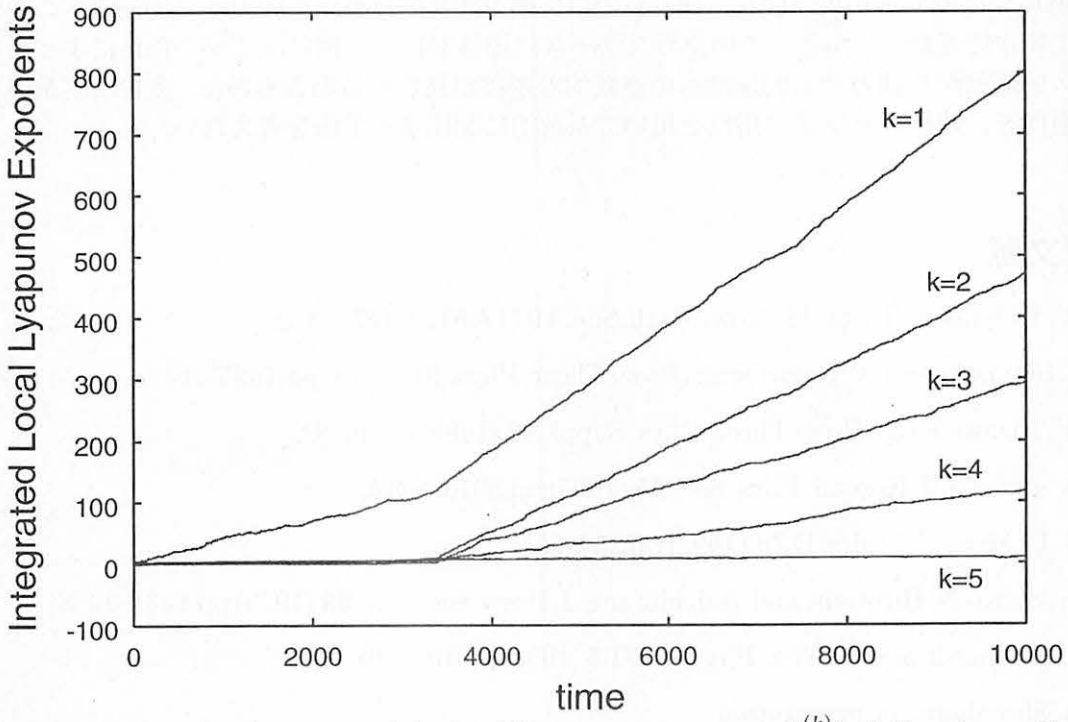

Fig.6 Cumulative functions of the local Lyapunov exponents $\lambda_0^{(k)}(z_t)$ $(k = 1, \cdots, 5)$ for the same trajectory as in Fig.5.

4.2 N=5 の場合

5 自由度 FPU モデル（$\alpha = 0, \beta = 1, E \approx 10.67$）において、初期に 3 番目のモードを励起した場合の、モードエネルギー E_3、および局所リャプノフ指数の積分値 $I_1, \cdots, I_5$ の時系列を、図 5 と図 6 にそれぞれ示す. スペクトルの対称性（式（13））があるため、図 6 では正のリャプノフ指数のみについて示してある.

図 5 の E_3 の変化から、$t \approx 3300$ で誘導時間が終了し、エネルギー分配が開始されることが分かる. 図 6 の $I_1, \cdots, I_5$ についても、$t \approx 3300$ で顕著な変化が見られる. すなわち、誘導時間の間は最大拡大方向の局所リャプノフ指数の積分値 I_1 のみが線形に増加し、他の拡大方向の値 $I_2, \cdots, I_5$ は、ゼロの近傍を揺らぐ. スペクトルの対称性（式（13））を考慮すれば、この結果は、10 次元接空間の 8 つの方向については強い拘束があることを意味し、実質的な運動の次元が $10 - 8 = 2$ であることを示唆する. 誘導時間が終了すると、全ての拡大方向について I_k が線形に増加し始める. I_1 については、誘導時間の間も有限の傾きを持っているが、誘導時間後は傾きが大きくなり、より不安定性の大きな領域に軌道が移ったことが分かる.

5 まとめ

2 自由度および 5 自由度の FPU モデルについて、局所リャプノフ指数の振舞いを調べた. 2 自由度系の結果から、軌道がトーラスに捕らえられている場合とエルゴード的に振舞う場合で、局所リャプノフ指数の積分値に明確な違いが現れることが分かった. また、5 自由度系の結果では、高次元のトーラスに捕らえられている軌道が、強カオス領域に移る際の、実質的な運動の次元の変化を捉えることが出来た.

誘導現象に関する結果（図 5、図 6）では、弱カオス的運動から強カオス的運動への遷移点は明確に特定できた. しかし、このようなケースは遷移過程の一例にすぎず、条件によっては、弱カオス的運動から強カオス的運動への連続的な遷移が見られる場合もある. 多自由度系の多様な緩和過程を、局所リャプノフ指数を用いて系統的に記述する手法を考えたい.

参考文献

[1] V. I. Oseldec, Trans. Moscow. Math. Soc. **19** (1968) pp.197–231.

[2] I. Shimada and T. Nagashima, Prog. Theor. Phys. **61** (1979) pp.1605–1616.

[3] Y. Aizawa et al, Prog. Theor. Phys. Suppl. **98** (1989) pp.36–82.

[4] Y. Aizawa, J. Korean. Phys. Soc. **95** (1995) pp.S310–S314.

[5] J. D. Meiss, Physica D **74** (1994) pp.254–267.

[6] N. Saito, N. Hirotomi and A. Ichimura, J. Phys. Soc. Jpn. **39** (1975) pp.1431–1438.

[7] B. Eckhardt and D. Yao, Physica D **65** (1993) pp.100–108.

[8] S. Shinohara, *in preparation.*

[9] A. J. Lichtenberg and M. A. Lieberman, *Regular and Chaotic Dyanamics* (1992) Springer.

A note on some special N-body Systems *

Masayoshi SEKIGUCHI

Kisarazu National College of Technology
Kiyomidai-higashi 2-11-1, Kisarazu
Chiba 292-0041, JAPAN
E-mail: masa@yana.kisarazu.ac.jp

Abstract

We are here concerned with a classification of special N-body systems, especially with the case of low degree of freedom. We describe the synthetic way of a new special problem of N bodies. It is important to study *Sub-homothetic Class* which we name.

1 Introduction

There are a lot of special cases of N-body gravitational systems with low degree of freedom. Other than a huge number of studies on the restricted three-body problem, for instance, studied were the Sitnikov Problem[1], the collinear three-body problem (C3BP for short) [2][7][8][9][13][17][20][21], the planar isosceles three-body problem (I3BP) [4][6][14], the symmetric collinear four-body problem (SC4BP) [5][19][23], and so on [3][5][10][11][12][15][16][18][22]. However, very few attempts have been made at a classification of such systems according to the phase flow.

Generally, gravitational systems are classified according to the number of bodies N. In other words, N is an index of the classification. Usually, a difference in degree of freedom provides some differences in the phase flow even if N is equal. On the other hand, there is a case where the phase flow resemble even if N is different. For instance, let us consider two trivial problems: the collinear two-body problem and the symmetric collinear three-body problem. These two systems consist of different number of bodies N although their phase flow are equivalent to each other except for the difference of time scale. Here is another example in the non-trivial cases: C3BP and SC4BP. There are some similar features pointed out by [23] (or see [2][5]). They are both two degree of freedom system in spite of the difference of the number of bodies N. It is necessary to introduce the degree of freedom f as an additional index of classification. We give a name (N, f)-*system* to the system of N bodies and f degree of freedom.

Here, we begin to discuss the case with low degree of freedom because it is too huge to study the gravitational systems in general. We introduce new terminology "Few Degree of Freedom System" (*FDFS* for short) as a gravitational system whose degree of freedom is 2 or 3. Our first purpose is to make a list of FDFS. On the way, we find the importance of a special class of gravitational systems: *Sub-homothetic class* whose systems consist of a combiantion of some homothetic systems.

Our next purpose is to compare some (N, f)-systems. We intend to study this subject in the near future. There are some FDFSs for a common fixed pair of indices (N, f). The example is the case: C3BP and I3BP. In C3BP, a homothetic solution of collinear case is realizable, while the collinear case and the equilateral case are possibleble in I3BP. Their phase flow are different from each other even though their indices (N, f) are same.

We assert that the other index is required to classify the gravitational systems. The index is related to the total collision manifold, the critical points on the manifold, and their stabilities. However, further studies are required to clarify how many indices are necessary for the classification,

*This research is partially funded by the National Astronomical Observatory of JAPAN.

what the most suitable index is, and whether such indices exist or not that identify a certain given gravitational system a priori.

In the present paper, we omit the case where some of bodies are massless.

2 Syntheses of Special Systems

We divide the general N-body systems into three cases according to the dimension of their configuration space. Here, symmetries are considered in each cases as well as the degree of freedom decreases. In each cases, some special systems are composed from other systems. We summarize the case of $f = 2$ except for trivial cases.

2.1 Collinear Systems

Generally, N bodies of masses $m_i, (i = 1, 2, \cdots, N)$ move on the fixed common line under the gravitational force. The degree of freedom f is $N - 1$ because the gravity center can be fixed on the origin.

Considering the symmetry of masses with respect to the gravity center, we have the symmetric collinear systems. Their degrees of freedom are reduced again. Therefore, we have

$$f = \left[\frac{N}{2}\right]. \tag{1}$$

2.2 Planar Systems

Generally, N bodies of masses $m_i, (i = 1, 2, \cdots, N)$ move on the fixed common plane. The degree of freedom f is $2N - 2$ because the gravity center can be fixed on the origin.

2.2.1 In the case with one symmetry

Let us consider one symmetry with respect to a certain line on the plane. We can let the line to be the x axis without loss of generality. Either masses and y coordinates are symmetry with respect to the x axis. Let the set of all bodies be $M = \{(m_i, x_i, y_i) \mid i = 1, 2, \cdots, N\}$. The set M can be divided into three subsets, i.e.,

$$M = M_+ \cup M_0 \cup M_-,$$

where

$$M_+ = \{(m_i, x_i, y_i) \mid y_i > 0\}, \quad M_0 = \{(m_i, x_i, y_i) \mid y_i = 0\}, \quad M_- = \{(m_i, x_i, y_i) \mid y_i < 0\}.$$

Let N_+ (resp. N_0, N_-) be the number of M_+ (resp. N_0 N_-). Let f_+ (resp. f_0, f_-) be the degree of freedom of M_+ (resp. f_0 f_-). Then, we have $N_0 \geq 0$, $N_+ = N_- > 0$, and

$$N = N_+ + N_0 + N_-,$$

while the degree of freedom is not additive.

Immediately, we have

$$f_+ = 2N_+, \quad f_0 = N_0, \quad f_- = 2N_-.$$

Therefore,

$$f = f_+ + f_0 - 1 = N - 1, \tag{2}$$

because the gravity center can be fixed on the origin.

2.2.2 In the case with two symmetries

Let us consider one another symmetry with respect to the y axis. Either masses and x (resp. y) coordinates are symmetry with respect to the y (resp. x) axis. The set M can be divided into the following nine subsets, i.e.,

$$M = M_1 \cup M_2 \cup M_3 \cup M_4 \cup M_{12} \cup M_{23} \cup M_{34} \cup M_{41} \cup M_0,$$

where

$$M_1 = \{(m_i, x_i, y_i) \mid x_i > 0, y_i > 0\}, \quad M_2 = \{(m_i, x_i, y_i) \mid x_i < 0, y_i > 0\},$$
$$M_3 = \{(m_i, x_i, y_i) \mid x_i < 0, y_i < 0\}, \quad M_4 = \{(m_i, x_i, y_i) \mid x_i > 0, y_i < 0\},$$
$$M_{12} = \{(m_i, x_i, y_i) \mid x_i = 0, y_i > 0\}, \quad M_{23} = \{(m_i, x_i, y_i) \mid x_i < 0, y_i = 0\},$$
$$M_{34} = \{(m_i, x_i, y_i) \mid x_i = 0, y_i < 0\}, \quad M_{41} = \{(m_i, x_i, y_i) \mid x_i > 0, y_i = 0\},$$
$$M_0 = \{(m_i, x_N, y_N) \mid x_N = 0, y_N = 0\}.$$

Let N_ξ denote the number of M_ξ and f_ξ be the degree of freedom, $(\xi = 1, 2, 3, 4, 12, 23, 34, 41)$. Then, we have

$$N_1 = N_2 = N_3 = N_4, \quad N_{12} = N_{34}, \quad N_{23} = N_{41},$$
$$N = N_1 + N_2 + N_3 + N_4 + N_{12} + N_{23} + N_{34} + N_{41} + N_0 = 4N_1 + 2N_{12} + 2N_{23} + N_0.$$

Naturally, $N_0 = 0$ iff N is even. Immediately, we have

$$f_i = 2N_i, (i = 1, 2, 3, 4),$$
$$f_i = N_i, (i = 12, 23, 34, 41),$$
$$f_0 = 0.$$

Therefore, we have

$$f = f_1 + f_{12} + f_{23} = 2N_1 + N_{12} + N_{23} = \left[\frac{N}{2}\right]. \tag{3}$$

2.2.3 In the case of the axis symmetry

The N bodies are divided into $[N/2]$ pairs. Each of pairs $(m_i, x_i, y_i) - (m_j, x_j, y_j)$ are symmetric with respect to the origin. Namely,

$$m_i = m_j, \quad x_i = -x_j, \quad y_i = -y_j. \tag{4}$$

Then, the degree of freedom is as follows.

$$f = 2\left[\frac{N}{2}\right].$$

2.2.4 Some special cases

In the case mentioned above, we assume that $N_1 = N_2 = N_3 = N_4 = 0$. Additionally, if homogeneity is required for the remaining bodies $M_{12} \cup M_{23} \cup M_{34} \cup M_{41} \cup M_0$, namely, $N_{12} = N_{23} = N_{34} = N_{41}$ are synchronously moving, the degree of freedom is reduced again. In fact,

$$N = N_{12} + N_{23} + N_{34} + N_{41} + N_0 = 4N_{12} + N_0,$$
$$f = f_{12} = N_{12} = \frac{N}{4}. \tag{5}$$

The schematic explanation for $(N, f) = (8, 2)$ is given in Fig.1-I. We can regard this system as a superposition of squares.

Similarly we obtain a system of a superposition of triangles (Fig.1-II), and a system of a superposition of hexagons (Fig.1-III).

Therefore, we have a sequence of systems which consist of a superposition of n regular polygons. They are n degree of freedom system.

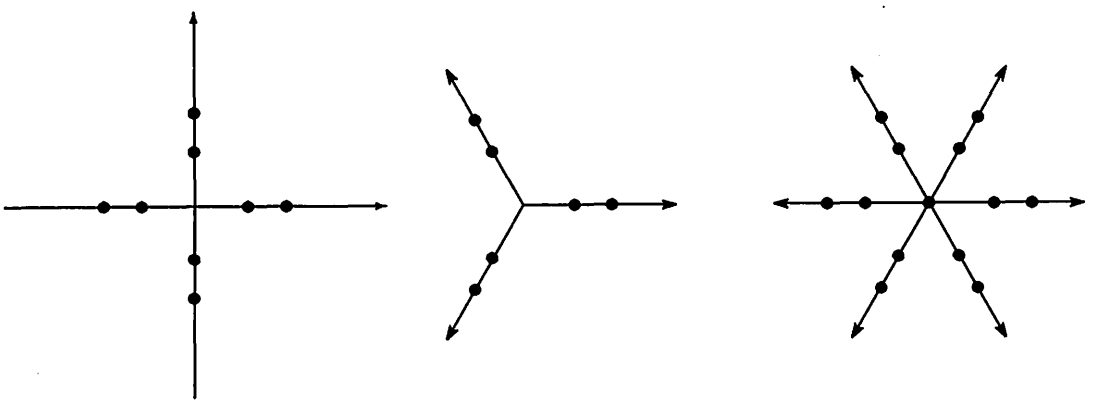

Figure 1: Schematic Explanation of the special case I(left), II(center), III(right).

2.3 Spatial Systems

Generally, the degree of freedom f is $3N-3$ because the gravity center can be fixed on the origin.

2.3.1 In the case with one symmetry

Let us consider one symmetry with respect to a certain plane. We can let the plane to be the xy plane without loss of generality. Either masses and z coordinates are symmetry with respect to the xy plane. Let the set of all bodies be $M = \{(m_i, x_i, y_i, z_i) \mid i = 1, 2, \cdots, N\}$. The set M can be divided into three subsets, i.e.,

$$M = M_+ \cup M_0 \cup M_-,$$

where

$$M_+ = \{(m_i, x_i, y_i, z_i) \mid z_i > 0\}, \quad M_0 = \{(m_i, x_i, y_i, z_i) \mid z_i = 0\}, \quad M_- = \{(m_i, x_i, y_i, z_i) \mid z_i < 0\}.$$

Let N_+ (resp. N_0, N_-) be the number of M_+ (resp. N_0 N_-). Let f_+ (resp. f_0, f_-) be the degree of freedom of M_+ (resp. f_0 f_-). Then, we have $N_0 \geq 0$, $N_+ = N_- > 0$, and

$$N = N_+ + N_0 + N_-,$$

while the degree of freedom is not additive.

Immediately, we have

$$f_+ = 3N_+, \quad f_0 = 2N_0, \quad f_- = 3N_-.$$

Therefore,

$$f = f_+ + f_0 - 2 = 3N_+ + 2N_0 - 2 = 2N - N_+ - 2, \tag{6}$$

because the gravity center can be fixed on the origin.

2.3.2 In the case with two symmetries

Let us consider one another symmetry with respect to the yz plane. Either masses and x (resp. z) coordinates are symmetry with respect to the yz (resp. xy) plane. The set M can be divided into the following nine subsets, i.e.,

$$M = M_1 \cup M_2 \cup M_3 \cup M_4 \cup M_{12} \cup M_{23} \cup M_{34} \cup M_{41} \cup M_0,$$

where

$$M_1 = \{(m_i, x_i, y_i, z_i) \mid x_i > 0, z_i > 0\}, \quad M_2 = \{(m_i, x_i, y_i, z_i) \mid x_i < 0, z_i > 0\},$$

$$M_3 = \{(m_i, x_i, y_i, z_i) \mid x_i < 0, z_i < 0\}, \quad M_4 = \{(m_i, x_i, y_i, z_i) \mid x_i > 0, z_i < 0\},$$

$$M_{12} = \{(m_i, x_i, y_i, z_i) \mid x_i = 0, z_i > 0\}, \quad M_{23} = \{(m_i, x_i, y_i, z_i) \mid x_i < 0, z_i = 0\},$$

$$M_{34} = \{(m_i, x_i, y_i, z_i) \mid x_i = 0, z_i < 0\}, \quad M_{41} = \{(m_i, x_i, y_i, z_i) \mid x_i > 0, z_i = 0\},$$

$$M_0 = \{(m_i, x_N, y_N, z_N) \mid x_N = 0, z_N = 0\}.$$

Let N_ξ denote the number of M_ξ and f_ξ be the degree of freedom, $(\xi = 1, 2, 3, 4, 12, 23, 34, 41)$. Then, we have

$$N_1 = N_2 = N_3 = N_4, \quad N_{12} = N_{34}, \quad N_{23} = N_{41},$$

$$N = N_1 + N_2 + N_3 + N_4 + N_{12} + N_{23} + N_{34} + N_{41} + N_0 = 4N_1 + 2N_{12} + 2N_{23} + N_0.$$

Naturally, N_0 is odd iff N is odd. Immediately, we have

$$f_i = 3N_i, (i = 1, 2, 3, 4),$$

$$f_i = 2N_i, (i = 12, 23, 34, 41),$$

$$f_0 = N_0.$$

Therefore,

$$f = f_1 + f_{12} + f_{23} + f_0 - 1 = 3N_1 + 2N_{12} + 2N_{23} + N_0 - 1 = N - N_1 - 1. \tag{7}$$

because the gravity center can be fixed on the origin.

2.3.3 In the case with three symmetries

Let us add one another symmetry with respect to the zx plane. Either masses and x (resp. y, z) coordinates are symmetry with respect to the yz (resp. zx, xy) plane. The set M can be divided into the following 27 subsets, i.e.,

$$M = \bigcup_{i=0}^{8} M_i \bigcup_{\xi \in \Xi} M_\xi \bigcup_{\eta \in H} M_\eta$$

where $\Xi = \{12, 15, 23, 26, 34, 37, 41, 48, 56, 67, 78, 85\}$, $H = \{1234, 1265, 1485, 2376, 3487, 5678\}$, and $M_0 = \{(m_i, x_N, y_N, z_N) \mid x_N = 0, y_N = 0, z_N = 0\}$,

$$M_1 = \{(m_i, x_i, y_i, z_i) \mid x_i > 0, y_i > 0, z_i > 0\}, \quad M_2 = \{(m_i, x_i, y_i, z_i) \mid x_i < 0, y_i > 0, z_i > 0\},$$

$$M_3 = \{(m_i, x_i, y_i, z_i) \mid x_i < 0, y_i < 0, z_i > 0\}, \quad M_4 = \{(m_i, x_i, y_i, z_i) \mid x_i > 0, y_i < 0, z_i > 0\},$$

$$M_5 = \{(m_i, x_i, y_i, z_i) \mid x_i < 0, y_i < 0, z_i < 0\}, \quad M_6 = \{(m_i, x_i, y_i, z_i) \mid x_i > 0, y_i < 0, z_i < 0\},$$

$$M_7 = \{(m_i, x_i, y_i, z_i) \mid x_i < 0, y_i < 0, z_i < 0\}, \quad M_8 = \{(m_i, x_i, y_i, z_i) \mid x_i > 0, z_i < 0, z_i < 0\}.$$

In addition, M_{ij} is a 2-dimensional region between M_i and M_j. M_{ijkl} is a 1-dimensional region between M_{ij} and M_{kl}. Let N_ζ denote the number of M_ζ and f_ζ be the degree of freedom, $(\zeta = 0, 2, \cdots, 8, \xi \in \Xi, \eta \in H)$. Then, we have

$$N_1 = N_2 = N_3 = N_4, \quad N_{12} = N_{34}, \quad N_{23} = N_{41},$$

$$N = \sum_{i=0}^{8} N_i + \sum_{\xi \in \Xi} N_\xi + \sum_{\eta \in H} N_\eta = N_0 + 8N_1 + 4(N_{12} + N_{56} + N_{15}) + 2(N_{1234} + N_{1265} + N_{1485}).$$

Naturally, N_0 is odd iff N is odd. Immediately, we have

$$f_i = 3N_i, (i = 1, 2, \cdots, 8),$$

$$f_\xi = 2N_\xi, (\xi \in \Xi),$$

$$f_\eta = N_\eta, (\eta \in H)$$

$$f_0 = N_0.$$

Therefore, we have

$$f = f_1 + f_{12} + f_{56} + f_{15} + f_{1234} + f_{1265} + f_{1485} + f_0$$

$$= 3N_1 + 2(N_{12} + N_{56} + N_{15}) + N_{1234} + N_{1265} + N_{1485} + N_0$$

$$= \left[\frac{N - N_0}{2}\right] - N_1 + N_0. \tag{8}$$

2.3.4 In the case of the axis symmetry

The N bodies are divided into N_1 pairs and N_0 indivisuals moving on the z axis, i.e., $N = 2N_1 + N_0$. Each of pairs $(m_i, x_i, y_i) - (m_j, x_j, y_j)$ are symmetric with respect to the z axis. Namely,

$$m_i = m_j, \quad x_i = -x_j, \quad y_i = -y_j.$$

Then, the degree of freedom is as follows.

$$f = 3N_1 + N_0 - 1 = N + N_1 - 1. \tag{9}$$

because the gravity center can be fixed on the origin.

2.3.5 Under stronger restriction

The degree of freedom in the homothetic solution is 1 or 2. If a system consists of two non-rotational homothetic systems, then the degree of freedom is just 2. We show two examples.

1. Non-rotational regular N polygon system is of 1 degree of freedom. Symmetric collinear system of two or three bodies is also of 1 degree of freedom. If we combine them perpendicularly at their gravity centers, we have a new two degree of freedom system.

2. If we combine two non-rotational regular N polygon systems symmetrically with respect to the xy-plane, we have a new two degree of freedom system.

We call such system *Sub-Homothetic Systems.*

3 Results

Here we limit ourselves to the case for $3 \leq N \leq 9$, $f = 2$. We obtain 31 FDFS in this case. We show their mass distribution and coordinates as follows.

N	Masses and Coordinates	Name	#Mass Parameters
3	$(m_i; x_i), i = 1,2,3$	C3BP	2
	$(m_1; \pm x_1, y_1), (m_2; 0, -2m_1y_1/m_2)$	I3BP	1
4	$(m_1; \pm x_1), (m_2; \pm x_2)$	SC4BP	1
	$(m; \pm x, \pm y)$	Rectangular 4BP	0
	$(m_1; \pm x_1, 0), (m_2; 0, \pm y_2)$	Rhomboidal 4BP	1
	$(m_1; 0, 0, z_1), (m_2; x_2, y_2, -m_1z_1/(3m_2))$	(None)	1
	(x_2, y_2) are vertices of regular triangle		
5	$(m_1; 0), (m_2; \pm x_2), (m_3; \pm x_3)$	SC5BP	2
	$(m_1; 0, 0), (m_2; \pm x_2, \pm y_2)$	(None)	1
	$(m_1; 0, 0), (m_2; \pm x_2, 0), (m_3; 0, \pm y_3)$	(None)	2
	$(m_1; 0, 0, z_1), (m_2; x_2, y_2, -m_1z_1/(4m_2))$	(None)	1
	(x_2, y_2) are vertices of regular quadrangle		
	$(m_1; 0, 0, \pm z_1), (m_2; x_2, y_2, 0)$	(None)	1
	(x_2, y_2) are vertices of regular triangle		
Even $N \geq 6$			
	$(m_i; x_i, y_i), i = 1,2$	(None, see Fig.1-II)	1
	(x_i, y_i) are vertices of regular $N/2$ polygon		
	$(m; x, y, \pm z)$	(None)	0
	(x, y) are vertices of regular $N/2$ polygon		
	$(m_1; 0, 0, z_1), (m_2; x_2, y_2, -m_1z_1/((N-1)m_2))$	(None)	1
	(x_2, y_2) are vertices of regular $(N-1)$-gon		
	$(m_1; 0, 0, \pm z_1), (m_2; x_2, y_2, 0)$	(None)	1
	(x_2, y_2) are vertices of regular $(N-2)$-gon		
	$(m_1; 0, 0, 0), (m_2; 0, 0, \pm z_2), (m_3; x_3, y_3, 0)$	(None)	2
	(x_2, y_2) are vertices of regular $(N-3)$-gon		
Odd $N \geq 7$			
	$(m_1, 0, 0), (m_i; x_i, y_i), i = 2,3$	(None, see Fig.1-III)	2
	(x_i, y_i) are vertices of regular $(N-1)/2$ polygon		
	$(m_1; 0, 0, 0), (m_2; x_2, y_2, \pm z_2)$	(None)	1
	(x_2, y_2) are vertices of regular $(N-1)/2$ polygon		
	$(m_1; 0, 0, z_1), (m_2; x_2, y_2, -m_1z_1/((N-1)m_2))$	(None)	1
	(x_2, y_2) are vertices of regular $(N-1)$-gon		
	$(m_1; 0, 0, \pm z_1), (m_2; x_2, y_2, 0)$	(None)	1
	(x_2, y_2) are vertices of regular $(N-2)$-gon		
	$(m_1; 0, 0, 0), (m_2; 0, 0, \pm z_2), (m_3; x_3, y_3, 0)$	(None)	2
	(x_2, y_2) are vertices of regular $(N-3)$-gon		

Table 1. A list of FDFS for $N \geq 3, f = 2$

References

[1] Moser,J.: 1973, 'Stable and Random Motions in Dynamical Systems', *Annals of Mathematics Studies*, **77**, Princeton University Press.

[2] McGehee,R.: 1974, 'Triple collision in the collinear three-body problem', *Inventiones Mathematicae*, **27**, pp.191-227.

[3] Mather,J. and McGehee,R.: 1975, 'Solutions of the collinear four-body problem which become unbounded in finite time', *Dynamical systems theory and its applications*, pp.573-597, Lecture notes in physics, Springer-Verlag.

[4] Devaney,R.L.: 1980, 'Triple collision in the planar isosceles three-body problem', *Inventiones Mathematicae*, **60**, pp.249-267.

[5] Simó,C. and Lacomba,E.: 1982, 'Analysis of some degenerate quadruple collisions', *Celes. Mech.*, **28**, pp.49-62.

[6] Simó,C. and Martinez,R.: 1988, 'Qualitative study of the planar isosceles problem', *Celes. Mech.*, **41**, pp.179-251.

[7] Mikkola,S. and Hietarinta,J.: 1989, 'A Numerical investigation of the one-dimensional Newtonian three-body problem', *Celes. Mech.*, **46**, pp.1-18.

[8] Mikkola,S. and Hietarinta,J.: 1990, 'A Numerical investigation of the one-dimensional Newtonian three-body problem II', *Celes. Mech.*, **47**, pp.321-331.

[9] Mikkola,S. and Hietarinta,J.: 1991, 'A Numerical investigation of the one-dimensional Newtonian three-body problem III', *Celes. Mech.*, **51**, pp.379-394.

[10] Xia,Z.: 1992, 'The existence of noncollision singularities in newtonian systems'. *Ann. Math.*, **135**, pp.411-468.

[11] Lacomba,E.A. and Pérez-Chavela,E.: 1992, 'A Compact Model For the Rhomboidal 4-Body Problem', *Celes. Mech. Dyn. Astr.*, **54**, pp.343-355.

[12] Lacomba,E.A. and Pérez-Chavela,E.: 1993, 'Motions Close to Escapes in the Rhomboidal Four Body Problem', *Celes. Mech. Dyn. Astr.*, **57**, pp.411-437.

[13] Hietarinta,J. and Mikkola,S.: 1993, 'Chaos in the one-dimensional gravitational three-body problem', *CHAOS*, **3**, pp.183-203.

[14] Zare,K. and Chesley,S.: 1998, 'Order and chaos in the planar isoceles three-body problem', *CHAOS*, **8**, pp.475-494.

[15] Steves,B.A. and Roy,A.E.: 1998, 'Some special restricted four-body problems — I. Modeling the Caledonian problem', *Planet. Space Sci.*, **46**(11/12), pp.1465-1474.

[16] Roy,A.E. and Steves,B.A.: 1998, 'Some special restricted four-body problems — II. From Caledonia to Copenhagen', *Planet. Space Sci.*, **46**(11/12), pp.1475-1486.

[17] Kaplan,S.R.: 1999, 'Symbolic Dynamics of the collinear three-body problem', *Contemporary Mathematics*, **246**, pp.143-162.

[18] Vidal,C.: 1999, 'The tetrahedral 4-body problem with rotation', *Celest. Mech. Dyn. Astr.*, **71**, pp.15-33.

[19] Sekiguchi,M. and Tanikawa,K.: 2000, 'On Escape Orbits in the Symmetric Collinear Four-Body Problem', *Proceedings of the 32nd Symposium on Celestial Mechanics, Kanagawa, Japan, 15-17 Mar. 2000*, pp.311-315.

[20] Tanikawa,K. and Mikkola,S.: 2000, 'Triple collisions in the one-dimensional three-body problem', *Celes. Mech. Dyn. Astr.*, **76**, pp.23-34.

[21] Tanikawa,K. and Mikkola,S.: 2000, 'One-dimensional three-body problem via symbolic dynamics', *CHAOS*, **10**, pp.649-657.

[22] Tanikawa,K. and Mikkola,S.: 2000, 'Multiple collisions in the one-dimensional free-fall four-body problem', *Proceedings of the 32nd Symposium on Celestial Mechanics, Kanagawa, Japan, 15-17 Mar. 2000*, pp.297-310.

[23] Sweatman,W.: 2001, 'The symmetrical one-dimensional Newtonian four-body problem: A numerical Investigation', to appear.

Celestial Mechanics in the 21st Century
21世紀の天体力学

Takashi Ito and Kiyotaka Tanikawa
伊藤孝士・谷川清隆 (文部科学省 国立天文台)
National Astronomical Observatory, Mitaka, Tokyo 181-8588, Japan

We review some of the major achievements in celestial mechanics and dynamical astronomy in the 20th century to look for their new directions in the 21st century.
20世紀の天体力学を振り返り、21世紀における天体力学の方向を探る。できれば新たなる方向を作りたい。他分野との境界領域に大いなる発展の可能性が存在している。

0. はじめに

天体力学のみならず世界のあらゆる局面で怒濤を巻き起こした20世紀が去った。かつて国立天文台あるいは東京大学東京天文台のメンバーを中心として開催されていた「天体力学研究会」は「N体力学研究会」へと発展解消し、量的にも質的にも大いなる変貌を遂げている。21世紀最初の年に開催された記念すべき草津N体力学研究会に際し、大胆にも20世紀の天体力学を振り返り、21世紀に於ける天体力学の方向を探ろうと試みたのが本稿である。もちろん非力な筆者らに前世紀の天体力学を完全にレビューし切れる力量があるはずはなく、況や今世紀の天体力学の発展の方向を完全に予測出来ようはずもない。改めて言うまでもないが、本稿に記したのは筆者自身が興味を持つ範囲内に於ける天体力学の来し方行く末についての偏った見方の露悪に過ぎない。その意味で、「21世紀の天体力学」という題目は大仰すぎるとの謗りを免れ得まい。ここに記載された内容は偏っているばかりでなく、筆者らの不勉強によりそもそも正しくない事柄が述べられている可能性もある。だが、21世紀は百年間継続する。筆者らの試みである20世紀天体力学の総括と21世紀天体力学の発展予測作業は今回で終わるものではなく、今世紀初頭の数年間に亘って継続するものと考えて頂きたい。本稿は私達がその端緒に付いたことを示すものである。なお、本稿で記した内容が極めて偏っていることは前述した通りだが、同様に引用文献の質・量についてもやはり大いに偏向し、且つ不完全なものである。この点についても筆者らの力量の低さが反映されていることは明らかなのだが、枉げて読者の寛恕を願う次第であると共に、不十分な点については各方面からの指摘を常に甘受する用意がある。

第一節では20世紀の天体力学の成果と諸問題について概観する。まず理論的(本稿では「数値的でない」くらいの意味で、「解析的」に近い)な研究の流れについて、三体問題、摂動論、KAM理論、アーノルド拡散、Aubry-Mather集合、可積分性カオス、自転運動理論などについて触れる。数値的研究に関しては、三体問題、惑星系の起源と進化、太陽系惑星の長期数値積分と安定性、数値計算法について触れる。第二節は第三節の準備として、21世紀の天体力学を考える際の指針の一例を示す。そもそも天体力学とは何であるかという定義を改めて考えておくことは重要であろう。然る後に第三節では、21世紀の天体力学の展望について私見を述べる。Lyapunov時間と不安定時間の関係の解明、惑星系、惑星探査の成果、星団の現実的数値積分、惑星の自転運動と公転運動の相互作用、三体問題、アーノルド拡散、カオスの世界、KAMの崩壊、解析的摂動論の精密化、天体の衝突破壊過程、数値計算法の発展、新世紀の現実生活への応用的側面、など、考えるべき領域は無数に存在する。以上の議論を踏まえた第四節では、主として理論的研究の立場から若干の議論を行う。

本稿の筆者は「伊藤孝士・谷川清隆」の順に記されているが、これは単に人名を五十音順に並べたに過ぎず、本稿への寄与は完全に対等である。執筆分担としては、理論的研究部分を主として谷川清隆が、それ以外の部分、特に惑星運動の数値計算に関する部分を伊藤孝士が担当した。文体を見ればいずれが執筆した部分であるかは自明であるが、時間の制約により調整が不完全な箇所もあり、一部内容の重複が見られる部分もある。この点についてはあらかじめお詫びしておきたい。なお、本稿は常に筆者のウェブページ (http://th.nao.ac.jp/~tanikawa/) にて最新版にアップグレードし続けられる予定である。

1. 20 世紀の天体力学の成果と諸問題

1.1 理論的研究

天体力学は、19 世紀末にポアンカレ (Poincaré) に流れ込み、ポアンカレから流れ出た。天体力学に於いて、摂動展開の無限級数は微小分母の存在のために一般に収束しない。摂動論をどんどん高次まで進めて行っても正しい解に辿り着かないことが明らかになった。摂動展開が収束するとは、系が積分可能であることを意味する。19 世紀末にわかったことは、天体力学の問題が一般には積分可能でないことである。世の中には積分可能な系の方が遙かに少ない。その典型例が剛体の回転 (コマ) 運動である。19 世紀末、ロシアにおいてリャプーノフが独自に安定性の議論を展開した (Lyapunov, 1892)。リャプーノフの仕事の成果は今日、リャプーノフ指数、リャプーノフ関数、リャプーノフの第一法および第二法、リャプーノフ安定性、漸近安定性などの用語として残っており、その影響の大きさが窺われる。

20 世紀の天体力学はバーコフから始まったと見てよい。バーコフは力学の定性論を本格的に開始した。個々の軌道を簡単な関数で表すことが出来ないなら、軌道の束の動きを知ることで我慢する。ここからいわゆる力学系という学問分野が発生した。一方、Siegel は三体問題が何故に可積分でないかを追究した。三体衝突が悪さをしている。Chazy (1922) の後、1940 年代から 1960 年代にかけて、旧ソ連では三体問題の定性論が盛んに展開された (Hagihara, 1971)。

太陽系の惑星運動の研究も進んだ。惑星の発見や小惑星の追跡発見は 19 世紀の天体力学の華であった。20 世紀も惑星の存在が予言され、冥王星の発見として結実した。小惑星の平山族の発見 (Hirayama, 1918) は太陽系小天体の起源および安定性の力学的問題の動機付けとなった.

新発見の惑星を加えた惑星暦の作製が天体力学のひとつの目標となった。ミランコビッチによる気候変動研究は摂動論を踏まえている。人工衛星の運動の研究も進んだ。1957 年のソ連によるスプートニク打ち上げ以後、Kozai (1962), Hori (1966, 1967, 1970, 1971), Kinoshita (1977) ら日本の天体力学研究者が人工衛星の軌道理論への大きな貢献を果たした。Hori (1966) の理論は新旧の正準変数が混じらない簡明かつ有用な手法を提供した。ハミルトン系の可積分性の研究では Yoshida (1983a, 1983b) が突破口を開いた。

運動方程式の数値積分法も大いに研究された。ルンゲクッタ法に始まり、予測子–修正子法、補外法らによって精度の向上が達成された。近年ではハミルトン系であることを明らさまに利用するシンプクティック法が考案され、少数多体系においては正則化法などが現在進行形で発展中である。

20 世紀天体力学の最大の成果は何かと問われれば、純理論的には KAM 理論であろうと答える。20 世紀の半ば、1957 年に人類が打ち上げたスプートニクは、天体力学に限らず 20 世紀人類の最高の成果のひとつであろう。これは技術革新の勝利とも言えるが、天体力学の立場から見ると摂動論の勝利とも言うことができる。

現在流行中のカオスもまた、ポアンカレに端を発する。ポアンカレは、双曲型不動点に流れ込んで再び流れ出す特別な流れや、安定多様体および不安定多様体の複雑な絡み合いを注意深く観察した。ポアンカレはニュートン力学が垣間見せた無限の深淵に身震いしたのであろう。パン屋のおやじがこねる生地そのままに、われらが世界は引き伸ばされ、折り畳まれる。Hénon & Heiles (1964) は 1960 年代に数値的に KAM 曲線の崩壊を観察して力学的カオスを発見し、1980 年代の始めに Wisdom (1983) は太陽系の惑星の運動に予測不可能な運命を見た。パワースペクトルもリャプーノフ指数もカオスの存在を示す。至る所にカオスが跳梁跋扈している。宇宙に於いて、太陽系に於いて、カオスが常態であることが 20 世紀後半の共通認識となった。

相対論を天体力学としてどう評価するか？ 相対論的天体力学、これは筆者らの手に負えない。1970 年代前半までの天体力学については相対論も含めて Hagihara (1970, 1972, 1974, 1975, 1976a, 1976b) が詳しい。

1.1.1 20 世紀の三体問題研究の流れ

19 世紀の末にポアンカレやブルンスにより三体問題の非可積分性が証明されて以来、定性的な方向への研究が盛んになった (Whittaker, 1904)。具体的な課題としては、19 世紀末に Painlevé (1895) が提出した非衝突特異性の存在または非存在の問題、Chazy (1922) が提出した振動解の存在または非存在の問題が挙げられる。前者は 1990 年代に Xia (1992) により解決され、後者は 1960 年にまず Sitnikov (1960) により考証され、Alexeev (1968a, 1968b, 1969) により摂動論を使って一般三体に拡張され、Xia (1994) によって平面問題に於いて解決された。Siegel (1941) は三体衝突が真性特異点であることを示した。旧ソ連では最終運動、初期運動の分類の研究が行われた (Merman, 1958; Hilmi, 1961)。これは軌道の束の行方を追う方法であり、一本一本の軌道を追うのに比べると遠慮した目標と言える。これにより、粒子の捕獲や交換の可能性、エスケープ (escape) など幾つもの成果が得られた。

Saari (1971) は衝突特異性と N 体問題に興味を持った。1974 年に McGehee (1974) の変数が導入され、三体問題の理論研究が再び盛んになった。Moeckel, Simo, Devaney 等は McGehee 変数を使って衝突近傍を通過する解の振舞いを考察した。最近では数値計算を援用する研究 (Tanikawa *et al.*, 1995; Umehara, 1997; Zare and Chesley, 1998; Umehara and Tanikawa, 2000; Tanikawa and Mikkola, 2000a; Tanikawa and Mikkola, 2000b; Tanikawa, 2000) により、相空間一般の構造を明らかにする方向で研究が進んでいる。エスケープの判定条件を求める分野もあり (例えば Marshal 1990)、現在は Yoshida (1972, 1974) の判定基準が最良のものと考えられている。

1.1.2 20 世紀の摂動論の簡単な流れ

20 世紀中盤に展開されてよく使われた Brouwer & van Woerkom (1950) の摂動論は、20 世紀初頭の Hill 理論の拡張および再構築であった (cf. Hill 1897)。ここでは木星と土星の六次の効果までを考慮し、惑星質量に関しては木星と土星の大均差 (the great inequality) について二次の効果を考慮した。Brouwer & van Woerkom (1950) の理論を拡張したのが Bretagnon (1974, 1992) であり、離心率と軌道傾斜角については四次の効果まで、惑星質量についてはすべて二次まで考えた解析的理論である。こうした流れを踏まえ、Laskar は離心率と軌道傾斜角については六次、惑星質量については二次までを考慮した精密な永年摂動論を構築した (Laskar 1985, 1986, 1988, 1990)。Laskar の理論は木星型四惑星に関する Duriez (1977, 1982) の永年摂動論の拡張であるが、永年摂動の運動方程式を数値積分で解き、その解をフーリエ展開して主要な周期成分の周期と振幅を求めた研究である。Laskar の理論は現代の永年摂動理論の業界標準として用いられている。

Milankovitch (1920, 1930, 1941) に代表されるように摂動論の範囲を自転運動にまで広げ、地球に入射する日射量の幾何的変動を検証しようとする試みも綿綿と続けられている。これについては中島 (1980) や木下 (1993) のレビューが詳しいので、そちらを参照のこと。

1.1.3 KAM 理論・アーノルド拡散・Aubry–Mather 集合

天体力学のみならず、20 世紀の数理科学すべてにとって KAM 理論 (Kolmogorov–Arnold–Moser) は一つの救いであった (Kolmogorov, 1954; Arnold, 1963; Moser, 1962)。18 世紀後半から 19 世紀第一四半世紀を生きた Laplace は、自著『確率の哲学的試論』(岩波文庫から内井惣七による邦訳あり) の中でいわゆる「ラプラスの魔」を考えた。われにすべての初期条件を与えよ、さすれば、未来のすべてを予言して見せよう、というわけである。これはまさにニュートン力学の勝利である。この線に沿って、19 世紀中は摂動論を発展させて、太陽系の未来ばかりでなくすべての力学系の未来は完全に予測可能あるいは解けると思われた。あるいは思いたかった。だが、19 世紀中に力学で説明のできない現象 (熱現象、電磁気現象など) が次々と研究の対象となり始め、力学的世界観および摂動論への信頼はゆるぎ始めた。最終的には、ポアンカレが摂動展開が一般には収束しないことを示してしまった。時まさに、統計力学が擡頭していた。振り子は揺れた。突然未来は統計的になった。粒子が多数になればなるほど、統計力学の領分に入る。

一方で太陽系の推定年齢はどんどん伸びていた。19 世紀には高々数千万年と思われ、20 世紀に入っても、1920 年代には宇宙年齢が 20 億年であった。太陽系の年齢が 45 億年となったのは 1950 年代である。これは摂動論が収束しないことにより太陽系が不安定になること、未来が統計的であることに対する強力な反証である。太陽系を記述する運動方程式が非可積分であっても、惑星達の運動が準周期的であるということは不安定性を妨げる障壁があるはずである。KAM 理論はこれに応えた。非可積分性が弱いときには、相空間のほとんどを障壁が占める。可積分系から遠ざかるにつれて障壁がまばらになる。こうして振り子はふたたび揺れた。大丈夫、未来はそれほど不確実ではない。

二つの問題が残った。ひとつは高次元の場合で、準周期運動の n 次元トーラスは $2n$ 次元の相空間を分離しない。従って、系が不安定になることを妨げる障壁にならない。準周期運動の間に狭まれていると思われた一般の運動は、次第に拡散していく。この現象はアーノルド拡散とよばれる (Arnold, 1964; Nekhoroshev, 1977)。この拡散の速度は如何？これが第一の問題。実際には拡散は非常に遅い。それは安定多様体と不安定多様体が織りなすネットワークに沿ってじわじわと進行する。ハミルトン関数を $H_0(I)+\varepsilon H_1(I,\varphi)$ として、適当に定数 a,b が取れて、タイムスケール $T=\frac{1}{\varepsilon}\exp(\frac{1}{\varepsilon^a})$ の間、作用変数は初期値から $|I(t)-I(0)|<\varepsilon^b$ だけ離れる。

準周期運動が滑らかな超曲面に閉じ込められなくなった時、それはどんな運動になるのか？トーラスが壊れたとき、その破片はどうなるのか？これが第二の問題である。この問題は Aubry & LeDaeron (1983) と Mather (1982) により、1980 年代の始めに解かれた。いわゆる KAM 曲面は、壊れると、きちんと編まれていたセーターの、横糸を失った縦糸のようにだらしなく緩んでしまう。横断面で見ると、連続曲線がカントール的な不連続集合、即ち Aubry–Mather 集合になる。ここから問題はカオスの領分に入る。

1.1.4 可積分性

ポアンカレやブルンスが三体問題の非可積分性を証明して以来、可積分であることは非常に稀なことであり、可積分系は特別なものであって、一般の力学系あるいは物理系を調べるのに役に立たないような印象が 20 世紀前半にはあったかもしれない。一般の系については摂動論的に攻

めるか、いっそ数値計算を使ってしまうかしかない。実際、その方向の研究はたくさん行われている。

1960 年代に、素朴な求積可能性から一歩進んで完全可積分性の概念が導入された。n 個の積分があって、どのふたつも Poisson 括弧を取ると 0 になる。これが Liouville の意味での求積可能性である。このとき相空間が n 次元トーラスによって層状に区分けされるとの幾何学的解釈がアーノルド (Arnold, 1978) によって行われ、完全可積分系と呼ばれるようになった。どうやって完全可積分な系を見つけるか、また、或る系が完全可積分でないとして、いくつ独立な積分を持つのか。進むべき道は？行動方針が欲しい。これが問題となった。1983 年以前の研究に関しては Kozlov (1983) が詳しい。

一方、不安定周期解の安定多様体と不安定多様体が横断的交差を持つこと (馬蹄を持つこと) が非可積分と同値であることが示された (Moser, 1974)。これは微分方程式の解の多価性を意味する。従って、系が非可積分であることを示すには、どこかに馬蹄があること、どこかで解が (無限) 多価になることを示せば良い。パンルベ性 (一般解が複素 t 面で一価であること) が可積分研究分野で重要な概念であることがわかる。

1970 年代中盤、有限戸田格子の可積分性が示された (Hénon, 1974; Flaschka, 1974)。Yoshida (1983a, 1983b) は weight-homogeneous な微分方程式系が可積分であるための必要条件を求める具体的方法を提示した。ある特異な解を特徴付けるコワレフスカヤ指数のすべてが有理数でないと、代数積分は存在しない。コワレフスカヤ指数のこの性質は解の一価性と関係する (Ziglin, 1982)。

相空間の一点を取ったときにそこを通る解、およびその近傍を通る解がどのように幾何学的に配置されているのか。この配置のされ方が非可積分性と関係する。次元が高くなればなるほど、場合分けの数は増える。一方の極端は相空間が超曲面 (トーラス) によって単純に区分けされる完全可積分系、もう一方の極端は、どんな超曲面もなく、解曲線が全次元を移り動く系。この違いが解の関数表現の違いとなって現れる。

1.1.5 カオス理論

カオスは気象学の Lorenz (1963)、生態学の May (1976)、電気回路の Ueda (1973, 1979)、一次元写像の Li and Yorke (1975)、Feigenbaum (1978)、乱流の Ruelle & Takens (1971) らがそれぞれの分野で独自に、あるいは自然発生的に発見した現象である。マンデルブロのいわゆる「フラクタル」(Mandelbrot, 1977) が共通項として存在することが知れ、その概念は一気に世に出た感がある。もちろん後になってみると、ポアンカレ、バーコフやスメールなどが見ていた現象と同根のものであることがわかるのであるが。

最初の驚きは、ランダムと思える現象が自由度の低い系に見られたことである。流体力学のランダウ的な観点からすると、静的な流れから乱流への移行に於いて、力学系としての自由度がどんどん増えて行く。完全な乱流は自由度無限大であるが、カオスを示す系は、常微分方程式で言えばわずか三元の連立方程式系でよい。ハミルトン系なら自由度 2 からすぐにカオスが始まる。カオスの本質は引き伸ばしと折り畳みである。これを図示したのが Smale (1967) であり、具体的には馬蹄写像である。四角形を伸ばして折り曲げて馬蹄形にし、もとの四角形の上に乗せる。あまりにも簡単なモデルであるが、これがカオスの本質を見せた。多項式写像でこれを表現したのが Hénon (1976) である。

カオス系は指数関数的に不安定であるが (引き伸ばし)、同じような場所に戻って来る (折り畳み)。引き伸ばしと折り畳みが繰り返され、初期値の記憶がどんどん失われる。いわゆる初期値に対する敏感な依存性である。もはやラプラスの魔も困り果てる。無限の精度で無限の未来を正確

に予言することにどれほどの意味があるのか？馬蹄が力学系の相空間の至る所に存在する。形の異なる馬蹄が近くに共存する。19 世紀の末にポアンカレを嘆かせた力学系のとてつもなく複雑な構造が、20 世紀の末に至って再び多くの研究者を悩ませている。この複雑性は宇宙のすべての階層にわたって普遍的に存在する。

J. Wisdom (Wisdom 1982, 1983, 1987a, 1987b) は小惑星や冥王星など太陽系天体の運動のカオスについて論じ、Hénon は制限三体問題でカオスを論じ、また Hénon 写像を作り出した。Lecar はリャプーノフ時間と大局的不安定性の不思議な関係 (大局不安定時間はリャプーノフ時間の 1.8 乗) を見つけ出した。理由は説明されていない。自由度 2 のハミルトン系に対応する二次元写像、特にねじれ写像を用いてカオスの始まり、カオスの発展、カオスの度合を調べる方向の研究もある (Tanikawa & Yamaguchi 1987, 1989, 1994, 1995, 2001; Yamaguchi & Tanikawa 2000, 2001)。

1.1.6 自転運動理論

惑星、特に地球の自転運動はタイムスケールによって全く研究分野が異なる。一日、更に一時間以下では弾性体としての地球が強調される。一年以下の時間スケールでは地球回転・自転速度変動として、20 世紀の四分の三の期間は恒星を用いた緯度観測や極運動観測が行われて来た。残り四分の一の期間は、地球回転が人工衛星レーザー測距、VLBI、GPS などの宇宙技術による高精度観測の対象となってきた。岩手県水沢市にあった緯度観測所の木村栄が極運動の z項 (木村項とも呼ばれる) を発見し (Kimura, 1902)、同じく緯度観測所の若生康次郎がこの z項を流体核の存在によって説明した (Wako, 1970)。数十年から数千年スケールの変動はデータとしては古代の天文現象 (日食、月食、星食) しかないので、古代史も関与する学際的な分野となる (Stephenson, 1997; 谷川, 相馬, 2001)。タイムスケールが数万年、数十万年となると、海洋のプランクトンの死骸、池に沈んだ巨木の年輪など、地質学的証拠が重要となる。ミランコビッチサイクルと呼ばれる地球軌道の長周期摂動とくに地軸の傾き変動に由来する日射量変化が気候変動に反映する (Milankovitch, 1941; Шараф and Будникова, 1969a; Шараф and Будникова, 1969b; Berger, 1976; Berger *et al.*, 1984; Berger, 1988; Berger, 1989)。数億年ともなると、月の軌道長半径の永年変化に対応する地球物理的な変動が観測されるはずである (Ito *et al.*, 1993)。地球自転が速いことが貝の模様に現れる (Abe *et al.*, 1992; 大野, 1993)。このタイムスケールの月運動論は Goldreich (1966) らに始まる。

より短い時間スケールの運動、すなわち剛体地球の歳差・章動の理論については、木下宙の功績が大である。国際天文学連合 (IAU) は長いこと 1950 年代に米国の Woolard が構築した理論 (Woolard, 1953) を正式に採用していた。が、VLBI を始めとする超精密観測時代に入ると Woolard の計算値は精度が不足し、なお且つ地球の形状軸ではなく瞬間自転軸の章動を計算しているという欠陥もあった。Kinoshita (1977) は剛体地球の章動理論構築にハミルトン力学を持ち込み、剛体地球の形状軸、瞬間自転軸、および角運動量軸の章動の精密な数値を計算し直した。Kinoshita (1977) で計算された章動の周期成分は 106 個であり、誤差精度は 1/10000 秒未満であった。この研究は更に Kinoshita (1990) で発展され、現在はフランスの J. Souchey らによって引き継がれている。なお、現在の観測値と理論値との差異は主として地球の非剛体部分が持つ不確定性が原因であるとされており、こちらに関しては笹尾哲夫の大いなる貢献があり (笹尾, 1979; Sasao *et al.*, 1980; 笹尾, 1993)、その後を白井俊道らが引き継いで精密な研究に取り組んでいる (Shirai and Fukushima, 2000; Shirai and Fukushima, 2001)。歳差・章動の理論は文字通りの超精密時代に入っており、自然科学研究というよりは高度技術開発という名称が当て嵌まるような段階に近付いている。真正の基礎天文学として、今後もしっかりと継承されて行くべき領域であろう。

1.1.7 相対論的天体力学

Hagihara (1931) は相対論的一体問題を解いた。観測精度が上がって、座標系の問題 (Fukushima *et al.*, 1986) が浮上した。最近はロシア学派の Brumberg (1995)、Kopeikin (1999, パルサータイミング)、Klioner (Klioner and Soffel, 1998) が活躍している。大質量星の重力崩壊があれば重力波が観測されると予測されている。

1.2 数値的研究

制限三体問題の数値積分は、20 世紀前半の手計算から後半の計算機による研究まで、切れ目なく続いている。一般三体問題も制限三体問題と同様、力学系そのものとしての興味や天文学の問題へのモデルとして、多くの研究者のターゲットとなった。理論的な取扱いのための正則化法は数値計算の時代には殊に有用となった。

1960 年代になると、重力多体問題を計算機で解くことが実用的になった。Aarseth (1985, 1988) に代表されるように、それ用の数値計算法やソースプログラムが次々と開発された。KAM 理論のチェックを数値的に行う研究も行われた (Hénon and Heiles, 1964)。数値計算法については、吉田春夫によるシンプレクティク数値積分法の理論、J. Wisdom らの手によるシンプレクティク数値積分法の実装、牧野淳一郎や福島登志夫らによる各種の多項式近似法、Levi-Civita や Kustaanheimo-Stiefel らによる正則化手法として花開いている。

杉本大一郎らによる重力多体問題専用計算機 GRAPE 類の成功は極めて大きい (Sugimoto *et al.*, 1990; Ebisuzaki *et al.*, 1993; Makino *et al.*, 1997; Makino and Taiji, 1998)。GRAPE 類を駆使して、井田茂・小久保英一郎らの東京工業大学グループが惑星集積過程の大規模直接計算に成功し、この分野に新時代を切り拓いた。ここ数年は惑星系力学の最盛期と言うこともでき、G. Wetherill, M. Holman, M. Duncan, H. Levison, J. Lissauer, J. Chambers らの活躍により次々と新しい成果が発表されている。惑星系のみならず、衛星・環系についても P. Goldreich や S. Tremaine ら以来研究の進展は著しい。特に天王星の楕円リングの起源や安定性維持の機構は、伝統的な解析的摂動論と新しい数値計算の融合領域の良い練習問題となっている。

計算機は理論の道具にもなっている。三体問題の理論の進展は、数値計算による相空間のサーベイによる。脳の延長として計算機を考えればよい。算盤や電卓の延長上にあるものである。

天体力学を代表する方向と言えば、ハミルトン力学一般、特殊な方程式としての N 体問題、特に三体問題であろう。20 世紀後半になぜ天体力学が亡びなかったのか？なぜカオス研究はこれほど流行るのか？答えは余りにも明らかである。計算機のおかげである。

1.2.1 制限三体問題

制限三体問題の数値積分は 20 世紀前半、細々と続けられた。手計算かそれともタイガー計算機か。コペンハーゲン学派の Strömgren (1935)、そして東北大学の松隈 (Matukuma, 1933)。大型計算機が導入されて、Hénon (1965) が系統的にコペンハーゲン派のシナリオに沿って周期解の探索を始めた。制限三体問題はその後、多くの人によって現実問題のモデルとして使われた。自転の起源 (Tanikawa *et al.*, 1989; Tanikawa *et al.*, 1991)、微惑星の集積 (Nakazawa *et al.*, 1989a; Nakazawa *et al.*, 1989b)、環の安定性 (Hénon and Petit, 1986; Petit and Hénon, 1987)、衛星の捕獲可能性 (Tanikawa, 1983) 等など。

Hénon (1965) は KAM 理論のチェックとして、一早く周期解の安定性を数値的に調べ始めた。正に計算機時代の申し子と言えよう。あるいはポアンカレ以来の伝統かしれない。その後、大型

計算機利用の恰好の題材として、制限三体問題は世界のあちこちで研究が行われた。主として周期軌道とその安定領域の数値的決定である。米国の Szebehely, Jefferys, 英国の Markellos などがこれに加わった。

1.2.2 一般三体問題

一般三体問題の数値計算も大型計算機の普及とともに本格的に開始された。薮下 (日本), Aarseth (ノルウエイ→英国), Anosova (ロシア), Broucke (ベルギー→米国), Mikkola (フィンランド), Heggie (英国), Zare (イラン→米国), Szebehely (ハンガリー→米国), Contopoulos (ギリシャ), 谷川 (日本)。世界中の研究者が参加した。三体問題には、直線問題、平面あるいは三次元二等辺問題、平面問題、階層問題、自由落下問題など、たくさんの変種がある。天文学的な応用のためには、単独星と連星の衝突、遭遇数値実験 (Heggie, Mikkola)、三体系が壊れるまでの時間 (Anosova) などが精力的に調べられている。S. Aarseth (http://www.ast.cam.ac.uk/~sverre/) は己の数値計算コードを一般に公開している。Harrington (1975) に始まる階層三体問題の安定性の研究は太陽系外惑星系の安定性の問題に繋がる可能性がある。

1.2.3 惑星系の起源と進化

林忠四郎や Safronov に始まる惑星系形成過程の定量的理論は、数値的研究の発展と共に急速な進展を遂げた典型的な分野である (Hayashi *et al.*, 1985)。これに天体力学が関与する部分は、原始太陽系星雲中の固体成分が凝縮して形成される微惑星の運動からである。林らのいわゆる「京都モデル」に於いては木星型惑星の形成時間が長くなり過ぎるということを研究の契機とし、1980 年代の後半には微惑星の成長が暴走的であることが Wetherill らの研究によって明らかにされて来た (Wetherill and Stewart, 1989)。この説を確定的にしたのが、東京大学教養学部および東京工業大学理学部のグループ (井田茂、小久保英一郎、牧野淳一郎、杉本大一郎、ら) が上述の重力多体問題専用計算機 GRAPE 類を使って行った一群の研究である (Kokubo and Ida, 1995; Kokubo and Ida, 1996; 小久保, 井田, 1997; Kokubo and Ida, 1998; 小久保, 1999; Kokubo and Ida, 2000; Kokubo and Ida, 2001)。Kokubo & Ida の一連の論文によれば、微惑星の暴走集積は必然であり、原始惑星と呼ばれる中間段階の天体へと寡占的に成長することがわかった。20 世紀の惑星形成過程理論が残した大きな課題のひとつはこの原始惑星から現在の惑星への成長の具体的描像であり、Chambers et al. (1996), Chambers & Wetherill (1998), Levison et al. (1998), Yoshinaga et al. (1999), Ito & Tanikawa (1999), Agnor et al. (1999), Chambers (2001) らによって幾つかの計算が行われ、今世紀への橋渡しが為された。

なお広い意味では惑星系の起源と同根だが、衛星–環系の起源と力学進化についての研究も Goldreich & Tremaine (1978, 1979) らに端を発して今や盛況である。衛星系には理論的にも興味深い共鳴現象が見られるし、惑星リングと相互作用して楕円リングを保持しているという説もあり、今後の発展が多いに待たれている。

1.2.4 太陽系惑星の長期数値積分と安定性

数値的研究の典型例のひとつが太陽系惑星の長期数値積分である。惑星系の安定性は Newton 以来の天体力学の大課題であり、現在でも研究が続けられている問題である。この問題に対する数値的アプローチは、世の中の計算機なるものが出現した 1950 年代から早速開始された。当時は計算機資源が極めて限られていたため、計算対象は専ら外五惑星であった。最初の有名な研究は Eckert

et al (1951) で、汎用大型計算機を用いて五外惑星の運動を 350 年間数値積分したというものであった。この後、Cohen & Hubbard (1965) による五外惑星運動の 12 万年数値積分、Cohen et al (1973) による五外惑星運動の 100 万年数値積分、Kinoshita & Nakai (1984) による五外惑星運動の 500 万年数値積分、Applegate et al (1986) の専用計算機による五外惑星運動の 217 万年数値積分などを経て、Roy et al (1988) に至って五外惑星運動の数値積分期間が一億年に到達し、五外惑星の数値積分に関しては太陽系年齢が視野に入る段階となった。この直後、Sussman & Wisdom (1988) が専用計算機 Digital Orrery を駆使して 8.45 億年の長期数値積分を実行し、外五惑星系の運動がカオス的であることを見い出した。外五惑星系については A. Milani らの LONGSTOP プロジェクトなどに於いても数値積分が継続され、Wisdom & Holman (1991) らの有名なシンプレクティク数値積分法の論文で発表された 11 億年間の数値積分、PC+i386 の組み合わせを用いて Kinoshita & Nakai (1996) が実行した±55 億年の数値積分を経て、積分期間は現在では Duncan & Lissauer (1998) や Ito et al. (1996) による 10^{11}年オーダーにまで到達した。この長期積分に於いてもやはり外五惑星系は安定であることが確認されている。

地球型四惑星も含めた数値積分では計算量が一気に 150 倍以上になる。現在でも標準とされる有名な研究は Quinn et al (1991) の 300 万年間の数値積分であり、月-地球系が受ける潮汐力や一般相対論的効果を慎重に扱った名論文と名高い。Sussman & Wisdom (1992) の一億年の数値積分により地球型惑星の Lyapunov 数が数百万年と非常に短いことが示された後には一時の数値積分ブームも去ったかに見えたが、安価な AT 互換機の跋扈と共に再び復活しつつあり、Duncan & Lissauer (1998) の約 10 億年の数値積分を経て、Ito & Tanikawa (2001) では±50 億年にわたる数値積分に於いて、カオスであるとは言いながらも大局的に安定である太陽系惑星の姿が明らかにされつつある。

付言しておくと、「太陽系は安定か？」という問いは極めて抽象的であり、その答を私達は既に知っているとも言えるし、知らないとも言える。これはひとつには、惑星の運動について「安定性」という用語が使われる場合にはその意味が非常に曖昧であることによる。実際のところ、太陽系惑星の運動に関して安定または不安定という厳密な定義を与えることは容易ではない。ここ数百年間に存在した研究者の数だけ安定性の定義があるとすら言えるかもしれない。そうした混乱の状況を A.M. Nobili は、自著 (Nobili *et al.*, 1989) の導入部分に於いて巧みな言い回しにより以下のように表現している。

> "... When the stability of our solar system is discussed, two objections often arise. Firstly, this problem has been around for too long, never getting to the point of stating clearly whether the system is stable or not; the few definite results refer to mathematical abstractions such as N-body models and do not really apply to the real solar system. Secondly, the solar system is macroscopically stable — at least for a few 10^9 years — since it is still there, and there is not much point in giving a rigorous argument for such an intuitive property. ..."

1.2.5 数値計算法

天体力学における数値計算で最も困難な部分は衝突の取り扱いである。これは理論の問題であると同時に数値計算法の問題でもある。ここでは 20 世紀の正則化の歴史をごく簡単にまとめる。

制限三体問題には二体衝突がある。Sundman (1912) は二体衝突に対応する微分方程式の特異性が真性でないこと、そして変数変換により取り除くことが可能であることを示した。二体衝突の正則化は Levi-Civita (1906), Birkhoff (1915), Thiele-Burrau (1906) らによって行われた。但

しこれらはすべて平面問題のための手法である。Levi-Civita は衝突点の周りに面を二枚用意し、軌道は衝突の度に面を移るとした。Birkhoff は第一天体および第二天体のどちらで衝突が起こっても良いように変数を選んだ。Thiele-Burrau は双曲線-楕円座標へと変数変換を行う。Lemaitre 変換 (Lemaitre, 1952) は Birkhoff 変換に似ているが、後者が元の変数と新変数の対応が 1 対 2 であるのに対し、前者は 1 対 4 である。Kustaanheimo & Stiefel (1965) は三次元問題の二体衝突の正則化に成功した。ここでは三次元の変数を四次元空間に埋め込んだ。

上記変換では時間変換はすべて $dt = rd\tau$ の形 (τ は新しい時間変数) である。ここで r は衝突する天体間の距離である。解は衝突を有限時間で通りすぎる。McGehee 変換では $dt = r^{3/2}d\tau$ なる形が採用される。この場合には時間を引き延ばし過ぎて、質点の衝突までに無限時間かかる。

Szebehely & Peters (1967) はピタゴラス問題 (三天体を 3-4-5 の直角三角形の頂点に置いた配置) を数値的に解き、動画を作った。これにより、三体問題の最終運動予測の難しさが多くの人に理解された。R.H. Miller (1964) は少数多体系の数値積分を行い、時間を進めて戻ってきたときに、途中に近接衝突があると初期条件への戻りが悪いことを見た。ハミルトン系は指数関数的に不安定であるから、数値積分の信頼性に問題があることを指摘した。この時期、32 体問題による国際プログラム比較が行われた。計算機が異なると、逃げる天体も同じではない。

2. 21 世紀の天体力学を考える際の指針

2.1 天体力学とは何か？

天体力学とは何か？この命題に関する研究者の見解はばらばらである。これは不思議なことではないかもしれない。だが天文学の他の分野に比べて、天体力学に於いては個々の研究者の間に自分達の守備範囲に関して暗黙の了解がなされていないことも確かである。伝統的には太陽系の天体の運動を扱う学問分野と呼べば良いか？けれども、伝統的という言葉は一体いつを指すのか？何しろ天文学の対象は 20 世紀に入ってからとてつもなく広がってしまった。18 世紀や 19 世紀の考えを伝統的と呼ぶならば、私達が取るべき態度としては二つが考えられる。18 世紀であれば、太陽系がほぼ宇宙そのものであった。19 世紀には系外銀河という概念はなかった。わが銀河が宇宙のすべてであった。星のスペクトル研究は 19 世紀の終りに始まったばかりで、その頃には原子核反応も知られていない。太陽系外天体の天体物理学研究も緒についたばかりである。やはり天体力学が天文学の中心であったろう。そこで、第一の態度は以下のようなものが考えられる：天体力学は宇宙を扱っていた。だから現在以降もそうあるべきである。一方、第二の態度は以下である：天体力学は今までずっと太陽系を中心的対象と考えて来た。従って、天体力学はやはりこれからも太陽系を対象とすべきである。

ともあれ、20 世紀に出版された書籍や論文のタイトルに「天体力学」のあるものを天体力学の守備範囲とするなら、極めて数学的なところから日常的なところまで範囲は非常に広い。19 世紀末のポアンカレの有名な教科書 "Les méthodes nouvelles de la méchanique céleste" (Poincaré, 1892) は日本語に訳せば「天体力学の新手法」となる。版を重ねた Whittaker の「解析力学」(1952) (1904 年から 1952 年まで) の副題は「三体問題への序付き」となっている。Siegel & Moser の教科書 (1971) は「天体力学講義」、萩原雄祐の「天体力学の基礎」(1950, 1976)、同じく 5 巻 9 冊の大著「天体力学」。これらはきわめて数学的である。日本語の標準的教科書「天体と軌道の力学」(木下, 1998)、「岩波講座第一巻 力学」(大貫, 吉田, 1994)、歴史に詳しい「古典力学の形成」(山本, 1997) が中間に位置し、「天体力学入門」(長沢, 1983) などは入門編に属する。毛色の変わったところでは四元数を縦横に駆使した「天体力学講義」(堀, 1988) があるが、非常に難解である。

具体的には、例えば新大学院生が初歩から天体力学を学ぶとすれば、以下のような道がひとつ提案できるかもしれない：長沢 (1983) や Danby (1992) で天体力学の初等的な部分の雰囲気を掴み、Brouwer & Clemence (1961) で古典的伝統芸能の全容を垣間見、木下 (1998) で Brouwer & Clemence (1961) の obsolete な部分を補う知識を得、Boccaletti & Pucacco (1996. 1998) でハミルトン力学やカオスに親しみ、Lichtenberg & Lieberman (1992) でカオス力学に更に深く触れ、惑星系の具体的な問題を扱う場合には Murray & Dermott (1999) をを参考にして研究を行う。人工衛星など更に精密で実際的な問題を扱う場合には Battin (1987) などが良い道標になろう。

余談になるが、解析力学に関する古典的な名著である H. Goldstein の "Classical Mechanics" (1980) 内での正準摂動論の記載は他のどの物理学の教科書よりも天体力学に寄っており、歴史的意義に関する記述も詳細である。正準摂動論の始原的な応用として「von Zeipel 法の第一版」とも言える 19 世紀の Delauney の仕事が紹介されており、Hori (1966) や Deprit (1970) の Lie 変換正準摂動論も紹介されている。筆者らが知る限り、正準変換の物理的意義についてこの Goldstein の教科書以上に執拗なる直感的説明を繰り返し続ける教科書は見当たらない。しかもその説明はどれも的を射ており、読むほどに味わい深い。この教科書が力学に関する名著中の名著との誉れを欲しい儘にする所以であろう。但し、数値積分の項で Cowell 法が「Crowell 法」と誤称されている部分はいただけないが。

話を戻すと、兎に角 Brown et al. (1922) が米国に於いて「天体力学」の活動報告を書いた時点で、既に天体力学とは何かについて迷いがあったと思われる。この報告の冒頭に「天体力学を最も広く解釈すれば、天文学のあらゆる分野に関わっている。狭く解釈すれば、重力相互作用する天体同士の公転運動や自転運動を扱う」とある。Brown も筆者と同じ悩みを抱えていた。報告書は、太陽系、天体力学の星々への応用、三体および多体問題の理論の三部構成であった。

この場合、自分がどこに居るかが重要である。「太陽系の天体の運動、それ以外でも宇宙の天体の運動に直接関わるような問題を相手にしない限り、天体力学とは呼べない」「制限三体問題や一般三体問題そのものを研究する時、それは天体力学とは言えない」と考えることも可能である。

ひとつの態度は、具体的な天体あるいは天文現象を想定することである。例えば太陽系の起源。これを力学的に追求する態度を保つ。もうひとつの態度は、天文学に現れるカオスの本性を追求することである。いずれにせよ、今後の発展方向のひとつが他の学問分野との境界領域にあることだけは明らかである。近いところでは天体物理学や地球惑星科学、あるいは生命科学、または人文社会科学などである。

2.2 計算機の性能向上と天体力学

TOP500 (http://www.top500.org/) に蓄積されたハイエンドコンピュータの性能変遷を見るまでもなく、この十年間で計算機の平均的性能は三桁以上向上しており、performance/cost 比は更にそれより数桁向上していると言って良い。天体力学業界もその恩恵に預かっていることは言を待たない。また、天体力学の分野では杉本大一郎・牧野淳一郎グループの GRAPE プロジェクトが大成功を納め、重力 N 体問題の分野に革命的な進展を持たらしたことは前述した。最新の GRAPE-6 は一筐体で 1 TFlops 以上の演算能力を持っており、その辺りの汎用ベクトル並列型スーパーコンピュータが束になっても届かない超高性能を誇っている。この GRAPE シリーズを利用し、小久保英一郎や井田茂らのグループは微惑星集積に関する力学過程を完全に解明し尽くした。GRAPE シリーズの開発は今も続けられており、専用計算機を使った重力 N 体問題研究の将来は明るいと言える。

一方、汎用のベクトル並列型スーパーコンピュータについては、市場に於ける存在自体が危う

くなっている。ベクトル計算機を製造するメーカは既に日本電気 (NEC) 以外になく、NEC にしても米国市場の販売のために CRAY と手を組んだりして四苦八苦している。富士通や日立製作所は既にベクトル機の開発から手を引いてしまった。一方では近年、ベクトル計算機を使って天体数 N がいくら小さくてもベクトル化による十分な高速演算を可能にする算法が福島登志夫によって開発された (Fukushima, 1997c; Fukushima, 1997e; Fukushima, 1999)。この方法は、運動方程式の解を Chebyshev 多項式で展開し、Picard 反復により逐次解を求めて行くという方法である。この方法は摂動が小さな太陽系の惑星運動の求解などに非常に有効と思われている。だがベクトル計算機自身の将来が見えない現在、この有効な方法の活路の存在も怪しげな状態になっている。ベクトル並列計算機に変わる新時代のスカラ超並列機の天体力学的活用については Saha & Tremaine (1997) らの算法が発表されているが、その実用性については未だ不明瞭な部分が多い。

低迷する大型計算機の領域に対比し、肥沃な資本主義経済支えられて performance/cost 比を上げ続ける PC については大いなる展望が開けている。伝統的な天体力学は基本的に小さな N の問題を扱うので、専用計算機や大型計算機に頼るケースは例外的であり、机上の PC でしこしこと長時間の数値積分を行うというスタイルが普遍的である。しかしこれには非常に長い時間がかかる。例えば、Ito & Tanikawa (2001) で行った太陽系 9 惑星の 50 億年間数値積分 (ひとつの初期値に対して) に必要な時間は、ちょっと前までの最速 PC であった alpha 21264 600MHz を用いたとして 6ヶ月近い時間を要する。すなわち一個の計算に 5000 時間以上の CPU time が必要ということである。カオス系である惑星運動の数値積分は一個の初期値で足りるはずはなく、少なくとも数個から数十個の初期値から出発して系の統計的な振舞いを検証する必要がある。こうなってしまうと、計算時間はあっと言う間に現実的な数字から遠ざかる値になる。PC の演算能力が現在の 1000 倍、すなわち太陽系 9 惑星の 50 億年間数値積分が 5 時間で終了する時代が訪れれば、この状況は質的に改善されるであろう (Tremaine, 1995)。けれども、汎用計算機の演算能力 (単一 CPU の高速化) はそろそろ原理的な上限—使用する素子中での電子運動の速度が律速になる段階—に到達しているという説もあり、従来のような「10 年で 1000 倍」という伸び率が期待できるということはなかろう。

3. 21 世紀の天体力学

3.1 Lyapunov 時間と不安定時間の関係の解明

カオス系の特徴的時間を表すスケールは Lyapunov 時間である (Benettin *et al.*, 1976)。Lyapunov 時間は、近接する初期値から出発した軌道が e 倍離れるまでの平均的時間として意味付けられている。けれども、Lyapunov 時間が過ぎたからと言って系が不安定化して瓦解するというわけではないことが話を混乱させる。例えば Sussman & Wisdom (1992) らの計算によれば太陽系の地球型惑星の運動の Lyapunov 時間はわずか数百万年と言うが、地球型惑星は今日に至るまで 50 億年近い間安定な運動を続けている。要するに、Lyapunov 時間 T_L と現実の不安定が発生するまでの時間 T_I の対応関係は不明であるというのが実状である。

惑星運動は一般に不安定までの時間が非常に長いので、T_L と T_I の関係を知る数値実験を繰り返すことは容易ではない。けれども、木星の摂動下にある小惑星には数百年から数千年で不安定化するものもあり、T_L と T_I の関係を検証するには良い例である。Lecar & Franklin (1992a, 1992b) はこの点に目を付け、多数の数値実験の後に $T_I \propto T_L^{\gamma}$ という関係を経験的に見出した。指数 γ は小惑星帯の場合には 1.8 に近いであろうという結論である。現在のところこの関係の物理的意義は解明されていないし、$\gamma \sim 1.8$ が何を意味するのかもわかっていない。Morbidelli & Froeschlé

(1996) らが解析的な説明を試みたりしてはいるものの、成功しているとは言えない。けれども、T_I と T_L の関係を知ることはカオスと現実の間に橋を掛けることに相当する。一般に Lyapunov 時間 T_L は大局的な不安定時間 T_I に比べるとずっと短いので、$T_I \propto T_L^{\gamma}$ という関係が成立するとすれば、実際の数値計算を行わずして系の不安定の時間スケールを知ることができることになる。

これに関連して、系の力学的間隔と不安定時間とのスケーリング則も経験的に知られている。Chambers et al. (1996) で指摘された事実は、原始惑星系の平均間隔 Δ (相互 Hill 半径で規格化したもの) と不安定までの時間 T_I の間に $\log T_I \propto \Delta$ という指数関数的な関係が成立することである。この関係は後に Yoshinaga et al. (1999) や Ito & Tanikawa (1999) によっても確認された。$\log T_I \propto \Delta$ という関係式の成立は、系の進化が或る種のカオス的な拡散に支配されているためと予想されているが、具体的な説明は未だ存在しない。T_I と T_L, あるいは Δ の関係の意味を知り、カオスと現実の架け橋を掛けることは、21 世紀の天体力学がまず最初に取り組むべき重要な課題であろう。

3.2 惑星系

惑星系の力学は 20 世紀も天体力学の中心的課題であり続け、その事実は 21 世紀も変わることはない。太陽系外惑星系の発見に伴い、天体力学と惑星系の関わりは私達の太陽系の問題と太陽系外惑星系の問題との二方向で進化して行くであろう。以下では 21 世紀に於ける惑星系の天体力学に関する諸問題を羅列して行く。

3.2.1 惑星集積過程

私達の太陽系に限るものではないが、微惑星の集積過程についての数値計算は重力多体問題専用計算機 GRAPE の活用を中心として更に進行するであろう。GRAPE は重力多体問題に正攻法で挑む王道だが、その一方で Tanikawa et al. (1991) に代表されるような制限問題を重ね合わせる手法も完全に死に絶えたわけではない。試験天体の個々の軌道の性質に関してより厳密な情報を得られることは、制限三体問題の唯一の長所だからである。

3.2.2 衛星の力学と物理

月を例に挙げるまでもなく、衛星の運動は前世紀以前から天体力学に極めて興味深い課題を提出し続けて来た。現在に於いても、天王星の楕円リングの維持機構と羊飼衛星の関係 (Kozai, 1992; Kozai, 1993; Kozai, 1995; Yamanaka, 1997; 山中, 1997)、逆行衛星とその力学的起源、土星の衛星に見られる各種の共鳴現象 (Greenberg, 1977) など、解かれるべき問題は山ほどある。これらの課題は間接的に、Europa に関して噂されている海の存在と生命の起源の問題と関連しているかもしれない。

3.2.3 太陽系外縁部

太陽系外縁部の力学的研究は、他のどの領域よりも観測と密接に結び付いている。幸いにも現在はその最盛期を迎えていると言っても良い。カイパーベルト天体は 2001 年夏現在で 400 個近く発見されており、十分に統計的な議論を行える段階に至った。けれどもその長い公転周期が原因し、カイパーベルト天体の力学的な構造はよく分かっているとは言い難い。今後の観測による正確な軌道決定や安定性解析の進展が望まれている。そしてその先には、未だ誰も目にしたことのないオールト雲の発見という難関が控えている。オールト雲は確かに遠く、暗く、その発見は

かなりの困難であろう。けれども、ひとたびオールト雲天体が発見されれば、長い間の謎であった彗星の軌道分布や微惑星の空間分布・速度分布に関する決定的な情報を得ることができるであろう。もしかするとネメシス、いわゆる惑星 X の存在あるいは非存在について何かを知ることができるかもしれない。国立天文台のすばる望遠鏡のみならず、世界中の大望遠鏡がその観測時間の多くを太陽系外縁部に向ける所以のひとつである。

3.2.4 太陽系外惑星系

1995 年の初発見以来 (Mayor and Queloz, 1995)、惑星系の天体力学の中でも太陽系外惑星系は圧倒的に 21 世紀天体力学の中心である (Boss, 1996; 井田, 1997)。何と言っても地球外生命や地球外文明、あるいは SETI と言った自然科学の究極目標のひとつに直結する太陽系外惑星系研究は、既に 70 例以上の観測結果を踏まえて怒濤の黄金時代に突入した (Marcy and Butler, 2000; Butler *et al.*, 2001; Jones *et al.*, 2001)。

太陽系外惑星系の多くは太陽系とは大きく異なる様相を呈しており、惑星形成理論にしても安定性研究にしてもその拡張と一般化が急務である (阿部, 1997; 渡邊, 井田, 1997)。従来は考えられなかったような初期条件や境界条件下での理論構築が待たれている。一方では、幾つかが既に発見されつつある複数惑星の系 (υ Andromedae, Gliese 876, HD 168443 など) で発現している各種の共鳴現象は、そのメカニズムなどは太陽系での現象と共通であるものの、起源の解明は大きな課題である (Lissauer, 1999; Laughlin and Adams, 1999; Rivera and Lissauer, 2000; Stepinski *et al.*, 2000; Nakai and Kinoshita, 2000; Barnes and Quinn, 2001; Ito and Miyama, 2001)。

現在発見されている太陽系外惑星系はその殆どが単独星の周囲のものである。観測対象が単独星であるからこれは当然でる。だが、宇宙の天体の多くは連星を形成している。この意味で、連星系の周りの惑星系の起源と進化・安定性に関して天体力学的見地からの検証を行うことは重要である (Holman and Wiegert, 1999; Whitmire *et al.*, 1998; Bennett *et al.*, 1999; Nelson, 2000)。Innanen & Mikkola (1997) が提唱した力学的剛性 (dynamical rigidity) や軌道要素の連動と安定性に関する研究 (Pauwels, 1983; Ito and Tanikawa, 2001b) などはその興味深い一例である。

現在発見されている太陽系外惑星は、観測限界によって大型のガス惑星ばかりであろうと思われている。いまから数年あるいは十数年の後、宇宙空間での光赤外干渉計観測などによって地球型の小型惑星が検出さることであろう。太陽系外惑星系に関する天体力学的研究の新たなる進展はそこから再び始まるはずである。

3.2.5 惑星探査の成果

天体力学の将来とは一見直接に結び付かないように聞こえるかもしれないが、将来の惑星探査ではロボット群が大活躍するであろう (発電ロボット、観測ロボット、送受信ロボット、工作ロボット、データ解析ロボット、...)。ロボットと言えば、何と言っても精密機械立国の日本が主導して行うべき方向である。上手く行けば惑星探査の実況放送が実現するかもしれない。惑星探査によって惑星系の起源に関して数多くの物質科学的情報が集まるという期待は言うに及ばず、天体力学に関係するデータも多く集まることが期待される。例えば族を成す小惑星や逆行衛星の組成を知ることで、これらに関する衝突起源説が真か否かを知る手掛りが得られる。最近流行の連星小惑星の起源についても同様である。物理探査との組み合わせで力学的性質を探るという手法は、将来の惑星探査に於いて明らかに重要である。

3.3 星団の現実的数値積分

多重恒星系 (三重連星、連星、惑星系) の多重度に関する情報は天体力学と言うよりも恒星系力学にとって重要であるが、今世紀に於ける大気圏外での観測により、その感度と分解能は共に向上する。これは恒星系の力学的進化 (星が星団として生まれ、その集団から次第に離れて行く過程) を知るための重要な鍵となる。理論的には、中心部に密な恒星系が出来上がった場合に、それらを取り込んだ部分系 (連星や三連星など) を含む超精密数値積分が必要となろう。また、星形成領域において集団として生まれた星の力学的進化の問題も大切な研究課題となる。

3.4 惑星の自転運動と公転運動の相互作用

言うまでもなく、天体力学は惑星の公転運動のみならず、自転運動をもカバーする。けれども、公転運動に比べて自転運動は一般に時間スケールが短く、精密かつ長期の議論をするには大きな困難が伴う。長い時間スケールの議論では公転運動と自転運動の相互作用 (spin-orbital coupling) の効果が大きくなり、自転と公転の運動方程式を組み合わせて解く必要が発生する (Goldreich and Peale, 1966; Laskar and Robutel, 1993; Laskar *et al.*, 1993b; Laskar *et al.*, 1993a)。また、自転運動の進化を追うためには惑星の内部構造モデルの確立が必須であり、伝統的な固体地球物理学の知識が必須となるため、天体力学の世界のみに閉じない話となる。

自転運動に関する問題と言えば、まずは惑星自転の起源と進化の解明が挙げられる。金星はどうして逆行自転しているのか、水星や月の自転はいつの段階で現在のように公転と同期するようになったのか、天王星の横倒し自転の起源は何かなど、解かれるべき問題は多い。これらについては 1960 年代から多くの研究が蓄積されているが、いずれの問題についても決定的な説は確立していない。

自転運動に関連する問題でおそらく私達がもっとも興味を持つべきものと言えば、やはり月-地球系の潮汐進化にとどめを刺す (Goldreich, 1966; Mignard, 1982; Abe *et al.*, 1992; 安部ほか, 1992; 安部, 1992; 安部, 大江, 1993)。大規模な天体衝突に始まった月の形成 (Lee *et al.*, 1997a; Ida *et al.*, 1997; 小久保, 1999; Kokubo *et al.*, 2000) 以降、地球の自転速度は低下して月は次第に遠ざかった。その様子は今まで極めて定性的にしか明らかではなかったが、昨今の地球内部物理学の研究成果を採り入れて、地球自転と月の公転運動の相互作用をすべて採り入れて数値的に解ける時代がそこまでやって来ている。もちろんこのためには、地球の海洋大陸分布の進化モデルのみならず、近い将来に行われるはずの月探査計画による月の内部物性に関する情報も必要である。月-地球系の進化を解明することは単に天体力学のみならず、地上の生命活動解明のための基礎的情報を私達に与えてくれるはずであり、誠に重要と言わざるを得ない (熊澤ほか, 2002)。

3.5 三体問題

「三体問題にだけは手を出すな」(古在由秀)、「相対論にだけは手を出すな」(海野和三郎) という戒めに代表されるように昔から危険視されて来た三体問題であるが、計算機の進歩によって数値計算に関しては身近な分野になるであろう。一般三体問題については「一部の人間の趣味として以外に生き残る道はあるのか?」と言う批判も強い。だが三体問題は、天体力学だけでなく、天文学や物理学に現れる微分方程式の中でも最も意味がはっきりしており、もっとも初等的な形を持ち、しかも解けない問題の代表である。その意味で、三体問題は一部の人間によって研究され続けるであろう。微分方程式あるいはハミルトン系、もっと広く見て一般の力学系に於いて開発された新しい数値的手法が有効であるかでどうかは、まずは三体問題に代表されるような性質を

良く知られた系で吟味されて来たし、これからも吟味されて行くことであろう。

三体問題はこれからも天文学に於ける数学モデルとして研究されるはずである。但し理論的研究はきわめて困難である。理論的研究も、数値計算による現象の発見と並行して行われると予測される。一方、宇宙には有限質量二天体の周りを動く無限小質量の天体の運動として近似できる現象がこれからも多く発見されるはずである。その意味で、制限三体問題はこれからも天体系のモデルとして愛用され続けると考えられる。

3.6 アーノルド拡散を数値的に見る

アーノルド拡散を見た者は未だ居ない (Morbidelli and Thomas, 1995; Morbidelli and Guzzo, 1996)。不変トーラス近傍の拡散速度はトーラスからの距離 d に依存する。もっと正確には、拡散はある閾値まで超指数関数的に遅く ($\sim 1/\exp[\exp(1/d)]$)、次の閾値までは指数関数的に遅く ($\sim 1/\exp(1/d)$)、最後の閾値までは二次的に遅い ($\sim d^2$)。最後の閾値は強いカオスへの移行の境界である。Xia (1992) は三体問題においてアーノルド拡散の存在を確認した。アーノルド拡散を見るには工夫が必要である。なんらかの方法で時間を縮めるか。あるいは、フラクタル図形の上を動く力学系を考えるのか。とにかくわからない。小惑星帯の安定性タイムスケールは短い。そこで、Morbidelli & Guzzo (1996) は、小惑星の大量の数値積分を行って、アーノルド拡散を観測しようではないかと提案している。

3.7 カオスの世界—KAM の崩壊を見る

カオス系の最終状態 ($t \to \infty$ の状態) は初期値に敏感に依存して変わる。初期値空間を最終状態に応じて分類して図示するとフラクタル図形が現れる。このフラクタル図形は、系の外部パラメータが変わると分岐する。しかもこの分岐自体がフラクタル的に生じる。KAM 曲線の生き残りはカントール集合であって、相点がこれを通り抜けるのに長い時間が必要である。自由度 2 のハミルトン系において、安定周期点のまわりの KAM 曲線が壊れて、それ以前には閉じ込められていた点が、外へと浸み出す。淀み層に捉えられる時間は長い。従って、何らかの次元解析により、やはり時間の短縮化が必要か。あるいは、特別なモデル力学系を考案するか。多倍長計算、誤差のない計算が必要とされるか。

3.8 解析的摂動論の精密化

伝統的な解析的摂動論の更なる精密化は天体力学の永遠の課題である。けれども現在の摂動論は解析的と言うよりも半解析的 (semi-analytic) あるいは半数値的 (semi-numerical) と言うべきほど、計算機の数式処理能力に頼っている。この路線を突き進んで行くと、或る将来には「天体力学用完全自動摂動展開プログラムパッケージ」なるものが完成され、人間は摂動展開のパラメータや次数を指定するだけで、ほしいだけの精度で解の展開を計算機が行ってくれる時代が来ないとも限らない。但しその場合には、天体力学用完全自動摂動展開プログラムパッケージの出力の意味を理解できる人間の存在が必要である。要するに、解析的摂動論の知識は天体力学業界の伝統芸能として、伝承して行く必要がある。それに携わる人数は多くある必要はないが、少なくとも世界のどこかの機関 (必ずしも日本である必要はない) では伝統芸能の継承が行われ続けることが、この業界の健全な将来へと繋がるであろう。但しこの伝統芸能は修得に夥しく長い時間が必要とされる割には地味な研究であり、現在の研究業界を支配する "Publish, or perish." の風潮

の下で大学院生が積極的に取り組む雰囲気を形成することは至難であるということも事実である (木下, 中井. 1994)。

太陽系外惑星の発見が相続く 21 世紀初頭、わが太陽系の長期安定性はほぼ示された。多種多様な系外惑星系の形態の雛形として、わが太陽系はいわば「責任ある立場」に置かれている。わが惑星系に見られる惑星間の相互作用を長短タイムスケールすべてにわたって、数え上げ、分類することが 21 世紀初頭の研究テーマであり、この研究は太陽系外惑星系の力学的研究の基礎となるはずである。このための手法としても、解析的摂動論の精密化は重要である。

3.9 天体の衝突破壊過程

微惑星の集積過程の数値計算に於いて常に問題となるのは、天体同士が衝突した際に合体したり跳ね返ったりせず、破壊して破片化してしまう場合の扱いである。相対速度が脱出速度より小さな衝突であれば、破壊しても再び集積すると考えて問題ないが、相対速度が脱出速度より大きな衝突ではそうも行かなくなる。木星の強い重力摂動の下にある小惑星帯などではこうした衝突破壊による破片化が系の力学進化に大きな影響を及ぼしていると考えられている (Yoshida *et al.*, 2001)。けれども、破片化した天体をひとつひとつ扱うのは非常に大きな計算量の増加となる。天体の衝突破片化に関しては幾つかの実際的な物理モデルが提案されているが (Alexander and Agnor. 1998; Leinhardt *et al.*, 2000)、それらの洗練をはじめ、衝突破壊過程の扱いは今世紀の天体力学の重要な課題のひとつと言える。

3.10 数値計算法の発展

21 世紀の天体力学で使われる数値計算法は、シンプレクティク数値積分法とそれ以外の方法に大別できるであろう。シンプレクティク数値積分法の発展については本稿の前半部分にある吉田春夫と伊藤孝士の解説、あるいは関連する諸論文 (Yoshida, 1990; Gladman *et al.*, 1991; Wisdom and Holman, 1991; Kinoshita *et al.*, 1991; Wisdom and Holman, 1992; Yoshida, 1992; Yoshida, 1993; Sanz-Serna and Calvo, 1994; 吉田, 1995; Wisdom *et al.*, 1996; 吉田, 1997; Yoshida, 2001) を読んでもらうのが最適であろう。現在の課題は天体同士の近接遭遇をどのように乗り切るかにある。シンプレクティク数値積分法は可変刻み幅に原理的に馴染まないため、近接遭遇の扱いには困難が伴う。近年になり、Duncan et al. (1998), Chambers (1999), Levison & Duncan (2000)、その他の研究 (Skeel and Biesiadecki. 1994; Lee *et al.*, 1997b; Levison and Duncan, 2000) によって近接遭遇を扱い得るシンプレクティク数値積分法が開発されて来ているが、計算効率の面からはまだ進展の余地があろう。この領域では Rauch & Holman (1999) が良いレビューとなっている。実用的な意味では、Saha & Tremaine (1992, 1994) による独立刻み幅と warm start の実装、Mikkola による正則化に関する一連の研究 (Mikkola, 1997; Mikkola and Innanen, 1999; Mikkola, 1999; Mikkola and Tanikawa, 1999; Mikkola and Palmer, 2000) が実際的に有益と言える。

シンプレクティク数値積分法以外の方法については、Makino (1991a, 1991b) や Makino & Aarseth (1992) らにより開発された四次の Hermite スキームやその発展形 (Kokubo *et al.*, 1998)、あるいは Quinlan & Tremaine (1990) の線形対称多段法が決定版となりつつある。Hermite スキームは単段法で可変刻み幅の方法であり、精度と効率を高いレベルでバランスさせた極めて実際的で効果的な方法である。重力多体問題専用計算機 GRAPE 類上で実装されている数値積分法もこの Hermite スキームをベースとしたものである。線形対称多段法は 10 次以上の超高精度の方法であり、固定刻み幅ではあるが、惑星運動のように円軌道に近く準周期的を扱う場合には有効な方法である。今後は PC クラスタのようにスカラ計算機を多数並列して計算を実行するケー

ス増えて行くであろうが、そのようなシステムの上で如何にして上記の数値積分法を実装して行くかという具体的な問題が大きな課題になって行くであろう。

付言だが、惑星運動の数値積分には不可避なケプラー方程式の求解については福島登志夫の一連の研究が非常に有効である (福島, 1982; Fukushima, 1996; Fukushima, 1997d; Fukushima, 1997a; Fukushima, 1997b; Fukushima, 1998)。

3.11 新世紀の現実生活への応用的側面

天体力学の現実生活への適用については、大雑把に以下の二通りに分類できるであろう。

- 人工衛星の精密位置決定 — これは天文学のみならず、人類の宇宙進出の補佐手段として重要である。地球上に人間が棲息する余地が限られている以上、今世紀中に宇宙空間への人類の進出は必定である。そのためには、宇宙開発技術の基礎の基礎としての人工天体の精密な位置決定が今までにも増して必要となることは言を待たない。まさに天体力学の現実応用的な側面の典型的な一例である。この中には、いわゆるスペースデブリの監視という側面も含まれる。人工衛星が多くなればなるほどその塵芥とも言えるスペースデブリは増加する。既に岡山県美星町や通信総合研究所鹿嶋などでは本格的な業務観測が行われており、宇宙科学研究所の吉川真や通信総合研究所の梅原広明らが精力的に研究を推進している。

- 太陽系内小天体目録 (地球接近小天体) — 地質学的過去に関する最近の成果によると、地表は小天体の衝突の危険に晒されている。但し、タイムスケールは長い。大量に発見されるであろう地球接近小天体の軌道をモニターし、天体同士の衝突を観測し、地球への接近を予報する。これは自然界での衝突実験であり、同時に宇宙災害予報でもある。世界的規模での『宇宙災害予知連』が確立されるかもしれない。

4. 議論

21 世紀の天文学に於ける理論的研究の本質的課題は何か？天体力学は変質するか？力学系理論の一部を取り込むのか、それとも力学系理論に飲み込まれるのか？

4.1 ハミルトン系の複雑さの程度の分類

ハミルトン系には沈点 (アトラクター) も湧点 (リペラー) もない。相点は一見あてどもなく相空間をうろつき回る。行く先々に構造がある。KAM 曲線に近づくと、淀み層があって、そこに捉えられる。なかなかそこから抜け出せない。相空間内の任意の場所での平均滞在時間を求めることはできそうにない。このような構造は、系が可積分系から遠ざかるにつれてますます複雑になる。そして複雑さの極限として、不思議なことにランダムな系が現れ、平均滞在時間は計算可能になる。その複雑さは何によるのか？基本的には周期解の数であろう。大きな構造は短周期軌道に関係し、小さな構造は長周期軌道に関係する。分岐で生じた周期軌道はあるものは最初から不安定であり、別のものは安定であるがいずれ不安定になる。不安定な周期点から出る安定・不安定多様体は別の周期点の不安定・安定多様体と交差して相空間内に複雑な網目を作る。相点はこの網に沿って動く。

この網目は与えられた系毎に異なるはずである。太陽系の相空間の網目、三体問題の相空間の網目。この網目を力学系ごとに解明することが大きな目標となる。大局的につながった網目の部

分は系の不安定性へと導く。そして自由度が3以上になると、相空間のどの点もこの大局的な網目につながっている (アーノルド拡散の起源)。

4.2 大気圏外での観測によるデータの高精度化・新天体の発見

21世紀には日本も独自に人工月衛星や人工惑星を打ち上げる。これにより、天体力学の基礎である天体の運動情報量が飛躍的に増大する。宇宙空間での位置天文学観測 (干渉計や三角視差)、物理観測 (視線測度や光度変化) により、データの精度が桁違いに向上する。銀河系内外にも新天体が続々発見されよう。太陽系内にもまだ未発見の種類の天体はいくつもあり得る。多くの天体力学者がみずからを太陽系内に閉じ込めてきたが、21世紀には太陽系外惑星系も含めて、天体力学者の視野が銀河系スケールにまで広がるであろう。

4.3 過去へ

わが惑星系の形成シナリオはますます地球の起源に迫り、地球科学は一層のこと過去に遡りつつある。海洋の起源や生命の起源などが多くの研究者の対象となる。惑星形成の最終段階、小天体の重爆撃、クレーターの形成、オールト雲の形成などの諸問題は21世紀初頭の天体力学の重要な問題である。その上、多様な太陽系外惑星系の中に形成途上のものが発見されることにより、わが太陽系の初期の状態に拘束条件が課される可能性がある。

4.4 21世紀の天文学

20世紀前半、天文学は観測波長を光から電波、赤外、紫外、X線、γ線へと広げた。20世紀後半、天文学は観測地を宇宙空間へと広げた。系外銀河の発見、宇宙膨張、3K背景輻射、クエーサー、中性子星 (パルサー) と発見が続く。ブラックホールの存在はほぼ確実、重力レンズ効果の発見、ダークマターの存在予想、γ線バーストの発見—これらの現象あるいは天体はどれひとつ取っても、宇宙の大局的な構造や進化の理解に欠かせない存在である。20世紀は盛りだくさんであった。まだ重力波は見つかっていないが、人間の世界観は変わった。もしかすると、われわれは繰り返しのない世界に生きている。自分の周りからどんどん他の物質が遠ざかり、孤独になってしまうかもしれない。地球上では小天体の衝突によって恐竜絶滅も起こったらしい。惑星系が次々と発見され、惑星形成過程が普遍的なものであることがはっきりしてきた。生命はどうか? 居住可能惑星の探索あるいは研究は21世紀天文学の最大の課題のひとつである。この世紀、人類は宇宙空間に自ら出向いて観測する。角分解能が干渉技術を用いて格段に上がり、現在の太陽系近傍を調べるように隣りの銀河を調べることができるであろう。もはや星間シンチレーションが問題になる水準である。

21世紀も天文学は急発展する。しかし、宇宙における天文現象のエネルギー源は重力ポテンシャルである。エネルギーをいくらでも汲み出せる。そのためのもっとも簡単な機構が三体相互作用である。宇宙の中の部分系の構造変化、あるいは進化は、注入されるエネルギー変化に応じると考えることもできる。「注入される」エネルギーは部分系自身の中に存在する。新たに発見される天体、現象の基本的な構造は力学によって解明されるはずである。もしそれが力学で説明がつかないなら、その天体はエネルギーを外部からもらっている。たとえば、大局磁場に貫かれたプラズマ、星の周囲の質量のごく小さなガス雲、など。すべての現象が天体力学で解明されるはずがないことはわかっているが、多くの現象はその外郭を天体力学によって明らかにされ得る。

*

天体物理学という大波に翻弄され、飲み込まれ、沈没しかけながらも、天体力学は 21 世紀も淡々と、黙々と、瓢々と、且つ粛々と発展を続けることであろう。この激動の時代に生き、新世紀に於ける天体力学の発展の端緒を目撃することが出来る私達の僥倖に感謝したい。

謝辞

本稿執筆に至るまでには数多くの人々との膨大な量の議論を経た。とりわけ吉田春夫氏と福島登志夫氏からの示唆は有益であった。この場を借りて御礼申し上げる。

参考文献

Aarseth, S.J. (1985) Direct method for N-body simulations, in Blackbill, J.U. and Cohen, B.I. eds., *Multiple Time Scales*, Academic Press, New York, 377–418.

Aarseth, S.J. (1988) Integration methods for small N-body systems, in Valtonen, M.J. ed., *The Few Body Problem*, Kluwer Academic Publisher, Dordrecht, 287–307.

Abe, M., Mizutani, H., Tamura, Y., and Ooe, M. (1992) Tidal evolution of the lunar orbit and the obliquity of the earth, *Proc. ISAS Lunar Planet. Symp.*, **25**, 226–231.

Agnor, C.B., Canup, R.M., and Levison, H.F. (1999) On the character and consequences of large impacts in the late stage of terrestrial planet formation, *Icarus*, **142**, 219–237.

Alexander, S.G. and Agnor, C.B. (1998) N-body simulations of late stage planetary formation with a simple fragmentation model, *Icarus*, **132**, 113–124.

Alexeev, V.M. (1968a) Quasirandom dynamical systems, I., *JMath. USSR-Sb*, **5**, 73–128.

Alexeev, V.M. (1968b) Quasirandom dynamical systems, II., *JMath. USSR-Sb*, **6**, 505–560.

Alexeev, V.M. (1969) Quasirandom dynamical systems, III., *JMath. USSR-Sb*, **7**, 1–43.

Applegate, J.H., Douglas, M.R., Gürsel, Y., Sussman, G.J., and Wisdom, J. (1986) The outer solar system for 200 million years, *Astron. J.*, **92**, 176–94.

Arnold, V.I. (1963) Small denominators and the problems of stability of motion in classical and celestial mechanics, *Russ. Math. Surveys*, **16**, 85–191, (English translation from Report to the IVth All-Union Mathematical Congress, Leningrad, 85–191, 1961).

Arnold, V.I. (1964) Instability of dynamical systems with several degrees of freedom, *Soviet Math. Dokl.*, **5**, 581–585, (English translation).

Arnold, V.I. (1978) *Mathematical Methods in Classical Mechanics*, Springer-Verlag, Berlin.

Aubry, S. and LeDaeron, P.Y. (1983) The discrete Frenkel-Kontorova model and its extensions, *Physica D*, **8**, 381–422.

Barnes, R. and Quinn, T. (2001) A statistical examination of the short-term stability of the υ Andromedae planetary system, *Astrophys. J.*, **550**. 884–889.

Battin, R.H. (1987) *An Introduction to The Mathematics and Methods of ASTRODYNAMICS*, American Institute of Aeronautics and Astronautics, Inc., New York.

Benettin, G., Galgani, L., and Strelcyn, J-.M. (1976) Kolmogorov entropy and numerical experiments, *Phys. Rev. A*, **14**. 2338–2345.

Bennett, D.P., Rhie, S.H., Becker, A.C., Butler, N., Dann, S., J. Kaspi, Leibowitz, E.M., Lipkin, Y., Maoz, D., Mendelson, H., Peterson, B.A., Quinn, J., Shemmer, O., Thomson, S., and Turner, S.E. (1999) Discovery of a planet orbiting a binary star system from gravitational microlensing, *nature*, **402**. 57–59.

Berger, A.L. (1976) Obliquity and precession for the last 5000000 years, *Astron. Astrophys.*, **51**, 127–135.

Berger, A.L. (1988) Milankovitch theory and climate, *Rev. Geophys.*, **26**, 624–657.

Berger, A.L. ed. (1989) *Climate and Geo-Science — A Challenge for Science and Society in the 21st Century*, Kluwer Academic Publishers, Dordrecht.

Berger, A.L., Imbrie, J., Hays, J., Kukla, G., and Saltzman, B. eds. (1984) *Milankovitch and Climate* —Understanding the Response to Astronomical Forcing, D. Reidel, Norwell, Mass.

Birkhoff, G.D. (1915) The restricted problem of three bodies, *Rend. Circ. Mat. Palermo*, **39**, 265–334.

Boccaletti, D. and Pucacco, G. (1996) *Theory of Orbits. 1. Integrable systems and non-perturbative methods*, Springer-Verlag, Berlin.

Boccaletti, D. and Pucacco, G. (1998) *Theory of Orbits. 2. Perturbative and geometrical methods*, Springer-Verlag, Berlin.

Boss, A.P. (1996) Extrasolar planets, *Physics Today*, **49**, 32–38.

Bretagnon, P. (1974) Termes à longues périodes dans le système solaire, *Astron. Astrophys.*, **30**, 141–154.

Bretagnon, P. and Francou, G. (1992) General theory for the outer planets, in *Chaos, resonance and collective dynamical phenomena in the solar system*, Kluwer Academic publishers, Dordrecht, 37–42.

Brouwer, D. and Clemence, G.M. (1961) *Methods of Celestial Mechanics*, Academic Press, New York.

Brouwer, D. and van Woerkom, A.J.J. (1950) The secular variations of the orbital elements of the principal planets, *Astron. Pap. Amer. Ephemeris. Naut. Alm.*, **13**, 2, 81–107.

Brown, E.W., Birkhoff, G.D., Leuschner, A.O., and Russell, H.N. (1922) Celestial Mechanics, *Bulletin of the National Research Counsil*, **4**, 1–22.

Brumberg, V.A. (1995) *Analytical Techniques of Celestial Mechanics*, Springer-Verlag, New York.

Burrau, C. (1906) Uber einige in Aussicht genommene Berechnun, betreffend einen spezialfall des Dreikorperproblems, *Vierteljahrsschrift Astron. Ges.*, **41**, 261.

Butler, R.P., Marcy, G.W., Fischer, D.A., Vogt, S.S., Tinney, C.G., Jones, H.R.A., Penny, A.J., and Apps, K. (2001) Statistical properties of extrasolar planets, in Penny, A., Artymowicz, P., Lagrange, A.-M., and Russell, S. eds., *ASP Conf. Ser. for IAU Symp. 202: 'Planetary Systems in the Universe'*, Kluwer Academic Publishers, in press.

Chambers, J.E. (1999) A hybrid symplectic integrator that permits close encounters between massive bodies, *Mon. Not. R. Astron. Soc.*, **304**, 793–799.

Chambers, J.E. (2001) Making more terrestrial planets, *Icarus*, in press.

Chambers, J.E. and Wetherill, G.W. (1998) Making the terrestrial planets: N-body integrations of planetary embryos in three dimensions, *Icarus*, **136**, 304–327.

Chambers, J.E., Wetherill, G.W., and Boss, A.P. (1996) The stability of multi-planet systems, *Icarus*, **119**, 261–268.

Chazy, M.J. (1922) Sur l'allure de mouvement dans le problème de trois corp quand le temps croit indéfiniment, *Ann. Sci. École Norm. Sup.*, **39**, 29–130.

Cohen, C.J. and Hubbard, E.C. (1965) Libration of the close approaches of Pluto to Neptune, *Astron. J.*, **70**, 10–13.

Cohen, C.J., Hubbard, E.C., and Oesterwinter, C. (1973) Planetary elements for 10000000 years, *Celes. Mech.*, **7**, 438–448.

Danby, J.M.A. (1992) *Fundamentals of Celestial Mechanics (second edition, third printing)*, Willmann-Bell Inc., Richmond, Virginia.

Deprit, A. (1969) Canonical transformations depending on a small parameter, *Celes. Mech.*, **1**, 12–30.

Duncan, M.J. and Lissauer, J.J. (1998) The effects of post-main-sequence solar mass loss on the stability of our planetary system, *Icarus*, **134**, 303–310.

Duncan, M.J., Levison, H.F., and Lee, M.H. (1998) A multiple time step symplectic algorithm for integrating close encounters, *Astron. J.*, **116**, 2067–2077.

Duriez, L. (1977) Théorie générale planétaire en variables elliptiques 1. Développement des equations, *Astron. Astrophys.*, **54**, 93–112.

Duriez, L. (1982) Théorie générale planétaire etendu au cas de la resonance et application au system des satellites Galileens de Jupiter (General planetary theory extended to the case of resonance and application to the Galilean satellite system of Jupiter), *Celes. Mech.*, **26**, 231–255.

Ebisuzaki, T., Makino, J., Fukushige, T., Taiji, M., Sugimoto, D., Ito, T., and Okumura, S.K. (1993) GRAPE project: an overview, *Publ. Astron. Soc. Japan*, **45**, 269–278.

Eckert, W.J., Brouwer, D., and Clemence, G.M. (1951) Coordinates of the five outer planets, *Astron. Pap. Amer. Ephemeris. Naut. Alm.*, **12**.

Feigenbaum, M. (1978) Quantative universality for a class of nonlinear transformations, *J. Stat. Phys.*, **19**, 25–.

Flaschka, H. (1974) Toda lattice II: existence of integrals, *Phys. Rev. B*, **9**, 1924–1925.

Fukushima, T. (1996) A fast procedure solving Kepler's equation for elliptic case, *Astron. J.*, **112**, 2858–2861.

Fukushima, T. (1997a) A method solving Kepler's equation for hyperbolic case, *Celes. Mech. Dyn. Astron.*, **68**, 121–137.

Fukushima, T. (1997b) A method solving Kepler's equation without transcendental function evaluations, *Celes. Mech. Dyn. Astron.*, **66**, 309–319.

Fukushima, T. (1997c) Picard iteration method, Chebychev polynomial approximation, and global numerical integration of dynamical motions, *Astron. J.*, **113**, 1909–1914.

Fukushima, T. (1997d) A procedure solving the extended Kepler's equation for the hyperbolic case, *Astron. J.*, **113**, 1920–1924.

Fukushima, T. (1997e) Vector integration of dynamical motions by the Picard-Chebychev method, *Astron. J.*, **113**, 2325–2328.

Fukushima, T. (1998) A fast procedure solving Gauss' form of Kepler's equation, *Celes. Mech. Dyn. Astron.*, **70**, 115–130.

Fukushima, T. (1999) Parallel/Vector integration methods for dynamical astronomy, *Celes. Mech. Dyn. Astron.*, **73**, 231–241.

Fukushima, T., Fujimoto, M.-K., Kinoshita, H., and Aoki, S. (1986) A system of astronomical constants in the relativistic framework, *Celes. Mech.*, **38**, 215–230.

Gladman, B., Duncan, M., and Candy, J. (1991) Symplectic integrators for long-term integrations in celestial mechanics, *Celes. Mech. Dyn. Astron.*, **52**, 221–240.

Goldreich, P. (1966) History of the lunar orbit, *Rev. Geophys.*, **4**, 411–439.

Goldreich, P. and Peale, S.J. (1966) Spin-orbit coupling in the solar system, *Astron. J.*, **71**, 425–438.

Goldreich, P. and Tremaine, S. (1978) The excitation and evolution of density waves, *Astrophys. J.*, **222**, 850–858.

Goldreich, P. and Tremaine, S. (1979) The excitation of density waves at the Lindblad and corotation resonances by an external potential, *Astrophys. J.*, **233**, 857–871.

Goldstein, H. (1980) *Classical Mechanics* (2nd edition), Addison-Wesley, Massachusetts, 邦訳は瀬川富士・矢野忠・江沢康生 訳『新版古典力学 (上・下)』, 吉岡書店, 1984.

Greenberg, R. (1977) Orbit-orbit resonances in the solar system: varieties and similarities, *Vistas Astron.*, **21**, 209–239.

Hagihara, Y. (1931) Theory of the relativistic trajectories in a gravitational field of Schwarzschild, *Annals of the Tokyo Astronomical Observatory*, **31**, 67–176.

Hagihara, Y. (1970) *Theories of Equilibrium Figures of a Rotating Homogeneous Fluid Mass*, NASA scientific and technical information office, Washington, D.C.

Hagihara, Y. (1971) Recent advances of celestial mechanics in the Soviet Union, *Vistas in Astronomy*, **13**, 15–47.

Hagihara, Y. (1972) *Celestial Mechanics II*, MIT Press, Cambridge, Massachusetts.

Hagihara, Y. (1974) *Celestial Mechanics*, Japan Society for the Promotion of Science, Tokyo.

Hagihara, Y. (1975) *Celestial Mechanics IV*, Japan Society for Promotion of Science, Tokyo.

Hagihara, Y. (1976) *Celestial Mechanics V*, Japan Society for Promotion of Science, Tokyo.

Harrington, R.S. (1975) Production of triple stars by the dynamical decay of stellar systems, *Astron. J.*, **80**, 1081–1086.

Hayashi, C., Nakazawa, K., and Nakagawa, Y. (1985) Formation of the solar system, in *Protostar & Planet II*, The University of Arizona Press, Tucson, Arizona, 1100–1153.

Hénon, M. (1965) Exploration numerique du probleme restreint I., *Annals Astrophysique*, **28**, 499–511.

Hénon, M. (1974) Integrals of the Toda lattice, *Phys. Rev. B*, **9**, 1921–1923.

Hénon, M. (1976) A two-dimensional mapping with a strange attractor, *Commun. Math. Phys.*, **50**, 69–77.

Hénon, M. and Heiles, C. (1964) The applicability of the third integral of motion: some numerical experiments, *Astron. J.*, **69**, 73–.

Hénon, M. and Petit, J.-M. (1986) Series expansion for encounter-type solutions of Hill's problem, *Celes. Mech.*, **38**, 67–100.

Hill, G.W. (1897) On the values of the eccentricities and longitudes of the perihelia of Jupiter and Saturn for distant epochs, *Astron. J.*, **17**, 81–87.

Hilmi, G.F. (1961) *Qualitative Methaods in the Many-Body Problem*, Gordon Breach, New York.

Hirayama, S. (1918) Groups of asteroids probably of common origin, *Astron. J.*, **31**, 185–188.

Holman, M. and Wiegert, P.A. (1999) Long-term stability of planets in binary systems, *Astron. J.*, **117**, 621–628.

Hori, G. (1966) Theory of general perturbations with unspecified canonical variables, *Publ. Astron. Soc. Japan*, **18**, 287–296.

Hori, G. (1967) Non-linear coupling of two harmonic oscillations, *Publ. Astron. Soc. Japan*, **19**, 229–241.

Hori, G. (1970) Comparison of two perturbation theories based on the canonical transformation, *Publ. Astron. Soc. Japan*, **22**. 191–198.

Hori, G. (1971) Theory of general perturbations for non-canonical systems, *Publ. Astron. Soc. Japan*, **23**, 567–587.

Ida, S., Canup, R.M., and Stewart, G.R. (1997) Lunar accretion from an impact-generated disk, *Nature*, **389**, 353–357.

Innanen, K.A., Zheng, J.Q., Mikkola, S., and Valtonen, M.J. (1997) The Kozai mechanism and the stability of planetary orbits in binary star systems, *Astron. J.*, **113**, 1915–1919.

Ito, T. and Miyama, S.M. (2001) An estimation of upper limit masses of υ Andromedae planets, *Astrophys. J.*, **552**, 372–379.

Ito, T. and Tanikawa, K. (1999) Stability and instability of the terrestrial protoplanet system and their possible roles in the final stage of planet formation, *Icarus*, **139**, 336–349.

Ito, T. and Tanikawa, K. (2001a) Long-term integrations and stability of planetary orbits in our solar system. *Mon. Not. R. Astron. Soc.*, submitted.

Ito, T. and Tanikawa, K. (2001b) Stability of terrestrial protoplanet systems and alignment of orbital elements. *Publ. Astron. Soc. Japan*, **53**, 143–151.

Ito, T., Kumazawa, M., Hamano, Y., Matsui, T., and Masuda, K. (1993) Long term evolution of the solar insolation variation over 4 Ga, *Proc. Jpn. Acad., Ser. B*, **69**, 233–237.

Ito, T., Kinoshita, H., Nakai, H., and Fukushima, T. (1996) Numerical experiments to inspect the long-term stability of the planetary motion −1, in *Proc. 28th Symp. Celes. Mech.*, National Astronomical Observatory, Mitaka, Tokyo, 123–136.

Iwasaki, K., Tanaka, H., Nakazawa, K., and Emori, H. (2001) The gas-drag effect on the orbital instability of a protoplanet-system. *Publ. Astron. Soc. Japan*, **53**, 321–329.

Jones, B.W., Sleep, P.N., and Chambers, J.E. (2001) The stability of the orbits of terrestrial planets in the habitable zones of known extraplanetary systems, *Astron. Astrophys.*, **366**, 254–262.

Kimura, H. (1902) A new annual term in the variation of latitude, independent of the components of the pole's motion, *Astron. J.*, **XXII**, 517, 107–108.

Kinoshita, H. (1977) Theory of the rotation of the rigid earth, *Celes. Mech.*, **15**, 277–326.

Kinoshita, H. and Nakai, H. (1984) Motions of the perihelions of Neptune and Pluto, *Celes. Mech.*, **34**, 203–217.

Kinoshita, H. and Nakai, H. (1995) The motion of Pluto over the age of the solar system, in Ferraz-Mello, S. *et al.* ed., *Dynamics, ephemerides and astrometry in the solar system*, Kluwer Academic publishers, Dordrecht, 61–70.

Kinoshita, H. and Nakai, H. (1996) Long-term behavior of the motion of Pluto over 5.5 billion years, *Earth, Moon, and Planets*, **72**, 165–173.

Kinoshita, H. and Souchay, J. (1990) The theory of the nutation of the rigid earth: Model at the second order, *Celes. Mech.*, **48**, 187–265.

Kinoshita, H., Yoshida, H., and Nakai, H. (1991) Symplectic integrators and their application to dynamical astronomy, *Celes. Mech. Dyn. Astron.*, **50**, 59–71.

Klioner, S.A. and Soffel, M. (1998) Nonrotating astronomical relativistic reference frames, *Astron. Astrophys.*, **334**, 1123–1135.

Kokubo, E. and Ida, S. (1995) Orbital evolution of protoplanets embedded in a swarm of planetesimals, *Icarus*, **114**, 247–257.

Kokubo, E. and Ida, S. (1996) On runaway growth of planetesimals, *Icarus*, **123**, 180–191.

Kokubo, E. and Ida, S. (1998) Oligarchic growth of protoplanets, *Icarus*, **131**, 171–178.

Kokubo, E. and Ida, S. (2000) Formation of protoplanets from planetesimals in the solar nebula, *Icarus*, **143**, 15–27.

Kokubo, E. and Ida, S. (2001) Formation of protoplanet systems, in Penny, A., Artymowicz, P., Lagrange, A.-M., and Russell, S. eds., *ASP Conf. Ser. for IAU Symp. 202: 'Planetary Systems in the Universe'*, Kluwer Academic Publishers, in press.

Kokubo, E., Yoshinaga, K., and Makino, J. (1998) On a time-symmetric Hermite integrator for planetary N-body simulation, *Mon. Not. R. Astron. Soc.*, **297**, 1067–1072.

Kokubo, E., Ida, S., and Makino, J. (2000) Evolution of a circumterrestrial disk and formation of a single moon, *Icarus*, **148**, 419–436.

Kolmogorov, A.N. (1954) Preservation of conditionally periodic movements with small change in the Hamitonian function, *Dokl. Akad. Nauk. USSR*, **98**, 527–531.

Kopeikin, S.M. (1999) Millisecond and binary pulsars as nature's frequency standards - II. The effects of low-frequency timing noise on residuals and measured, *Mon. Not. Roy. Astron. Soc.*, **305**, 563–590.

Kozai, Y. (1962) Secular perturbations of asteroids with high inclination and eccentricity. *Astron. J.*, **67**, 591–598.

Kozai, Y. (1992) Shepherding satellites and dynamical structure of the rings of Uranus, *Publ. Astron. Soc. Japan*, **44**, 135–139.

Kozai, Y. (1993) Shepherding satellites and dynamical structure of the rings of Uranus. II, *Publ. Astron. Soc. Japan*, **45**, 263–267.

Kozai, Y. (1995) Dynamical structure of the Uranian rings, *J. Astrophys. Astron. Suppl.*, **16**, 373–375.

Kozlov, V.V. (1983) Integrability and non-integrability in Hamiltonian mechanics. *Russ. Math. Survey*, **38**, 1–76.

Kustaanheimo, P. and Stiefel, E. (1965) Perturbation theory of Keplarian motion based on Spinor regularization, *J. Math.*, **218**, 204–.

Laskar, J. (1985) Accurate methods in general planetary theory, *Astron. Astrophys.*, **144**, 133–146.

Laskar, J. (1986) Secular terms of classical planetary theories using the results of general theory, *Astron. Astrophys.*, **157**, 59–70.

Laskar, J. (1988) Secular evolution of the solar system over 10 million years, *Astron. Astrophys.*, **198**, 341–362.

Laskar, J. (1990) The chaotic motion of the solar system: A numerical estimate of the size of the chaotic zones, *Icarus*, **88**, 266–291.

Laskar, J. and Robutel, P. (1993) The chaotic obliquity of the planets, *Nature*, **361**, 608–612.

Laskar, J., Joutel, F., and Boudin, F. (1993a) Orbital, precessional, and insolation quantities for the earth from −20Myr to +10Myr, *Astron. Astrophys.*, **270**, 522–533.

Laskar, J., Joutel, F., and Robutel, P. (1993b) Stabilization of the Earth's obliquity by the Moon, *Nature*, **361**, 615–617.

Laughlin, G. and Adams, F.C. (1999) Stability and chaos in the υ Andromedae planetary system, *Astrophys. J.*, **526**, 881–889.

Lecar, M. and Franklin, F. (1992) On the original distribution of the asteroids IV. numerical experiments in the outer asteroid belt, *Icarus*, **96**, 234–250.

Lecar, M., Franklin, F., and Murison, M. (1992) On predicting long-term orbital instability: a relation between the Lyapunov time and sudden orbital transitions, *Astron. J.*, **104**, 1230–1236.

Lee, D.-C., Halliday, A.N., Snyder, G.A., and Taylor, L.A. (1997a) Age and origin of the moon, *Science*, **278**, 1098–1103.

Lee, M.H., Duncan, M.J., and Levison, H.F. (1997b) Variable time step integrators for long-term orbital integrations, *Astron. Soc. Pac. Conf. Ser.*, **123**, 32–37.

Leinhardt, Z.M., Richardson, D.C., and Quinn, T. (2000) Direct N-body simulations of rubble pile collisions, *Icarus*, **146**, 133–151.

Lemaitre, G. (1952) Cordonnées symétriques dans le probléme des trois corps, *Bull. Classe. Sci. Acad. Roy. Belg.*, **38**, 582–.

Levi-Civita, T. (1906) Sur la résolution qualitative du probléme des trois corps, *Acta Math.*, **30**, 305–.

Levison, H.F. and Duncan, M.J. (2000) Symplectically integrating close encounters with the Sun, *Astron. J.*, **120**, 2117–2123.

Levison, H.F., Lissauer, J.J., and Duncan, M.J. (1998) Modeling the diversity of outer planetary systems, *Astron. J.*, **116**, 1998–2014.

Li, T.Y. and Yorke, J.A. (1975) Period three implies chaos, *Am. Math. Monthly*, **82**, 985–992.

Lichtenberg, A.J. and Lieberman, M.A. eds. (1992) *Regular and Chaotic Dynamics*, Springer-Verlag, New York.

Lissauer, J.J. (1999) Three planets for Upsilon Andromedae, *nature*, **398**, 659.

Lorenz, E.N. (1963) Deterministic nonperiodic flow, *J. Atoms. Sci.*, **20**, 130–.

Lyapunov, A.M. (1892) *The General Problem of Stability of Motion*, Kharikov, (in Russian: English translation is published by Taylor & Francis, London, 1992).

Makino, J. (1991a) A modified Aarseth code for GRAPE and vector processors, *Publ. Astron. Soc. Japan*, **43**, 859–876.

Makino, J. (1991b) Optimal order and time-step criterion for Aarseth-type N-body integrators. *Astron. J.*, **369**, 200–212.

Makino, J. and Aarseth, S.J. (1992) On a Hermite integrator with Ahmad-Cohen scheme for gravitational many-body problems, *Publ. Astron. Soc. Japan*, **44**, 141–151.

Makino, J. and Taiji, M. eds. (1998) *Scientific Simulations with Special-Purpose Computers — the GRAPE systems*, John Wiley & Sons, New York.

Makino, J., Taiji, M., Ebisuzaki, T., and Sugimoto, D. (1997) GRAPE-4: a massively parallel special-purpose computer for collisional N-body simulations, *Astrophys. J.*, **480**, 432–446.

Mandelbrot, B. (1977) *Fractals: Form, Chance, and Dimension*, W.H. Freeman & Co, San Francisco.

Marcy, G.W. and Butler, R.P. (2000) Planets orbiting other suns, *Publ. Astron. Soc. Pac.*, **112**, 137–140.

Marshal, C. (1990) *The Three-Body Problem*, Elsevier. Amsterdam.

Mather, J.N. (1982) Existence of quasi-periodic orbits for twist homeomorphisms of the annulus, *Topology*, **21**, 457–467.

Matukuma, T. (1933) On the periodic orbits in Hill's case, *Proc. imp. Acad. Japan*, **9**, 364–.

May, R.M. (1976) Simple mathematical models with very complicated dynamics, *nature*, **261**, 459–.

Mayor, M. and Queloz, D. (1995) A Jupiter-mass companion to a solar type star, *Nature*, **378**, 355–359.

McGehee, R. (1974) Triple collision in the collinear three-body problem, *Invent. Math.*, **27**, 191–227.

Merman, G.A. (1958) Qualitative investigations of the three-body problem. *Bull. Inst. Teoret. Astronom.*, **6**, 687–712, (in Russian).

Mignard, F. (1982) Long time integration of the Moon's orbit, in Brosche, P. and Sündermann, J. eds., *Tidal Friction and the Earth's Rotation II*, Springer, Berlin.

Mikkola, S. (1997) Practical symplectic methods with time transformation for the few-body problem, *Celes. Mech. Dyn. Astron.*, **67**, 145–165.

Mikkola, S. (1999) Efficient symplectic integration of satellite orbits, *Celes. Mech. Dyn. Astron.*, **74**, 275–285.

Mikkola, S. and Innanen, K. (1999) Symplectic tangent map for planetary motions, *Celes. Mech. Dyn. Astron.*, **74**, 59–67.

Mikkola, S. and Palmer, P. (2000) Simple derivation of symplectic integrators with first order correctors, *Celes. Mech. Dyn. Astron.*, **77**. 305–317.

Mikkola, S. and Tanikawa, K. (1999) Explicit symplectic algorithms for time-transformed Hamiltonians, *Celes. Mech. Dyn. Astron.*, **74**, 287–295.

Milankovitch, M. (1920) *Théorie mathématique des phénomènes thermique produis par la radation solaire*, Gautier-Villars, Paris.

Milankovitch, M. (1930) *Mathematische Klimalehre und astronomische Theorie der Klimaschwankungen*, Springer-Verlag, in "Handbuch der Klimatologie" (Köppen and Geiger eds.), Band 1. Teil A.

Milankovitch, M. (1941) *Kanon der Erdbestrahlung und seine Anwendung auf das Eiszeitproblem*, Vol. 133 of *Königlich Serbische Academie Publication*, Königlich Serbische Academie, 邦訳は『ミランコビッチ気候変動の天文学理論と氷河時代』, 柏谷健二・山本淳之・大村誠・福山薫・安成哲三 訳, 古今書院, 1992.

Miller, R.H. (1964) Irreversibility in small stellar dynamical systems, *Astrophys. J.*, **140**, 250–585.

Morbidelli, A. and Froeschlé, C. (1996) On the relationship between Lyapunov times and macroscopic instability times, *Celes. Mech. Dyn. Astron.*, **63**, 227–239.

Morbidelli, A. and Guzzo, M. (1996) The Nekhoroshev theorem and the asteroid belt dynamical system, *Celes. Mech. Dyn. Astron.*, **65**, 107–136.

Morbidelli, A. and Thomas, F. (1995) The resonant structure of the Kuiper belt and the dynamics of the first five trans-Neptunian objects, *Icarus*, **118**, 322–340.

Moser, J. (1962) Oninvariant curves of area-preserving mappings of an annulus, *Nachr. Akad. Wiss. Gottingen. II Math. Phys.*, **1**, 1–20.

Moser, J. (1974) *Stable and Random Motions in Dynamical Systems*, Princeton University Press.

Murray, C.D. and Dermott, S.F. eds. (1999) *Solar System Dynamics*, Cambridge University Press, Cambridge.

Nakai, H. and Kinoshita, H. (2000) Stability of the υ Andromedae planetary system, in *Proc. 32th Symp. Celes. Mech.*, National Astronomical Observatory, 206–215.

Nakazawa, K., Ida, S., and Nakagawa, Y. (1989a) Collisional probability of planetesimals revolving in the solar gravitational field I. Basic formulation, *Astron. Astrophys.*, **220**, 293–300.

Nakazawa, K., Ida, S., and Nakagawa, Y. (1989b) Collisional probability of planetesimals revolving in the solar gravitational field II. The validity of the two-body approximation, *Astron. Astrophys.*, **221**, 342–347.

Nekhoroshev, N.N. (1977) An exponential estimate of the time of stability of nearly integrable Hamiltonian systems, *Russ. Math. Survey*, **32**, 1–65.

Nelson, A.F. (2000) Planet formation is unlikely in equal-mass binary systems with $a \sim 50$ AU, *Astrophys. J.*, **537**, L65–L68.

Newhall, X X., Standish, E.M., and Williams, J.G. (1983) DE102: a numerically integrated ephemeris of the Moon and planets spanning forty-four centuries, *Astron. Astrophys.*, **125**, 150–167.

Nobili, A.M., Milani, A., and Carpino, M. (1989) Fundamental frequencies and small divisors in the orbits of the outer planets, *Astron. Astrophys.*, **210**, 313–336.

Painlevé, P. (1897) *Lecon sur la Theorie analytique des equation differentielle*, A. Hermann, Paris.

Pauwels, T. (1983) Secular orbit-orbit resonance between two satellites with nonzero masses, *Celes. Mech.*, **30**, 229–247.

Petit, J.-M. and Hénon, M. (1987) A numerical simulation of planetary rings. I—Binary encounters, *Astron. Astrophys.*, **173**, 389–404.

Poincaré, H. (1892) *Les Méthode nouvelles de la Méchanique céleste*, Gauthier-Villars.

Quinlan, G.D. and Tremaine, S. (1990) Symmetric multistep methods for the numerical integration of planetary orbits, *Astron. J.*, **100**, 1694–1700.

Quinn, T.R., Tremaine, S., and Duncan, M. (1991) A three million year integration of the earth's orbit, *Astron. J.*, **101**, 2287–2305.

Rauch, K.P. and Holman, M. (1999) Dynamical chaos in the Wisdom-Holman integrator: origins and solutions, *Astron. J.*, **117**, 1087–1102.

Richardson, D.L. and Walker, C.F. (1989) Numerical simulation of the nine-body planetary system spanning two million years, *J. Astronaut. Sci.*, **37**, 159–182.

Rivera, E.J. and Lissauer, J.J. (2000) Stability analysis of the planetary system orbiting υ Andromedae, *Astrophys. J.*, **530**, 454–463.

Roy, A.E., Walker, I.W., Macdonald, A.J., Williams, K., I.P. Fox, Murray, C.D., Milani, A., Nobili, A.M., Message, P.J., Sinclair, A.T., and Carpino, M. (1988) Project LONGSTOP, *Vistas Astron.*, **32**, 95–116.

Ruelle, D. and Takens, F. (1971) On the nature of turbulence, *Comm. Math. Phys.*, **23**, 343–.

Saari, D.G. (1971) Implications of the inverse-square model, *Astrophys. J.*, **165**, 399–1971.

Saha, P. and Tremaine, S. (1992) Symplectic integrators for solar system dynamics, *Astron. J.*, **104**, 1633–1640.

Saha, P. and Tremaine, S. (1994) Long-term planetary integrations with individual time steps, *Astron. J.*, **108**, 1962–1969.

Saha, P. and Tremaine, S. (1997) A parallel integration method for solar system dynamics, *Astron. J.*, **114**, 409–415.

Sanz-Serna, J.M. and Calvo, M.P. (1994) *Numerical Hamiltonian Problems*, Chapman & Hall, London.

Sasao, T., Okubo, S., and Saito, M. (1980) A simple theory on the dynamical effects of a stratified fluid core upon nutational motion of the Earth, in Fedrov, E.P., Smith, M.L., and Bender, P.L. eds., *Nutation and the Earth's Rotation*, Reidel, Dordrecht, Netherlands, 165–183, International Astronomical Union Symposium No.78.

Шараф, Ш.Г. and Будникова, Н.А. (1969a) О вековых изменениеых элементов орбиты Земли, влияющих на климаты геологического прощлого, БЮЛЛЕТЕНЬ ИНСТИТУТА ТЕОРЕТИЧЕСКОЙ АСТРОНОМИИ, **11**, 231–261, English translation is in NASA TT F–12, *467*, 1–37.

Шараф, Ш.Г. and Будникова, Н.А. (1969b) ВЕКОВЫЕ ИЗМЕНЕНИЯ ЭЛЕМЕНТОВ ОРБИТЫ ЗЕМЛИ И АСТРОНОМИЧЕСКАЯ ТЕОРИЯ КОЛЕБАНИЙ КЛИМАТА, ТРУДЫ ИНСТИТУТА ТЕОРЕТИЧЕСКОЙ АСТРОНОМИИ, **14**, 48–84, Japanese translation is available from http://th.nao.ac.jp/~tanikawa/list08/list08.html.

Shirai, T. and Fukushima, T. (2000) Numerical convolution in the time domain and its application to the nonrigid-earth nutation theory, *Astron. J.*, **119**, 2475–2480.

Shirai, T. and Fukushima, T. (2001) Construction of a new forced nutation theory of the nonrigid earth, *Astron. J.*, **121**, 3270–3283.

Siegel, C. (1941) Der Dreierstoss, *Acta Math.*, **42**, 127–168.

Siegel, C. and Moser, J. (1971) *Lectures on Celestial Mechanics*, Springer-Verlag, Berlin.

Sitnikov, K. (1960) The existence of oscillatory motions in the three-body problem, *Dokl. Akad. Nauk USSR*, **133**, 303–306.

Skeel, R.D. and Biesiadecki, J.J. (1994) Symplectic integration with variable stepsize, *Ann. Numer. Math.*, **1**, 191–198.

Smale, S. (1967) Differential dynamical systems, *Bull. Amer. Math. Soc.*, **73**, 747–817.

Stephenson, F.R. (1997) *Historical Eclipses and Earth's Rotation*, Cambridge University press.

Stepinski, T.F., Malhotra, R., and Black, D.C. (2000) The υ Andromedae system: models and stability, *Astrophys. J.*, **545**, 1044–1057.

Strömgren, E. (1935) Fortgesetzte untersuchungen uber asymptotische bahnen im probleme restreint, *Bulletine Astronomiques*, **9**, 87, (also in *Publ. Copenhague Obs.* no. 100).

Sugimoto, D., Chikada, Y., Makino, J., Ito, T., Ebisuzaki, T., and Umemura, M. (1990) A special-purpose computer for gravitational many-body problem, *Nature*, **345**, 33–35.

Sundman, K. (1912) Mémoire sur le probléme des trois corps, *Acta Math.*, **36**, 105–179.

Sussman, G.J. and Wisdom, J. (1988) Numerical evidence that the motion of Pluto is chaotic, *Science*, **241**, 433–437.

Sussman, G.J. and Wisdom, J. (1992) Chaotic evolution of the solar system, *Science*, **257**, 56–62.

Szebehely, V. and Peters, C.F. (1967) Complete solution of a general problem of three bodies, *Astron. J.*, **72**, 876–883.

Tanikawa, K. (1983) Impossibility of the capture of retrogarde satellites in the restricted three-body problem, *Celes. Mech.*, **29**, 367–402.

Tanikawa, K. (2000) A Search for collision orbits in the free-fall three-body problem II., *Celes. Mech. Dyn. Astron.*, **76**, 157–185.

Tanikawa, K. and Mikkola, S. (2000a) One-dimensional three-body problem via symbolic dynamics, *Chaos*, **10**, 649–657.

Tanikawa, K. and Mikkola, S. (2000b) Triple collision in the one-dimensional three-body problem, *Celes. Mech. Dyn. Astron.*, **76**, 23–34.

Tanikawa, K. and Yamaguchi, Y. (1987) Coexistence of periodic points in reversible dynamical systems on a surface, *J. Math. Phys.*, **28**, 921–928.

Tanikawa, K. and Yamaguchi, Y. (1989) Coexistence of periodic points in the Standard Map, *J. Math. Phys.*, **30**, 608–616.

Tanikawa, K. and Yamaguchi, Y. (1994) Stable and unstable manifolds in a zone of instability, *J. Math. Phys.*, **35**, 2408–2412.

Tanikawa, K. and Yamaguchi, Y. (1995) Stable and unstable manifolds in a zone of instability II., *J. Math. Phys.*, **36**, 3608–3612.

Tanikawa, K. and Yamaguchi, Y. (2001) Forcing relation of symmetric non-Birkhoff periodic points in Standard-like mappings. *Chaos*, in press.

Tanikawa, K., Manabe, S., and Broucke, R. (1989) On the origin of the planetary spin angular momentum by accretion of planetesimals: property of collision orbits, *Icarus*, **79**, 208–222.

Tanikawa, K., Kikuchi, N., and Sato, I. (1991) On the origin of the planetary spin by accretion of planetesimals II. collisional orbits at the Hill surface, *Icarus*, **94**, 112–125.

Tanikawa, K., Umehara, H., and Abe, H. (1995) A search for collision orbits in the free-fall three-body problem I. Numerical procedure, *Celes. Mech. Dyn. Astron.*, **62**, 335–362.

Tremaine, S. (1995) Is the solar system stable?, CITA–95–3, in *Proceedings of Rosseland Centenary Symposium of Astrophysics*, Oslo, June 16–17, 1994.

Ueda, Y. (1979) Randomly transitional phenomena in the system governed by Duffing's equation, *J. Stat. Phys.*, **20**, 181–.

Ueda, Y., Hayashi, C., and Akamatsu, N. (1973) Computor simulation of nonlinear ordinary differential equations and nonperiodic oscillations, *Electron. Comm. Japan*, **56A**, 27–.

Umehara, H. (1997) *The free-fall three-body problem: escape and collisions*, PhD thesis, The Graduate University for Advanced Studies, Hayama, Kanagawa, Japan.

Umehara, H. and Tanikawa, K. (2000) Binary and triple collisions causing instability in the free-fall three-body problem, *Celes. Mech. Dyn. Astron.*, **76**, 187–214.

Wako, Y. (1970) Interpretation of Kimura's annual Z-term, *Publ. Astron. Soc. Japan*, **22**, 525–.

Wetherill, G.W. and Stewart, G.R. (1989) Accumulation of a swarm of small planetesimals, *Icarus*, **77**, 330–357.

Whitmire, D.P., Matese, J.J., Criswell, L., and Mikkola, S. (1998) Habitable planet formation in binary star systems, *Icarus*, **132**, 196–203.

Whittaker, E.T.. (1904) *A Treatise on the Analytical Dynamics of Particles and Rigid Bodies*, Cambridge University press, (revised in 1952).

Williams, J.G. and Benson, G.S. (1971) Resonances in the Neptune-Pluto system, *Astron. J.*, **76**, 167–177.

Wisdom, J. (1982) The origin of the Kirkwood gaps: a mapping for asteroidal motion near the 3/1 commensurability, *Astron. J.*, **87**, 577–593.

Wisdom, J. (1983) Chaotic behavior and the origin of the 3/1 Kirkwood gap, *Icarus*, **56**, 51–74.

Wisdom, J. (1987a) Chaotic behavior in the solar system, *Proc. R. Soc. London Ser.*, **413**, 109–129.

Wisdom, J. (1987b) Urey prize lecture: chaotic dynamics in the solar system, *Icarus*, **72**, 241–275.

Wisdom, J. (1992) Long term evolution of the solar system, in *Chaos, resonance and collective dynamical phenomena in the solar system*, Kluwer Academic publishers, Dordrecht, 17–24.

Wisdom, J. and Holman, M. (1991) Symplectic maps for the N-body problem, *Astron. J.*, **102**, 1528–1538.

Wisdom, J. and Holman, M. (1992) Symplectic maps for the n-body problem: stability analysis, *Astron. J.*, **104**, 2022–2029.

Wisdom, J., Holman, M., and Touma, J. (1996) Symplectic correctors, in Marsden, J.E., Patrick, G.W., and Shadwick, W.F. eds., *Integration Algorithms and Classical Mechanics*, Vol. 10 of Fields Institute Communications, American Mathematical Society, Providence, Rhode Island, 217–244.

Woolard, E.M. (1953) Theory of the rotation of the Earth around its center of mass, *Astron. Pap. Amer. Ephem. Naut. Alm.*, **15**, 3–165.

Xia, Z. (1992) The existence of noncollision singularities in newtonian systems, *Annals of Mathematics*, **135**, 411–468.

Xia, Z. (1994) Arnold diffusion and oscillatory solutions in the planar three-body problem, *J. Differential Equations*, **110**, 289–321.

Yamaguchi, Y. and Tanikawa, K. (2000) Symmetrical non-Birkhoff period-3 orbits in the standard-like mappings, *Prog. Theor. Phys.*, **104**, 943–954.

Yamaguchi, Y. and Tanikawa, K. (2001) Geometrical approach to the splitting of separatrix for standard-like mappings, *Phys. Lett. A*, **280**, 33–36.

Yamanaka, Y. (1997) Stability of Uranian elliptical ring, in *Proc. 29th Symp. Celes. Mech.*, National Astronomical Observatory, Mitaka, Tokyo, Japan, 290–305.

Yoshida, J. (1972) Improved criteria for hyperbolic-elliptic motion in the general three-body problem, *Publ. Astron. Soc. Japan*, **24**, 391–408.

Yoshida, J. (1974) Improved criteria for hyperbolic-elliptic motion in the general three-body problem II., *Publ. Astron. Soc. Japan*, **26**, 367–377.

Yoshida, H. (1983a) Necessary conditions for the existence of algebraic first integrals I., *Celestial Mechanics*, **31**, 363–379.

Yoshida, H. (1983b) Necessary conditions for the existence of algebraic first integrals II., *Celestial Mechanics*, **31**, 383–399.

Yoshida, H. (1990) Construction of higher order symplectic integrators, *Phys. Lett. A*, **150**, 262–268.

Yoshida, H. (1992) Symplectic integration for Hamiltonian systems: basic theory, in *Chaos, resonance and collective dynamical phenomena in the solar system*, Kluwer Academic publishers, Dordrecht, 407–412.

Yoshida, H. (1993) Recent progress in the theory and application of symplectic integrators, *Celes. Mech. Dyn. Astron.*, **56**, 27–43.

Yoshida, H. (2001) Non-existence of the modified first integral by symplectic integration method, *Phys. Lett. A*, **282**, 276–283.

Yoshida, F., Nakamura, T., Fuse, T., Komiyama, Y., Yagi, M., Miyazaki, S., Okamura, S., Ouchi, M., and Miyazaki, M. (2001) First Subaru observations of sub-km main belt asteroids, *Publ. Astron. Soc. Japan*, in press.

Yoshinaga, K., Kokubo, E., and Makino, J. (1999) The stability of protoplanet systems, *Icarus*, **139**, 328–335.

Zare, K. and Chesley, S. (1998) Order and chaos in the planar isosceles three-body problem, *Chaos*, **8**, 475–494.

Ziglin, S.L. (1982) Splitting of separatrices, branching of solutions and nonexistence of an integral in the dynamics of a solid body, *Trans. Moscow Math. Soc.*, **41**, 283–298.

安部正真, 水谷仁, 大江昌嗣, 田村良明 (1992) 地球-月潮汐進化における太陽潮汐力の効果, 太陽系科学シンポジウム, **14**, 226–231.

安部正真 (1992) 地球月系潮汐進化に及ぼす海洋大陸配置の影響, 修士論文, 東京大学.

安部正真, 大江昌嗣 (1993) 地球-月系力学進化の問題点, 地球, **15**, 306–310.

阿部豊 (1997) 太陽系の起源, 松井孝典（編）, 比較惑星学, 岩波講座 地球惑星科学, No. 1, 岩波書店, 第 5 章, 219–280.

井田茂 (1997) 太陽系外惑星の発見：比較惑星系形成論の幕開け, 天文月報, **90**, 3, 116–121.

大貫義郎, 吉田春夫 (1994) 力学, 岩波講座 現代の物理学, No. 1, 岩波書店.

大野照文 (1993) Wells 以来—地球月力学系の歴史を記録した化石や堆積物の縞状構造解読 30 年の歩み, 地球, **16**, 53–59.

木下宙 (1993) ミランコヴィチ周期計算の基礎について, 地球, **15**, 314–315.

木下宙, 中井宏 (1994) 最果ての星・冥王星の奇妙な運動, 天文月報, **87**, 100–107.

木下宙 (1998) 天体と軌道の力学, 東京大学出版会.

熊澤峰夫, 吉田茂生, 伊藤孝士（編） (2002) 全地球史解読, 東京大学出版会.

小久保英一郎, 井田茂 (1997) 惑星集積 —微惑星から惑星へ—, 日本物理学会誌, **52**, 77–82.

小久保英一郎 (1999) 名残の月 —巨大衝突により形成された周地球円盤から—, 天文月報, **92**, 6, 296–303.

笹尾哲夫 (1979) 流体核をもつ地球の運動, 現代天文学講座 1 地球回転, 恒星社, 109–167.

笹尾哲夫 (1993) 地球の章動, 地球, **16**, 4–7.

谷川清隆, 相馬充 (2001) 推古 36 年の皆既日食記事の信憑性, 天体力学 N 体力学研究会集録, 国立天文台, 東京都三鷹市, *ibid.*, 2001 年 3 月 16 日–3 月 18 日, 草津セミナーハウス.

中井宏, 木下宙 (1995) 外惑星系の数値シミュレーション, 第 27 回天体力学研究会集録, 国立天文台, 三鷹, 東京, 1–9.

中島映至 (1980) 地球軌道要素の変動と気候, 気象研究ノート, **140**, 81–114.

長沢工 (1983) 天体力学入門（上・下）, 地人書館.

萩原雄祐 (1950) 天体力学の基礎 I (下), 河出書房, 東京.

福島登志夫 (1982) Newton 反復に対する安定な出発値とその Kepler 方程式への応用, 第 15 回天体力学研究会集録, 国立天文台, 33–36.

堀源一郎 (1988) 天体力学講義, 東京大学出版会.

山中右次 (1997) 天王星楕円リングの安定性, 修士論文, 日本大学理工学部.

山本義隆 (1997) 古典力学の形成 — ニュートンからラグランジュへ, 日本評論社, 東京.

吉田春夫 (1995) シンプレクティク数値解法, 数理科学, **384**, 37–46.

吉田春夫 (1997) ハミルトン力学系のためのシンプレクティク数値積分法, 共同研究「非線型現象の数理科学」・湘南レクチャー「非線型現象の数理」 論文集, 総合研究大学院大学, 68–83.

渡邊誠一郎, 井田茂 (1997) 比較惑星系形成論, 松井孝典（編）, 比較惑星学, 岩波講座 地球惑星科学, No. 12, 岩波書店, 第 3 章, 131–232.

電子航海暦

河合雅司，　門村英城，　渡部佳吾
（富山商船高等専門学校）

Computer Nautical Almanac

Masashi KAWAI, Hideki KADOMURA and Keigo WATANABE
Toyama National College of Maritime Technology,
Shinminato, Toyama, 933-0293, Japan
e-mail:mkawai@toyama-cmt.ac.jp (Masashi KAWAI)

Abstract

The learned frame of navigation was established through development of technique for astronomical positioning about 300 years ago. Therefore the astronomical navigation has been lectured in nautical colleges even in the today in which satellite navigation system has been most prevalent positioning system and astronomical positioning almost has not been used.

A computer nautical almanac has been developed to be used in the lecture on astronomical navigation. This almanac is fortran program to compute geocentric apparent places of the sun and planets which are based on JPL ephemerides and those of fixed stars used in the astronomical positioning which are based on Fifth Fundamental Catalogue(FK5).

It was made a comparison between apparent places of the computer nautical almanac and those of Japanese Ephemeris. The mean of differences between moon apparent places based on JPL DE200/LE200 and those of Japanese Ephemeris is about 2 milliseconds in right ascension and about 0.01 arc seconds in declination, and that between those based on JPL DE403/LE403 or DE405/LE405 and those of Japanese Ephemeris is about 1 millisecond in right ascension and about 0.02 arc seconds in declination.

１．電子航海暦(Computer Nautical Almanac)

海上で天体を観測して船の位置を求めるためには，太陽系天体や恒星の世界時に対する視位置(視赤経，視赤緯）及び恒星時に関する情報が必要である。航海者のためにこれらの情報を表にまとめたものが航海暦（Nautical Almanac）であり、公式に発行された最初の暦は、英国の1767年用航海暦"Nautical Almanac and Astronomical Ephemeris"であった。現在、毎年発行されている航海暦には、U.S. Naval Observatory(USNO:米国海軍天文台）と Her Majesty's Nautical Almanac Office (HMNAO)の米英航海暦"The Nautical Almanac" や日本の海上保安庁の"天測暦" 等がある。

天体を観測して位置を求める技術（天文航法）は１７～１８世紀にヨーロッパで開発された。そして、この天文航法の開発により航海学の学問体系が確立したと考えられている。人工衛星までの距離を電波で観測して位置を求める衛星航法が広く普及した現在、天文航法はほとんど利用されなくなっているが、測位計算の基礎を学ぶ上で非常に重要であり、現在でも商船系の教育機関で教えられている。教育に計算機が広く取り入れられるようになった現在、天測計算（天体観測データを船位に変換する計算）や航海算法等の航海計算は表ではなく計算機で行われるようになっており、計算機上で動作する航海暦すなわち電子航海暦があれば非常に便利である。海上保安庁発行の天測暦にはコンピュータ用天体位置計算式が紹介されているので、この計算式を用いて電子航海暦を作ることが可能であるが、この場合は毎年膨大な係数を計算機にキーボード入力する必要があり、非常に不便である。そこで、天測計算や人工衛星軌道計算等で利用出来る、係数のキーボード入力等を必要としない高精度電子航海暦を開発した。ここで、紹介する電子航海暦はＪＰＬエフェメリスと星表ＦＫ５を利用して、光行差、視差、太陽重力場による光の屈折等の補正を行い、４５個の常

用恒星と太陽系天体（太陽、水星、金星、火星、木星、土星、月）の視位置（視赤経・視赤緯)、グリニジ時角、Ｅ値等を計算するためのFortranプログラムである。

２．天体暦と星表

ここでは、電子航海暦の基礎となる天体暦と星表について簡単に説明する。　太陽系天体の位置を時間の関数として表現したものが天体暦（Ephemeris）であり、天体暦は基本暦（Fundamental ephemeris）と視天体暦（Apparent ephemeris）に分けることができる。基本暦は、天体の運動方程式を積分して得られる天体の幾何学的な位置・速度及び座標に関する情報であり、これらを直接観測することは出来ない。これに対して視天体暦は、基本暦の天体位置に光行差や重力場による光の屈折等の補正と座標変換を行うことにより得られる天体の視位置等の情報である。

現行の視天体暦には、海上保安庁の発行する天体位置表や米国海軍天文台と Her Majesty's Nautical Almanac Officeが発行する米英暦 The Astronomical Almanac 等がある。計算機上で利用する視天体暦としては、米国海軍天文台天文応用部(The Astronomical Applications Department of the U.S. Naval Observatory, http://aa.usno.navy.mil/AA/)により開発された電子天体暦(MICA:Multiyear Interactive Computer Almanac)が、Willmann-Bell, Inc. から24.95ドル（2000年現在）で販売されている。

基本暦については、米国航空宇宙局（NASA）のジェット推進研究所（Jet Propulsion Laboratory:JPL)が電子天体暦 JPL Planetary and Lunar Ephemerides を開発し一般に公開している。このＪＰＬ暦は現在最も優れた天体暦として定評があり、国際地球回転観測事業（International Earth Rotation Service:IERS）の標準天体暦となっており、その最新版は、DE405/LE405 である。

星表は、太陽系外の天体の位置と位置の時間変化を表にまとめたものであり、最も精度が高く現在広く利用されているのが、独天文計算研究所（Astronomisches Rechen-Institut:ARI）が刊行している第５基本星表（Fifth Fundamental Catalogue:FK5)でありＦＫ５には4652個の恒星の位置がカタログされている。このＦＫ５もＪＰＬ暦と同様に一般利用者に無料で公開されている。ＪＰＬ暦及びＦＫ５の入手先を次に示す。

(1) ＪＰＬエフェメリス（http://ssd.jpl.nasa.gov/eph_info.html)
(2) 星表ＦＫ５(http://www.ari.uni-heidelberg.de/fk6/)

天文航法で使用する４５個の常用恒星に関するＦＫ５をTable 1 に示す。

３．座標系

天体の位置は地球の赤道面及び春分点（地球赤道面と地球公転軌道面との交点）を基準とした座標系で定義されるが、地球赤道面及び春分点は歳差、章動によって宇宙空間に対して絶えず動いている。つまり、位置を表すために用いる座標系そのものが、動いているのである。従って天体の位置を表現する時は、座標系の基準時点（元期）を指定し、又章動を考慮しているかどうかを明示する必要がある。天体の位置を表す座標系には次のようなものがある。

(1) Mean of J2000.0 赤道面座標系(Mean of J2000.0 Coordinate System)

力学時2000年 1月 1.5日(J2000.0)における平均赤道面，平均春分点を基準とする座標系。ＪＰＬ暦DE200/LE200 及び星表ＦＫ５の座標系は、座標系原点を太陽系重心においたMean of J2000.0 赤道面座標系である。

(2) 国際天球座標系(The International Celestial Reference System;ICRS)

銀河系外の電波星を利用して宇宙空間に固定された天球座標系であり、１９９８年から国際天文学連合(IAU)により採用されている。座標系の原点は太陽系重心であり、その赤道面及び赤経の原点は、J2000.0の平均赤道面及び平均春分点とほぼ一致している。J2000.0平均赤道面の極は、ICRSの極に対して１２時の方向へ17.3mas(milli arc second)、１８時の方向へ 5.1masずれており、J2000.0平均春分点の方向はICRSの赤経の原点に対して78masずれている。(ICRSにおけるJ2000.0平均春分点の赤経は78mas。)

ＪＰＬ暦DE403/LE403、DE405/LE405及び星表ＦＫ６の座標系はICRSである。

(3) Mean of Date 赤道面座標系(Mean of Date Coordinate System)

Table 1 Mean Places of Civil Stars in FK5 (2000 Jan. 1d 12h TT)

$\alpha_{2000.0}$: Right ascension , $d_{2000.0}$: Declination

PM(α) : Proper motion in right ascension [s / Julian century]

PM(d) : Proper motion in declination ["/ Julian century]

π : Parallax ["] , V_R : Radial velocity [km / s]

Star Name (FK5 No.)	$\alpha_{2000.0}$	PM(α)	$d_{2000.0}$	PM(d)	π	V_R
	H M S	s	. . ..	..	..	km/sec
1 POLARIS (907)	2 31 48.704	19.877	89 15 50.72	-1.52	0.0030	-17.40
2 KOCHAB (550)	14 50 42.346	-0.763	74 09 19.78	1.22	0.0310	16.90
3 DUBHE (417)	11 03 43.666	-1.675	61 45 03.22	-6.65	0.0310	-8.90
4 β CASSIOP. (2)	0 09 10.695	6.827	59 08 59.18	-18.09	0.0720	11.80
5 MERAK (416)	11 01 50.482	0.988	56 22 56.65	3.40	0.0420	-12.00
6 ALIOTH (483)	12 54 01.748	1.328	55 57 35.47	-0.58	0.0080	-9.30
7 SCHEDIR (21)	0 40 30.450	0.636	56 32 14.46	-3.19	0.0090	-3.80
8 MIZAR (497)	13 23 55.539	1.411	54 55 31.38	-2.00	0.0370	-9.00
9 A. PERSEI (120)	3 24 19.365	0.246	49 51 40.34	-2.46	0.0290	-2.40
10 BENETNASCH (509)	13 47 32.434	-1.249	49 18 47.95	-1.09	0.0040	-10.90
11 CAPELLA (193)	5 16 41.353	0.728	45 59 52.90	-42.47	0.0730	30.20
12 DENEB (777)	20 41 25.917	0.027	45 16 49.31	0.23	0.0000	-4.60
13 VEGA (699)	18 36 56.332	1.726	38 47 01.17	28.61	0.1230	-13.90
14 CASTOR (287)	7 34 35.997	-1.347	31 53 18.53	-9.87	0.0720	6.00
15 ALPHERATZ (1)	0 08 23.265	1.039	29 05 25.58	-16.33	0.0240	-11.70
16 POLLUX (295)	7 45 18.946	-4.740	28 01 34.26	-4.59	0.0930	3.30
17 α COR. BOR. (578)	15 34 41.276	0.906	26 42 52.94	-8.86	0.0430	1.70
18 ARCTURUS (526)	14 15 39.677	-7.714	19 10 56.71	-199.84	0.0900	-5.20
19 ALDEBARAN (168)	4 35 55.237	0.439	16 30 33.39	-18.97	0.0480	54.10
20 MARKAB (871)	23 04 45.658	0.436	15 12 18.90	-4.25	0.0300	-3.50
21 DENEBOLA (444)	11 49 03.580	-3.422	14 34 19.35	-11.41	0.0760	-0.10
22 A OPHIUCHI (656)	17 34 56.076	0.822	12 33 36.14	-22.64	0.0560	12.70
23 REGULUS (380)	10 08 22.315	-1.693	11 58 01.89	0.64	0.0390	3.50
24 ALTAIR (745)	19 50 47.002	3.629	8 52 06.03	38.63	0.1980	-26.30
25 BETELGEUSE (224)	5 55 10.307	0.173	7 24 25.35	0.87	0.0050	21.00
26 BELLATRIX (201)	5 25 07.857	-0.059	6 20 58.74	-1.39	0.0260	18.20
27 PROCYON (291)	7 39 18.113	-4.755	5 13 30.06	-102.29	0.2880	-3.20
28 RIGEL (194)	5 14 32.268	0.003	-8 12 05.98	-0.13	0.0000	20.70
29 α HYDRAE (354)	9 27 35.247	-0.093	-8 39 31.15	3.28	0.0170	-4.30
30 SPICA (498)	13 25 11.587	-0.278	-11 09 40.71	-2.83	0.0210	1.00
31 SIRIUS (257)	6 45 08.871	-3.847	-16 42 57.99	-120.53	0.3750	-7.60
32 β CETI (22)	0 43 35.372	1.637	-17 59 11.82	3.25	0.0570	13.10
33 ANTARES (616)	16 29 24.439	-0.071	-26 25 55.15	-2.03	0.0190	-3.20
34 σ SAGITTARII (706)	18 55 15.924	0.099	-26 17 48.23	-5.42	0.0000	-11.00
35 FOMALHAUT (867)	22 57 39.055	2.551	-29 37 20.10	-16.47	0.1440	6.50
36 λ SCORPII (652)	17 33 36.534	-0.011	-37 06 13.72	-2.92	0.0000	0.00
37 CANOPUS (245)	6 23 57.119	0.245	-52 41 44.50	2.07	0.0180	20.50
38 α PAVONIS (764)	20 25 38.852	0.082	-56 44 06.38	-8.91	0.0000	2.00
39 ACHERNAR (54)	1 37 42.852	1.173	-57 14 12.18	-3.47	0.0230	19.00
40 β CRUCIS (481)	12 47 43.237	-0.631	-59 41 19.46	-1.36	0.0000	20.00
41 β CENTAURI (518)	14 03 49.408	-0.426	-60 22 22.79	-1.93	0.0160	-12.00
42 α CENTAURI (538)	14 39 35.885	-49.826	-60 50 07.44	69.93	0.7510	-22.20
43 α CRUCIS (462)	12 26 35.871	-0.524	-63 05 56.58	-1.21	0.0000	-11.20
44 α TRI. AUST. (625)	16 48 39.869	0.260	-69 01 39.82	-3.40	0.0240	-3.60
45 β CARINAE (348)	9 13 11.957	-3.108	-69 43 01.95	10.78	0.0380	-5.00

瞬時（観測時）の平均赤道面、平均春分点を基準とする座標系。章動は考慮していない。

(4) True of Date 赤道面座標系(True of Date Coordinate System)

瞬時の真の赤道面、真の春分点を基準とする座標系。歳差と章動を考慮した座標系である。この座標系における天体の位置は真位置である。

真位置(True Place)：固有運動、歳差、章動を考慮した天体の位置

天測暦に掲載されている天体位置は地心視位置でありこれは、恒星の場合は真位置に年周視差、年周光行差、重力場による光の曲がりを補正した位置であり、太陽系天体の場合は、光差、年周光行差、重力場による光の曲がりを補正した位置である。分かりやすく言えばある時刻に見えている天体と地球中心とを結ぶ直線と地球表面との交点（地位）の緯度（地心緯度）が視赤緯で経度が（視赤経）－（グリニジ視恒星時）である。

地球を球と仮定し、更に地球極位置の変動（極運動）を無視すると、地位と視位置（視赤緯，視赤経）との間には次の関係式が成立する。

$l_S = d$，　$L_S = \alpha - \theta_G$，$\alpha = \theta_G - (U+E)$，　$h_G = U+E$　　(1)

l_S, L_S：天体の地位の緯度, 経度　U：世界時　E：E値

α, d：天体の視赤経, 視赤緯　θ_G: グリニジ視恒星時　h_G: グリニジ時角

天測暦には太陽，月，惑星，常用恒星（45個）の視赤緯と E値が掲載されており、これらの値を用いて (1)式により天体の地位の緯度，経度を求めて、天測位置の計算を行っている。

３．１　座標系の変換

天体の地心視位置を得るためには、国際天球座標系及びMean of J2000.0 赤道面座標系をTrue of Date 赤道面座標系に変換する必要がある。電子航海暦で用いられた座標変換式について簡単に紹介する。

$$[MJ2000] = [P]\cdot[N]\cdot[TDE] \quad (2)$$

$$[ICRS] = R_Z(\theta_Z)\cdot R_Y(\theta_Y)\cdot R_X(\theta_X)\cdot[P]\cdot[N]\cdot[TDE] \quad (3)$$

$$\theta_X = 5.1\text{mas},\ \theta_Y = -17.3\text{mas},\ \theta_Z = 78.0\text{mas}$$

$$[P] = R_Z(\varsigma_A)\cdot R_Y(-\theta_A)\cdot R_Z(Z_A)$$

$$[N] = R_X(-\varepsilon_A)\cdot R_Z(\Delta\varphi)\cdot R_X(\varepsilon_A + \Delta\varepsilon)$$

$$\varsigma_A = 2306.''2181\cdot t + 0.''30188\cdot t^2 + 0.''017998\cdot t^3$$

$$\theta_A = 2004.''3109\cdot t - 0.''42665\cdot t^2 - 0.''041833\cdot t^3$$

$$Z_A = 2306.''2181\cdot t + 1.''09468\cdot t^2 + 0.''018203\cdot t^3$$

$$\varepsilon_A = 84381.''448 - 46.''8150\cdot t - 0.''00059\cdot t^2 + 0.''001813\cdot t^3$$

$$t = (TT - TT_{2000.0})/36525$$

[MJ2000]: Mean of J2000.0 赤道面座標系

[TDE]: True of Date 赤道面座標系

[ICRS]: 国際天球座標系(ICRS)

$R_X(\theta)$: X軸周りの座標回転マトリクス　$R_Y(\theta)$: Y軸周りの座標回転マトリクス

$R_Z(\theta)$: Z軸周りの座標回転マトリクス

$\Delta\varphi$: 黄経の章動(IAU 1980)　$\Delta\varepsilon$: 黄道傾角の章動(IAU 1980)

TT: 地球時におけるユリウス日

$TT_{2000.0}$: 地球時2000年 1月1.5日のユリウス日

座標軸周りの座標回転式は、回転前の座標を(X, Y, Z)、回転後の座標を(X', Y', Z')とすると次のようになる。

＜X軸周りの座標回転＞

$$R_X(\theta)=\begin{pmatrix}1 & 0 & 0\\ 0 & \cos\theta & \sin\theta\\ 0 & -\sin\theta & \cos\theta\end{pmatrix},\qquad \begin{pmatrix}X'\\ Y'\\ Z'\end{pmatrix}=R_X(\theta)\begin{pmatrix}X\\ Y\\ Z\end{pmatrix}$$

＜Y軸周りの座標回転＞

$$R_Y(\theta)=\begin{pmatrix}\cos\theta & 0 & -\sin\theta\\ 0 & 1 & 0\\ \sin\theta & 0 & \cos\theta\end{pmatrix},\qquad \begin{pmatrix}X'\\ Y'\\ Z'\end{pmatrix}=R_Y(\theta)\begin{pmatrix}X\\ Y\\ Z\end{pmatrix}$$

＜Z軸周りの座標回転＞

$$R_Z(\theta)=\begin{pmatrix}\cos\theta & \sin\theta & 0\\ -\sin\theta & \cos\theta & 0\\ 0 & 0 & 1\end{pmatrix},\qquad \begin{pmatrix}X'\\ Y'\\ Z'\end{pmatrix}=R_Z(\theta)\begin{pmatrix}X\\ Y\\ Z\end{pmatrix}$$

４．時刻

時刻は、周期的な物理現象を観測することにより決定することが出来る。原子時はセシウム１３３原子の振動を、世界時や恒星時は地球自転運動を、力学時は太陽系天体の公転運動を観測することにより得られる。天体暦で使用される時刻は力学時であり、これは天体運動方程式を積分して太陽系天体の位置を求める時の時間引数である。１９６０年頃から１９８０年代中頃までは、天体暦の時刻として暦表時が使用されていたが、相対性理論（１９１５年）により時間と空間は分離することが出来ず、運動速度や加速度（重力）の大きさにより時間の進み方が変化し、時間の進み方が場所に依存していることが明らかになってきた。そこで、地球のジオイド上の固有時である地球力学時(Terrestrial Dynamical Time:TDT)すなわち地球時(Terrestrial Time:TT)及び太陽系重心における太陽系力学時(Solar System Barycentric Dynamical Time:TDB)なるものを定義し、１９８０年代中頃以降は暦表時に代わって、これらの力学時が使用されている。(太陽系力学時の平均的な進み方は、理論的に地球時よりも遅いが、これでは天体暦の扱いに不都合が生じるので、時刻の平均的な進み方は地球時と同じになる様に定義されている。)地球時と太陽系力学時の関係は次式で与えられる。

$$TDB=TDT+1.66\cdot\sin(M_A)\ \ [ms] \qquad (4)$$

TDB：太陽系力学時,　　TDT:地球力学時(地球時)

M_A:地球･月重心の平均近点離角　ms：ミリ秒

一般的に、太陽系重心を原点とした赤道面座標系で幾何学的天体位置を求める天体暦（例えばＪＰＬ暦）における時間引数は、太陽系力学時が用いられている。又、地球力学時と国際原子時（International Atomic Time:TAI）の関係については、１９７６年に開かれた国際天文学連合第１６回総会の勧告により、次のように定義されている。

1997年 1月 1日 0時 TAI において,　TDT-TAI=32.184秒

(1997年 1月 1.0日 TAI= 1997年 1月 1.0003725日 TDT)

天体位置計算で使用される力学時に対し、我々の日常生活で使用される時刻は世界時（Universal Time）である。世界時と国際原子時の関係は、国際地球回転事業（International Earth Rotation Service:IERS）のＷｅｂサイト（http://www.iers.org/）で公表されている地球回

転パラメタを用いて得ることが出来る。そして、グリニジ視恒星時（Greenwich Apparent Sidereal Time）と世界時の関係は次式で定義されている。

$$GAST=12^H+UT1+\alpha_m+\Delta\varphi\cdot\cos\varepsilon \quad (5)$$

$$GMST=12^H+UT1+\alpha_m$$

$$\varepsilon=\varepsilon_A+\Delta\varepsilon$$

$$\alpha_m=18^H41^M50.54841^S+8640184.812866^S\cdot Tu+0.093104^S\cdot Tu^2-0.0000062^S\cdot Tu^3$$

GAST：グリニジ視恒星時　　UT1：世界時

α_m: グリニジ基準天体の瞬時の平均春分点に対する赤経

Tu：2000年 1月 1日12時UT1から36525日単位で測った世界時

$\Delta\varphi$：黄経の章動　　ε：真黄道傾角　　ε_A: 平均黄道傾角　　$\Delta\varepsilon$：黄道傾角の章動

ここで、グリニジ基準天体とは、赤道上を一様に運動する仮想的な太陽であり、この仮想太陽のグリニジ時角から１２時間を引いたものが世界時である。

４．１　航海暦における時刻の変換

航海暦（NAUT200,NAut403）は世界時、航海暦（NADT200,NADT403）は地球力学時に対する天体位置を計算するようになっているが、位置計算過程で地球力学時と世界時の変換を行う必要がある。1987年11月20日から2000年12月 1日 0時まで（2000年12月 1日 0時は含まない）は、IERS BULLETIN-B の地球回転パラメタを用いて次式により世界時と地球力学時との変換を行ない、2000年12月 1日 0時以降については、IERS BULLETIN-A に紹介されている式により世界時と協定世界時の差を予測して変換している。

（電子航海暦の地球回転パラメタファイル"IERSEOP.DAT"には、1987年11月20日から2000年12月 1日までの地球回転パラメタが入っており、2000年12月 1日以降については、予測式によりパラメタを予測して計算している。そして、1987年11月20日以前についてはデータがないので時刻の変換が出来ない。）

＜2000年12月 1日 0時以前＞

$$UT1R=UT1-\Delta UT1,\quad \Delta UT1=\sum_{i=1}^{41}A_i\sin\xi_i \quad (6)$$

$$UTC=UT1R-(UT1R-UTC)$$

$$TDB=TDT+1.66\cdot\sin(M_A)\ [ms]$$

TDT-UTC：IERS BULLETIN Cの値，　UT1R-UTC：IERS BULLETIN Bの値

A_i, ξ_i (i=1～41)：IERS TECHNICAL NOTE 21 参照

TDT-UTCは、IERS BULLETIN C の値を使用し、(UT1R-UTC)は、IERS BULLETIN-B の値を使用する。ΔUT1は、地球回転の潮汐変動であり、係数A及びξはIERS TECHNICAL NOTE 21 に示されている。

＜2000年12月 1日 0時以降＞

$$UT1-UTC=0.1108-0.00070\cdot(MJD-51862)-(UT2-UT1)\ [sec] \quad (7)$$

$$UT2-UT1=0.0220\cdot\sin(2\pi T)-0.0120\cdot\cos(2\pi T)-0.0060\cdot\sin(4\pi T)+0.0070\cdot\cos(4\pi T)\ [sec]$$

$$T=2000.000+(MJD-51544.03)/365.2422$$

$$TDT-UTC=64.184\ [sec]$$

$$TDB=TDT+1.66\cdot\sin(M_A)\ [ms]$$

MJD：修正ユリウス日　UTC：協定世界時　UT1：世界時

TDT：地球力学時　　TDB：太陽系力学時　π：円周率

M_A: 地球・月重心の平均近点離角　　ms：ミリ秒

地球回転パラメタには、速報版であるBULLETIN-A(Rapid data and predictions)と確定版であるBULLETIN-B(Monthly earth orientation data)及び BULLETIN-C(Leap second announcement)があり、インターネットで公開されている。そのURL は、http://www.iers.org/iers/products/eop/である。

5．地心視位置の計算方法

電子航海暦では、太陽系天体の位置についてはＪＰＬ暦、常用恒星の位置については星表ＦＫ５に基づいている。そして、ＪＰＬ暦DE200/LE200 及び星表ＦＫ５は、座標系原点を太陽系重心においたMean of J2000.0 赤道面座標系であり、ＪＰＬ暦DE403/LE403、DE405/LE405 の座標系は、国際天球座標系（ICRS）である。ここでは、これらの座標系における天体位置を天体位置表の基礎理論に基づいて地心視位置に変換している。変換方法については天体位置表に詳しく解説されているので、その方法の概略について簡単に紹介する。（以下、地心視位置を単に視位置と表記する。）

＜１＞　太陽系天体の視位置計算手順

(1) 天体(X)の視位置を求める日時を世界時で入力し、これを太陽系力学時に変換して時刻Ｔを求める。（Ｔ：ユリウス日）世界時と力学時の変換方法については、３．２に示されている。
(2) 光差方程式を解き、天体(X)を光が発した時刻Ｔ’を求める。この時、地球、天体(X)、及び太陽の位置は、ＪＰＬ暦で求める。（重力により光の経路を曲げる天体として太陽のみを考慮した。）
(3) 時刻Ｔにおける地球重心から時刻Ｔ’における天体(X)への方向ベクトルを求める。この時、太陽重力場による光の曲がりの補正を行う。
(4) 方向ベクトルをLorentz変換して光行差を補正する。
(5) 歳差と章動による座標回転を行い、国際天球座標系及びMean of J2000.0 赤道面座標系をTrue of Date 赤道面座標系に変換する。（座標変換については、２．４参照）
(6) 方向ベクトルを球面座標（赤経、赤緯）に変換して、天体(X)の視赤経と視赤緯を得る。

＜２＞　常用恒星の視位置計算法

(1) 星表ＦＫ５の位置（赤経、赤緯）を方向ベクトルに変換する。
(2) 固有運動と年周視差の補正を行なうを得る。
(3) 太陽系天体の場合と同様に、太陽重力場による光の曲がりを補正する。

(4)～(6)の手順については太陽系天体の場合と同じである。又、常用恒星の場合は、地球力学時と太陽系力学時の差は無視している。

6．電子航海暦のインストール

今回開発された電子航海暦はFORTRANプログラムであり、次の３種類がある。

(1) ＪＰＬ暦DE200/LE200と星表ＦＫ５による電子航海暦

常用恒星の位置は星表FK5、太陽系天体についてはDE200/LE200を用いた電子航海暦。ＪＰＬ暦DE200/LE200は、NASAジェット推進研究所の Standishによって開発されたもので1990年当時に国立天文台の大型汎用計算機 FACOM M780/10S 上で動作していたものである。又、ＪＰＬ暦は、国際地球回転観測事業(International Earth Rotation Service, IERS) の標準天体暦になっている。世界時で指定した日時に対する天体の地心視位置を計算するプログラムNAUT200.FORと、力学時で指定した日時に対する天体の地心視位置を計算するプログラムNADT200.FORがある。

(2) ＪＰＬ暦DE403/LE403と星表ＦＫ５による電子航海暦

常用恒星の位置は星表FK5、太陽系天体についてはDE403/LE403を用いた電子航海暦で、世界時で指定した日時に対する天体の地心視位置を計算するプログラムNAUT403.FORと、力学時で指定した日時に対する天体の地心視位置を計算するプログラムNADT403.FORがある。

(3) ＪＰＬ暦DE403/LE403と星表ＦＫ５による電子航海暦

常用恒星の位置は星表FK5、太陽系天体についてはDE405/LE405を用いた電子航海暦であり、DE405/LE405はＪＰＬ暦の最新版である。世界時で指定した日時に対する天体の地心視位置を計算するプログラムNAUT405.FORと、力学時で指定した日時に対する天体の地心視位置を計算するプログラムNADT405.FORがある。

これらの航海暦をインストールするためには、事前にFORTRANコンパイラを準備する必要があり、現在のところ最終的に得られるものは、天体のグリニジ時角（GREENWICH HOUR ANGLE)、Ｅ値、赤緯

(DECLINATION) 及び天体視位置 (TRUE OF DATE COORDINATE(APPARENT PLACE)) である。次にインストール方法とその使用方法について説明する。

6．1　インストール手順

インターネット経由 (http://www.toyama-cmt.ac.jp/~mkawai/) で下記の全てのファイルをダウンロードする。

＜説明書＞	READ.DOC
＜共通データファイル＞	CIVILSTAR.FK5, IERSEOP.DAT
＜NAUT200関係ファイル＞	NAUT200.FOR, NADT200.FOR, CONVDE20.FOR
	DE200.DAT, X200.BAT
＜NAUT403関係ファイル＞	NAUT403.FOR, NADT403.FOR, ASC2EPH.FOR
	INFILE.403, X403.BAT
＜NAUT405関係ファイル＞	NAUT405.FOR, NADT405.FOR, ASC2EPH.FOR
	INFILE.405, X405.BAT

インストール方法等についてはテキストファイルREAD.DOCに説明されている。ここでは例として電子航海暦NAUT403のインストール及び実行方法について紹介する。

＜NAUT403のインストール＞

NAUT403.FOR 及び ASC2EPH.FOR　をコンパイル&リンクする。

バッチファイル X403.BAT を実行する。

NAUT403 実行KEY (NAUT403を起動) でプログラムが動くので、日付、時間 (世界時) 及び天体番号を入力する。その一例を次に示す。

```
>NAUT403
 INPUT DATE - YEA,MON,DAY       ?
 2000,4,1
 INPUT TIME [UT] - H. M. S.     ?
 2,0,0

 ＜恒星及び太陽系天体の天体番号が画面に表示される＞
 INPUT STAR NUMBER              ?
 100

*** STAR NAME(100): SUN           ***
 DATE:2000YEAR  4MON.  1DAY   TIME[UT] :  2H  0M  0.00S
 GREENWICH HOUR ANGLE= 13H 56M  6.747S (E= 11H 56M  6.747S)
          DECLINATION=  4D 36.41M
 G.TRUE SIDEREAL TIME= 14H 38M 57.589S

 DATE:2000YEAR  4MON.  1DAY   TIME[TDT]:  2H  1M  3.91S
 TRUE OF DATE COORDINATE(APPARENT PLACE)
 R.ASCENSION=  0H 42M 50.842S   DECLINATION=  4D 36M 24.43S
```

7．天体位置表との比較

電子航海暦を実行したときに、最後に表示される天体位置 TRUE OF DATE COORDINATE(APPARENT PLACE)が天体の視赤経と視赤緯であり、海上保安庁発行の天体位置表に記載されている天体視位置 (視赤経、視赤緯) と同じものである。天体位置表では、力学時に対する視位置が掲載されており、これと比較するためには電子航海暦により、力学時に対する天体視位置を計算する必要がある。2000年 1月 1日から12月31日までの 366日間の力学時 (地球時) 0時における月の天体位置表と電子航海暦による地心視位置の差を求めた。ＪＰＬ暦DE200/LE200に基づく電子航海暦NADT200と天体位置表との差は視赤経で0.002秒、視赤緯で0.01″程度、ＪＰＬ暦DE403/LE403に基づく電子航海暦NADT403及びＪＰＬ暦DE405/LE405に基づく電子航海暦NADT405と天体位置表との差は視赤経で0.001秒、視赤緯で0.02″程度であった。これらの結果からＪＰＬ暦DE403/LE403及びDE405/LE405の月位置の天体位置表との差は、ＪＰＬ暦DE200/LE200に比べて赤経では小さくなっているが、赤緯では逆に

大きくなっていることが分かる。

８．結言

ここで紹介された電子航海暦は、太陽系天体についてはＪＰＬ暦に基づいている。DE403/LE403以降のＪＰＬ暦は、座標系が Mean of J2000.0赤道面座標系から国際天球座標系(ICRS)に変更されており、ICRSとTrue of Date 赤道面座標系との変換は(3)式により行った。(3)式の θ_X, θ_Y, θ_Z の符号は逆になっているように思われるが、地心視位置の値が天体位置表（海上保安庁発行）の値と一致するように変換するためには(3)式を用いる必要がある。この様に座標変換に関する若干の疑問点はあるが、この電子航海暦により天体位置表とほぼ同じ精度で、天文航海学で利用される天体の地心視位置が得られることを確認した。

商船学校等の船舶職員養成施設は船舶職員法施行規則及びその告示で最新の天測暦を備えることが義務付けられており、毎年海上保安庁水路部が発行する天測暦を購入する必要がある。そこで、天文航海学の授業及び船舶職員法施行規則に対応するために開発されたのがこの電子航海暦である。本航海暦は、インターネットで公開し毎年更新していく予定である。商船学校等の機関で広く利用して頂ければ幸いである。

謝辞

本報告書をまとめるにあたり、貴重な助言をして頂いた国立天文台の中井宏氏に心から感謝の意を表する。

参考文献

(1) 海上保安庁水路部：天体位置表，海上保安庁.

(2) 河合雅司，中谷俊彦：”静止衛星を測位に用いた場合の座標変換と測位計算”，日本航海学会誌，第119号，平成６年３月.

(3) Minoru Sasaki:"ALGORITHM FOR DETERMINATION OF SATELLITE ORBIT AND GEODETIC PARAMETERS BY USING LASER RANGING DATA AND PRELIMINARY RESULTS OF ITS APPLICATION", Report of Hydrographic Researches, No.19,March 1984.

(4) Dennis D. McCarthy : IERS TECHNICAL NOTE 21, Central Bureau of IERS- Observatoire de Paris, 1996.

Reliability of the totality of the eclipse in AD628 in Nihongi
推古天皇36年の皆既日食記事の信憑性

Kiyotaka TANIKAWA and Mitsuru SOMA
National Astronomical Observatory
Mitaka, Tokyo, 181-8588, Japan
谷川清隆, 相馬 充(国立天文台)

Abstract

It is generally accepted that the solar eclipse on April 10, 628 (the second day, the third month, the thirty-sixth year of Empress Suiko) recorded in Nihongi is not total but partial though it is written as a total eclipse. We argue for the record appealing to the contemporary total or near total eclipses in Chinese history books and Japanese occultation observation. If the value of the tidal term in the lunar longitude(the coefficient of T^2 term) is different from the present value by about $-2''/\mathrm{cy}^{-2}$, then there disappears an apparent contradiction of ΔT around AD600 derived from lunar and solar eclipses. Grazing occultation data are found to be useful.

1 序.

三月丁未朔戊申, 日有蝕盡之

この記述は日本書紀の推古天皇三十六年の項にある. 長い伝統を持つ中国史書の規則どおりに読むと, これは皆既日食である. 計算によると (渡邊敏夫, 日食月食宝典), 確かにこの日皆既日食はあった. 西暦 (ユリウス暦)628 年 4 月 10 日の日食である. 問題は皆既帯が日本列島上を通ったかどうかである.

1.1 この日食記事を取り上げた理由

1.1.1 日本書紀の最初の日食記事

書き手が意識して書いた日食記事として最初のものであることを注意しておく. 帝紀の書き方に則っている. 日本書紀, 神代上に有名な天の岩戸記事がある. 「是時, 天照大神..., 入干天石窟, 閉磐戸而幽居焉」これは江戸時代以来, 日食記事であると理解する研究者も多い. ただしこの記事は「日食」を意味する記事であって, 「日食記事」ではない.

1.1.2 倭国の歴史上重要な時点に対応する

倭国の興隆の歴史を中国の史書に見る. 以下に掲げる魏志倭人伝, 宋書倭国伝, 隋書たい国伝の記事を見ればわかるように, 3 世紀, 5 世紀, 7 世紀と順に倭は国として成長していることがわかる. 7 世紀の大業三年 (西暦 607 年) の倭からの国書は独立宣言であると見ることができる. これは大方の歴史学者の認めるところである (西嶋, 1994). ただし独立することの意味については意見が別れるように窺える. 独立国家は何をするか. 筆者の考えによれば, (1) 法律を定めること, (2) 度量衡を定めること, (3) 暦を作ること, および (4) 歴史を書くこと, である. 最初の 3 項目は必須である. これらは同一国内の住人同士に会話なり契約なりを成立させるため必要な規則だからである. 第 4 項目は時間軸方向にも国としてのまとまりを示すために必要な事業であるとの解釈ができる. もっとまともな解釈があるかもしれない. 中国に属している間は中国のものを借用すればよい. 独立直後は中国の制度をまねる. ただ中国には複数の国が並立することがあるから, どの国から制度を輸入するかは輸入する側の事情によるだろう.

中国は有史以来, 日食, 月食, その他の天文現象を記録し続けてきた. この記録は上記項目 (3) と (4) に関係して重要視された. とくに暦の狂いを補正するためには日食と月食の観測データが重要である. 朔 (新月) が月初からずれると改暦が必要になる. 改暦のためには長期にわたる観測データが必要である. 独立国家はこのデータを独自に持たなければならない. 独立した倭国はデータをすでに蓄積していたか? それはわからない. だが, 独立宣言 (西暦 607 年) 直後の皆既日食記事 (西暦 628 年) はデータを蓄積しようという姿勢を見せたと思えないか? それはほぼ確実である. というのは, その後, 天文観測記事が連綿として続くからである (神田 茂, 日本天文史料, 1978). 日食記事だけではない. 彗星 (634 年), 流星 (637 年), 月食 (643 年), 月星接近 (640 年), 惑星現象 (692 年), 星昼見 (702 年) などの観測も始まった. 暦を作る作業は複雑であり, 江戸時代, 渋川春海による貞享暦 (1685 年) に至ってようやく日本独自の暦を作ることができた. それ以前はいつも中国暦を用いていた. 中国の暦の精度が良かったからである (薮内, 1969).

3 世紀 (魏志倭人伝, 参考文献 11) – 卑弥呼

- 倭人は帯方の東南大海の中にあり. 山島に依りて国邑をなす. 旧百余国. 漢の時朝見する者あり, 今, 使訳通ずる所三十国. ...
- 景初二年六月 (紀元 238 年), 倭の女王, 大夫難升米等を遣わし, 郡に詣り, 天子に朝献せんことを求む. ...
- 景初二年十二月「... 汝がある所はるかに遠きも, 乃ち使を遣わし貢献す. 我れ甚だ汝を哀れむ. 今汝をもって親魏倭王となし, ...」

5 世紀 (宋書倭国伝, 参考文献 12) – 倭の五王

- 倭国は高驪の東南大海の中にあり. 世々貢職を修む.
- 高祖の永初二年 (421 年), 詔していわく, 「倭讃, 万里を修む. ..., 除授を賜うべし」と.
- 太祖の元嘉二年 (425 年), . .. 讃死して弟珍立つ. ... 詔して安東将軍・倭国王に除す.
- (元嘉) 二十年 (443 年), 倭国王済, 使を遣わして奉献す. また以って安東将軍・倭国王となす.
- (元嘉) 二十八年 (451 年), ... 済死す. 世子興, 使を遣わして貢献す.

- 世祖の大明六年 (462 年), 詔していわく, 「倭王世子興, ..., 安東将軍・倭国王とすべし. 」興死して弟武立ち, ... 安東大将軍・倭国王と称す.
- 順帝の昇明二年 (478 年), 使を遣わして表を上げる. いわく「封国は偏遠にして, ... 窃かに自ら開府儀同三司を仮し, ...」 ... 安東大将軍・倭国王に除す.

7 世紀 (隋書たい国伝, 参考文献 13) – 日出処天子致書日没処天子無恙

- 倭国は百済・新羅の東南にあり. ... 則ち「魏誌」のいわゆる邪馬台なる者なり.
- 開皇二十年 (600 年), 倭王あり. 姓は阿毎, 字は多利思比孤, 阿輩き弥と号す.
- **大業三年 (607 年)**, その王多利思比孤, 使を遣わして朝貢す. ... その国書にいわく, 「日出処天子致書日没処天子無恙」と. 帝, ... 「夷蛮の書, 無礼なる者あり. 復た以て聞するなかれ」と.
- 大業四年 (608 年), 文林郎はい清を遣わして倭国に使せしむ.
- その後遂に絶つ.

1.1.3 千年規模の地球自転変動, 月運動を求めること

現在, 月レーザー測距観測により, 月が徐々に遠ざかっていること, それが年に数 cm(3.8cm) であることも知られている. このことから, 月の軌道周期の増加率も計算できる. この増加率は千年前も同じであったのか. また地球自転は遅くなっている. この遅くなり方は, 現在と千年前と同じであろうか. このような問題に答えるための理論はない. 正確に言うと, 理論の精度は足りない. 海あり大気あり, 地下にマグマあり, 流体核ありのこの地球と月, 太陽, 惑星の相互作用を解いて, 地球の自転運動を千年にわたって追う. これは現代の科学ではまだできないことである. 唯一, 日食, 月食, その他の天文現象の古代記録を使うと, 自転がどうであったか, 月の公転周期がどうであったかを決めることができる.

1.2 この記事に関する通説

通説では, 推古天皇三十六年の皆既日食記事は誇張表現であるとされている (渡邊敏夫「日食月食宝典」,1979; 内田正男「日本暦日原典」, 1975; 斉藤国治「星の古記録」, 1982). 代表して内田正男氏の見解を掲げておこう. 「この日食記事を当時暦法をすでに採用していた証とする説がある. 私は必ずしもそうは思わない. この日食は飛鳥地方で, 午前 9 時半前に食甚となり, 食分は 9 割を越えたが皆既とはならなかった. しかし皆既とはならなくとも, 9 割以上もかければ気温は下り, 一種異様な雰囲気となる. 別に暦に予報されなくとも誰でも気付く現象である. 書紀の記録を実見の記録とすれば, 暦法の施行とは必ずしも結びつかないであろう.」 (内田正男, 1975 年, 525 ページ.)

この通説には根拠がある. 西暦 600 年あたりの $\Delta T = 4000$ 秒とすると, 推古天皇三十六年日食の皆既帯は, 日本列島上ではなく, 太平洋上にある. もうひとつは, 古代日食の信憑性である. 中国の史書の天文記事の中には信用ならないものもある. とくに皆既食の場合はそうである. これが通説の強い支えになっているものと思われる. それについては次節で述べよう.

ここでは外国人研究者のコメントを挙げておく.

Stephenson(1997, p.267) による 628 年日食の計算

'The recorded date proves to be in accurate accord with that of a computed solar eclipse. Although the obscuration of the Sun was said to be total, further description is lacking, so that I have included the observation in the lowest category. It is noteworthy that event does not seem to be linked in any way with the Empress' death by the chronicler(unlike several similar occurrences in China – see above).

Steele(2000),

'In common with all of the other observations in the Nihongi, this record is not very detailed. No times are ever recorded for any of the eclipse records in this work.'

表 I. 中国歴代史書に載る日食記事の検証[1]

西暦	日食数	的中	的中率	夜食・不食	非食
春秋	37	35	95	1	1
史記 (戦国)	10	4	40	6	0
漢書	61	42	69	1	18
後漢書	88	65	74	7	16
三国志	12	11	92	0	1
晉書	82	49	60	16	17
宋書	83	60	72	16	7
魏書	61	41	67	16	4
南斉書	5	4	(80)	1	0
梁書・陳書	10	7	70	10	0
南史	35	23	66	10	2
北斉書	2	2	(100)	0	0
周書	22	7	32	15	0
北史	82	46	56	34	2
隋書・梁	3	2	(67)	1	0
隋書・陳	1	0	0	1	0
隋書・斉	1	1	(100)	0	0
隋書・周	10	2	20	8	0
隋書・隋	8	3	(37)	5	0
旧唐書	99	69	70	25	5
新唐書	93	66	71	25	2
旧五代史	20	15	75	5	0
新五代史	18	14	78	4	0

[1] 中国古代の天文記録の検証 (斉藤国治・小沢賢二, 雄山閣, 平成 4 年, p.17).

1.3 古代中国の日食記事の信憑性

古代中国の日食記事の信憑性を斉藤・小沢(1992)が調べた. 彼らは, 春秋から五代に至る中国の史書からすべての天文記事を抜き出し, それを現在の知識で再現し得る現象とそうでない現象とに分類した. ここでは日食記事に関して彼らの結果を紹介し, 若干のコメントを述べる.

表 II. 五 ～ 九世紀の皆既日食全記録

西暦	国と年月	食分 (斉藤・小沢) $\Delta T = 4000$?	谷川・相馬 $\Delta T = 2000$
453.08.20	(宋) 元嘉三十年七月辛丑朔, 日有蝕之, **既** 星辰畢見	不食	
454.08.10	(宋) 孝建元年七月丙申朔, 日有蝕之, **既**	0.96	0.97
516.04.18	(梁) 天監十五年三月, 日有蝕之, **既**	0.97	0.94
522.06.10	(梁) 普通三年五月壬辰朔, 日有蝕之, **既**	皆既直後に日出	0.97 非・日出帯食
562.10.14	(北周) 保定二年九月戊辰朔, 日有食之, **既**	0.35 周書には「既」なし	0.225
616.05.21	(隋) 大業十二年五月丙戌朔, 日有食之, **既**	0.90 記事の" 既" は不当	0.967
702.09.26	(則周) 長安二年九月乙丑朔, 日有食之, **幾既**, 在角初度	0.99	1.016
	日有蝕之, 不尽如鈎, 京師及四方見之	旧唐書	
754.06.25	(唐) 天宝十三載六月乙丑朔, 日有食之, **幾既**. 在東井十九度. 京師分也	0.87	0.854
	日有蝕之, 不尽如鈎	旧唐書	
756.10.28	(唐) 至徳元年十月辛巳朔, 日有食之, **既** 在てい十度	0.96	0.886
		旧唐書, 既なし	
761.08.05	(唐) 上元二年七月癸未朔, 日有食之, **既** 大星皆見, 在張四度	0.99	1.011
	蝕既, 大星皆見	旧唐書	
846.12.22	(唐) 会昌六年十二月戊辰朔, 日有食之, 在南斗十四度	0.85	0.818
	皆蝕	旧唐書	
879.04.25	(唐) 乾符 六年四月庚申朔, 日有食之, 既 在胃八度	非食	
		旧唐書, 記述なし	

表1は斉藤・小沢(1992)の17ページの表そのものである. 表中, 日食の的中率とは史書の日食記事のうち, 本当に起こったものの百分率である. この表を見てはじめに不思議に思うのは,

的中率が必ずしも時代とともに上がらないことである. これには理由がある. そのために, 表中の夜食, 不食, 非食なる用語を説明しておく. 古代中国においては, 暦法を使って日食推算が行われていた. ただし必ずしも予測は成功せず, 予測した日食が地球の裏側であったり (夜日食あるいは夜食), 予測した日食が南半球であったりあるいは北半球でもずっと北の方であって観測地では食が起こらなかったり (不食), 地球上のどこで見ても日食が起こらなかったり (非食) した. 予測が行われていたことは驚きであるが, それがすでに前漢や後漢の時代に行われていたとするとさらに驚きである.

以上のことからすると, 個々の日食記事の信憑性を問うことには危険がつきまとう. 特定の日食があったかなかったをわれわれはチェックできるので, 記事の信憑性をしらべることができるように見える. ところが, 当時の天文官が日食を見たかどうかをわれわれははっきり断言できない. 曇っていたかもしれない. 日食をみたのではなく, 予測が当たったのかもしれないからである. さらに, われわれの計算に使用したパラメータが正しいかどうか保証がない.

皆既日食記事, あるいはほぼ皆既 (幾既) の日食記事の場合, 問題はもう少し微妙である. ほとんどの場合, この記事に対応してたしかに日食はあった. しかし, 天文官あるいは, 天文官のいた首都の住人は本当に「皆既」を見たのであろうか. この問題に関する斉藤・小沢 (1992) の答えを表 II に掲載した. 斉藤・小沢の計算によると, どの「皆既食」も実は皆既食ではない. ほかの研究者も同様の意見を持っている. 「大体食分 0.9 ぐらいになると, 皆既と記したものと解してよいようである. この点でも「既」とある記録をそのまま受け入れるわけにはいかない」(渡邊敏夫, 日食・月食宝典, 1979).

著者は素朴に疑問に思う. 5 世紀から 9 世紀の間, 長安や洛陽の住民は皆既食を一度も見なかったのだろうか. この疑問が今回の研究のきっかけである. 皆既帯が緯度線にほぼ平行で, 皆既帯を東西にずらしても長安あるいは洛陽が決して皆既帯に入らない日食もある. たとえば 754 年 6 月 25 日の日食である. この場合, たしかに, 「皆既」記事は誇張であろう. 皆既食帯が緯度線を斜めに横切る場合は, 異なるパラメータで再計算してみる価値はある. パラメータの値を変えても皆既帯が東西にしかずれない理由は 2.1 節参照.

1.4 Stephenson(1997) の結果 – 研究の発端

Stephenson(1997) のグラフ (1997, p. 508) で 600 年前後の日月食の結果を見ると, 585 年から 596 年の中国における月食の結果 (これらの個々の数値は p. 301 の表に掲載されている) からは $TT - UT = 5000$ sec 前後の大きな値が得られているのに対して, 680 年ころの中国の日食の結果 (グラフ上の×印) からは $TT - UT = 2000$ sec 前後の値が得られていて, 滑らかな曲線は日食の結果からはずれ, 月食の結果に合うように引かれていることがわかる. 628 年の日本の日食の記録はこれらの日食の記録とほぼ一致しており, その結果滑らかな曲線からはずれているのである. そこで日食と月食の結果がどうして食い違っているのかが問題になる.

2 日月食と地球自転速度の永年変化

日食・月食は太陽・地球・月が一直線上に来ることによって起こる現象である. 太陽まわりの地球の公転運動, 地球まわりの月の公転運動, 地球の自転運動がどれも不変であれば, 日月食

は周期的あるいは準周期的に生起する. 上記3つの運動が永年的に変化すると, 日月食の起こり方は準周期的でなくなる. 以下では, この三千年間, 太陽まわりの地球の公転運動は不変であるとして (歳差, 章動などを無視するわけではない), 残りの2つの運動が永年的に変化した場合の日月食の生起の永年変化を定性的に調べる.

現代の理論からは計算できないのが, 数千年間の地球自転の遅れと, 月の永年加速量である. われわれは, 月が遠ざからないとして計算した地球まわりの月の公転運動を得ることができる. また地球自転は変化しないとする.

地球自転の永年変化, 月距離の永年変化に関してはそれぞれ, 40年 (国際極運動事業), 20年程度 (月レーザー測距) のデータしかない. つまり, 永年変化の瞬間値しか知ることができない. その値が2000年, 3000年にわたって正しい保証はない.

2.1 地球自転減速と月の永年加速項の効果

この節で記述することはすべて知られていることである. 記述を一貫したものにするために付け加えた.

2.1.1 永年変化なしの場合

われわれは過去の日食の生起場所, 時刻, 継続時間などを計算することができる. この場合, 歴史記録はわれわれの計算のチェックにしか使えない. 「永年変化なし」は現実ではない.

2.1.2 地球自転が遅くなる場合

過去, 地球自転が速いとする. ただし, その変化は定量的にはわからないとする. 一方, 月の公転速度はいまと変わらないとする. 太陽系を北から見る. 簡単のため, 地軸は傾いていないとし, 地球の北極の真上から物事を見る. 地球の自転を巻き戻す. 過去 (例えば1000年前のある月のある日) に皆既日食が, ある場所で観測されたとする. (その日食が記録されていることを意味する.) 過去の日食記録が有用となる.

地球の公転運動, 月の公転運動は現在の理論で過去に戻れるので, 一様時間で見て, 地球・月・太陽が一直線上に来る時刻は計算可能である. 問題は, その時刻に地球のどの部分が日食の場所に来るかである. 過去の方が自転が速いので, 自転が一定であると考えて巻き戻す場合よりも, 余分に (西へ) 巻き戻す必要がある. したがって, 予想 (自転が一定であるとした場合) よりも東で日食が起きる.

一様に流れる時間で測った時刻をTT, 地球の自転が変わらないとして流れる時間で測った時刻をUTとし, 近代のある時に時計合わせをしておく. すると, それ以前にはUTの進みが速いから, 時刻にすると, UTの値が小さい.

$$\Delta T = \mathrm{TT} - \mathrm{UT}$$

この時刻の差は, 1時間に15° 自転するとして, 実際の日食点と予想した日食点の回転角度の差である. その際, この1時間をTTで測ろうと, UTで測ろうと違いはない. ここ数千年では自転速度の差は非常に小さい.

当時の ΔT を求めるには, 観測地点が皆既帯の西端に来る場合と東端にくる場合を両極端として, その中間の ΔT がすべて可能である. 日食の継続時間の記録があれば, もっと絞り込める.

2.1.3 月公転が遅くなる場合

過去, 月公転が速いとする. ただし, その変化は定量的にはわからないとする. 一方, 地球の自転速度はいまと変わらないとする. 前節と同様な視点で日食の場所を推定する.

月公転が今も昔も変わらないとして日食を予想する. 太陽・月・地球が一直線上にあり, 観測点が本影に入るはずである. ところが, 過去, 月の公転は速かった. だから時間を巻き戻すと, 月は予想より西にいる. 月の位置が予想と少ししかずれていないとする. 過去数千年間はこれが成り立つ. すると, 月は太陽からの平行光線の中にいる. 月の影は西にできる. つまり, 月の公転速度が過去ほど速いことの効果は, 過去の日食が予想より西に起こることである. これは地球自転減速の効果と逆であることに注意しよう.

2.1.4 地球自転が遅くなり, 月公転が遅くなる場合

この場合, 地球自転が遅くなる効果で, 日食地点は予想より東に来る. 月公転が遅くなる効果で, 日食地点は予想より, 西に来る. 併せた効果を知るには, 地球自転の遅くなる割合と, 月公転の遅くなる割合の関係を求める必要がある.

地球・月系の角運動量保存を考える. 簡単のため, 地球・月系の重心の動きは等速直線運動であるとする. 地球, 月の質量をそれぞれ $M_\oplus$, $M_{\rm moon}$ と書く. $M_t = M_\oplus + M_{\rm moon}$ と書く. 地球・月間の平均距離を R とする. 地球・月系の重心を O と書く. O に関する地球・月系の全角運動量を L_t, 共通重心 O に関する地球重心, 月重心の角運動量を $L_\oplus^{\rm orb}$, $L_{\rm moon}^{\rm orb}$, また, 地球重心, 月重心のまわりのそれぞれのスピン角運動量を $L_\oplus^{\rm spin}$, $L_{\rm moon}^{\rm spin}$ と書くと,

$$L_t = L_\oplus^{\rm orb} + L_{\rm moon}^{\rm orb} + L_\oplus^{\rm spin} + L_{\rm moon}^{\rm spin}.$$

以下, 右辺各項の表現を求める. 簡単のため, 地球・月の相互運動は円運動であるとする. 地球・月系の互いの重心のまわりの公転運動の周期 (または平均運動) を求めよう.

$$GM_t = n^2R^3 \quad \text{または} \quad n = \sqrt{\frac{GM_t}{R^3}}.$$

すると, $\mu = M_\oplus M_{\rm moon}/M_t$ と置いて

$$L_\oplus^{\rm orb} = M_\oplus \left(\frac{M_{\rm moon}}{M_t}R\right)^2 n = \mu M_{\rm moon}\sqrt{\frac{GR}{M_t}},$$
$$L_{\rm moon}^{\rm orb} = M_{\rm moon} \left(\frac{M_\oplus}{M_t}R\right)^2 n = \mu M_\oplus \sqrt{\frac{GR}{M_t}}.$$

両者を加えると,

$$L_\oplus^{\rm orb} + L_{\rm moon}^{\rm orb} = \mu\sqrt{GRM_t}.$$

一方, 自転角運動量は, 自転角速度をそれぞれ $\omega_\oplus$, $\omega_{\rm moon}$ とし, 慣性モーメントをそれぞれ $I_\oplus$, $I_{\rm moon}$ として

$$L_\oplus^{\rm spin} = I_\oplus \omega_\oplus,$$
$$L_{\rm moon}^{\rm spin} = I_{\rm moon}\omega_{\rm moon}.$$

各項の大きさを見積もる. $G = 6.672\times10^{-11}$MKS, $R = 3.844\times10^8$m, $M_\oplus = 5.974\times10^{24}$kg, $M_{\rm moon} = 1.23\times10^{-2}M_\oplus$, 球と考えて, $I_\oplus = \frac{2}{5}M_\oplus r_\oplus^2$, $I_{\rm moon} = \frac{2}{5}M_{\rm moon}r_{\rm moon}^2$, ただし, $r_\oplus, r_{\rm moon}$ は地球および月の半径, $\omega_\oplus = 2\pi/(24\,\text{時間})$, $\omega_{\rm moon} = 2\pi/(27.3\,\text{日})$. MKS 単位で,

$$L_\oplus^{\rm orb} = 3.47\times10^{32},\quad L_{\rm moon}^{\rm orb} = 2.82\times10^{34},\quad L_\oplus^{\rm spin} = 7.07\times10^{33},\quad L_{\rm moon}^{\rm spin} = 2.37\times10^{29}$$

これからわかるとおり,

(地球・月重心のまわりの) 月の公転角運動量 > 地球の自転角運動量 >
(地球・月重心のまわりの) 地球の公転角運動量 > 月の自転角運動量.

さて, 月が永年的に遠ざかり, 地球自転が徐々に遅くなる場合の, 角運動量の再配分のされ方を見ることにより, この節の目的を達成しよう.

$$L_t = \mu\sqrt{GRM_t} + I_\oplus\omega_\oplus + I_{\rm moon}\omega_{\rm moon},$$

を時間で微分して, 全角運動量が保存されることを考慮すると,

$$0 = \frac{\mu}{2}\sqrt{\frac{GM_t}{R}}\dot{R} + I_\oplus\dot{\omega}_\oplus + I_{\rm moon}\dot{\omega}_{\rm moon}.$$

ケプラーの第三法則を時間で微分して

$$2\dot{n}R = -3n\dot{R}\quad \text{または}\quad \dot{R} = -\frac{2}{3}R^2\sqrt{\frac{R}{GM_t}}.$$

これらを上式に代入すると

$$I_\oplus\dot{\omega}_\oplus = \frac{\mu}{3}R^2\dot{n} - I_{\rm moon}\dot{\omega}_{\rm moon},$$

あるいは

$$\dot{\omega}_\oplus = \frac{5}{6}\left(\frac{M_{\rm moon}}{M_t}\right)\left(\frac{R^2}{r_\oplus^2}\right)\dot{n} - \left(\frac{M_{\rm moon}}{M_\oplus}\right)\left(\frac{r_{\rm moon}^2}{r_\oplus^2}\right)\dot{\omega}_{\rm moon}.$$

月の自転が公転周期にロックされていると考えれば, $\dot{\omega}_{\rm moon} = \dot{n}$ である. その場合には,

$$\dot{\omega}_\oplus = \left[\frac{5}{6}\left(\frac{M_{\rm moon}}{M_t}\right)\left(\frac{R^2}{r_\oplus^2}\right) - \left(\frac{M_{\rm moon}}{M_\oplus}\right)\left(\frac{r_{\rm moon}^2}{r_\oplus^2}\right)\right]\dot{n}.$$

$\dot{\omega}_\oplus$ と $\dot{n}$ の関係式である. これが求めるものであった. 数値を入れると

$$\dot{\omega}_\oplus = \left(36.8 - 9.1\times10^{-4}\right)\dot{n} \simeq 36.8\dot{n}.$$

第二項の影響は 4 桁ほど小さい. それゆえ, 3 桁の精度の話をするなら, 月の自転が公転周期にロックされていると考える必要はない.

2.2 ΔT と月の永年加速

2.1.4 節において, 簡単な近似のもとで, 地球自転速度の変化率と月公転速度の変化率に簡単な関係があることがわかった.

いま過去のある時点における ΔT が判ったとする. そのときの月の公転速度は判るか? これが問題. 同じことだが, 地球自転速度はわかるか. 判らない. これが答えである. 複数の日付のデータがあれば, その限りでない.

そこで, ここでは地球自転鈍化の効果で皆既帯が東にずれる効果と同等な月公転の鈍化の効果を求めよう. 月は太陽平行光線の中を動くと考えてよいから, 月が軌道上で動いた距離は地上で月の影が動いた距離である. 月が軌道上 1 秒角動くと, 月の影は地上で 1.86km 動く. 地球自転を赤道上で測ると, 1 秒間に 0.463km である. つまり ΔT の 1 秒は 0.463km. 月の軌道上の 1 秒角は ΔT の 4.0 秒に対応する. したがって, たとえば, ΔT の 2000 秒は月の軌道上の位置の違いで 500 秒角に相当する.

2.3 日食と月食の結果の不一致と月の潮汐項の効果

月食観測から得られた TT − UT の値は記録にある月食の開始・終了などの時刻を現在の暦から計算した時刻と比較して求めたものである. それに対して日食の方は (当時の中国の日食については Stephenson の本 (1997) や論文 (Stephenson and Morrison, 1995) に詳しい記述がなく実際の記録が未調査なのではっきりしないが, 少なくとも 628 年の日本の日食については) 時刻観測ではなく, 皆既食の見られた場所から TT − UT の値が推定されている. そこで, 当時の夜間における時刻観測の精度なども検討する必要があると思うが, ここでは, 月の運動理論にまだ不確定性が残っている月の黄経の潮汐項がこれらの決定に及ぼす効果について考察しておく.

月の黄経の潮汐項としてはこれまで次のような値が得られていた. T は 100 年単位で測った時間である.

Spencer Jones (1939)	$-11''.22T^2$	(Moon vs planets)
Van Flandern (1970)	$(-28'' \pm 8'')T^2$	(Moon vs Brown)
Morrison (1973)	$(-21'' \pm 3'')T^2$	(Moon vs Brown)
Van Flandern (1975)	$(-32''.5 \pm 9'')T^2$	(Moon vs Num. Int.)
Morrison & Ward (1975)	$(-13'' \pm 1'')T^2$	(Moon vs Mercury Transits)
Calame & Mulholland (1978)	$(-12''.3 \pm 2''.5)T^2$	(LLR)
Williams et al. (1978)	$(-11''.9 \pm 2''.0)T^2$	(LLR)
Ferrari et al. (1980)	$(-11''.9 \pm 1''.3)T^2$	(LLR)
Dickey et al. (1982)	$(-11''.9 \pm 0''.8)T^2$	(LLR)
Dickey et al. (1994)	$(-12''.94 \pm 0''.25)T^2$	(LLR)

現在の潮汐項の採用値は $-13''T^2$ である. 暦による潮汐項の差の例として, DE200 と DE405 の月の位置の差を 1600 年から 2000 年まで 50 年毎に示しておく.

DE405 - DE200　　Moon

date			long	lat	dist	d-long	d-lat	d-dist
			o	o	au	"	"	km
1600	1	1	104.77143	+1.41719	0.002561	-40.91810	+3.67448	-3.48105
1650	1	0	245.58877	-0.85420	0.002415	-25.18135	+2.29119	+0.83199
1700	1	0	26.53991	-3.28175	0.002557	-10.42751	+0.71961	+1.42244
1750	1	0	180.28823	-5.20741	0.002703	-4.47492	+0.09208	+0.07907
1800	1	0	335.71660	-4.33024	0.002589	-2.98036	-0.17168	-0.37561
1850	1	0	119.43714	-2.18999	0.002395	-1.80050	-0.15803	-0.09627
1900	1	0	258.26803	-0.18464	0.002492	-0.61495	-0.06873	+0.05555
1950	1	0	49.31906	+3.00530	0.002689	-0.06852	-0.01840	-0.00134
2000	1	0	205.08024	+5.17687	0.002655	-0.04320	+0.01766	-0.00966

例えば，DE406 の潮汐項への補正として $-2''.0T^2$ を採用して計算すると，600 年ころの月食の時刻は 10 分程度異なるだけであり，当時の時刻観測精度からして無視できる量であるが，皆既日食の見られた場所は大きく異なり，628 年の日食に対しては TT − UT の値を 1000 sec 大きくして TT − UT = 3000 sec としないと日本で見られたことにならない．これにより当時の日食と月食の結果から得られた TT − UT の値の不一致は解消されることになる．現在の月の暦の潮汐項に $-2''.0T^2$ もの補正が必要だというのは現在の月レーザー測距データとは相容れないが，この事実は過去千数百年間に潮汐項が変化した可能性を示唆している．

3　検証

3.1　日食

推古天皇 36 年の皆既日食は TT − UT として Stephenson による 4000 sec を仮定すると斉藤らの言うように皆既帯が太平洋上を通り，日本では部分食になる．これを TT − UT = 2000 sec とすると日本書紀にいうように日本で皆既日食が見られたことになる．ただし，この場合，1.4 節で述べたように，日食と月食から求めた TT − UT の値に大きな隔たりがある．そこで，月の暦の潮汐項に $-2''.0T^2$ の補正を加えてみる．先にも述べたように，この補正では月食から求めた TT − UT の値には大きな変化がない．しかし日食については，TT − UT = 3000 sec 程度の値を仮定しないと日本で皆既日食が見られたことにはならない．これによって，日食と月食による TT − UT の値の不一致はかなり解消されることになる．結果は図 1 に示した．

3.2　星食による検証

古記録の中には月が惑星や恒星を隠す星食もある．星食が見られる範囲は部分日食と同様に一般に広いため，パラメータの値を求めるのに役立つものは少ないが，限界線に近いところで起きるものでは役に立つものがある．ここでは，そのような現象のうち，681 年 11 月 3 日の火星食が我々の議論に重要な役割を果たすことが判明したので紹介しておく．

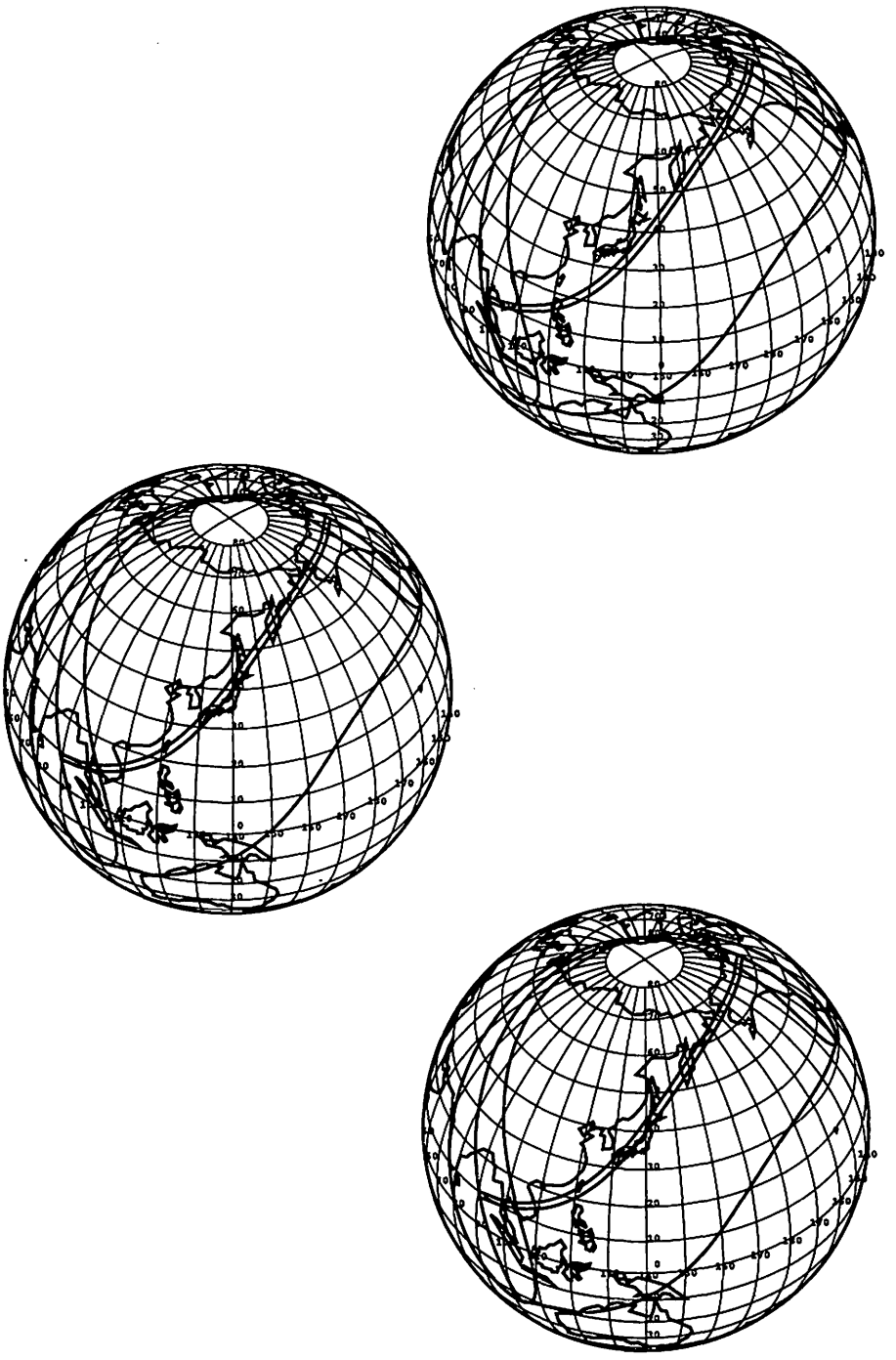

a

図 1: The solar eclipse on Arpil 10, 628(The second day, the third month, the thirty sixth year of Empress Suiko). Shown are the bands of total eclipse. From the top, ΔT = TT − UT = 4000s, Corr. to tidal term = 0"T^2; ΔT = 2000s, Corr. to tidal term = 0"T^2 ; ΔT = 3000s, Corr. to tidal term = -2"T^2.

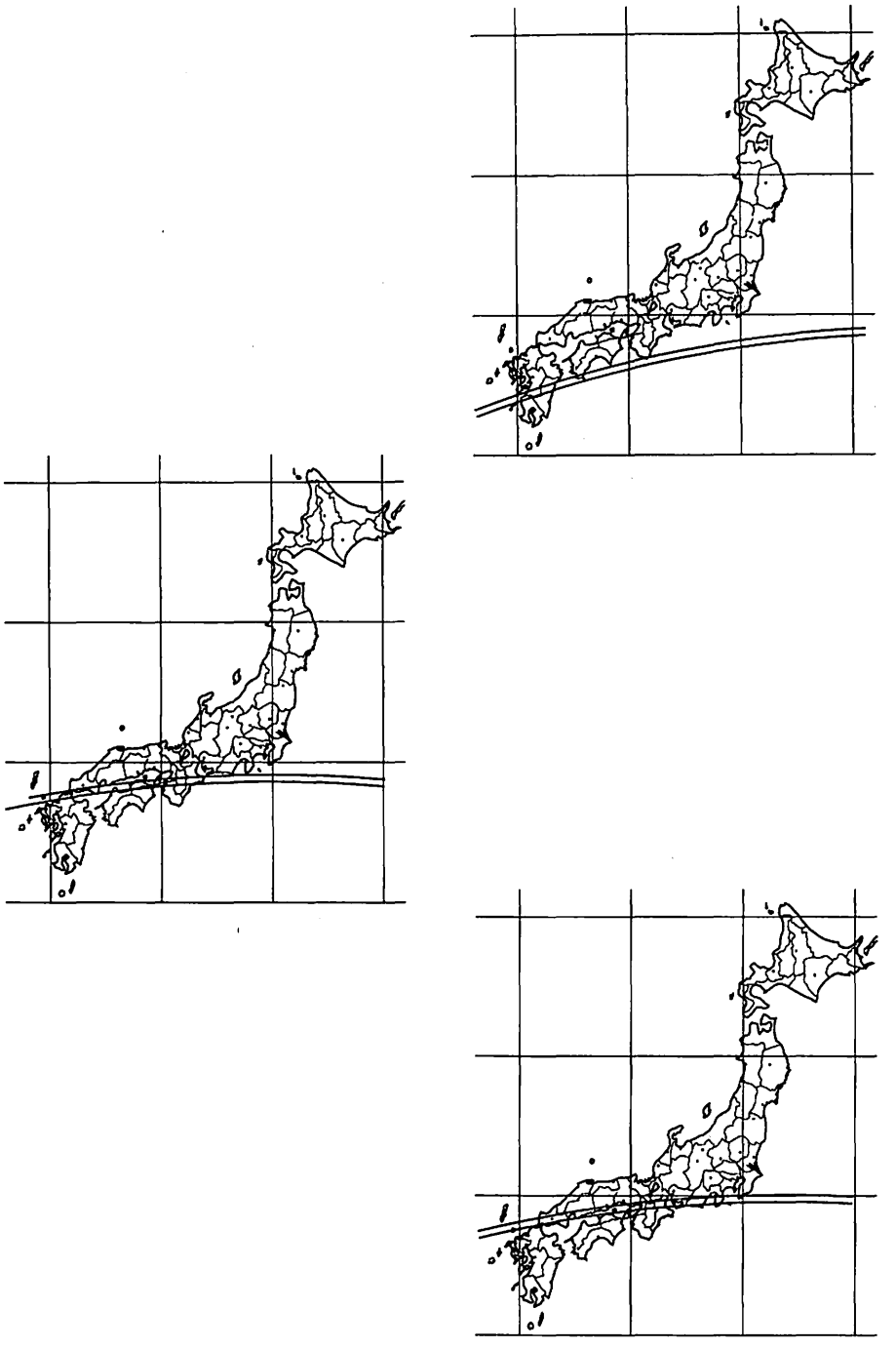

図 2: Occultation of Mars by the Moon on November 3, 681. Shown are the bands of partial eclipse. The total occultation took place to the south of the band. From the top, ΔT = TT − UT = 4000s, Corr. to tidal term = 0"T^2; ΔT = 2000s, Corr. to tidal term = 0"T^2; ΔT = 3000s, Corr. to tidal term = -2"T^2.

日本書紀には「天武天皇10年9月癸丑，蛍或月に入る」(「蛍」の「虫」は「火」) とある．斉藤 (1982b, p.14) は「蛍或とは火星のこと．この夜の光度は −1.3 等，月齢 17.3 日，月の見かけの半径 0°.28．計算によると，ユリウス暦 XI 4, 2h a.m. に蛍或が月の北へりの外 0°.04 のへんを通過したことになる．『日本書紀』原文には「入月」とあるが，実はわずかにはずれて「犯」である．観測者は，月齢 17.3 日の月体の明るさに幻惑されて，食と見誤ったのであろう.」としている．月が月齢 17.3 日（満月から約 2 日後）の明るさだったとしても，−1.3 等の火星を月の縁から 0°.04 で見失うというのは不自然に思える．確かに現在の月の潮汐項を採用し，TT − UT = 4000sec とすれば日本では九州南部などを省いて食にならないが，TT − UT = 2000sec とすると近畿南部でも星食が見られたことになるし，さらに潮汐項に $-2''/\mathrm{cy}^2$ の補正を施して TT − UT = 3000sec とすれば飛鳥地方でも食が見られたことになるのである．日本書紀のこの星食記事は我々の仮定している TT − UT と潮汐項の値を支持しているのである．(図参照．なお, 図で, 2 本の線で挟まれた地域では火星の一部が月に隠され, それより南では完全に隠され, 北では食は見られない．)

4 議論

われわれは日本書紀の記事が必ずしも誇張表現でない可能性のあることを指摘したい．

その理由をまとめると,

1. TT − UT = 2000.0sec とすれば西日本で皆既食になったはず．これは無理な値ではない．
2. 倭国は紀元 607 年に独立した (独立宣言を中国に送っている)．
3. 日食 (628 年) だけでなく, 彗星 (634 年), 流星 (637 年), 月星接近 (640 年), 月食 (643 年) などの記録が始まっている．このことから, 天文官がいたと思われる (河鰭, 2001)．
4. 倭国と通じていた百済の採用した元嘉暦を使っていた可能性が大きい (小川, 1997)．

謝辞. 国立天文台の中村 士氏および杏林大学の横尾広光氏は参考文献を紹介し, 議論してくれた．ここに謝意を表する．

参考文献

1. 内田正男 編, 日本暦日原典, 雄山閣, 1975 年.
2. 渡辺敏夫, 日食月食宝典, 雄山閣, 1994 年 (1979 年).
3. 小川清彦, 日本書紀の暦日について, 小川清彦著作集-古天文・暦日の研究-(斉藤国治編著), 1997 年.
4. 神田 茂, 日本天文史料, 原書房, 昭和五十三年.
5. J.M. Steele, Observation and Predictions of Eclipse Times by Early Astronomers, Kluwer Academic Press, 2000.
6. F.R. Stephenson, Historical eclipses and earth's rotation, Cambridge University Press, 1997.
7. 斉藤国治, 星の古記録 (岩波新書, 1982a), 飛鳥時代の天文学 (河出書房新社, 1982b).

8. 斉藤國治, 小沢賢二, 中国古代の天文記録の検証, 雄山閣, 1992.

9. 薮内 清, 中国の天文暦法, 平凡社, 昭和 44 年.

10. 西嶋定生, 邪馬台国と倭国, 吉川弘文館, 平成 6 年.

11. 三国志, 陳寿 撰, 中華書局, 1959.

12. 南史, 李延寿 撰, 中華書局, 1975.

13. 隋書, 中華書局.

14. F.R. Stephenson and L.V. Morrison, Long-term fluctuations in the Earth's rotation: 700BC to AD1990 *Phil. Trans. R. astr. Soc. London* **A 351**, 163-202, 1995. (http://th.nao.ac.jp/~tanikawa/に翻訳あり.)

15. 河鰭公昭, Private communication, 2001.

Symposium Program/プログラム

＜第 1 日 16 日 (金) ＞

14:00-15:00　受けつけ
15:00-15:10　小久保 英一郎 (国立天文台)
　　はじめに

【力学系他】　(座長 篠原 晋)
15:10-15:30　井上 猛 (京都産業大学)
　　「Le Verrier 中間軌道」の正しい把捉
15:30-15:50　Vincent Naudot (国立天文台)
　　Linearisation of smooth vector fields. The LMT method
15:50-16:10　谷川 清隆 (国立天文台)
　　Forcing relations among symmetric non-Birkhoff
　　periodic points in the Standard-like mappings. I
16:10-16:30　山口 喜博 (帝京平成大学)
　　Forcing relations among symmetric non-Birkhoff
　　periodic points in the Standard-like mappings. II

【ポスター発表】　(座長 武田 隆顕)
16:40-17:40　ポスター 3 分発表
18:00-19:00　夕食
19:30-　ポスターセッション兼ウェルカムパーティー

＜第 2 日 17 日 (土) ＞

07:30-08:30　朝食
09:00-10:00　ポスターセッション
　　受けつけ

【招待講演】　(座長 梅原 広明)
10:00-11:15　吉田 春夫 (国立天文台)
　　Symplectic Integration から Geometric Integration へ
12:00-13:00　昼食
13:00-14:00　ポスターセッション
14:00-15:15　伊藤 孝士 (国立天文台)
　　Symplectic 数値積分法の天体力学的応用

【惑星系形成】 (座長 古屋 泉)

15:30-15:50 今枝 佑輔 (東京大学/国立天文台)
連星系を取り巻く原始惑星系円盤のダイナミクス

15:50-16:10 小南 淳子 (東京工業大学)
原始惑星系円盤との重力相互作用を考慮した地球型惑星形成

16:10-16:30 井田 茂 (東京工業大学)
原始系外惑星による微惑星散乱と中心星の重元素存在度

【系外惑星系】 (座長 吉田 二美)

16:40-17:00 長沢 真樹子 (東京工業大学)
系外惑星系における永年共鳴の移動

17:00-17:20 木下 宙 (国立天文台)
惑星永年摂動で永年共鳴は存在するか?

17:20-17:40 木下 宙 (国立天文台)
GJ876 惑星系の安定性

18:00- 懇親会

<第3日 18日 (日)>

07:30-08:30 朝食

09:00-10:00 ポスターセッション

【太陽系・他】 (座長 長澤 真樹子)

10:00-10:20 眞崎 良光 (総合研究大学院大学)
Triton 摂動を考慮した Nereid 運動の解析的表現に向けて

10:20-10:40 Sebastian Bouquillon (国立天文台)
Extension of Cassini's Laws

10:40-11:00 福島 登志夫 (国立天文台)
相対論的トルクによる歳差・章動

11:00-11:20 吉川 真 (宇宙科学研究所)
火星探査機「のぞみ」の軌道決定における諸問題

Author Index and Participant List/参加者リスト

天体力学N体力学研究会

平成13年3月16日-18日 草津セミナーハウス